

Pertanika Journal of

SCIENCE &

TECHNOLOGY

JST

VOL. 32 (5) AUG. 2024



PERTANIKA
JOURNALS

A scientific journal published by Universiti Putra Malaysia Press

PERTANIKA JOURNAL OF SCIENCE & TECHNOLOGY

About the Journal

Overview

Pertanika Journal of Science & Technology is an official journal of Universiti Putra Malaysia. It is an open-access online scientific journal. It publishes original scientific outputs. It neither accepts nor commissions third party content.

Recognised internationally as the leading peer-reviewed interdisciplinary journal devoted to the publication of original papers, it serves as a forum for practical approaches to improve quality on issues pertaining to science and engineering and its related fields.

Pertanika Journal of Science & Technology currently publishes 6 issues a year (*January, March, April, July, August, and October*). It is considered for publication of original articles as per its scope. The journal publishes in **English** and it is open for submission by authors from all over the world.

The journal is available world-wide.

Aims and scope

Pertanika Journal of Science & Technology aims to provide a forum for high quality research related to science and engineering research. Areas relevant to the scope of the journal include: bioinformatics, bioscience, biotechnology and bio-molecular sciences, chemistry, computer science, ecology, engineering, engineering design, environmental control and management, mathematics and statistics, medicine and health sciences, nanotechnology, physics, safety and emergency management, and related fields of study.

History

Pertanika Journal of Science & Technology was founded in 1993 and focuses on research in science and engineering and its related fields.

Vision

To publish a journal of international repute.

Mission

Our goal is to bring the highest quality research to the widest possible audience.

Quality

We aim for excellence, sustained by a responsible and professional approach to journal publishing. Submissions can expect to receive a decision within 90 days. The elapsed time from submission to publication for the articles averages 180 days. We are working towards decreasing the processing time with the help of our editors and the reviewers.

Abstracting and indexing of Pertanika

Pertanika Journal of Science & Technology is now over 27 years old; this accumulated knowledge and experience has resulted the journal being abstracted and indexed in SCOPUS (Elsevier), Clarivate Web of Science (ESCI), EBSCO, ASEAN CITATION INDEX, Microsoft Academic, Google Scholar, and MyCite.

Citing journal articles

The abbreviation for Pertanika Journal of Science & Technology is *Pertanika J. Sci. & Technol.*

Publication policy

Pertanika policy prohibits an author from submitting the same manuscript for concurrent consideration by two or more publications. It prohibits as well publication of any manuscript that has already been published either in whole or substantial part elsewhere. It also does not permit publication of manuscript that has been published in full in proceedings.

Code of Ethics

The *Pertanika* journals and Universiti Putra Malaysia take seriously the responsibility of all of its journal publications to reflect the highest in publication ethics. Thus, all journals and journal editors are expected to abide by the journal's codes of ethics. Refer to *Pertanika*'s **Code of Ethics** for full details, or visit the journal's web link at http://www.pertanika.upm.edu.my/code_of_ethics.php

Originality

The author must ensure that when a manuscript is submitted to *Pertanika*, the manuscript must be an original work. The author should check the manuscript for any possible plagiarism using any program such as Turn-It-In or any other software before submitting the manuscripts to the *Pertanika* Editorial Office, Journal Division.

All submitted manuscripts must be in the journal's acceptable similarity index range:
≤ 20% – PASS; > 20% – REJECT.

International Standard Serial Number (ISSN)

An ISSN is an 8-digit code used to identify periodicals such as journals of all kinds and on all media—print and electronic.

Pertanika Journal of Science & Technology: e-ISSN 2231-8526 (Online).

Lag time

A decision on acceptance or rejection of a manuscript is reached in 90 days (average). The elapsed time from submission to publication for the articles averages 180 days.

Authorship

Authors are not permitted to add or remove any names from the authorship provided at the time of initial submission without the consent of the journal's Chief Executive Editor.

Manuscript preparation

For manuscript preparation, authors may refer to *Pertanika*'s **INSTRUCTION TO AUTHORS**, available on the official website of *Pertanika*.

Editorial process

Authors who complete any submission are notified with an acknowledgement containing a manuscript ID on receipt of a manuscript, and upon the editorial decision regarding publication.

Pertanika follows a **double-blind peer-review** process. Manuscripts deemed suitable for publication are sent to reviewers. Authors are encouraged to suggest names of at least 3 potential reviewers at the time of submission of their manuscripts to *Pertanika*, but the editors will make the final selection and are not, however, bound by these suggestions.

Notification of the editorial decision is usually provided within 90 days from the receipt of manuscript. Publication of solicited manuscripts is not guaranteed. In most cases, manuscripts are accepted conditionally, pending an author's revision of the material.

The journal's peer review

In the peer-review process, 2 to 3 referees independently evaluate the scientific quality of the submitted manuscripts. At least 2 referee reports are required to help make a decision.

Peer reviewers are experts chosen by journal editors to provide written assessment of the **strengths** and **weaknesses** of written research, with the aim of improving the reporting of research and identifying the most appropriate and highest quality material for the journal.

Operating and review process

What happens to a manuscript once it is submitted to *Pertanika*? Typically, there are 7 steps to the editorial review process:

1. The journal's Chief Executive Editor and the Editor-in-Chief examine the paper to determine whether it is relevance to journal needs in terms of novelty, impact, design, procedure, language as well as presentation and allow it to proceed to the reviewing process. If not appropriate, the manuscript is rejected outright and the author is informed.
2. The Chief Executive Editor sends the article-identifying information having been removed, to 2 to 3 reviewers. They are specialists in the subject matter of the article. The Chief Executive Editor requests that they complete the review within 3 weeks.

Comments to authors are about the appropriateness and adequacy of the theoretical or conceptual framework, literature review, method, results and discussion, and conclusions. Reviewers often include suggestions for strengthening of the manuscript. Comments to the editor are in the nature of the significance of the work and its potential contribution to the research field.

3. The Editor-in-Chief examines the review reports and decides whether to accept or reject the manuscript, invite the authors to revise and resubmit the manuscript, or seek additional review reports. In rare instances, the manuscript is accepted with almost no revision. Almost without exception, reviewers' comments (to the authors) are forwarded to the authors. If a revision is indicated, the editor provides guidelines for attending to the reviewers' suggestions and perhaps additional advice about revising the manuscript.
4. The authors decide whether and how to address the reviewers' comments and criticisms and the editor's concerns. The authors return a revised version of the paper to the Chief Executive Editor along with specific information describing how they have addressed the concerns of the reviewers and the editor, usually in a tabular form. The authors may also submit a rebuttal if there is a need especially when the authors disagree with certain comments provided by reviewers.
5. The Chief Executive Editor sends the revised manuscript out for re-review. Typically, at least 1 of the original reviewers will be asked to examine the article.
6. When the reviewers have completed their work, the Editor-in-Chief examines their comments and decides whether the manuscript is ready to be published, needs another round of revisions, or should be rejected. If the decision is to accept, the Chief Executive Editor is notified.
7. The Chief Executive Editor reserves the final right to accept or reject any material for publication, if the processing of a particular manuscript is deemed not to be in compliance with the S.O.P. of *Pertanika*. An acceptance letter is sent to all the authors.

The editorial office ensures that the manuscript adheres to the correct style (in-text citations, the reference list, and tables are typical areas of concern, clarity, and grammar). The authors are asked to respond to any minor queries by the editorial office. Following these corrections, page proofs are mailed to the corresponding authors for their final approval. At this point, **only essential changes are accepted**. Finally, the manuscript appears in the pages of the journal and is posted on-line.

Pertanika Journal of
**SCIENCE
& TECHNOLOGY**

Vol. 32 (5) Aug. 2024



A scientific journal published by Universiti Putra Malaysia Press

EDITOR-IN-CHIEF

Luqman Chuah Abdullah
Chemical Engineering

CHIEF EXECUTIVE EDITOR

Mohd Sapuan Salit

UNIVERSITY PUBLICATIONS COMMITTEE

CHAIRMAN

Zamberi Sekawi

EDITORIAL STAFF

Journal Officers:

Ellyianur Puteri Zainal
Kanagamalar Silvarajoo
Siti Zuhaila Abd Wahid
Tee Syin Ying

Editorial Assistants:

Ku Ida Mastura Ku Baharom
Siti Juridah Mat Arip
Zulinaardawati Kamarudin

English Editor:

Norhanizah Ismail

PRODUCTION STAFF

Pre-press Officers:

Nur Farrah Dila Ismail
Wong Lih Jiun

WEBMASTER

IT Officer:

Illi Najwa Mohamad Sakri

EDITORIAL OFFICE

JOURNAL DIVISION

Putra Science Park
1st Floor, IDEA Tower II
UPM-IMTDC Technology Centre
Universiti Putra Malaysia
43400 Serdang, Selangor Malaysia.

General Enquiry

Tel. No: +603 9769 1622 | 1616

E-mail:

executive_editor.pertanika@upm.edu.my

URL: www.journals-jd.upm.edu.my

PUBLISHER

UPM Press

Universiti Putra Malaysia
43400 UPM, Serdang, Selangor, Malaysia.
Tel: +603 9769 8851
E-mail: penerbit@putra.upm.edu.my
URL: <http://penerbit.upm.edu.my>



ASSOCIATE EDITOR

2023-2024

Adem Kilicman

Mathematical Sciences
Universiti Putra Malaysia, Malaysia

Miss Laiha Mat Kiah

Security Services Sn: Digital Forensic,
Steganography, Network Security,
Information Security, Communication
Protocols, Security Protocols
Universiti Malaya, Malaysia

Saidur Rahman

Renewable Energy, Nanofluids, Energy
Efficiency, Heat Transfer, Energy Policy
Sunway University, Malaysia

EDITORIAL BOARD

2022-2024

Abdul Latif Ahmad

Chemical Engineering
Universiti Sains Malaysia, Malaysia

Ho Yuh-Shan

Water research, Chemical Engineering
and Environmental Studies
Asia University, Taiwan

Mohd Zulkifly Abdullah

Fluid Mechanics, Heat Transfer,
Computational Fluid Dynamics (CFD)
Universiti Sains Malaysia, Malaysia

Ahmad Zaharin Aris

Hydrochemistry, Environmental
Chemistry, Environmental Forensics,
Heavy Metals
Universiti Putra Malaysia, Malaysia

Hsiu-Po Kuo

Chemical Engineering
National Taiwan University, Taiwan

Mohd. Ali Hassan

Bioprocess Engineering, Environmental
Biotechnology
Universiti Putra Malaysia, Malaysia

Azlina Harun@Kamaruddin

Enzyme Technology, Fermentation
Technology
Universiti Sains Malaysia, Malaysia

Ivan D. Rukhlenko

Nonlinear Optics, Silicon Photonics,
Plasmonics and Nanotechnology
The University of Sydney, Australia

Nor Azah Yusof

Biosensors, Chemical Sensor, Functional
Material
Universiti Putra Malaysia, Malaysia

Bassim H. Hameed

Chemical Engineering: Reaction
Engineering, Environmental Catalysis &
Adsorption
Qatar University, Qatar

Lee Keat Teong

Energy Environment, Reaction
Engineering, Waste Utilization,
Renewable Energy
Universiti Sains Malaysia, Malaysia

Norbahiah Misran

Communication Engineering
Universiti Kebangsaan Malaysia,
Malaysia

Biswajeet Pradhan

Digital image processing, Geographical
Information System (GIS), Remote
Sensing
University of Technology Sydney,
Australia

Mohamed Othman

Communication Technology and
Network, Scientific Computing
Universiti Putra Malaysia, Malaysia

Roslan Abd-Shukur

Physics & Materials Physics,
Superconducting Materials
Universiti Kebangsaan Malaysia,
Malaysia

Daud Ahmad Israf Ali

Cell Biology, Biochemical, Pharmacology
Universiti Putra Malaysia, Malaysia

Mohd Shukry Abdul Majid

Polymer Composites, Composite
Pipes, Natural Fibre Composites,
Biodegradable Composites, Bio-
Composites
Universiti Malaysia Perlis, Malaysia

Wing Keong Ng

Aquaculture, Aquatic Animal Nutrition,
Aqua Feed Technology
Universiti Sains Malaysia, Malaysia

INTERNATIONAL ADVISORY BOARD

2021-2024

CHUNG, Neal Tai-Shung

Polymer Science, Composite and
Materials Science
National University of Singapore,
Singapore

Mohamed Pourkashanian

Mechanical Engineering, Energy, CFD
and Combustion Processes
Sheffield University, United Kingdom

Yulong Ding

Particle Science & Thermal Engineering
University of Birmingham, United
Kingdom

Hiroshi Uyama

Polymer Chemistry, Organic
Compounds, Coating, Chemical
Engineering
Osaka University, Japan

Mohini Sain

Material Science, Biocomposites,
Biomaterials
University of Toronto, Canada

ABSTRACTING AND INDEXING OF PERTANIKA JOURNALS

The journal is indexed in SCOPUS (Elsevier), Clarivate-Emerging Sources Citation Index (ESCI), BIOSIS, National Agricultural Science (NAL), Google Scholar, MyCite, ISC. In addition, Pertanika JSSH is recipient of "CREAM" Award conferred by Ministry of Higher Education (MoHE), Malaysia.

The publisher of Pertanika will not be responsible for the statements made by the authors in any articles published in the journal. Under no circumstances will the publisher of this publication be liable for any loss or damage caused by your reliance on the advice, opinion or information obtained either explicitly or implied through the contents of this publication.

All rights of reproduction are reserved in respect of all papers, articles, illustrations, etc., published in Pertanika. Pertanika provides free access to the full text of research articles for anyone, web-wide. It does not charge either its authors or author-institution for refereeing/publishing outgoing articles or user-institution for accessing incoming articles.

No material published in Pertanika may be reproduced or stored on microfilm or in electronic, optical or magnetic form without the written authorization of the Publisher.

Copyright © 2021 Universiti Putra Malaysia Press. All Rights Reserved.

Pertanika Journal of Science & Technology
Vol. 32 (5) Aug. 2024

Contents

Foreword	i
<i>Mohd Sapuan Salit</i>	
 <i>Review Article</i>	
A Review on the Development of Microcarriers for Cell Culture Applications	1939
<i>Sia Yiik Swan, Muhammad Auni Hairunnaja, Nurhusna Samsuddin, Syed Mahmood, Mohd Aizudin Abd Aziz and Mohd Azmir Arifin</i>	
Facial Emotion Recognition with Deep Neural Network: A Study of Visual Geometry Group-16 (VGG16) Technique with Data Augmentation for Improved Precision	1963
<i>Sarthak Kapaliya, Debabrata Swain, Ritu Sharma, Kanishka Varyani and Jyoti Thakar</i>	
 <i>Review Article</i>	
The Compatibility of Cement Bonded Fibreboard Through Dimensional Stability Analysis: A Review	1979
<i>Nurul Huda Azmi, Nik Mohd Zaini Nik Soh and Hasniza Abu Bakar</i>	
Mesh Optimisation for General 3D Printed Objects with Cusp-Height Triangulation Approach	1997
<i>Qais Ahmed Habash, Noor Ali Sadek, Ahmed Faeq Hussein and Abbas AlZubaidi</i>	
Comparing CNN-based Architectures for Dysgraphia Handwriting Classification Performance	2013
<i>Siti Azura Ramlan, Iza Sazanita Isa, Muhammad Khusairi Osman, Ahmad Puad Ismail and Zainal Hisham Che Soh</i>	
Learning Discriminative Features Using ANN-based Progressive Learning Model for Efficient Big Data Classification	2033
<i>Nandita Bangera and Kayarvizhy</i>	
Bending Effects on Polyvinyl Alcohol Thin Film for Flexible Wearable Antenna Substrate	2055
<i>Amirudin Ibrahim, Ahmad Rashidy Razali, Muzammil Jusoh, Najwa Mohd Faudzi and Aiza Mahyuni Mozi</i>	

- The Riblet Short-Slot Coupler Using Substrate Integrated Waveguide (SIW) for High-frequency Applications 2069
Nurehansafwanah Khalid, Siti Zuraidah Ibrahim, Mohd Nazri A Karim, Wee Fwen Hoon, Aliya Ashraf Dewani, Khuzairi Masrakin and Saidatul Norlyana Azemi
- Cytotoxicity Assessment of α Helix Antarctic Yeast Oriented Antifreeze Peptide (Afp1m) on *M. dunni* (Clone III8C) Cells 2083
Muhammad Shuaib Khan, Mohd Basyaruddin Abdul Rahman, Mohd Zuki Abu Bakar, Mohammed Mustapha Noordin, Shakeeb Ullah, Adamu Abdul Abubakar, Saifur Rehman, Aisha Saddiqua and Loqman Mohammad Yusof
- Aluminium Hydroxide/Graphene-reinforced Rigid Polyurethane Foam Hybrid Composites 2095
Aisha Elhadi Abosnina, Zurina Mohamad, Rohah Abdul Majid and Raji Muhammed Abdulwasii
- Inoculations of *R. erythropolis* and *B. subtilis* Stimulate Indigenous Bacteria and Improve the Properties of Low-fertilized Agricultural Soils 2121
Abd Aziz Amin, Hideki Okuda, Mizuho Kawamura, Nurjannah and Andi Kurniawan
- Application of UAV Technology for Vegetation Community Identification in Coastal BRIS Wetland 2137
Syazuani Mohd Shariff, Edlic Sathiamurthy, Rohani Shahrudin, Idham Khalil and Mohd Sofiyam Sulaiman
- Comparative Analysis of Filtering Techniques for AGV Indoor Localization with Ultra-Wideband Technology 2151
Nuradlin Borhan, Izzati Saleh and Wan Rahiman
- Review Article*
- Exploring Probability of Detection (POD) Analysis in Nondestructive Testing: A Comprehensive Review and Potential Applications in Phased Array Ultrasonic Corrosion Mapping 2165
Jan Lean Tai, Mohamed Thariq Hameed Sultan, Farah Syazwani Shahar, Noorfaizal Yidris, Adi Azriff Basri and Ain Umaira Md Shah
- Review Article*
- Formulation of Lubricating Grease from Waste Oil: A Review 2193
Nur Amira Fatihah Bashari, Mohd Aizudin Abd Aziz, Muhammad Auni Hairunnaja and Mohd Azmir Arifin
- Microwave Electro-technological Installation for Processing Vegetable-origin Organic Materials and Agricultural Crops 2213
Midhat Tukhvatullin and Eduard Khasanov

- Prevalence of *Vibrio parahaemolyticus*, *Vibrio cholerae*, and *Vibrio alginolyticus* in a White-leg Shrimp (*Litopenaeus vannamei*) Farm in Sarawak
Dalene Lesen, Elexson Nillian, Dayang Najwa Awang Baki and Tunung Robin 2233
- Modeling Respiration Rate of Bell Pepper (*Capsicum anuum* L.) Under Hypobaric Storage Through Dimensional Analysis
Dewi Maya Maharani, Nursigit Bintoro, Joko Nugroho Wahyu Karyadi and Arifin Dwi Saputro 2259
- A Reliable Multimetric Straggling Task Detection
Lukiman Saheed Ajibade, Kamalrulnizam Abu Bakar, Muhammed Nura Yusuf and Babangida Isyaku 2281
- Comparative Analysis of Contaminant Levels in Leachate and Soil from Young and Old Landfills
Amir Detho, Aeslina Abdul Kadir and Muhammad Aizat Azhar 2299
- Physical and Mechanical Properties of Palm Frond-based Fiberboard Composite
Moraida Hasanah, Tengku Jukdin Saktisahdan, Susilawati, Frannoto, Adjie Padriansyah and Irfan Hafizh 2313
- Smoothing RRT Path for Mobile Robot Navigation Using Bio-inspired Optimization Method
Izzati Saleh, Nuradlin Borhan and Wan Rahiman 2327
- Early Triage Prediction for Outpatient Care Based on Heterogeneous Medical Data Utilizing Machine Learning
Omar Sadeq Salman, Nurul Mu'azzah Abdul Latiff, Sharifah Hafizah Syed Arifin and Omar Hussein Salman 2343
- Finite Element Analysis of a Portable Bamboo Girder Used in Emergency Responses
Azrul Affandhi Musthaffa, Norazman Mohamad Nor, Abdulrahman Alhayek, Mohammed Alias Yusof and Mohd Yuhazri Yaakob 2369
- Some Aspects of the Biology of Invasive Fish Species from a Langat River Tributary, Selangor, Malaysia
Abdulwakil Olawale Saba, Muhammad Shakir Zufayri Mohd Arshad, Muhammad Afifuddin Abdul Razak, Amirah Mustafa Kamal, Muhammad Rasul Abdullah Halim, Intan Faraha A Ghani, Mohd Lokman Ilham-Norhakim and Mohammad Noor Azmai Amal 2385

Foreword

Welcome to the fifth issue of 2024 for the Pertanika Journal of Science and Technology (PJST)!

PJST is an open-access journal for studies in Science and Technology published by Universiti Putra Malaysia Press. It is independently owned and managed by the university for the benefit of the world-wide science community.

This issue contains 25 articles; four review articles and the rest are regular articles. The authors of these articles come from different countries namely Australia, Bangladesh, Canada, France, India, Indonesia, Iraq, Malaysia, Nigeria, Pakistan, Russia and Sultanate of Oman.

In their article “Microwave electro-technological installation for processing vegetable-origin organic materials and agricultural crops,” Midhat Tukhvatullin and Eduard Khasanov from Bashkir State Agrarian University, Russia, present a unique study. They have identified the optimal process conditions, involving the operation of 7 magnetrons and a rotation mechanism for vegetable-origin organic materials. The processing time is less than 15 hours, and the final humidity does not exceed 7% with uniform temperature change. The temperature at a depth of 1/4 of the thickness of the samples differs from the temperature on the surface of the samples by 0.5–1.0°C. The differences in the calculated and experimental data on the humidity of organic materials of plant origin do not exceed 3.8%. This innovative approach of creating a microwave installation for the simultaneous microwave processing of vegetable organic materials and agricultural crops will significantly increase the energy and economic efficiency of the installation by reducing the processing time and increasing the quality of dried material quality. The detailed information of this study is available on page 2213.

The next article discussed the smoothing Rapidly Exploring Random Tree (RRT) path for mobile robot navigation using the bio-inspired optimization method. The main objective is to improve the smoothness of RRT-generated trajectories and reduce significant path curvature. A novel approach is proposed, integrating the RRT path planner with a modified version of the Whale Optimization Algorithm (RRT-WOA). The modified WOA algorithm incorporates parameter variation (\vec{C}) specifically designed to optimize trajectory smoothness. Additionally, Piecewise Cubic Hermite Interpolating Polynomial instead of conventional splines for point interpolation further smoothes the generated paths. The modified WOA algorithm is thoroughly evaluated through a comprehensive comparative analysis, outperforming other popular population-based optimization algorithms such as Particle Swarm Optimization, Artificial Bee Colony, and Firefly Algorithm in terms of optimization time, trajectory smoothness, and improvement from the initial guess. The resultant optimized path is also validated using hardware to ensure path validity. This research contributes a refined trajectory planning approach and highlights the competitive advantage of the modified WOA algorithm in achieving smoother and more efficient trajectories compared to existing methods. Details of this study are available on page 2327.

An investigation on early triage prediction for outpatient care based on heterogeneous medical data utilizing machine learning (ML) was conducted by Omar Sadeq Salman et al. from Universiti Teknologi Malaysia and AL Iraqia University, Iraq. A comparative study was conducted to ascertain how well different supervised ML models evaluated patient triage outcomes for outpatient care. Hence, data from diverse, rapidly generated sources is crucial for informed patient triage decisions. Collected through The Internet of Medical Things (IoMT) enabled sensors, it includes sensory data (electrocardiogram, blood pressure, oxygen saturation, temperature) and non-sensory text frame measurements. The study examined six supervised ML algorithms. These models were trained using patient medical data and validated by assessing their performance. Supervised ML technology was implemented in Hadoop and Spark environments to identify individuals with chronic illnesses accurately. A dataset of 55,680 patient records was used to evaluate methods and determine the best match for disease prediction. The simulation results highlight the powerful integration of ML in telemedicine to analyze data from heterogeneous IoMT devices, indicating that the Decision Tree algorithm outperformed the other five ML algorithms by 93.50% in terms of performance and accuracy metrics. This result provides practical insights for developing automated triage models in telemedicine systems. Further details of the investigation can be found on page 2343.

We anticipate that you will find the evidence presented in this issue to be intriguing, thought-provoking and useful in reaching new milestones in your own research. Please recommend the journal to your colleagues and students to make this endeavour meaningful.

All the papers published in this edition underwent Pertanika's stringent peer-review process involving a minimum of two reviewers comprising internal as well as external referees. This was to ensure that the quality of the papers justified the high ranking of the journal, which is renowned as a heavily-cited journal not only by authors and researchers in Malaysia but by those in other countries around the world as well.

We would also like to express our gratitude to all the contributors, namely the authors, reviewers, Editor-in-Chief and Editorial Board Members of PJST, who have made this issue possible.

PJST is currently accepting manuscripts for upcoming issues based on original qualitative or quantitative research that opens new areas of inquiry and investigation.

Chief Executive Editor

Mohd Sapuan Salit

executive_editor.pertanika@upm.edu.my

Review Article

A Review on the Development of Microcarriers for Cell Culture Applications

Sia Yiik Swan¹, Muhammad Auni Hairunnaja¹, Nurhusna Samsuddin², Syed Mahmood³, Mohd Aizudin Abd Aziz¹ and Mohd Azmir Arifin^{1*}

¹Faculty of Chemical and Process Engineering Technology, University Malaysia Pahang Lebuhraya Tun Razak, 26300 Gambang, Pahang, Malaysia

²International Institute for Halal Research and Training, Level 3, Block A, KICT Building, International Islamic University Malaysia, Jalan Gombak, Selangor, Malaysia

³Faculty of Pharmacy, University Malaya 50603 Kuala Lumpur, Federal Territory of Kuala Lumpur, Malaysia

ABSTRACT

Microcarrier-based cell culture systems have gained significant attention and popularity in tissue engineering and regenerative medicine. In this culture system, tissue cells are grown as a monolayer on the surface of small solid particles called microcarriers (100 to 300 μm), kept suspended in the culture medium by stirring. This technology has paved the way for creating engineered tissues, one of the cutting-edge topics in tissue engineering and regenerative medicine. Microcarrier-based approaches have been proposed for three-dimensional (3D) cell culture in which cellular morphology and functions are maintained *in vivo*. This paper provides an overview of the optimal characteristics such as microcarriers' size, shape, density and porosity. Various methods of preparation of microcarriers and surface modification techniques have been elaborated. Recent advances and applications of microcarriers in biotechnology fields, like the production of viral vaccines and recombinant proteins, culture and expansion of stem cells (SC), are described.

ARTICLE INFO

Article history:

Received: 08 July 2023

Accepted: 01 February 2024

Published: 08 August 2024

DOI: <https://doi.org/10.47836/pjst.32.5.01>

E-mail addresses:

crystalsia96@gmail.com (Sia Yiik Swan)

mauliduni97@gmail.com (Muhammad Auni Hairunnaja)

nurhusna@iiu.edu.my (Nurhusna Samsuddin)

syedmahmood@um.edu.my (Syed Mahmood)

maizudin@ump.edu.my (Mohd Aizudin Abd Aziz)

mazmir@ump.edu.my (Mohd Azmir Arifin)

* Corresponding author

Keywords: Biomolecule immobilization, microcarrier, polymer, preparation, surface modification

INTRODUCTION

Cell culture technology has recently played a vital role in producing biological products such as vaccines, hormones, antibodies,

interferons, and clotting factors. Wezel first put forward the concept of a microcarrier-based culture system (1967). He proposed to culture cells as monolayers on the surface of small beads called microcarriers to support the attachment of adherent cells in bioreactors. This technology was believed to be used to produce inactivated poliomyelitis vaccines in 1972. Pharmacia Biotech AB (Sweden) collaborated with Wezel and developed Cytodex microcarriers, which are now commercially available (Badenes et al., 2016). The first microcarriers used were diethylaminoethyl (DEAE)-Sephadex A-50 resin beads (cross-linked dextran polymers), commonly used for column packing in ion-exchange chromatography (Badenes et al., 2016). Microcarriers based on biopolymers are preferred because of their superior biocompatibility and biodegradability. They can be made from natural or synthetic polymers. Alginates, chitosan, cellulose, and collagen are examples of natural polymers. Synthetic polymers include polycaprolactone (PCL), polyethylene glycol (PEG), polyglycolic acid (PGA), and polylactic acid (PLA). Several types of microcarriers are available commercially, like Cytodex (1, 2 and 3), Cytopore (1 and 2), CultiSpher (G, S and GL), Hillex II-170, ProNectin F, FACT III, and CGEN 102-L factors (Chen et al., 2020; Zhou et al., 2019).

Earlier cells were cultured on static surfaces such as T-flasks, multi-tray systems, and roller bottles. However, these conventional methods have a smaller surface area for cell culture, thus decreasing productivity (Merten, 2015). Microcarriers, on the other hand, can provide a surface area to volume ratio that is up to 10 times higher (Cytodex can offer a ratio of $30 \text{ cm}^2/\text{cm}^3$ in 1 mL medium) than T-flasks (ratio of $3 \text{ cm}^2/\text{cm}^3$ in 1 mL medium) (Clapp et al., 2018). Another limitation of the static culture system is its inefficiency in establishing multidirectional cellular interactions as they occur in the microenvironment *in vivo*. It may alter the morphology of cells and the expression of genes (Azahar et al., 2023; Tavassoli et al., 2018). Microcarriers have been proposed as a strategic alternative as they can facilitate cell attachment, have higher cell yields, and provide a more efficient environment for transporting gases and nutrients (Silva et al., 2015). These benefits have led to extensive research into the microcarrier for the 3D cell culture in cell therapy applications, tissue repair and regeneration.

This paper aims to discuss the different properties of microcarriers, such as size and shape, concentration, density, porosity, elasticity, and polymers, that are suitable for their preparation. Efforts to improve microcarrier surface properties are also discussed, and various techniques used for surface modification and biomolecule immobilization are discussed. An overview of the methods used for preparing microcarriers, namely emulsion-solvent evaporation and suspension polymerization, is given. In addition, applications of microcarriers in cell culture technology for producing vaccines, recombinant proteins, and stem cells are elaborated.

PROPERTIES OF MICROCARRIERS

Size and Shape

Microcarriers should have a uniform size distribution and be within the 100 to 300 μm diameter range, enabling them to remain suspended during stirring (Clapp et al., 2018). Uniform size distribution enables even distribution of cells and ensures a homogeneous culture (Chen et al., 2013; Merten, 2015). The proliferation of cells on microcarriers is affected by their size. Small-sized microcarriers may aggregate, leading to decreased cell viability due to insufficient nutrition and growth factors. At the same time, large-sized microcarriers provide a larger surface area to volume ratio on which large volumes of cells can be cultured (Clapp et al., 2018).

The size and shape of microcarriers are known to affect cell behavior. Hence, it is important to investigate their impact on cell expansion and proliferation (Clainche et al., 2021). The existing microparticles have different shapes, such as spherical and cylindrical shapes. Spherical microspheres are particularly interesting due to their ease of fabrication, injectability and large proportion among commercial microcarriers. Small-size microspheres can be injected directly into the targeted tissue defect or tumor sites with minimally invasive surgical procedures (Chen et al., 2013). The high sphericity of these microspheres facilitates improved and direct delivery of cells to the target site and lowers inflammatory responses associated with foreign body implantations (Chen et al., 2020; Hossain et al., 2015). Besides, spherical microcarriers can generate higher cell yield by producing open aggregates with thinner cell layers compared to cylindrical microcarriers with compact aggregates (Ornelas-González et al., 2021). They have been applied in biomedical applications such as controlled-release vehicles for vaccines, drug encapsulation, and hormone and therapeutic agent carriers.

Concentration of Microcarriers

The concentration of microcarriers affects the hydrodynamic environment of the culture. Theoretically, cell concentration should be increased with the microcarrier concentration due to the greater surface area available for cell adhesion. However, studies showed that increasing microcarrier concentration might be deleterious as higher microcarrier concentration may cause higher collision frequency (Maillot et al., 2022; Tsai et al., 2020). It has been proved by Luo et al. (2021) and Croughan et al. (1998) that a higher concentration of Cytodex-1 microcarrier resulted in lower cell growth rate and lower cell expansion fold during culture of Chinese Perch Brain cell (CPB) and FS-4 fibroblast cells. Croughan et al. (1998) discovered that the impact of microcarrier concentration varied according to the degree of agitation. In a laboratory-scale vessel, microcarrier concentration had no adverse effect during mild agitation. However, interactions between microcarriers and eddies at

high degrees of agitation caused hydrodynamic damage. The interaction increases the collision frequency, resulting in cell damage. A higher agitation rate will also decelerate cell attachment on the microcarrier due to loss in contact between cells and microcarriers (Luo et al., 2021). Besides, higher microcarrier concentrations may be accompanied by cytotoxicity of the culture system as increased cellular metabolites are produced, which leads to faster consumption of the culture medium and can be detrimental to cell viability. Due to high cell density, a more frequent medium change is required to overcome nutrient limitations and metabolite accumulation (Tsai et al., 2020). Thus, various factors such as agitation speed, availability of culture media, labor cost and time consumption need to be considered to obtain the optimal microcarrier concentration for maximum cell concentration (Luo et al., 2021).

Density of Microcarriers

Researchers have comprehensively investigated the relationship of microcarrier density on cell adherence and proliferation. Their density should be slightly higher than that of the culture medium to facilitate the separation of cells from the medium. Microcarriers with a density close to the culture medium can remain suspended with mild stirring, reducing the chances of shear stress and collisions (Zhou et al., 2019). A density range of 1.02–1.04 g/cm³ is regarded as optimal for microcarriers; most commercially available microcarriers have densities falling within this range (Chen et al., 2020). Cell adhesion efficiency of PCL microcarriers with a density range of 1.05–1.06 g/cm³ is up to 80%, whereas adhesion efficiency decreases to 35% with higher density range of 1.10–1.14 g/cm³. Microcarriers with high densities (~1.14 g/cm³) are difficult to suspend in stirred bioreactors and form large aggregates with cells leading to necrosis (Li et al., 2017).

Porosity of Microcarriers

Depending on their porosity, microcarriers are classified as non-porous, microporous, and macroporous. Microcarriers like Plastic Plus and FACT III from SoloHill Engineering are non-porous, providing a smooth cell adhesion and proliferation surface. The transfer of nutrients and the elimination of toxic products occur efficiently (Pörtner, 2015). Microporous microcarriers like Cytodex and SoloHill have small pores, which might limit cell infiltration to microcarrier surfaces only. Cells continue to proliferate under sufficient nutrients, but an arrest in proliferation is seen once confluence is reached as the microcarrier surfaces are fully attached to cells. There are no more surfaces available for cell proliferation. In the case of macroporous microcarriers such as Cytoline, CultiSpher and Fibracell, cells embed themselves within large pores and proliferate inside. These large pores shield the embedded cells from shear stress generated in a bioreactor and enhance productivity by offering a larger surface area for attachment and proliferation of

cells (Clapp et al., 2018). These macroporous microcarriers provide a multilayer culture system that resembles the *in vivo* cellular environment and facilitates multidirectional cellular interactions (Huang et al., 2018). The pore spaces can harbor a variety of cells like skeletal myoblasts, hepatocytes, articular chondrocytes, preosteoblasts, and mouse gastric stem cells (mGSCs) (Kankala et al., 2019).

The porous microcarriers are prepared with different porogens such as camphene, paraffin, sodium chloride, water and gelatin (Ravikumar, 2016; Samsudin et al., 2018; Zhou et al., 2019). Fabrication of porous microcarriers can be achieved by a two-step procedure of porogen leaching and freeze-drying (Zhou et al., 2019). Other methods involving microfluidic technology have also been successful in generating highly porous microcarriers (Kankala et al., 2019). Although porous microcarriers have been extensively explored for their applications in cell culture, currently, there are no studies to establish the optimum pore size for different types of cells.

Elasticity of Microcarriers

The elastic modulus of microcarriers is evaluated using the atomic force microscopy (AFM)--based nanoindentation technique. The elasticity of microcarriers plays a critical role in providing anchorage to cells. It ensures that the adherent cells remain undisturbed while experiencing turbulence or shear stress while stirring the culture medium (Huang et al., 2018). It is crucial in cellular differentiation and designing microcarriers with ideal mechanical properties for tissue regeneration. Soft matrix (1 kPa) promotes adipogenic, neuronal, and chondrogenic cell differentiation. Muscle cell differentiation is promoted by matrix having intermediate stiffness (11 kPa), while stiffer surfaces (34 kPa) promote osteogenic differentiation (Huang et al., 2018). The concentration and degree of cross-linking of polymers can be adjusted to control the elastic properties of microcarriers. Fabricated microcarriers have different elastic modulus ranging from 33.93 kPa to 132.68 kPa by blending different ratios of gelatin and chitosan (Ding et al., 2022).

POLYMERS USED IN THE PREPARATION OF MICROCARRIERS

Microcarriers have been produced using a variety of natural and synthetic polymers due to their chemical flexibility, biocompatibility, and biodegradability. They can also be immobilized with desired biomolecules. Natural polymers are the preferred candidates for biomedical applications since they are biodegradable with inherent bioactivity, biocompatibility, and bioresorbability (Reddy et al., 2021). They are non-toxic as they have biochemical similarities with human extracellular matrix (ECM) components and are thus safe for human use. Natural polymers are plant origin (cellulose, starch, dextran, and pectin) or animal origin (chitosan, collagen, chondroitin, and gelatin). Microcarriers made from synthetic polymers can be categorized into biodegradable or non-biodegradable

microcarriers. Biodegradable polymers are susceptible to enzymatic and/or chemical deterioration associated with living organisms and are easily decomposed. The demand for synthetic biodegradable polymers has grown exponentially over the years because of their excellent degradation ability and biocompatibility. Various polymers are used extensively for biomedical engineering and as microcarriers for drug delivery. Some examples of the most widely used polymers are PCL, PGA, PLA and PLGA (Tavassoli et al., 2018; Zhou et al., 2019). Non-biodegradable polymers are comprised of long chains of carbon and hydrogen atoms and are resistant to environmental degradation. Polycarbonate (PC), polyethylene terephthalate (PET), and polystyrene (PS) are examples of non-biodegradable synthetic polymers involved in cell culture (Tavassoli et al., 2018).

Some disadvantages of natural polymers are weak structural integrity, poor mechanical strength, lack of industrially acceptable processability and economic viability. These factors have restricted its application in tissue engineering. Conversely, synthetic polymers are versatile, have strong mechanical properties, desired flexibility and stability, and resist chemical degradation. However, synthetic polymers can induce inflammatory reactions and are considered toxic. They often lack cell adhesion and require chemical modifications (Reddy et al., 2021). These constraints can be overcome by introducing natural polymers on the surface of synthetic polymers or by creating a combination of natural and synthetic polymers (Reddy et al., 2021). Natural-synthetic polymer blends have enhanced cell adhesion and mechanical properties. Blended polymeric materials were created by grafting cellulose on polylactide (PLLA) polymers, which exhibited improved adhesion of hepatocellular liver carcinoma cells (HepG-2) as opposed to microcarriers fabricated solely from PLLA (Yang et al., 2016). Blending PCL with hydroxyapatite (HA), an essential element required for bone regeneration, has shown promising results in bone tissue engineering applications (Zheng et al., 2017).

SURFACE MODIFICATION OF MICROCARRIERS

Surface properties are fundamental for the good design and functioning of microcarriers. Surface energy and hydrophilicity are crucial in regulating cell-polymer interactions in culture systems (Omran et al., 2020). However, it has been observed that polymers often lack the desired surface properties required for specific applications. Hence, surface properties are modified to create an advanced multifunctional product. Hydrophilic surfaces are more favorable for cell adhesion as adhesion molecules on the cell membrane surface tend to adhere to the hydrophilic surfaces compared to the hydrophobic surfaces. The high hydrophobicity and low bioabsorption of synthetic polymers make it difficult for cells to adhere to their surfaces (Shahrifi et al., 2020). Numerous research has led to the development of various surface modification methods that enhance the physical and chemical characteristics of polymer microcarriers without changing their bulk properties.

Physical methods like surface abrasion and chemical methods like wet chemical oxidation are commonly used (Omrani et al., 2020).

Additionally, high-energy methods such as ultraviolet-ozone treatment (UVO) and plasma treatment can enhance wettability and immobilization of biomolecules by incorporating functional groups on microcarrier surfaces (Recek et al., 2016). The chemical nature of the groups is dependent on the gases used. For instance, nitrogen-containing groups (C-N, N-C=O) are from nitrogen and ammonia plasma, oxygen-containing groups (C-CO₂, C=O, O-C=O) are from oxygen plasma, and fluorine-containing groups (C-CF_n, C-F, CF₂, CF₃) are from sulfur hexafluoride plasma (Minati et al., 2017). Omrani et al. (2020) demonstrated increased adhesion of mouse embryonic fibroblasts onto the plasma-treated polyether ether ketone (PEEK) surface. The general objectives of microcarrier surface modification are presented in Table 1.

Table 1
Objectives of microcarrier surface modification (Minati et al., 2017; Recek et al., 2016)

Microcarrier surfaces are usually modified to:
<ul style="list-style-type: none"> • Microcarrier surfaces are usually modified to: • Introduce random or specific functional groups • Improve hydrophilicity • Improve surface energy • Enhance surface conductivity • Facilitate adsorption of biomolecules • Facilitate adhesion of microorganisms • Eliminate contaminants • Change surface morphology and roughness • Change chemical or biological reaction kinetics

TECHNIQUES FOR SURFACE MODIFICATION OF MICROCARRIERS

Plasma Treatment

Surface modification using plasma is a highly productive technique in regenerative medicine and tissue engineering, such as stem cell generation, wound healing, and skin tissue engineering. (Mozaffari et al., 2021). It is done to improve the hydrophilic properties of the microcarrier surface, thereby enhancing the materials' biocompatibility. Plasma is an ionized gas; the gas in the cell ionizes to a plasma state and emits UV light. The formed ions will collide with the neutral gas molecules to produce numerous reactive species. The interactions between the reactive species and the polymer surfaces placed inside the chamber will result in surface modification by forming functional groups derived from gas particles introduced to the polymer surface. Examples of gases include oxygen, ammonia, sulfur dioxide, nitrogen and argon (Laput et al., 2022; Minati et al., 2017). Recek et al. (2016) have treated PCL surfaces with oxygen, ammonia, and sulfur dioxide plasma and concluded that surfaces treated with oxygen and ammonia exhibited better cell adhesion. The proliferation of HUVEC increased by more than 60% for oxygen and ammonia plasma-treated PCL compared to sulfur dioxide plasma-treated PCL, which showed a 40% increase in cell viability. Besides, the sulfur dioxide plasma-treated PCL also demonstrated poorer cell adhesion through SEM analysis. However, Syromotina et al. (2016) demonstrated that ammonia plasma-treated poly(3-hydroxybutyrate) surfaces showed better adhesion

and proliferation of mouse embryonic fibroblasts as compared to oxygen-treated surfaces. Hence, the efficiency of different plasma treatments needs further investigation to ensure their applicability and biocompatibility.

UVO TREATMENT

UVO treatment is a photosensitized oxygenation process introducing oxygen-based functional groups to the treated surface. It has been demonstrated to have potential in cell culture, such as the generation of skin and stem cells. (Samsudin et al., 2018; Suzuki et al., 2021). During the treatment, UV-driven ozone-oxygen synthesis and dissociation cycle produce atomic oxygen continuously (Özçam et al., 2014). UV rays with wavelengths between 184.9 nm and 253.7 nm are emitted from low-pressure mercury lamps. Atomic oxygen is a very reactive oxygen species, which may interact with the polymer chain, ambient oxygen molecules, ozone, and water vapor in various reaction pathways to form oxygen-containing functional groups such as C-O, COO-, C=O, -OH. The atomic oxygen also reacts with the carbon atoms of the polymer chain, producing alkyl radicals that may react with the molecular oxygen, producing peroxy radicals and then forming peroxide intermediates. The hydroxyl, peroxy, and hydroperoxide groups may oxidize, producing carbonyl compounds with ketone, ester, or carboxylic acid groups (Arifin et al., 2022; Sia et al., 2023).

In recent years, this method has effectively improved the surface chemistry of polymers (with respect to surface energy and hydrophilicity). The surface energy of polyurethane was increased to ~38.8% by using UVO treatment (Kuang & Constant, 2015). In another study, the hydrophilicity of polymer surfaces, namely poly(dimethyl siloxane) (PDMS) and poly(vinylmethylsiloxane) (PVMS), were significantly improved by UVO treatment (Özçam et al., 2014). This technique is cost-effective, feasible, offers a high degree of control, and does not leave residues or contaminants. Additionally, this treatment is suitable for heat-unstable materials as it can be easily carried out at room temperatures with different gases, solvents and solutions (Yusilawati et al., 2010).

Wet Chemical Method

The wet chemical-based method is a classical approach to microcarrier surface modification. This technique uses liquid reagents to generate reactive functional groups on the surfaces (Govindarajan & Shandas, 2014). Introducing functional groups (such as amino, carboxyl, hydroxyl, and sulfate) modifies and enhances the hydrophilicity of the treated surfaces (Tham et al., 2014). Wet chemicals penetrate porous surfaces deeper than high energy-based modification approaches, producing a more stable and noncorrosive immobilization surface. It is an attractive alternative due to its affordability and high-yield production (Govindarajan & Shandas, 2014). However, monitoring the concentration of liquid reagents

is crucial in preventing bulk degradation of the polymers (Tham et al., 2014). Wet chemical modification is achieved by aminolysis and hydrolysis.

During aminolysis, amine groups are introduced on microcarrier surfaces. Certain polymer surfaces are hydrophobic and lack interaction with biomolecules, with the introduction of amine groups on polymer surfaces. Subsequent grafting onto the biomolecules is achieved through conjugation (Holmes & Tabrizian, 2015). 1-6-hexanediamine and ethylenediamine are common diamines used during the aminolysis of polymers (Holmes & Tabrizian, 2015; Shi et al., 2019). In general, aminolysis increases the roughness and wettability of polymer surfaces and hence improves the interactions of the protein with the surfaces. However, it should be noted that aminolysis is a non-specific method, and there is a possibility of surface degradation of polymers, so reactions should be carried out under controlled conditions to avoid adverse effects on the bulk properties of polymers (Holmes & Tabrizian, 2015).

During hydrolysis, hydroxyl and carboxyl groups are introduced on polymer surfaces. These are produced due to hydrolysis of ester linkages, which are the backbones of polymers. PGA, PLA, PLGA, and PCL are examples of polymers used during hydrolysis (Holmes & Tabrizian, 2015; Tham et al., 2014). Hydrolyzed microcarrier surfaces allow the grafting of biomolecules, thus promoting cell adhesion and proliferation. Tham et al. (2014) subjected PLA microcarriers, which are relatively hydrophobic and lack adequate cellular interaction, to alkaline hydrolysis. Post-treatment, the hydrolyzed PLA microcarriers showed enhanced hydrophilicity. In another study, Zhou et al. (2019) hydrolyzed PCL microcarriers in an alkaline solution before conjugating them with HA to produce a hydrophilic substrate more conducive to human fibroblasts' growth and proliferation. However, this method could cause irregular topography of the surface, which might affect the bulk properties of polymers (Holmes & Tabrizian, 2015).

The research was performed simultaneously during aminolysis and hydrolysis to analyze the influence of each reaction on material biocompatibility. Shi et al. (2019) conducted aminolysis and hydrolysis of PLA microcarriers. Then, they compared the end products of each reaction for their potential to induce the growth of human osteoblast-like cells. Both methods showed good cell adhesion and growth, but hydrolyzed PLA proved to be a better substrate for cell cultivation.

Biomolecule Immobilization

An effective approach to enhance polymer-based microcarriers' biological functionalities is immobilizing biomolecules on their surfaces. High hydrophobicity and low bioadsorption of synthetic polymer-based microcarriers pose difficulty for cell adhesion (Shahrifi et al., 2020). The attachment of natural hydrophilic polymers like cellulose, collagen or gelatin improves the surface energy and hydrophilicity of the microcarriers, making

them suitable for cell adhesion and proliferation. Ma et al. (2002) immobilized gelatin or collagen on PLLA and proved that immobilization improved surface wettability. In another study, arginine was immobilized on polyetherimide films. These surface-modified films showed approximately 85% increase in cell adhesion in less than two hours as opposed to untreated films (Sengupta & Prasad, 2018). Examples of ECM proteins, like collagen, gelatin, and fibronectin, as well as short peptide sequences, can be incorporated to create biomaterials/biological systems that closely mimic the natural cell environments. Apart from providing structural support to cells, these biomaterials can also regulate cellular morphology, attachment, differentiation, migration, and immune responses (Nikolova & Chavali, 2019). This biomimetic approach has been applied in biomedical applications like tissue engineering, device implantation, diagnostic assays, and drug delivery systems (Nikolova & Chavali, 2019).

Techniques for Biomolecule Immobilization

Albumin and heparin are two common biomolecules immobilized using different techniques (Frey et al., 2020). The method used depends on the type of biomolecule involved and the surface properties of polymers (Mohamad et al., 2015). Surface properties like the presence of functional groups, hydrophobicity, and surface charge influence the efficiency of biomolecule immobilization. Surface modification techniques such as plasma and UVO treatment tend to introduce polar and hydrophilic functional groups on the polymers. These functional groups decrease the hydrophobicity of polymer surfaces and are often applied in protein immobilization with a coupling agent such as EDAC (Arifin et al., 2022; Guo et al., 2020). Besides, the charges on the polymer surface also affect biomolecule immobilization, as shown in a previous study that showed higher efficiency of biomolecule immobilization between oppositely charged polymer surfaces and biomolecules (Guo et al., 2020).

Physical and chemical methods immobilize biomolecules. Physical methods are immobilization by weaker, mono-covalent interactions such as hydrophobic interactions, hydrogen bonding, van der Waals forces, ionic binding, and mechanical entrapment of biomolecules within polymer matrices. Covalent bonds are formed in chemical methods through amide, ether or thio-ether linkages between the biomolecules and polymer surfaces. These bonds confer stronger and lasting immobilization (Mohamad et al., 2015). Three main methods exist to immobilize biomolecules: physical adsorption, entrapment, and covalent binding (Frey et al., 2020).

Physical Adsorption

The physical adsorption technique is the simplest approach to introduce biomolecules on microcarrier surfaces. Polymer samples are soaked in a dissolved biomolecule solution and incubated for immobilization. Alternatively, the process can be carried out by drying

the biomolecule solution on polymer surfaces and then rinsing away the non-adsorbed molecules with an appropriate buffer solution (Mohamad et al., 2015). The adsorption of biomolecules occurs spontaneously via non-specific intermolecular forces such as hydrogen bonding, hydrophobic interactions, van der Waals forces, and ionic binding (Frey et al., 2020). These intermolecular forces are highly influenced by environmental conditions like ionic strength, pH, or polarity of the solvent; hence, fluctuations in these environmental conditions may potentially reverse the adsorption process (Wieland et al., 2020).

Guo et al. (2020) found that the charge of the attached molecules influences immobilization efficiency. In a previous study, heparin molecules were immobilized by ion attraction on aminolyzed PCL surfaces. These heparin molecules were then used to adsorb lysozyme (LZM) and bovine serum albumin (BSA) protein molecules. It was observed that the negatively charged heparin molecules absorbed more of the positively charged LZM. Clara-Trujillo et al. (2019) created a biomimetic environment for cell culture by using magnetic microspheres. The microspheres were prepared by immobilizing acrylates and acrylic acid and coated with fibronectin (FN) (Clara-Trujillo et al., 2019). Cell adhesion of porcine mesenchymal stem cells (pMSCs) onto these magnetic microspheres was observed. These microspheres provided a flexible 3D environment for cells to remodel and reorganize during cell development and homeostasis. Levato et al. (2015) observed that physical adsorption allowed rapid and uncontrolled release of adhered cells. Using a combination of physical adsorption and covalent bonding could control the release rate of cells, and this approach could be used to design efficient biomaterials for controlled cell delivery.

It is a simple and inexpensive strategy for immobilizing biomolecules without toxic or complicated linker chemistry, which may have a larger commercial potential due to its ability to preserve the activity and integrity of biomolecules (Guo et al., 2020). However, there is progressive leaching of the immobilized biomolecules as the intermolecular forces holding them together are relatively weak and cannot control the orientation and conformation of biomolecules. The leaching of immobilized biomolecules will slowly revert the surface properties of polymers to initial hydrophobic properties, which is not conducive to cell adhesion (Mohamad et al., 2015). Besides, this method's poor reproducibility and low operational stability have only limited its applications in laboratory procedures and preliminary studies.

Covalent Bonding

Covalent bonding is the most popular method for immobilizing biomolecules on microcarrier surfaces (Mohamad et al., 2015). Growth factors, proteins, and ECM components are a few examples of biomolecules covalently grafted on microcarriers. The formation of strong covalent bonds between functional groups of biomolecule microcarriers carries out immobilization. Cross-linking reagents link biomolecules directly

to the immobilization surfaces (zero-length crosslinkers) or indirectly work by introducing molecular spacers between the cross-links. Carbodiimides, Woodward's reagent K (N-ethyl-3-phenylisoxazolium-3'-sulfonate), and N,N'-carbonyldiimidazole are the most widely used zero-length crosslinkers. Among the carbodiimides, 1-ethyl-3-(3dimethylaminopropyl) carbodiimide hydrochloride (EDAC/EDC) is the most popular reagent. To obtain more stable conjugates, EDC is often cross-linked with N-hydroxysuccinimide (NHS) or Sulfo-NHS (water-soluble analog of NHS). A few research that have used EDAC with NHS (or Sulfo-NHS) for bioconjugation are listed in Table 2.

The activity of covalently bonded biomolecules is largely dependent on the shape and composition of polymer surfaces and the nature of the coupling method used (Mohamad et al., 2015). The main advantage of this technique is that there is no leaching of biomolecules into the environment, although solutions or substrates of high ionic strength are present (Wieland et al., 2020). This technique is more robust, provides uniform immobilization, has higher surface coverage, and is able to increase the immobilized biomolecules' thermal stability compared to physical adsorption (Mohamad et al., 2015). However, this technique has disadvantages such as longer incubation time, toxic and complex linkage chemistry applications, tedious protocols, and expensive operational costs (Wieland et al., 2020).

Table 2

Researches that used EDAC/NHS (Or Sulfo-NHS) reagents for bioconjugation

Title of Paper	Conjugation	References
"Ocular biocompatibility of gelatin microcarriers functionalized with oxidized hyaluronic acid."	Oxidized hyaluronic acid onto gelatin microcarriers	Lai & Ma, 2017
"Surface Modification of Microporous of Polycaprolactone (PCL) Microcarrier to Improve Microcarrier Biocompatibility"	Gelatin onto PCL microcarriers	Samsudin et al., 2018
"Biomimetic microspheres for 3D mesenchymal stem cell culture and Characterization"	Hyaluronic acid onto acrylic acid incorporated ethyl acrylate and ethyl methacrylate copolymer microspheres	Clara-Trujillo et al., 2019
"Droplet-based vitrification of adherent human induced pluripotent stem cells on alginate microcarrier influenced by adhesion time and matrix elasticity"	Matrigel onto alginate microcarriers	Meiser et al., 2021

METHODS FOR PREPARATION OF MICROCARRIERS

Emulsion-solvent Evaporation Method

Emulsion methods used to produce nanosized microcarriers (size < 10 µm) are commonly classified as single-emulsion methods and double-emulsion methods. Single emulsion methods such as oil-in-water (O/W), water-in-oil (W/O), oil-in-oil (O/O); double emulsion methods such as water-in-oil-in-water (W/O/W). In O/W emulsions, oil droplets are

dispersed in an aqueous phase, whereas in W/O emulsions, water droplets are dispersed in an oil phase. The O/O emulsion system consists of two immiscible oils (the first oil phase dispersed as droplets in a continuous second oil phase). The W/O/W emulsion system extends the W/O emulsion method in which the W/O emulsion is dispersed in the second aqueous phase (Campos et al., 2013).

O/W emulsions are the simplest emulsion systems used to prepare microcarriers. The method of O/W emulsion-solvent evaporation comprises four steps (Figure 1): (1) The dissolution of polymers in a suitable organic solvent followed by dispersion of the active compound in the organic phase, (2) Emulsification of the organic phase in an immiscible aqueous phase, (3) Evaporation and subsequent removal of the solvent, with consequent hardening of the dispersed phase into solid microspheres, and (4) Harvesting of the microspheres by filtration or centrifugation, followed by drying (Campos et al., 2013). PCL and PLGA microcarriers have been fabricated using an O/W emulsion system (Samsudin et al., 2018). Keratin-based microcarriers, fabricated using W/O emulsion systems, act as good substrates for bone marrow-derived MSC (BM-MSC) (Thompson et al., 2020).

Although emulsion-solvent evaporation methods, especially single emulsion, have been widely practiced for microcarrier production due to ease of fabrication, this method has several shortcomings. The main disadvantages faced are the difficulty in controlling the evaporation rate, low encapsulation efficiency, uneven distribution of particles, and

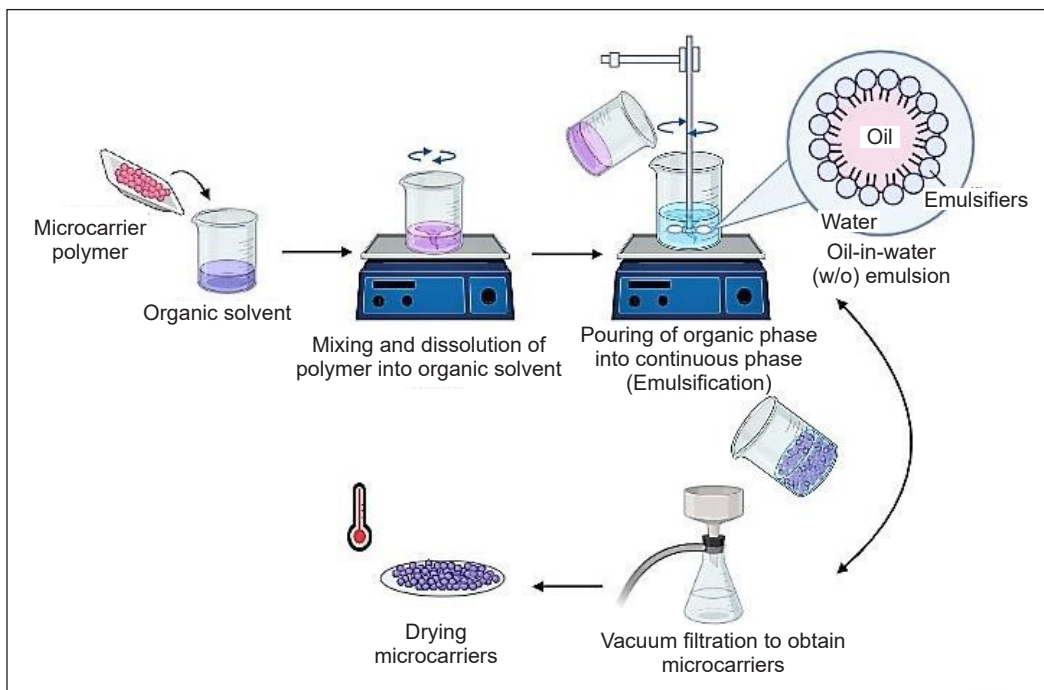


Figure 1. Steps involved in the oil-in-water emulsion-solvent evaporation technique (Lagreca et al., 2020; Campos et al., 2013)

unpredictable release of drugs or growth factors (Dashtimoghadam et al., 2020). Hence, double emulsion is emerging as an attractive microcarrier due to its high level of sample isolation and convenient cargo loading, which gives it a high potential for controlled release. However, this technique is more complicated to ensure on-demand core release and trajectory control during application (Zhang et al., 2022). Besides, microfluidic-assisted technology has been used with the emulsion-solvent evaporation technique to produce microcarriers with uniform shapes and sustained release ability. Dashtimoghadam et al. (2020) encapsulated vascular endothelial growth factor (VEGF) into PLGA microcarriers using a microfluidic-assisted double emulsion-solvent evaporation technique. The microcarriers produced exhibited a biphasic release pattern of VEGF, with rapid release followed by sustained release due to slow diffusion from the matrix.

Suspension Polymerization

This method produces 5 to 1000 μm particles and larger than those produced during emulsion-solvent evaporation (May 2016). In suspension immobilization, the dispersed phase consisting of monomers and monomer-soluble initiators is added to an immiscible solvent, which forms the continuous phase in the presence of surfactants or stabilizers. The solution is then heated to activate the initiator for radical immobilization. The microspheres are then collected and washed to remove the stabilizer. A major shortcoming of this approach is that the microcarriers produced have high polydispersity; micro-sieving is required to obtain well-defined particles, which reduces the yields (Saralidze et al., 2010). Cer et al. (2007) used suspension immobilization to design PEG-based microcarriers, which exhibited high cell adhesion and proliferation rates and could be used as a potential alternative to commercial microcarriers. Thermosensitive microcarriers have also been prepared by suspension immobilization. Gümüřdereliođlu et al. (2013) first prepared poly(2-hydroxyethyl methacrylate) (PHEMA) beads using this technique, then grafted N-isopropylacrylamide (NIPAAm) onto the PHEMA beads leading to the production of thermosensitive PHEMA-gPNIPAAm microcarriers.

APPLICATIONS OF MICROCARRIERS

Production of Viral Vaccines

One of the earliest and major uses of animal cell culture is the replication of viruses in culture medium to produce vaccines. Vaccines are being produced industrially using continuous or immortalized cell lines for viral replication. The most used cell lines are Vero, Chinese hamster ovary (CHO), BHK-21, Madin-Darby Bovine Kidney (MDBK), and human fetal lung fibroblasts (Verma et al., 2020). These cell lines are preferred as they are susceptible to infections, extremely resistant to genetic modifications, and can be grown

frequently *in vitro*. Initially, cells were cultivated in T-flasks, roller bottles, and cell factories; now, they are cultivated in microcarrier cultures to produce inactivated vaccines (Ismail et al., 2021). Microcarrier-based cell culture systems have demonstrated great potential in vaccine production and are good alternatives to egg-based vaccine production processes.

Stainless steel stirred-tank bioreactors equipped with marine impellers are the most typical bioreactors used for vaccine production (Silva et al., 2015). According to reports, the maximum size of stirred-tank bioreactors used to culture cells on microcarriers is 6,000 L, which Baxter Biosciences has used for producing influenza vaccines using Vero cells grown on Cytodex microcarriers (Eisenkraetzer, 2014). Wave-mixed bioreactors have also shown promising results for the culture of cells on microcarriers and have been employed to produce mink enteritis vaccines (Silva et al., 2015). The conditions within the bioreactors need to be monitored constantly throughout the culture process. For instance, temperature is mostly maintained at $37^{\circ}\text{C} \pm 0.5^{\circ}\text{C}$ for mammalian cells, and pH is mostly maintained within a narrow range at 7.2 ± 0.1 . Oxygen partial pressure $p\text{O}_2$ needs to be optimal with approximately 20-50% of air saturation, and carbon dioxide partial pressure $p\text{CO}_2$ needs to be varied to control the pH of the medium used containing sodium bicarbonate (Pörtner, 2015). Table 3 enlists various vaccines produced by the microcarrier culture system.

Table 3
Vaccines produced by microcarrier culture system

Vaccines against	Cell Line	Microcarrier	References
Yellow fever 17DD virus	Vero cells	Cytodex™ 1	Mattos et al., 2015
Enterovirus A71(EV-A71)	Vero cells	Cytodex™ 1	Chia et al., 2018
Louis Pasteur 2061 (LP2061) rabies virus	Vero cells	Cytodex™ 1	Trabelsi et al., 2019
Recombinant vesicular stomatitis virus–Zaire Ebola virus (rVSV-ZEBOV)	Vero cells	Cytodex™ 1	Kiesslich et al., 2020
Human parainfluenza virus type 3 (PIV3), respiratory syncytial virus (RSV), Severe acute respiratory syndrome coronavirus (SARS-CoV), and varicella-zoster virus (VZV)	Primary human bronchiotracheal cells (HBTCs), BEAS-2B cells, normal human neural progenitor (NHNP) cells	CultiSpher-G	Goodwin et al., 2015

Production of Recombinant Proteins

Recombinant proteins are widely used in pharmaceuticals for therapeutic treatments and prevention of diseases such as diabetes, cancers, and infectious diseases. They are exogenous proteins encoded by recombinant DNA cloned in a production organism (Burnett & Burnett, 2020). Microcarrier-based cell culture technology serves as a promising tool for producing a variety of recombinant proteins that are being used in basic research as well as pharmaceutical development. Over the last two decades, mammalian cell protein

expression has become the dominant recombinant protein production system for clinical applications; about 60-70% of all recombinant proteins are produced in mammalian cells. The most used mammalian cell is the immortalized CHO cell. Other cell lines like BHK, mouse myeloma (NS0), and human retinal cells have also gained regulatory approval to produce recombinant proteins (Fliedl & Kaisermayer, 2014).

These cell lines are cultured on microcarriers in stirred tanks and fluidized-bed bioreactors. Compared to normal suspension cultures, microcarriers show increased cell growth and excellent harvest yields (Tharmalingam et al., 2011). Chevalot et al. (1994) observed higher cell densities and higher amounts of human gamma-glutamyl transferase (GGT) when recombinant CHO cells were cultured on microcarriers. Similarly, Shirokaze et al. (1995) showed that the growth of recombinant CHO cells with microcarriers gave about double the yields interleukin-4 compared to the amount obtained through suspension culture. Table 4 lists commercially available recombinant proteins manufactured using microcarrier-based cell culture technology.

Table 4

Commercially available recombinant proteins produced using microcarrier-based cell culture technology

Product	Cell line	Microcarrier	Manufacturer
Aldurazyme™ (recombinant human α L-iduronidase or rhIDU)	CHO cells	Cytopore™	Biomarin
Myozyme™ (recombinant human acid alpha-glucosidase)	CHO cells	CytoPore™	Genzyme
Cerezyme™ (imiglucerase)	CHO cells	CytoPore™	Genzyme
GONAL-F® (recombinant human follicle stimulating hormone)	CHO cells	Cytodex™ 3	Merck
Luveris® (recombinant human luteinizing hormone)	CHO cells	Cytodex™ 3	Merck

Expansion of SCs

SCs have recently made significant progress in targeting the modulation of immune responses and tissue and organ regeneration. They are used to treat a myriad of diseases and conditions of the blood and immune system. This requirement of SCs for future cell therapy has evoked interest in applying microcarriers as the preferred platform for SC expansion. These cells have a remarkable capacity to self-renew and differentiate into other cell types (Mattiasson, 2018). SCs for clinical use are mostly produced through conventional static adherent cultures unsuitable for large-scale production. Conventional static adherent culture models, such as T-flask roller bottles, have smaller surface areas compared to microcarriers. Besides, 2D cell culture cannot provide an environment for multidirectional interactions between cells and the extracellular matrix, which might cause cellular morphology and gene expression changes. In contrast, microcarriers enable the scaling up of cell production in small volumes of the medium by supplying a large

surface area for cell growth in suspension cultures and providing a 3D environment for multidirectional cell interactions (Huang et al., 2020; Tavassoli et al., 2018). Numerous strategies (using different bioreactors, microcarriers and culture mediums) are being applied to shift the production to microcarrier suspension cultures to fulfill the future demand for quality-assured SCs (Kumar & Starly, 2015). Table 5 lists various research studies that have successfully cultured SCs using microcarrier-based culture systems.

Table 5
Culturing of different types of stem cells using microcarriers

Cell type	Microcarrier	Reactor type	Purpose	References
Human embryonic stem cells (hESCs)	Cytodex 1 and Cytodex 3	Spinner flask	Expansion and differentiation	Park et al., 2014
Mesenchymal stem cells (MSCs)	Corning®Synthemax®II polystyrene and CELLstart™coated SoloHill plastic microcarriers	Spinner flask	Expansion	Silva et al., 2014
	Corning® Enhanced Attachment, Corning® Low Concentration Synthemax®II, Corning® Collagen, SoloHill® Plastic Plus, SoloHill® Glass Coated, SoloHill® Collagen Coated, SoloHill® Pronectin F	Spinner flask	Expansion and differentiation	Heathman et al., 2018
	SoloHill® Plastic P102L, Cytodex-3 and Hillex	Spinner flask	Expansion	Rafiq et al., 2018
	Cytodex-1, Corning, GhaterDisc-1, GhaterDisc-2 and GhaterDisc-3	Spinner flask	Expansion	Clainche et al., 2021

CONCLUSION

Microcarriers are gaining considerable attention due to their overwhelming potential in numerous fields, especially regenerative medicine and bioengineering. Morphology, physical and chemical properties of microcarriers have been deeply studied to determine the suitability of microcarriers in cell cultures. Modifying surface properties of microcarriers and immobilizing biomolecules on their surfaces have successfully enhanced their biocompatibility and made them more conducive for cell growth and differentiation. Surface modification methods like plasma treatment, UVO treatment, and wet chemical methods can improve the hydrophilicity and wettability of microcarriers without altering their bulk properties. Microcarrier-based cell culture technology has appeared as a robust platform for tissue engineering. This review concludes that microcarriers have great potential in cell culture technology; the availability of a large surface area enables mass cultivation of cells. More detailed studies on microcarriers, including clinical studies, are required to understand

the mechanism of interactions of microcarriers with various biological molecules and cells for greater development in medical and bioengineering fields.

ACKNOWLEDGEMENTS

This work was supported by the Ministry of Higher Education Malaysia (MOHE) under the Fundamental Research Grant Scheme (Grant no. FRGS/1/2019/STG05/UMP/02/9) and Universiti Malaysia Pahang Al-Sultan Abdullah (UMPSA) under the UMP Research Grant Scheme (Grant no PGRS210320).

REFERENCES

- Arifin, M. A., Mel, M., Swan, S. Y., Samsudin, N., Hashim, Y. Z., & Salleh, H. M. (2022). Optimization of ultraviolet/ozone (UVO3) process conditions for the preparation of gelatin coated polystyrene (PS) microcarriers. *Preparative Biochemistry & Biotechnology*, 52(2), 181–196. <https://doi.org/10.1080/10826068.2021.1923031>
- Azahar, N. I., Mokhtar, N. M., Mahmood, S., Aziz, M. A. A., & Arifin, M. A. (2023). Evaluation of *Piper betle* L. extracts and its antivirulence activity towards *P. aeruginosa*. *Jurnal Teknologi*, 85(1), 133-140. <https://doi.org/10.11113/jurnalteknologi.v85.18892>
- Badenes, S. M., Fernandes-Platzgummer, A., Rodrigues, C. A. V., Diogo, M. M., da Silva, C. L., & Cabral, J. M. S. (2016). Microcarrier culture systems for stem cell manufacturing. In J. M. S. Cabral, C. L. de Silva, L. G. Chase & M. M. Diogo (Eds.), *Stem Cell Manufacturing* (pp. 77–104). Elsevier. <https://doi.org/10.1016/b978-0-444-63265-4.00004-2>
- Burnett, M. J., & Burnett, A. C. (2020). Therapeutic recombinant protein production in plants: Challenges and opportunities. *Plants, People, Planet*, 2(2), 121–132. <https://doi.org/10.1002/ppp3.10073>
- Campos, E., Branquinho, J., Carreira, A. S., Carvalho, A., Coimbra, P., Ferreira, P., & Gil, M. H. (2013). Designing polymeric microparticles for biomedical and industrial applications. *European Polymer Journal*, 49(8), 2005–2021. <https://doi.org/10.1016/j.eurpolymj.2013.04.033>
- Cer, E., Gürpınar, Ö. A., Onur, M. A., & Tuncel, A. (2007). Polyethylene glycol-based cationically charged hydrogel beads as a new microcarrier for cell culture. *Journal of Biomedical Materials Research Part B: Applied Biomaterials*, 80(2), 406–414. <https://doi.org/10.1002/jbm.b.30611>
- Chen, A. K. L., Reuveny, S., & Oh, S. K. W. (2013). Application of human mesenchymal and pluripotent stem cell microcarrier cultures in cellular therapy: Achievements and future direction. *Biotechnology Advances*, 31(7), 1032-1046. <https://doi.org/10.1016/j.biotechadv.2013.03.006>
- Chen, X. Y., Chen, J. Y., Tong, X. M., Mei, J. G., Chen, Y. F., & Mou, X. Z. (2020). Recent advances in the use of microcarriers for cell cultures and their *ex vivo* and *in vivo* applications. *Biotechnology Letters*, 42(1), 1-10. <https://doi.org/10.1007/s10529-019-02738-7>
- Chevalot, I., Visvikis, A., Nabet, P., Engasser, J. M., & Marc, A. (1994). Production of a membrane-bound proteins, the human gamma-glutamyl transferase, by CHO cells cultivated on microcarriers, in aggregates and in suspension. *Cytotechnology*, 16(2), 121-129. <https://doi.org/10.1007/BF00754614>

- Chia, M. Y., Chung, W. Y., Wang, C. H., Chang, W. H., & Lee, M. S. (2018). Development of a high-growth enterovirus 71 vaccine candidate inducing cross-reactive neutralizing antibody responses. *Vaccine*, *36*(9), 1167-1173. <https://doi.org/10.1016/j.vaccine.2018.01.041>
- Clainche, T. L., Moisan, A., Coll, J. L., & Martel-Frchet, V. (2021). The disc-shaped microcarriers: A new tool for increasing harvesting of adipose-derived mesenchymal stromal cells. *Biochemical Engineering Journal*, *174*, Article 108082. <https://doi.org/10.1016/j.bej.2021.108082>
- Clapp, K. P., Castan, A., & Lindskog, E. K. (2018). Upstream processing equipment. In G. Jagschies, E. Lindskog, K. Łacki & P. Galliher (Eds.), *Biopharmaceutical Processing: Development, Design, and Implementation of Manufacturing Processes* (pp. 457-476). Elsevier. <https://doi.org/10.1016/B978-0-08-100623-8.00024-4>
- Clara-Trujillo, S., Marín-Payá, J. C., Córdón, L., Sempere, A., Ferrer, G. G., & Ribelles, J. L. G. (2019). Biomimetic microspheres for 3D mesenchymal stem cell culture and characterization. *Colloids and Surfaces B: Biointerfaces*, *177*, 68-76. <https://doi.org/10.1016/j.colsurfb.2019.01.050>
- Croughan, M. S., Hamel, J. F. P., & Wang, D. I. (1988). Effects of microcarrier concentration in animal cell culture. *Biotechnology and Bioengineering*, *32*(8), 975-982. <https://doi.org/10.1002/bit.260320805>
- Dashtimoghadam, E., Fahimipour, F., Tongas, N., & Tayebi, L. (2020). Microfluidic fabrication of microcarriers with sequential delivery of VEGF and BMP-2 for bone regeneration. *Scientific Reports*, *10*(1), Article 11764. <https://doi.org/10.1038/s41598-020-68221-w>
- Ding, S. L., Liu, X., Zhao, X. Y., Wang, K. T., Xiong, W., Gao, Z. L., Sun, C. Y., Jia, M. X., Li, C., Gu, Q., & Zhang, M. Z. (2022). Microcarriers in application for cartilage tissue engineering: Recent progress and challenges. *Bioactive Materials*, *17*, 81-108. <https://doi.org/10.1016/j.bioactmat.2022.01.033>
- Eisenkraetzer, D. (2014). 6.1 Bioreactors for animal cell culture. In H. Hauser & R. Wagner (Eds.), *Animal Cell Biotechnology* (pp. 389-426). De Gruyter. <https://doi.org/10.1515/9783110278965.389>
- Fliedl, L., & Kaisermayer, C. (2014). Scalable transient gene expression in adherent mammalian cells using polyethylenimine. In R. Pörtner (Ed.), *Animal Cell Biotechnology: Methods and Protocols* (pp. 29-34). Springer https://doi.org/10.1007/978-1-62703-733-4_3
- Frey, S. J., Hoffman, A. S., Hubbell, J. A., & Kane, R. S. (2020). Surface-immobilized biomolecules. In *Biomaterials Science* (pp. 539-551). Academic Press. <https://doi.org/10.1016/b978-0-12-816137-1.00036-2>
- Goodwin, T. J., McCarthy, M., Cohrs, R. J., & Kaufer, B. B. (2015). 3D tissue-like assemblies: A novel approach to investigate virus-cell interactions. *Methods*, *90*, 76-84. <https://doi.org/10.1016/j.ymeth.2015.05.010>
- Govindarajan, T., & Shandas, R. (2014). A survey of surface modification techniques for next-generation shape memory polymer stent devices. *Polymers*, *6*(9), 2309-2331. <https://doi.org/10.3390/polym6092309>
- Gümüşderelioğlu, M., Çakmak, S., Timuçin, H. Ö., & Çakmak, A. S. (2013). Thermosensitive PHEMA Microcarriers: ATRP synthesis, characterization, and usabilities in cell cultures. *Journal of Biomaterials Science, Polymer Edition*, *24*(18), 2110-2125. <https://doi.org/10.1080/09205063.2013.827104>
- Guo, J., Li, K., Ning, C., & Liu, X. (2020). Improved cellular bioactivity by heparin immobilization on polycarbonate film via an aminolysis modification for potential tendon repair. *International Journal of Biological Macromolecules*, *142*, 835-845. <https://doi.org/10.1016/j.ijbiomac.2019.09.136>

- Heathman, T. R. J., Nienow, A. W., Rafiq, Q. A., Coopman, K., Kara, B., & Hewitt, C. J. (2018). Agitation and aeration of stirred-bioreactors for the microcarrier culture of human mesenchymal stem cells and potential implications for large-scale bioprocess development. *Biochemical Engineering Journal*, *136*, 9–17. <https://doi.org/10.1016/j.bej.2018.04.011>
- Holmes, C., & Tabrizian, M. (2015). Surface functionalization of *Biomaterials*. In A. Vishwakarma, P. Sharpe, S. Shi & M. Ramlingam (Eds.), *Stem Cell Biology and Tissue Engineering in Dental Sciences* (pp. 187–206). Academic Press. <https://doi.org/10.1016/b9780-12-397157-9.00016-3>
- Hossain, K. M. Z., Patel, U., & Ahmed, I. (2015). Development of microspheres for biomedical applications: A Review. *Progress in Biomaterials*, *4*(1), 1–19. <https://doi.org/10.1007/s40204-014-0033-8>
- Huang, L., Abdalla, A. M. E., Xiao, L., & Yang, G. (2020). Biopolymer-based microcarriers for three-dimensional cell culture and engineered tissue formation. *International Journal of Molecular Sciences*, *21*(5), Article 1895. <https://doi.org/10.3390/ijms21051895>
- Huang, L., Xiao, L., Jung Poudel, A., Li, J., Zhou, P., Gauthier, M., Liu, H., Wu, Z., & Yang, G. (2018). Porous chitosan microspheres as microcarriers for 3D cell culture. *Carbohydrate Polymers*, *202*, 611–620. <https://doi.org/10.1016/j.carbpol.2018.09.021>
- Ismail, N. A., Abd Aziz, M. A., Hisyam, A., & Abidin, M. A. (2021). Separation of samarium from medium rare earth mixture using multi-stage counter-current extraction. *Chemical Engineering Communications*, *208*(5), 764–774. <https://doi.org/10.1080/00986445.2020.1746654>
- Kankala, R. K., Zhao, J., Liu, C., Song, X., Yang, D., Zhu, K., Wang, S., Zhang, Y. S., & Chen, A. (2019). Highly porous microcarriers for minimally invasive in situ skeletal muscle cell delivery. *Small*, *15*(25), Article 1901397. <https://doi.org/10.1002/smll.201901397>
- Kiesslich, S., Losa, J. P. V. C., Gélinas, J. F., & Kamen, A. A. (2020). Serum-free production of rVSV-Zebov in *Vero Cells*: *Microcarrier Bioreactor* versus scale-XTM hydro fixed-bed. *Journal of Biotechnology*, *310*, 32–39. <https://doi.org/10.1016/j.jbiotec.2020.01.015>
- Kuang, P., & Constant, K. (2015). Increased wettability and surface free energy of polyurethane by ultraviolet ozone treatment. In M. Aliofkhaezrai (Ed.), *Wetting and Wettability* (pp. 85-102). InTech. <https://doi.org/10.5772/60798>
- Kumar, A., & Starly, B. (2015). Large scale industrialized cell expansion: Producing the critical raw material for Biofabrication processes. *Biofabrication*, *7*(4), Article 044103. <https://doi.org/10.1088/1758-5090/7/4/044103>
- Lagrec, E., Onesto, V., Di Natale, C., La Manna, S., Netti, P. A., & Vecchione, R. (2020). Recent advances in the formulation of PLGA microparticles for controlled drug delivery. *Progress in Biomaterials*, *9*(4), 153–174. <https://doi.org/10.1007/s40204-020-00139-y>
- Lai, J. Y., & Ma, D. H. K. (2017). Ocular biocompatibility of gelatin microcarriers functionalized with oxidized hyaluronic acid. *Materials Science and Engineering: C*, *72*, 150–159. <https://doi.org/10.1016/j.msec.2016.11.067>
- Laput, O. A., Vasenina, I. V., Shapovalova, Y. G., Ochered'ko, A. N., Chernyavskii, A. V., Kudryashov, S. V., & Kurzina, I. A. (2022). Low-temperature barrier discharge plasma modification of scaffolds based on polylactic acid. *ACS Applied Materials & Interfaces*, *14*(37), 41742–41750. <https://doi.org/10.1021/acsaami.2c11027>

- Levato, R., Planell, J. A., Mateos-Timoneda, M. A., & Engel, E. (2015). Role of ECM/peptide coatings on SDF-1 α triggered mesenchymal stromal cell migration from microcarriers for cell therapy. *Acta Biomaterialia*, *18*, 59–67. <https://doi.org/10.1016/j.actbio.2015.02.008>
- Li, J., Lam, A. T. L., Toh, J. P., Reuveny, S., Oh, S. K. W., & Birch, W. R. (2017). Tunable volumetric density and porous structure of spherical poly- ϵ -caprolactone microcarriers, as applied in human mesenchymal stem cell expansion. *Langmuir*, *33*(12), 3068–3079. <https://doi.org/10.1021/acs.langmuir.7b00125>
- Luo, X., Niu, Y., Fu, X., Lin, Q., Liang, H., Liu, L., & Li, N. (2021). Large-scale microcarrier culture of Chinese perch brain cell for viral vaccine production in a stirred bioreactor. *Vaccines*, *9*(9), Article 1003. <https://doi.org/10.3390/vaccines9091003>
- Ma, Z., Gao, C., Ji, J., & Shen, J. (2002). Protein immobilization on the surface of poly-L-lactic acid films for improvement of cellular interactions. *European Polymer Journal*, *38*(11), 2279–2284. [https://doi.org/10.1016/s0014-3057\(02\)00119-2](https://doi.org/10.1016/s0014-3057(02)00119-2)
- Maillot, C., Isla, N. D., Loubiere, C., Toye, D., & Olmos, E. (2022). Impact of microcarrier concentration on mesenchymal stem cell growth and death: Experiments and modeling. *Biotechnology and Bioengineering*, *119*(12), 3537–3548. <https://doi.org/10.1002/bit.28228>
- Mattiasson, B. (2018). *Immobilized cells and organelles: Volume I*. CRC Press. <https://doi.org/10.1201/9781351073394>
- Mattos, D. A., Silva, M. V., Gaspar, L. P., & Castilho, L. R. (2015). Increasing vero viable cell densities for yellow fever virus production in stirred-tank bioreactors using serum-free medium. *Vaccine*, *33*(35), 4288–4291. <https://doi.org/10.1016/j.vaccine.2015.04.050>
- May, C. P. (2016). *The study and fabrication of a novel thermally responsive microcarrier for cell culture application* [Unpublish doctoral thesis]. University of Nottingham, England.
- Meiser, I., Majer, J., Katsen-Globa, A., Schulz, A., Schmidt, K., Stracke, F., Koutsouraki, E., Witt, G., Keminer, O., Pless, O., Gardner, J., Claussen, C., Gribbon, P., Neubauer, J. C., & Zimmermann, H. (2021). Droplet-based vitrification of adherent human induced pluripotent stem cells on alginate microcarrier influenced by adhesion time and matrix elasticity. *Cryobiology*, *103*, 57-69. <https://doi.org/10.1016/j.cryobiol.2021.09.010>
- Merten, O. W. (2015). Advances in cell culture: Anchorage dependence. *Philosophical Transactions of the Royal Society B: Biological Sciences*, *370*(1661), Article 20140040. <https://doi.org/10.1098/rstb.2014.0040>
- Minati, L., Migliaresi, C., Lunelli, L., Viero, G., Dalla Serra, M., & Speranza, G. (2017). Plasma assisted surface treatments of biomaterials. *Biophysical Chemistry*, *229*, 151–164. <https://doi.org/10.1016/j.bpc.2017.07.003>
- Mohamad, N. R., Marzuki, N. H., Buang, N. A., Huyop, F., & Wahab, R. A. (2015). An overview of technologies for immobilization of enzymes and surface analysis techniques for immobilized enzymes. *Biotechnology & Biotechnological Equipment*, *29*(2), 205–220. <https://doi.org/10.1080/13102818.2015.1008192>
- Mozaffari, A., Gashti, M. P., Mirjalili, M., & Parsania, M. (2021). Argon and argon–oxygen plasma surface modification of gelatin nanofibers for tissue engineering applications. *Membranes*, *11*(1), Article 31. <https://doi.org/10.3390/membranes11010031>

- Nikolova, M. P., & Chavali, M. S. (2019). Recent advances in biomaterials for 3D scaffolds: A review. *Bioactive Materials*, 4, 271–292. <https://doi.org/10.1016/j.bioactmat.2019.10.005>
- Omrani, M. M., Kumar, H., Mohamed, M. G., Golovin, K., S. Milani, A., Hadjizadeh, A., & Kim, K. (2020). Polyether ether ketone surface modification with plasma and gelatin for enhancing cell attachment. *Journal of Biomedical Materials Research Part B: Applied Biomaterials*, 109(5), 622–629. <https://doi.org/10.1002/jbm.b.34726>
- Ornelas-González, A., González-González, M., & Rito-Palomares, M. (2021). Microcarrier-based stem cell bioprocessing: GMP-grade culture challenges and future trends for regenerative medicine. *Critical Reviews in Biotechnology*, 41(7), 1081–1095. <https://doi.org/10.1080/07388551.2021.1898328>
- Özçam, A. E., Efimenko, K., & Genzer, J. (2014). Effect of ultraviolet/ozone treatment on the surface and bulk properties of poly (dimethyl siloxane) and poly (vinylmethyl siloxane) networks. *Polymer*, 55(14), 3107–3119. <https://doi.org/10.1016/j.polymer.2014.05.027>
- Park, Y., Chen, Y., Ordovas, L., & Verfaillie, C. M. (2014). Hepatic differentiation of human embryonic stem cells on microcarriers. *Journal of Biotechnology*, 174, 39–48. <https://doi.org/10.1016/j.jbiotec.2014.01.025>
- Pörtner, R. (2015). Bioreactors for mammalian cells. In M. Al-Rubeai (Ed.), *Animal Cell Culture* (pp. 89–135). Springer. https://doi.org/10.1007/978-3-319-10320-4_4
- Rafiq, Q. A., Ruck, S., Hanga, M. P., Heathman, T. R. J., Coopman, K., Nienow, A. W., Williams, D. J., & Hewitt, C. J. (2018). Qualitative and quantitative demonstration of bead-to-bead transfer with bone marrow-derived human mesenchymal stem cells on microcarriers: Utilising the phenomenon to improve culture performance. *Biochemical Engineering Journal*, 135, 11–21. <https://doi.org/10.1016/j.bej.2017.11.005>
- Ravikumar, M. N. V. (2016). *Handbook of polyester drug delivery systems*. CRC Press.
- Recek, N., Resnik, M., Motaln, H., Lah-Turnšek, T., Augustine, R., Kalarikkal, N., Thomas, S., & Mozetič, M. (2016). Cell adhesion on polycaprolactone modified by plasma treatment. *International Journal of Polymer Science*, 2016, Article 7354396. <https://doi.org/10.1155/2016/7354396>
- Reddy, M. S., Ponnamma, D., Choudhary, R., & Sadasivuni, K. K. (2021). A comparative review of natural and synthetic biopolymer composite scaffolds. *Polymers*, 13(7), Article 1105. <https://doi.org/10.3390/polym13071105>
- Samsudin, N., Hashim, Y. Z., Arifin, M. A., & Salleh, H. M. (2018). Surface modification of microcoporous of polycaprolactone (PCL) microcarrier to improve Microcarrier biocompatibility. *International Journal on Advanced Science, Engineering and Information Technology*, 8(4–2), Article 1642. <https://doi.org/10.18517/ijaseit.8.4-2.7060>
- Saralidze, K., Koole, L. H., & Knetsch, M. L. W. (2010). Polymeric microspheres for medical applications. *Materials*, 3(6), 3537–3564. <https://doi.org/10.3390/ma3063537>
- Sengupta, P., & Prasad, B. L. V. (2018). Surface modification of polymers for tissue engineering applications: Arginine acts as a sticky protein equivalent for viable cell accommodation. *ACS Omega*, 3(4), 4242–4251. <https://doi.org/10.1021/acsomega.8b00215>

- Shahrifi, B. H., Mohammadi, M., Manoochehri, M., & Atashi, A. (2020). Mechanical and biological properties of polycaprolactone/fibrin nanocomposite adhesive produced by electrospinning method. *Bulletin of Materials Science*, 43(1), Article 135. <https://doi.org/10.1007/s12034-020-02111-9>
- Shi, X., Cui, L., Sun, H., Jiang, N., Heng, L., Zhuang, X., Gan, Z., & Chen, X. (2019). Promoting cell growth on porous PLA microspheres through simple degradation methods. *Polymer Degradation and Stability*, 161, 319–325. <https://doi.org/10.1016/j.polymdegradstab.2019.01.003>
- Shirokaze, J., Yanagida, K., Shudo, K., Konomoto, K., Kamiya, K., & Sagara, K. (1995). IL-4 production using macroporous microcarrier. In E. C. Beuvery, J. B. Griffiths & W. P. Zeijlemaker (Eds.), *Animal Cell Technology: Developments Towards the 21st Century* (pp. 877–881). Springer. https://doi.org/10.1007/978-94-011-0437-1_141
- Sia, Y. S., Azahar, N. I., Aziz, M. A. A., & Arifin, M. A. (2023). Sequential adaptation to Serum-free medium for Vero cells cultivation on ultraviolet/ozone (UVO) treated microcarrier. *Materials Today: Proceedings*. <https://doi.org/10.1016/j.matpr.2023.08.031>
- Silva, A. C., Roldão, A., Teixeira, A., Fernandes, P., Sousa, M. F., & Alves, P. M. (2015). Cell immobilization for the production of viral vaccines. In M. Al-Rubeai (Ed.), *Animal Cell Engineering* (pp. 541–563). Springer. https://doi.org/10.1007/978-3-319-10320-4_17
- Silva, C. L. D., Carmelo, J. G., Fernandes-Platzgummer, A., Weber, J. L., Bear, M., Hervy, M., Diogo, M. M., & Cabral, J. S. (2014). Scalable production of human mesenchymal stem/stromal cells in microcarrier-based culture systems. *Cytotherapy*, 16(4), S101-S102. <https://doi.org/10.1016/j.jcyt.2014.01.377>
- Suzuki, H., Kasai, K., Kimura, Y., & Miyata, S. (2021). UV/ozone surface modification combined with atmospheric pressure plasma irradiation for cell culture plastics to improve pluripotent stem cell culture. *Materials Science and Engineering: C*, 123, Article 112012. <https://doi.org/10.1016/j.msec.2021.112012>
- Syromotina, D. S., Surmenev, R. A., Surmeneva, M. A., Boyandin, A. N., Epple, M., Ulbricht, M., Oehr, C., & Volova, T. G. (2016). Oxygen and ammonia plasma treatment of poly(3-hydroxybutyrate) films for controlled surface zeta potential and improved cell compatibility. *Materials Letters*, 163, 277–280. <https://doi.org/10.1016/j.matlet.2015.10.080>
- Tavassoli, H., Alhosseini, S. N., Tay, A., Chan, P. P. Y., Weng Oh, S. K., & Warkiani, M. E. (2018). Large-scale production of stem cells utilizing microcarriers: A biomaterials engineering perspective from academic research to commercialized products. *Biomaterials*, 181, 333–346. <https://doi.org/10.1016/j.biomaterials.2018.07.016>
- Tham, C. Y., Hamid, Z. A., Ahmad, Z. A., & Ismail, H. (2014). Surface engineered poly (lactic acid) (PLA) microspheres by chemical treatment for drug delivery system. *Key Engineering Materials*, 594–595, 214–218. <https://doi.org/10.4028/www.scientific.net/kem.594-595.214>
- Tharmalingam, T., Sunley, K., Spearman, M., & Butler, M. (2011). Enhanced production of human recombinant proteins from CHO cells grown to high densities in macroporous microcarriers. *Molecular Biotechnology*, 49(3), 263–276. <https://doi.org/10.1007/s12033011-9401-y>
- Thompson, M., Giuffre, A., McClenny, C., & Dyke, M. V. (2020). A keratin-based microparticle for cell delivery. *Journal of Biomaterials Applications*, 35(6), 579–591. <https://doi.org/10.1177/0885328220951892>

- Trabelsi, K., Zakour, M. B., & Kallel, H. (2019). Purification of rabies virus produced in vero cells grown in serum free medium. *Vaccine*, *37*(47), 7052–7060. <https://doi.org/10.1016/j.vaccine.2019.06.072>
- Tsai, A. C., Jeske, R., Chen, X., Yuan, X., & Li, Y. (2020). Influence of microenvironment on mesenchymal stem cell therapeutic potency: From planar culture to microcarriers. *Frontiers in Bioengineering and Biotechnology*, *8*, Article 640. <https://doi.org/10.3389/fbioe.2020.00640>
- Verma, A., Verma, M., & Singh, A. (2020). Animal tissue culture principles and applications. In S. Verma & A. Singh (Eds.), *Animal Biotechnology* (pp. 269–293). Academic Press. <https://doi.org/10.1016/b978-0-12-8117101.00012-4>
- Wezel, V. A. L. (1967). Growth of cell-strains and primary cells on microcarriers in homogeneous culture. *Nature*, *216*(5110), 64–65. <https://doi.org/10.1038/216064a0>
- Wieland, F., Bruch, R., Bergmann, M., Partel, S., Urban, G. A., & Dincer, C. (2020). Enhanced protein immobilization on polymers — A plasma surface activation study. *Polymers*, *12*(1), Article 104. <https://doi.org/10.3390/polym12010104>
- Yang, L., Zhang, J., He, J., Zhang, J., & Gan, Z. (2016). Fabrication, hydrolysis and cell cultivation of microspheres from cellulose-graft-poly(L-lactide) copolymers. *RSC Advances*, *6*(21), 17617–17623. <https://doi.org/10.1039/c5ra25993b>
- Yusilawati, A. N., Maizirwan, M., Hamzah, M. S., Ng, K. H., & Wong, C. S. (2010). Surface modification of polystyrene beads by ultraviolet/ozone treatment and its effect on gelatin coating. *American Journal of Applied Sciences*, *7*(6), 724–731. <https://doi.org/10.3844/ajassp.2010.724.731>
- Zheng, P., Yao, Q., Mao, F., Liu, N., Xu, Y., Wei, B., & Wang, L. (2017). Adhesion, proliferation and osteogenic differentiation of mesenchymal stem cells in 3D printed poly-ε-caprolactone/hydroxyapatite scaffolds combined with bone marrow clots. *Molecular Medicine Reports*, *16*(4), 5078–5084. <https://doi.org/10.3892/mmr.2017.7266>
- Zhou, A., Ye, Z., Zhou, Y., & Tan, W. (2019). Bioactive poly(ε-caprolactone) microspheres with tunable open pores as microcarriers for tissue regeneration. *Journal of Biomaterials Applications*, *33*(9), 1242–1251. <https://doi.org/10.1177/0885328218825371>

Facial Emotion Recognition with Deep Neural Network: A Study of Visual Geometry Group-16 (VGG16) Technique with Data Augmentation for Improved Precision

Sarthak Kapaliya¹, Debabrata Swain¹, Ritu Sharma^{2*}, Kanishka Varyani² and Jyoti Thakar²

¹School of Technology, Pandit Deendayal Energy University Raisan, Gandhinagar- 382426, Gujarat, India

²School of Liberal Studies, Pandit Deendayal Energy University, Raisan, Gandhinagar- 382426, Gujarat, India

ABSTRACT

Emotions play a significant role in both verbal and nonverbal communication. Facial emotion recognition has applications in various sectors where we can get real-time feedback about student activeness by detecting their expression. In this paper, we aim to provide an improved deep-learning technique to detect emotions by using publicly available datasets to perform this detection. To get more data for the well-being of the Machine Learning Model, we have used data augmentation using the TensorFlow framework. Visual Geometry Group-16 (VGG16) is a convolutional neural network of 16 layers deep. There has been an alteration to the default VGG16 structure to get better classification results. Various optimization algorithms and loss functions increase the model's accuracy. We have used many evaluation parameters from the technical side, like precision, accuracy, recall, Area Under the Receiver Operating Characteristic Curve (AUC), and F1 Score. The proposed model has an accuracy of 89% while having a precision of 81 percent for classification. We have achieved an F1 Score of 0.42 and an area under the ROC curve (AUC) of 0.734.

Overall, it would be beneficial for analyzing and categorizing positive and negative emotions, which would aid in detecting signs of stress, anxiety, and burnout, as well as taking preventive actions to enhance well-being.

ARTICLE INFO

Article history:

Received: 26 July 2023

Accepted: 10 January 2024

Published: 08 August 2024

DOI: <https://doi.org/10.47836/pjst.32.5.02>

E-mail addresses:

kapaliyasarthak@gmail.com (Sarthak Kapaliya)

Debabrata.Swain@sot.pdpu.ac.in (Debabrata Swain)

dr.sharmaritu@gmail.com (Ritu Sharma)

kanishkavaryani@gmail.com (Kanishka Varyani)

jyoti.thakar85@gmail.com (Jyoti Thakar)

* Corresponding author

Keywords: Deep learning, emotion, facial emotion, human-computer interaction, image classification, neural networks

INTRODUCTION

The last decade has seen a significant increase in the integration of emotions and technology. It has led to a multidisciplinary study of computer science, cognitive science, psychology, and neuroscience (Shank, 2014). Emotions play a significant role in both verbal and nonverbal communication in humans. It can be most effectively understood through facial affect, which refers to the feelings and emotions humans experience. Face expressions are widely regarded as the universal language of internal emotional states since people of all cultural backgrounds understand them, and they also help in understanding the moods of individuals. Facial experiences are regarded as a universal language to understand emotions and are recognized and interpreted similarly across all cultures. The universality hypothesis by Darwin (1872) suggests that humans can express six internal emotions, i.e., happiness, surprise, fear, disgust, anger, and sadness (Ekman, 2009).

Further research by Ekman and Friesen (1971) suggested a similar concept. He proposed that there are six universal primary emotions in humans: anger, disgust, fear, happiness, sadness, and surprise, and argued that these emotions are expressed with the same facial expressions regardless of culture or language. Therefore, the terms facial expressions or emotional expressions are often used to describe the various emotions and moods of individuals universally (Ortony, 2022).

While talking about facial emotions, the issues of universality and cultural specificity have often been considered (Barrett et al., 2019). There has been enough empirical evidence to prove that emotions in facial expressions are recognized similarly in different cultures. The facial expressions of basic emotions are considered innate and universal (Mandal, 2004). Facial expressions represent a person's state of mind, which informs other people how a person is feeling and is most useful when communicating with others. Facial expressions can be analyzed in various fields, such as psychology (Song, 2021).

Recently, with the growth of digital technologies, various social media platforms have introduced emoticons and animated graphics interchange formats representing emotions. These visual elements provide a more detailed and expressive way to communicate emotions and sentiments. Many tech companies like Microsoft Azure (2018) and Google Inc. have developed software to read emotions objectively by understanding facial expressions. Additionally, facial expressions, which can indicate emotional states, help identify and manage psychiatric illnesses. Treatment plans for people with Autism Spectrum Disorder (ASD) and other Neurological disorders also include emotional expression and facial recognition. A study recently observed that emotion recognition technologies teach children with ASD (Autism Spectrum Disorder) how to express and identify emotions (Garcia-Garcia et al., 2022). Rapid human-computer interaction development, such as Artificial intelligence (AI), Cloud computing, and various machine-driven learning, has enhanced their application in Psychology.

With the increase in suicide rates in India, with 12 deaths per 100,000 people reported in 2021 (Salve, 2022) and also over the world (<https://ourworldindata.org/grapher/death-rate-from-suicides-ghe>), this technology can be utilized by counselors to comprehend and understand the emotional state of their clients, especially in a virtual setting. By analyzing subtle changes in their facial expressions, counselors can tailor their approach toward their clients and provide more effective treatment.

Facial emotion recognition technology can identify potential threats and suspicious behavior in law enforcement and crime. By analyzing the emotions expressed in a suspect's facial expressions, new ways of identifying individuals involved in criminal activity can be evolved. It can also analyze the emotions expressed in surveillance footage, providing valuable insights into criminal behavior and aiding the investigation. In the field of forensics, it can be used to identify individuals in photographs when their faces are partially obscured, or images are of poor quality, supplementary to traditional methods of solving crimes.

Overall, facial emotion recognition technology has the potential to revolutionize a wide range of fields and applications. This technology can help improve outcomes and enhance our understanding of the complex nature of human emotions.

The environment today generates an enormous amount of data, which is accumulated to improve the situation in various settings such as education, organizations, research, and more. However, when a large amount of data is generated, it becomes crucial to remove subjectivity and inaccuracy in interpreting emotional cues to make the data more meaningful, personalized, and objective (Saini et al., 2023).

However, accurately interpreting emotional cues could be challenging. Subjectivity and inaccuracy can arise due to differences in cultural expressions, state of mind, and interpretation. For instance, people with social anxiety have been found to interpret facial expressions of emotions based on prior knowledge and expectations (Song et al., 2022).

Human-computer interaction can help to mitigate these issues by using facial recognition technology to recognize emotional cues accurately. The significance of facial recognition of emotions has been documented in various studies. The study done by Pabst et al. (2023) on facial recognition technology helped us to discover how healthy individuals and individuals with severe alcohol use disorder reacted to various socio-emotional cues.

Saini et al. (2023) recognized the importance of technology and media in communication. They conducted a study to compare three speech emotion recognition machine learning methods to determine feelings and sentiments in speeches. Studying emotions in the workplace becomes imperative, as an employee's state of affect can lead an organization to flourish or fail. Such technology can help take preventive measures by tracking employees' moods and emotional states (Subhashini & Niveditha, 2015).

Siam et al. (2022) used machine learning techniques to detect emotion. They used principal component analysis with basic models like support vector machine and logistic

regression. The model achieved a validation accuracy of 70% on the face emotion dataset. Jaymon et al. (2021) proposed the detection of emotion on actual feeds that grasp the information about personalities. To build the model, they used TensorFlow, the framework of a Convolutional Neural Network, which gave them an accuracy of 65%

In addition, as the number of studies that concentrate on enhancing or increasing facial emotion detection has increased, the problem of a restricted database of photos for model training has also been brought to light (Devi & Preetha, 2023). Data augmentation, which increases the image count by modifying it at various levels, can increase the image count, thereby training the model for better precision and accuracy and contributing to refining human-computer interaction. It is accomplished by increasing the levels at which the data is modified.

This research highlights the need for extensive application of this technology. Language is full of emotions, which help in decoding the underlying meaning behind the intent of communication. Facial recognition of emotion in human-computer interaction is imperative to create more personalized, meaningful experiences for users in various industries. By incorporating facial recognition technology, we can better understand and respond to the user's emotional needs, leading to increased productivity, innovation, and well-being.

RESEARCH OBJECTIVES

The main contributions of the work can be summarized as follows:

1. A new fast and robust emotion detection framework for cyber-physical vision applications is proposed.
2. A comparison between traditional psychological and modern AI methods is evaluated to recognize human emotion.
3. Exploration of data augmentation to help us increase the data and introduce variability in the datasets.
4. Performing emotion classification using deep learning techniques.
5. A brief model implementation uses a live camera feed and images.

This approach system is based on Convolutional Neural Networks for facial expression recognition. A new architecture is proposed in which the system's input is an image; then, a Convolutional Neural Network (CNN) is used to predict the facial expression labels.

METHOD

Data Preprocessing System

Emotions are the most important part of a human being. Humans can recognize and differentiate between faces. Recognizing facial emotions and differentiating between them is believed to be achieved by computers nowadays. Recognizing facial expressions that

communicate fundamental emotions like fear, happiness, and disgust is known as facial emotion recognition. A highly accurate emotion identification model has been developed thanks to the development of computer vision techniques.

Data Collection

We have collected different types of facial emotion data from many online dataset repositories. We have used the Facial Expression Recognition 2013 dataset for training purposes. It contains approximately 30000 facial images in Red, Blue, and Green (RGB) form of differential expression with a size restricted to 48×48 pixels. It contains mainly seven types of emotion labels: angry (0), disgusted (1), fear (2), Happy (3), Sad (4), Surprise (5), and Neutral (6).

We used different data for model testing. CK+48 is a small dataset containing seven classes: fear, sadness, anger, disgust, happiness, contempt, and surprise. The images are 48×48 and have a grey-scaled color palette. Good variations and feature distributions can be used in testing to obtain good results. It has a frontal view with clear images of faces.

Data Augmentation

Data augmentation (Alamsyah et al., 2022) is a group of methods for creating additional data points from previously collected data to artificially increase the amount of data. It includes making minor adjustments to the data or creating new data points using deep learning models. By creating new and varied examples, this has a wide range of applications for enhancing the performance and results of machine learning models.

We have used the Tensorflow framework for the deep learning model. Tensorflow provides an image preprocessing technique for data augmentation by generating batches of tensor images. We have done the following data augmentation operation:

1. Rotation: In this, we rotate the image to a certain degree. If the rotation degree is set to 40, the new image will be 40 degrees and rotate to the original one.
2. Shearing: It is also used to transform the orientation of the image. Additionally, it implies that the image will be warped along a particular axis, typically to alter or modify the perception angles.
3. Zooming: It allows us to either zoom in or zoom out. The specified zoom-in range allows us to get a different image, which can help train the ML model.
4. Flipping allows us to flip the orientation of the image. We can use horizontal or vertical flips. This operation can be misleading for a model. If the image is flipped along the wrong axis, it can make no sense during the training of the deep learning model. So, in face detection, we do not need vertical flips.
5. Rescale: We rescale the image pixel in the range 0 to 255.
6. Shifting: We shift the image by a certain length, making it different from the real image. It has a height and width shift.

For instance, here demonstrates how Data Augmentation changes the Face image. It creates different types of images similar to the original ones. It is applied to the whole dataset to increase the dataset. We can see the implementation of these techniques on an image, as shown in Figure 1.

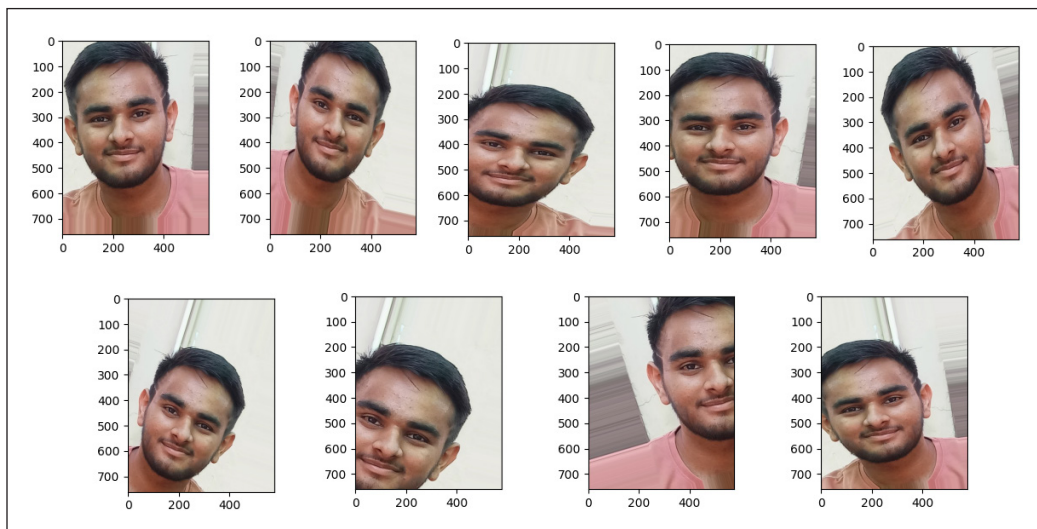


Figure 1. Image augmentation

Data augmentation plays an important role in this research. By using augmentation techniques, we increase the number of data samples from 30,000 to 50,000, which helps achieve better accuracy. Many machine learning techniques include data augmentation, as it increases the amount of data and helps achieve more useful information from the images. It makes Data Augmentation necessary for image-based multi-classification. This technique has been utilized extensively for various purposes and is useful for resolving data generation and precision issues. Several techniques, including posture transfer, hairdo transfer, expression transfer, cosmetics transfer, and age transfer, have been suggested to change the appearance of a genuine face image. In the meantime, the simulated virtual faces can also be improved to match the realism of the genuine ones. One can increase the training data's variety and strengthen the trained model's resilience using any augmentation technique.

Model Training

A neural network with three or more layers is what machine learning essentially is, which includes deep learning. Although these neural networks try to emulate how the human brain works, they cannot match it, allowing the computer to “learn” from enormous amounts of data. Even if a neural network with only one layer can still provide approximate predictions, more hidden layers can help to tune and improve accuracy.

Here, we have used VGG16 as a deep-learning model. There are several reasons for the choice of VGG16 as a primary architecture for this study, as mentioned below:

1. Facial emotion involves capturing special details and unique features, which can be done using VGG16 hierarchical representations, capturing both low-level and high-level features in facial expressions.
2. VGG16 leverages the power of pre-trained weights using the ImageNet Large Scale Visual Recognition Challenge Dataset; this helps the model acquire general knowledge during training and enhances detection accuracy.
3. With transfer learning capabilities, VGG 16 uses small filter sizes and contains several convolutional layers, which provide a balanced receptive field. This receptive field helps the model capture local and global features from the images.

VGG16 is a convolutional neural network that is 16 layers deep. It is a pre-trained model that has been trained on the ImageNet database. The pre-trained model can categorize 1000 different types of objects. The network has, therefore, acquired rich feature representations for various images. The network can accept images up to 224×224 in size. This model has achieved 92% in the ImageNet Challenge for 14 million images belonging to 1000 classes. It has a fixed input size of 224×224 and RGB channels, resulting in $(224, 224, 3)$ tensor. Here, it calculates the probabilities of different classes. After every prediction, we get probabilities associated with different classes based on similarity. The classification vector has to ensure that these probabilities add to 1 and check it. We use the Softmax function.

The 16 in VGG16 refers to 16 layers with weights (Figure 2). VGG16 has 13 convolutional layers, five max-pooling layers, and three dense layers, i.e., learnable parameters layer. It contains a 3×3 filter with Stride 1 and the same padding and max pool layer of a 2×2 filter with Stride 2. The convolutional and max pool layers are consistently arranged throughout the whole structure.

The VGG16 model is a deep convolutional neural network trained on the Image Net dataset. It consists of 13 convolutional layers and three fully connected layers. By using the VGG16 model as the base model, the pre-trained weights are used as initial weights for the model, which can improve performance and reduce training time. After the VGG16 base model, a dropout layer with a rate of 0.5 is added to prevent overfitting. Then, a flattened layer is added to flatten the output from the base model to a 1-dimensional tensor. A batch normalization layer is added to normalize the output. Then, three dense layers are added with 32 units, each followed by a batch normalization layer, the rectified linear activation unit (ReLU) activation function, and a dropout layer with a rate of 0.5. The ReLU activation function is used to introduce non-linearity into the model. Finally, a dense layer with seven units is added, and the softmax activation function is used to output a probability distribution over the seven classes.

This model is suitable for classification tasks on images with seven classes, and the use of a pre-trained VGG16 base model can lead to improved performance and faster

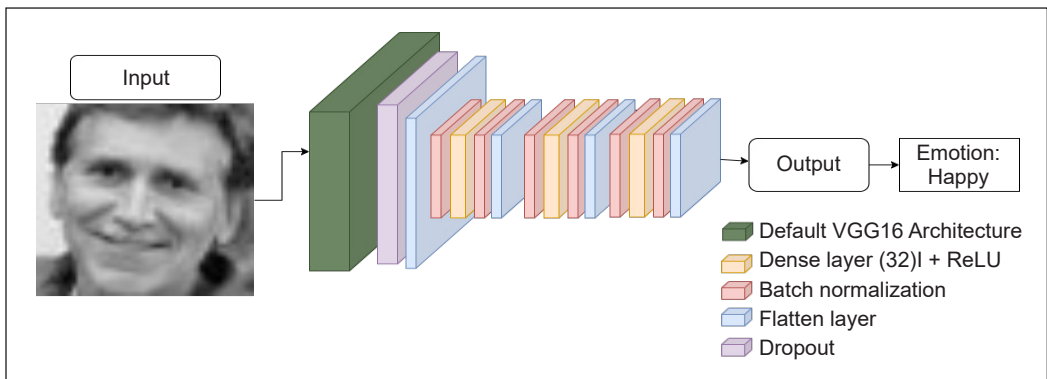


Figure 2. Improved VGG 16 Block Diagram

Source: Input image taken from the public dataset

training time. A good optimizing algorithm can help a deep learning model train by getting differences in results in minutes, hours, and days. In this case, we will apply the Adam optimization method. In addition to stochastic gradient descent, the Adam optimizer is used.

Adam Optimization

Adam optimization is a gradient descent algorithm for optimizing the parameters in a neural network. It uses momentum and adaptive learning rates to converge to the minimum of the cost function faster than traditional gradient descent methods.

The algorithm shows the working of Adam Optimization

Initialize $V_{dw}=0, S_{dw}=0, V_{db}=0, S_{db}=0$

On iteration t :

1. Computer dw, db using current mini-batch gradient descent
2. $V_{dw} = \beta_1 V_{dw} + (1 - \beta_1)dw, V_{db} = \beta_1 V_{db} + (1 - \beta_1)db$
3. (momentum β_1 exponentially weighted average)
4. $S_{dw} = \beta_2 S_{db} + (1 - \beta_2)dw^2, S_{db} = \beta_2 S_{db} + (1 - \beta_2)db$
5. (RMSProp β_2)
6. $V_{dw}^{corr} = V_{dw} / (1 - \beta_1^t), V_{db}^{corr} = V_{db} / (1 - \beta_1^t)$
7. $S_{dw}^{corr} = S_{dw} / (1 - \beta_2^t), S_{db}^{corr} = S_{db} / (1 - \beta_2^t)$
8. $W = W - \alpha V_{dw}^{corr} / \sqrt{(S_{dw}^{corr} + \epsilon)}, b = b - \alpha V_{db}^{corr} / \sqrt{(S_{db}^{corr} + \epsilon)}$

Where Hyper parameter choices:

α : Learning rate. It needs to be tuned.

β_1 : beta 1 moving average weight of dw . Default value 0.9

β_2 : beta 2 moving average weight of dw^2 and db^2 . Default value 0.999

ϵ : 10^{-8}

The algorithm starts by initializing two variables, V_{dw} and S_{dw} , and V_{db} and S_{db} , to zero. On each iteration, the gradients dw and db are computed using the current mini-batch of data. Then, it updates the moving average of the first and second moments of the gradients (V_{dw} , V_{db} , S_{dw} , S_{db}) using exponential decay rates (β_1 and β_2). It also corrects these moving averages to prevent bias towards zero at the beginning of the training by dividing them by $(1-\beta_1^t)$ and $(1-\beta_2^t)$.

Finally, it updates W and B parameters using the corrected moving averages and a learning rate α . The learning rate determines the step size of the parameter updates and needs to be tuned. The β_1 and β_2 values have default values of 0.9 and 0.999, respectively. ϵ is a small value added to the denominator to avoid division by zero.

These days, deep learning applications for computer vision and natural language processing are commonly regarded as dependable. Adam is a shortened version of adaptive moment estimation. Using estimated values for the first and second moments of the gradients, it calculates individual adaptive learning rates for various parameters. It uses momentum and scaling terms for the gradient cost function. Adam additionally uses the average of the second moments of the gradients, as opposed to adjusting the parameter learning rates based on the average first moment as in root mean squared propagation (RMSProp). It combines the idea of moment optimization with RMSProp and exponential decay.

How Adam Works

Adam optimization combines the Moment's and RMSProp methods, which accelerate the gradient descent algorithm with exponentially weighted averages of the gradient.

Moment's Method

Generally, the main aim is to accelerate the gradient descent algorithm with an exponentially weighted gradient average. We use averages to converge faster toward minima, as shown in Equations 1 and 2.

$$w_{t+1} = w_t - \alpha_t \cdot m_t \quad [1]$$

Where

$$m_t = \beta \cdot m_{t-1} + (1 - \beta) [\partial L / \partial w_t] \quad [2]$$

Where m_t = total gradients at time t [present]. (m_t initially equals 0); m_{t-1} = the sum of gradients at time $t-1$; w_t = weights at time t ; w_{t+1} = weights at time $t+1$; α = learning rate at time t ; ∂L = derivative of Loss Function; ∂w_t = derivative of weights at time t ; β = moving average parameter (constant = 0.9)

RMSP Method

It avoids the early stopping problem by accumulating recent gradients through exponential decay. Here, we take the exponential moving average, as shown in Equations 3 and 4.

$$v_t = \beta \cdot v_{t-1} + (1 - \beta) * [\partial L / \partial w_t] \quad [3]$$

$$w_{t+1} = w_t - \alpha_t / (v_t + \epsilon)^{1/2} * [\partial L / \partial w_t] \quad [4]$$

Where w_t = weights at time t ; $w_t + 1$ = weights at time $t + 1$; α_t = learning rate at time t ; $\#L$ = derivative of Loss Function; $\#w_t$ = derivative of weights at time t ; v_t = sum of the square of past gradients. [i.e $\text{sum}(\partial L / \partial W t - 1)$] (initially, $Vt = 0$); β = moving average parameter (constant = 0.9); ϵ = a small positive constant (10 – 8)

Adam Optimizer inherits the strength or the positive attributes of the above two methods and builds upon them to give optimized results, as shown in Equation 5.

$$m_t = \beta_1 m_{t-1} + (1 - \beta_1) \left[\frac{dL}{dw_t} \right], v_t = \beta_2 v_{t-1} + (1 - \beta_2) \left[\frac{dL}{dw_t} \right]^2 \quad [5]$$

Parameters used:

1. $\epsilon = 10 - 8$
2. $\beta_1 + \beta_2$ = average of gradients in the above methods ($\beta_1 = 0.9$ & $\beta_2 = 0.999$)
3. α = learning rate (0.001)

Cross Entropy Loss Function

The loss function measures how far the algorithm's current output deviates from the desired output. This information theory-derived function aims to compare two averages of the distribution's bit count. Cross-entropy is used as the Log Loss function to compare two probability distribution functions (not the same, but they measure the same thing).

We have employed binary and multiclass problems; categorical cross-entropy is utilized; the label must be encoded as a categorical, one-hot encoding representation (for three classes: [0, 1, 0], [1, 0, 0]).

Model Evaluation

The most crucial phase, model evaluation, allows us to assess and enhance our model. Validation and testing methodologies were the primary assessment criteria that we employed. Twenty-eight thousand photos from seven distinct classes/emotions were used to train the model. Eight thousand photos were used to validate the model as it was being improved. Only the Facial Expression Recognition (FER) 2013 dataset was utilized for training and validation. For testing, we used photos from the CK+48 dataset, which contains various images from the FER2013 data. The CK+48 data includes 981 pictures.

We used different evaluation metrics. We used five classification metrics: (1) Accuracy, (2) Precision, (3) Recall, (4) AUC, and (5) F1 Score.

RESULTS AND DISCUSSION

In this paper, we have proposed an Emotion detection model. Deep neural networks are used to precisely predict emotion from facial images. Features are extracted using deep learning methods. Classification metrics like Precision Recall F1 Score and Accuracy evaluate the effectiveness of the Deep learning Pre-trained model. We have used two different types of datasets that are available publicly. The FER2013 dataset contains over 30000 images, of which we have used 28000 for training the VGG16 Pre-Trained Model. The Rest of the Images were used to validate the model while training, which uses transfer learning methods. For the testing of the model, we used the CK+48 dataset. The model performs well in detecting all emotions provided in the dataset.

Instead of using cross-validation, we used a different strategy for dividing the data into training, validation, and testing sets. The dimensions and properties of the employed datasets impacted this choice. Due to the FER2013 dataset's size, we could assign a sizeable fraction for training and validation, creating a solid base for model learning. The CK+48 dataset, used only for testing, guarantees a fair assessment of the model's performance on omitted data. Even while cross-validation is a useful approach, its use may be impacted by computing limitations and dataset size, so we decided to use a partitioned training-validation-testing strategy in this situation.

We have evaluated it using the classification metrics. The graphs in Figure 3 represent the status of the metrics during the model training. We can see that validation Accuracy is greater than training accuracy for the 30 epochs. It shows that the model is not overfitting.

We have also practically implemented the model using the Open Source Computer Vision Library and Tensorflow. The model can detect facial emotion through live video and image feeds. Some of the implementation examples are shown in Figure 4.

The proposed model's classification accuracy is 89%, while its precision is 81% (Table 1). We have achieved an F1 Score of 0.42 and an AUC of 0.734.

The model performs well in terms of overall accuracy, categorizing dataset instances correctly 89% of the time, as shown in Table 2. When the model predicts a positive class, a precision of 81% shows a pretty good level of accuracy. A balanced performance in terms of precision and recall is indicated by the F1 Score of 0.42. The model's ability to differentiate between positive and negative classes is modest, according to the AUC of 0.734. Additionally, we are working on a research trend where the proposed approach is being implemented on hardware. Additionally, this problem can be resolved using additional machine learning techniques, including dictionary learning and semi-supervised learning.

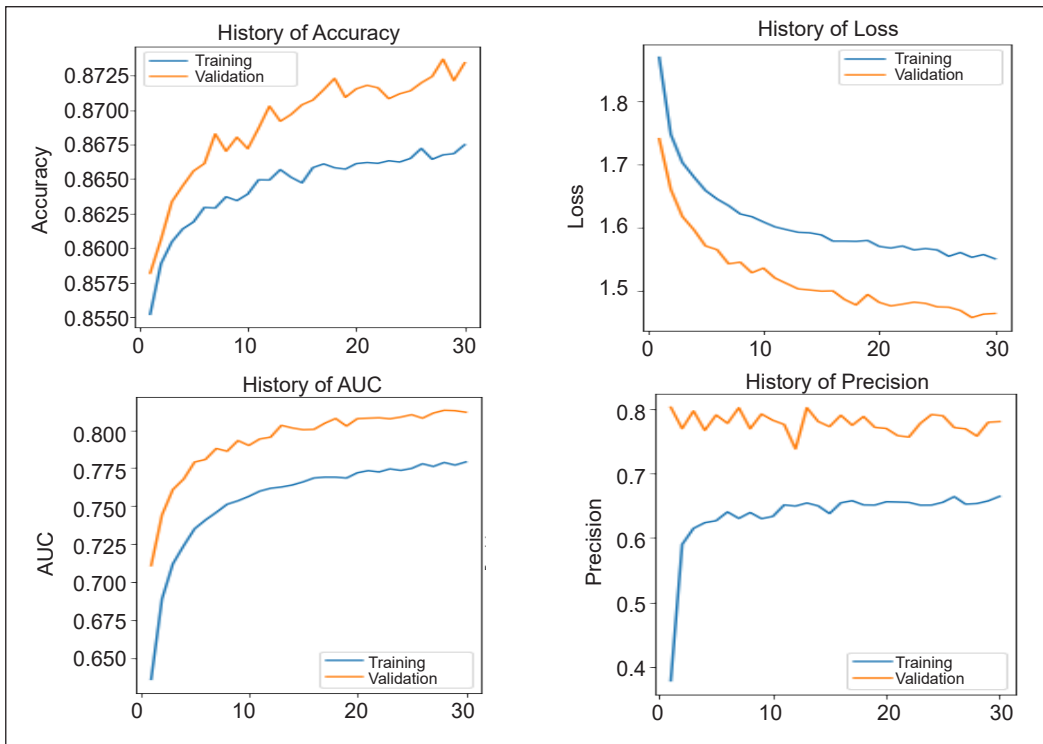


Figure 3. Graphical representation of model performance

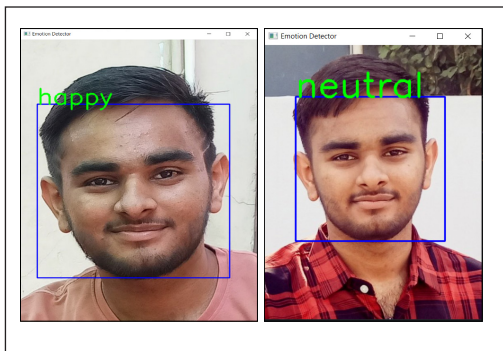


Figure 4. Test result of the model
Source: Personal images of the first author

Table 1
Result analysis of VGG16

Metrics	Score
Accuracy	89%
Precision	81
F1 Score	0.42
AUC	0.734

In Figure 3, the interaction of a sizable dataset and the intrinsic complexity of the VGG16 model may be responsible for the observed difference in loss between training and validation after 30 epochs. Given the complexity of VGG16, attaining convergence in a constrained number of epochs may present difficulties. However, various overfitting mitigation strategies, one of which is using regularization techniques like weight regularization and extra dropout layers to provide a more balanced output, can overcome this issue.

It is important to understand that assessing the model's performance only in terms of the loss graph might not give a complete picture. Despite the observed variation in loss, the model demonstrates

Table 2
Result comparison with our proposed results

Topic	Methodology	Framework	Validation Accuracy	Reference
Deploying machine learning techniques for human emotion detection. Computational Intelligence and Neuroscience	Reducing Dimension of Data Using Principal Component Analysis	Support Vector Machine, Logistic Regression	70%	Siam et al. (2022)
Real-time emotion detection using deep learning. 2021 International Conference on Advances in Electrical, Computing, Communication and Sustainable Technologies	Convolutional Neural Network (TensorFlow)	CNN	65%	Jaymon et al. (2021)
Proposed VGG16 Model (our Result)	Applied Data Augmentation techniques on the dataset and evaluated the model using separate real-time test data.	Modified VGG16 Transfer Learning Model	89%	

promising classification results, achieving an overall precision of 81% and an AUC of 73%. These metrics affirm the model’s efficacy in classification tasks. Another reason this solution has not been employed is that this research is computationally expensive. We need better computing resources to train a model using a better hyperparameter.

We did not employ certain alternatives, such as adding extra regularization, due to their high computational cost. We require more potent computational resources to improve the model’s hyperparameters. Although the loss graph shows possible overfitting, we must weigh this against our actual practical constraints. The model still does well in categorization, demonstrating the importance of considering metrics and resource limitations when evaluating a system.

CONCLUSION AND THE WAY FORWARD

Emotions are an innate part of human beings. They direct and impact communication, relationships, and social distance. Emotions involve three distinct components: a subjective experience, a physiological response, and a behavioral or expressive response. The need to accurately decipher emotions has arisen with the advent and advancement of technology. The study mentioned above assists in doing so. It has collected data from different types of facial emotion expression data from many digital repositories of around 30,000 facial images. It has used the deep neural networks model VGG16 technique to decipher the seven emotional expressions: happiness, sadness, anger, fear, disgust, surprise, and neutral expressions. The data gathered was augmented to produce more data and enrich

the modeling technique for more precision. The model has achieved 89% precision and 81% emotion classification.

This study will help to achieve better accuracy in decoding, comprehending, and classifying facial emotional expressions across various media such as images, media, and virtual reality environments and thus benefit several industries such as organization, education, entertainment, and research. Due to the high computational cost of certain alternatives, such as adding extra regularization, we did not employ them. We require more potent computational resources to improve the model's hyperparameters. It can be improved in the future with better resources. Therefore, we conclude that human emotions are innate and directly impact their lives. The new advanced technologies, such as virtual and augmented reality, may impose novel challenges to people's mental well-being, hence making it imperative to employ such approaches to detect emotional changes in a person's conduct. Overall, it would be beneficial to analyze and classify positive and negative emotions, which would help detect signs of stress, anxiety, and burnout and take preventive measures to enhance well-being.

ACKNOWLEDGEMENTS

The authors would like to express their gratitude to all the participants and stakeholders of Pandit Deendayal Energy University, India, for their support in this research work.

REFERENCES

- Alamsyah, T. M. S. N., Abidin, T. F., Ferdhiana, R., Dirhamsyah, M., & Chaidir, M. (2022, December 8-9). *Analysis of face data augmentation in various poses for face recognition model*. [Paper presentation]. Seventh International Conference on Informatics and Computing (ICIC), Bali, Indonesia. <https://doi.org/10.1109/ICIC56845.2022.10006997>
- Barrett, L. F., Adolphs, R., Marsella, S., Martinez, A. M., & Pollak, S. D. (2019). Emotional expressions reconsidered: Challenges to inferring emotion from human facial movements. *Psychological Science in the Public Interest*, 20(1), 1–68. <https://doi.org/10.1177/1529100619832930>
- Darwin, C. (1872). *The expression of the emotions in man and animals*. John Murray. <https://doi.org/10.1037/10001-000>
- Devi, B., & Preetha, M. M. S. J. (2023). A descriptive survey on face emotion recognition techniques. *International Journal of Image and Graphics*, 23(1), Article 2350008. <https://doi.org/10.1142/S0219467823500080>
- Ekman, P. (2009). Darwin's contributions to our understanding of emotional expressions. *Philosophical Transactions of the Royal Society B: Biological Sciences*, 364(1535), 3449–3451. <https://doi.org/10.1098/rstb.2009.0189>
- Ekman, P., & Friesen, W. V. (1971). Constants across cultures in the face and emotion. *Journal of Personality and Social Psychology*, 17(2), 124–129. <https://doi.org/10.1037/h0030377>

- Garcia-Garcia, J. M., Penichet, V. M. R., Lozano, M. D., & Fernando, A. (2022). Using emotion recognition technologies to teach children with autism spectrum disorder how to identify and express emotions. *Universal Access in the Information Society*, 21(4), 809–825. <https://doi.org/10.1007/s10209-021-00818-y>
- Jaymon, N., Nagdeote, S., Yadav, A., & Rodrigues, R. (2021, February 19-20). *Real-time emotion detection using deep learning*. [Paper presentation]. International Conference on Advances in Electrical, Computing, Communication and Sustainable Technologies (ICAECT), Bhilai, India. <https://doi.org/10.1109/ICAECT49130.2021.9392584>
- Mandal, M. K. (2004). *Emotion*. Affiliated East-West Press.
- Ortony, A. (2022). Are all “basic emotions” emotions? A problem for the (basic) emotions construct. *Perspectives on Psychological Science*, 17(1), 41–61. <https://doi.org/10.1177/1745691620985415>
- Pabst, A., Bollen, Z., Masson, N., Billaux, P., Timary, P. D., & Maurage, P. (2023). An eye-tracking study of biased attentional processing of emotional faces in severe alcohol use disorder. *Journal of Affective Disorders*, 323, 778–787. <https://doi.org/10.1016/j.jad.2022.12.027>
- Salve, P. (2022, October 3). *India's suicide rate has increased. But is it because of better reporting or rising distress?* Croll.in. <https://scroll.in/article/1034045/indias-suicide-rate-has-increased-but-is-it-because-of-better-reporting-or-rising-distress>
- Saini, A., Khaparde, A. R., Kumari, S., Shamsher, S., Joteeswaran, J., & Kadry, S. (2023). An investigation of machine learning techniques in speech emotion recognition. *Indonesian Journal of Electrical Engineering and Computer Science*, 29(2), Article 875. <https://doi.org/10.11591/ijeecs.v29.i2.pp875-882>
- Shank, D. B. (2014). Technology and emotions. In J. E. Stets & J. H. Turner (Eds.), *Handbook of the sociology of emotions: Volume II* (pp. 511–528). Springer. https://doi.org/10.1007/978-94-017-9130-4_24
- Siam, A. I., Soliman, N. F., Algarni, A. D., El-Samie, F. E. A., & Sedik, A. (2022). Deploying machine learning techniques for human emotion detection. *Computational Intelligence and Neuroscience*, 2022, Article 8032673. <https://doi.org/10.1155/2022/8032673>
- Song, S., Zhao, S., Gao, Z., Lu, M., Zhang, M., Gao, S., & Zheng, Y. (2022). Influence of affective verbal context on emotional facial expression perception of social anxiety. *International Journal of Psychophysiology*, 181, 141–149. <https://doi.org/10.1016/j.ijpsycho.2022.09.002>
- Song, Z. (2021). Facial expression emotion recognition model integrating philosophy and machine learning theory. *Frontiers in Psychology*, 12, Article 759485. <https://doi.org/10.3389/fpsyg.2021.759485>
- Subhashini, R., & Niveditha, P. R. (2015). Analyzing and detecting employee's emotions for amelioration of organizations. *Procedia Computer Science*, 48, 530–536. <https://doi.org/10.1016/j.procs.2015.04.131>

Review Article

The Compatibility of Cement Bonded Fibreboard Through Dimensional Stability Analysis: A Review

Nurul Huda Azmi*, Nik Mohd Zaini Nik Soh and Hasniza Abu Bakar

Faculty of Civil Engineering and Built Environment, Universiti Tun Hussein Onn Malaysia, 86400 Parit Raja, Batu Pahat, Johor Darul Takzim, Malaysia

ABSTRACT

Natural fibre in cement matrix was used to reinforce, increase tensile strength, and protect against matrix cracking. The various properties of the matrix, which were introduced by the shrinkage and thermal stresses, can be attributed to the microcracks on the composites. The composites experienced significant negative changes due to the spread of microcracks. Changes in moisture have an impact on the dimensional stability of cement-bonded fibreboards. The increasing moisture content caused the expansion of cement-bonded fibreboard, whereas shrinkage was caused by the moisture being evaporated. Since natural fibres connect ineffectively with the cement matrix due to their hydrophilicity, fibre-cement composites are dimensionally unstable. Hot water treatments operate by clearing the fibre's surface of volatile compounds, impurities, and waxy elements and facilitating water absorption. Numerous variables, including the mixing ratio, the targeted density, and the pre-treatment technique used on natural fibre, influence the dimensional stability of cement-bonded fibreboard. The compatibility of cement-bonded fibreboard increases with increasing cement/fibre mixing ratio, density of cement-bonded fibreboard, hot water treatment temperature and duration.

Keywords: Cement bonded fibreboard, dimensional stability, hot water treatment, mechanical properties, physical properties

ARTICLE INFO

Article history:

Received: 27 July 2023

Accepted: 01 February 2024

Published: 08 August 2024

DOI: <https://doi.org/10.47836/pjst.32.5.03>

E-mail addresses:

nurulhudaazmi99@gmail.com (Nurul Huda Azmi)

nikzaini@uthm.edu.my (Nik Mohd Zaini Nik Soh)

hasniza@uthm.edu.my (Hasniza Abu Bakar)

* Corresponding author

INTRODUCTION

Natural plant fibres in cement composites have been shown in numerous studies to increase tensile strength, toughness, crack and impact resistance, and ductility (Zhao et al., 2019). Wax, nitrogenous materials, and inorganic salts are among the non-structural

extractives that are present in the fibre (Surid et al., 2021). The structural composition is unstable because of moisture and poor adhesion in the fibre surrounding the matrix (Amin et al., 2022; Geremew et al., 2021). According to Viju and Thilagavathi (2022), hot water treatment is a cost-effective and environmentally friendly fibre modification treatment since the process simply uses fibre and water as a medium. Scapini et al. (2021) studies defined that the hot water treatment application can enhance hemicellulose dissolution, boost the yield of procedures such as enzymatic hydrolysis, and prevent the ability to recover. Many factors influenced the dimensional stability of the composite, especially the mixing ratio (Adelusi, Adedokun et al., 2019; Frybort et al., 2008), density (Adelusi, Olaoye et al., 2019; Ogunjobi, Temitope et al., 2019), and hydrophilicity of fibre that required suitable fibre treatment (Ibrahim et al., 2016; Zuraidda et al., 2018). Therefore, this study will cover the compatibility of cement-bonded fibreboard correlated to dimensional stability composites.

DIMENSIONAL STABILITY ANALYSIS

Dimensional Stability of Cement Bonded Fibreboard Based on the Mixing Ratio

Frybort et al. (2008) stated that the compatible properties of the composites rely on the composition of cement and fibre. Earlier researchers have conducted numerous studies on the effect of the cement/fibre ratio on the compatibility of cement-bonded fibreboard. Atoyebi et al. (2018) mentioned that the Thickness Swelling (TS) and Water Absorption (WA) results play important roles in the dimensional stability of composite final performance. Figures 1 and 2 show the effect of different cement/fibre mixing ratios of the cement-bonded fibreboard on the TS and WA percentage values. Based on the charts, the TS and WA shared by previous researchers show the same result pattern where when the cement/fibre mixing ratio increases, the percentage mean value of TS and WA of the composites decreases (Adelusi, Adedokun et al., 2019; Adelusi, Olaoye et al., 2019; Ogunjobi, Ajibade et al., 2019; Dadile et al., 2019; Budiman et al., 2021; Fabiyi, 2004; Sotannde et al., 2012; Castro et al., 2018; Ogunjobi, Temitope et al., 2019).

According to Figures 1 and 2, a study by Ogunjobi, Ajibade et al. (2019) found that the higher fibre content and low cement content (cement/fibre mixing ratio of 1:3) produce excessive TS (16.67%) and WA (135.76%) values. It can also be highlighted that the same mixing ratio (1:1) produces a high percentage of TS and WA values, which are 11.67% and 118.07%. The rapid changes in the TS and WA values are shown by Dadile et al. (2019) and Sotannde et al. (2012) studies, from the 2:1 and 2.5:1 mixing ratios to 3:1 and 3.5:1 mixing ratios. Based on the chart, the value of TS was found on the 2:1 mixing ratio (17% and 5.28%) and lessened drastically to the 3.5:1 mixing ratio (4.01% and 1.96%). The same goes for the WA values, which decreased from 10.29% and 48.19% to 5.86% and 14.82%. This situation is supported by Abdullah et al. (2011) and Singh et al. (2018) studies that the low cement/fibre mixing ratio causes the higher fibre to absorb more water.

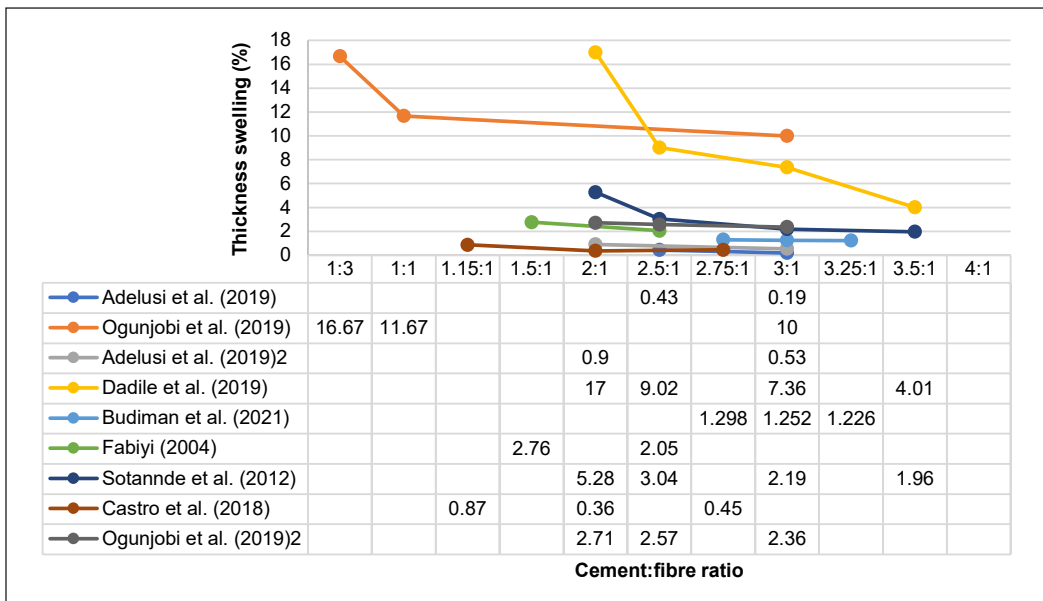


Figure 1. Previous studies on the effect of cement/fibre mixing ratio on TS

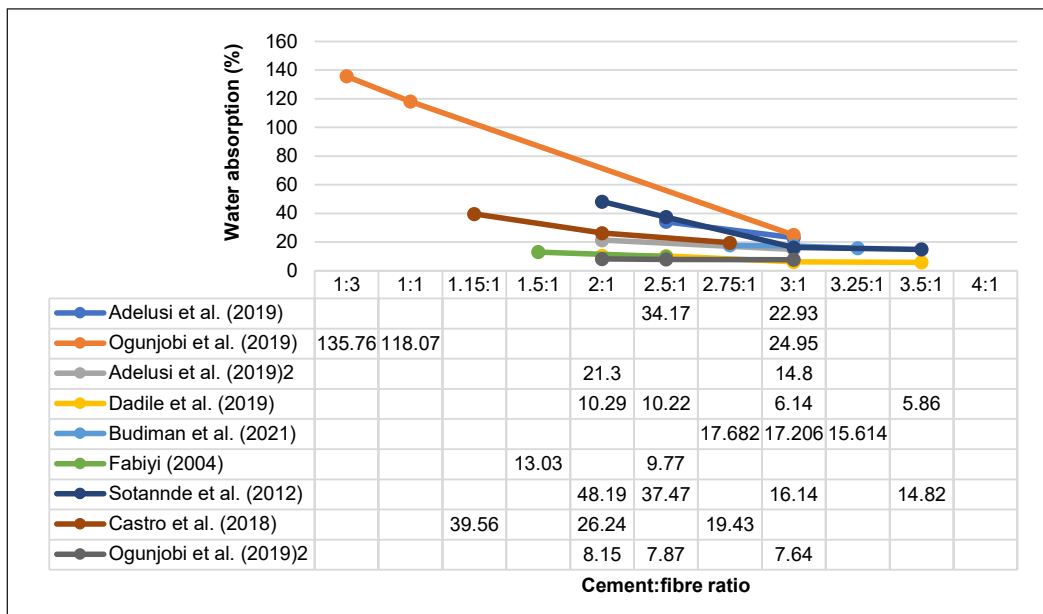


Figure 2. Previous studies on the effect of cement/fibre mixing ratio on WA

This outcome results from the materials' compatibility, which prevents void spaces from allowing the materials to absorb water. Water may not be able to enter the air void spaces because of the complete coating between the cement and natural fibre (Adelusi, Adedokun et al., 2019). Figures 3 and 4 show the previous study conducted to determine

the relationship between the cement/fibre mixing ratio and the mechanical properties of cement-bonded fibreboard through Modulus of Elasticity (MOE) and Modulus of Rupture (MOR) testing. As pictured in the charts below, each study on different mixing ratios applied produced the same conclusion: the increasing cement/fibre mixing ratio generates high mechanical performance on the composites. Comparable to the physical properties results shown above, Ogunjobi, Ajibade et al. (2019) found that the low fibre content (1:3) and same mixing ratio (1:1) resulted in the lowest MOE (23.39 N/mm² and 76.99 N/mm²) and MOR (0.20 N/mm² and 0.63 N/mm²) values. This condition shows that the cement-

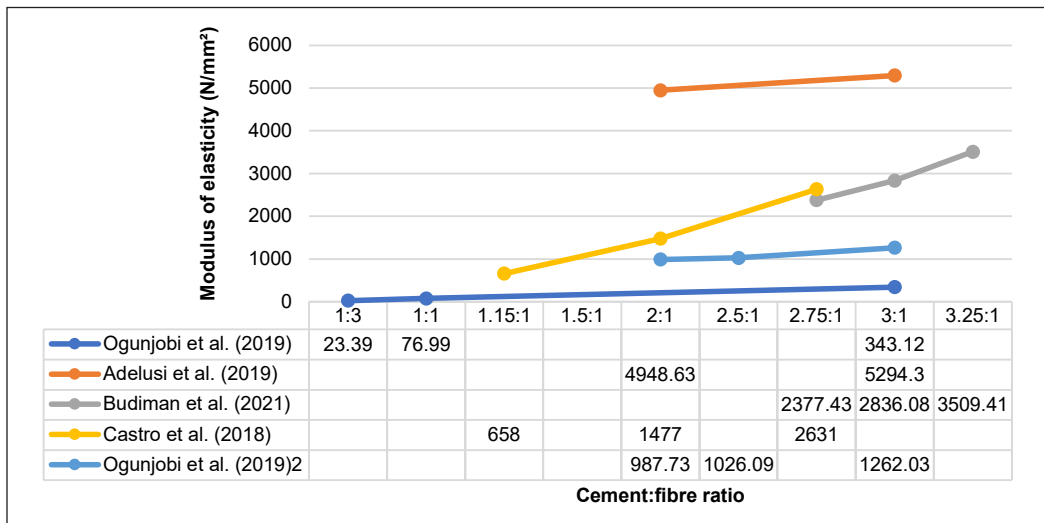


Figure 3. Previous studies on the effect of cement/fibre mixing ratio on MOE

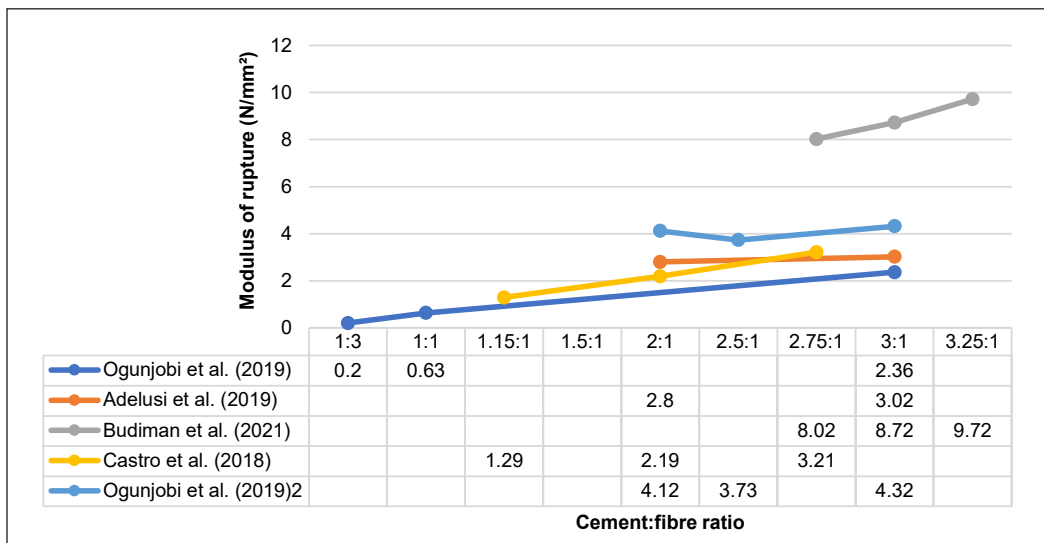


Figure 4. Previous studies on the effect of cement/fibre mixing ratio on MOR

bonded fibreboard has higher fibre content and only produces dimensionally unstable and incompatible composites.

Although each study shows different values of mechanical properties due to the type of fibre, treatment, and fabrication procedure used, the flow of high mixing ratio generates high strength composite can be analysed. The cement-bonded fibreboard with a cement/fibre ratio of 3.25:1 found by Budiman et al. (2021) reveals the higher MOE (3509.41 N/mm²), MOR (9.72 N/mm²), and IB (7.30 N/mm²) value compared to 2.75:1 and 3:1. According to Abdullah et al. (2011), the increasing fibre content will result in a decrease in compressive strength. The findings of Thong et al. (2020) shared that the flexural strength of the composite that contains a higher amount of fibre is related to a lower amount of cement matrix, which leads to a decreasing tendency of the adhesion between the fibre and cement. According to the studies, it found that the cement/fibre mixing ratio of 3.5:1 is an ideal targeted parameter in producing dimensional stable and highly compatible cement-bonded fibreboard due to the results obtained by Sotannde et al. (2012) and Dadile et al. (2019).

Dimensional Stability of Cement Bonded Fibreboard Based on Density

Limited studies have covered the effect of density on the properties of cement-bonded fibreboard. Figures 5 and 6 show earlier research studies conducted by analysing the physical properties based on the density of the composites. According to Rahim and Yunus (2021), Ridzuan et al. (2023), Ogunjobi, Temitope et al. (2019), and Nasser (2014) studies, it was discovered that the increment of cement bonded fibreboard density generates positive results on physical properties. The mean value of the TS and WA percentages decreased when the higher density was applied to the composite. Based on Figures 5 and 6, it can be highlighted that all the composite with a density of 1300 kg/m³ shows the lowest value

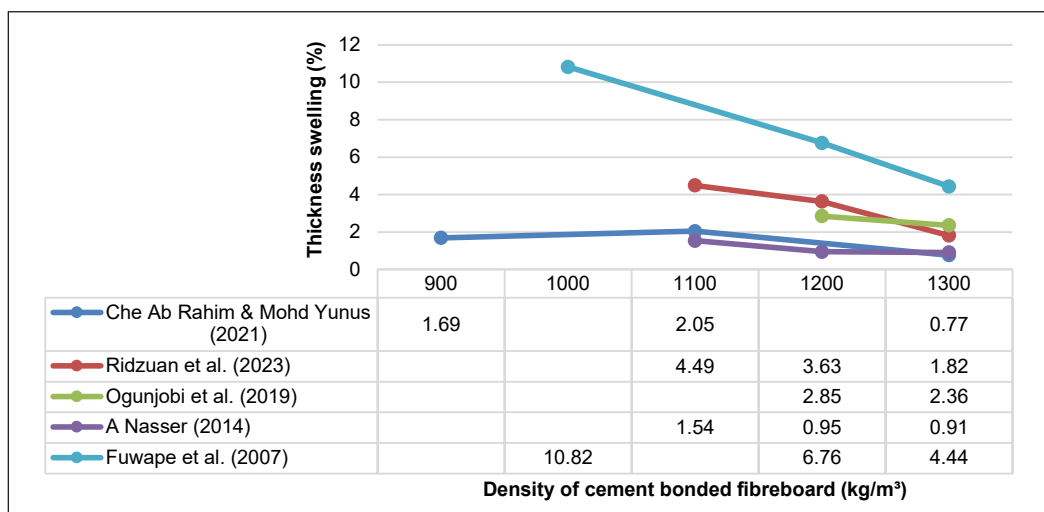


Figure 5. Previous studies on the effect of density on TS

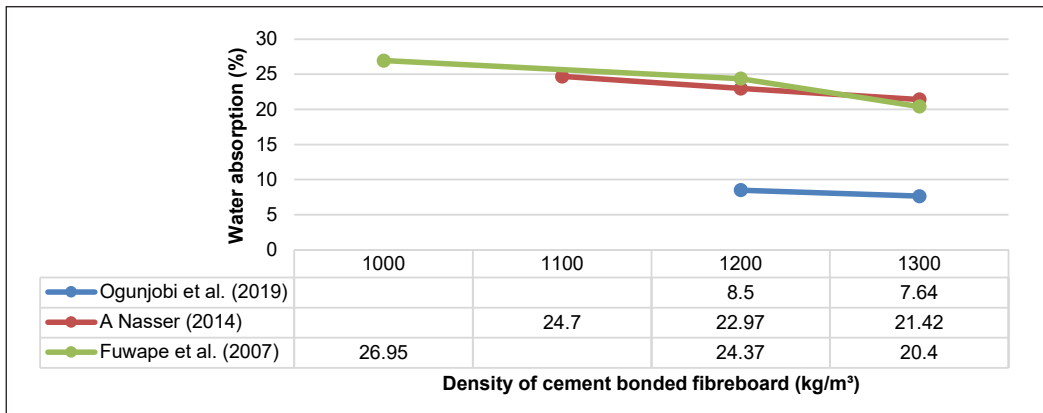


Figure 6. Previous studies on the effect of density on WA

from each study. TS results generate a major reduction from low density (1.69%, 4.49%, 2.85%, 1.54%, and 10.82%) to higher density (0.77%, 1.82%, 2.36%, 0.91%, and 4.44%). The same goes for the mean percentage value of WA, where the percentage of moisture absorbed in the composite reduced from 8.50%, 24.70%, and 26.95% to 7.64%, 21.42%, and 20.40%.

Ogunjobi, Temitope et al. (2019) found that this situation is related to the small or no void between the fibre and cement matrixes for the water to retain when the higher density is applied due to a higher board compaction ratio. The porosity in cement-bonded fibreboard decreases with the degree of coverage as density rises (Rahim & Yunus, 2021). The mechanical properties in Figures 7 and 8 also show the same constant pattern in the researcher’s studies. Higher density, such as 1300 kg/m³, generates the highest MOE and MOR value. According to the bar charts, cement-bonded fibreboard with a density of 1300 kg/m³ produces high MOE and MOR, especially in a study by Fuwape et al. (2007) (5300 N/mm² and 11.55 N/mm²) and Nasser (2014) (4142 N/mm² and 12.28 N/mm²). At the same time, Yel et al. (2011) study shows a major difference between the MOE (1199 N/mm² and 2979 N/mm²) and MOR (3.45 N/mm² and 10.99 N/mm²) values between density 800 kg/m³ and 1200 kg/m³. This result clearly showed the increment of density related to the stiffness and strength of the composite.

Fuwape et al. (2007) shared that the enhancement of mechanical properties of the composites when the higher density is applied can be elaborated by the tight compaction between the fibre. Therefore, the fibre helps prevent the brittle cement from fracturing and delaying the bond-line failure, increasing the flexural stiffness of the bonded fibreboard. According to Ogunjobi, Temitope et al. (2019), a cement-bonded fibreboard with a higher density avoids hydrostatic stress against the bonds and has less or no void space for water to retain in it. It was also acknowledged that increasing board density might make heavier, stronger, and stiffer boards. This result also can be supported by Akasah et al. (2019),

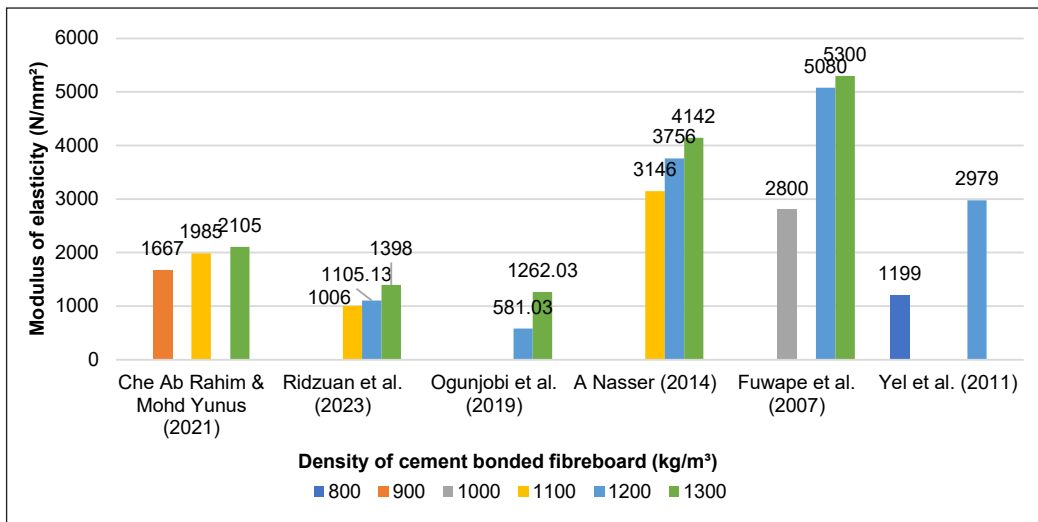


Figure 7. Previous studies on the effect of density on MOE

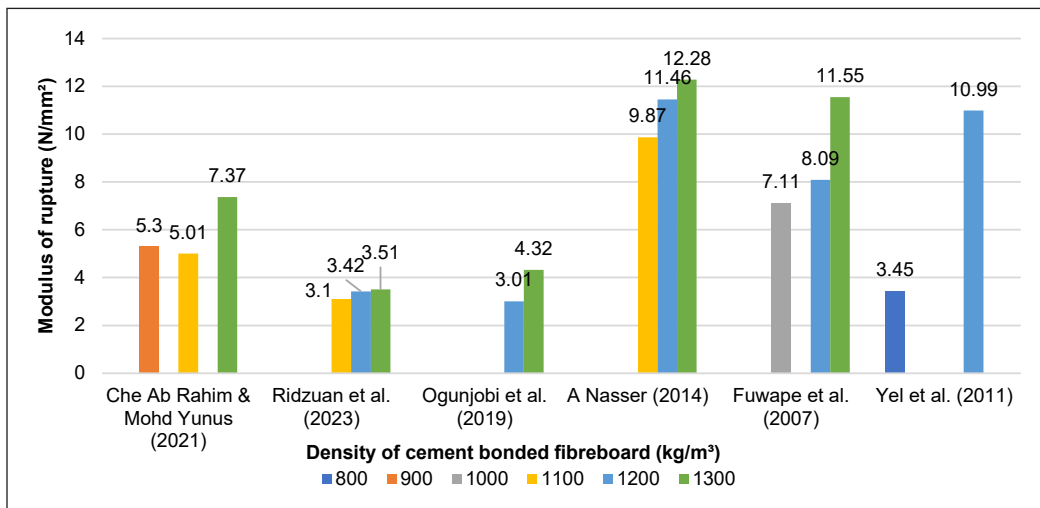


Figure 8. Previous studies on the effect of density on MOR

Maynet et al. (2023), Hassan et al. (2021), and Peter et al. (2020) studies which chose 1300 kg/m³ as the targeted density for fabricating the cement bonded fibreboard due to the optimum density in producing compatible cement bonded fibreboard.

Dimensional Stability of Cement Bonded Fibreboard Based on Hot Water Pre-treatment

According to Viju and Thilagavathi (2022), hot water treatments eliminate volatile substances, impurities, and waxy substances from the fibre's surface and improve water absorption. Figure 9 shows the scanning electron microscopy (SEM) analysis for untreated

and hot water-treated fibre. Based on Figure 9, the volatile substances and extractives were removed after applying hot water treatment. The residue on the surface of untreated fibre in Figure 9(a) was seen compared to the treated fibre in Figure 9(b). Futami et al. (2021) stated that the treated fibre produced a rougher and cleaner surface, which gave an advantage for the adhesion process in cementitious composite due to the removal of lignin molecules and deposition on the fibre's surface. Momoh et al. (2020) stated that cracking occurs on the cross-section of the fibre after the hot water treatment, as shown in Figures 9(c) and 9(d) happens due to the pressure build-up from the temperature of hot water treatment (100°C) between the fibre which produces radial cracking. Figures 9(e) and 9(f) show the SEM of the fibre's cross-section with magnifications of 500×. According to Olonade and Junior (2023), the treated fibre produced more compacted lumens than the untreated fibre, which generates firmer and more stable fibre. These factors can enhance the binding between cement and natural fibre and produce composites with outstanding physical and mechanical properties.

The dimensional stability of cement-bonded fibreboard can be analysed based on the composite's physical and mechanical properties. Figure 10 shows the TS results on the cement-bonded fibreboard, which generates a major difference between the untreated and hot water-treated fibre. The relationship between the TS and hot water treatment is very clear, where the hot water treatment applied with higher temperatures produces a low TS percentage. Earlier researchers supported that the hot water treatment influences the TS

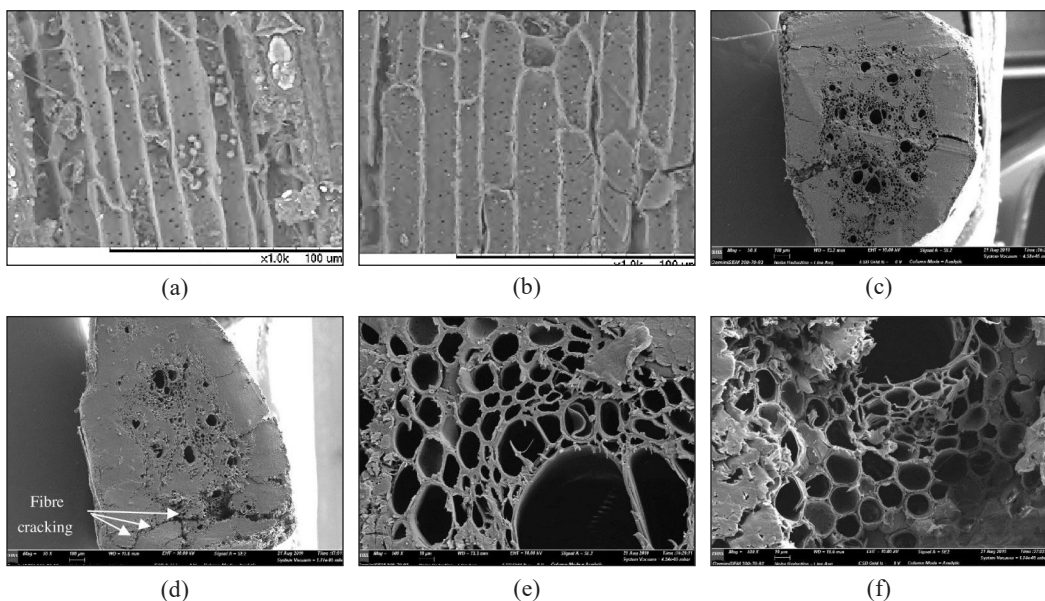


Figure 9. SEM analysis: (a) longitudinal section of untreated fibre; (b) longitudinal section of hot water treated fibre; (c) cross-section of untreated fibre 50×; (d) cross-section of hot water treated 100×; (e) cross-section of untreated fibre 500×; and (f) cross-section of hot water treated fibre 500×

Source: Cabral et al., 2018; Momoh et al., 2020

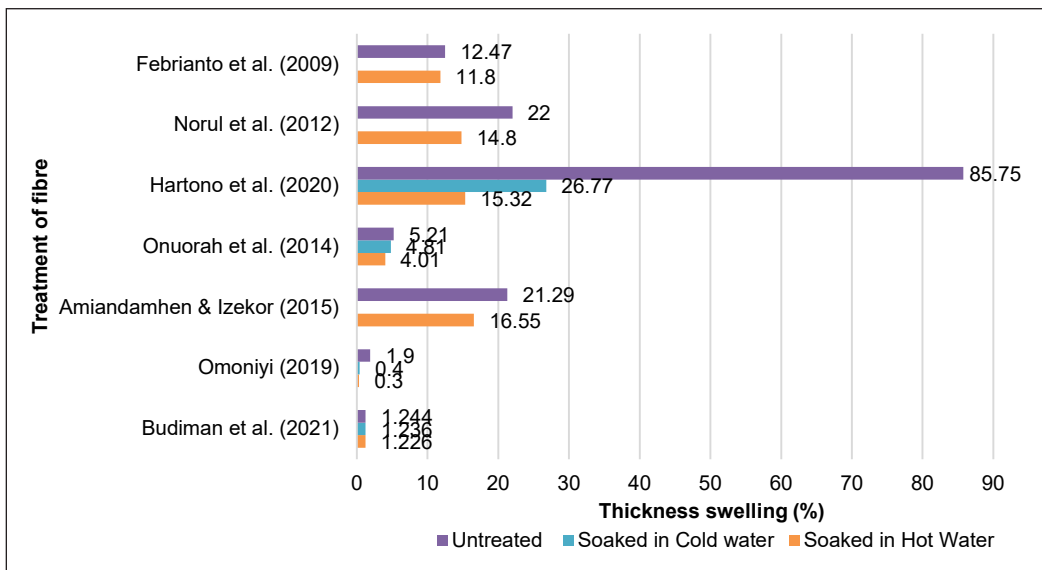


Figure 10. Previous studies on TS of cement-bonded fibreboard with untreated, cold water-treated, and hot water-treated fibre

performance of cement-bonded fibreboard whereby when the temperature of hot water treatment increases, the TS of cement-bonded fibreboard decreases (Amiandamhen & Izezor, 2015; Budiman et al., 2021; Febrianto et al., 2009; Hartono et al., 2018; Izani et al., 2012; Omoniyi, 2019; Onuorah et al., 2014).

The consistent pattern of decreasing TS performance between the untreated, cold water treated, and hot water treated fibre is remarked. The untreated fibre has the highest value of TS compared to the treated fibre, which is the fibre soaked in hot water and has the lowest value of TS. Izani et al. (2012) highlighted that the reduction of TS is related to the degradation of hemicellulose and lignin content during hot water treatment, where these substances have a high ability for water absorption. The low percentage of TS value shows that the cement-bonded fibreboard is sturdy where the composites do not easily swell and absorb water. Therefore, the removal of the hydroxyl group is related to the swelling of the cement-bonded fibreboard. These show that the hydroxyl group in the fibre was ultimately removed when the fibre was soaked in hot water.

Earlier studies had discovered the relationship between the WA of cement-bonded fibreboard and the effect of the application of hot water-treated fibre compared to untreated fibre. Based on the results of the previous study, as shown in Figure 11, it was found that the higher the temperature of hot water treatment applied, the lower the WA percentage value recorded (Amiandamhen & Izezor, 2013; Amiandamhen & Izezor, 2015; Budiman et al., 2021; Febrianto et al., 2009; Izani et al., 2012; Omoniyi, 2019). Budiman et al. (2021) and Omoniyi (2019) displayed that the fibre treated with cold water (16.774% and 14.6%) has a slightly lower WA percentage value than the fibre soaked in hot water (15.614% and

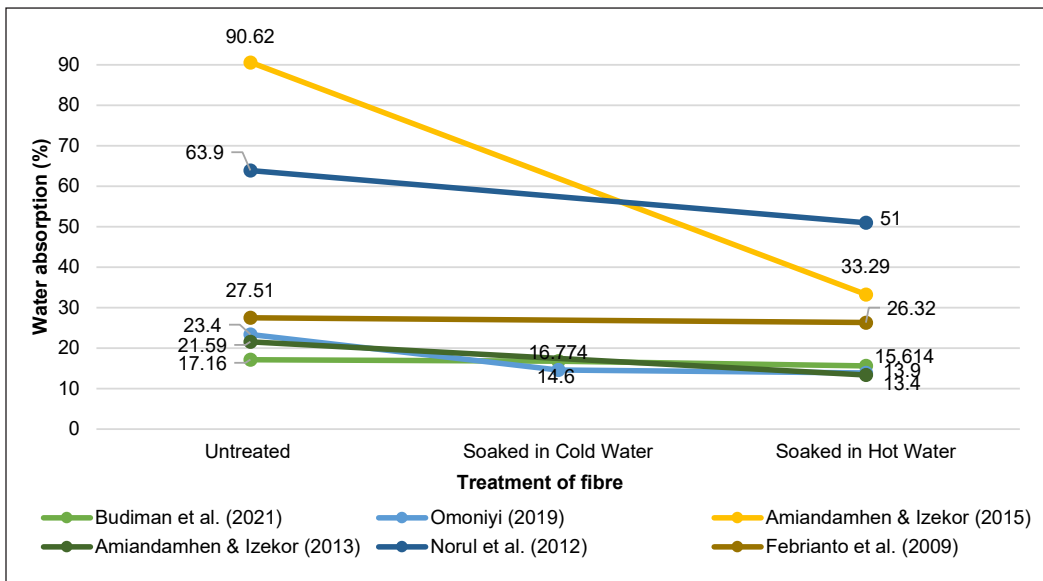


Figure 11. Previous studies on WA of cement bonded fibreboard with untreated, cold water treated, and hot water treated fibre

13.9%) with a temperature of 100°C. Eventually, the reduction of WA percentage value in the cement-bonded fibreboard is related to the adhesion between the matrix and fibre after treatment, leading to the presence of capillaries (pores) that had a high suction effect on the composite structure for better bonding (Halip et al., 2019).

For cementitious composites, the amount of WA decreases as the TS value decreases. The reduction of TS and WA generates more dimensional stable cement-bonded fibreboard by enhancing the bonding between the fibre and cement (Amiandamhen & Izezor, 2015). The higher the temperature of hot water applied to the fibre, the higher the content of extractive substances removed. Removing lignin and hemicellulose from the fibre helps the binding composites penetrate easily and improves the adhesion between the fibre and cement. The water molecules are unable to be absorbed in the fibre easily because it is covered with cement. However, the water is still able to penetrate between the fibre pores due to the capillary effect (Zalinawati et al., 2020). The presence of water in the cell wall can also be carried in the bonding tissues of composites (Hartono et al., 2018).

It was noticed through the earlier research shown in Figures 12 and 13 that there is a similar pattern where the cement-bonded fibreboard pre-treated with hot water has a higher MOE and MOR value compared to the untreated fibre. The untreated fibre of cement bonded fibreboard had a mean value in a range of 10.3 N/mm² to 9111 N/mm² (MOE) and 0.45 N/mm² to 50.12 N/mm² (MOR) compared to the hot water treated fibre which shows higher range value 1275.75 N/mm² to 14736 N/mm² (MOE) and 2.31 N/mm² to 67.89 N/mm² (MOR). This situation can be related to the study of Zheng et al. (2023), whereby the

treatment applied to fibre led to an improvement in MOE (stiffness) and MOR (strength) of the cement-bonded fibreboard. The increased crystallinity in fibre, removal of extractive, and rearrangement of cellulose molecules after the treatment increased the fibre’s stiffness and generated high flexural properties. The treated fibre and cement matrix leads to higher strength and more rigid composite due to improved linking structures.

Figure 14 shows earlier studies’ internal bonding (IB) results, which compare untreated and hot water-treated fibre in cement-bonded fibreboard. A similar trend was observed according to the IB mean value where the hot water treatment improves the

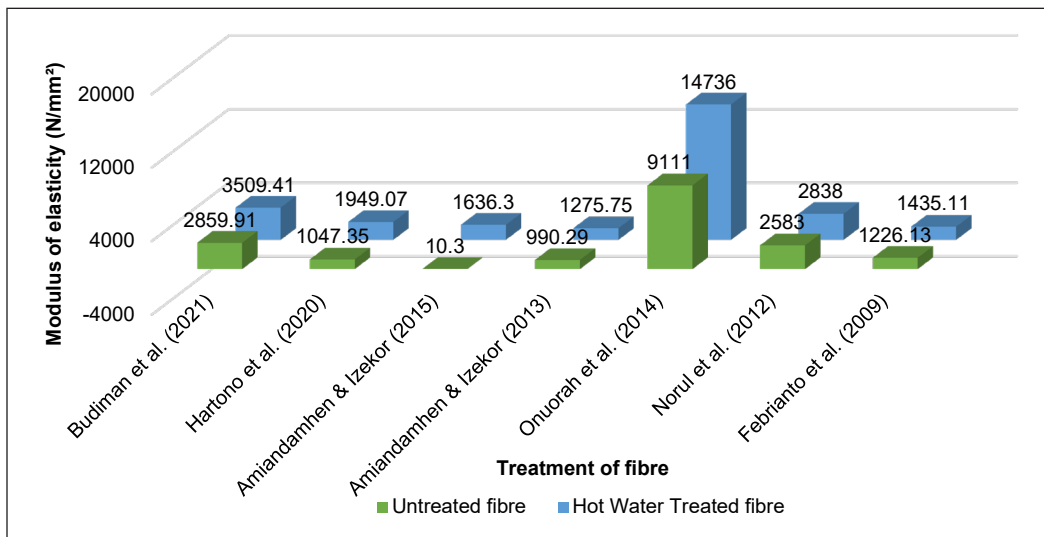


Figure 12. Previous studies on MOE of cement-bonded fibreboard with untreated and hot water-treated fibre

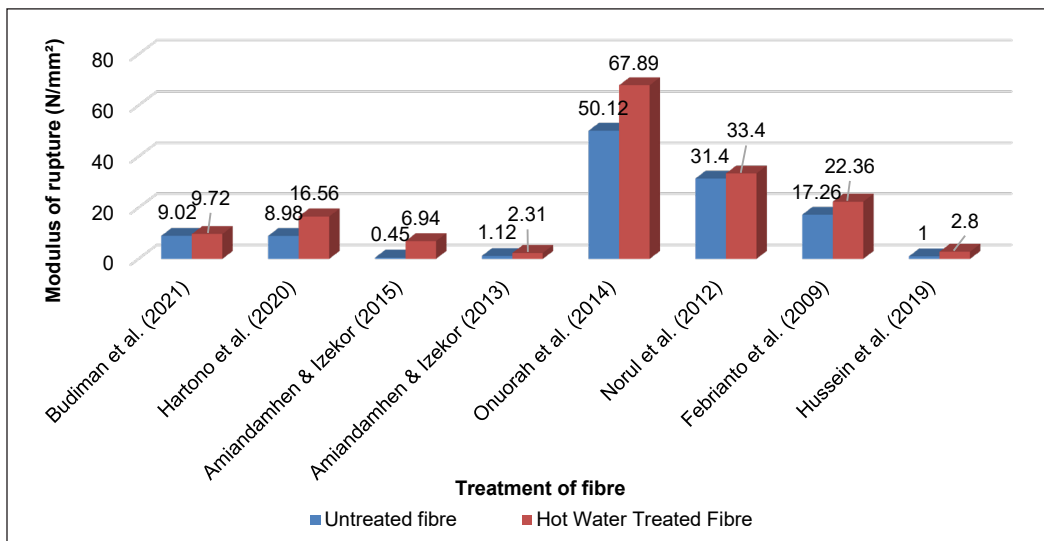


Figure 13. Previous studies on MOR of cement-bonded fibreboard with untreated and hot water-treated fibre

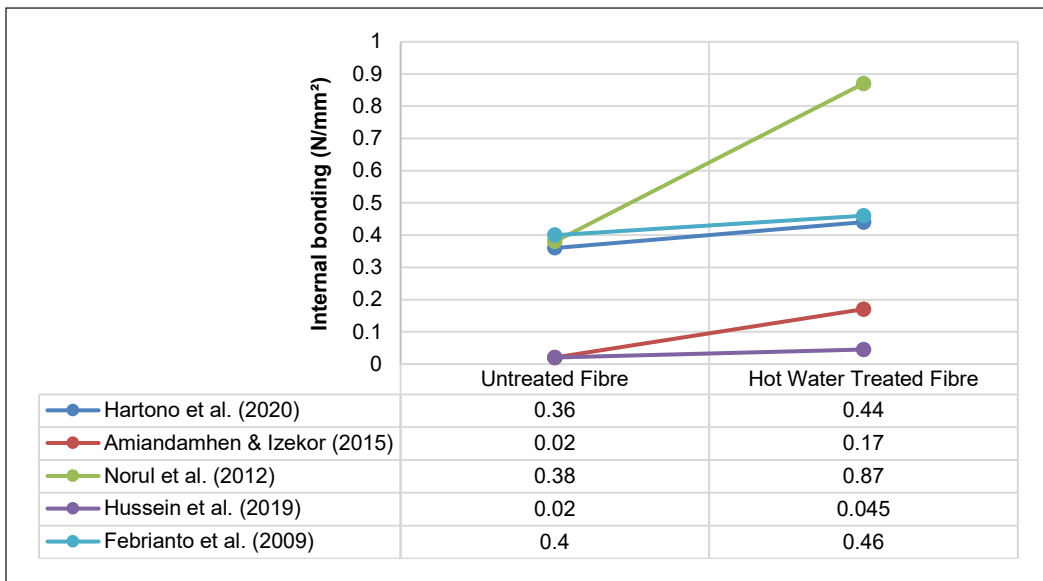


Figure 14. Previous studies on IB of cement-bonded fibreboard with untreated and hot water-treated fibre

mechanical properties of composites through internal bonding ability (Amiandamhen & Izekor, 2015; Febrianto et al., 2009; Hartono et al., 2018; Hussein et al., 2019; Izani et al., 2012). Amiandamhen and Izekor (2015) explained that the positive results from hot water treatment on fibre are related to the fibrillation of the fibre surface throughout the treatment process, creating great bonding on the fibre and matrixes. The hot water treatment helps enhance the mechanical properties of composites caused by fibre particle properties and changes in chemical composition (Iswanto et al., 2018). The strength of the matrix interlocking may decrease as extractive content rises. The reduced mechanical strength was also caused by increased adhesive failure due to the increased extractive level (Hartono et al., 2018).

It is proven by previous studies on physical and mechanical performance that the hot water treatment is an effective treatment that can be applied to the fibre to produce more dimensionally stable and compatible cement-bonded fibreboard. Omoniyi (2019) found that the cement-bonded composites pre-treated with 100°C of hot water produced more compatible results compared to fibre treated with 60°C of hot water, cold water, and untreated fibre. Based on the outcome, the compatibility of the composite is shown by the reduction of WA and TS values from untreated fibre to the hot water-treated fibre with the highest temperature. The untreated fibre generates the highest mean value of WA and TS (23.4%–26.2% and 1.9%–2.5%), while the cold water-treated fibre produces 14.6%–17.9% of WA and 0.4%–0.9% of TS. When the fibre was treated with hot water, the WA and TS decreased, followed by the temperature where 14.2%–16.2%, 0.3%–0.6% for 60°C of hot water and 13.9%–15.4%, 0.3%–0.6% for 100°C.

Most researchers are using hot water treatment with a temperature of 100°C as a pre-treatment method to remove the water-soluble sugar and hemicellulose in producing more compatible and dimensional stable cement bonded fibreboard (Amiandamhen et al., 2021; Dadile et al., 2019; Hassan, 2018; Ogunjobi, Ajibade et al., 2019). Other researchers' application and performance results of hot water treatment at 100°C have supported Omoniyi's (2019) research that this temperature is the optimum temperature for stable and high-strength composites. The duration of the pre-treatment method also played an important role in removing the extractives and hemicellulose content from the fibre surface. Drpić et al. (2022) conducted a study of the difference in time applied (30 minutes and 60 minutes) in using the hot water treatment (100°C) on a wooden chip. According to the findings, the cellulose content of the wooden chip after the hot water treatment for 60 minutes is 48.68%, which is increased compared to 30 minutes (47.61%) and untreated wooden chips (46.12%).

The increase of cellulose content for wooden chips treated with hot water for 60 minutes was discussed, resulting from the lower degradation reactions of wood tissues. Elmoudnia et al. (2023) also found that the fibre treated with hot water for 60 minutes has the highest crystallinity index than those treated for 15 and 30 minutes. In addition, the fibre treated for 60 minutes produced a rough surface, which demonstrated the elimination of amorphous components (Elmoudnia et al., 2023). Based on the mentioned studies, it can be found that higher temperature and duration of hot water treatment on fibre helps remove higher extractive content and increase the cellulose content, which benefits composite performance. Therefore, hot water treatment with controlled temperature and duration, such as 100°C for 60 minutes, is the ideal parameter that can be applied to produce compatible and dimensional stable cement-bonded fibreboard.

CONCLUSION

The dimensional stability of cement-bonded fibreboard is influenced by many factors, mainly the mixing ratio, the targeted density, and the method of pre-treatment of natural fibre. The higher mixing ratio and density produced a more compatible cement-bonded fibreboard. Based on the review, the mixing ratio of cement/fibre is 3.5:1, and a targeted density of 1300 kg/m³ may produce a compatible cement-bonded fibreboard. The other important aspect of dimensional stability in cement-bonded fibreboard is the natural fibre treatment method. The hot water treatment is the most sustainable, environmentally friendly, and cost-effective treatment compared to the other methods. The reviews show that the higher the temperature and duration applied to the hot water treatment, the higher the compatibility of cement-bonded fibreboard. The temperature of 100°C and 60 minutes of treatment are the ideal parameters for conducting the hot water treatment for producing cement-bonded fibreboard.

ACKNOWLEDGMENTS

This research was supported by Universiti Tun Hussein Onn Malaysia (UTHM) through GPPS (vot Q291). The authors thank the Faculty of Civil Engineering and Built Environment, Universiti Tun Hussein Onn Malaysia, for using the facilities.

REFERENCES

- Abdullah, A., Jamaludin, S. B., Anwar, M. I., Noor, M. M., & Hussin, K. (2011). Assessment of physical and mechanical properties of cement panel influenced by treated and untreated coconut fiber addition. *Physics Procedia*, 22, 263-269. <https://doi.org/10.1016/j.phpro.2011.11.042>
- Adelusi, E. A., Adedokun, S. A., & Adelusi, F. T. (2019). Dimensional stability of cement bonded boards produced from *Thaumatococcus Danielli* stalk. *Journal of Material Science Research and Reviews* 4(2), Article 51497.
- Adelusi, E. A., Olaoye, K. O., & Adebawo, F. G. (2019). Strength and dimensional stability of cement bonded boards manufactured from mixture of *Ceiba Pentandra* and *Gmelina Arborea* Sawdust. *Journal of Engineering Research and Reports* 8(1), Article 51983. <https://doi.org/10.9734/JERR/2019/v8i116980>
- Akasah, Z. A., Soh, N. M. Z. N., Dullah, H., Aziz, A. A., & Aminudin, E. (2019). The influence of oil palm empty fruit bunch fibre geometry on mechanical performance of cement bonded fibre boards. *International Journal of Mechanical Engineering and Robotics Research*, 8(4), 547-552. <https://doi.org/10.18178/ijmerr.8.4.547-552>
- Amiandamhen, S. O., & Izekor, D. N. (2015). Assessment of the physical and mechanical properties of treated Kenaf fibre cement composites. *Ife Journal of Technology*, 23(2), 14-17.
- Amiandamhen, S., & Izekor, D. (2013). Effect of wood particle geometry and pre-treatments on the strength and sorption properties of cement-bonded particle boards. *Journal of Applied and Natural Science*, 5(2), 318-322.
- Amiandamhen, S. O., Agwu, C. U., & Ezenwaegbu, P. N. (2021). Evaluation of cement-bonded particleboards produced from mixed sawmill residues. *Journal of the Indian Academy of Wood Science*, 18(1), 14-19. <https://doi.org/10.1007/s13196-021-00273-5>
- Amin, M. N., Ahmad, W., Khan, K., & Ahmad, A. (2022). A comprehensive review of types, properties, treatment methods and application of plant fibres in construction and building materials. *Materials*, 15(12), Article 4362. <https://doi.org/10.3390/ma15124362>
- Atoyebi, O. D., Awolusi, T. F., & Davies, I. E. (2018). Artificial neural network evaluation of cement-bonded particle board produced from red iron wood (*Lophira alata*) sawdust and palm kernel shell residues. *Case Studies in Construction Materials*, 9, Article e00185. <https://doi.org/10.1016/j.cscm.2018.e00185>
- Budiman, I., Sumarno, A., Prasetyo, A. M., Widodo, E., Akbar, F., Subiyanto, B., & Nugroho, A. (2021). The properties of cement boards reinforced with coconut coir fibre (*Cocos nucifera*) as building materials. *In IOP Conference Series: Earth and Environmental Science*, 762(1), Article 012074. <https://doi.org/10.1088/1755-1315/762/1/012074>

- Cabral, M. R., Nakanishi, E. Y., Santos, V. D., Palacios, J. H., Godbout, S., Savastano, H., & Fiorelli, J. (2018). Evaluation of pre-treatment efficiency on sugarcane bagasse fibers for the production of cement composites. *Archives of Civil and Mechanical Engineering*, 18, 1092-1102. <https://doi.org/10.1016/j.acme.2018.02.012>
- Castro, V., Parchen, C., & Iwakiri, S. (2018). Particle sizes and wood/cement ratio effect on the production of vibro-compacted composites. *Floresta e Ambiente*, 25, Article e20150213. <https://doi.org/10.1590/2179-8087.021315>
- Dadile, A. M., Sotannde, O. A., & Alao, J. S. (2019). Physico-mechanical properties of cement bonded particleboards made from date palm fibres (*Phoenix dactylifera*) and obeche sawdust (*Triplochyton schleroxylon*). *Journal of Materials Science Research and Reviews*, 4(4), Article JMSRR.54083.
- Drpić, A., Popović, J., Popović, M., & Điporović-Momčilović, M. (2022). Analysis of the influence of pre-treatment with liquid hot water (LHW) on the chemical composition of wooden chips. *Advanced Technologies 2022*, 11(2), 40-47. <https://doi.org/10.5937/savteh2202040D>
- Elmoudnia, H., Faria, P., Jalal, R., Waqif, M., & Saâdi, L. (2023). Effectiveness of alkaline and hydrothermal treatments on cellulosic fibres extracted from the Moroccan *Pennisetum Alopecuroides* plant: Chemical and morphological characterization. *Carbohydrate Polymer Technologies and Applications*, 5, Article 100276. <https://doi.org/10.1016/j.carpta.2022.100276>
- Fabiyi, J. S. (2004). Effects of chemical additive concentrations on strength and sorption of cement-bonded board. *Journal of Tropical Forest Science*, 16(3), 336-342.
- Febrianto, F., Royama, L. I., Hidayat, W., Bakar, E. S., Kwon, J. H., & Kim, N. H. (2009). Development of oriented strand board from acacia wood (*Acacia mangium* Willd): Effect of pretreatment of strand and adhesive content on the physical and mechanical properties of OSB. *Journal of the Korean Wood Science and Technology*, 37(2), 121-127.
- Futami, E., Shafiqh, P., Katman, H. Y. B., & Ibrahim, Z. (2021). Recent progress in the application of coconut and palm oil fibres in cement-based materials. *Sustainability*, 13(22), Article 12865. <https://doi.org/10.3390/su132212865>
- Fuwape, J. A., Fabiyi, J. S., & Osuntuyi, E. O. (2007). Technical assessment of three layered cement-bonded boards produced from wastepaper and sawdust. *Waste Management*, 27(11), 1611-1616. <https://doi.org/10.1016/j.wasman.2006.09.005>
- Frybort, S., Mauritz, R., Teischinger, A., & Müller, U. (2008). Cement bonded composites-A mechanical review. *BioResources*, 3(2), 602-626.
- Geremew, A., Winne, P. D., Demissie, T. A., & Backer, H. D. (2021). An overview of the characterization of natural cellulosic fibres. *Key Engineering Materials*, 881, 107-116. <https://doi.org/10.4028/www.scientific.net/KEM.881.107>
- Halip, J. A., Hua, L. S., Ashaari, Z., Tahir, P. M., Chen, L. W., & Uyup, M. K. A. (2019). Effect of treatment on water absorption behavior of natural fiber-reinforced polymer composites. In M. Jawaid, M. Thariq & N. Saba (Eds.) *Mechanical and Physical Testing of Biocomposites, Fibre-Reinforced Composites and Hybrid Composites* (pp. 141-156). Woodhead Publishing.

- Hartono, R., Iswanto, A. H., Sucipto, T., & Lubis, K. M. (2018). Effect of particle pre-treatment on physical and mechanical properties of particleboard made from oil palm trunk. *In IOP Conference Series: Earth and Environmental Science*, 166(1), Article 012006. <https://doi.org/10.1088/1755-1315/166/1/012006>
- Hassan, M. S. (2018). Moisture sensitivity and dimensional stability of carbonated fibre–cement composites. *Advances in Cement Research*, 30(9), 413-426. <https://doi.org/10.1680/jadcr.17.00141>
- Hasan, K. F., Horváth, P. G., & Alpár, T. (2021). Development of lignocellulosic fiber reinforced cement composite panels using semi-dry technology. *Cellulose*, 28, 3631-3645. <https://doi.org/10.1007/s10570-021-03755-4>
- Hussein, Z., Ashour, T., Khalil, M., Bahnasawy, A., Ali, S., Hollands, J., & Korjenic, A. (2019). Rice straw and flax fiber particleboards as a product of agricultural waste: An evaluation of technical properties. *Applied Sciences*, 9(18), Article 3878. <https://doi.org/10.3390/app9183878>
- Ibrahim, Z., Ahmad, M., Aziz, A. A., Ramli, R., Jamaludin, M. A., Muhammed, S., & Alias, A. H. (2016). Dimensional stability properties of medium density fibreboard (MDF) from treated oil palm (*Elaeis guineensis*) empty fruit bunches (EFB) fibres. *Open Journal of Composite Materials*, 6(4), 91-99. <https://doi.org/10.4236/ojcm.2016.64009>
- Iswanto, A. H., Supriyanto, Fatriasari, W., & Susilowati, A. (2018). Effect of particle treatment and adhesive type on physical, mechanical, and durability properties of particleboard made from *Sorghum Bagasse*. *IOP Conference Series: Earth and Environmental Science*, 126(1), Article 012016. <https://doi.org/10.1088/1755-1315/126/1/012016>
- Izani, M. A. N., Paridah, M. T., Astimar, A. A., Nor, M. Y. M., & Anwar, U. M. K. (2012). Mechanical and dimensional stability properties of medium-density fibreboard produced from treated oil palm empty fruit bunch. *Journal of Applied Sciences*, 12(6), 561-567.
- Maynet, W. A., Samsudin, E. M., Zaini Nik Soh, N. M., Ismail, L. H., Bakar, H. A., & Elgadi, A. (2023). Effects of fibre length on the physical properties of oil palm empty fruit bunch cement board (OPEFB-CB). *Pertanika Journal of Science & Technology*, 31(3), 1279 - 1290. <https://doi.org/10.47836/pjst.31.3.09>
- Momoh, E. O., Osofero, A. I., & Menshykov, O. (2020). Physicomechanical properties of treated oil palm-broom fibres for cementitious composites. *Journal of Materials in Civil Engineering*, 32(10), Article 04020300. [https://doi.org/10.1061/\(ASCE\)MT.1943-5533.0003412](https://doi.org/10.1061/(ASCE)MT.1943-5533.0003412)
- Nasser, R. A. (2014). Influence of board density and wood/cement ratio on the properties of wood-cement composite panels made from date palm fronds and tree prunings of buttonwood. *Alexandria Science Exchange Journal*, 35, 133-145. <https://doi.org/10.21608/asejaiqsae.2014.2588>
- Ogunjobi, K. M., Ajibade, M. A., Gakenou, O. F., & Gbande, S. (2019). Physical and mechanical properties of cement bonded particle board produced from anogeissus leiocarpus (DC.) guill and perr wood species. *African Journal of Agriculture Technology and Environment*, 8(1), 192-99.
- Ogunjobi, K. M., Temitope, B. F., Oluwaseun, F. G., Ayanleye, S. O., & Thompson, O. E. (2019). Effects of board density and mixing ratio on the physio-mechanical properties of cement bonded particle board produced from *Ceiba pentandra* Sawdust. *Agriculture and Forestry Journal*, 3(2), 58-63.
- Olonade, K. A., & Junior, H. S. (2023). Performance evaluation of treated coconut fibre in cementitious system. *SN Applied Sciences*, 5(8), Article 218. <https://doi.org/10.1007/s42452-023-05444-2>

- Omoniyi, T. E. (2019). Potential of oil palm (*elaeisguineensis*) empty fruit bunch fibres cement composites for building applications. *AgriEngineering*, 1(2), 153-163. <https://doi.org/10.3390/agriengineering1020012>
- Onuorah, E. O., Nnabuife, E. C., & Nwabanne, J. T. (2014). Potentials of *Bambusa vulgaris* grown in southeast nigerian for the manufacture of wood-cement composite panels. *Journal of Minerals and Materials Characterization and Engineering*, 2(5), Article 48500. <https://doi.org/10.4236/jmmce.2014.25041>
- Peter, P., Soh, N. N., Akasah, Z. A., & Mannan, M. A. (2020). Durability evaluation of cement board produced from untreated and pre-treated empty fruit bunch fibre through accelerating ageing. *IOP Conference Series: Materials Science and Engineering*, 713(1), Article 012019. <https://doi.org/10.1088/1757-899X/713/1/012019>
- Rahim, N. H. C. A., & Yunus, N. Y. M. (2021). Cement board filled with aged oil palm trunk strands: Effect of board densities and strand sizes. *Gading Journal of Science and Technology*, 4(2), 50-57.
- Ridzuan, M. N., Bakar, H. A., Samsudin, E. M., Soh, N. M. Z. N., & Ismail, L. H. (2023). Effects of density variation on the physical and mechanical properties of Empty Fruit Bunch Cement Board (EFBCB). *Pertanika Journal of Science & Technology*, 31(3), 1157-1172. <https://doi.org/10.47836/pjst.31.3.02>
- Scapini, T., Dos Santos, M. S., Bonatto, C., Wancura, J. H., Mulinari, J., Camargo, A. F., Klanovicz, N., Zabot, G. L., Tres, M. V., Fongaro, G., & Treichel, H. (2021). Hydrothermal pretreatment of lignocellulosic biomass for hemicellulose recovery. *Bioresource Technology*, 342, Article 126033. <https://doi.org/10.1016/j.biortech.2021.126033>
- Singh, A., Singh, J., & Ajay, S. (2018). Properties of fiber cement boards for building partitions. *International Journal of Applied Engineering Research*, 13(10), 8486-8489.
- Sotannde, O. A., Oluwadare, A. O., Ogedoh, O., & Adeogun, P. F. (2012). Evaluation of cement-bonded particle board produced from *afzelia* africanawood residues. *Journal of Engineering Science and Technology*, 7(6), 732-743.
- Surid, S. M., Maraz, K. M., Shahida, S., Ahmed, A., & Khan, R. A. (2021). A review on the properties of natural fibres and manufacturing techniques of fibre reinforced biocomposites. *Modern Concepts in Material Science*, 4(4), 1-15. <https://doi.org/10.33552/MCMS.2021.04.000592>
- Thepthong, C., Ksapabutr, B., Chaiyut, N., & Panapoy, M. (2020). Enhanced mechanical performance of cement board composite reinforced with coconut coir fiber and tire rubber waste. *IOP Conference Series: Materials Science and Engineering* 773(1), Article 012057. <https://doi.org/10.1088/1757-899X/773/1/012057>
- Viju, S., & Thilagavathi, G. (2022). Hot water treatment on nettle fibres: An environment- friendly/economical process for the production of oil sorbent. *Journal of Natural Fibres*, 19(2), 761-769. <https://doi.org/10.1080/15440478.2020.1761929>
- Yel, H., Cavdar, A. D., & Kalaycioğlu, H. (2011). Mechanical and physical properties of cement-bonded particleboard made from tea residues and hardboards. *Key Engineering Materials*, 471, 572-577. <https://doi.org/10.4028/www.scientific.net/KEM.471-472.572>
- Zalinawati, M., Siregar, J. P., Tezara, C., Jaafar, J., Sazali, N., Oumer, A. N., & Hamdan, M. H. M. (2020). The effect of fibre treatment on water absorption and mechanical properties of buri palm (*Corypha utan*) fibre reinforced epoxy composites. *Journal of Mechanical Engineering and Sciences*, 14(4), 7379-7388. <https://doi.org/10.15282/jmes.14.4.2020.06.0580>

- Zhao, K., Xue, S., Zhang, P., Tian, Y., & Li, P. (2019). Application of natural plant fibres in cement-based composites and the influence on mechanical properties and mass transport. *Materials*, *12*(21), Article 3498. <https://doi.org/10.3390/ma12213498>
- Zheng, S., Chen, M., Wu, J., & Xu, J. (2023). Effect of heat treatment on properties and interfacial compatibility of poplar veneer/polyethylene film composite plywood. *Polymer Testing*, *122*, Article 108006. <https://doi.org/10.1016/j.polymertesting.2023.108006>
- Zuraida, A., Insyirah, Y., Maisarah, T., & Zahurin, H. (2018). Influence of fiber treatment on dimensional stabilities of rattan waste composite boards. *IOP Conference Series: Materials Science and Engineering*, *290*(1) Article 012029. <https://doi.org/10.1088/1757-899X/290/1/012029>

Mesh Optimisation for General 3D Printed Objects with Cusp-Height Triangulation Approach

Qais Ahmed Habash¹, Noor Ali Sadek¹, Ahmed Faeq Hussein^{1*} and Abbas AlZubaidi²

¹Biomedical Engineering Department, College of Engineering, Al-Nahrain University, Bagdad, 10001, Iraq

²University of Saskatchewan, Saskatoon, SK S7N 5A2, Canada

ABSTRACT

3D printing (3DP) is increasingly utilized to achieve quick turnaround on various geometric designs and prototypes, being the growing part of additive manufacturing technology (AMT). The 3DP technique effectively improves the production of complex models in terms of low-cost, time-consuming production, and with less material volume. The key to results optimisation with 3DP is the preparation of the geometry. The following techniques can effectively reduce the required time of the 3D printing process for complex and non-linear CAD files. The fused deposition modelling/fabrication (FDM/FFF) techniques become the first choice in many applications, including biomedical ones. Still, some obstacles exist in the geometry roughness and quality zones. This paper proposes an optimisation method for 3D printed shapes used in biomedical devices and instrumentation by minimising the support structure attached to the model using the FDM technique. In this research, we proposed a method for dynamic compensation against gravity-affected parts extended from the main object's geometry using a forward planar learning (FPL) algorithm to minimise cusp height in 3D printed objects. After the slicing stage, the outcomes proved to be of good quality, optimised the object's surfaces, and minimised the printing time by 32%–38%. The proposed method is promising in defining a better setting for slicing and toolpath for FDM 3D printing. However, this method was not tested on other 3DP methods (Stereolithography

(SLA), Selective laser sintering (SLS), and Digital Light Processing (DLP)), as more verification efforts need to be done on these 3D printing processes.

Keywords: 3D printing, 3D policing, cartesian 3DP, cusp-high compensation, fused deposition modelling (FDM), geometric roughness, mesh optimization, stereo-lithography

ARTICLE INFO

Article history:

Received: 02 August 2023

Accepted: 01 February 2024

Published: 08 August 2024

DOI: <https://doi.org/10.47836/pjst.32.5.04>

E-mail addresses:

Qais.Habash@gmail.com (Qais Ahmed Habash)

Noor.Sadek@gmail.com (Noor Ali Sadek)

sabrean2555@gmail.com (Ahmed Faeq Hussein)

Abbas.ubaidi@gmail.com (Abbas AlZubaidi)

* Corresponding author

INTRODUCTION

3D printing (3DP) as part of additive manufacturing (AM) is conveniently used for producing customised objects and applies to a number of general and biomedical applications. Research interest is increasing with the development of printing techniques and materials suitable for particular medical applications (Aimar et al., 2019; Sharaf et al., 2021). The recent developments show that exciting and important advances have already been made in different areas of research, teaching, surgical planning, and prosthetic/medical restoratives. Other applications like personalised drugs and organ printing are at an early stage of development (Bächer et al., 2014).

Recently, most 3D printing technologies have been based on layered manufacturing. One of these techniques is fused deposition modelling or stereolithography. The later technology considered the first attempt appeared in 1981, describing the first functional system for rapid prototyping using photo-based polymers. In this slice-by-slice approach, the effective printing resolution, accuracy, and surface smoothness are highly anisotropic at the initial time of this technology application (Jalil et al., 2017).

It shows a considerable variance in surface quality and textural mapping, visual and haptic, depending on the spatial orientation of the printing process, especially when a larger layer thickness is chosen to save printing time, reduce cost and maximise quality. It is a crucial aspect of biomedical instrumentation technologies (Musialski et al., 2019).

The problem is amplified in the case of fused deposition modelling (FDM), which has become one of the widespread standards in additive manufacturing and rapid prototyping fields. Printing with FDM faces several technical and implementation challenges due to several factors that govern the fabrication and process parameters (e.g., z-axis control, thermal loads and capacity, transition and travelling time).

Generally, in all 3D printers, the optimal quality of the mesh surface is maintained by making the printing axis perpendicular to the surface normal. The relatively high x/y-resolution plus the physical smoothing effect may rise, such as from the melted polymeric filament in FDM-based printers, which may lead to an uncontrolled explosion. As a rule of thumb, the higher staircase artefacts that appear between deposited layers are related to greater surface normal alignment with the (positive or negative) printing direction (Umetani & Schmidt, 2019).

Moreover, by tilting the surface normally towards the negative printing direction (“floating” or “overhang”), auxiliary support structures are generated. It leads to poor printing quality in the surface region that touches the support structures, as shown in Figure 1. Dismissal of this structure may cause extra damage and distortion to the model’s surface. Furthermore, many complex objects with many branches and anastomosis are difficult to print with high quality using one global orientation. Such a kind complex object needs excessive support structures, which are adverse to object smoothness and

can damage the surface or even break some parts of the model if removed (Sharaf et al., 2020).

In this paper, we propose an approach to decomposing the input model into a set of parts to overcome the limitations of support structure needs and improve the surface quality in 3D printing. Assuming the printing direction is vertical, each component is oriented to reduce the surface's normal deviation from the horizontal axis.

In this decomposition, more constraints should be taken into account to ensure that the shape of individual pieces remains compact and that the parts can reassemble in order. We initially defined the parts according to the intersection of convex spatial cells with the input model's volume to achieve this.

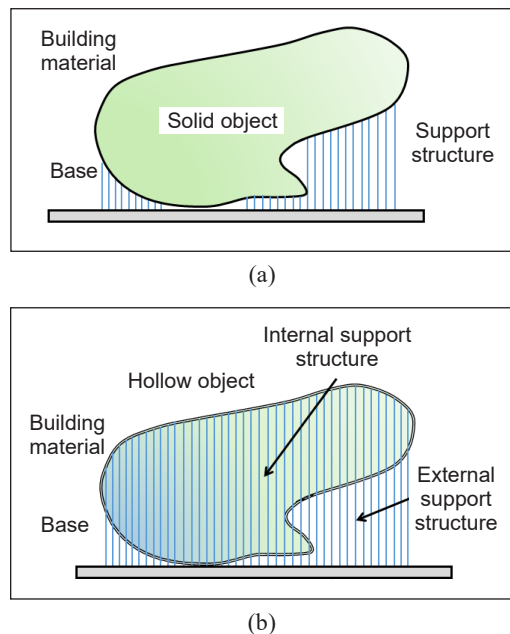


Figure 1. Schematic of support structure configuration in 3D printing: (a) for a solid object; and (b) for a hollow one

Fused Filament Fabrication (FFF) Method

Consumers love the fused Fabrication (FFF) method since it is cheap and popular compared to SLS and SLA printing methods. The printer head of these machines heats a polymer-based filament until it melts, then deposits the melted filament in predetermined spots that match the model's geometry (Ultraker's RepRap technology) (Sharaf et al., 2020).

Once placed over the layer profile, the molten polymer (semi-liquid) cools and immediately solidifies. The process continued layer by layer until the model's shape was fully formed. The most common material for 3D printing is polylactic acid (PLA), but other thermoplastics, such as acrylamide butadiene styrene (ABS), are also acceptable. The level of detail and features produced by parametric models made using FFF is typically lower than that of models made using other 3D parametric techniques (Yamanaka et al., 2014). In order to prevent the gravity effect and gap-printing defects that can occur with FDM, geometric-support profiles and structures may be necessary, in contrast to SLS and inkjet.

Geometry-related 3D Printing Artifacts Categories

The most common file format used in the 3D printing process is (STL), which has several definitions as abbreviations (e.g. Standard Triangle, Triangulation Language, or Stereo-Lithography). Most Computer-Aided Design/Engineering (CAD/CAE) software allows

users to generate the (STL) file format and export it for the final 3D printing production stage (Wang et al., 2013). However, the generated file may face several hurdles and inconsistencies during production, such as tessellation, refining, vertices computation, and exporting/writing processes.

Therefore, a wide spectrum of geometry correction algorithms was developed to overcome any distortion or deformation in the generated object (Zhu et al., 2017). This paper discussed one effective technique to compensate for geometric distortion occurring during the abovementioned procedures. We focused on vertically aligned surfaces as a treatment spot for the over-hanged shapes (extensions outside z-axis 3D printing) (Zhou et al., 2016).

Some work related to mesh optimisation for 3DP structure focused on reducing gap distance and mesh overlapping errors during the assembly process of the 3D model from printed anatomical structures (e.g., bone fragments) by calculating and analysing detectable boundaries for each contact region in clinical image datasets used to generate the STL medical model.

Supporting Structure in FDM 3D Printing

Based on the geometry characteristics of the printed parts, which can be hollow surfaces or solid entities, the support computation of the hollow surface geometry tends to use only the external support structure and ignore the internal one to minimise the cost and travel pattern complexity of the XYZ-motor driving system and minimise the power consumed by the extruder itself.

This solution is economical for hollow parts because it minimises the total material volume (V_{total}) of the filament used in printing and fabrication time. Therefore, each printed layer contains information on extruded filament (volume, weight and relative length) and travel patterns for shells, walls and top regions in vertically aligned parts. These factors will enhance the overall quality of the 3D-printed shape. Figure 2 demonstrates the cross-sectional Hollow part, while Figure 3 depicts the FDM-based 3D printing processes supported by structure terminology.

Background and Problem Identification

Regarding the input geometries to 3D printers, there is an understudied issue regarding the design of shapes with less

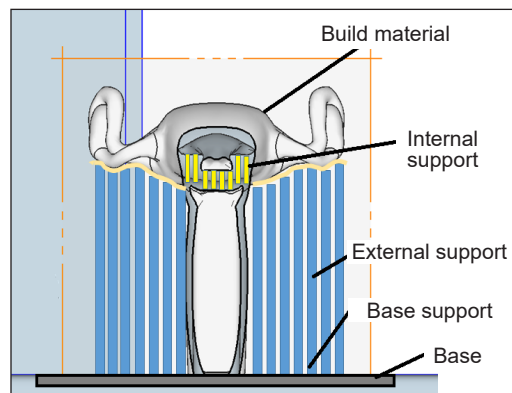


Figure 2. The hollow part cross-sectional view shows external and internal support structures with a printing base

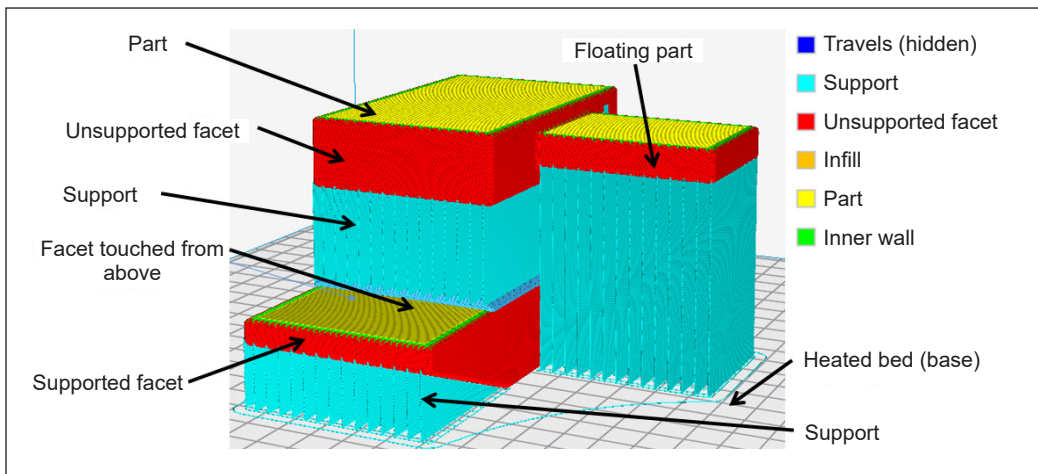


Figure 3. Schematics of the support structure terminology used in the 3D printing process in solid objects with colour-coded territories (blue: travelling direction, magenta: support structure, red: unsupported facets, orange: infill, yellow: parts, green: inner wall region). This coding approach is important to identify the region of geometric processing

support structure models that are more suited for printing, with less roughness in the external layer and walls. A key idea in the FFF method is finding the optimal orientation for the 3D-printed component, and there are a number of ways to handle this aspect of fabrication. Numerous researchers have devised diverse ways for computing optimal orientation, utilising ML algorithms to determine the ideal extruder travel pathway and the most time-effective deposition scenario.

The open-source slicing programme, which prepares the STL file for final printing, already implements many of these methods. Most studies focused on stereolithography (SLS) and stereolithography (SLA) 3D printing processes, although they discovered that FDM and FFF produced superior results.

When it comes to the cost, quality, and integrity of 3D printed components, orientation is typically one of the most important factors among many others. If not, all parameters are included when dealing with general orientation characteristics (GOCs), an error-prone process will be developed by integrating automatic orientation computation in the slicing profile.

We can summarise this characteristic as follows:

- Part's height in the printing direction, which is related to the overall building time and final cost
- Usage of the external support structure, which includes several factors (total volume, entire density and area of contact with 3D printed geometry, inter-support gap distance, and travelling overlapping ratio)
- The quality of faces used in external 3D printed walls (i.e. shells) as its total surface area (TSA) determines the face exposed to the staircase effect.

- Total surface area (SA) of support structure contact with the main shape and also with the base (i.e. heated bed)

Additionally, in addition to the criteria listed above, there are also the considerations of hot-end relative drainage during the printing process (this impact is almost insignificant in tiny nozzle diameters less than 1 mm) and the mechanical strength of the objects that are being built, both of which are not taken into consideration in this optimisation process of the printing process.

The FDM process can have an effect on the computation of GOCs as well as their influence on the final part finishing and cost. For instance, the computation of the FDM support structure considers several elements during the determination process. These considerations include the overall weight of the support structure, the optimal vertical orientation, the base vs the facet supporting profile, surface homogeneity, vertex orientation/angle, and the gravity contact system. Consequently, the computation of the standards will be optimised based on these factors whenever there is a change in the orientation of the 3D product creation process. Therefore, the Cusp-Height Triangulation Approach has been utilised in this work for Mesh Optimisation for General 3D Printed Objects.

MATERIALS AND METHODS

Methodology and Geometry Optimisation for 3D Printed Objects

The staircase effect is the main cause of inaccuracy. Figure 4 depicts the produced vertical and horizontal surfaces (K4 and K1, respectively) that exactly match the proposed models prepared in CAD. However, the process presents some errors according to inaccuracies; they are considered insignificant when compared to errors caused by stair steps (Figure 4). The close horizontal surface (K2) is significantly more affected by inaccuracy than the close vertical surface (K3). For this reason, the facet accuracy should be considered horizontal or

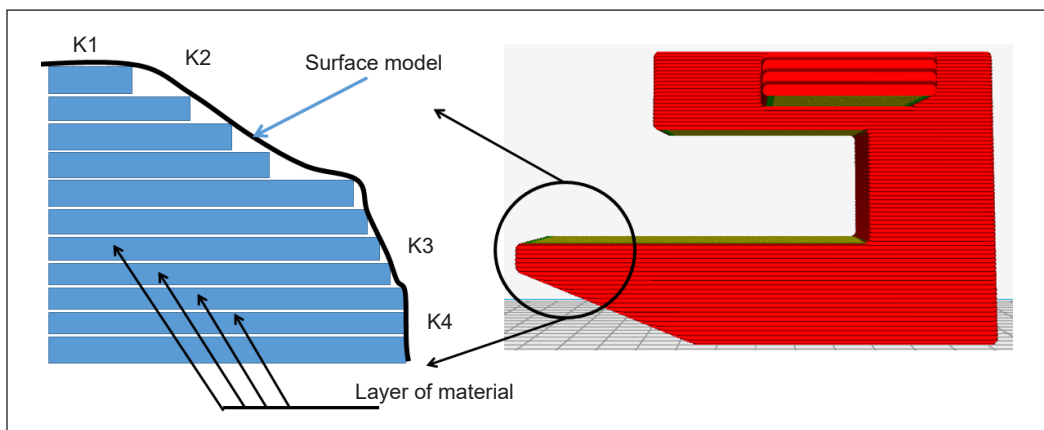


Figure 4. Layer variation in the manufacturing process of 3D printing using FDM technology is due to the staircase effect compared to the real model surface variation

vertical to maximise it, where the “face” entity resembles it over the printing direction. It is not attainable at all times. Therefore, orienting it as close to vertical as possible is desirable.

It is usual for the staircase effect to be the primary cause of surface roughness and loss of fine features in FDM 3D printing. In the worst circumstances, it can also result in the loss of overlapping structure inside the shape (Goh et al., 2022). Therefore, accuracy measurement is done by different researchers (Blumenthal et al., 2013; Jalil et al., 2017). Therefore, many study directions concentrated on digital models in graphical mode, which frequently consist of a large number of triangles. When these triangular edges are immediately mapped to a wire-frame model for 3D printing, the result is complicated structures that directly oppose the goal of a quick production process. Because their definition of the roughness of the CAD model is dependent on the expansion plane (P), which generates an inclination angle that ranges from (90-θ) to the direction of printing, this plane is the one that generates the roughness. An additional parameter that plays a role in the definition of roughness is the maximum distance measured from the surface of the CAD model to the first printable portion (cusp height), also known as (h), because it is significantly dependent on the thickness of the layer and (θ), the angle specified by the cusp-step measure. (Hedges et al., 2012).

The roughness of the local (plane) or surface, sometimes referred to as “cusp height,” which is generated from the fabrication of layers during an object’s 3D printing process, can be measured by Equation 1:

$$e_{\theta} = | \cos(\theta) | * h = | n^T T | * h \tag{1}$$

where (L) is the thickness of the segmented layer and q is the angle between surface normal n and the direction of printing d, as shown in Figure 5.

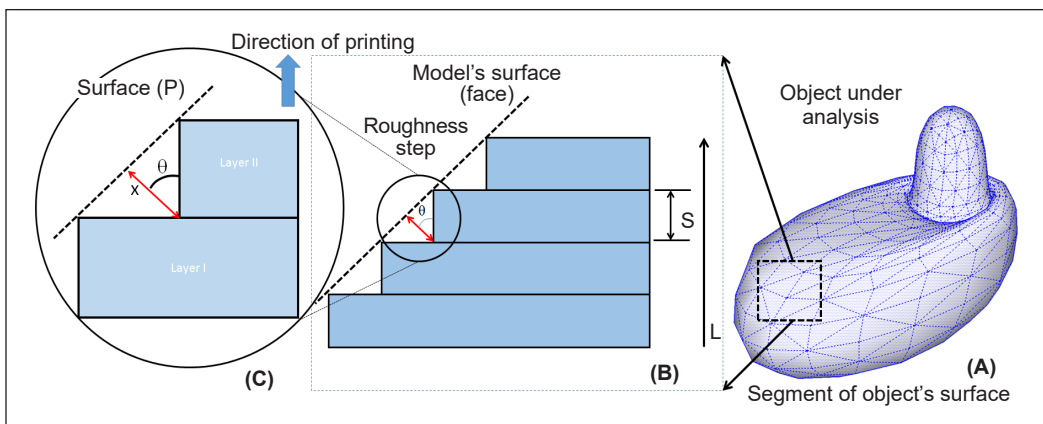


Figure 5. Illustration of Cusp-height error presented in the 3D printed structure (A) the main shape geometry showing the vertices on the surface, (B) the cusp-height error in staircase model of the geometry and (C) Close-up for cusp height of the 3D printed object

To guarantee an acceptable quality for the geometry’s surface, we require that for each triangle, the angle between surface normal (\hat{n}) and printing direction (\hat{d}) lies in some interval $\theta_{neg} < \theta < \theta_{pos}$ with $\theta < 90$ large enough so that the roughness step’s height remains small and $\theta_{pos} > 90$ slightly small enough, so no support structures are required in this case.

Therefore, the definition of cusp height is used to measure the shape accuracy and surface quality from the geometry of the part, layer thickness, printing direction, and tolerance of the hot-end nozzle. In light of Equation 1, which applies only in the 2D regime, further modification can be used to apply the same equation in slicing free-form geometries. As many orientations optimisation can be applied in this regime, treating irregular STL faceted shapes could be implemented using the nominal surface interpolation method. This technique is used to minimise energy profiles in facet object-based convex-hull computation.

To clearly approximate the surface optimisation problem, let us consider a single facet present on a surface (S), as depicted in Figure 6. In this approximation, we propose an angle (θ) between the unit vector along the printing direction (\hat{b}) and the unit-normal of the surface (\hat{n}); hence, the absolute angle value is defined by their dot product, as shown in Equation 2.

$$| \cos\theta | = | \hat{b} \cdot \hat{n} | \tag{2}$$

Triangulating the surface facet allows the accuracy and cusp height to be estimated with Equation 3.

$$h = z_t | \hat{b} \cdot \hat{n} | \tag{3}$$

The 3D object, which composes a higher number of facets as part of the triangulation and meshing process in different directions, may need an adjustable cusp height for higher accuracy. As a result, this compensation mechanism requires comparative weights for all generated facets of the object. A new definition was raised due to this variation in cusp height, and it is called the “ influence zone” for the facet’s cusp height. This definition is governed by the area (A_{facet}) of the facet itself. It considers the new weighting function relative to other neighbouring facets, as stated in Equation 4.

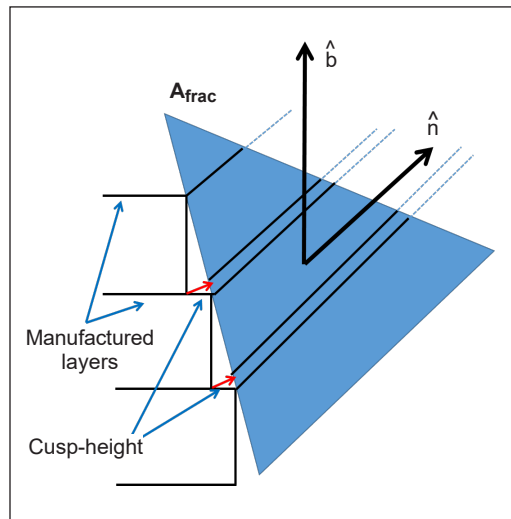


Figure 6. Diagram of STL file accuracy based on one triangular facet approximation

$$h_w = h \cdot A_{facet} \quad [4]$$

Therefore, combining two adjacent facets, even with high-irregular triangulation at their margins, a higher surface area over the cusp height will make the optimisation more influential than a smaller one. We try to “soften” the intersection edges for both facets. This observation iteration can be automated with predictive-surface distortion via (recurrent neural network or tree-model prediction) as this technique is widely used in scaffold quality analysis and validation in tissue engineering applications.

Slicing Implementation

In the process of the part’s orientation calculation, the lower facet has a higher cusp height than the large facet, which has a smaller one. It will affect the accuracy of sliced geometry in large surface areas and may generate a wobbling effect in the upward direction. Therefore, slicing implementation for cusp-height (CH) difference correction will be used in the pre-slicing profile for better support structure optimisation in vertically aligned shapes. Therefore, based on the part’s accuracy defined in Equation 4, the cusp height computation, which is not sufficient for the total definition of the part’s orientation, it is practical to compute the normal of this height variation. Hence, three cases have been defined in slicer software for facets processing in a regular-based model as follows:

- Downward-facing supported facets
- Top-touched facets with supporting skeleton
- Non-supported facets

As a result of this implementation, the inaccuracy in the printed model was reduced to more than 82% based on roughness criteria defined earlier in cusp-height computation, as described in Figure 7. The mesh-optimisation sequence was implemented within the g-code generated during slicing using computed parameters aligned with slice-layer thickness and initial travel time for each layer. This technique will provide more flexibility in the implementation strategy for different iterations in this context.

Segmentation and Mesh Generation

In 3D printed replicas or models, the segmentation is an optional process; however, practically, it is essential in most biomedical and clinical-based applications. The aim of pre- or post-processing is to identify the ROI (region of interest) within an imaging database, which is called segmentation. Besides that, surface extracting from segmented datasets, known as “meshed superficial facet”, is another important aim researchers try to achieve.

The thresholding technique permits one to set a series of values from the reserved data while disregarding that drop outside the range. It is an effective and useful tool for retaining or removing regions of interest related to tissue types of density values. Besides,

growing the seed-based region is another segmenting tool. Using this tool, the user chooses zones from the image in simple steps, an initial point or seed, and selects voxel density parameters. The software package then adds extra voxels to the point that agrees with the defined density standards. The added voxels are then added to subsequent adjacent voxels that meet the standards.

When the segmentation is broad, a surface extraction process is started. This management is achieved by extracting the volumetric data by adapting the data from voxel form into a mesh collected faces based on a sequence of triangular facets. It can be accomplished by means of automated rendering tools of surfaces contained within certain software discussed earlier. The conversion from a voxel to a polygonal model, which results in a flatter surface, is an estimate of the original image.

RESULTS AND DISCUSSION

3D Printing Results and Post-processing

Results were obtained by applying the optimisation pipeline for surface roughness reduction and support structure elimination using the forward-adaptive mesh optimisation (MO) algorithm in the slicing software. Results displayed in Figure 8 show a visible reduction of support structure percentage used in the slice-fading profile with open-source slicing software Cura (Ultimaker) and a bold definition of surface roughness reduction due to fine-tuning of layer thickness over a single layer during the 3D printing process shown in Figure 7. In addition, this reduction is even more relevant if we increase the layer heights (initial and standard ones) over the geometric profile in the printing queue. The total iteration presented is averaged for each of the 83 batches in the slicing profile to reach the optimal results with each minimisation percentage, as indicated in Figure 7.

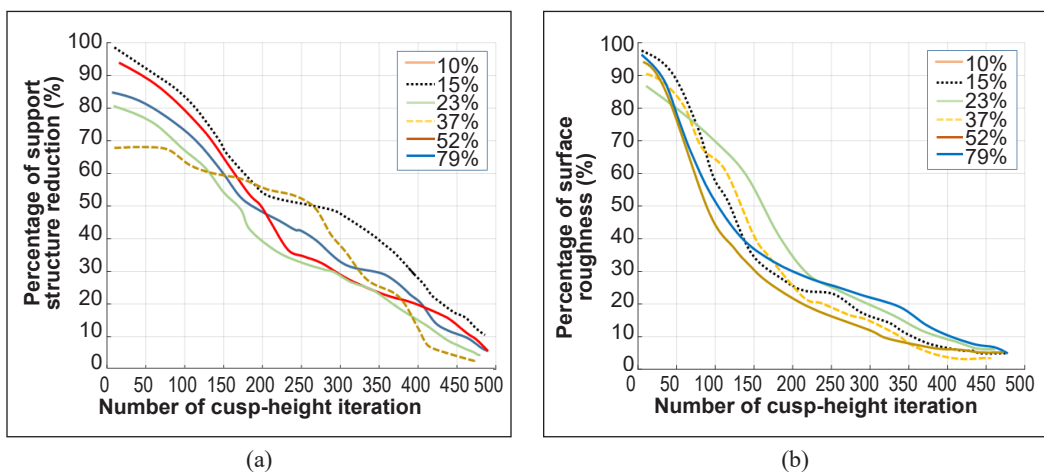


Figure 7. Optimisation result: (a) Support structure elimination; and (b) geometry’s surface roughness reduction with 0.4 mm nozzle hot end setting @ 0.2 mm layer thickness

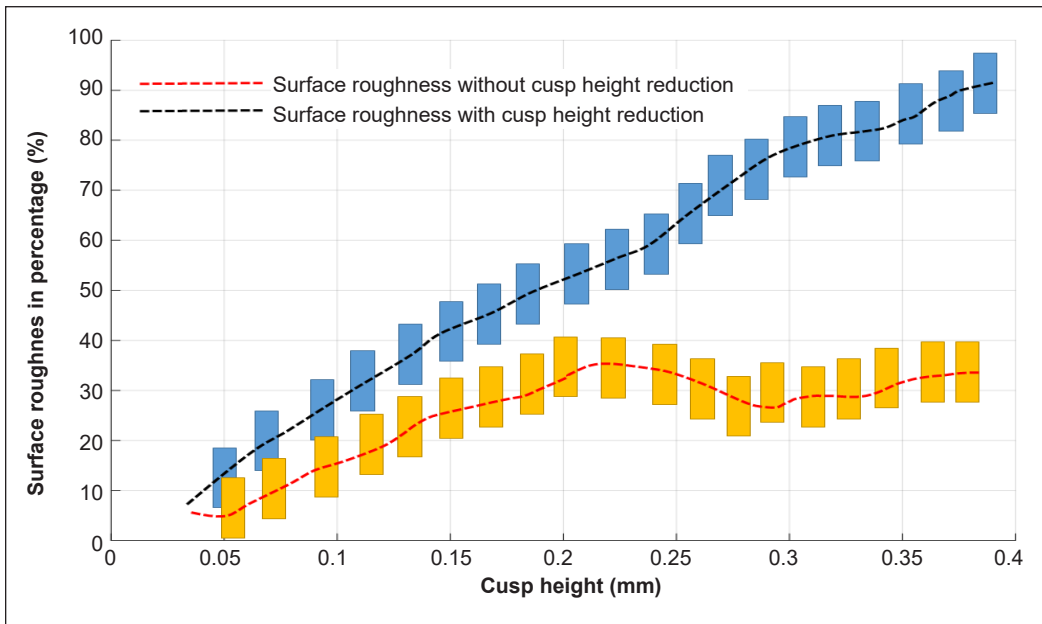


Figure 8. Surface roughness determination for different cusp-height variations with/without CH reduction, as this indicator can be adjusted over the course of printing

Surface roughness is a parameter that represents the average roughness of a surface. It is often used to express surface roughness and the units of measurement for it are either micrometres (μm) or microinches (μin). One of the less prevalent ways to convey roughness is through the proportion of surface roughness present.

With careful examination of the roughness measurement for 3D printed objects, we noticed that with the lower layer height, the lower roughness on the meshed surface, despite the large step size for the cusp-height parameter. It is due to the optimisation level for cusp height (CH) in reference to the layer thickness and invariance of height adjustment during the slicing process. Determination of the relative roughness for performed iteration was measured for each printed sample, as shown in Table 1.

Table 1

Smoothness computation for variable cusp-height versus layer-thickness in FFF 3D printing after using cusp-height (degree) optimisation in slicing profile

Iteration	Layer-height (mm)	Cusp height (mm)	Support (%)	Relative roughness (%)
1	0.175	0.021	11	27
2	0.165	0.025	15	22
3	0.155	0.028	16	19
4	0.145	0.032	19	16
5	0.135	0.035	23	12
6	0.125	0.042	26	10

Moreover, the surface roughness in the case of inclination-based measurement (support structures) may suffer from other tolerance-related values, which may be generated especially in the zones of higher accuracy demands; the sample with specific Y-axis values has a large support area compared to the lower accuracy zone. It is because the sectional computation is performed perpendicularly to the object edge-sand, hence, on or inside a starting step.

For a specific iteration of measuring surface roughness on different 3D printed parts, which is tabulated in Table 2, the value of Ra with different orientations (0° , 45° and 90°) has been registered with all mean and standard deviations for four different faces of the 3D printed parts produced with the cusp-height optimisation technique.

Table 2

Practical measurement of surface roughness for four printed examples used in this research with combined cusp-height optimisation technique

Printed part	Surface roughness	Inner face				Mean	SD
		Face 1	Face 2	Face3	Face4		
nozzle diameter =0.4 mm with layer height =0.175 mm							
1	Ra@0deg	3.5095	4.1734	0.9037	1.824	2.60	1.50
	Ra@45deg	22.7945	22.4523	24.671	24.0782	23.50	1.05
	Ra@90deg	19.8834	20.4995	23.0288	21.4029	21.20	1.37
nozzle diameter =0.4 mm with layer height =0.185 mm							
2	Ra@0deg	1.7052	6.4298	6.2361	4.6017	4.74	2.19
	Ra@45deg	15.7584	18.5059	14.029	12.0904	15.10	2.72
	Ra@90deg	15.2823	14.4466	17.7571	15.4151	15.72	1.42
nozzle diameter =0.4 mm with layer height =0.2 mm							
3	Ra@0deg	2.0394	2.0662	2.8696	1.2892	2.07	0.65
	Ra@45deg	22.4323	21.8081	20.6335	28.9004	23.44	3.71
	Ra@90deg	21.7547	20.904	19.7598	26.2476	22.17	2.84
nozzle diameter =0.4 mm with layer height =0.22 mm							
4	Ra@0deg	1.4446	1.344	1.6269	0.9773	1.35	0.27
	Ra@45deg	37.0573	36.4608	37.633	36.7085	36.96	0.51
	Ra@90deg	33.2943	32.6814	33.4522	31.7007	32.78	0.79

Limitations and Technical Restrictions

Due to limited FDM-based 3DP technology in the current stage, there is a need for optimal slicing techniques based on machine learning and stepper motor drive and operation over a long period are needed. In addition, to smooth the driving transition, a stable Cartesian movement phasing for the extruder could be implemented to avoid over- or under-extruding for printing samples with large and complex geometric models and parts.

This paper has described a mesh optimisation methodology for a wide range of applications in 3D printing and bioprinting in medicine. Here, we will look at lessons

learned from recent developments and try to make realistic predictions for emerging applications.

As the roughness of 3D printed objects becomes a crucial point in producing high-quality fabricated surgical parts, avoidance of micro-surface scaffolding is important to decrease the opportunities of prosthetic failure and histo-compatibility issues, as many biological 3D printed geometries which possess a high degree of irregularities and non-linearities. It is also true for different shapes printed in various applications. An example of a 3DP shape without/with cusp-height (CH) optimisation approach was demonstrated in Figure 9 for both cases displayed for convenient comparison. As a demonstration of roughness enhancement in 3D printed surfaces, Figure 9 shows different medical parts used in biomedical instrumentation (A-Fan mounting in ventilator systems, Proximal connection in prosthetic hand, B-modular MCU box for Holter cardiac monitor, Brain SpO₂ sensor holder), which can see the effect of CH-optimization algorithm.

Contrary to many researchers focused on different parameters of mesh optimisation, such as minimum length scale and maximum overhang angle, our outcomes support structure elimination with a higher ratio than adjusting chemical additives, which may add extra expenses to the single 3D printing process. However, our method does not cover the non-Newtonian effects on optimal configurations because we focused on solid structure only and not semi-solid or cartilaginous-like materials (i.e. flexible printing material). Mesh optimisation is also in higher demand for 3D bio-printing; it has also facilitated research on early conceptual work for new therapy perspectives, exemplified by the work. Although irregular shapes and geometries associated with these types of bio 3D-printed objects can adversely affect the printing quality, a mesh optimisation technique with cusp height (CH) should be considered in future applications for such fields. In addition, integrating mesh optimisation in microfluidics with 3D bio-printing builds complex co-cultures and tissue structures in test tubes.

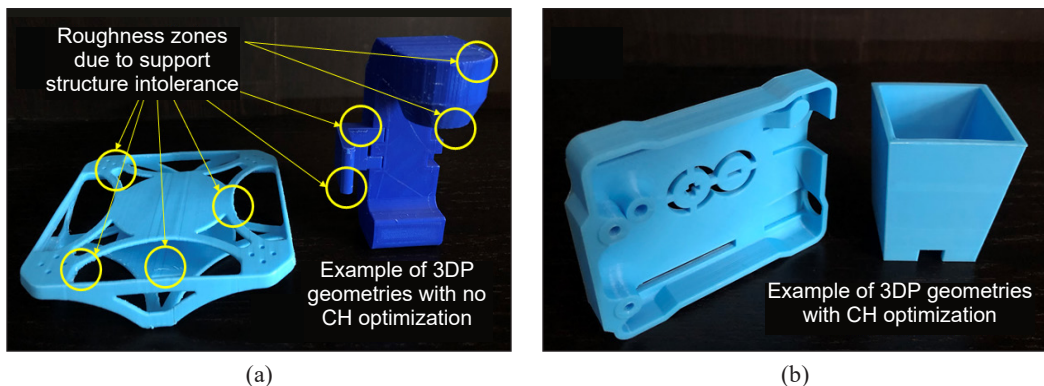


Figure 9. Examples of 3D printed objects used for validation cusp-height (CH) optimisation technique for minimisation of support structures and lowering roughness percentage of the external wall of shapes: (a) with roughness displayed on parts surface; and (b) with smoothness all over the part surface due to CH utilisation

CONCLUSION

Mesh optimisation in 3D printing research continues its maturity, and its capacity to provide more accurate models in research of different domains, such as the modelling of cancerous lesions, is the subject of increasing research interest. Developments in the direction of cusp-height minimisation to suppress the low-resolution effect of FDM 3D printing will boost the usage of this technology to hydrogel matrices, printing techniques, and better integration with microfluidics are all important steps to move towards obtaining functioning, robust artificial organs by bio-printing. The latest bio-printers can extrude angiogenic microfluidics networks alongside tissue printing.

Our method, as simulated with slicing iteration, proves that it has an advantage over the orthogonal array method developed in terms of parameters optimised, such as print pattern (linear), orientation on the X-axis (0-180°), support angle (45°) and sidewalk (0.175 mm). The slicing profile was implemented to get better surface roughness results and proved to be a smoother transition in support structure utilisation in different segments of 3D printed parts. However, more optimisation is needed in slicing algorithms to deal with other 3D printing technologies, such as the SLA method. The integration of topology-based slicing and segmentation will help smoothen the printing procedure. However, these steps should be accompanied by a better energy-convergent function in terms of minimal failure rate during the deposition phase.

ACKNOWLEDGEMENT

The authors thank Al-Nahrain University, Bagdad, Iraq, for the great support.

REFERENCES

- Aimar, A., Palermo, A., & Innocenti, B. (2019). The role of 3D printing in medical applications: A state of the art. *Journal of Healthcare Engineering*, 2019, Article 5340616. <https://doi.org/10.1155/2019/5340616>
- Bächer, M., Whiting, E., Bickel, B., & Sorkine-Hornung, O. (2014). Spin-it: Optimizing moment of inertia for spinnable objects. *ACM Transactions on Graphics (TOG)*, 33(4), Article 96. <https://doi.org/10.1145/2601097.2601157>
- Blumenthal, T., Fratello, V., Nino, G., & Ritala, K. (2013). Conformal printing of sensors on 3D and flexible surfaces using aerosol jet deposition. *Nanosensors, Biosensors, and Info-Tech Sensors and Systems*, 8691, 118-126. <https://doi.org/10.1117/12.2009278>
- Goh, G. L., Dikshit, V., Koneru, R., Peh, Z. K., Lu, W., Goh, G. D., & Yeong, W. Y. (2022). Fabrication of design-optimized multifunctional safety cage with conformal circuits for drone using hybrid 3D printing technology. *The International Journal of Advanced Manufacturing Technology*, 120(3), 2573-2586. <https://doi.org/10.1007/s00170-022-08831-y>
- Hedges, M., & Marin, A. B. (2012, March 14-15). *3D aerosol jet® printing-adding electronics functionality to RP/ RM*. [Paper presentation]. Fraunhofer Direct Digital Manufacturing Conference (DDMC), Berlin, Germany.

- Jalil, N. A. A., Sharaf, H. K., & Salman, S. (2017). A simulation on the effect of ultrasonic vibration on ultrasonic assisted soldering of Cu/SAC305/Cu joint. *Journal of Advanced Research in Applied Mechanics*, 36(1), 1-9
- Musialski, P., Auzinger, T., Birsak, M., Wimmer, M., & Kobbelt, L. (2015). Reduced-order shape optimization using offset surfaces. *ACM Transaction Graphics*, 34(4), Article 102. <https://doi.org/10.1145/2766955>
- Sharaf, H. K., Ishak, M. R., Sapuan, S. M., & Yidris, N. (2020a). Conceptual design of the cross-arm for the application in the transmission towers by using TRIZ–morphological chart–ANP methods. *Journal of Materials Research and Technology*, 9(4), 9182-9188. <https://doi.org/10.1016/j.jmrt.2020.05.129>
- Sharaf, H. K., Salman, S., Abdulateef, M. H., Magizov, R. R., Troitskii, V. I., Mahmoud, Z. H., Mukhutdinov, R. H., & Mohanty, H. (2021). Role of initial stored energy on hydrogen microalloying of ZrCoAl (Nb) bulk metallic glasses. *Applied Physics A*, 127(1), Article 28. <https://doi.org/10.1007/s00339-020-04191-0>
- Umetani, N., & Schmidt, R. (2013). Cross-sectional structural analysis for 3D printing optimization. *SIGGRAPH Asia Technical Briefs*, 2013, Article 5. <https://doi.org/10.1145/2542355.2542361>
- Wang, W., Wang, T. Y., Yang, Z., Liu, L., Tong, X., Tong, W., Deng, J., Chen, F., & Liu, X. (2013). Cost-effective printing of 3D objects with skin-frame structures. *ACM Transactions on Graphics (TOG)*, 32(6), Article 177. <https://doi.org/10.1145/2508363.2508382>
- Yamanaka, D., Suzuki, H., & Ohtake, Y. (2014, December 3-6). *Density aware shape modeling to control mass properties of 3D printed objects*. [Paper presentation]. Computer Graphics and Interactive Techniques (SIGGRAPH-ASIA), Shenzhen, China.
- Zhu, B., Skouras, M., Chen, D., & Matusik, W. (2017). Two-scale topology optimization with microstructures. *ACM Transactions on Graphics (TOG)*, 36(4), Article 120b. <https://doi.org/10.1145/3072959.3095815>
- Zhou, Y., Kalogerakis, E., Wang, R., & Grosse, I. R. (2016, October). Direct shape optimization for strengthening 3D printable objects. *Computer Graphics Forum*, 35(7), 333-342. <https://doi.org/10.1111/cgf.13030>

Comparing CNN-based Architectures for Dysgraphia Handwriting Classification Performance

Siti Azura Ramlan, Iza Sazanita Isa*, Muhammad Khusairi Osman, Ahmad Puad Ismail and Zainal Hisham Che Soh

Electrical Engineering Studies, College of Engineering, Universiti Teknologi MARA, Cawangan Pulau Pinang, Permatang Pauh Campus, 13500 Permatang Pauh, Penang, Malaysia

ABSTRACT

Deep learning algorithms are increasingly being used to diagnose dysgraphia by concentrating on the issue of uneven handwriting characteristics, which is common among children in the early stage of basic learning of reading and writing skills. Convolutional Neural Network (CNN) is a deep learning model popular for classification tasks, including the dysgraphia detection process in assisting traditional diagnosis procedures. The CNN-based model is usually constructed by combining layers in the extraction network to capture the features of offline handwriting images before the classification network. However, concerns have been expressed regarding the limited study comparing the performance of the Directed Acyclic Graph (DAG) and Sequential Networks in handwriting-related studies in identifying dysgraphia. The proposed method was employed in this study to compare the two network structures utilized for feature extraction in classifying dysgraphia handwriting. To eliminate this gap. Therefore, a new layer structure design in the Sequential and DAG networks was proposed to compare the performance of two feature extraction layers. The findings demonstrated that the DAG network outperforms the Sequential network with 1.75% higher accuracy in classification testing based on confusion matrix analysis. The study provides valuable insights into the efficiency of various network structures in recognizing inconsistencies identified in dysgraphia handwriting, underlining the need for additional research and improvement in this field. Subsequently, these findings highlight the necessity of deep learning approaches to advance dysgraphia identification and establish the framework for future research.

ARTICLE INFO

Article history:

Received: 14 August 2023

Accepted: 07 March 2024

Published: 08 August 2024

DOI: <https://doi.org/10.47836/pjst.32.5.05>

E-mail addresses:

sitiazura@uitm.edu.my (Siti Azura Ramlan)

izasazanita@uitm.edu.my (Iza Sazanita Isa)

khusairi@uitm.edu.my (Muhammad Khusairi Osman)

ahmadpuad127@uitm.edu.my (Ahmad Puad Ismail)

zainal872@uitm.edu.my (Zainal Hisham Che Soh)

* Corresponding author

Keywords: Convolutional Neural Network, deep learning, directed acyclic graph, dysgraphia handwriting, handwriting analysis

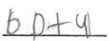



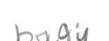

INTRODUCTION

Dysgraphia is a complex learning disability that affects language skills, including writing, spelling, and comprehension, and causes difficulties in a child’s academic and social life (Deuel, 1995). Writing skills are key abilities that children must develop during their school years. Dysgraphia children, on the other hand, suffer from handwriting difficulties and lack the writing skills that are expected for his or her age and cognitive level (Chung et al., 2020; Vlachos & Avramidis, 2020). Dysgraphia children’s handwriting products exhibit indications of inconsistent handwriting, improper letter size, reversed letter form, and corrected handwriting (Biotteau et al., 2019). Some scholars have also detected dysgraphia in children presented with spelling impairment (Šafářová et al., 2021; Vlachos & Avramidis, 2020) that affects writing skills, prohibiting children from writing words quickly and consistently. Table 1 presents examples of dysgraphia and normal handwriting images by children aged 7 to 12.

Addressing dysgraphia and finding appropriate interventions are critical in increasing learning and ensuring success in education. Furthermore, traditional techniques of detecting dysgraphia rely primarily on subjective assessments, such as scoring tests and observations-based methods, which can be time-consuming, biased, and lacking objectivity (Dimauro et al., 2020). These constraints emphasize the need for more accurate and efficient dysgraphia detection systems. In recent years, computer-based approaches have emerged as a potential solution for dysgraphia detection. These approaches leverage various features and algorithms to analyze and interpret dysgraphia symptoms, such as inconsistent handwriting with redundant form, reversal and corrected letters (Vaivre-Douret et al., 2021). The accuracy and efficiency of dysgraphia detection are improved by computer-based methods, providing an objective and quantitative evaluation.

By automatically learning and extracting information from dysgraphia-related data, machine learning and deep learning algorithms have improved dysgraphia identification. These methods, particularly Convolutional Neural Networks (CNNs), have been performed in image classification tasks with various input images. CNNs comprise learnable layers that extract hierarchical information from input images (Almisreb et al., 2022). The Directed Acyclic Graph Network (DAGN) and Sequential Network (SN) are two leading CNN architectures that could be implemented to extract features of layer network construction. SN is a simple network built on a single or multi-layer architecture with no shortcuts between the layers. In contrast, DAGN uses skip

Table 1
Dysgraphia and normal handwriting images by school-age children

Dysgraphia handwriting	Normal handwriting
	
	
	

connections, allowing direct connections between non-adjacent layers and improving gradient flow, resulting in improved classification performance. Moreover, by capturing specific features from dysgraphia handwriting, CNNs have shown the potential to be explored in detecting dysgraphia. Nonetheless, the performance comparison of DAGN and SN designs in dysgraphia detection is limited and current research lacks a detailed analysis of various network designs and their effects on classification. The same number of convolutional layers in the network could be used to better understand the advantages and disadvantages of DAGN and SN, which could help improve dysgraphia detection methods based on the performance of both networks.

This study compares the performance of DAGN and SN architectures for dysgraphia handwriting classification. By evaluating accuracy, precision, recall, and F1-score on a large dataset, it seeks to provide insights into the effectiveness of these network designs. The findings will advance dysgraphia detection methods and guide the development of more accurate deep-learning models for identifying dysgraphia based on handwriting characteristics. The proposed layer structure network could achieve significant output as a considerable network structure to integrate with another model in improving the dysgraphia detection approach.

RELATED WORK

Numerous methods have been presented for detecting the presence of dysgraphia symptoms in children and adults using various input domains. The domain of online and offline handwriting was utilized and extracted to obtain an accurate diagnosis. Most researchers focus on accurate diagnosis by implementing a machine-learning algorithm. Online handwriting frequently extracts acceleration, pressure, and pen tilt, typically using additional instruments such as a tablet (Asselborn et al., 2020; Dankovicova et al., 2019; Kunhoth et al., 2023). In the meantime, digitized offline handwriting could be extracted as static features (letter shape, missing letters/words, uneven slanting, and inconsistent letter size) based on the output of handwriting on paper. Researchers have investigated both domains, exponentially demonstrating the potential of machine learning techniques for detecting dysgraphia symptoms.

More research in machine learning techniques has been conducted on classification algorithms and feature extraction. Machine learning algorithms, support vector machines (SVM), AdaBoost, and decision trees were applied to extracted features, and a dysgraphia diagnostic model was developed, as Kunhoth et al. (2023) demonstrated. From the study, the AdaBoost classifier has shown high accuracy with 80.8% accuracy, 1.3% more than the state-of-the-art method, similar to the research of Devillaine et al. (2021) that presented a machine learning algorithm-based pre-diagnosis tool for dysgraphia in France. From the study, Random Forest obtained the best accuracy score of 73.4% compared to Extra Trees

and Multi-Layers Perceptron (MLP). In a similar perspective of the input domain, Sihwi et al. (2019) developed a Support Vector Machine (SVM) with several kernels, including Linear, Polynomial, and Radial Base Functions (RBF), to classify the collected data and identify dysgraphia. By handling the Synthetic Minority Over-sampling Technique (SMOTE) for unbalanced data, the RBF kernel produced the highest accuracy score of 82.51%.

A study by Dankovicova et al. (2019) explored the application of various machine learning techniques, which are random forest, support vector machine, and adaptive boosting, to analyze and extract attributes from irregular handwriting and identify dysgraphia characteristics. While the study employs hyperparameter tuning, 3-fold stratified cross-validation, and normalized data to predict and assess the handwriting data, the principal component analysis has been used to visualize these attributes in a two-dimensional space with a success rate of approximately 67%. The performance indicates a significant finding based on the various input domains and extracted features used in the previous study. It might be improved more accurately by aiding the diagnosis procedure with minimal consumption. The knowledge of machine learning has grown, and a more advanced concept known as deep learning promises high performance in computer vision.

As deep learning research continues to grow, it offers the promise of additional revolutionary advancements in a variety of disciplines, including dysgraphia identification. Deep learning has shown outstanding performance in a variety of input domains used and across various disciplines. In computer vision, convolutional neural networks (CNNs) have achieved state-of-the-art performance in image classification, object detection, and image segmentation tasks (Chai et al., 2021). The effectiveness of CNNs in extracting feature spatial hierarchies has resulted in advances in image classification. Based on previous studies, several research studies have been conducted using the CNN-based model to classify dysgraphia and non-dysgraphia handwriting symptoms. A hybrid CNN-LSTM Random Forest model has been performed in classifying handwriting characters for Parkinson's patients (Masood et al., 2023). The combination of CNN and LSTM layer construction captured spatial and sequential information from the images, while Random Forest enhanced the classification performance. With different feature extraction methods, Devi and Kavya (2023) implemented a combined feature extraction formula of Kekre-Discrete Cosine Transform with Deep Transfer Learning (K-DCT-DTL) to select prominent handwriting and geometrical features. Another CNN-based model has been presented by Vilasini et al. (2022), which was performed to identify and detect abnormal handwriting among children with learning disability. The CNN model and Vision Transformers (ViT) were utilized, and they have contributed to developing an efficient approach to dysgraphia detection research.

A study by Ghouse et al. (2022) demonstrated the use of balancing parameters in the loss function to balance the class during training and eliminating the features to reduce

overfitting problems in classifying dysgraphia and non-dysgraphia by implementing Non-Discrimination Regularization in Rotational Region Convolutional Neural Network (NDR-R2CNN) model. By using graphic tablets to capture the dynamic features of letter writing, Zolna et al. (2019) developed a Recurrent Neural Network model (RNN) to identify children with dysgraphia. The sequential CNN-based model was explored and experimented with using letter handwriting images, and it was shown that the performance could be improved through different layer construction, such as the number of convolutional layers and different activation function layers (Ramlan et al., 2022). The experimental results predicted that the classification performance could increase if the convolutional layers increase. Prior research indicated that numerous implementations of input domain features, such as offline or online handwriting image features, have utilized CNN-based models to detect and identify dysgraphia in children and adults.

CNN-based models have shown gradual growth in dysgraphia identification and classification based on handwriting features extracted during model training. Besides the model design, the datasets used in classifying dysgraphia handwriting are one of the crucial parameters to be considered. These datasets often include a diverse range of writing styles, ages, and severity levels of dysgraphia. Additionally, some studies employed data augmentation techniques to increase the size and diversity of the training dataset, such as rotation, scaling, and noise injection. The use of assistive tools such as a graphic tablet to preserve the dynamic features of handwriting aids in the performance of classification tasks, but it comes at a cost. Static features of handwriting products (offline handwriting) can supplement the limitations of employing online handwriting. However, functional CNN layer building is required to ensure that effective feature extraction can be done and classified appropriately. Most research studies focused on the performance accuracy of the model developed. However, limited research has investigated the impact of layer construction and hyperparameter comparison in handwriting image classification, especially in dysgraphia identification.

To summarize, deep learning has emerged as a dominant framework in machine learning, adapting several fields and delivering outstanding performance in complex tasks. A CNN-based model is a focus model designed to identify dysgraphia symptoms and assist in dysgraphia diagnosis. Limited research has been conducted on a Directed Acyclic Graph (DAG) network to investigate the effect of the layer construction on classification performance. This study compares the performance of two models in classifying dysgraphia offline handwriting products, namely Sequential and DAG network designs.

METHODOLOGY

An experimental study is used to achieve the research objective of comparing the performance between two different construction layers in extracting the features of

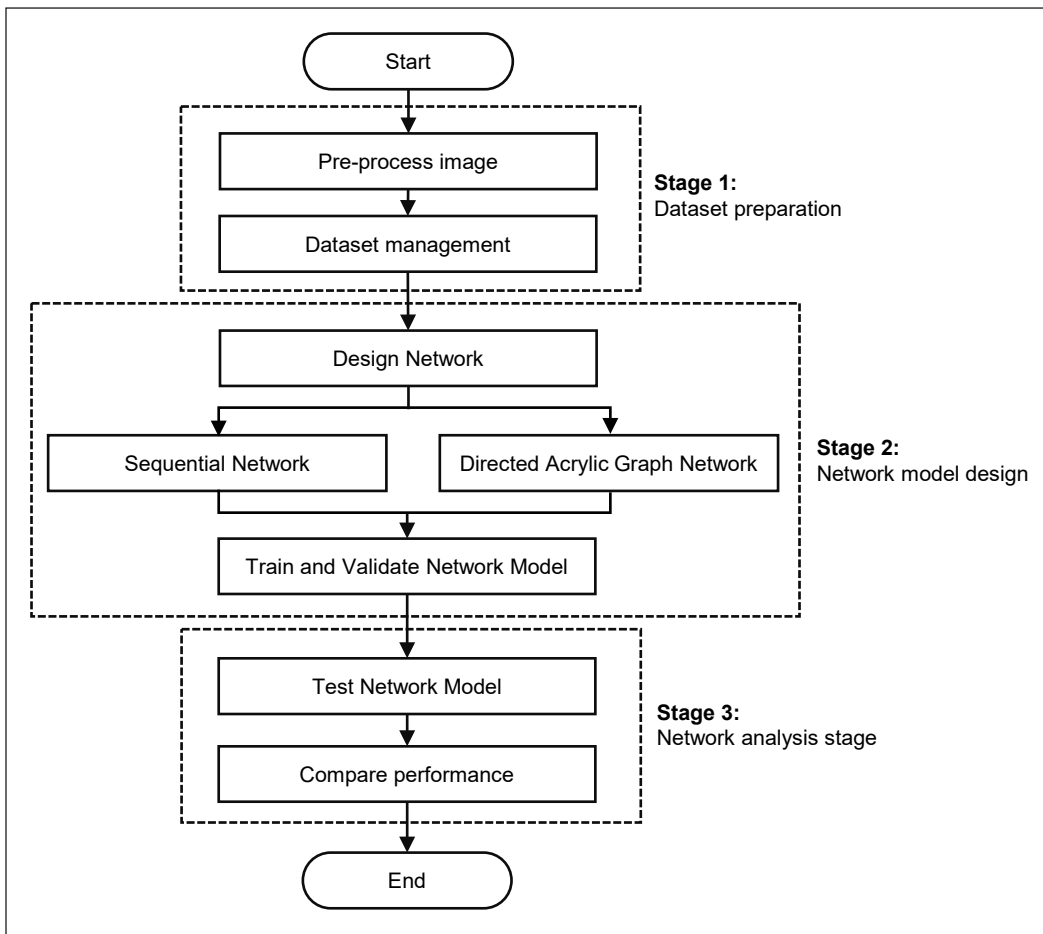


Figure 1. Overall experimental procedure for comparing networks performance of dysgraphia classification

handwriting images. This methodology focuses on the novel network layer structures proposed for Sequential and DAG feature extraction networks.

The overall experimental procedure depicted in Figure 1 is divided into three major stages: (1) preparing the dataset, (2) continuing network development, (3) and network analysis activities to complete the procedure. The first stage entails preprocessing the images using image processing techniques, including resizing and rotating to normalize the data. Then, the dataset is split into train and test portions to prepare it for input to the next stage.

The network architecture is developed in the second stage by considering the layer construction, activation function, and connectivity patterns. A model is developed in this second step, which could effectively learn and extract useful features from the input data. The hyperparameters, the adjustable parameters that control the network's learning process, include learning rate, batch size, number of epochs, optimized function and regularization techniques. Tuning these hyperparameters is critical for optimizing network performance

and generalization capability. The network model is trained and validated using the prepared dataset after the hyperparameters have been determined. The model learns from the training data during training and adjusts its parameters based on the set loss function and optimization method—the validation phase aids in monitoring the model’s performance on unseen data and preventing overfitting.

The model is then tested using a separate dataset in the third stage. This step assesses the network’s generalization capabilities, offering insight into how well it operates on unseen data. The test results evaluate the model’s performance and usefulness in addressing the target problem. When the execution is complete, the next step is to compare the network model’s performance against other models or benchmarks. Based on this comparison, decisions about the feasibility and effectiveness of the established network can be made, marking the end of the process. If the execution is incomplete, the workflow returns to the training and validation phase. This iteration allows further model refining by altering hyperparameters, changing the network topology, or experimenting with other training procedures.

Following this iterative process, the proposed workflow ensures a systematic approach to designing, training, and assessing network models for a specific task. MATLAB 2021a environment was used with supported hardware that included a 2.50GHz Intel® Core™ i5-10500H CPU and an NVIDIA GeForce RTX 3060 graphics processing unit to complete the overall experimental procedure.

Dataset Preparation

The dataset utilized in this experiment was obtained from the Kaggle database (<https://www.kaggle.com/datasets/drizasazanitaisa/dyslexia-handwriting-dataset>), which consists of an established image dataset (Rosli et al., 2021). The dataset preparation process establishes the image dataset and aims to ensure that it is suitable for execution as an input in deep neural networks. It consists of two key parts: preprocessing all images and the dataset management process.

Preprocess Image

The preprocessing steps collectively prepare the image data for training deep learning models, making the input more suitable for the classification task. Figure 2 illustrates the preprocessing stages, which include binarization, inversed black-and-white pixels, image resizing, noise injection, and rotation.

Initially, the image undergoes binarization, where pixel values are simplified to binary form based on a threshold. The image’s colors are then inverted, changing white pixels into black and vice versa. The image is then resized to 32×32 dimensions to meet standardized input sizes. Controlled amounts of random noise are injected to enhance the model’s

robustness by exposing it to variations in real-world data. Finally, the image undergoes rotation to a specified degree to diversify the training dataset, ensuring the model’s ability to handle variations in object orientation. These preprocessing stages work together to produce a refined and optimal input for further analysis and CNN model training (Rosli et al., 2021).

Dataset Management

This procedure organizes all preprocessed data images into specified classes before they are entered into the network models. After completing the preprocessing activities, the established collection now contains 267,930 images, which include noise injection and rotated images. Therefore, each class has a balanced representation of the collection. The dataset input size is 32 × 32 pixels, encompassing rows and columns for dysgraphia and normal class. Table 2 presents the percentage proportion and numerical distribution of the training and testing datasets. About 85% of the dataset is used for training, and the remaining 15% is used for testing. However, 30% of the training dataset was randomly selected for the validation phase.

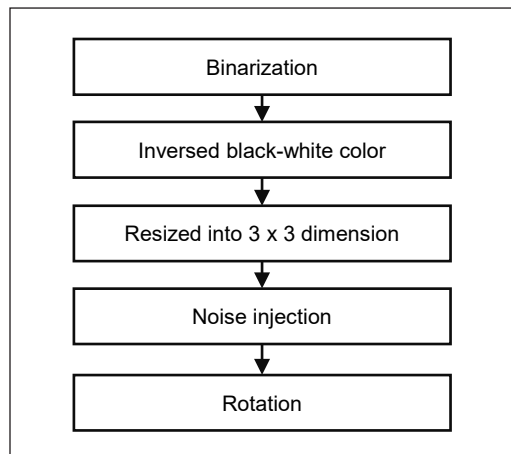


Figure 2. Preprocessing steps

Table 2
Dataset division of training and testing

Dataset Category	Number of Images	Percentage
Training	228816	85%
Testing	39114	15%

Network Model Design

Network Design

As illustrated in Figure 3, the overall network construction consists of an extraction network and a classification network. This experiment used two types of new layer structures for extraction networks, as shown in Figures 4 and 5. The following classification network employed a fully connected Softmax layer and yielded the predicted output class at the end of the network.

Figure 4 depicts the architecture of SN, which includes three convolutional layers, batch normalization, and ReLU as an activation function. Before proceeding to the classification network, each layer block finishes with the max pooling layer.

Figure 5 demonstrates the DAGN layer architecture, which includes three convolutional layers (Conv), batch normalization (BaN), and activation function using ReLu. A skip connection is a network connection between the two layers that enables the gradient to move directly from the output to the input levels. During the forward and backward propagation training phases, this connection allows the network to bypass one or more layers. Mixing inputs from distinct layers requires an additional layer to complete the acyclic graph. By

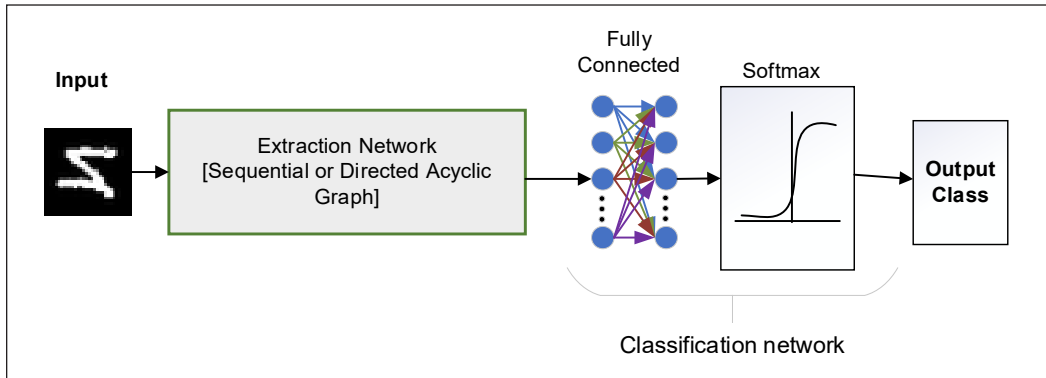


Figure 3. Overall network construction for Sequential Network and Directed Acyclic Graph Network

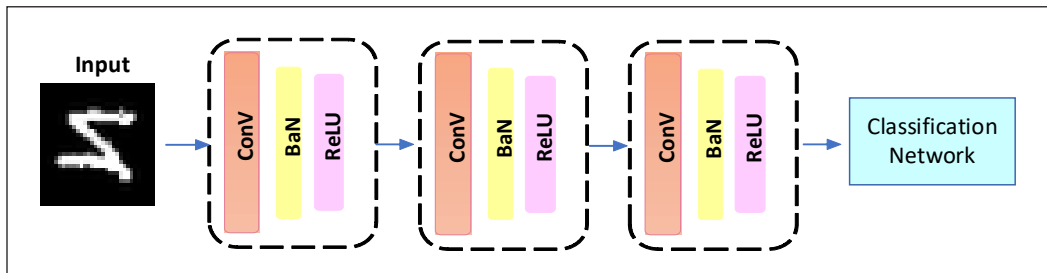


Figure 4. A new structure layer of Sequential Network architecture
 Note. Conv = Convolutional layers, BaN = Batch normalization

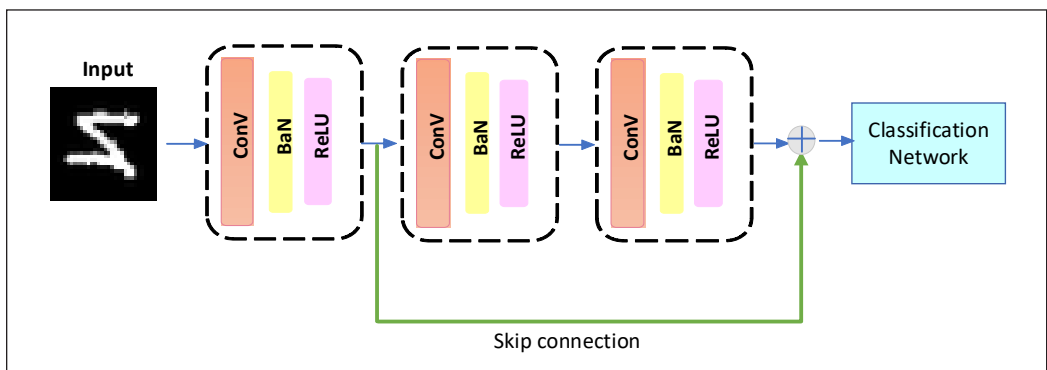


Figure 5. A new structure layer of Directed Acyclic Graph Network architecture
 Note. Conv = Convolutional layers, BaN = Batch normalization

using an average pooling prior classification network, the average of the items identified in the filtered area of the feature map is determined.

For each network, the neural network model parameters for dysgraphia screening using handwriting images were independently adjusted, as presented in Table 3. Both networks used the “sgdm” optimizer (Stochastic Gradient Descent with Momentum). The learning rate was set to 0.001 for SN and 0.01 for DAGN, which defines the step size for minimizing the loss. It implies that the model iterates and adjusts the weights each time. The model is trained for eight epochs, which means the network processes the dataset eight times during training. Each epoch has 1251 iterations, with the weights adjusted every 30 iterations. The optimizer, learning rate, epochs, and iterations per epoch are all factors that affect the performance and training duration of the neural network model used to classify handwriting images as dyslexic or normal.

Table 3

Parameter set up for Sequential Network (SN) and Directed Acyclic Graph Network model (DAGN)

Parameter	SN	DAGN
Optimizer	SGDM	SGDM
Learning Rate	0.001	0.01
Number of epochs	8	8

Train and Validate Model

Training and validating a deep learning network model require a structured process to ensure the model learns meaningful representations from the input data. During the training phase, the CNN model is given a labeled dataset and iteratively modifies its internal parameters to reduce the discrepancy between predicted and actual outputs (Alzubaidi et al., 2021). This optimization is often accomplished through backpropagation and gradient descent. Meanwhile, the validation phase is important for determining the model’s performance on unseen data. In this phase, the model’s generalization skills are evaluated using a separate dataset not used during training. To avoid overfitting, fine-tune the model based on the validation results and repeat this iterative procedure until the model achieves satisfactory performance on both the training and validation datasets.

Network Analysis

Performance evaluation assesses the neural network model’s capacity to detect potential dysgraphia and normal handwriting. This experiment uses performance evaluation to track and measure how the CNN model performs during training and testing. In this phase, network analysis involves analyzing the network’s performance based on the testing results obtained from untested data and subsequent to the comparison of both SN and DAGN performances.

Network Testing

The testing phase evaluates the model’s overall performance on a completely independent dataset, finalizing its capability to make accurate predictions in real-world scenarios. This

process ensures that the CNN-based model is robust and accurate and can generalize well beyond the training data. The binary class confusion matrix was used to evaluate the effectiveness of each model in achieving network testing. The performance was assessed using accuracy, precision, recall, and the F1-score. All computations are based on a binary confusion matrix (Sokolova & Lapalme, 2009) to identify potential dysgraphia and normal handwriting.

Performance Comparison

The final measurement involves comparing SN and DAGN performances according to the best achievement of accuracy, precision, recall, and f1-score as harmonic values to validate the performance measurement.

RESULTS

The classification performance of both SN and DAGN on potential dysgraphia handwriting images is analyzed using the confusion matrix and loss graph. Additionally, the extraction of layer networks influences classification performance through the result of accuracy, precision, recall, F1-score and loss obtained were analyzed. It also discusses how the conclusions may improve dysgraphia detection methods based on deep learning, especially Convolutional Neural Network (CNN).

The results shown in Figure 6 emphasize the classification performance of two network models: SN and DAGN. The SN model attained an impressive training accuracy of 94.27%, but its validation accuracy was slightly lower, and its testing accuracy decreased to 86%. In contrast, the DAGN model outperformed all other models in all phases. It outperformed the SN model in terms of training accuracy, achieving 96.17%, and demonstrated improved generalization, with a validation accuracy of 95.2%. Notably, the DAGN model exceeded the SN model in testing accuracy, scoring 87.75%. These data highlight the DAGN model's improved performance and generalization capability in dysgraphia classification compared to the SN model. The finding shows that the DAGN model outperforms the SN model in terms of accuracy during training, validation, and testing. The finding shows

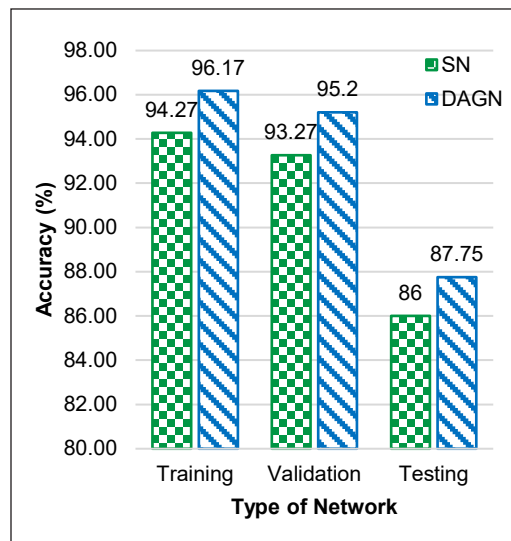


Figure 6. Accuracy performance for Sequential Network (SN) and Directed Acyclic Graph Network (DAGN)

that the DAGN model is more capable of learning and adapting properly to new unseen data. The higher accuracy achieved by the DAGN model on the testing dataset shows that it is more reliable and effective than the SN model in accurately classifying handwriting images. The DAGN model took 117 minutes and 9 seconds to train, while the SN model took somewhat longer at 121 minutes and 49 seconds. Although the SN model finished significantly faster, the time difference between the two models is relatively small.

The results presented in Figure 7 show the training and validation accuracies across multiple epochs. The training accuracy of the SN model begins at 46.09% at epoch 0 and steadily increases over consecutive epochs, reaching the highest at 94.53% at epoch 4. In subsequent epochs, it varied with slight decreases and increases. Similarly, the validation accuracy for the SN model began at 48.17% in epoch 0 and reached a maximum of 93.67% at epoch 8. Overall, the SN model improved training and validation accuracy over the length of the epochs. On the contrary, the DAGN model has better training accuracy across most epochs. It outperformed the SN model at 60.94% in epoch 0 and maintained relatively good training accuracy. At epoch 8, the highest training accuracy was obtained, 98.44%. Similarly, the DAGN model’s validation accuracy began at 54.77% at epoch 0 and steadily rose to 95.20% at epoch 8. In terms of training and validation accuracy, the DAGN model consistently outperformed the SN model. The findings revealed that the DAGN model exhibited enhanced predictive capabilities and improved accuracy as the epoch progressed. These findings highlight the importance of network architecture, with the DAGN model’s structure contributing to its higher performance over the SN model. The structure of layers, activation functions, or connection patterns in the DAGN model may allow it to extract relevant features and produce better predictions.

The loss graph for training and validation progress is shown in Figure 8. The training loss for the SN model began at 0.91 at epoch 0 and gradually reduced over subsequent

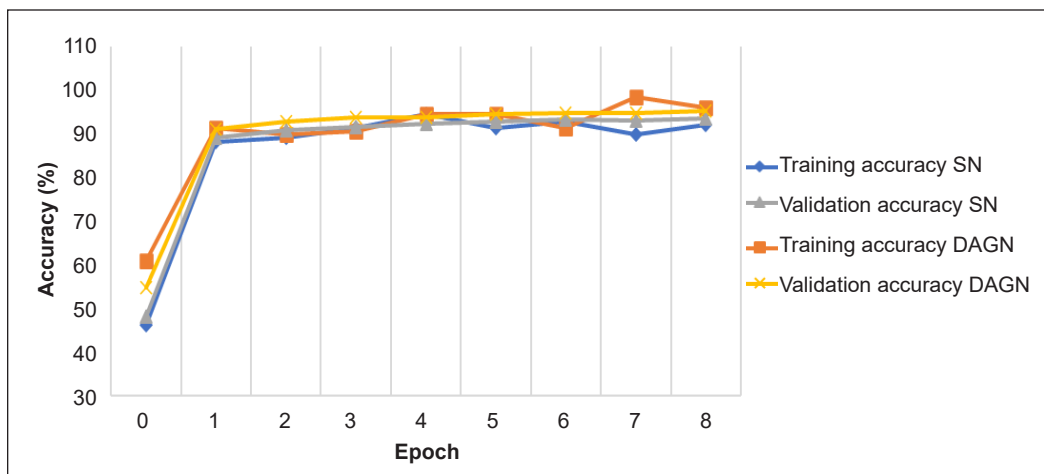


Figure 7. Accuracy performance graph for training and validation

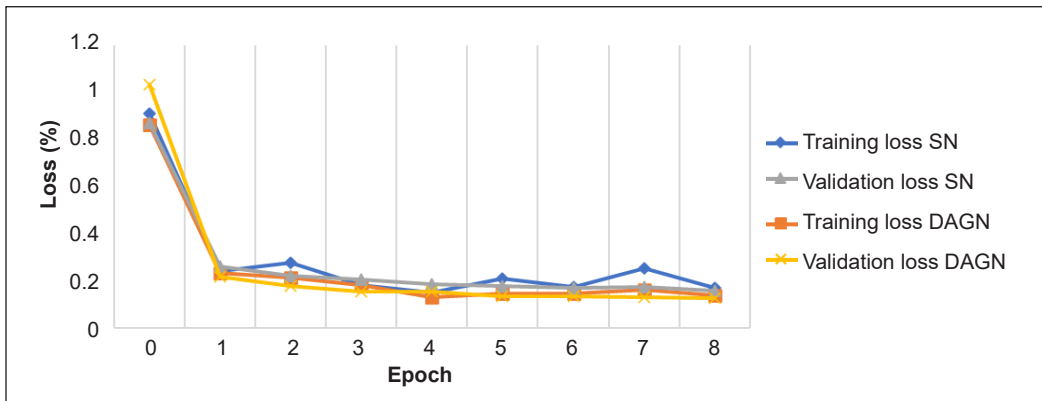


Figure 8. Loss graph for training and validation

Note. SN = Sequential Network, DAGN = Directed Acyclic Graph Network

epochs. It reached the lowest at 0.15 at epoch 4 and continued relatively low in subsequent epochs. Similarly, the validation loss for the SN model began at 0.87 at epoch 0 and decreased across the epochs, reaching a low of 0.16 at epoch 8. Over the training period, the SN model showed a reduction in training and validation losses. At the instance of the DAGN model, the training loss begins at 0.86 at epoch 0 and decreases progressively over the epochs. The validation loss for the DAGN model started at 1.03 at epoch 0 and rapidly reduced in the following epochs, reaching 0.13 at epoch 8. The DAGN model consistently reduced training and validation losses throughout the training process. The decreasing trend in losses suggests that both models are learning and adjusting their parameters to better capture the patterns in the data. These findings highlight the importance of network architecture and emphasize the potential benefits of utilizing the DAGN model for classifying handwriting images.

The data shown in Figure 9 compares the predicted classifications for DAGN to the actual classifications for two categories, namely dysgraphia and non-dysgraphia. In the first actual row, 42.0% (16,416) of the handwriting cases were correctly identified as dysgraphia, whereas 4.2% (1,652) cases of the actual dysgraphia handwriting were wrongly classified as non-dysgraphia which indicates a false negative rate. The second actual row shows that 8.0% (3,141) of the handwriting cases that were actually non-dysgraphia were wrongly labeled as dysgraphia, indicating a false positive rate. Meanwhile, 45.8% (17,90) of cases were correctly classified as non-dysgraphia.

The testing confusion matrix of SN is depicted in Figure 10, and it was discovered that 43.9% (17,152) of the occurrences that were dysgraphia were accurately recognized as such. However, 7.8% (3,070) of those with dysgraphia were misclassified as non-dysgraphia. The second row shows that 6.1% (2,405) of the cases that were actually non-dysgraphia were misclassified as dysgraphia. However, 42.2% (16,48) of the truly non-dysgraphia examples were appropriately classified as such. Generally, the model successfully classifies

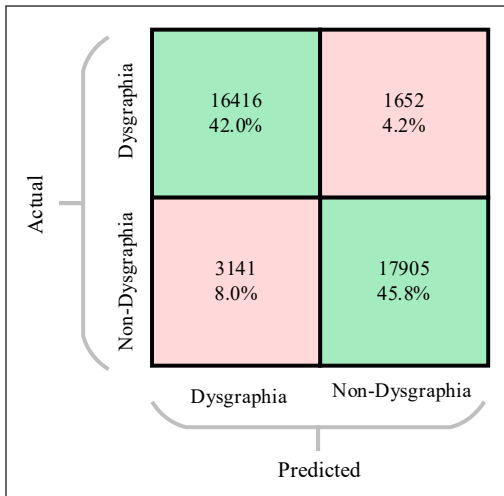


Figure 9. Testing confusion matrix of Directed Acyclic Graph Network

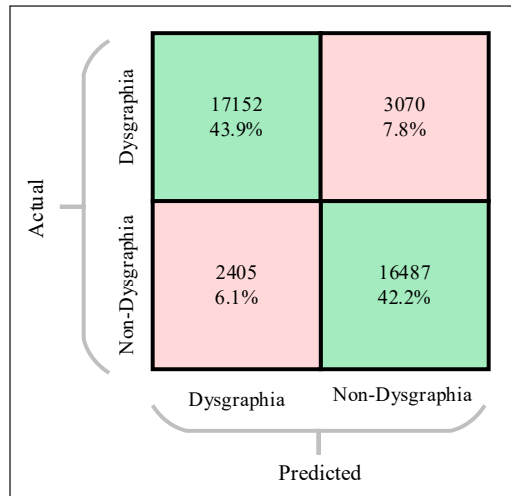


Figure 10. Testing confusion matrix of Sequential Network

dysgraphia with a higher rate of true predictions than misclassifications. However, more research is required to lower the false negative rate and ensure that all dysgraphia cases are correctly diagnosed. Similarly, with a higher percentage of accurate classifications, the model’s performance in detecting non-dysgraphia cases is beneficial.

A more comprehensive insight into the model’s performance is offered in Table 4 through additional analysis, including precision, recall, and F1-score. Precision for the dysgraphia class is high in training, validation, and testing for both SN and DAGN. The DAGN consistently outperforms the SN in terms of precision. During validation, the highest precision for SN was 92.90%, whereas DAGN yielded the highest precision with 97.07% accuracy. The recall scores for the dysgraphia class, SN, and DAGN are comparable, with SN having slightly higher recall values during validation and testing. The highest recall for DAGN is achieved during testing with 91.55% accuracy. For the dysgraphia class, the F1 scores for SN and DAGN are relatively close, with both models showing comparable performance during training, validation, and testing. During testing, the difference in performance between the SN and DAGN scores is only 0.12%.

For the non-dysgraphia class, the precision performance revealed that SN consistently outperforms DAGN at all training, validation, and testing. The maximum precision for SN was observed during testing, with 87.27% accuracy. Meanwhile, the recall score for DAGN increased at every stage of training, validation, and testing. The non-dysgraphia class achieved a high accuracy during testing, which was 7.15% greater than the SN class. SN and DAGN have similar F1 scores in the dysgraphia class and obtained the results with DAGN reaching slightly higher accuracy. DAGN achieved the greatest F1 score during testing and demonstrated 88.20% accuracy.

Table 4
Precision, recall and F1-score

	Type of Network	Training (%)		Validation (%)		Testing (%)	
		Dysgraphia	Non-Dysgraphia	Dysgraphia	Non-Dysgraphia	Dysgraphia	Non-Dysgraphia
Precision	SN	93.39	95.18	92.90	94.63	84.82	87.27
	DAGN	97.91	94.55	97.07	93.48	90.86	85.08
Recall	SN	95.27	93.26	94.74	92.76	87.70	84.30
	DAGN	94.35	97.99	93.22	97.18	83.94	91.55
F1 score	SN	94.32	94.09	93.81	93.56	86.24	85.29
	DAGN	95.96	96.24	94.92	95.29	86.36	88.20

Note. SN = Sequential Network, DAGN = Directed Acyclic Graph Network

The results show that SN and DAGN performance changes across the dysgraphia and non-dysgraphia classes. The DAGN model demonstrated exceptional performance throughout validation and testing, with accuracy rates of 95.2% and 87.75%, respectively. In contrast, the SN model obtained a meager 93.27% in validation and 86.0% in testing. Significantly superior in testing, the DAGN model exhibited a 1.75% improvement over the SN model. DAGN has higher precision and recall values in all classes, demonstrating a superior ability to classify handwriting. However, in terms of precision, SN outperforms the non-dysgraphia class. Both models have similar F1 scores, but the DAGN model performs better, with 86.36% and 88.20% accuracy in both classes.

DISCUSSION

The investigation results of this study demonstrate that the DAGN outperforms the SN in terms of accuracy and F1-score value. This finding indicates that the DAGN of extraction layer architecture is better suited for offline handwriting images in classifying dysgraphia and non-dysgraphia. The higher accuracy achieved by DAGN implies it is more effective at capturing and learning the underlying patterns and features than the SN.

The loss and training progress graphs presented in Figures 6 and 7 further support the superior performance of DAGN. The graphs clearly show that the DAGN model displays a faster convergence rate and lower training loss compared to the SN. It indicates that the DAGN layer construction is more efficient in optimizing the model parameters and minimizing the difference between predicted and actual classification. The consistent improvement in the loss and training progress throughout the training process indicates the efficiency and consistency of the DAGN model.

The testing confusion matrix in Figures 8 and 9 provides valuable details on the accuracy of predictions presented by both models. The confusion matrix demonstrates the DAGN's lower error rate in predicting target labels, highlighting its more accurate performance when compared to the SN. The confusion matrix demonstrates that the DAGN

model has a higher accuracy in correctly classifying the target labels, with fewer instances of misclassification between different classes.

Furthermore, the precision, recall, and F1 scores indicated in Table 4 prove that DAGN outperformed SN. These metrics comprehensively evaluate the model's performance by considering true positives, false positives, and false negatives. Precision can be defined as true positives (actual dysgraphia class predicted as dysgraphia) proportion to all handwriting in actual dysgraphia class. Therefore, precision scores demonstrate the DAGN model's ability to correctly identify dysgraphia handwriting as actual instances in the dysgraphia class. Meanwhile, the recall score demonstrates that the DAGN model can effectively recognize each class from the overall handwriting input images. As a result, the F1 score presented the harmonic mean value of precision and recall score, indicating that DAGN is greater than SN for both classes.

Overall, our findings highlight the superiority of the DAGN architecture over the SN in terms of accuracy, loss optimization, prediction accuracy, and comprehensive evaluation metrics. The DAGN model's ability to capture complex patterns, faster convergence rate, and lower error rate in predicting the target labels indicate its robustness and efficacy. It is supported by the DAGN structure, which enables skip connections in layer construction. Skip connections enable CNNs to bypass some layers and connect directly to deeper or shallower ones (Mohammed et al., 2022). It could help to differentiate patterns from the image data. Additionally, skip connections can help address the problem of vanishing gradients by offering alternate paths for the gradients to flow (Qiao et al., 2018). Furthermore, they can make it easier and faster to train deeper networks with greater expressive capacity and the ability to extract more features from data images. These results contribute to the growing evidence supporting the advantages of utilizing DAGN architectures in similar problem domains. Future research should focus on exploring the underlying reasons behind the improved performance of DAGN and investigate its applicability to other domains and datasets.

Based on the investigation, several studies have been compared to the proposed study, which provides excellent results with more than 80% testing accuracy, as depicted in Table 5. According to Table 5, the proposed CNN has 87.75% testing accuracy for a simple DAG construction network with automated feature extraction and 86.0% for a simple sequential network. In a study by Devi and Kavya (2023), hand-crafted feature extraction was executed using the Kekre-Discrete Cosine Transform method and classified using deep transfer learning for offline handwriting, which yielded the highest performance at 99.75% accuracy. Hand-crafted feature extraction is not competent in representing the overall performance because it is usually not robust, and the computational requirement is high, especially for high-dimension images. The performance of the proposed CNN-based model does not show the highest percentage of accuracy. However, this proposed CNN is the simplest network,

Table 5
State-of-the-art performance comparison

Author	Model	Input Domain	Performance
Masood et al., 2023	CNN-LSTM Random Forest	Parkinson handwriting	92.6%
Devi & Kavya, 2023	Kekre-Discrete Cosine Transform with Deep Transfer Learning (K-DCT-DTL)	Offline handwriting	99.75%
Vilasini et al., 2022	Convolutional Neural Networks (CNN) and Vision Transformers (ViT)	Offline handwriting (letter form)	79.47% (CNN) 86.22% (ViT)
Ghouse et al., 2022	Non-Discrimination Regularization in Rotational Region Convolutional Neural Network (NDR-R2CNN)	Offline handwriting	98.2%
Zolna et al., 2019	Recurrent Neural Network model (RNN).	Online handwriting	>90% diagnosed as dysgraphia
Proposed CNN	Sequential CNN (three Convolutional layers (SN))	Offline handwriting	86%
	DAG network	Offline handwriting	87.75%

and it has been successfully executed with automated feature extraction and only requires minimal time to complete the training and testing. However, the proposed CNN-based model demonstrated noteworthy performance, which is substantial enough to warrant its integration with another model in the future.

CONCLUSION

This paper focused on the classification performance of SN and DAGN on potential dysgraphia handwriting images and compared both network models. According to the experimental results, this study demonstrates that DAGN can significantly improve classification performance on dysgraphia screening using children's handwriting products. This finding is consistent with previous research that found skip connections in DAGN improved classification performance by addressing the issue of vanishing gradients during backpropagation. In addition, skip connections provide a different route that acts as a shortcut, preventing information loss and distortion across the network. Hence, DAGN has been proven to be a useful tool for image classification tasks, as it uses skip connections to improve training speed, accuracy, and stability. Besides, this improved performance may be contributed by the DAGN model's layer structure, activation functions, or connection patterns, which enable more efficient feature extraction and representation. The proposed CNN-based network model shows significant performance in children's handwriting classification and could be a considerable network structure to be integrated with another model to assist the dysgraphia detection process.

The performance in this study is based on a specific dataset, limiting the generalizability of the models. Additional validation on larger and more diverse data sets is required to establish the validity of the findings. Future research could investigate the interpretability of

model predictions to comprehend the underlying characteristics and patterns that contribute to dysgraphia detection in handwriting. Incorporating additional features and conducting comparative analyses with other advanced architectures or traditional algorithms would extend dysgraphia detection research while improving model precision and reliability. This study shows that using DAGN as a promising strategy for identifying dysgraphia-related handwriting symptoms has the potential to improve understanding of dysgraphia and stimulate the development of improved tools and interventions for people with this learning difference.

ACKNOWLEDGMENTS

This project is funded by the Malaysia Ministry of Higher Education Grant Scheme (FRGS), “A Formulation on Optimum Resnet-CNN Layer Architecture Based on Dilated Method for Dysgraphia Severity Classification”(Ref: FRGS/1/2021/ICT02/UITM/02/4). The authors thank members of the Research Intervention for Dysgraphia: Learning & Technology (RIDyLT) and the Centre for Electrical Engineering Studies, Universiti Teknologi MARA, Cawangan Pulau Pinang, Malaysia, for their help and guidance during the fieldwork. Finally, the authors express their gratitude to Universiti Teknologi MARA, Cawangan Pulau Pinang, Malaysia, for their exceptional administrative support.

REFERENCES

- Almisreb, A. A., Tahir, N. M., Turaev, S., Saleh, M. A., & Al Junid, S. A. M. (2022). Arabic handwriting classification using deep transfer learning techniques. *Pertanika Journal of Science and Technology*, 30(1), 641–654. <https://doi.org/10.47836/PJST.30.1.35>
- Alzubaidi, L., Zhang, J., Humaidi, A. J., Al-Dujaili, A., Duan, Y., Al-Shamma, O., Santamaría, J., Fadhel, M. A., Al-Amidie, M., & Farhan, L. (2021). Review of deep learning: Concepts, CNN architectures, challenges, applications, future directions. *Journal of Big Data*, 8, Article 53. <https://doi.org/10.1186/s40537-021-00444-8>
- Asselborn, T., Chapatte, M., & Dillenbourg, P. (2020). Extending the spectrum of dysgraphia: A data driven strategy to estimate handwriting quality. *Scientific Reports*, 10(1), Article 3140. <https://doi.org/10.1038/s41598-020-60011-8>
- Biotteau, M., Danna, J., Baudou, É., Puyjarinet, F., Velay, J. L., Albaret, J. M., & Chaix, Y. (2019). Developmental coordination disorder and dysgraphia: Signs and symptoms, diagnosis, and rehabilitation. *Neuropsychiatric Disease and Treatment*, 15, 1873–1885. <https://doi.org/10.2147/NDT.S120514>
- Chai, J., Zeng, H., Li, A., & Ngai, E. W. T. (2021). Deep learning in computer vision: A critical review of emerging techniques and application scenarios. *Machine Learning with Applications*, 6, Article 100134. <https://doi.org/10.1016/j.mlwa.2021.100134>
- Chung, P. J., Patel, D. R., & Nizami, I. (2020). Disorder of written expression and dysgraphia: Definition, diagnosis, and management. *Translational Pediatrics*, 9(Suppl 1), S46–S54. <https://doi.org/10.21037/TP.2019.11.01>

- Dankovicova, Z., Hurtuk, J., & Fecilak, P. (2019, September 12-14). *Evaluation of digitalized handwriting for dysgraphia detection using random forest classification method*. [Paper presentation]. IEEE 17th International Symposium on Intelligent Systems and Informatics, Proceedings (SISY), Subotica, Serbia. <https://doi.org/10.1109/SISY47553.2019.9111567>
- Deuel, R. K. (1995). Developmental dysgraphia and motor skills disorders. *Journal of Child Neurology*, *10*(1_suppl), S6-S8. <https://doi.org/10.1177/08830738950100S103>
- Devi, A., & Kavya, G. (2023). Dysgraphia disorder forecasting and classification technique using intelligent deep learning approaches. *Progress in Neuro-Psychopharmacology and Biological Psychiatry*, *120*, Article 110647. <https://doi.org/10.1016/j.pnpbp.2022.110647>
- Devillaine, L., Lambert, R., Boutet, J., Aloui, S., Brault, V., Jolly, C., & Labyt, E. (2021). Analysis of graphomotor tests with machine learning algorithms for an early and universal pre-diagnosis of dysgraphia. *Sensors*, *21*(21), Article 7026. <https://doi.org/10.3390/s21217026>
- Dimauro, G., Bevilacqua, V., Colizzi, L., & Di Pierro, D. (2020). TestGraphia, a software system for the early diagnosis of dysgraphia. *IEEE Access*, *8*, 19564–19575. <https://doi.org/10.1109/ACCESS.2020.2968367>
- Ghouse, F., Paranjothi, K., & Vaithyanathan, R. (2022). Dysgraphia classification based on the non-discrimination regularization in rotational region convolutional neural network. *International Journal of Intelligent Engineering and Systems*, *15*(1), 55–63. <https://doi.org/10.22266/IJIES2022.0228.06>
- Kunhoth, J., Maadeed, S. A., Saleh, M., & Akbari, Y. (2023). Biomedical signal processing and control exploration and analysis of on-surface and in-air handwriting attributes to improve dysgraphia disorder diagnosis in children based on machine learning methods. *Biomedical Signal Processing and Control*, *83*, Article 104715. <https://doi.org/10.1016/j.bspc.2023.104715>
- Masood, F., Khan, W. U., Ullah, K., Khan, A., Alghamedy, F. H., & Aljuaid, H. (2023). A hybrid CNN-LSTM random forest model for dysgraphia classification from hand-written characters with uniform/normal distribution. *Applied Sciences*, *13*(7), Article 4275. <https://doi.org/10.3390/app13074275>
- Mohammed, A. B., Al-Maftji, A. A. M., Yassen, M. S., & Sabry, A. H. (2022). Developing plastic recycling classifier by deep learning and directed acyclic graph residual network. *Eastern-European Journal of Enterprise Technologies*, *2*(10), 42–49. <https://doi.org/10.15587/1729-4061.2022.254285>
- Qiao, J., Lv, Y., Cao, C., Wang, Z., & Li, A. (2018). Multivariate deep learning classification of alzheimer's disease based on hierarchical partner matching independent component analysis. *Frontiers in Aging Neuroscience*, *10*, Article 417. <https://doi.org/10.3389/fnagi.2018.00417>
- Ramlan, S. A., Isa, I. S., Osman, M. K., Ismail, A. P., & Soh, Z. H. C. (2022). Investigating the impact of CNN layers on dysgraphia handwriting image classification performance. *Journal of Electrical and Electronic Systems Research*, *21*, 73–83. <https://doi.org/https://doi.org/10.24191/jeesr.v21i1.010>
- Rosli, M. S. A., Isa, I. S., Ramlan, S. A., Sulaiman, S. N., & Maruzuki, M. I. F. (2021, August 27-28). *Development of CNN transfer learning for dyslexia handwriting recognition*. [Paper presentation]. 11th IEEE International Conference on Control System, Computing and Engineering (ICCSCE), Penang, Malaysia. <https://doi.org/10.1109/iccsce52189.2021.9530971>

- Šafářová, K., Mekyska, J., & Zvončák, V. (2021). Developmental dysgraphia: A new approach to diagnosis. *The International Journal of Assessment and Evaluation*, 28(1), 143–160. <https://doi.org/10.18848/2327-7920/CGP/v28i01/143-160>
- Sihwi, S. W., Fikri, K., & Aziz, A. (2019). Dysgraphia identification from handwriting with support vector machine method. *Journal of Physics: Conference Series*, 1201(1), Article 012050. <https://doi.org/10.1088/1742-6596/1201/1/012050>
- Sokolova, M., & Lapalme, G. (2009). A systematic analysis of performance measures for classification tasks. *Information Processing and Management*, 45(4), 427–437. <https://doi.org/10.1016/j.ipm.2009.03.002>
- Vilasini, V., Rekha, B. B., Sandeep, V., & Venkatesh, V. C. (2022, August 11-12). *Deep learning techniques to detect learning disabilities among children using handwriting*. [Paper presentation]. Third International Conference on Intelligent Computing Instrumentation and Control Technologies (ICICICT), Kannur, India. <https://doi.org/10.1109/ICICICT54557.2022.9917890>
- Vaivre-Douret, L., Lopez, C., Dutruel, A., & Vaivre, S. (2021). Phenotyping features in the genesis of pre-scriptural gestures in children to assess handwriting developmental levels. *Scientific Reports*, 11(1), Article 731. <https://doi.org/10.1038/s41598-020-79315-w>
- Vlachos, F., & Avramidis, E. (2020). The difference between developmental dyslexia and dysgraphia: Recent neurobiological evidence. *International Journal of Neuroscience and Behavioral Science*, 8(1), 1–5. <https://doi.org/10.13189/ijnbs.2020.080101>
- Zolna, K., Asselborn, T., Jolly, C., Casteran, L., Johal, W., & Dillenbourg, P. (2019). The dynamics of handwriting improves the automated diagnosis of dysgraphia. *arXiv:1906.07576*, Article 1906.07576. <https://doi.org/10.48550/arXiv.1906.07576>

Learning Discriminative Features Using ANN-based Progressive Learning Model for Efficient Big Data Classification

Nandita Bangera^{1,2*} and Kayarvizhy¹

¹B.M.S College of Engineering, Bangalore, Karnataka 560019, India

²RV Institute of Technology and Management, Bangalore 560076, India

ABSTRACT

Progressive techniques encompass iterative and adaptive approaches that incrementally enhance and optimize data processing by iteratively modifying the analysis process, resulting in improved efficiency and precision of outcomes. These techniques contain a range of components, such as data sampling, feature selection, and learning algorithms. This study proposes the integration of an Artificial Neural Network (ANN) with a Progressive Learning Model (PLM) to enhance the efficacy of learning from large-scale datasets. The SMOTE and Pearson Correlation Coefficient (PCC) methods are commonly employed in imbalanced dataset handling and feature selection. The utilization of progressive weight updating is a notable strategy for improving performance optimization in neural network models. This approach involves the incremental modification of the network's progressive weights during the training phase rather than relying on gradient values. The proposed method gradually obtains the localization of discriminative data by incorporating information from local details into the overall global structure, effectively reducing the training time by iteratively updating the weights. The model has been examined using two distinct datasets: the Poker hand and the Higgs. The performance of the suggested method is compared with that of classification algorithms: Population and Global Search Improved Squirrel Search Algorithm (PGS-ISSA) and Adaptive E-Bat (AEB). The convergence of Poker's is achieved after 50 epochs with ANN-PLM; however, without PLM, it takes 65 epochs.

Similarly, with the Higgs, convergence is achieved after 25 epochs with PLM and 40 without PLM.

Keywords: Artificial neural network, big data classification, data imbalance, Pearson correlation coefficient-based feature selection, progressive learning model, weight updating

ARTICLE INFO

Article history:

Received: 22 August 2023

Accepted: 01 February 2024

Published: 08 August 2024

DOI: <https://doi.org/10.47836/pjst.32.5.06>

E-mail addresses:

nanditamanohar@gmail.com (Nandita Bangera)

kayarvizhyn.cse@bmsce.ac.in (Kayarvizhy)

* Corresponding author

INTRODUCTION

Information technologies have achieved extraordinary growth in data. Large amounts of data from various applications are combined as big data, which has resulted in the complexity of dealing with big data (Wang et al., 2021) and enhancing convergence. Big data is either structured or unstructured. The number of data created is represented as volume (Dubey et al., 2021), data's creation speed is defined as velocity and structured and unstructured characteristics are represented as data's variety (Jain et al., 2022; Kantapalli & Markapudi, 2023). Big data gathers huge attention in numerous areas, such as electronic commerce, online social networks, the Internet of Things, bioinformatics, and e-health because those applications have progressively achieved an enormous amount of raw data (Brahmane & Krishna, 2021; Hassib et al., 2020; Park et al., 2021; Xing & Bei, 2020).

Big data applications have revolutionized various industries by providing unprecedented opportunities to extract valuable insights from massive and complex datasets. However, the volume and complexity of big data often pose challenges in terms of response time, as processing such large-scale data can be time-consuming and resource-intensive. Many techniques have emerged as promising approaches to reduce response time and improve the efficiency of big data applications in addressing these challenges,

Data preparation techniques can reduce processing time in large-scale data applications. Preprocessing refers to a set of operations that increase the quality and usability of data, such as data cleansing, transformation, and integration. Preprocessing processes that are executed efficiently can decrease unnecessary computational overhead, resulting in faster processing time. Sampling approaches are an alternate method for dealing with the issue of time limits. Sampling is a statistical strategy in which a representative subset of data is chosen for examination rather than the complete dataset. It is feasible to achieve large savings in computing complexity and processing time while receiving important insights using a smaller sample size. It is also critical to ensure that the sampling approach maintains the statistical traits and characteristics of the initial dataset. In machine learning, data classification is an extensive operation that involves understanding the targeted data to predict the class of unseen data (Banchhor & Srinivasu, 2021). The existence of prominent redundancy of information in data is required to be noted while examining the openly accessible tabular big data issues because these redundant features cause an impact on storage and scalability (Basgall et al., 2020). The training of an efficient learning system is difficult in data mining when the given class distribution is imbalanced in a training data set. Moreover, the classification of rare objects is more complex than that of general objects in most data mining approaches (Abhilasha & Naidu, 2022). The imbalance (Juez-Gil et al., 2021) decreases the classifier's generalization abilities and makes it inefficient for minority classes (Sleeman & Krawczyk, 2021). Therefore, feature selection is combined with progressive learning to improve big data classification in this work. Feature selection

is choosing appropriate features and eliminating redundant features from the dataset. Moreover, preserving the strong features makes the predictive model highly discriminative, which enhances performance (Al-Thanoon et al., 2021; BenSaid & Alimi, 2021).

The timely completion of data processing and machine learning model training is critical for generating efficient and timely results. Numerous approaches have been proposed in scholarly publications, including feature selection, dimensionality reduction, ensemble learning, approximation, transfer learning, progressive sampling algorithms, mini-batch learning, and online learning to overcome this barrier. Using these strategies, researchers can effectively reduce training time while maintaining acceptable levels of precision, allowing for faster and more effective application of machine learning models.

The use of iterative and incremental strategies in model construction and data analysis distinguishes progressive approaches in machine learning. These strategies aim to gradually improve the accuracy of machine learning models by incorporating new data and modifying model parameters. Researchers and data scientists can iteratively improve the precision and efficacy of their models by implementing progressive methodologies. Progressive techniques have been developed to decrease the temporal complexity of training time, resulting in faster learning. This advancement is particularly significant for big data applications. However, it is important to note that these techniques also have certain drawbacks. Progressive networks present a model framework that enables transfer through lateral connections to characteristics of previously acquired columns. This mechanism mitigates the issue of catastrophic forgetting by establishing a distinct neural network, referred to as a column, for each task being performed. During training, the system maintains a reservoir of pre-trained models and leverages lateral connections from existing models to extract valuable characteristics for novel tasks. The network's last layer, along with its associated weights, increases in size as each new class is introduced. All these models necessitate additional overhead in establishing new connections and incorporating additional columns to retain the acquired data. The trade-off involves an increase in model complexity, which refers to including a greater number of parameters to be trained for each extra column. If a new class is introduced, it becomes necessary to retrain the entire model. The implementation of progressive learning paradigms necessitates a fundamental alteration in the arrangement of layers and neurons, augmenting the process's intricacy.

Progressive learning is a concept in artificial neural networks (ANNs) that refers to incrementally improving a neural network's performance over time. There are many progressive learning techniques for ANN and CNN. The techniques differ in the way the network carries out the learning. Recent literature has focused on developing progressive learning algorithms that are more efficient, robust, and flexible. Some approaches include incremental, transfer, lifelong, and meta-learning. Incremental learning methods gradually learn new tasks while preserving previously learned knowledge. Transfer learning

approaches leverage knowledge from previously learned tasks to improve learning on new tasks. Lifelong learning methods learn continuously over an extended period while maintaining a growing knowledge base. Meta-learning methods aim to learn how to learn, facilitating faster and more efficient learning.

This research uses the ANN with PLM to perform big data classification without changing the overall structure of the ANN and maintaining the process of traditional ANN. In this proposed system, the incremental learning of weights according to the batches of data is termed a progressive learning model. This research highlights feature selection, data imbalance, and progressive learning methods, which collectively reduce the training time of neural networks.

The contributions of this work are concise as follows—the ANN-PLM approach is used to localize discriminative data from local details to the global structure, which is further used to enhance classification by combining the output of the last multiple stages and progressively updating the probabilities of the weight. PLM helps the neural network learn from the data effectively and efficiently, leading to better accuracy and faster training times.

The possible research questions that arise and which have been addressed in the paper are:

- RQ1: How does combining a Progressive Learning Model (PLM) with an Artificial Neural Network (ANN) impact learning effectiveness from extensive datasets?
- RQ2: What is the specific impact of progressive weight updating on reducing the training time of the ANN-PLM model, and how does this compare to traditional gradient-based weight updating methods?
- RQ3: What is the comparative performance of the ANN-PLM model about traditional classification algorithms like Population and Global Search improved Squirrel search Algorithm (PGS-ISSA) and Adaptive E-Bat (AEB)?

RELATED WORK

We discuss further the related work on big data classification and progressive learning, along with its advantages and limitations.

Du et al. (2022) developed a progressive training approach that operated in a zooming-out manner to perform fine-grained visual classification. This progressive training was executed in various steps to accomplish the feature learning and acquire the essential complementary characteristics between various granularities. The Category-Consistent Block Convolution (CCBC) was proposed, which integrated the operation of block convolution with the feature Category-Consistency Constraint (CCC). This CCC was used to overcome the overfitting issue and confirmed that the acquired multi-granularity regions are expressive and related to classes. The classification of developed progressive training mainly depends on the block numbers of convolutional layers.

Rebuffi et al. (2017) proposed a method for incremental learning that addresses the problem of catastrophic forgetting. It uses a combination of exemplar-based rehearsal and feature expansion to learn new tasks while preserving old ones. All these methods have the overhead of storing the old, learned data.

A newly developed learning method that could help learn new classes while keeping information from older courses was proposed by Venkatesan and Er (2016). The number of classes did not bind it. The neural network structure is automatically reconstructed by enabling new neurons and interconnections when a new class that is not native to the knowledge obtained so far is encountered, and the parameters are computed so that the knowledge learned thus far is kept. This approach is suited for real-world applications where it is necessary to learn online using real-time data and where the number of classes is frequently uncertain. The consistency and intricacy of the progressive learning method are studied. The proposed method used the ELM technique, where the output layer structure changes every time a new class is introduced.

Chatterjee et al. (2017) created an approach for systematically creating a large artificial neural network employing a progression property in this paper. The systematic design handles network size selection and parameter regularization. A network's number of nodes and layers grows over time to constantly lower a reasonable cost. Each layer is optimized individually, with optimal parameters learned via convex optimization. Certain weight matrices' random occurrences reduced the number of parameters to learn. However, instead of utilizing a back propagation-based learning strategy, they applied a nonlinear modification at each layer.

In this Progressive method, a deep network is developed unsupervised by PSL, a progressive stage-wise learning framework for unsupervised visual representation learning (Li et al., 2021). Early learning stages concentrate on simple tasks, whereas later learning stages are guided to glean deeper knowledge from more challenging tasks. They have used the gradient flow concept from one step to the next.

The suggested network architecture prevents prior knowledge from being forgotten and allows previously learned knowledge to be leveraged through lateral connections to previously learned classes and their attributes (Siddiqui & Park, 2021). Furthermore, the suggested technique is scalable and does not necessitate structural changes to the network trained on the old task; both are critical qualities in embedded systems, but this proposed method requires a pool of pre-trained models. Progressive Neural Networks (ProgNN) is a method for incremental learning (Rusu et al., 2016). ProgNN adds new neural networks to the architecture to solve new tasks while retaining knowledge from previous tasks. Each new network is trained on the new task and connected to the previous networks, forming a chain of expertise.

This work is based on a cross-entropy loss to learn the new classes and a distillation measure to retain the knowledge from the old classes (Castro et al., 2018). It requires extra memory space to store the old class data.

Movassagh et al. (2021) suggest a Hierarchical Convolutional Neural Network (HCNN) for image classification in this paper, which consists of numerous subnetworks utilized to categorize images progressively. The images with the revised weights are utilized to train the following sub-networks. If the prediction confidences in a sub-network are above a certain threshold, the results are output immediately. Otherwise, the following sub-networks must acquire deeper visual properties sequentially until a reliable image classification result or the last sub-network is reached. Otherwise, the following sub-networks must acquire deeper visual properties one after the other until a reliable image classification result or the last sub-network is reached. The model's accuracy is relatively high; however, it necessitates the maintenance of subnetworks, which adds overhead. All the research on progressive learning depicts the stupendous effort to retain knowledge, creating an overhead in time and memory.

The remaining portion of the associated study is based on data imbalance and classification techniques used for ANN. Smote plays an important role in solving the issues related to data imbalance. Sleeman and Krawczyk (2021) presented Apache Spark, including a SMOTE, to overcome spatial restrictions in big data analytics. The developed multi-class sampling approaches, i.e., SMOTE, under- and oversampling, were augmented with informative sampling and partitioning for SMOTE in Spark nodes. Therefore, clustering-based data partitioning was used to avoid the issue of the absence of spatial coherence between the instances from each class because of the random data splitting between the nodes. The probability of generating erroneous artificial instances was minimized by using the SMOTE in Spark. For an effective classification, feature selection was required to be considered for selecting the optimal features.

Ali and Balakrishnan (2021) developed the Population and Global Search Improved Squirrel Search Algorithm (PGS-ISSA) for feature selection. The developed PGS-ISSA was used to overcome the issue of local optimum and minimize the convergence rate in the conventional squirrel search algorithm. The main modification of this PGS-ISSA was the development of chaos theory to improve the population initialization, which is used to maximize the search space. The optimal features were chosen according to the minimum error rate used in the fitness to enhance the classification. The classification's SVM does not perform better when processed with larger datasets.

Mujeeb et al. (2021) presented the optimization-based MapReduce framework (MRF) for dealing with imbalanced data using the deep learning approach in classification. An adaptive E-Bat (AEB) approach was used to select the feature using the mappers in the MRF. The developed AEB integrated the Exponential Weighted Moving Average (EWMA) and the Bat algorithm (BA). The AEB was used to modify the update expression of E-Bat by creating an adaptive one for handling real-time data. The Deep Belief Network was used to classify the features according to the chosen ones. The developed AEB required

many training data to provide better classification accuracy. In most of the work mentioned above, the categorization of the generated progressive training was mostly based on the convolutional layer block counts, and a large amount of training data was needed.

Zhou et al. (2021) presented the region proposal and progressive learning, namely PRP-Net, for recognizing vegetable disease under a complex background. The attention proposal subnetwork, APN, was developed to acquire the disease’s key regions from the background. The developed APN provided highly discriminative data for extracting the features. Next, these acquired regions were integrated with progressive learning to support the model in concentrating on fine-grained areas to obtain multiscale features. The channel attention mechanism was used to estimate the features for classification. The database’s knowledge information was required to be enhanced to assist the training process; only then can it process the data from various times and planes. Hassanat et al. (2021) developed a supervised machine learning Magnetic Force (MF) classifier for big data classification according to iron-filling attraction to magnetic force. Here, the class was denoted by certain magnets, and iron filings denoted the unknown data points required to be categorized in big data classification. The inverse square law was applied to computing each class’s force over each point in feature space. The developed MF was sensitive to the information skewed by the class.

MATERIALS AND METHODS

With a progressive learning model, ANN is developed to improve big data classification in this research. The important processes of the proposed method are (1) data acquisition, (2) class imbalance processing using SMOTE, (3) feature selection using PCC, and (4) classification using ANN-PLM. Here, the PCC is used to choose the optimal features from the feature vector, which leads to improving the classification. The localization of discriminative data from local details to the global structure is used to perform an effective classification. Figure 1 shows the block diagram of the proposed method.

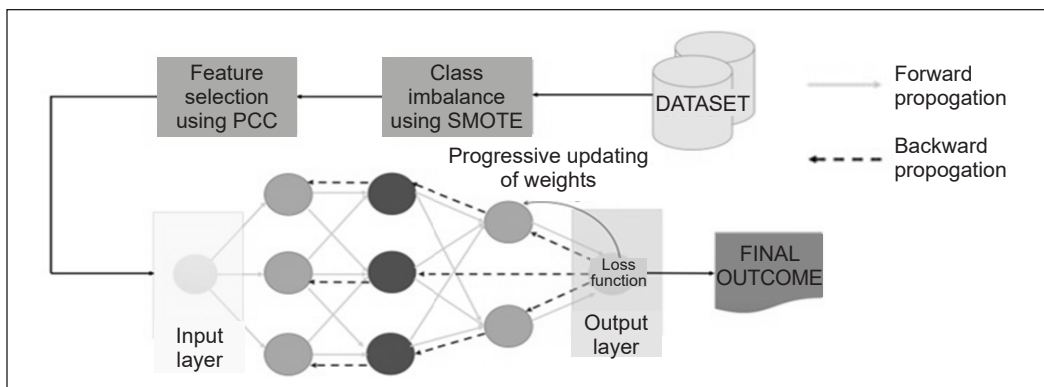


Figure 1. Block diagram of the proposed method

Dataset Acquisition

In this research, two datasets, the Poker hand dataset and the Higgs dataset, are taken from the UCI and Kaggle machine repository. The links for the dataset are: <https://archive.ics.uci.edu/ml/datasets/Poker+Hand>; and <https://archive.ics.uci.edu/ml/datasets/HIGGS>.

Few research methodologies have used these datasets, considering their voluminous structure, which consumes much processing time. The proposed method experimented with the PLM training method on this dataset to achieve considerably good results.

The Poker hand dataset includes the 1025010 instances and 11 attributes with categorical and integer features. The nature of this Poker hand dataset is multivariate.

Poker is a 5-card poker hand used in each instance of the dataset, with each card having two attributes (suite and rank) and the poker-hand label. It is an all-categorical trait and highly imbalanced dataset, with the first two classes representing 90% of the samples in both the training and testing sets. In the Higgs dataset, the number of attributes and instances are 28 and 1100000, respectively. Monté Carlo simulations were used to generate the data. The first column is the class label (s for the signal for background), followed by the 28 features (21 low-level features, then 7 high-level features). The first 21 features (columns 2–22) are kinematic attributes measured by the accelerator's particle detectors. The final seven features are functions of the first 21 features. These are high-level features developed by physicists to aid in distinguishing between the two groups.

Class Imbalance Processing Using SMOTE

The data acquired from the datasets are processed using the synthetic minority over-sampling technique (SMOTE) approach to avoid issues related to imbalanced data. SMOTE is a classical oversampling in that the number of samples of the minority class is maximized in proportion to the majority class. The main principle of SMOTE is to include new data at random places among the minority data and its neighbors. Initially, the K-nearest neighbors are investigated using minority-class data. Equation 1 shows the interpolation expression of SMOTE.

$$D'_i = D + rand(0,1) \times (NN_i - D) \quad [1]$$

The data sample of minority class samples is denoted as D ; the random number between $[0,1]$ is denoted as $rand(0,1)$; the i th nearest neighbors are denoted as NN_i , and the interpolated sample is denoted as D'_i .

Figure 2 shows the imbalance property of both datasets, whereas Figure 3 depicts the class distribution before and after applying SMOTE in the Higgs Dataset.

The Higgs dataset contained imbalanced data, with the background class representing almost 90% of data and the signal class around 50% after the application of SMOTE. Oversampling equally distributed the classes.

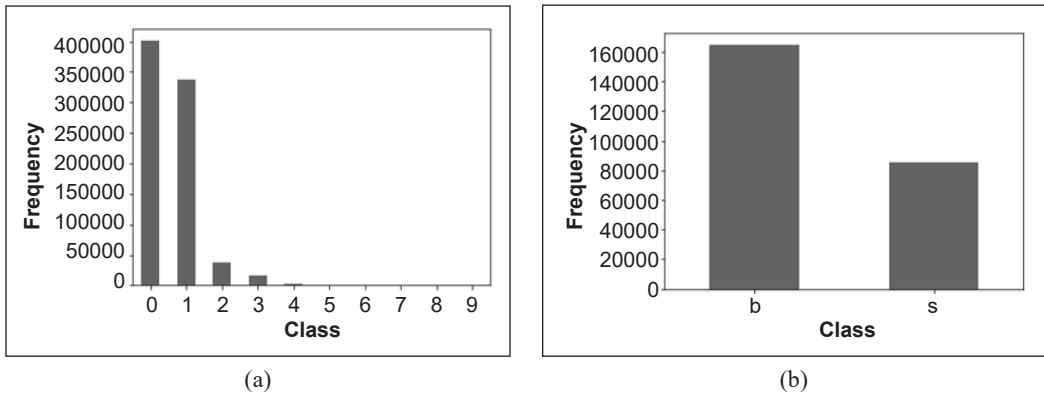


Figure 2. Depiction of total imbalance distribution of classes in: (a) Poker dataset; and (b) Higgs dataset before applying SMOTE

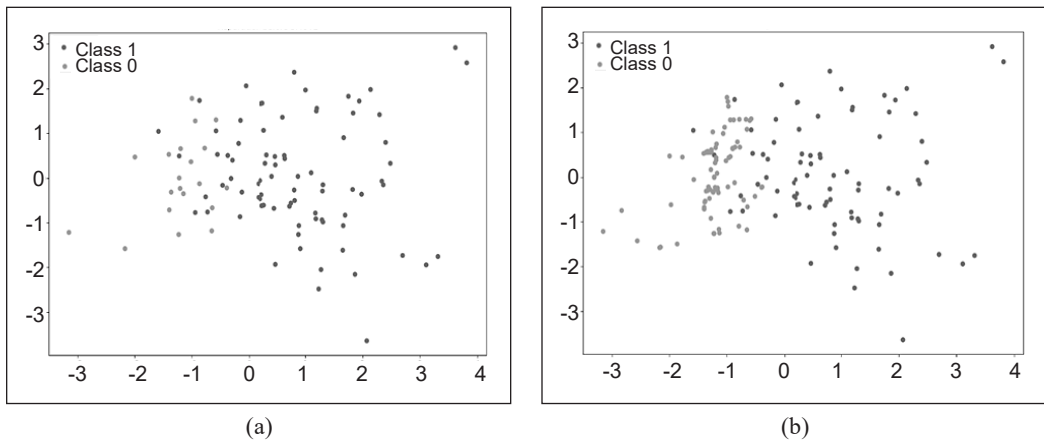


Figure 3. Distribution of classes in Higgs dataset: (a)Before; and (b) after applying SMOTE

Feature Selection Using Pearson Correlation Coefficient

Pearson Correlation Coefficient (PCC) is a linear dependence degree measured between the two random features, i.e., real-valued vectors obtained from the dataset. PCC of two variables, D'_1 and D'_2 , is generally defined as the ratio between the covariance (COV) of the two variables and the standard deviation's product expressed in Equation 2.

$$\rho_{D'_1, D'_2} = \frac{COV(D'_1, D'_2)}{\sigma_{D'_1} \sigma_{D'_2}} \tag{2}$$

Where the PCC is denoted as $\rho_{D'_1, D'_2}$; standard deviations of D'_1 and D'_2 are denoted as $\sigma_{D'_1}$ and $\sigma_{D'_2}$; Hence, the relevant features are selected based on derived PCC, and it is processed further in the ANN with PLM for big data classification. The coefficient correlation value less than 0.5 was not considered for the training dataset.

Classification Using ANN-PLM

PLM Process

The training process, which is performed using PLM, starts from a lower stage and progressively updates the learning weights of all stages to perform the overall training. The phenomena considered in progressive learning is the computation of progressive weight based on cross-entropy loss. This cumulative progressive weight is updated to the previous layer via backpropagation. In normal backpropagation, the gradient value is updated as feedback to the previous layer, but ANN-PLM updates the progressive weight to the previous layer. This progressive weight-based feedback helps to achieve trained layers with optimal performance in an earlier stage compared to the conventional ANN. The PLM is required to obtain the discriminative data from local details to overcome the lower stage's restriction of representation capacity and receptive field. Here, the representation capacity denotes the data training capacity of neurons in an ANN layer, and the receptive field represents the response attainable from the neurons according to the previous stage output. The ANN steadily discovers discriminative data from local (i.e., layer) details to the global structure along with the increment of stages, where the global structure is cumulative of all hidden layers.

In general, the ANN output is the trained weights of the hidden layers, whereas the ANN-PLM's output is the weight of the global structure. The changes in the local layer's weight create an impact on the adjacent layers. Consequently, the global structure varies as a result of progressive learning.

Steps in the PLM Process

The flowchart of the proposed system is shown in Figure 4.

The main objective is to develop progressive training to reduce classification loss in various intermediate stages. Therefore, the convolution block of B_l^{conv} considers the output of stage S_l as input and minimizes vector depiction. $V_l = B_l^{conv}(S_l)$ The classification module B_l^{class} is defined for predicting the probability distribution, whereas B_l^{class} has exponential linear units, batch norm, and two fully connected stages. The probability distribution $y_l = B_l^{class}(V_l)$ is obtained by giving V_l as input to the classification.

The cross-entropy loss L_{CE} expressed in Equation 3 is adopted in PLM for reducing the distance among the label of ground truth y and distribution of prediction probability y_l

$$L_{CE}(y_l, y) = - \sum_{i=1}^m y^i \times \log(y_l^i) \quad [3]$$

Where the number of categories is represented as m ; the probability that the input X of the category i and stage l is represented as y_l^i . The outputs of multiple previous stages are combined, as shown in Equation 4, to enhance the classification.

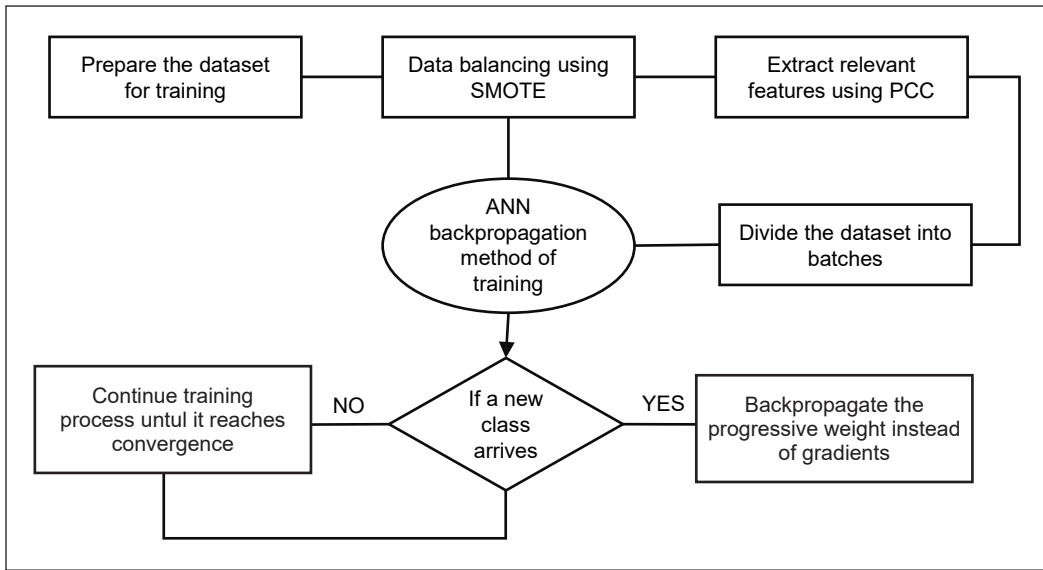


Figure 4. Flowchart of proposed ANN-PLM method

$$V_{concat} = concat[V_{L-S+1}, \dots, V_{L-1}, V_L] \tag{4}$$

Where the amount of the last stages is represented as S , and it is followed by the classification, $y_{concat} = H_{concat}^{class}(V_{concat})$, where H is an output. Subsequently, the PLM is optimized using the cross-entropy loss, expressed in Equation 5.

$$L_{CE}(y_{concat}, y) = - \sum_{i=1}^m y^i \times \log(y_{concat}^i) \tag{5}$$

The parameters used in the current estimation are optimized and are updated in the previous step to help every stage in the PLM operate together in the ANN. The probability distribution of discovery, such as y_l and y_{concat} , is obtained in PLM. The outcome of PLM is derived as Equation 6 when it only uses the y_{concat} in the discovery.

$$C = argmax(y_{concat}) \tag{6}$$

The identifications of each stage are complementary and unique; therefore, all outcomes are integrated to obtain the final prediction, as shown in Equation 7, which is modified from Equation 6.

$$C = argmax \left(\sum_{l=L-S+1}^L y_l + y_{concat} \right) \tag{7}$$

Pseudocode for ANN-PLM with an Experimental Setup

Input: Initialize the hyperparameters of the network such as learning rate =0.01, hidden layers =10, Number of neurons = 30, Maximum number of epochs =100, batch size =8, Test ratio = 20%, Train ratio=80%and Activation function = Sigmoid.

- m = number of classes
- B_i^{conv} = convolution block
- V_i = vector
- L_{CE} = cross loss entropy
- \log = the natural log
- y = ground truth label for i-th sample
- y_l = predicted label for i-th sample
- V_{concat} = outputs of multiple previous stages
- y_{concat} = predicted labels for the concatenated output
- Δy^i = new class sample

Preprocess the input data for classification.

For epochs 1, N do # N defines the number of epochs

With probability p with random learning weight

Calculate $L_{CE}(y_l, y)$ for each class of data

$L_{CE}(y_l, y) = -\sum_{i=1}^m y^i \times \log(y_l^i)$ // Calculate loss for each batch of training data as in Equation 4.

Calculate $L_{CE}(y)$ for each class

Repeat

Calculate Δy^i

$$L_{CE}(y_l, \Delta y^i) = -\sum_{i=1}^m (y^i + \Delta y^i) \times \log(y_l^i + \Delta y^i)$$

If $(L_{CE}(y_l, y^i) < L_{CE}(y_l, \Delta y^i))$ // Check, new class data arrived.

$$L_{CE}(y_{concat}, y) = -\sum_{i=1}^m y^i \times \log(y_{concat}^i) // \text{Update learning weights and back-propagate the progressive weight}$$

//Find the loss probabilities

Else continue

End if

End For

Evaluate prediction for test data in the trained model

Compute performance measures.

Output: Classified information of big data.

The input data must be pre-processed before classification during the initialized training phase. The learning weights are randomly initialized, and the training data loss in every batch is calculated using Equation 4. For several epochs, this process is repeated

for every class, and the loss of the training data is evaluated and checked for new class data. If new class data arrives to calculate the new learning weights, the learning weights are updated using Equation 6. Else, continue the epochs. The trained model is evaluated based on the test data prediction, and the performance measure is calculated, resulting in big data classification.

RESULTS AND DISCUSSION

The design and simulation of the proposed method are performed in Python 3.7. The system configurations used to run this big data classification are an i5 processor, 16 GB RAM, and 6 GB GPU. The datasets used to analyze the big data classification using the proposed method are the Poker hand and the Higgs datasets. Of these datasets, 80% were taken for training and 20% for testing. The performance metrics such as accuracy, precision, recall, F-measure, and specificity are used in this study. The ROC curve, Confusion Matrix, was also derived for both datasets. Training validation accuracy and loss are calculated for 100 epochs. Finally, the convergence rate of the datasets concerning accuracy and epochs is also derived to provide more insights into the proposed model.

Performance Analysis of the Proposed Method

Higgs Dataset

Figure 5 shows the ROC Curves for the Higgs dataset. The ROC curve is the reference point for evaluating the classifier's performance. A ROC curve is a graph that displays the performance of the classification model at different classes (0 to 9). Figure 5 observes that the ROC curve of class 9 (area 1.00) reaches a stable point of 1.0 to achieve superior results for the Higgs dataset. Figure 6 displays that training accuracy reaches 0.01820 at 100 epochs, while validation accuracy achieves 0.01860 at 100 epochs. Figure 7 shows the graphical representation of training and validation loss for the Higgs dataset. Training loss values stabilize at 5.020 for 100 epochs, while the validation loss stabilizes at 5.009.

Figure 8 shows the early convergence of the ANN-PLM method as compared to ANN. The epochs required to attain convergence is 25 compared to the conventional ANN method, which takes 40 epochs with a uniform accuracy rate.

Figure 8 also shows the Graphical representation of accuracy performance for the Higgs dataset. It can be observed that the proposed ANN-PTM with SMOTE achieved

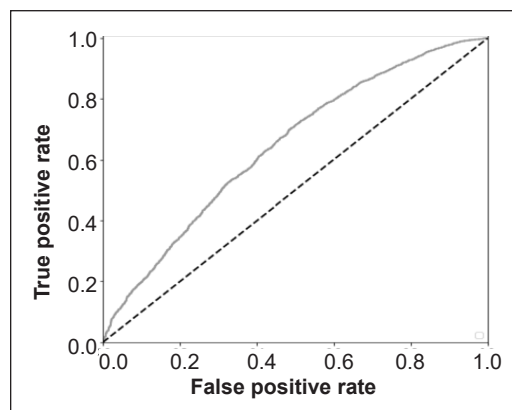


Figure 5. ROC characteristics of Higgs dataset

better accuracy, 0.98, at a cut-off range of 25 epochs, where the accuracy starts to stabilize and is maintained the same till it reaches 100 epochs. While considering the ANN process, it achieved an accuracy of 0.95 at a cut-off range of 40 epochs. The performance evaluation of the proposed method with the Higgs dataset with and without PCC and SMOTE is shown in Table 1. The ANN-PLM performs better with and without PCC and SMOTE than the ANN, KNN, and SVM.

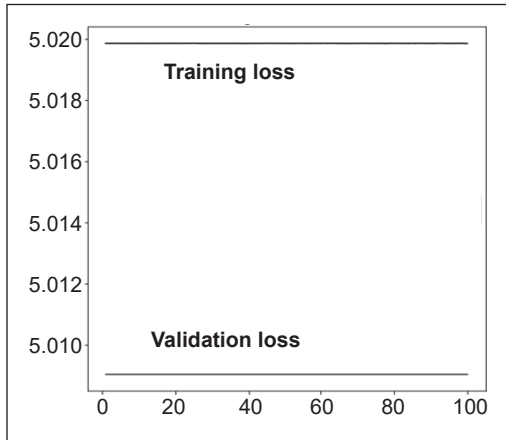


Figure 6. Epochs vs. training-validation loss

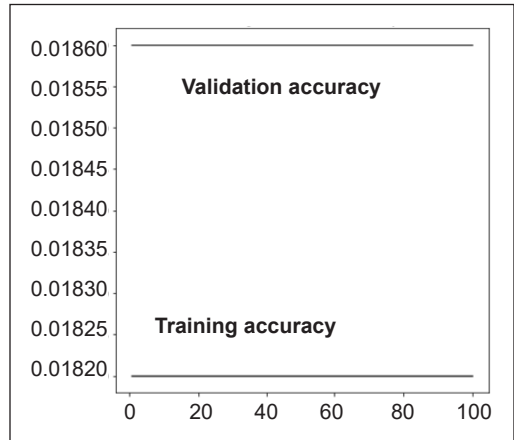


Figure 7. Epochs vs. training-validation accuracy

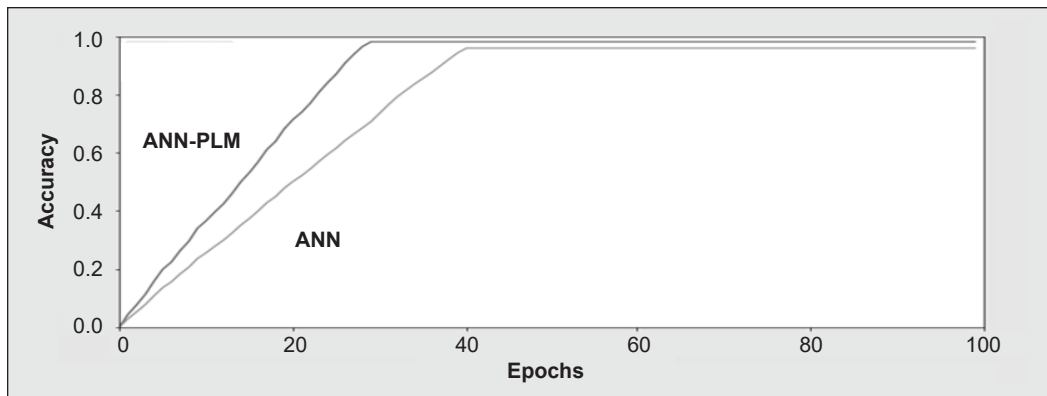


Figure 8. Convergence graph of Higgs dataset with ANN and ANN-PLM

Table 1
Performance evaluation of the proposed method for the Higgs dataset

Feature selection	Classifiers	Accuracy (%)	Precision (%)	Recall (%)	Fmeasure (%)	Specificity (%)
Without PCC	ANN	91.804	91.372	89.264	91.176	89.955
	KNN	93.882	94.217	94.153	94.386	96.357
	SVM	94.454	95.280	95.969	95.373	96.116
	ANN-PLM	97.220	95.166	96.671	96.092	96.104

Table 1 (continue)

Feature selection	Classifiers	Accuracy (%)	Precision (%)	Recall (%)	Fmeasure (%)	Specificity (%)
With PCC	ANN	93.110	93.948	94.893	95.057	94.463
	KNN	96.170	97.006	95.487	96.533	95.382
	SVM	97.597	97.637	96.784	97.362	96.735
	ANN-PLM	99.329	99.121	99.004	99.536	99.668
Without SMOTE	ANN	90.60	70.40	80.39	78.50	80.39
	KNN	93.689	96.456	95.336	91.337	92.896
	SVM	92.081	96.189	94.667	95.321	88.542
	ANN-PLM	96.227	95.780	96.548	97.168	78.660
With SMOTE	ANN	93.80	77.4	87.1	82.0	86.10
	KNN	94.657	93.778	96.932	92.436	93.786
	SVM	93.180	97.005	95.457	96.879	89.865
	ANN-PLM	97.325	96.532	97.278	98.568	80.578

Pokers Dataset

In Figure 9, the ROC curve contains two constraints, (i.e.) True Positive Rate (TPR) and False Positive Rate (FPR). In general, a ROC of more than 0.9 is considered outstanding. Figure 9 shows that the ROC curve reaches the value of 0.98, which is closer to 1, i.e., it produces better classification results for the Poker hand dataset. The ROC curve signifies that all ten classes are properly classified within the range of 0.97 and 1.

Figure 10(a) shows the graphical representation of Training and Validation accuracy for the Higgs dataset. The training accuracy reaches 0.821 at 100 epochs, while the validation accuracy achieves 0.86 at 100. As shown in Figure 10 (b), training loss reaches -1.3 for 100 epochs, while the validation loss reaches -1.4 at 100 epochs.

Figure 11 shows the graphic representation of accuracy performance for the Poker hand dataset. Figure 11 shows that the proposed ANN-PTM achieved better accuracy, 0.92,

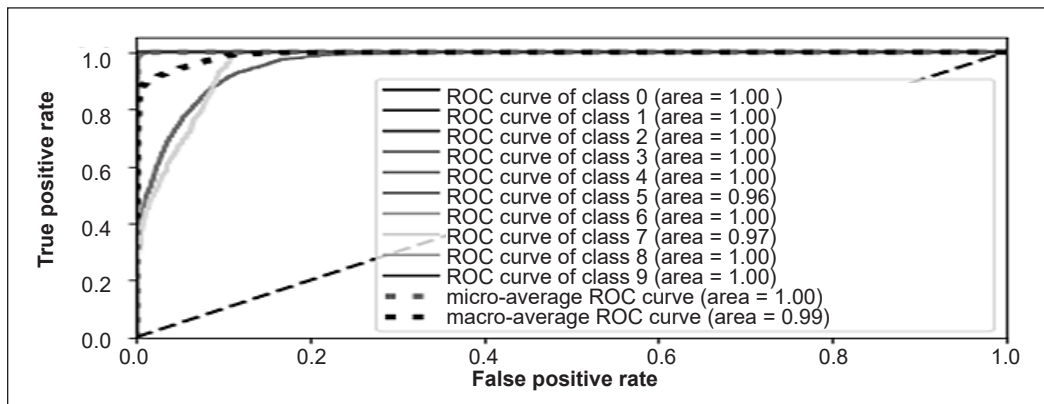
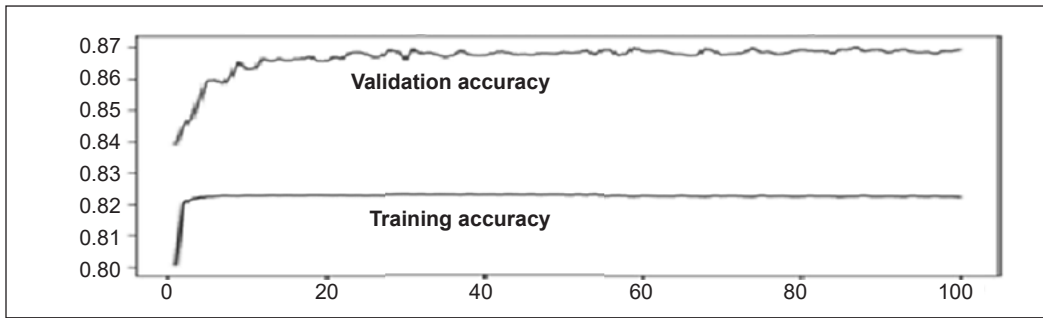
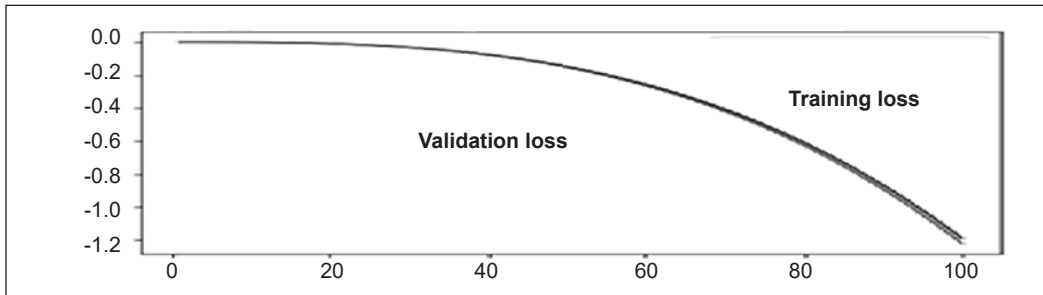


Figure 9. ROC characteristics for Pokers data



(a)



(b)

Figure 10. (a) Training and validation accuracy; and (b) Training and validation loss

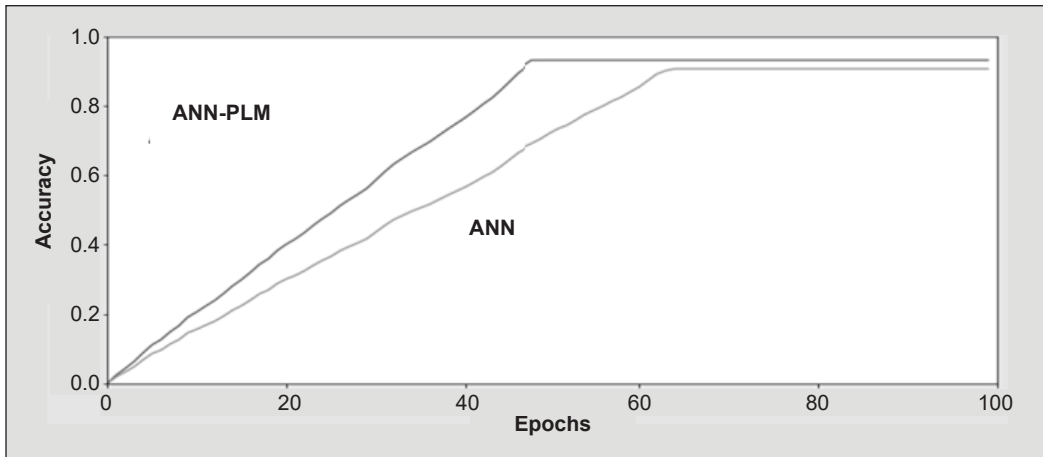


Figure 11. Convergence graph of Pokers dataset with ANN and ANN-PLM

at a cut-off range of 50 epochs, where the accuracy starts to stabilize and is maintained the same until it reaches 100 epochs. While considering the ANN process, it achieved an accuracy of 0.89 at a cut-off range of 65 epochs.

Table 2 shows the performance evaluation of the proposed method with the Pokers' dataset with and without PCC and SMOTE. The ANN-PLM performs better with and without PCC and SMOTE than the ANN, KNN, and SVM.

Table 2
Performance evaluation of the proposed method for the Poker hand dataset

Feature selection	Classifiers	Accuracy (%)	Precision (%)	Recall (%)	F-measure (%)	Specificity (%)
Without PCC	ANN	91.804	91.372	89.264	91.176	89.955
	KNN	93.882	94.217	94.153	94.386	96.357
	SVM	94.454	95.280	95.969	95.373	96.116
	ANN-PLM	97.220	95.166	96.671	96.092	96.104
With PCC	ANN	93.110	93.948	94.893	95.057	94.463
	KNN	96.170	97.006	95.487	96.533	95.382
	SVM	97.597	97.637	96.784	97.362	96.735
	ANN-PLM	99.329	99.121	99.004	99.536	99.668
Without Smote	ANN	90.60	70.40	80.39	78.50	80.39
	KNN	93.689	96.456	95.336	91.337	92.896
	SVM	92.081	96.189	94.667	95.321	88.542
	ANN-PLM	96.227	95.780	96.548	97.168	78.660
With Smote	ANN	93.80	77.4	87.1	82.0	86.10
	KNN	94.657	93.778	96.932	92.436	93.786
	SVM	93.180	97.005	95.457	96.879	89.865
	ANN-PLM	97.325	96.532	97.278	98.568	80.578

Comparative Analysis of Other Classification Methods Using Higgs and Poker Dataset

The existing research on big data classification, such as MF [28], PGS-ISSA [19], Genetic Programming, Multilayer feedforward Backpropagation, and AEB [20] are used to compare the proposed method. A comparison is made between the Poker hand and the Higgs datasets. In that, the PGS-ISSA [19] is analyzed for the Poker hand dataset, and AEB [20] is analyzed for the Higgs dataset, while MF [28] is used for both data set comparisons. Tables 3 and 4 show the comparative analysis of the proposed method with Higgs and Poker hand datasets, respectively. Tables 3 and 4 show that the proposed method provides better performance than the existing methods. The graphical representation is shown in Figures 12 and 13 for the Higgs and Pokers datasets, respectively.

Table 3
Comparative analysis of the Higgs dataset

Method	Accuracy (%)
MF	52
PGS-ISSA	64.72
Cartesian Genetic Programming Using Random Sampling	65
Proposed method	96.566

Table 4
Comparative analysis of Poker hand dataset

Method	Accuracy (%)
MF	50
AEB	89.93
Multilayer Feedforward Propagation Method	94
Proposed method	98.629

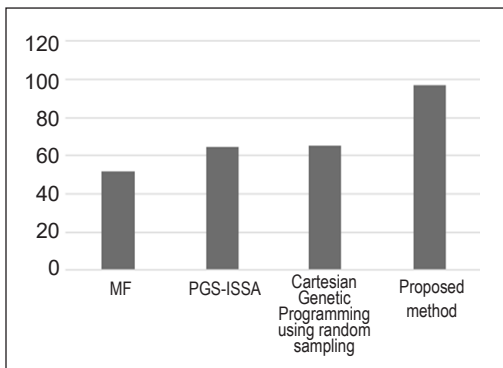


Figure 12. Accuracy comparison of Higgs dataset

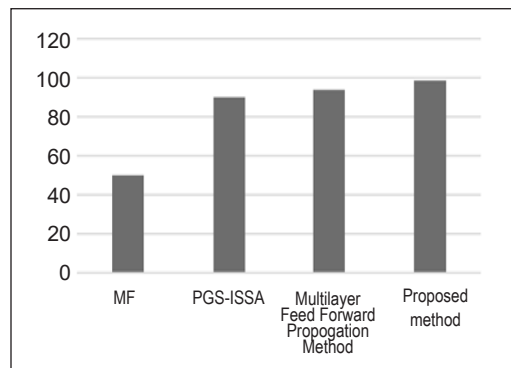


Figure 13. Accuracy comparison of Poker dataset

CONCLUSION

This research proposed a methodology for the classification of huge amounts of data. The strategy combines the use of the ANN-PLM technique, which stands for Artificial Neural Network with Progressive Learning Method, with feature selection based on the Pearson Correlation Coefficient (PCC). The Synthetic Minority Over-sampling Technique (SMOTE) is used as a means of data augmentation in the classification procedure to mitigate the issues related to class imbalance and overfitting. The PCC feature selection approach is utilized to identify the most pertinent features from the feature vector, improving the classification performance. The Pearson correlation coefficient (PCC) aids in the identification of the most suitable collection of features by evaluating their correlation with the target variable. This process enhances the classification model's ability to differentiate across classes.

In addition, we integrate the notion of discriminative data localization, which entails iteratively adjusting the weights of the neural network model by considering both local particulars and global structure. This localization methodology allows the network to concentrate on significant patterns and characteristics in the data, increasing the categorization accuracy. The experimental results demonstrate that the proposed ANN-PLM strategy exhibits superior performance compared to traditional ANN approaches in terms of convergence epochs and other classification performance criteria. The suggested method demonstrates significantly improved accuracy on the Higgs and Poker datasets when utilizing the PLM technique compared to currently available methods.

In summary, the efficacy of integrating ANN-PLM, PCC-based feature selection, SMOTE, and data localization approaches for the classification of huge data is demonstrated by our suggested strategy. The findings underscore the effectiveness of the suggested approach to precision, convergence speed, and overall classification performance. It underscores its potential as a reliable and efficient option for addressing classification issues involving large datasets.

In future research, it would be beneficial to evaluate the performance of this method on imbalanced data, as the current study only assessed its effectiveness on balanced data. This limitation can be further experimented with.

ACKNOWLEDGEMENTS

The author extends sincere gratitude to Dr. Kayarvizhy N for invaluable advice and constructive feedback throughout the development of this manuscript. Her expertise and guidance were instrumental in shaping the final version of this paper. The author also wishes to acknowledge the open-access resources and online communities that offered valuable insights and data, enabling the author to pursue this research independently.

REFERENCES

- Abhilasha, A., & Naidul, P. A. (2022). Self-boosted with dynamic semi-supervised clustering method for imbalanced big data classification. *International Journal of Software Innovation*, 10(1), 1-24. <https://doi.org/10.1007/s11042-022-12038-4>
- Ali, I. M. S., & Balakrishnan, M. (2021). Population and global search improved squirrel search algorithm for feature selection in big data classification. *International Journal of Intelligent Engineering & Systems*, 14(4), 177-189. <https://doi.org/10.22266/ijies2021.0831.17>
- Al-Thanoon, N. A., Algamal, Z. Y., & Qasim, O. S. (2021). Feature selection based on a crow search algorithm for big data classification. *Chemometrics and Intelligent Laboratory Systems*, 212, Article 104288. <https://doi.org/10.1016/j.chemolab.2021.104288>
- Banchhor, C., & Srinivasu, N. (2021). Analysis of Bayesian optimization algorithms for big data classification based on map reduce framework. *Journal of Big Data*, 8(1), Article 81. <https://doi.org/10.1186/s40537-021-00464-4>
- Basgall, M. J., Naiouf, M., & Fernández, A. (2021). FDR2-BD: A fast data reduction recommendation tool for tabular big data classification problems. *Electronics*, 10(15), Article 1757. <https://doi.org/10.3390/electronics10151757>
- BenSaid, F., & Alimi, A. M. (2021). Online feature selection system for big data classification based on multi-objective automated negotiation. *Pattern Recognition*, 110, Article 107629. <https://doi.org/10.1016/j.patcog.2020.107629>
- Brahmane, A. V., & Krishna, B. C. (2021). Big data classification using deep learning and apache spark architecture. *Neural Computing and Applications*, 33(2), 15253-15266. <https://doi.org/10.1007/s00521-021-06145-w>
- Castro, F. M., Marín-Jiménez, M. J., Guil, N., Schmid, C., & Alahari, K. (2018, September 8-14). *End-to-end incremental learning*. [Paper presentation]. Proceedings of the European Conference on Computer Vision (ECCV), Munich, Germany. <https://doi.org/10.48550/arXiv.1807.09536>
- Chatterjee, S., Javid, A. M., Sadeghi, M., Mitra, P. P., & Skoglund, M. (2017). Progressive learning for systematic design of large neural networks. *arXiv*, Article 1710.08177. <https://doi.org/10.48550/arXiv.1710.08177>

- Dubey, A. K., Kumar, A., & Agrawal, R. (2021). An efficient ACO-PSO-based framework for data classification and preprocessing in big data. *Evolutionary Intelligence*, 14, 909-922. <https://doi.org/10.1007/s12065-020-00477-7>
- Du, R., Xie, J., Ma, Z., Chang, D., Song, Y. Z., & Guo, J. (2021). Progressive learning of category-consistent multi-granularity features for fine-grained visual classification. *IEEE Transactions on Pattern Analysis and Machine Intelligence*, 44(12), 9521-9535. <https://doi.org/10.1109/TPAMI.2021.3126668>
- Hassanat, A. B., Ali, H. N., Tarawneh, A. S., Alrashidi, M., Alghamdi, M., Altarawneh, G. A., & Abbadi, M. A. (2022). Magnetic force classifier: A novel method for big data classification. *IEEE Access*, 10, 12592-12606. <https://doi.org/10.1109/ACCESS.2022.3142888>
- Hassib, E. M., El-Desouky, A. I., Labib, L. M., & El-Kenawy, E. S. M. (2020). WOA+BRNN: An imbalanced big data classification framework using whale optimization and deep neural network. *Soft Computing*, 24(8), 5573-5592. <https://doi.org/10.1007/s00500-019-03901-y>
- Jain, D. K., Boyapati, P., Venkatesh, J., & Prakash, M. (2022). An intelligent cognitive-inspired computing with big data analytics framework for sentiment analysis and classification. *Information Processing Management*, 59(1), Article 102758. <https://doi.org/10.1016/j.ipm.2021.102758>
- Juez-Gil, M., Arnaiz-Gonzalez, A., Rodriguez, J. J., Lopez-Nozal, C., & Garcia-Osorio, C. (2021). Approx-SMOTE: Fast SMOTE for big data on Apache spark. *Neurocomputing*, 464, 432-437. <https://doi.org/10.1016/j.neucom.2021.08.086>
- Kantapalli, B., & Markapudi, B. R. (2023). SSPO-DQN spark: Shuffled student psychology optimization based deep Q network with spark architecture for big data classification. *Wireless Networks*, 29(1), 369-385. <https://doi.org/10.1007/s11276-022-03103-9>
- Li, Z., Liu, C., Yuille, A., Ni, B., Zhang, W., & Gao, W. (2021, June 19-25). *Progressive stage-wise learning for unsupervised feature representation enhancement*. [Paper presentation]. Proceedings of the IEEE/CVF Conference on Computer Vision and Pattern Recognition, Nashville, USA. <https://doi.org/10.48550/arXiv.2106.05554>
- Movassagh, A. A., Alzubi, J. A., Gheisari, M., Rahimi, M., Mohan, S., Abbasi, A. A., & Nabipour, N. (2021). Artificial neural networks training algorithm integrating invasive weed optimization with differential evolutionary model. *Journal of Ambient Intelligence and Humanized Computing*, 14, 6017-6025. <https://doi.org/10.1007/s12652-020-02623-6>
- Mujeeb, S. M., Sam, R. P., & Madhavi, K. (2021). Adaptive exponential bat algorithm and deep learning for big data classification. *Sādhanā*, 46(1), Article 15. <https://doi.org/10.1007/s12046-020-01521-z>
- Park, S. T., Kim, D. Y., & Li, G. (2021). An analysis of environmental big data through the establishment of emotional classification system model based on machine learning: Focus on multimedia contents for portal applications. *Multimedia Tools and Applications*, 80, 34459-34477. <https://doi.org/10.1007/s11042-020-08818-5>
- Rebuffi, S. A., Kolesnikov, A., Sperl, G., & Lampert, C. H. (2017). icarl: Incremental classifier and representation learning. In *Proceedings of the IEEE conference on Computer Vision and Pattern Recognition* (pp. 2001-2010). IEEE Publishing. <https://doi.org/10.48550/arXiv.1611.07725>

- Rusu, A. A., Rabinowitz, N. C., Desjardins, G., Soyer, H., Kirkpatrick, J., Kavukcuoglu, K., Pascanu R. & Hadsell, R. (2016). Progressive neural networks. *arXiv*, Article 1606.04671. <https://doi.org/10.48550/arXiv.1606.04671>
- Siddiqui, Z. A., & Park, U. (2021). Progressive convolutional neural network for incremental learning. *Electronics*, 10(16), Article 1879. <https://doi.org/10.3390/electronics10161879>
- Sleeman IV, W. C., & Krawczyk B. (2021). Multi-class imbalanced big data classification on spark. *Knowledge-Based Systems*, 212, Article 106598. <https://doi.org/10.1016/j.knosys.2020.106598>
- Venkatesan, R., & Er, M. J. (2016). A novel progressive learning technique for multi-class classification. *Neurocomputing*, 207, 310-321. <https://doi.org/10.1016/j.neucom.2016.05.006>
- Wang, H., Xiao, M., Wu, C., & Zhang, J. (2021). Distributed classification for imbalanced big data in distributed environments. *Wireless Networks*, 2021, 1-12. <https://doi.org/10.1007/s11276-021-02552-y>
- Xing, W., & Bei, Y. (2019). Medical health big data classification based on KNN classification algorithm. *IEEE Access*, 8, 28808-28819. <https://doi.org/10.1109/ACCESS.2019.2955754>
- Zhou, J., Li, J., Wang, C., Wu, H., Zhao, C., & Wang, Q. (2021). A vegetable disease recognition model for complex background based on region proposal and progressive learning. *Computers and Electronics in Agriculture*, 184, Article 106101. <https://doi.org/10.1016/j.compag.2021.106101>

Bending Effects on Polyvinyl Alcohol Thin Film for Flexible Wearable Antenna Substrate

Amirudin Ibrahim¹, Ahmad Rashidy Razali^{1*}, Muzammil Jusoh², Najwa Mohd Faudzi¹ and Aiza Mahyuni Mozi¹

¹Electrical Engineering Studies, College of Engineering Universiti Teknologi MARA, Cawangan Pulau Pinang, Permatang Pauh Campus, Permatang Pauh, Pulau Pinang 13500, Malaysia

²Advanced Communication Engineering, Centre of Excellence, Faculty of Electronic Engineering, Universiti Malaysia Perlis, Perlis, Malaysia

ABSTRACT

Polyvinyl Alcohol (PVA) has been used in various applications, including the medical health industry and electronics. It is a synthetic polymer with advantages such as being transparent, flexible, biocompatible, biodegradable, and a simpler synthesis process. These advantages make PVA a very promising material for human wearable antennae. In this research, the bending effect of an antenna using a PVA substrate is studied to analyze its durability in the wearable application. Firstly, the thin film substrate synthesis is performed using PVA 2488 with the measured average dielectric constant and tangent loss of 1.24 and 0.066, respectively, across S-Band frequency. Later, a 5G antenna is designed and fabricated using the PVA substrate. Finally, the bending effects of the fabricated antenna are measured at different bending radii. Four different antenna-bending radii are selected to represent different curvatures of human body parts. Results show that bending does not have a significant effect on the reflection coefficient of the antenna, where the frequency shifts from 2.2% up to 7.4% only for all bending conditions. Hence, in that aspect of finding, the PVA thin film is a potential candidate for flexible and wearable antenna material in various human body parts in biomedical applications.

ARTICLE INFO

Article history:

Received: 24 August 2023

Accepted: 01 February 2024

Published: 08 August 2024

DOI: <https://doi.org/10.47836/pjst.32.5.07>

E-mail addresses:

amirudin4854@uitm.edu.my (Amirudin Ibrahim)

ahmad073@uitm.edu.my (Ahmad Rashidy Razali)

muzammil@unimap.edu.my (Muzammil Jusoh)

najwafaudzi@uitm.edu.my (Najwa Mohd Faudzi)

aiza_mahyuni@uitm.edu.my (Aiza Mahyuni Mozi)

* Corresponding author

Keywords: Antenna, bending, biocompatible, flexible, PVA, polymer, wearable

INTRODUCTION

A polymer is a large molecule composed of repeating structural monomer units connected by covalent bonds. Polymers such as proteins, cellulose, and starch can be

naturally occurring or synthetic, such as plastics, synthetic fibers, and rubber. Polymers are versatile materials with a wide range of properties and applications. For example, some polymers are rigid and stiff, while others are flexible and resilient. Some are transparent, and others are opaque. Some are thermoplastic, meaning they can be melted and reshaped, while others set into a permanent shape when heat and pressure are applied. The properties of a polymer can be tailored by adjusting its composition and molecular structure. It can be achieved through copolymerization, blending, and cross-linking. Polymers have numerous practical applications, including in packaging, construction, textiles, electronics, and medicine (Rhazi et al., 2018; Turek et al., 2020; Wu et al., 2021; Zhang, Biesold et al., 2022; Zhong et al., 2020). For example, polyethylene is commonly used to make plastic bags, while polyvinyl chloride (PVC) is used in pipes and upholstery. Polyurethane is used in foam insulation, cushions, and adhesives; nylon is used in clothing and ropes. On the other hand, in recent years, there has been a growing concern about the environmental impact of synthetic polymers, particularly plastic. It has led to increased research into biodegradable and renewable polymer alternatives, as well as recycling and waste management strategies for conventional polymers.

Wireless on the body refers to wireless communications around the human body area to transmit data between wearable devices attached to the human body. This purpose includes medical sensors, fitness trackers and smartwatches. Hence, those technologies allow the collection of real-time data and monitoring of various physiological and environmental parameters, allowing for personalized and adaptive applications in healthcare, sports, and other fields. Therefore, a special flexible material needs to be used for a flexible, robust, biocompatible, and environmentally friendly antenna. Polymer materials such as Polyimide (PI), Polyethylene terephthalate (PET/PETE), Polydimethylsiloxane (PDMS) and Liquid Crystal Polymer (LCP) have been widely used as antenna substrates because those materials are highly flexible, and some are not biocompatible and biodegradable. Previous work on antennae using those materials is summarized in Table 1.

Interestingly, physical hydrogels based on poly (vinyl alcohol) (PVA), which contains a significant number of reactive groups (-OH groups), are notable for their remarkable biocompatibility, superior mechanical properties, and chemical stability (Xu et al., 2023). PVA is a more human-friendly wearable material than others because it is biocompatible and biodegradable, easy to synthesize and transparent (Ibrahim et al., 2022).

In addition, it is also a synthetic and water-soluble polymer that has been widely used in pharmaceutical, food packaging and electronics sensors. However, researchers have overlooked using PVA as a flexible material for wearable antennae. Most work that uses PVA as potential wearable sensors and other electronics applications has only been applied at frequencies lower than 1 GHz, such as work by Reddy et al. (2019), Mousa & Taha (2022), Ambrosio et al. (2018) and Hamad and Hashim (2022). With the potential, there is a need to

Table 1
Previous flexible material in antenna design

Flexible material	Author	Technique	Antenna operating frequency (GHz)	Dielectric constant (ϵ_r)	Tangent loss ($\tan\delta$)
PDMS	Shakirul et al., 2021b	Patch antenna	3.5	3.0	0.008
PTFE	Fujiwara et al., 2014	Patch antenna	2.4	2.1	0.002
LCP	Paul et al., 2013	Patch antenna	2.45 & 5.8	2.6	0.0025
PI Kapton	Khaleel, 2014	Patch antenna	3.1–10.6	3.5	0.02
Jeans	Gil & Fernández-García, 2016	Patch antenna	1.575	1.7	0.025
PVA/CaCO ₃	Appusamy et al., 2020	Patch antenna	2.4	1.67	0.039
Polyimide PI	Zhang, Huang et al., 2022	Patch antenna	5.8	3.6	0.02
PET	Hassan et al., 2017	Patch antenna	26–40	3.2	0.022
PDMS	Salleh et al., 2022	Patch antenna	3.5	2.54	0.05
Proposed work		Patch antenna	3.5	1.24	0.066

study several robustness elements of the material as part of wearable antennae, specifically the bending effects. Table 1 shows the previous flexible materials used in antenna design.

METHODOLOGY

A PVA thin film substrate was prepared using a simple synthesis process. This process involved several stages, starting with the preparation of the PVA substrate material.

Preparation of Antenna Substrate

The antenna substrate was prepared using a simple synthesis process. The formulation of the mixture was adopted from Appusamy et al. (2020) but modified. The PVA used in this project was PVA 2488, and in the modification, it was used with an 88% degree of hydrolysis. Normally, this material is applied to adhesion, coating, film packaging, the textile industry, personal care, and cosmetics (Achutha et al., 2023; Haque et al., 2021).

The synthesis started by measuring 4.3g of PVA 2488 powder and diluting it in 100 ml of double-distilled water. The solution was constantly stirred using a magnetic stirrer and heated at 80°C for



Figure 1. Fabricated PVA thin film substrate

2 hours until the PVA powder was completely dissolved and a homogenous solution was produced.

After that, the solution was poured into a petri dish and dried using Universal Oven for 12 hours. Then, the PVA thin film was peeled off from the cast, as in Figure 1, before its dielectric properties were measured.

Substrate Measurement

The PVA thin film substrate’s dielectric constant and tangent loss were measured using coaxial probe N1501A from Keysight Technologies and Vector Network Analyzer (VNA) from Agilent. A thin film PVA sample with a minimum thickness of 3 mm was used, as in Figure 2. Moreover, the thickness of the substrate sample plays an important role in determining the accurate dielectric and tangent loss value. The dielectric constant and tangent loss were measured and averaged in the S-Band range from 2 GHz to 4 GHz. The measurement result is as in Figure 3.

The average measured values for dielectric constant and tangent loss across S-Band frequency for pure PVA thin film are 1.24 and 0.066, respectively. The dielectric and tangent loss at 3.5 GHz is 1.27 and 0.066, respectively. These two values are not much different from the average value across the S-Band frequency range. The proposed PVA dielectric and tangent loss is compared with other wearable, flexible materials, as in Table 1.

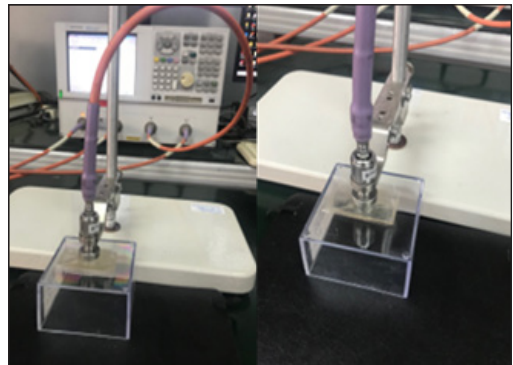


Figure 2. PVA thin film measurement technique using Keysight N1501 and Vector Network Analyzer

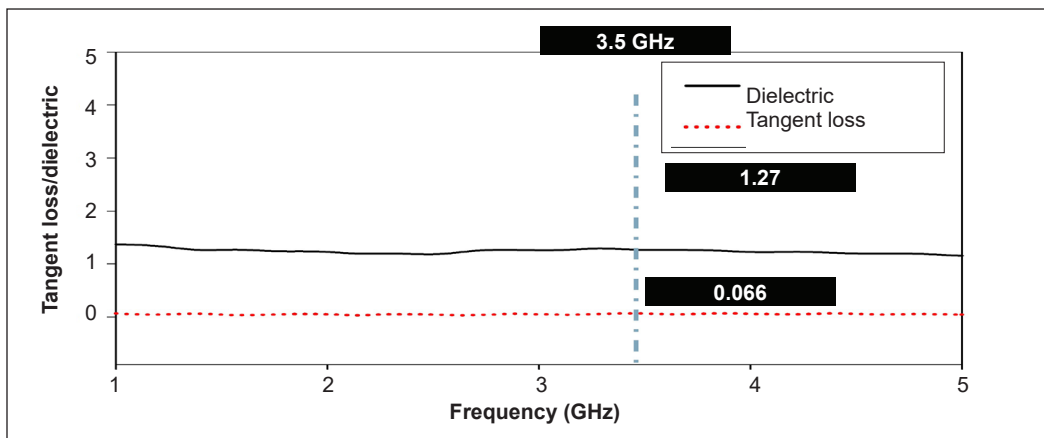


Figure 3. Result for PVA thin film (3 mm) substrate measurement using Keysight N1501 and Vector Network Analyzer

Antenna Design and Fabrication

The antenna design substrate used the average dielectric and tangent loss values. The microstrip patch antenna was designed with a resonance frequency of 3.5 GHz, located in the sub-6 5G band, which is the most popular 5G frequency.

The antenna dimensions of the microstrip patch were calculated using Equations 1 to 4 (Dewan et al., 2021). The patch width (W_p) was calculated using Equation 1. The dielectric constant (ϵ_r) of the substrate and desired resonance frequency (f_r).

$$W_p = \frac{c}{2 \times f_r} \times \sqrt{\frac{2}{\epsilon_r + 1}} \quad (1)$$

After that, the effective dielectric constant (ϵ_{reff}) is determined as a function of W_p and substrate high (h), considering edge effects and the propagation speed of the field waves in the antenna provided by Equation 2.

$$\epsilon_{reff} = \frac{\epsilon_r + 1}{2} + \frac{\epsilon_r - 1}{2} \times \left[1 + 12 \times \frac{h}{W_p} \right]^{-\frac{1}{2}} \quad (2)$$

Then, the length extension is calculated using Equation 3.

$$\Delta L = 0.412 \times h \times \left[\frac{(\epsilon_{reff} + 0.3) \left(\frac{W_p}{h} + 0.264 \right)}{(\epsilon_{reff} - 0.258) \left(\frac{W_p}{h} + 0.813 \right)} \right] \quad (3)$$

Finally, the length of the patch (L_p) is calculated by substituting the effective dielectric constant ϵ_{reff} and length extension ΔL values in Equation 4.

$$L_p = \frac{c}{2 \times f_r \sqrt{\epsilon_{reff}}} \times 2 \times \Delta L \quad (4)$$

The calculated formula used the starting parameters dimensions to design, simulate, and improve the rectangular patch antenna using Computer Simulation Technology (CST) software. The calculated values for $W_p = 40.47$ mm, $\epsilon_{reff} = 1.228$, $\Delta L = 0.514$ mm and $L_p = 37.62$ mm were used as the dimension references in antenna simulation in CST Software. This calculation and simulation process was completed before the antenna was constructed as a prototype.

Copper tape with a thickness of 0.025 mm was used as the conductive patch radiator and ground. The design structures are listed in Table 2, where these values are based on calculations. Besides, some optimization modification was done, and the optimal structures of the antenna substrate were 50×50 mm² with a thickness of 0.8 mm.

Antenna Bending Analysis

The intended design and functional PVA wearable antenna must have good mechanical characteristics; thus, the bending effect on the designed antenna is investigated. Both simulation and measurement were carried out, and the results were compared.

Normally, antenna bending is used to investigate the robustness performance of a wearable antenna. The bending also represents the curve of human body parts, such as the head, arm, leg and chest, where it is normally attached.

The simulation has been done in CST Microwave Studio, and the bending effect was simulated on XZ-plane, and TE mode will be contributed to the frequency resonant shift. A cylinder structure was used in the simulation to bend the antenna, hence representing several body parts (Shakhirul et al., 2021a; Zaidi et al., 2022; Zhang, Huang et al., 2022).

In the simulation process, four bending radii were chosen, which are $R = 18\text{ mm}$, $R = 25\text{ mm}$, $R = 38\text{ mm}$ and $R = 50\text{ mm}$ (Figure 4). The radius represents the several body part curvature conditions and shapes as in practical conditions explained by Zaidi et al. (2022), Salleh et al. (2022), and Zhang, Huang et al. (2022). The performance in reflection coefficients S_{11} , gain and directivity are compared on those works with different wearable substrates and operating frequency.

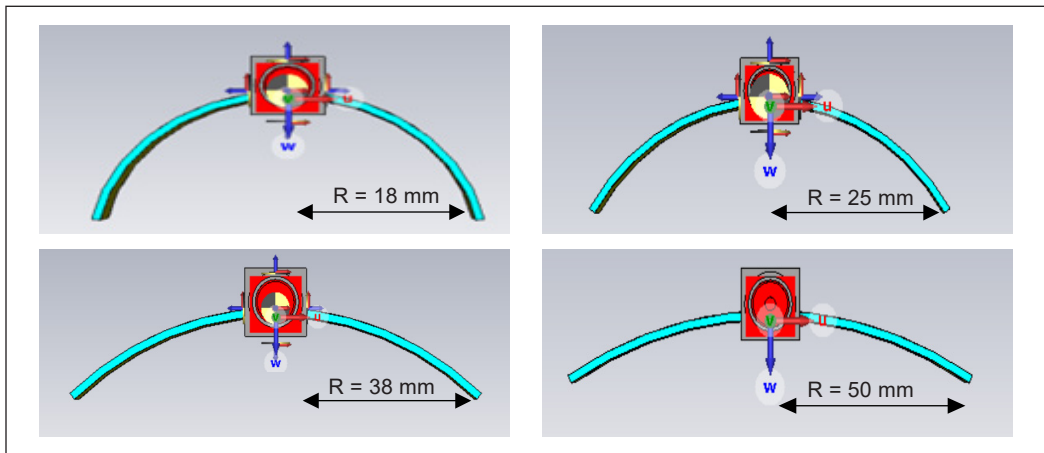


Figure 4. Antenna bending for radius $R = 18\text{ mm}$, 25 mm , 38 mm and 50 mm in CST Simulation Software

RESULTS AND DISCUSSION

This project starts with simulation, fabrication, and measurement processes to achieve the research aim of PVA antenna bending effects. Typically, the initial step involves conducting the substrate synthesis process to obtain the dielectric and tangent loss values. Subsequently, the focus shifts to simulating the prototype and proceeding with the fabrication and measurement of the antenna. The final design is finally subjected to the study of its bending characteristics.

Antenna Simulation and Prototype

Equations 1 to 4 were used as the reference dimension for the antenna design. However, some modifications and optimizations were done to produce good antenna performance, such as S_{11} , radiation pattern, bandwidth, directivity, and gain.

The antenna has been designed and simulated in Computer Simulation Technology (CST) Studio Suite, as in Figure 5, using the optimized values from Table 2. In contrast, the fabricated prototype antenna is shown in Figure 6.

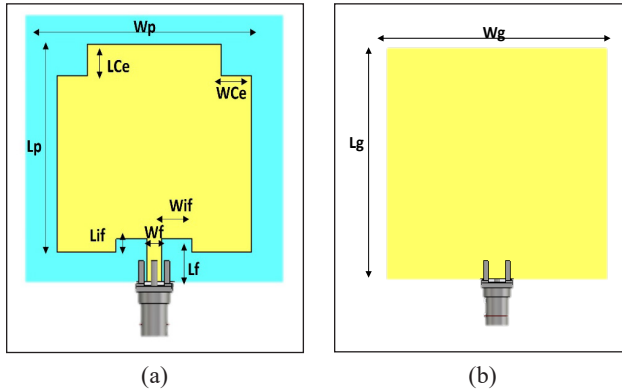


Figure 5. View of antenna in CST simulation: (a) Front; and (b) back

Table 2
Dimension for antenna structure

Antenna structure	Dimension (mm)
Width substrate	50.0
Length substrate	50.0
Thickness substrate	0.80
Feedline (Lf)	9.97
Feedline width (Wf)	2.90
Patch width (Wp)	38.00
Patch length (Lp)	38.99
Length edge cut (Lce)	5.98
Width edge cut (Wce)	5.98
Width inset feed (Wif)	5.97
Length inset feed (Lif)	2.48
Ground width (Wg)	50.0
Ground length (Lg)	50.0
Copper thickness	0.025

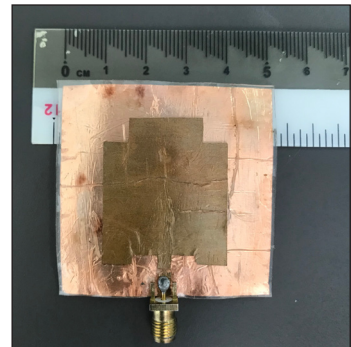
Flat Condition Test

Basically, wearable antennae will be designed and simulated under two major conditions: flat and bending. Table 3 compares the simulation and measurement of the designed antenna under flat conditions. It will ensure that the fabricated antenna’s practicality is suitable for flexible wearable conditions.

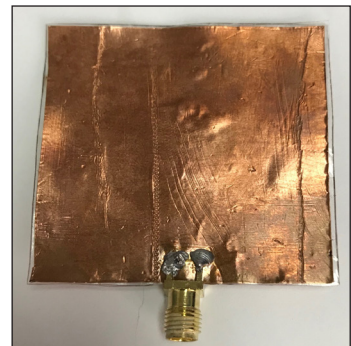
Table 3 compares the simulation and measurement results. The reflection coefficient S11 for the flat condition shows a good correlation between the simulation and measurement. The simulation S11 is -22.627 dB at 3.5 GHz, while the measurement S11 is -20.966 dB at 3.42 GHz, as shown in Figure 7. The operating frequency shift is about 2.2% from the 3.5 GHz resonant frequency.

Table 3
Antenna performance comparison

Parameter	Simulation	Measurement
S11 (dB)	-22.627	-20.966
Bandwidth (MHz)	143	400
VSWR	1.08	1.20
Impedance Matching (Ω)	50	41



(a)



(b)

Figure 6. View of the fabricated antenna: (a) Front; and (b) back

Bending Condition Test

The fabricated antenna has been tested under different bending conditions for simulation and measurement analyses. For measurement, it has been tested on polystyrene foam with a different radius, R , as in Figure 8. The antenna will be placed on top of the polystyrene foam and taped to produce some bending conditions.

Based on the bending simulation result in Figure 9, the resonant frequencies were shifted to the lower frequency, around 3.42 GHz. It represents the shifted frequency of 2.2% at the maximum shift. The reflection coefficient for all bending radiuses, R , was below -10 dB. This result significantly proves that the bending condition is less affected by the radius. However, the smaller the antenna bending radius, the higher the shift, as seen in the results.

Similarly to the antenna bending measurements in Figure 10, the resonant frequencies were shifted from the original

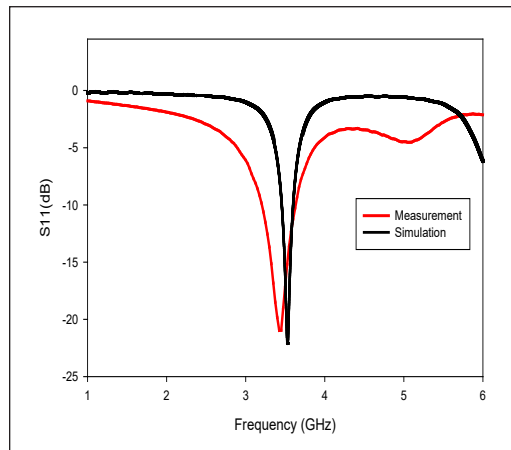


Figure 7. S11 for simulation and measurement under flat condition

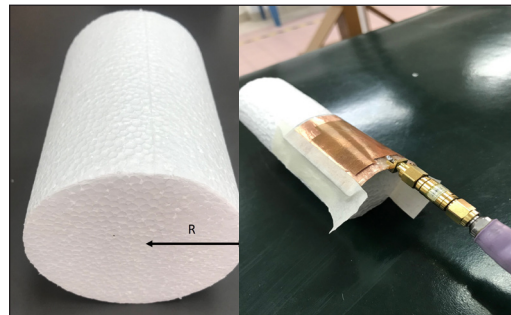


Figure 8. Antenna bending setup on polystyrene foam with different radius R

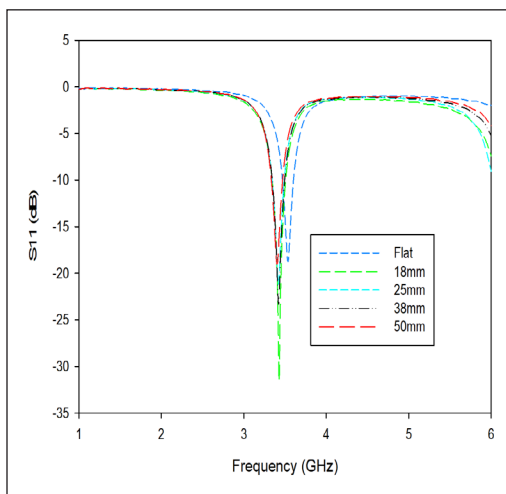


Figure 9. Antenna bending simulation with different radii R

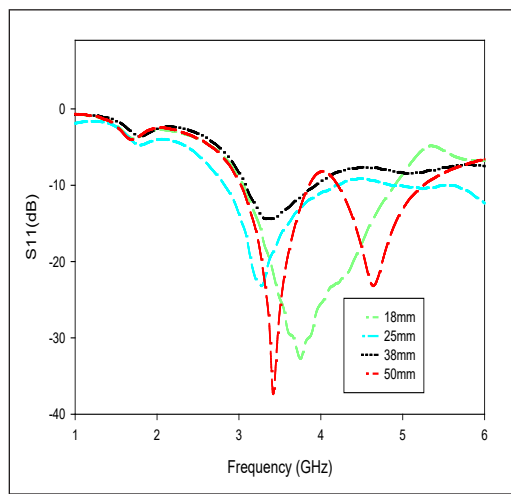


Figure 10. Antenna bending measurement on polystyrene foam with different radii R

flat position (without bending) resonant frequency. Most resonant frequencies were shifted to a maximum of 7.7%, as recorded in the results. Overall, there are weak correlations between simulation and measurement results due to human and equipment errors during the fabrication and measurement process. However, it can be concluded that the antenna's performance is still in the range of 3.4 GHz to 3.6 GHz, which is allocated bandwidth for the 3.5GHz sub-6 band.

The radiation patterns for E and H-Plane were evaluated for flat and four different bending radii. The radiation pattern for flat and four different bending radiuses shows an almost similar pattern, a monopole directional pattern, as in Figure 11. However, this pattern is desired, especially when the antenna is designed for wearable applications, because it minimizes radiation from the back lobe to the human body.

Apart from radiation, the performance of the antenna, such as S11, realized gain, directivity, efficiency, and bandwidth, were evaluated and summarized in Table 4. The bending radius has a significant impact on the antenna, particularly on its gain performance.

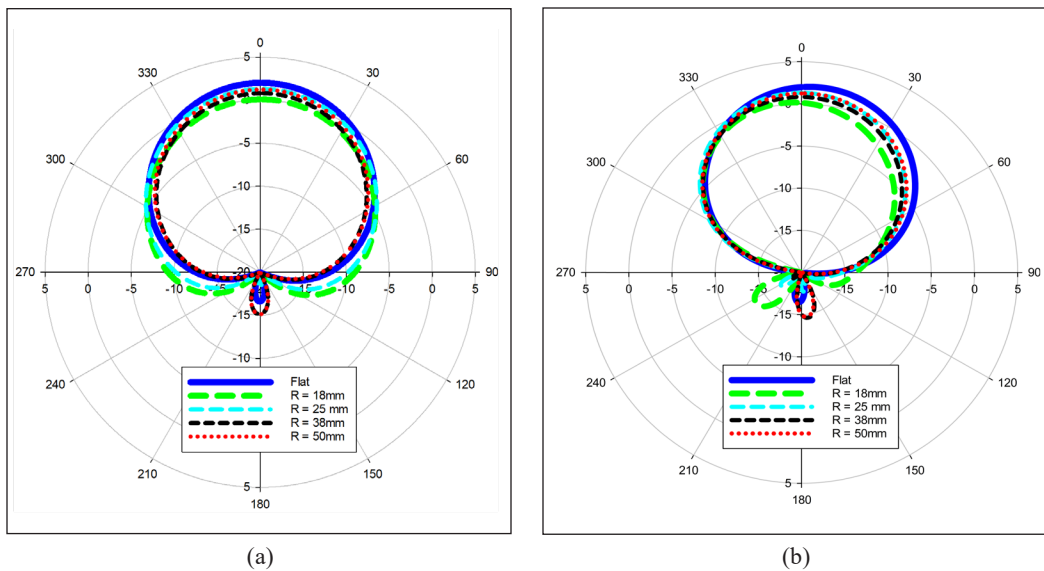


Figure 11. Radiation pattern for flat and bending conditions: (a) E-plane; and (b) H-plane

Table 4
Antenna bending performance under various bending conditions

Parameter/ Radius	18 mm	25 mm	38 mm	50 mm
S11 (dB)	-17.497	-17.676	-19.471	-18.543
Gain (dBi)	0.212	1.32	0.825	1.26
Directivity (dBi)	6.106	7.248	7.184	5.75
Efficiency	25.75%	25.54%	23.13%	23.24%
Bandwidth (MHz)	130	133	137	135

The gain performance of an antenna is reduced when it has a smaller radius bending angle because more energy is trapped inside the antenna as it is bent on the small bending radius. Therefore, the shorter the bending radius, the lower the gain.

Figure 12 shows the relationship between the antenna bending radius with realized gain and directivity. The gain and directivity were increased when the bending radius varied from the lower to the higher bending radius. It shows $R = 18$ mm having the lowest gain and directivity, while $R = 50$ mm shows the best performance.

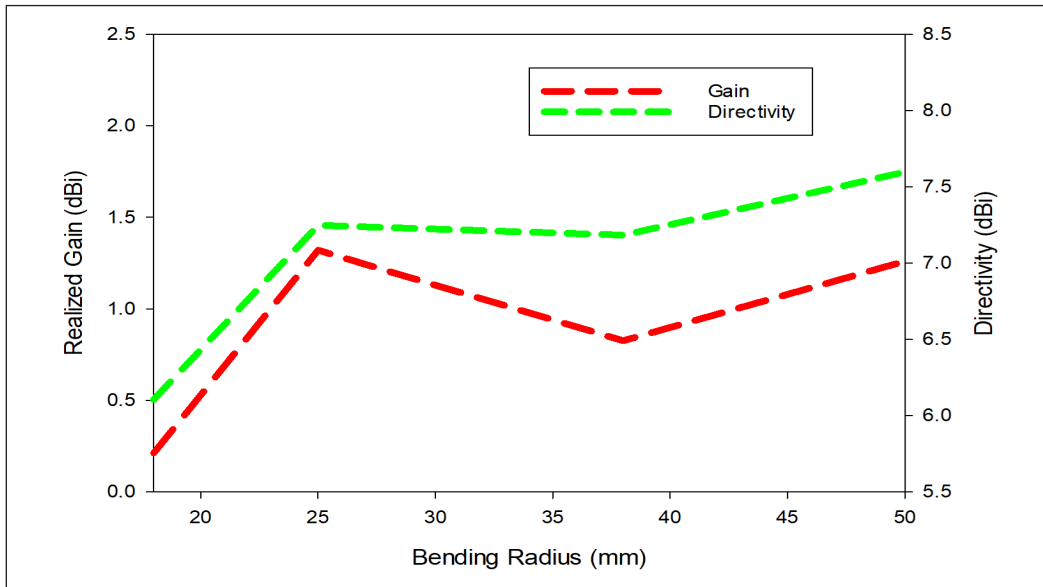


Figure 12. Gain and directivity of the antenna under various bending radius

CONCLUSION

In conclusion, an analysis of the bending effects on the PVA antenna substrate has been carried out. When the antenna is in flat condition, the return loss S_{11} is resonated at 3.5 GHz while under the bending condition from 18 mm to 50 mm, the return loss S_{11} was shifted to the lower frequency band by 269MHz shift, which is still acceptable under the 3.5GHz bandwidth allocation. In the study, it is found that at the bending conditions, the resonant frequency did not severely affect the original return loss due to the lower dielectric constant value of the PVA thin film substrate, which is around 1.24 on average across the S-Band and closer to the dielectric constant of the air. The obtained resonant frequency shifts are around 2.2% to 7.7% from the desired resonant frequency at S_{11} less than -10 dB.

This finding indicates that apart from its human-wearable-friendly material properties, PVA thin film holds substantial promise as a flexible material in the design of wearable antennas for wireless on-body monitoring, showcasing its significant potential in the robustness of flexible wearable antennas in biomedical applications.

ACKNOWLEDGEMENTS

The authors express their sincere gratitude to Institut Pengajian Siswazah (IPSiS) and Universiti Teknologi MARA, Cawangan Pulau Pinang, Malaysia, for their invaluable support throughout the research work. In particular, the authors extend their heartfelt appreciation to the Electrical Engineering Studies and Chemical Engineering Studies, College of Engineering and Antenna and the Microwave Research Group (AMRG) for their guidance, encouragement, and equipment resources, which have been instrumental in the successful completion of this study. The authors are truly grateful for the opportunities enabling us to pursue academic and research endeavors. Their support has significantly contributed to the advancement of knowledge in the field.

REFERENCES

- Achutha, S., Nisha, S. K., Pushpa, S. B., & Andrews, S. (2023). Antimicrobial polyvinyl alcohol/neem oil flexible film for food packaging applications. *Materials Today: Proceedings*. <https://doi.org/10.1016/J.MATPR.2023.07.061>
- Ambrosio, R., Carrillo, A., Mota, M. L., de la Torre, K., Torrealba, R., Moreno, M., Vazquez, H., Flores, J., & Vivaldo, I. (2018). Polymeric nanocomposites membranes with high permittivity based on PVA-ZnO nanoparticles for potential applications in flexible electronics. *Polymers*, *10*(12), Article 1370. <https://doi.org/10.3390/polym10121370>
- Appusamy, S., Thangavelu, S., Gopikrishna, M., & Raman, S. (2020, August 29-September 5). *A flexible PVA/CaCO₃ dielectric film for microwave antenna applications*. [Paper presentation]. XXXIIIrd General Assembly and Scientific Symposium of the International Union of Radio Science, Rome, Italy. <https://doi.org/10.23919/URSIGASS49373.2020.9232264>
- Dewan, A. R., Ibrahim, A., Dewan, R., Razali, A. R., & Bakar, A. A. (2021). Multiband microstrip patch antenna for LTE application. *International Journal of Nanoelectronics and Material*, *14*(2), 169–178.
- Rhazi, M. E., Majid, S., Elbasri, M., Salih, F. E., Oularbi, L., & Lafdi, K. (2018). Recent progress in nanocomposites based on conducting polymer: Application as electrochemical sensors. *International Nano Letters*, *8*(2), 79–99. <https://doi.org/10.1007/s40089-018-0238-2>
- Fujiwara, K., Shimasaki, H., Morimoto, K., & Kuwahara, N. (2014, November 4-7). *Studies on a polyester fabric substrate of the feed line to a flexible slot antenna*. [Paper presentation]. Asia-Pacific Microwave Conference, Sendai, Japan.
- Gil, I., & Fernández-García, R. (2016, August 8-11). *Wearable GPS patch antenna on jeans fabric*. [Paper presentation]. Progress in Electromagnetics Research Symposium (PIERS), Shanghai, China. <https://doi.org/10.1109/PIERS.2016.7734859>
- Hamad, Z. S., & Hashim, A. (2022). Dielectric characteristics of PVA/ZrO₂-SiC nanostructures for electronics applications. *Nanosistemi, Nanomateriali, Nanotehnologii*, *20*(1), 159–164. <https://doi.org/10.15407/nnn.20.01.159>

- Haque, A. N. M. A., Zhang, Y., & Naebe, M. (2021). A review on lignocellulose/poly (vinyl alcohol) composites: Cleaner approaches for greener materials. *Cellulose* 28(17), 10741–10764. <https://doi.org/10.1007/s10570-021-04234-6>
- Hassan, A., Ali, S., Hassan, G., Bae, J., & Lee, C. H. (2017). Inkjet-printed antenna on thin PET substrate for dual band Wi-Fi communications. *Microsystem Technologies*, 23(8), 3701–3709. <https://doi.org/10.1007/s00542-016-3113-y>
- Ibrahim, A., Razali, A. R., Jusoh, M., Faudzi, N. M., & Mozi, A. M. (2022, December 19-21). *SAR evaluation of 5G antenna using polyvinyl alcohol thin film substrate*. [Paper presentation]. IEEE International RF and Microwave Conference (RFM), Kuala Lumpur, Malaysia. <https://doi.org/10.1109/RFM56185.2022.10064758>
- Khaleel, H. R. (2014). Design and fabrication of compact inkjet printed antennas for integration within flexible and wearable electronics. *IEEE Transactions on Components, Packaging and Manufacturing Technology*, 4(10), 1722–1728. <https://doi.org/10.1109/TCPMT.2014.2352254>
- Mousa, E., & Taha, E. O. (2022). Synergetic effects of nano-SiO₂/glycerol on the electrical and optical properties of PVA for embedded electronics and optical applications. *Journal of Materials Science: Materials in Electronics*, 33(29), 23088-23106. <https://doi.org/10.1007/s10854-022-09075-y>
- Paul, D., Zhang, L., & Zheng, L. (2013, May 2024). *Flexible dual-band LCP antenna for RFID applications*. [Paper presentation]. International Symposium on Electromagnetic Theory, Hiroshima, Japan.
- Reddy, P. L., Deshmukh, K., Chidambaram, K., Ali, M. M. N., Sadasivuni, K. K., Kumar, Y. R., Lakshmipathy, R., & Pasha, S. K. K. (2019). Dielectric properties of polyvinyl alcohol (PVA) nanocomposites filled with green synthesized zinc sulphide (ZnS) nanoparticles. *Journal of Materials Science: Materials in Electronics*, 30(5), 4676–4687. <https://doi.org/10.1007/s10854-019-00761-y>
- Salleh, S. M., Ain, M. F., Ahmad, Z., Abidin, I. S. Z., & Isa, C. M. N. C. (2022). Development of stretchable and bendable polymer wearable antenna for 5G applications. *Express Polymer Letters*, 16(12), 1267-1279. <https://doi.org/10.3144/expresspolymlett.2022.92>
- Shakhirul, M. S., Ain, M. F., Ahmad, Z., Abidin, I. S. Z., & Ali, M. Z. (2021a). Bending analysis of polydimethylsiloxane composite substrate patch antenna for 5G application. *AIP Conference Proceedings*, 2339(1), Article 020047. <https://doi.org/10.1063/5.0044273>
- Shakhirul, M. S., Ain, M. F., Ahmad, Z., Abidin, I. S. Z., & Ali, M. Z. (2021b). Stretch analysis of polydimethylsiloxane composite microstrip patch antenna for 5G application. *AIP Conference Proceedings*, 2339(1), Article 020117. <https://doi.org/10.1063/5.0044274>
- Turek, P., Budzik, G., Oleksy, M., & Bulanda, K. (2020). Polymer materials used in medicine processed by additive techniques. *Polimery/Polymers* 65(7–8), 510-515. <https://doi.org/10.14314/polimery.2020.7.2>
- Wu, F., Misra, M., & Mohanty, A. K. (2021). Challenges and new opportunities on barrier performance of biodegradable polymers for sustainable packaging. *Progress in Polymer Science*, 117, Article 101395. <https://doi.org/10.1016/j.progpolymsci.2021.101395>
- Xu, Q., Wu, Z., Zhao, W., He, M., Guo, N., Weng, L., Lin, Z., Taleb, M. F. A., Ibrahim, M. M., Singh, M. V., Ren, J., & El-Bahy, Z. M. (2023). Strategies in the preparation of conductive polyvinyl alcohol hydrogels

- for applications in flexible strain sensors, flexible supercapacitors, and triboelectric nanogenerator sensors: An overview. *Advanced Composites and Hybrid Materials*, 6(6), Article 203. <https://doi.org/10.1007/s42114-023-00783-5>
- Zaidi, N. I., Rahman, N. H. A., Yahya, M. F., Nordin, M. S. A., Subahir, S., Yamada, Y., & Majumdar, A. (2022). Analysis on bending performance of the electro-textile antennas with bandwidth enhancement for wearable tracking application. *IEEE Access*, 10, 31800-31820. <https://doi.org/10.1109/ACCESS.2022.3160825>
- Zhang, J., Huang, J., Sun, P., Meng, F., Zhang, J., & Zhao, P. (2022). Analysis method of bending effect on transmission characteristics of ultra-low-profile rectangular microstrip antenna. *Sensors*, 22(2), Article 602. <https://doi.org/10.3390/s22020602>
- Zhang, M., Biesold, G. M., Choi, W., Yu, J., Deng, Y., Silvestre, C., & Lin, Z. (2022). Recent advances in polymers and polymer composites for food packaging. *Materials Today*, 53, 134-161. <https://doi.org/10.1016/j.mattod.2022.01.022>
- Zhong, Y., Godwin, P., Jin, Y., & Xiao, H. (2020). Biodegradable polymers and green-based antimicrobial packaging materials: A mini-review. *Advanced Industrial and Engineering Polymer Research*, 3(1), 27-35. <https://doi.org/10.1016/j.aiepr.2019.11.002>

The Riblet Short-Slot Coupler Using Substrate Integrated Waveguide (SIW) for High-frequency Applications

Nurehansafwanah Khalid¹, Siti Zuraidah Ibrahim^{1,2*}, Mohd Nazri A Karim¹, Wee Fwen Hoon^{1,2}, Aliya Ashraf Dewani³, Khuzairi Masrakin¹ and Saidatul Norlyana Azemi^{1,2}

¹Faculty of Electronic Engineering & Technology, Universiti Malaysia Perlis (UniMAP), 02600 Arau, Perlis, Malaysia

²Centre of Excellence for Advanced Communication Engineering (ACE), Universiti Malaysia Perlis (UniMAP), 02600 Arau, Perlis, Malaysia

³Center for Wireless Monitoring and Applications, School of Electrical Engineering, Griffith University, Brisbane, Australia

ABSTRACT

Substrate Integrated Waveguide (SIW) involves the conductive via holes immersed in a dielectric substrate that connects two substrate plates. This article presents a new SIW technique to enhance the operational bandwidth of the Riblet Short-Slot coupler. To demonstrate the proposed SIW technique, two Riblet Short-Slot couplers are designed and investigated at two different high-frequency ranges, Ku-band and K-band. The bandwidth of the proposed couplers is improved by introducing multiple layers of SIW vias at the center of the couplers' side wall. Applying this approach minimizes the leakage loss between vias, indicating an improved overall operating bandwidth of 36.31% and 26.32% for Ku-band and K-band, respectively. All vias in both prototypes are realized using an alternative method, without using the Plated-Through-Hole Printed-Circuit-Board (PTH-PCB) machine. In addition, experimental results agree well with the simulated results.

ARTICLE INFO

Article history:

Received: 04 September 2023

Accepted: 01 February 2024

Published: 08 August 2024

DOI: <https://doi.org/10.47836/pjst.32.5.08>

E-mail addresses:

nurehansafwanah@yahoo.com (Nurehansafwanah Khalid)

sitizuraidah@unimap.edu.my (Siti Zuraidah Ibrahim)

nazrikarim@unimap.edu.my (Mohd Nazri A Karim)

fhwee@unimap.edu.my (Wee Fwen Hoon)

a.ashraf@griffith.edu.au (Aliya Ashraf Dewani)

khuzairimasrakin@gmail.com (Khuzairi Masrakin)

snorlyana@unimap.edu.my (Saidatul Norlyana Azemi)

* Corresponding author

Keywords: K-band, Ku-band, Riblet Short-Slot coupler, substrate integrated waveguide

INTRODUCTION

These days, there is a high demand for low loss, high level, and ease of high-frequency integration. Microstrips are essential in producing low-cost and easy fabrication. Recently, some applications have utilized

microstrip circuits at low frequencies in the Radio Frequency (RF) range. However, these circuits experience high losses magnetically and electrically (Tu et al., 2022). Therefore, developing and designing RF and microwave integrated circuits with this technology platform is impractical.

Lately, there is considerable interest in planar circuits known as the Substrate Integrated Waveguide (SIW) method as it has many benefits, such as exhibiting low leakage loss (negligible), low insertion loss, and insensitivity to outside interference (Arnieri et al., 2022; Kumar & Raghavan, 2018; Kumar & Rosaline, 2021). The SIW method controls excessive losses through a conducting layer on two sides of a substrate that covers the SIW components. This technology is one of the well-known techniques for transforming the conventional square waveguide into a Printed Circuit Board (PCB) and photo-imageable process (Nayak et al., 2022). This technology is in demand due to its efficiency and high RF and microwave application reliability.

Nonetheless, only a few works of literature are reported on coupler devices that employ the SIW technique for high-frequency applications. For frequency operating lower than 12 GHz, the design of an SIW coupler was successfully established by Sabri et al. (2013), Nasri et al. (2016) and Srivastava et al. (2015). Nevertheless, the presented results in Sabri et al. (2013) and Nasri et al. (2016) are limited to simulation with operational bandwidth of merely 11% in Sabri et al. (2013) and 20% in Nasri et al. (2016). The simulated performance of the SIW coupler in Srivastava et al. (2015) was validated through experiments, but the bandwidth is limited to just 12%. A SIW coupler operating higher than 12 GHz was demonstrated by Carrera et al. (2010). However, the proposed prototypes are not compact due to the usage of numerous vias. A good performance of the SIW coupler with 24% operational bandwidth within a range of 28–38 GHz was verified by Doghri et al. (2015). Nevertheless, it is unpractical to integrate the three-dimensional SIW coupler Doghri et al. (2015) with a planar circuit.

Therefore, a Riblet Short-Slot coupler employing the SIW technique that features a compact size and broader operational bandwidth operating at Ku-band and K-band is demonstrated in this article. The bandwidth of the proposed coupler is enhanced by employing three layers of conductive vias that act as a guiding wall of the coupling section. By employing this approach, the bandwidth is significantly broadened compared to the other SIW coupler designs, which operate at lower operational bandwidth (Carrera et al., 2010; Nasri et al., 2016; Sabri et al., 2013; Srivastava et al., 2015). Furthermore, introducing multiple layers via the coupling sidewall leads to good coupling performance and low insertion loss at the investigated operating frequency range. Two Riblet Short-Slot couplers are developed and studied at two distinct high-frequency bands, Ku-band and K-band, to demonstrate the proposed SIW approach.

METHODOLOGY

The proposed structure of a Riblet Short-Slot coupler employing a SIW method is illustrated in Figure 1.

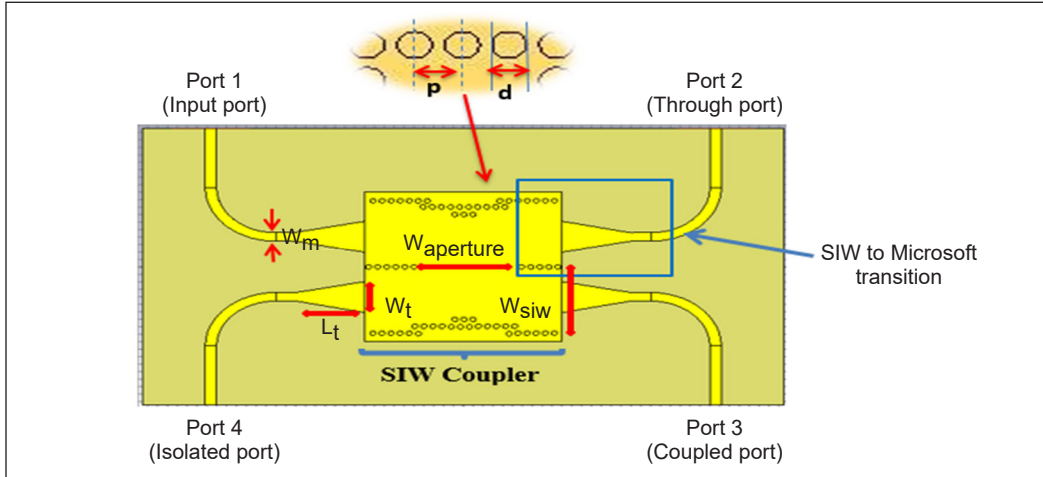


Figure 1. The proposed structure of a Riblet Short-Slot using the SIW technique

The Riblet Short-Slot waveguide coupler is two parallel waveguides with a common sidewall (Haro-Baez et al., 2020; Kumar et al., 2017; Ruiz-Cruz et al., 2011, 2007). The waveguide’s sidewall is represented by several vias by means of the SIW technique. The coupler is utilized to distribute the microwave signal through the input port to the two outputs with 90° phase differences between the two output ports. The ports of the coupler in Figure 1 are denoted as an input port (P1), through port (P2), coupled port (P3), and isolated port (P4).

The initial dimensions of the structure in Figure 1 are obtained by determining the width SIW, W_{siw} and W_{equi} , which can be determined through the mathematical Equations 1 and 2 (Aloui et al., 2018; Khalid et al., 2017).

$$W_{siw} = W_{equi} + p(0.766e^{0.4482\frac{d}{p}} - 1.176e^{-1}) \quad [1]$$

$$W_{equi} = \frac{c}{2f_c\sqrt{\epsilon_{eff}}} \quad [2]$$

Where S_{siw} is the width of the Riblet Short-Slot SIW coupler, and W_{equi} is the waveguide port. Moreover, f_c is the cutoff frequency for standard operating frequency, while ϵ_r is the relative permittivity of the substrate. Note that the following conditions should be fulfilled to reduce leakage loss between vias (Wu et al., 2021):

$$0.5 < \frac{d}{p} < 0.8. \quad [3]$$

where the diameter, d , and the pitch of via p in Equation 3 are provided as Equations 4 and 5 (Kordiboroujeni & Bornemann, 2014):

$$0.5 < \frac{\lambda_g}{5} \tag{4}$$

$$p \leq 2d \tag{5}$$

$$\lambda_g = \frac{2\pi}{\sqrt{\frac{\epsilon_r(2\pi f)^2}{c^2} - \left(\frac{\pi}{w}\right)^2}} \tag{6}$$

In Equation 6, the cutoff frequency, c , is the speed of light, and (ϵ_r) is the permittivity of the substrate. In the design, $d = 0.6$ mm is assumed. Therefore, the applicable range for this design is $0.75 < p < 1.2$. The parameter $W_{aperture}$ in Figure 1 is the common sidewall of the Riblet Short-Slot coupler. The length of $W_{aperture}$ is determined using Equation 7 to control the coupling coefficient from input port P1 to the output port P3:

$$W_{aperture} \geq \frac{\lambda_g}{2} \tag{7}$$

To ensure integration compatibility with the planar microstrip technique, the SIW to microstrip taper transition is applied in the design structure in Figure 1. The W_m is the width of microstrip transmission lines that can be determined by Equations 8 to 10 (Kumar et al., 2012):

$$\frac{w}{h} = \begin{cases} \frac{8e^A}{e^{2A}-2} & \text{for } \frac{w}{h} < 2 \\ \frac{2}{\pi} \left[B - 1 - \ln(2B - 1) + \frac{\epsilon_r - 1}{2\epsilon_r} \left\{ \ln(B - 1) + 0.39 - \frac{0.61}{\epsilon_r} \right\} \right] & \text{for } \frac{w}{h} > 2 \end{cases} \tag{8}$$

$$A = \frac{Z_0}{60} \sqrt{\frac{\epsilon_r + 1}{2}} + \frac{\epsilon_r - 1}{\epsilon_r + 1} \left(0.23 + \frac{0.11}{\epsilon_r} \right) \tag{9}$$

$$B = \frac{377\pi}{2Z_0\sqrt{\epsilon_r}} \tag{10}$$

where Z_0 is the characteristic impedance of the microstrip line. In the design, $Z_0 = 50$ ohms is assumed. The width of the transition taper, W_t , is determined using Equation 11:

$$W_t = W_m + 0.1547 W_{siw} \tag{11}$$

where W_m is the width of the microstrip transmission lines, and W_{siw} is the width of the Riblet Short-Slot SIW coupler. The length of the transition taper, L_t , can be obtained using Equations 12 and 13.

$$L_t = 0.2368 \lambda_{g-ms} \tag{12}$$

$$\lambda_{g-ms} = \frac{\lambda_{g0}}{\sqrt{\epsilon_{reff}}} \tag{13}$$

Where (λ_{g-ms}) is the guided wavelength of the microstrip line, (λ_0) is the wavelength in free space, and (ϵ_{reff}) is the permittivity, which can be determined using Equation 14 (Aloui et al., 2018).

$$\epsilon_{reff} = \frac{\epsilon_r + 1}{2} \left(1 - \frac{1}{2h} \left(\frac{\epsilon_r - 1}{\epsilon_r + 1} \right) \right) \left(\ln \left(\frac{\pi}{2} \right) + \frac{1}{\epsilon_r} \ln \left(\frac{4}{\pi} \right) \right) \quad [14]$$

Where h is the thickness of the substrate, the designs are demonstrated at two frequency ranges to validate the proposed Riblet Short-Slot SIW technique (Ku-band and K-band). After optimization of the designs at the center frequency of 14 GHz for Ku-band and 23 GHz for K-band, the final dimensions of the two designs are presented in Table 1.

Table 1
Optimized dimensions of both proposed Riblet Short-Slot SIW coupler

Parameters	Description	Dimension (mm) Ku-band	Dimension (mm) K-band
D	Diameter of via	0.60	0.60
P	Distance between via	0.92	0.92
W_t	Width transition taper	4.13	2.80
L_t	Width of transition taper	7.15	5.26
$W_{aperture}$	Width of aperture	10.92	6.48
W_{siw}	Width of SIW	8.85	6.58
W_m	Width of microstrip TL	1.15	1.10

DESIGN DEVELOPMENT

The SIW Coupler is designed by simulating and analyzing the standard single-row circular metallic via's performance. The parameters, such as the diameter of metallic vias, the pitch between holes waveguide, and the multi-rows of metallic vias with basic rectangular waveguide structures, are studied to initiate the design of the SIW coupler.

The structure of the circular metallic transition on the side wall is designed in layers, as shown in Figure 2. Furthermore, the metallic circular via position is positioned across from another row of via. According to analysis, a broader bandwidth is provided by the triple rows circular metallic via compared to a standard coupler. Additionally, using the suggested SIW coupler, fewer circular metallic via are produced.

As a first step, an SIW is designed with a single row of metallic vias using an equivalent rectangular waveguide model. The E-field distribution is like a traditional rectangular waveguide. The basic waveguide coupler configuration is shown in Figure 2(a). After that, the vias are added in other rows to demonstrate the coupler's performance and effect. As depicted in Figure 2(c), the proposed technique is triple rows of vias, illustrating that vias act as electric side walls to prevent radiation loss.

The magnitude of the electric field of the proposed coupler is shown in Figure 3. The coupling coefficient is optimized such that the sum of the coupled power at port 4 goes to

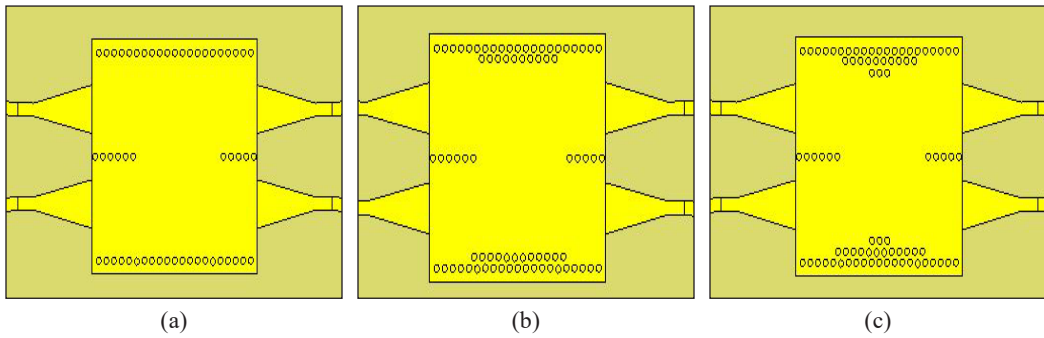


Figure 2. Evolution structure of SIW coupler: (a) Single rows; (b) Dual rows; and (c) Triple rows

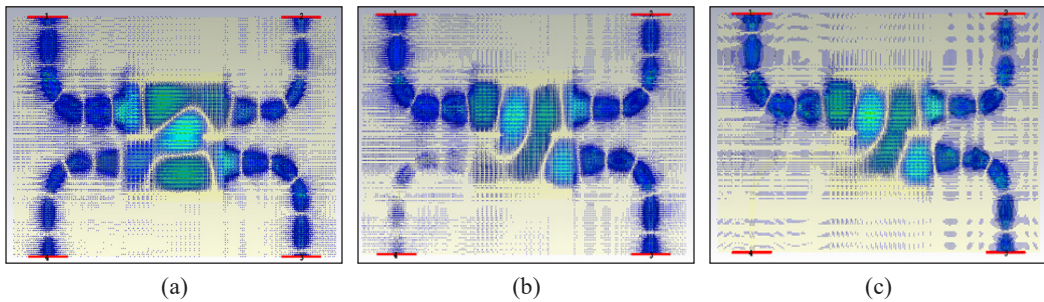


Figure 3. E-field distribution : (a) Single rows Via; (b) Dual rows Via; and (c) Triple rows Via

zero to exhibit good isolation at that port, as depicted in Figure 3(c). However, the designed coupler with single and dual rows is not in ideal condition, as there is a small amount of signal passing through port 4 (isolated), as illustrated in Figures 3(a) and 3(b).

The parametric analysis is done using an electromagnetic simulation tool to optimize the appropriate number of vias rows. The two rows of side wall vias function as a boundary to avoid leakage and to guide electromagnetic waves.

From Figure 4(a), the single rows via have a narrow operating frequency bandwidth from 12 GHz to 15 GHz. Correspondingly, dual rows via produce a narrow bandwidth that operates from 13 GHz to 17 GHz. We observed better performance with a wide bandwidth of reflection coefficient (S11) in triple rows via, which performed below -40 dB compared to dual rows via, as shown in Figure 4(a). Moreover, Figure 4(b) portrays a better performance of the reflection coefficient (S11), which is triple rows via (at operating frequency 20 GHz to 26 GHz) compared to other layers. Hence, this parametric study validates that the triple rows via perform good SIW coupler performance.

Figures 5(a) and (b) illustrate isolation coefficient (S41) responses for the same variations of rows vias. Based on the results, the parameter of triple rows vias produces the best performance with achieved isolation of more than -45 dB at both operating frequencies. At Ku-band, parameters of dual rows vias and triple rows vias show equal bandwidth

performance. However, the best performance is shown by triple rows vias because the isolation coefficient is more than -50 dB compared to dual rows vias.

As depicted in Figures 6(a) and (b), that graphical result presents the output and transmission coefficient (S_{21}) by different rows of circular metallic via. From Figure 6(a), the basic single rows via is shown slightly above -3 dB in contrast with dual rows via, which are more than -5 dB with amplitude imbalance. Additionally, as shown in Figure 6(b), the triple rows via show a flat amplitude compared to single and dual rows vias. As a result, the dotted lines (green) are producing flat amplitude, and the output transmission coefficient (S_{21}) is shown to be at -3 dB \pm 1.5 dB. Based on this result, the bandwidth of a coupler with triple rows vias performs higher bandwidth compared to a coupler with single rows vias and dual rows vias.

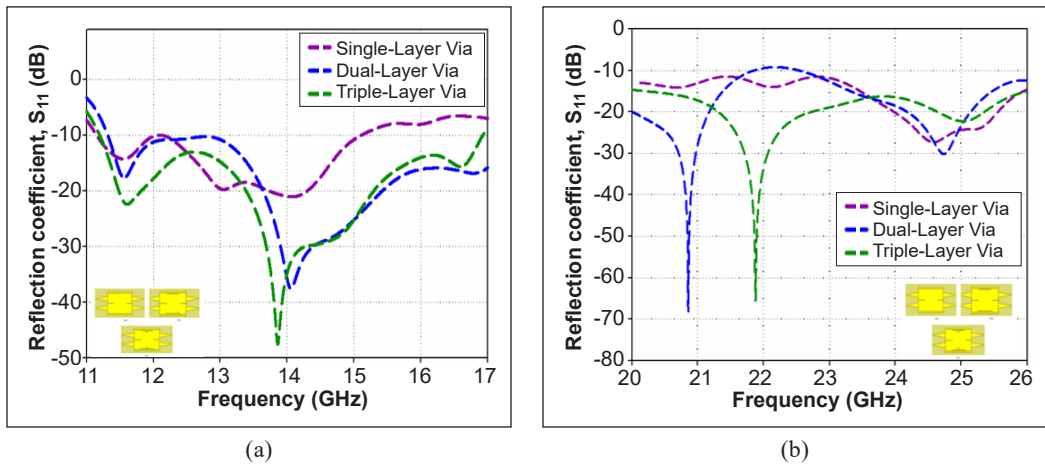


Figure 4. Reflection coefficient, S_{11} (dB) with different rows of vias: (a) Ku-band; and (b) K-band

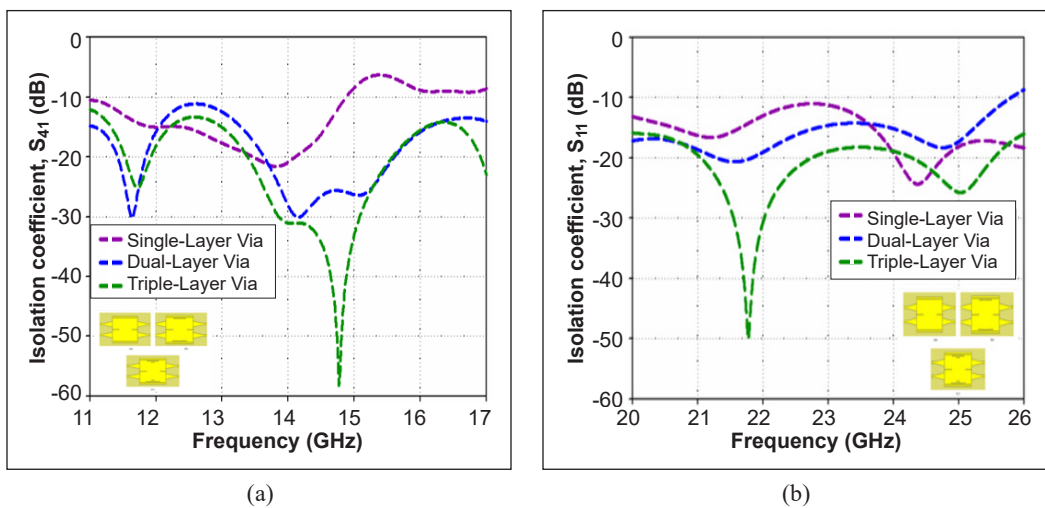


Figure 5. Isolation coefficient, S_{41} (dB) with different rows of vias: (a) Ku-band; and (b) K-band

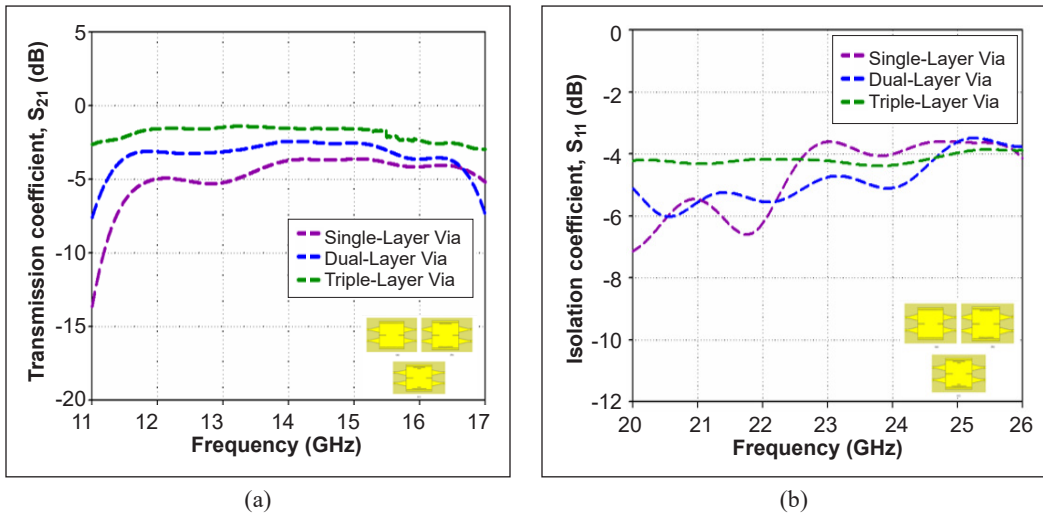


Figure 6. Transmission coefficient, S_{21} (dB) with different rows of vias: (a) Ku-band; and (b) K-band

RESULTS AND DISCUSSION

The prototypes for both designs are constructed with the assistance of a Rogers RO4003c substrate with dielectric permittivity ($\epsilon_r = 3.38$), thickness (h)=0.508 mm, and attenuation ($\tan \theta$) = 0.0027. A photograph of both fabricated couplers is displayed in Figure 7. An additional length of tapered microstrip transition is included to attach the SubMiniature version A (SMA) connectors at all ports for measurement purposes. The prototypes of Riblet Short-Slot SIW couplers are fabricated using a PCB machine, and the holes are drilled by a Computerized Numerical Control (CNC) Bungard drilling machine. Finally, the SIW via holes is metalized by soldering all the inserted copper wires into the via holes to ensure the connectivity (ohmic contact) between the conductive layers. By using this approach, it is validated that vias may possibly be constructed using an alternative

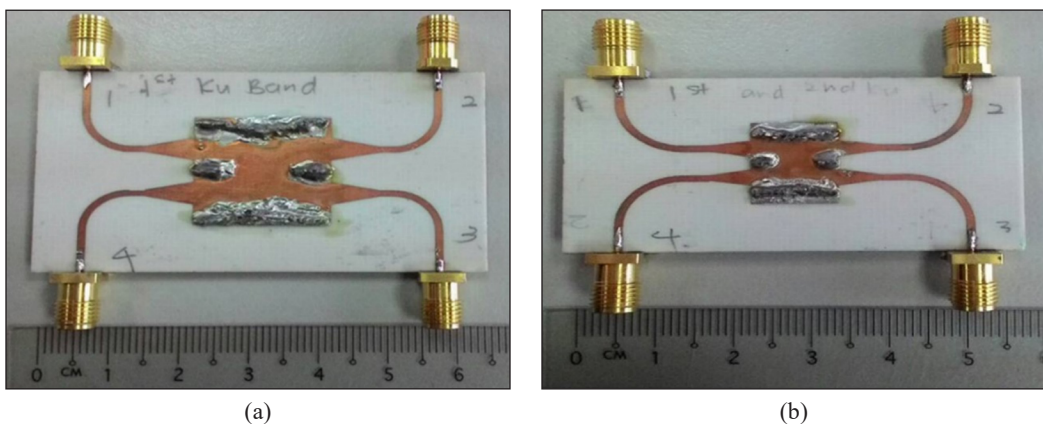


Figure 7. Photograph of the fabricated prototypes: (a) Ku-band; and (b) K-band

method, as demonstrated in this article, without using the PCB Plated Through Hole (PTH) machine. The final dimensions of the fabricated prototypes are 65 mm × 37 mm and 58 mm × 30 mm for the respective Ku-band and K-band design couplers, including the SIW to microstrip transition length.

The experimental results for the S-parameters performance for both designs are obtained through Agilent PNA-X 5245A PNA Network Analyzer. The simulated and measured S-parameters magnitude for the Ku-band design is illustrated in Figure 8. As displayed in Figure 8, the simulated and measured magnitudes of S11 and S41 are better than 10 dB in the whole operating frequency of Ku-band (12–18GHz). Furthermore, S21 and S31 parameters with coupling coefficients of 3 ±1.5 dB are observed in the same frequency range for both simulated and measured results. Considering all these parameters, a relative bandwidth of 36.31% can be obtained.

There is a slight discrepancy between the proposed SIW coupler's simulated and fabricated performances. A possible reason is dimensional accuracy. The microstrip technique must be fabricated with high precision for high-frequency applications to ensure that it resonates at the desired frequency. Deviations from the desired dimensions can lead to shifts in the resonant frequency or changes in the bandwidth of the resonant response. Errors in the fabrication process, such as non-uniform etching or deposition, can also impact the properties of the SIW and introduce additional scattering or loss.

The simulated and measured results for the K-band coupler are displayed in Figure 9, where the magnitude of S11 and S41 is better than 10 dB in the frequency range of 20–26 GHz. It is observed that the simulated reflection coefficient value of port one, S11, suggests excellent performance with a return loss better than 68 dB at the operating frequency of 21.9 GHz. Furthermore, a 3-dB flat coupling response represented by S21 and S31 parameters is observed in the same frequency range with a tolerance of 0.5 dB. Overall, a bandwidth of 26.32% is obtained for both simulated and measured results based on these parameters.

The phase difference between two output ports is one of the critical parts in the coupler designs, where the simulated and measured Ku-band coupler results are illustrated in Figure 10. Figure 10 indicates a flat phase response with $90^\circ \pm 5^\circ$ is observed within the 11.5 GHz to 16 GHz frequency range. Furthermore, a good response to the simulated and measured phase difference of $90^\circ \pm 5^\circ$ for the K-band design is observed in Figure 11.

The errors between both results are tabulated in Tables 2 and 3 for Ku-band and K-band, respectively, to verify the simulated and measured data. As depicted in Tables 2 and 3, the realized magnitude and phase at the 14 GHz and 23 GHz center frequencies of the simulated and measured S-parameters are very close to the theoretically predicted values. Meanwhile, it can be observed that the computed relative mean error is very low, which makes the proposed design unique and has vastly improved performance. Table 4 presents the comparison between the proposed couplers with previously published works.

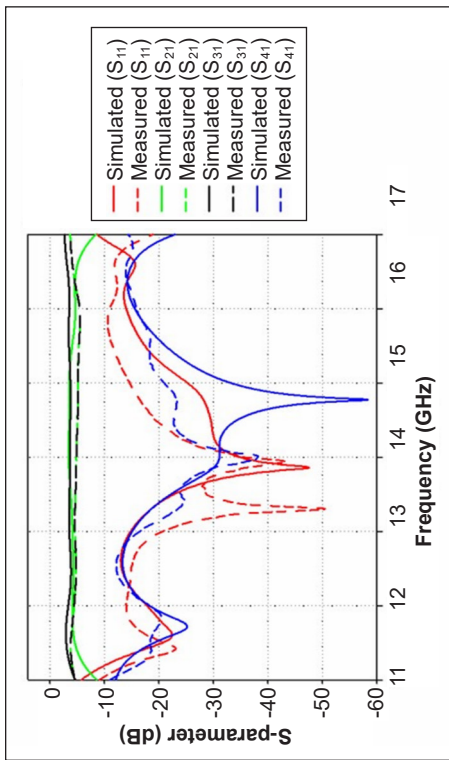


Figure 8. Simulated and measured parameters of Ku-band

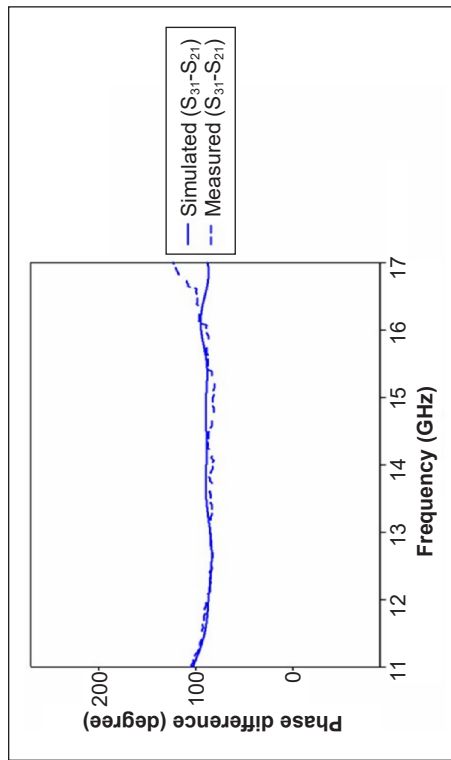


Figure 11. Simulated and measured phase difference of K-band coupler

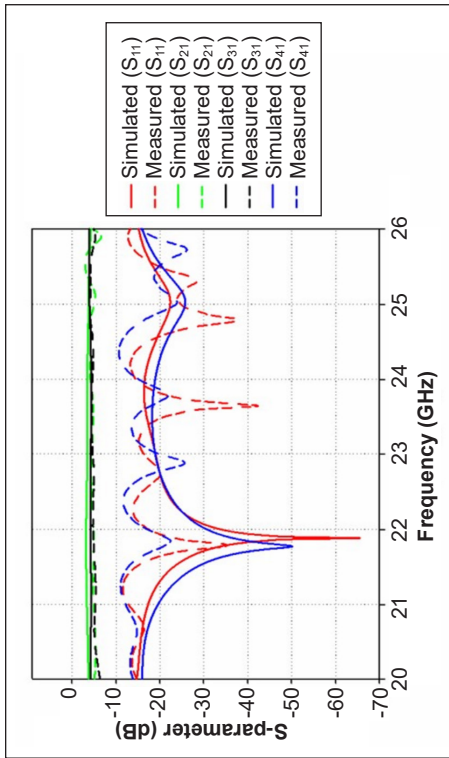


Figure 9. Simulated and measured parameters of K-band

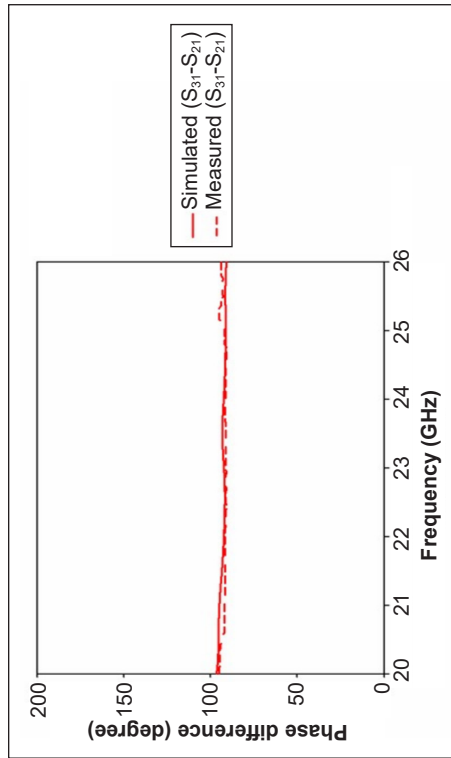


Figure 10. Simulated and measured phase difference of Ku-band coupler

Table 2

The values simulated against the measured result of the Ku-band coupler

S-Parameters (Ku-band)	S11	S21	S31	S41	S31-S21
Theory (Moscato et al., 2016)	<0.1	0.5/0.355	0.5/0.355	<0.1	90°±5
Simulation (SM)	0.00	0.47	0.43	0.00	89.67°
Measurement (M)	0.00	0.33	0.33	0.00	87.00°
Error btw SM & Theory	-	0.14	0.14	-	0.37
Error btw SM & M	0.00	0.29	0.23	0.00	2.97

Table 3

Simulated against the measured result of the K-band coupler

S-Parameters (K-band)	S11	S21	S31	S41	S31-S21
Theory (Moscato et al., 2016)	<0.1	0.5/0.355	0.5/0.355	<0.1	90°±5
Simulation (SM)	0.01	0.45	0.44	0.01	92.38°
Measurement (M)	0.06	0.37	0.38	0.01	91.10°
Error btw SM & Theory	-	0.10	0.12	-	2.57
Error btw SM & M	0.83	0.18	0.14	0	1.38

Table 4

Performance comparison with other works

S-Parameters (K-band)	S11@S41 (dB)	S21@S31 (dB)	S31-S21	Bandwidth (%)
Sabri et al., 2013	<-10	-3±0.5 dB	90°±5°	11
Nasri et al., 2016	<-10	-3±0.5 dB	90°±5°	20
Srivastava et al., 2015	<-10	-3±0.5dB	90°±5°	12
Doghri et al., 2015	<-10	-3±0.5 dB	90°±5°	24
Proposed work	<-10	-3±0.5 dB	90°±5°	Ku-band (36) K-band (26)

CONCLUSION

The proposed Riblet Short-Slot coupler employing SIW technology for Ku-band and K-band frequencies has been successfully simulated and implemented. The designs are performed through multiple layers of sidewall via. A wide bandwidth of 36.31% was obtained in the Ku-band coupler, with return loss and isolation being better than 10 dB and 13 dB, respectively. Moreover, a bandwidth of 26.32% has been accomplished in the K-band coupler with a return loss and isolation higher than 10 dB. Furthermore, the flat phase response of simulated and measured results for both couplers indicates a minimum error. The simulated and measured results mostly agree well over the intended frequency range.

ACKNOWLEDGEMENTS

This research was funded by the Ministry of Higher Education (MOHE), Malaysia, grant number FRGS/1/2019/STG02/UNIMAP/02/5 and the financial support in the form of a publication incentive grant from Universiti Malaysia Perlis (UniMAP), Malaysia. The authors fully acknowledged MOHE and UniMAP for the approved fund, which makes this important research viable and effective.

REFERENCES

- Aloui, R., Houaneb, Z., & Zairi, H. (2018, December 16-19). *Modeling a ka-band resonator cavity with SIW 3-D technology*. [Paper presentation]. International Conference on Microelectronics (ICM), Sousse, Tunisia. <https://doi.org/10.1109/ICM.2018.8704106>
- Arnieri, E., Greco, F., Boccia, L., & Amendola, G. (2022). Vertical waveguide-to-microstrip self-diplexing transition for dual-band applications. *IEEE Microwave and Wireless Components Letters*, 32(12), 1407–1410. <https://doi.org/10.1109/LMWC.2022.3193166>
- Carrera, F., Navarro, D., Baquero-Escudero, M., & Rodrigo-Peñarrocha, V. M. (2010, September 28-30). *Compact substrate integrated waveguide directional couplers in ku and k bands*. [Paper presentation]. The 40th European Microwave Conference, Paris, France. <https://doi.org/10.23919/EUMC.2010.5616711>
- Doghri, A., Djeraji, T., Ghiotto, A., & Wu, K. (2015). Substrate integrated waveguide directional couplers for compact three-dimensional integrated circuits. *IEEE Transactions on Microwave Theory and Techniques*, 63(1), 209–219. <https://doi.org/10.1109/TMTT.2014.2376560>
- Haro-Baez, R. V., Ruiz-Cruz, J. A., Córcoles, J., Montejo-Garai, J. R., & Rebollar, J. M. (2020). A new 4 x 4 rectangular waveguide short-slot coupler in 3d printed technology at Ku-band. *Electronics*, 9(4), Article 610. <https://doi.org/10.3390/electronics9040610>
- Juneja, S., Pratap, R., & Sharma, R. (2021). Semiconductor technologies for 5G implementation at millimeter wave frequencies – Design challenges and current state of work. *Engineering Science and Technology, an International Journal*, 24(1), 205–217. <https://doi.org/10.1016/j.jestech.2020.06.012>
- Khalid, N., Ibrahim, S. Z., & Wee, F. H. (2017). Substrate Integrated Waveguide (SIW) coupler on green material substrate for internet of things (IoT) applications. *MATEC Web of Conferences*, 140, Article 01022. <https://doi.org/10.1051/mateconf/201714001022>
- Kordiboroujeni, Z., & Bornemann, J. (2014). New wideband transition from microstrip line to substrate integrated waveguide. *IEEE Transactions on Microwave Theory and Techniques*, 62(12), 2983–2989. <https://doi.org/10.1109/TMTT.2014.2365794>
- Kumar, A., & Raghavan, S. (2018). Planar cavity-backed self-diplexing antenna using two-layered structure. *Progress in Electromagnetics Research Letters*, 76, 91–96. <https://doi.org/10.2528/pierl18031605>
- Kumar, A., & Rosaline, S. I. (2021). Hybrid half-mode SIW cavity-backed diplex antenna for on-body transceiver applications. *Applied Physics A*, 127(11), Article 834. <https://doi.org/10.1007/s00339-021-04978-9>

- Kumar, G. A., Biswas, B., & Poddar, D. R. (2017). A compact broadband riblet-type three-way power divider in rectangular waveguide. *IEEE Microwave and Wireless Components Letters*, 27(2), 141–143. <https://doi.org/10.1109/LMWC.2016.2646999>
- Kumar, H., Jadhav, R., & Ranade, S (2012). A review on substrate integrated waveguide and its microstrip interconnect. *IOSR Journal of Electronics and Communication Engineering*, 3(5), 36–40. <https://doi.org/10.9790/2834-0353640>
- Moscato, S., Moro, R., Pasian, M., Bozzi, M., & Perregrini, L. (2016). Innovative manufacturing approach for paper-based substrate integrated waveguide components and antennas. *IET Microwaves, Antennas and Propagation*, 10(3), 256–263. <https://doi.org/10.1049/iet-map.2015.0125>
- Nasri, A., Zairi, H., & Gharsallah, A. (2016). Design of a novel structure SIW 90° Coupler. *American Journal of Applied Sciences*, 13(3), 276–280. <https://doi.org/10.3844/AJASSP.2016.276.280>
- Nayak, A. K., Filanovsky, I. M., Moez, K., & Patnaik, A. (2022). A broadband coaxial line-to-SIW transition using aperture-coupling method. *IEEE Microwave and Wireless Components Letters*, 32(11), 1271–1274. <https://doi.org/10.1109/LMWC.2022.3182933>
- Ruiz-Cruz, J. A., Montejo-Garai, J. R., & Rebollar, J. M. (2011). Short-slot E- and H-plane waveguide couplers with an arbitrary power division ratio. *International Journal of Electronics*, 98(1), 11–24. <https://doi.org/10.1080/00207217.2010.488913>
- Ruiz-Cruz, J. A., Montejo-Garai, J. R., Rebollar, J. S. M., Daganzo, A. I., & Hidalgo-Carpintero, I. (2007, June 9-15). *Design of riblet-type couplers for Ka band applications*. [Paper presentation]. IEEE Antennas and Propagation Society International Symposium, Honolulu, USA. <https://doi.org/10.1109/APS.2007.4396486>
- Sabri, S. S., Ahmad, B. H., & Othman, A. R. (2013, September 22-25). *Design and fabrication of X-band substrate integrated waveguide directional coupler*. [Paper presentation]. IEEE Symposium on Wireless Technology and Applications (ISWTA), Sarawak, Malaysia. <https://doi.org/10.1109/ISWTA.2013.6688784>
- Srivastava, R., Mukherjee, S., & Biswas, A. (2015, July 19-24). *Design of broadband planar substrate integrated waveguide (SIW) transvar coupler*. [Paper presentation]. IEEE International Symposium on Antennas and Propagation & USNC/URSI National Radio Science Meeting, Vancouver, Canada. <https://doi.org/10.1109/APS.2015.7305090>
- Tu, H., Hong, H., Zhang, Y., Zhou, L., & Li, X. (2022). The effect of conductive layer thickness on the function of screen printing fabric-based microstrip line. *The Journal of the Textile Institute*, 114(8), 1119–1124. <https://doi.org/10.1080/00405000.2022.2109104>
- Wu, K. E., Bozzi, M., & Fonseca, N. J. G. (2021). Substrate integrated transmission lines: Review and applications. *IEEE Journal of Microwaves*, 1(1), 345–363. <https://doi.org/10.1109/JMW.2020.3034379>

Cytotoxicity Assessment of α Helix Antarctic Yeast Oriented Antifreeze Peptide (Afp1m) on *M. dunnii* (Clone III8C) Cells

Muhammad Shuaib Khan^{1,2}, Mohd Basyaruddin Abdul Rahman³, Mohd Zuki Abu Bakar⁴, Mohammed Mustapha Noordin⁵, Shakeeb Ullah², Adamu Abdul Abubakar⁶, Saifur Rehman², Aisha Siddiqua⁷ and Loqman Mohammad Yusuf^{1*}

¹Department of Companion Animal Medicine and Surgery, Faculty of Veterinary Medicine, Universiti Putra Malaysia, 43400 UPM, Serdang, Selangor, Malaysia

²Faculty of Veterinary and Animal Sciences Gomal University, Dera Ismail Khan 29111, Pakistan

³Department of Chemistry, Faculty of Science, Universiti Putra Malaysia, 43400 UPM, Serdang, Selangor, Malaysia

⁴Department of Pre-Clinical Veterinary Studies, Faculty of Veterinary Medicine, Universiti Putra Malaysia, 43400 UPM, Serdang, Selangor, Malaysia

⁵Department of Veterinary Pathology and Microbiology, Faculty of Veterinary Medicine, Universiti Putra Malaysia, 43400 UPM, Serdang, Selangor, Malaysia

⁶Department of Veterinary Medicine, College of Applied and Health Sciences, A'Sharqiyah University, Ibra 1108 Sultanate of Oman

⁷Gomal Centre of Biochemistry and Biotechnology, Gomal University, Dera Ismail Khan 29111, Pakistan

ABSTRACT

In order to assess the cytotoxic effects of the cryoprotectant helix Antarctic yeast-orientated antifreeze peptide Afp1m on normal mouse skin fibroblasts, an *in vitro* model was developed for cytotoxicity assessment. In order to evaluate the cytotoxic effects of Afp1m, the cells of *M. dunnii* (Clone III8C) were subjected to various amounts of Afp1m. The cell viability was assessed using MTT Assay (Tetrazolium dye MTT 3-(4, 5 dimethylthiazol-2-yl)-2, 5-10 diphenyltetrazolium bromide) against the positive control cells (Clone III8C) that

were cultured with 10% FBS (Foetal Bovine Serum) using an Elisa reader and in medium containing various amounts (10, 5, 2, 1 and 0.5 mg/mL) of Afp1m, the control group (10% FBS) displayed varying survival percentages ($78.86 \pm 10.17\%$, $88.38 \pm 3.19\%$, $88.75 \pm 7.19\%$, $90.61 \pm 7.11\%$, $91.19 \pm 4.52\%$, and $100.00 \pm 0.0\%$) throughout 24 hr. At 72 hr of treatment, the cell viability scores of Afp1m at 5, 2, 1, and 0.5 mg/mL were significantly higher ($p < 0.05$) than those of 10mg/mL, which

ARTICLE INFO

Article history:

Received: 12 September 2023

Accepted: 01 February 2024

Published: 08 August 2024

DOI: <https://doi.org/10.47836/pjst.32.5.09>

E-mail addresses:

anatomistkhan@gmail.com (Muhammad Shuaib Khan)

basya@upm.edu.my (Mohd Basyaruddin Abdul Rahman)

zuki@upm.edu.my (Mohd Zuki Abu Bakar)

noordinmm@upm.edu.my (Mohammed Mustapha Noordin)

shakeebullah@gmail.com (Shakeeb Ullah)

adamu.abubakar@asu.edu.om (Adamu Abdul Abubakar)

saifur.rehman-2019@fkh.unair.ac.id (Saifur Rehman)

draisha@gu.edu.pk (Aisha Siddiqua)

loqman@upm.edu.my (Loqman Mohamad Yusuf)

* Corresponding author

showed 86.73 ± 6.92 % viability of cells (103.9 ± 6.56 %, 104.3 ± 5.13 %, 100.9 ± 1.71 %, 102.8 ± 1.24 %, and 100.00 ± 0.0 %). At 24, 48, and 72 hr, retarded development was noted in 10 mg/mL Afp1m. Development was observed, albeit more slowly than in the positive control and treated with lesser concentrations. The findings of this work indicate that Afp1m exhibits cryoprotective properties without inducing toxicity when used for the cryopreservation of *M. dunni* (Clone III8C) cells.

Keywords: Cytotoxicity, fetal bovine serum, *M. dunni*, non-toxic cryoprotective, subzero temperatures, α helix

INTRODUCTION

Previous research has indicated that Anti-Freeze proteins (AFP) have a non-toxic cryoprotective effect on tissues, even at high concentrations. It is attributed to their elevated molecular weight, solubility, and ability to be incorporated into various solutions (Degner et al., 2014; Hirano et al., 2008). Using AFP as a cryopreservative for cells and tissues in hypothermic circumstances presents an alternative to conventional liquid nitrogen storage, which requires extremely low temperatures. Further investigation is warranted to explore the potential of utilising AFPs and their separated peptides for cryopreservation applications in various cell types and tissues and to ascertain their viability for future utilisation.

All types of cell preservation require low temperatures rather than freezing during storage. Effective use of cell culture technology is determined by the reproducible performance of particular cell lines and their continuous availability. Many laboratories rely on the continuous availability of various cell lines with consistent specialised properties, as well as a significant amount of other research resources. This can be achieved by keeping collections and stocks of cell cultures (Grout et al., 1990).

Previous research has failed to find evidence of a direct interface between anti-freeze peptides and cell membranes. In the presence of the liposomes, neither the antifreeze proteins (AFPs) nor the antifreeze glycoproteins (AFGPs) could change the behaviour phase of the phospholipid liposomes. Furthermore, the platelet membrane and the peptide's secondary structure were unaffected. Moreover, AFPs had a slighter protecting effect than other cryopreservatives on phospholipid systems as trans-monounsaturated or fully saturated lipids (Beirão et al., 2012). Cryopreservation of cells using AFP might have a wide range of applications for *in vitro* research and medical technology. It was also thought that AFPs were a non-toxic preservative that would not distress the cells in different solutions and buffers (Adler et al., 1993; Hirano et al., 2008). Due to their higher molecular weight could be soluble in buffer solutions (Baardsnes et al., 2001).

It has been shown that AFP does not contain chemical tissue toxicity at higher concentrations of up to 40 mg/mL. If used in the buffer solution, it is a non-toxic

cryopreservative that will not disturb the cells and tissue. Due to its higher molecular weight, AFP is soluble in buffer solutions (Degner et al., 2014; Hirano et al., 2008).

The utilisation of Antifreeze peptide (Afp1m) involves the application of a compact peptide that imitates the biological functionality exhibited by the parent Antifreeze Proteins (AFPs). The Afp1m protein is constructed using a sequence of 25 amino acids derived from the helix-1 of the helix sections found in *Glaciozyma Antarctica*. This sequence is modified by introducing specific substitutions. The modifications made to the sequence were implemented to facilitate the creation of helix structures by introducing salt bridges into the peptide sequence. Due to these alterations, Afp1m is expected to form a more stable helix structure than the other isolated peptides. Therefore, it is thought to have higher antifreeze activity (Shah et al., 2012). Afp1m may be useful in the future as a quality storage media of the cells and tissue at low-temperature preservation conditions and can keep the tissue without freezing damage at very low temperatures.

The exact molecular mechanism of action of Afp1m needs to be clearly understood. This study was designed to investigate the interactions of Afp1m in cryomedia and ice crystal effects on post-cryopreservation cell viability. The objectives of this study were to estimate the cytotoxicity level of Afp1m in growing *M. dunni* (Clone III8C) cells at 37°C for 24, 48 and 72 hr.

MATERIALS AND METHODS

All cell culture *M. dunni* (Clone III8C) incubations took place in a 37°C incubator with 5% CO₂ and standard humidity (95%) (Figure 1). Prospectively used solutions were pre-warmed at room temperature before being applied to the cells. *M. dunni* (Clone III8C) (ATCC® CRL-2017™) was purchased from ATCC. *M. dunni* Clone III8C was derived from the dermal layer of the skin of a normal female mouse (*Mus dunni*). These cells resembled fibroblasts. These cells lack most endogenous murine leukaemia virus-linked sequences. The confluent culture of *M. dunni* (Clone III8C) remains more firmly attached in a growing medium composed of RPMI 1640 or DMEM + 10% of FBS during the assays. These cells are mainly resistant to the infections. The base medium used for this cell line was McCoy's 5A Medium Modified (ATCC-formulated). Fetal bovine serum (FBS) at a concentration of 10% was added to the base medium to modify McCoy's 5A Medium (Weng & Hsu, 2008).

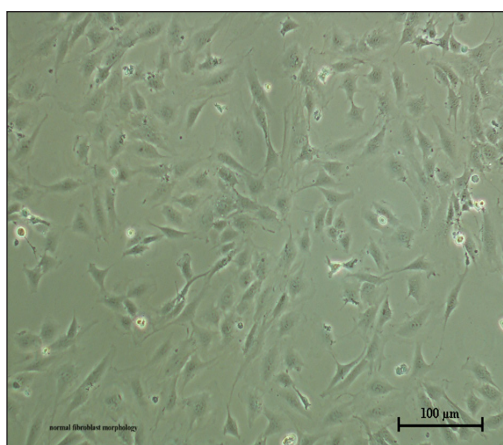


Figure 1. Morphology of normal mouse epidermis fibroblasts *M. dunni* Clone III8C (Scale bar = 100 μ m \times 10)

Normal mouse skin fibroblasts (*M.dunni* Clone1118C) employed in an *in vitro* cryopreservation experiment for the protein Afp1m showed the following morphology.

Subculture Procedure

A cryovial of *M. dunni* (Clone III8C) cells was rapidly thawed by gentle spinning in the 37°C water bath. The cap and the O-rings of the cryovial were kept out on the water surface to reduce the risk of contamination. The cryovial was disinfected by spraying with 70% ethanol in the biohazard safety cabinet type II. The cell suspension of *M. dunni* cells was transferred from the cryovial into a 15 mL conical tube containing 10 mL of ATCC-formulated McCoy's 5A Medium supplemented with 10% fetal bovine serum (FBS). Cells were pelleted using a centrifuge at $200 \times g$ for 5 minutes at room temperature. After pelleting, the supernatant was removed, and cells were resuspended in 5 to 10 mL McCoy's 5A Medium, 10% FBS supplemented and transferred into a 25 cm² tissue culture flask (T25) by adding 5 mL of McCoy's 5A medium. Suspension was transferred to tissue culture flasks and vented caps. The flask was incubated in a 37°C incubator with 5% CO₂. Cells were monitored daily or every other day up to the time until they reached 90% confluence. Media was changed every 3 days until the cells reached 80%–90% confluence and were passed into the new flasks (Freshney, 2005; Ho et al., 2012).

Maintenance of Cell Culture

M. dunni (Clone III8C) cells stopped growing and started to die after they reached confluence; therefore, it was extremely important to monitor cells and subculture them until they reached confluent monolayers. Actively grown cells usually double roughly in numbers every 24 (Chen & Okayama, 1987). The frequency of cell passaging, often ranging from 2 to 3 times each week, is contingent upon the initial quantity of cells planted in the flask as well as the size of the flask.

The growth medium was removed from a confluent monolayer of *M. dunni* (Clone III8C) cells. Cells were washed twice with 5 mL of Phosphate-Buffered Saline (PBS) to remove serum containing trypsin inhibitors. 5 mL of 1× trypsin-EDTA was added, and the cells were incubated at 37°C for 2 to 3 minutes until they started to detach from the surface of the flask.

Moderate shaking and tapping of the flask were performed on the flask surface to help the cells detach from the flask. McCoy's 5A Medium (5 mL) was added with 10% FBS to inactivate the trypsin-EDTA. The cell suspension was pipetted up and down to break up any clump of cells. Cells with media were removed from the flask, transferred to a sterile 15 mL falcon tube, and then centrifuged at $200 \times g$ at room temperature for 5 minutes. The supernatant was removed, and cells were resuspended in 10 mL McCoy's 5A Medium with 10% FBS. The desired dilution of cells in 12 to 20 mL of McCoy's 5A Medium with 10%

FBS was added to 75 cm² cell culture flasks with vented caps. Cells were monitored daily or every alternate day. Media was changed after every 3 to 4 days. When cells reached 80%–90% of the confluent monolayer level, by repeating this protocol, cells were passaged again (Ammerman et al., 2008).

Cytotoxicity Determination

M. dunnii (Clone III8C) cells suspended in McCoy's 5A medium, which was modified with 10% FBS, cells were plated before treatment. About 1×10^5 cells/mL were seeded in the 96-well titration plate (Becton Dickinson, USA), and the plate was kept at 37 °C with a 5% CO₂ incubator for 24 h. On the following day, the cells were treated with different Afp1m concentrations. The old medium was removed, and the sub-diluted extracts were then transferred into a 96-well titer plate using sterile pipette tips. The concentrations of both types of cells were determined using a haemocytometer. The cells were suspended in supplemented McCoy's 5A medium, containing the different concentrations of Afp1m and 10 mg/mL.

A 4 mg/mL was prepared and then diluted by serial dilution in 96-well microtitration plates to achieve the required concentration of a 20 mg/mL stock solution. The titration plate was placed for incubation at 37°C with 5% CO₂ for 24, 48 and 72 h. Cells were suspended in a growth medium containing McCoy's 5A supplemented with 10% FBS for positive control.

After 24, 48 and 72 hr incubation at 37°C with 5% CO₂, MTT reagent (20 μ L) was added to each well, and the plate was incubated for 3 hr in an incubator at 37°C with 5% CO₂. The generated purple formazan was dissolved by adding 150 μ L of dimethyl sulfoxide (DMSO) in a dark environment at room temperature. The solution was then agitated on an orbital shaker for approximately 15 minutes. The absorption measurement was conducted using a microplate reader, with the recorded values at 570 nm and a reference value at 630 nm.

The trials were conducted in triplicate, resulting in three sets of data. After the incubation period, the fraction of survived cells was determined relative to the untreated cell population by the MTT assay. The data were analysed using Graph Pad Prism Version 9, which showed the graph of viability percentages after cytotoxicity tests and cryopreservation.

Statistical Analysis

The dose-response of each concentration, temperature and period was determined from those summarised and presented by bar graphs with a mean (\pm) standard deviation after analysing data as depicted in Figures 2 to 5. The score data were evaluated parametrically using one-way ANOVA and two-way ANOVA tests. The multiple comparison tests of Sidak and Tukey were conducted, and statistical significance was determined based on the observed p-value ($p < 0.05$) (Parvaneh et al., 2017).

RESULTS

Cytotoxicity Determination

This study employed the MTT test to evaluate the cytotoxic effects of Afp1m on *M. dunnii* (Clone III8C) cells. The cells were cultured with Afp1m in a 37°C incubator with 5% CO₂, and the percentage of viable cells was assessed at various time intervals (24, 48, and 72 hr).

Cytotoxicity After 24 hr Treatment with Afp1m at 37°C (Cell Viability %)

The % values of live cells following 24 hr of treatment with different concentrations of Afp1m, *i.e.* 10, 5, 2, 1 and 0.5 mg/mL with positive and negative controls were 78.86 ± 10.17%, 88.38 ± 3.19%, 88.75 ± 7.19%, 90.61 ± 7.11%, 91.19 ± 4.52%, and 100.00 ± 0.0%, respectively.

One-way ANOVA observed a significant difference ($p < 0.01$) among different concentrations following 24 hr treatment at 37°C (Figure 2). There was a significant difference ($p < 0.05$) between 10 mg/mL and all lower concentrations, *i.e.* 5, 2, 1, 0.5 mg/mL and control percentages. A significant difference ($p < 0.05$) was observed between the control and 5, 2, 1 and 0.5 mg/mL percentages. There was no significant difference ($p > 0.05$) between 5 mg/mL and lower concentrations.

Cytotoxicity Following a 48-hour Afp1m Therapy at 37°C (Cell Viability %)

The % of live cells following 48 hr of treatment with different concentrations of Afp1m with positive and negative controls were 83.37 ± 8.74%, 97.46 ± 1.71%, 95.80 ± 6.24%, 94.2 ± 4.81%, 95.29 ± 5.53%, and 100.00 ± 0.0%, respectively. A significant ($p < 0.01$) difference was observed between different concentrations at 48 hr.

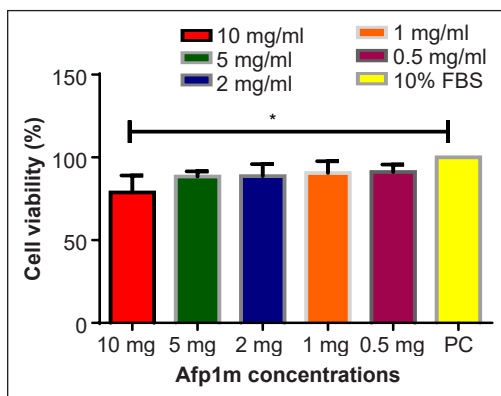


Figure 2. Cell viability for different concentrations of Afp1m incubated for 24 hr at 37°C (A statistically significant difference ($p < 0.01$) was discovered using a one-way analysis of variance (ANOVA) when examining the percentage of reported viable cells following an incubation time of 24 hours at 37°C with 5% CO₂)

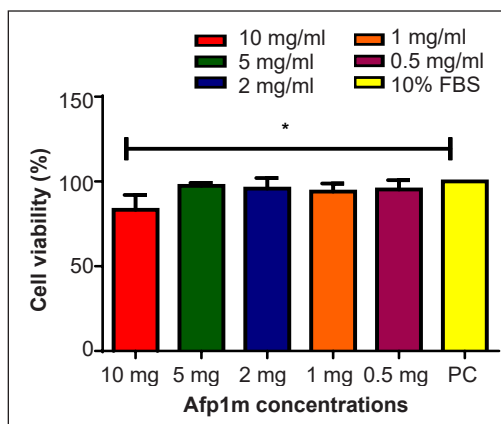


Figure 3. Cell viability for different concentrations of Afp1m incubated for 48 hr at 37°C (Following a 48-hour incubation period at 37 degrees Celsius and 5% carbon dioxide, a One-way Analysis of Variation (ANOVA) was performed. The results showed a statistically significant difference ($p < 0.01$) in the percentage of cell survival.)

Cell viability in 10 mg/mL was significantly lower ($p < 0.01$) than all lower concentrations, i.e. 5, 2, 1, and 0.5 mg/mL with control percentages. There was no significant difference ($p > 0.05$) between 5 mg/mL and lower concentrations, i.e. 2, 1 and 0.5 mg/mL with control percentage (Figure 3).

Cytotoxicity Following a 72-hour Afp1m Therapy at 37°C (Cell Viability %)

The % of live cells following 72 hr of treatment with different concentrations of Afp1m, i.e. 10, 5, 2, 1 and 0.5 mg/mL with positive and negative controls were $86.73 \pm 6.92\%$, $103.9 \pm 6.56\%$, $104.3 \pm 5.13\%$, $100.9 \pm 1.71\%$, $102.8 \pm 1.24\%$, and $100.00 \pm 0.0\%$, respectively. One-way ANOVA suggests a significant difference ($p < 0.01$) between different concentrations at a 72 hr time point. Tukey's multiple comparison tests revealed a noteworthy distinction ($p < 0.01$) between 10 mg/mL and all lower concentrations, i.e. 5, 2, 1, 0.5 mg/mL and control percentages. There was no significant difference ($p > 0.05$) between 5 mg/mL and lower concentrations of 2, 1 and 0.5 mg/mL with control percentage (Figure 4).

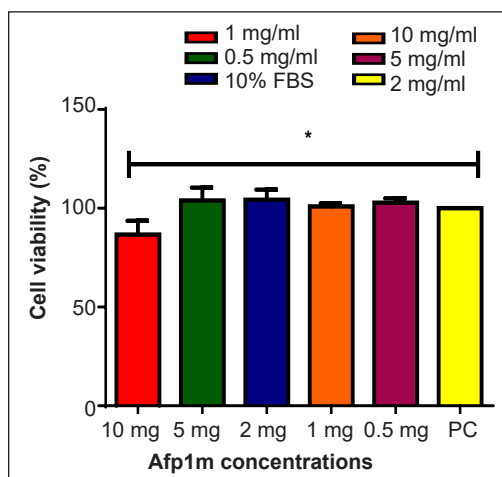


Figure 4. Cell viability for different concentrations of Afp1m incubated for 72 hr at 37°C

Cytotoxicity Comparisons Between Different Afp1m Concentrations at 72 hr (Cell Viability %)

One-way ANOVA showed a significant difference ($p < 0.01$) between 24, 48 and 72 hr of cell viability percentages. Multiple comparison tests depicted a significant difference at 24 and 48 hr, 24 and 72 hr, and 48 and 72 hr. Cell number was significantly increased from 24 to 48 hr and 48 to 72 hr (Figure 5).

Afp1m Concentration 10 mg/mL

A statistically significant variation ($p < 0.01$) was seen in the viability of cell percentages

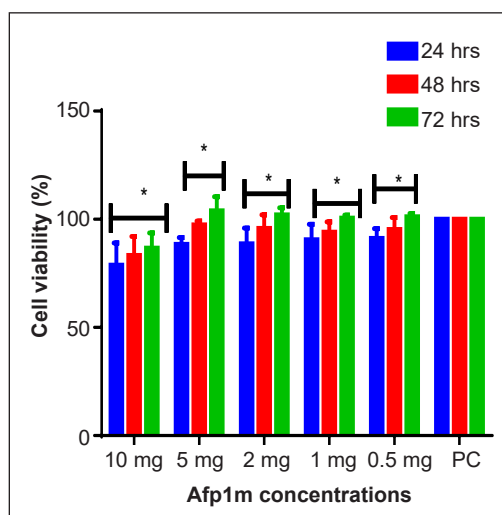


Figure 5. The viability of cells at 37°C for different amounts of Afp1m at different times

between the time points of 24 and 72 hrs. No statistically significant difference ($p > 0.05$) was seen between the 24-hour and 48-hour time points. At the same time, a significant difference ($p < 0.05$) was also observed between 48 and 72 hr (Figure 5).

Afp1m Concentration 5 mg/mL

At a dosage of 5 mg/mL, there was a statistically significant difference ($p < 0.01$) in cell viability percentages between the 24 and 48-hour and 24- and 72-hour time points. Furthermore, after 48 and 72 hr, a statistically significant difference was seen ($p < 0.05$) (Figure 5).

Afp1m Concentration 2 mg/mL

The proportion of cells that survived between the time points of 24 and 48 hr, as well as between 48 and 72 hr, showed statistically significant differences ($p < 0.05$) at a dose of 2 mg/mL. Furthermore, a highly significant ($p < 0.01$) difference was discovered between the 48- and 72-hour intervals (Figure 5).

Afp1m Concentration 1 mg/mL

No significant difference ($p > 0.05$) was observed in cell viability percentages at 1 mg/mL at 24 h. In contrast, a significant difference was observed in cell viability percentages between 1 mg/mL between 48 and 72 h, while a high significant difference ($p < 0.01$) was also observed between 24 and 72 hr (Figure 5).

Afp1m Concentration 0.5 mg/mL

No statistically significant differences ($p > 0.05$) were found in the cell viability percentages at a concentration of 0.5 mg/mL between the time points of 24 and 48 hr, as well as between 48 and 72 hr. On the other hand, a highly significant difference was seen at the time points of 24 and 72 hr ($p < 0.01$) (Figure 5).

DISCUSSION

Different Afp1m treated cells showed different survival percentages after growing the cells in media containing different Afp1m concentrations at 37°C with 0.05% CO₂. The percentage of cell viability in different concentrations, i.e. 10 mg/mL, was increased from 78.86% to 86.73%, 5 mg/mL (from 88.38% to 103.9%), 2 mg/mL (from 88.75% to 104.3%), 1 mg/mL (90.61% to 100.9%), and 0.5 mg/mL (from 91.19% to 102.8%). At the 72-hour mark of treatment, the concentrations of Afp1m at 2 and 5 mg/mL showed notable differences, surpassing the scores obtained by the concentrations of 1 mg/mL and

0.5 mg/mL. Impaired growth was found in the 10 mg/mL AFP solution at 24, 48, and 72 hr. The growth rate of the samples treated with a concentration of 10 mg/mL was slower than that of those treated with lower concentrations.

These results were in partial agreement with the studies in which it was mentioned that protective effects may be narrowed at higher Afp1m concentrations and were in agreement with the study that the maximum concentration of AFP1 may produce damage to cryopreserved tissue (Chao et al., 1996). These findings also align with a study by Liu et al. (2007), which used human liver and kidney cells treated with AFGP8 and produced different results. The study showed that a higher concentration of more than 2 mg/mL AFGP8 showed higher toxicity, subsequently 20 hr of incubation at 37°C (Liu et al., 2007). Findings also showed similarity to the study where the cryoprotectant like DMSO was the most toxic of the cryoprotectant to zebra fish blastomeres when exposed at room temperature (Ritar, 1999). These results agree with previous findings where an anti-freeze peptide from *Pleuronectes americanus* was successfully used as a cryoprotectant at 37°C. They gave 50% viability when Vero cells were grown with different concentrations of Afp1m from *P. americanus* (Migliolo et al., 2012).

Previous studies reported using anti-freeze glycopeptides as cryoprotectants characteristically worked at concentrations greater than 10 mg/mL. One of these reports designated the cytotoxicity in spinach thylakoid membranes (Biggs et al., 2017; Hinch et al., 1993; Sun et al., 2022). In this study, Afp1m has been mentioned to be a good vitrification agent that protects cells and enhances growth at subzero temperatures and lower temperatures like 0°C and in fresh cell suspensions (Bang et al., 2013; Katkov et al., 2012).

CONCLUSION

The finding of the current study revealed that cryopreservation with Afp1m was safe. Cryopreservation of cells with the Afp1m concentration like 10 mg/mL and above and very low concentrations like 2 mg/mL and 1 mg/mL may need further studies to confirm the effects of peptide on the cell morphology. Using damage-specific N-glycosylases will help researchers assess the various types and amounts of damage. It will allow researchers to compare the role of numerous DNA repair pathways in DNA damage caused by tissue cryopreservation. Therefore, the use of Afp1m in the cryopreservation of cells and tissue should be further investigated.

ACKNOWLEDGEMENTS

This work was supported by grants from the Ministry of Higher Education Malaysia (02-01-13-1200FR) and Universiti Putra Malaysia (UPM) (GP/2017/9567000). The authors thank the Faculty of Veterinary Medicine and UPM staff for their assistance with this project.

REFERENCES

- Adler, K., Arkona, C., Manteuffel, R., & Süss, K. H. (1993). Electron-microscopical localization of chloroplast proteins by immunogold labelling on cryo-embedded spinach leaves. *Cell Biology International*, *17*(2), 213-220. <https://doi.org/10.1006/cbir.1993.1057>
- Ammerman, N. C., Beier-Sexton, M., & Azad, A. F. (2008). Growth and maintenance of Vero cell lines. *Current Protocols in Microbiology*, *11*(1), A.4E.1-A.4E.7. <https://doi.org/10.1002/9780471729259.mca04es11>
- Baardsnes, J., Jelokhani-Niaraki, M., Kondejewski, L. H., Kuiper, M. J., Kay, C. M., Hodges, R. S., & Davies, P. L. (2001). Antifreeze protein from shorthorn sculpin: Identification of the ice-binding surface. *Protein Science*, *10*(12), 2566-2576. <https://doi.org/10.1110/ps.ps.26501>
- Bang, J. K., Lee, J. H., Murugan, R. N., Lee, S. G., Do, H., Koh, H. Y., Shim, H. E., Kim, H. C., & Kim, H. J. (2013). Antifreeze peptides and glycopeptides, and their derivatives: potential uses in biotechnology. *Marine Drugs*, *11*(6), 2013-2041. <https://doi.org/10.3390/md11062013>
- Beirão, J., Zilli, L., Vilella, S., Cabrita, E., Schiavone, R., & Herráez, M. P. (2012). Improving sperm cryopreservation with antifreeze proteins: effect on gilthead seabream (*Sparus aurata*) plasma membrane lipids. *Biology of Reproduction*, *86*(2), 59-1. <https://doi.org/10.1095/biolreprod.111.093401>
- Biggs, C. I., Bailey, T. L., Graham, B., Stubbs, C., Fayter, A., & Gibson, M. I. (2017). Polymer mimics of biomacromolecular antifreezes. *Nature Communications*, *8*(1), Article 1546. <https://doi.org/10.1038/s41467-017-01421-7>
- Chao, H., Davies, P. L., & Carpenter, J. F. (1996). Effects of antifreeze proteins on red blood cell survival during cryopreservation. *Journal of Experimental Biology*, *199*(9), 2071-2076. <https://doi.org/10.1242/jeb.199.9.2071>
- Chen, C., & Okayama, H. (1987). High-efficiency transformation of mammalian cells by plasmid DNA. *Molecular and Cellular Biology*, *7*(8), 2745-2752. <https://doi.org/10.1128/mcb.7.8.2745-2752.1987>
- Degner, B. M., Chung, C., Schlegel, V., Hutkins, R., & McClements, D. J. (2014). Factors influencing the freeze-thaw stability of emulsion-based foods. *Comprehensive Reviews in Food Science and Food Safety*, *13*(2), 98-113. <https://doi.org/10.1111/1541-4337.12050>
- Freshney, R. I. (2005). Culture of specific cell types. In *Culture of Animal Cells: A Manual of Basic Technique* (pp. 375-420). John Wiley & Sons. <https://doi.org/10.1002/0471747599.cac023>
- Grout, B., Morris, J., & McLellan, M. (1990). Cryopreservation and the maintenance of cell lines. *Trends in Biotechnology*, *8*, 293-297.
- Hincha, D. K., De Vries, A. L., & Schmitt, J. M. (1993). Cryotoxicity of antifreeze proteins and glycoproteins to spinach thylakoid membranes - comparison with cryotoxic sugar acids. *Biochimica et Biophysica Acta (BBA)-Biomembranes*, *1146*(2), 258-264. [https://doi.org/10.1016/0005-2736\(93\)90364-6](https://doi.org/10.1016/0005-2736(93)90364-6)
- Hirano, Y., Nishimiya, Y., Matsumoto, S., Matsushita, M., Todo, S., Miura, A., Komatsu, Y., & Tsuda, S. (2008). Hypothermic preservation effect on mammalian cells of type III antifreeze proteins from notched-fin eelpout. *Cryobiology*, *57*(1), 46-51. <https://doi.org/10.1016/j.cryobiol.2008.05.006>

- Ho, W. Y., Yeap, S. K., Ho, C. L., Rahim, R. A., & Alitheen, N. B. (2012). Development of multicellular tumor spheroid (MCTS) culture from breast cancer cell and a high throughput screening method using the MTT assay. *Plos One*, 7(9), Article e44640. <https://doi.org/10.1371/journal.pone.0044640>
- Katkov, I. I., Bolyukh, V. F., Chernetsov, O. A., Dudin, P. I., Grigoriev, A. Y., Isachenko, V., Isachenko, E., Lulat, A. G. M., Moskovtsev, S. I., Petrushko, M. P., Pinyaev, V. I., Sokol, K. M., Sokol, Y. I., Sushko, A. B., & Yakhnenko, I. (2012). Kinetic vitrification of spermatozoa of vertebrates: What can we learn from nature? In I. I. Katkov (Ed.), *Current Frontiers in Cryobiology* (pp.3-40). INTECH Open Access Publisher. <https://www.intechopen.com/chapters/31227>
- Liu, J. X., Srivastava, R., Che, P., & Howell, S. H. (2007). An endoplasmic reticulum stress response in Arabidopsis is mediated by proteolytic processing and nuclear relocation of a membrane-associated transcription factor, bZIP28. *The Plant Cell*, 19(12), 4111-4119. <https://doi.org/10.1105/tpc.106.050021>
- Migliolo, L., Silva, O. N., Silva, P. A., Costa, M. P., Costa, C. R., Nolasco, D. O., Barbosa, J. A. R., Silva, M. R. R., Bemquerer, M. P., Lima, L. M. P., Romanos, M. T. V., Freitas, S. M., Magalhães, B. S., & Franco, O. L. (2012). Structural and functional characterization of a multifunctional alanine-rich peptide analogue from *Pleuronectes americanus*. *Plos One*, 7(10), Article e47047. <https://doi.org/10.1371/journal.pone.0047047>
- Parvaneh, S., Mohler, J., Toosizadeh, N., Grewal, G. S., & Najafi, B. (2017). Postural transitions during activities of daily living could identify frailty status: Application of wearable technology to identify frailty during unsupervised condition. *Gerontology*, 63(5), 479-487. <https://doi.org/10.1159/000460292>
- Ritar, A. J. (1999). Artificial insemination with cryopreserved semen from striped trumpeter (*Latris lineata*). *Aquaculture*, 180(1-2), 177-187. [https://doi.org/10.1016/S0044-8486\(99\)00109-X](https://doi.org/10.1016/S0044-8486(99)00109-X)
- Shah, S. H. H., Kar, R. K., Asmawi, A. A., Rahman, M. B. A., Murad, A. M. A., Mahadi, N. M., Basri, M., Rahman, R. N. Z. A., Salleh, A. B., Chatterjee, S., Tejo, B. A., & Bhunia, A. (2012). Solution structures, dynamics, and ice growth inhibitory activity of peptide fragments derived from an antarctic yeast protein. *Plos One*, 7(11), Article e49788. <https://doi.org/10.1371/journal.pone.0049788>
- Sun, Y., Maltseva, D., Liu, J., Hooker, T., Mailänder, V., Ramløv, H., DeVries, A. L., Bonn, M., & Meister, K. (2022). Ice recrystallization inhibition is insufficient to explain cryopreservation abilities of antifreeze proteins. *Biomacromolecules*, 23(3), 1214-1220. <https://doi.org/10.1021/acs.biomac.1c01477>
- Weng, C. H., & Hsu, M. C. (2008). Regeneration of granular activated carbon by an electrochemical process. *Separation and Purification Technology*, 64(2), 227-236. <https://doi.org/10.1016/j.seppur.2008.10.006>

Aluminium Hydroxide/Graphene-reinforced Rigid Polyurethane Foam Hybrid Composites

Aisha Elhadi Abosnina^{1*}, Zurina Mohamad¹, Rohah Abdul Majid¹ and Raji Muhammed Abdulwasiiu²

¹*Department of Bioprocess and Polymer Engineering, Faculty of Chemical and Energy Engineering, Universiti Teknologi Malaysia, 81310, Skudai, Johor, Malaysia*

²*INSA Center Val de Loire, University Orleans, PRISME EA 4229, 18022 Bourges, France*

ABSTRACT

In this study, rigid polyurethane foams (RPUF) were successfully modified using 30 wt.% aluminium hydroxides (ATH), 1.0 pphp silicone surfactant, and different concentrations of graphene, using a one-shot one-step foaming method. This study aims to improve the compressive strength, flame retardancy, and thermal properties of RPUF by creating a synergistic effect between ATH and graphene in fire-retardant RPUF hybrid composites. The effects of a fixed amount of ATH and silicone surfactant and various loadings of graphene on RPUF were investigated. The results show that 0.5 wt.% graphene loading confers the best compression performance on the hybrid composite. Their compressive strength value of 12.58 KPa was higher than virgin RPUF (4.07 KPa) and RPUF/ATH (9.89 KPa). FTIR confirmed the functional groups in the virgin RPUF but could not identify new functional groups in most modified composites. The smallest amount of graphene addition (0.5 wt.%) produced a more stable hybrid composite structure. At 3.0 wt.% graphene addition,

the maximum decomposition temperature of the RPUF/ATH hybrid composite was recorded (539°C), which was enhanced by 50% compared to virgin RPUF (296°C), and the highest char residue of 17.46% was observed. The incorporation of graphene enhanced the thermal firmness of the hybrid composite. The study also revealed an enhancement in the fire resistance of the hybrid composite. The LOI and UL-94 results showed that incorporating 3.0 wt.%

ARTICLE INFO

Article history:

Received: 17 September 2023

Accepted: 25 March 2024

Published: 15 August 2024

DOI: <https://doi.org/10.47836/pjst.32.5.10>

E-mail addresses:

aisha.abosnina@gmail.com (Aisha Elhadi Abosnina)

r-zurina@utm.my (Zurina Mohamad)

r-rohah@utm.my (Rohah Abd Majid)

rajiabdul85@gmail.com (Abdulwasiiu Muhammed Raji)

* Corresponding author

enables increased LOI value and V-0 classification compared to virgin samples. This hybrid composite can be used in high-performance building insulation applications.

Keywords: Aluminium hydroxides (ATH), fire behaviour, flammability, graphene, hybrid flame retardant, rigid polyurethane foam

INTRODUCTION

Owing to their durability and versatility, polyurethanes (PU) are in high demand in the fields of construction, automobiles, and refrigeration for thermal insulation (Dhaliwal et al., 2020; Kavšek et al., 2022; Liu & Hu, 2020). Polyurethane foam is the most common application of PUs in the central consumer segment (Shoaib et al., 2014). According to studies by Eaves (2004) and Titow (2001), polyurethane (PU) still accounts for 67% of the global foam market, ahead of polyvinyl chloride (PVC) and polystyrene (PS) (Muhammed et al., 2023). PU foam is divided into rigid and flexible categories based on its intended use. Each category differs in the functionality and polyol type used for synthesis (Baguian et al., 2021; Shoaib et al., 2014).

Among the listed categories, rigid polyurethane foam (RPUF) has been more widely studied because of its superior application ranges in transportation (Tiuc et al., 2019), sealants (Eling et al., 2020), insulation materials (Srihanum et al., 2022; Tiuc et al., 2022), packaging (Jonjaroen et al., 2020), and construction (Ju et al., 2020; Lorusso et al., 2017), among others. RPUF is used as a structural material owing to its lightweight, excellent strength-to-weight ratio, and capacity to absorb energy (Alis et al., 2019; Kumar & Kaur, 2017). RPUFs are produced with a higher isocyanate (NCO) content, which increases the hard segment composition of the system. They are highly crosslinked three-dimensional polymers with closed-cell structures, low thermal conductivities, high compression strengths, and low densities. These attributes are attributed to their high porosity, strength-to-weight ratio, and low moisture permeability (Chen et al., 2014; Kerche et al., 2020). Similar to other PU foams, the properties of RPUF can be easily modified by incorporating inorganic hydroxide fillers and nanoparticles into the polymer matrix to produce composites with superior mechanical and thermal performance (Mohamad et al., 2021; Peng et al., 2019; Sałasińska et al., 2021).

Traditional inorganic hydroxide fillers, such as magnesium hydroxide, aluminium hydroxide (ATH), and layered double hydroxides, are non-toxic and ecologically friendly. They are commonly used as reinforcing materials in a polymer matrix to enhance their mechanical, thermal, and flammability properties (Pang et al., 2019; Rocha et al., 2021; Wang et al., 2017). ATH, in particular, is a popular choice owing to its chemical inertness, ease of handling, odourless, low cost, and non-volatility. When composites filled with ATH are heated and burned, they absorb heat. It leads to a uniform distribution of absorbed heat within the ATH particles, thereby reducing the heating rate of the composite (Cheng et

al., 2014; Modesti et al., 2002). On the other hand, nanoparticle fillers like graphene are used in smaller quantities compared to traditional particles, which has little impact on the PU foaming process. The dispersion of the filler in the matrix played a significant role in the reinforcement effect. Graphene is well-known for its excellent mechanical properties, including a fracture strength of 125 GPa, high Young's modulus of 1.1 TPa (Lee et al., 2008), and an ideal specific surface area of 2630 m²/g (Stoller et al., 2008).

Despite its unique properties, RPUF has significant limitations, including ease of ignition, high flammability, low mechanical strength, and low thermal stability. Additionally, their low dimensional stability creates problems in insulation (Liu et al., 2016; Srihanum et al., 2022). RPUF is a flammable polymer. In a fire outbreak, foams release a large amount of heat and toxic gases such as carbon monoxide and hydrogen cyanide (Chen et al., 2018). Previous studies have shown that incorporating more than one type of flame retardant (FR) (such as organic and inorganic FR) into polymer foam can significantly enhance the mechanical, thermal, and flammability properties of foam composites (Feng et al., 2016; Huang et al., 2020). Członka et al. (2021) reported the effect of montmorillonite (MMT)-modified sage filler on the mechanical and thermal properties of RPUF composites. The results showed that modifying salvia (SO) filler with MMT improved the interphase compatibility between the filler surface and PUR matrix. This modification also results in RPUF composites with improved compressive strength, thermal stability, and flame retardancy.

Wang et al. (2018) used magnesium hydroxide (MH) nanosheets to create core-shell expandable graphite (EG) flame-retardant fragments using a hetero-coagulation technique. Thus, the storage modulus and cell structure of RPUF-EG@MH were enhanced. The MH nanosheet shell successfully increased the foam's limiting oxygen index (LOI), and the interface adhesion between the expandable graphite (EG) and the matrix was improved. Pen et al. (2019) compared the effects of MH and ATH on the combustion resistance, compressive stress, and cell structure of RPUF. They found that ATH performed better than MH-modified RPUF composites because the RPUF/ATH composite had larger cells, higher maximum compressive stress, and an optimal LOI value. Various studies have compared the effects of graphene and its derivatives on the properties of polymer foam composites. In a recent survey by Thiyagu et al. (2021), different amounts of graphene were incorporated into polyurethane foam, and the thermal stability and morphology of the composites were investigated. The SEM results confirmed that graphene was evenly dispersed in the PU matrix, and its incorporation increased the thermal stability of the foam composites. Based on the results of Yao et al. (2020), the addition of flexible graphene sheets enhanced the flexibility, fire behaviour, and thermal degradation temperature of PU composites.

Several studies have been conducted on the influence of dual fillers and nanofillers on the preparation and properties of rigid polyurethane foams. Sałasińska et al. (2021) developed a

dual non-halogen flame retardants (FRs) system using graphene-oxide (GO) and histidine for rigid PU foam to reduce smoke emissions and enhance its fire retardancy. Liu et al. (2021) examined the impact of different concentrations of GO-hollow glass microspheres on the morphology, density, and compressive properties of RPUF. Liu et al. (2020) summarised the improvements in the thermal stability and fire safety of RPUF attributed to the synergistic relationship between expandable graphite and phosphorus/nitrogen compounds. A summary of previous studies on the flame-retardant behaviour of RPUF is presented in Table 1.

This study aims to address the existing research gap by investigating and comparing the morphology, compressive strength, and thermal and flammability properties of a hybrid composite system utilising aluminium hydroxide (ATH) and graphene as reinforcing fillers in rigid polyurethane foam (RPUF). To the best of our knowledge, no previous studies have explored the performance of hybrid ATH/graphene fillers in RPUF composite systems, specifically in terms of their morphology, compressive strength, flammability, and thermal properties. In addition, we incorporated a silicone surfactant into the RPUF formulation to control the cell size of the rigid foam and reduce its surface tension. Therefore, this

Table 1

Summarises past and recent literature on the flame-retardant behaviour of RPUF

Paper Title/Focus	Contribution	Reference
Fire behaviour of PU foam with non-halogen fire retardants (histidine/modified graphene oxide) system	The authors obtained a reduction in the total heat release rate, heat release rate, maximum average rate of heat emission, total heat release (THR) and total smoke release for modified RPUF.	Sařasińska et al., 2021
Preparation and evaluation of RPUF flame retardant (functionalised graphene oxide)	3 wt.% functionalised GO enhanced the flame retardancy of the foam: reduction in peak heat release rate (PHRR) by 25% and total smoke production by 15% compared to pure RPUF.	Zhou et al., 2023
Incorporation of multiple inorganic fillers as viable synergistic agents for enhancing the flame retardancy of intumescent flame retardant (IFR)	RPUF/IFR had a good performance, with a low PHRR of 82.12 kW/m ² , THR of 15.15 MJ/m ² , and a high LOI value of 36% compared to the untreated sample.	Lee et al., 2022
Flammability properties of novel IFR (APP/sepiolite/melamine) in RPUF	The composite's limiting oxygen index (LOI) value increased to 23.20% compared to 17.0% for pure RPUF. The V-0 rating was obtained for RPUF/IFR 16 phr in the UL-94 test. The lowest after-flame time after ignition (21.4 s) was obtained at this formulation compared to other samples.	Mohammad et al., 2021
RPUF was prepared and reinforced by incorporating hydrolysed keratin (HK) to enhance foam smoke suppression and flame retardancy.	The addition of HK improved the LOI and PHRR of the foam, but the THR of the modified foam decreased. The HRR of foam/HK5 was reduced by 28.8 kW/m ² compared with pure foam, and the THR of foam/HK5 is 0.74 MJ/m ² lower than the untreated foam. HK5 wt.% had the most obvious smoke suppression effect	Zhang et al., 2023

study investigates and compares the performance of RPUF-based composites using pure RPUF and ATH/graphene/silicone surfactant hybrid filler systems. This manuscript presents experimental findings regarding the developed composites' structure, morphology, compressive strength, flammability, and thermal properties. The results provide valuable insights into the potential of a hybrid filler system for enhancing the properties of RPUF and contribute to the advancement of materials with improved performance characteristics.

MATERIALS AND METHODS

Materials

This study prepared a flame-retardant rigid polyurethane foam by incorporating a hybrid ATH/graphene. The experiment employed polyol (4500 series), consisting of Part A (with a hydroxyl number of approximately 400–455 mg KOH/g) and Part B. Part A of the formulation has been enhanced with several additional substances, including a catalyst, specifically benzyl-dimethylamine, present at a concentration of 1%. Furthermore, a blowing agent, namely 1,1-dichloro-1-fluoroethane, has been inserted at a concentration of 20%. Finally, a crosslinker, tetramethyl hexamethylenediamine, has been introduced at a concentration of 0.1%. Part B refers to a polymeric diphenylmethane diisocyanate compound, commonly known as P-MDI. Wee Tee Tong Chemicals Pte Ltd., a Malaysia-based company, manufactures Polyol and P-MDI. The foam stabiliser employed in this study was Niax Silicone L-5440, manufactured by Momentive Performance in the United States. Odourless, white, powdered Al (OH)₃ (purchased from Merck KGaA, Germany) and graphene sourced from Soochow Hengqiu Technology were used as flame retardants.

Preparation of Rigid Polyurethane Foam and Composites

Virgin RPUF and ATH/graphene/RPUF foams were prepared in our laboratory using a one-shot, one-stop foaming method. The RPUF and RPUF hybrid composite samples were synthesised in a plastic container. The amounts of ATH and silicone surfactant in the formulations were kept constant at 30 wt.% and 1.0 pphp, respectively, while the graphene content was varied at three different concentrations of 0.5, 2.5, and 3.0 wt.%. First, ATH, graphene, and the silicone surfactant were added to a beaker containing polyol (Part A). The initial mixture was agitated at a rotational speed of 500 revolutions per minute (RPM) for five min using a mechanical stirring device to achieve a uniform and consistent solution. After the flame retardants were completely wetted and dispersed in the mixture, diisocyanate (Part B) was added to the pre-mixed solution with continuous stirring for a few seconds. The ratio of parts A and B was maintained at 1:1. Subsequently, the resulting mixture was poured into a stainless-steel mould to facilitate the creaming and self-rising processes. The modified foams were cured for 24 h at ambient temperature before being cut into samples for analysis. Table 2 shows the formulations of the RPUF and RPUF composites.

Table 2
The formulations of RPUF and hybrid RPUF composites

Sample Code	P-DMI (g)	Polyol (g)	ATH (wt.%)	Graphene (pphp)*
RPUF	50	50	0	0
RPUF/A	50	50	30	0
RPUF/A/GNP	50	50	30	0.5
RPUF/A/GNP	50	50	30	2.5
RPUF/A/GNP	50	50	30	3.0

Note. *(pphp): Parts per hundred polyols in weight

Characterisation of Specimens

The morphological analysis consisted of field emission scanning electron microscopy (FESEM). Field emission scanning electron microscopy (FESEM) was used to examine the spatial arrangement of graphene and aluminium trihydrate (ATH) within a rigid polyurethane (PU) foam. Furthermore, it was necessary to investigate the distribution of closed and open cells within the foam samples to analyse the surface morphology of the samples and examine the foam structure. The SEM used was a Hitachi Japan Tabletop Microscope 3000 model. RPUF/ATH was evaluated using scanning electron microscopy (SEM), and further analysis of the FESEM images was performed using the Zeiss Ks300 imaging system software (3.0 release). Initially, the internal surfaces of the specimens were coated with an auto fine coating to facilitate observation and prevent electrical charge. Subsequently, a thin layer of platinum was applied, and an operating voltage of 2 kilovolts (2 kV) was employed.

For the compressive strength test, the foams were cut to dimensions of $50 \times 50 \times 30$ mm³ (width \times length \times thickness). The test was conducted using a Zwick/Roll Proline Universal Testing Machine from (Ulm, Germany) at room temperature, following the ASTM D 1621-1 standard method. The rise direction of the RPUF was marked, and a crosshead speed rate of 5 mm/min was used. A load cell size was applied until the compressed foam stress reached 10% strain. The strengths of six specimens per sample were measured, and the average of these values was reported.

Fourier Transform Infrared (FTIR) spectroscopy was conducted to determine the presence of specific functional groups in the rigid polyurethane (PU) samples, including urethane linkages and carbonyl groups. The modified samples were also analysed to identify their functional groups. The scanning rate was set from 4000 cm^{-1} to 500 cm^{-1} . A Nicolet iS10 smart modal was used to scan the samples, and the obtained absorption spectra were analysed.

Thermogravimetric analysis (TGA, Q500 V20) was performed to analyse the thermal degradation of the samples. The weight decreases of the samples were measured at different temperatures. Approximately 6.4770 mg of each sample was carefully placed in a platinum

container. The analysis involved subjecting the samples to a temperature range of 28–700°C, with a heating rate of 10°C/min, in the presence of nitrogen gas at a constant flow rate of 100 ml/min. The rate of mass change or weight loss of each sample was carefully measured and recorded throughout the experiment.

The LOI (Limiting Oxygen Index) test was conducted by preparing seven samples for each formulation. Following the specifications outlined in ASTM D2863-97, the minimum burning duration was estimated to be three min. The samples used in the experiment were 100 mm long, 12.5 mm wide, and 12.5 mm thick. The samples were positioned vertically in a clear chimney, and the oxygen and nitrogen flow regulation was carefully controlled. The test was conducted multiple times by varying the oxygen and nitrogen levels to determine the minimal oxygen concentration required for the sample to undergo combustion within three minutes. The LOI of each formulation was assessed by averaging the results of the seven samples.

The flame retardancy of the RPUF/ATH/graphene composites was tested using the Underwriter Laboratories vertical burning test, UL94-V, following the ASTM D 3801-10 standard. The vertical height of the flame during the combustion was 20 mm. Seven samples were prepared for testing, each with dimensions of (130 × 10 × 10) mm³. The samples were then exposed to a flame emitted by the burner for 10 s. The duration for which the flame remained active without external intervention was measured, and the combustion characteristics, including the occurrence of dripping, were carefully monitored. Seven samples for each formulation were tested, and the burning rate was determined using the equation $V = 60 L/t$, where L represents the average length (mm), and t represents the average time (s).

RESULTS AND DISCUSSION

Morphology of RPUF and Hybrid RPUF Composites

Scanning electron microscopy (SEM) was used to analyse the compositions and internal structure of RPUF (Rigid Polyurethane Foam) composites. A hybrid composite system was created by incorporating a 30 wt.% ATH, 1.0 pphp silicone surfactant, and three different concentrations of graphene (0.5, 2.5, and 3.0 wt.%). Figure 1 illustrates the internal structure of the RPUF/ATH composites and the RPUF hybrid composites containing ATH and graphene as hybrid fillers. A surfactant prevents foam collapse by preventing the build-up of gases produced by blowing agents (Baferani et al., 2018). In general, the RPUF hybrid composite exhibited smaller cell sizes than the RPUF/ATH composites, attributed to the nucleation effect of graphene, which produces more bubbles and denser cells. Previous studies have shown that nanoparticles, such as graphene, act as nucleation points, leading to a larger number of cells and, consequently, a smaller cell size (Lorusso et al., 2017).

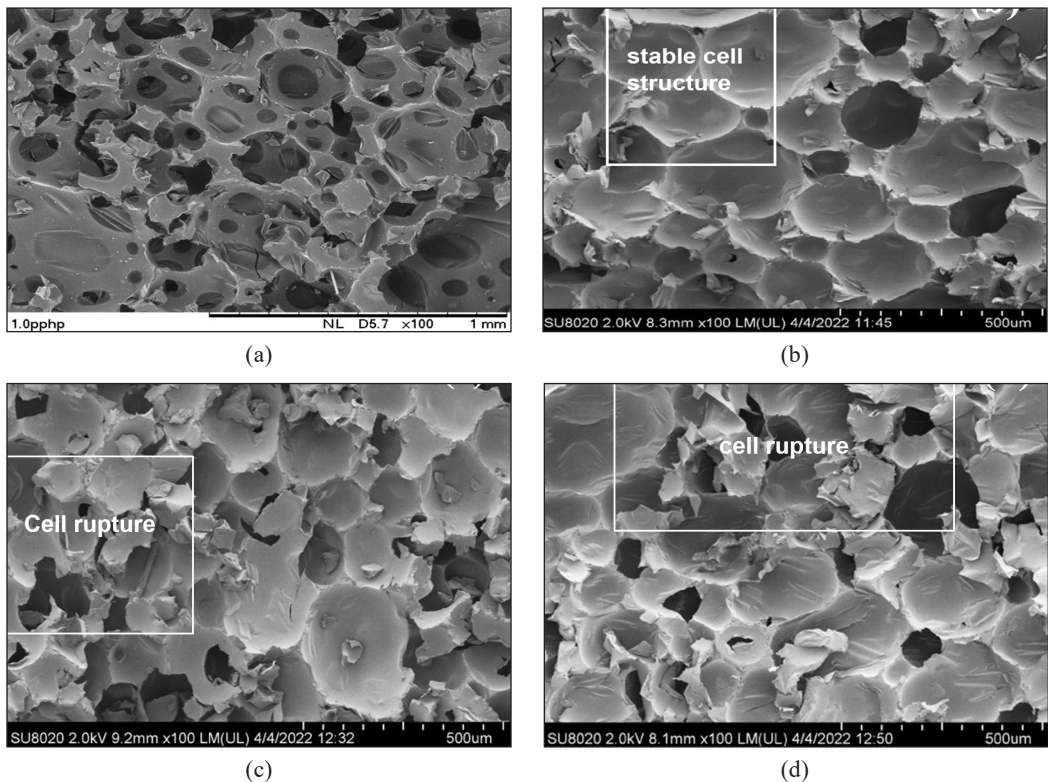


Figure 1. SEM micrographs of RPUF/ATH containing different graphene content: (a) 0 wt.%, (b) 0.5 wt.%, (c) 2.5 wt.%, (d) 3.0 wt.% (Magnification 100 \times).

At a graphene concentration of 0.5 wt.%, the RPUF hybrid composite demonstrates a more stable cell structure with fewer broken cells [Figure 1(b)]. However, as the graphene content was increased to 2.5 wt.% [Figure 1(c)], the internal space becomes compact, and noticeably broken cells are observed. It can be attributed to the presence of graphene, which incorporates rigid particles and hinders the formation and expansion of bubbles during the foaming, leading to further deterioration of the foam structure at higher concentrations (Zhang et al., 2021). Furthermore, an increase in the quantity of graphene resulted in non-uniform cell sizes in the RPUF hybrid composites, as shown in Figures 1(b), 1(c) and 1(d). As the graphene content exceeds 0.5 wt.%, the cell structure collapses rapidly. The research suggests that adding 2.5 to 3.0 wt.% of graphene to RPUF leads to smaller cell growth, but a significant portion of cells collapse, resulting in a disorganised cellular structure. However, the SEM images did not show significant clustering of graphene fillers. This finding is consistent with the observations of other researchers that graphene is beneficial for PU foam. However, excessive concentrations can decrease cell size and create intricate pathways within the foam. Previous studies have attributed the reduction in foam cell size to graphene acting as nucleation points, generating more cells and resulting in a smaller

size. Increasing the graphene content induced rapid changes in the rigid foam structure. While higher concentrations of solid particles, such as graphene, typically reduce cell size and increase cell density, excessive concentrations can decrease and create complex pathways (Chen et al., 2019; Kim et al., 2017; Lorusso et al., 2017).

As observed in other studies, hybrid composites take advantage of the synergies between two fillers in polyurethane systems, enhancing the mechanical and thermal properties (Liu et al., 2021; Pinto et al., 2020). For instance, the SEM result of a multiple FR system (ATH, APP, and others) in RPUF revealed closed-cell structures with adjoining spherical cells, attributed to the strong bond between the flame-retardant system and the PU matrix (Lee et al., 2022). The SEM image of a biobased RPU foam in the presence of ATH shows an elliptical cell shape in two different directions but with the same cross-sectional area (Silva et al., 2022). However, SEM analysis of the RPUF hybrid composites incorporating graphene revealed a smaller cell size, attributed to graphene acting as a nucleation point. However, excessive concentrations of graphene lead to cell collapse and a disorganised cellular structure. Recent studies support these findings and highlight the importance of optimising the graphene concentration to achieve the desired foam and composite properties while avoiding structural deterioration (Jesiak et al., 2023; Yuan et al., 2018). The use of hybrid composites has the potential to further enhance foam properties, and future research can continue to explore the synergistic effects of different fillers on polyurethane systems.

In Figures 2(b), 2(c) and 2(d), the higher magnification images (300 \times) display the cell morphology of the hybrid composites with varying graphene content. The hexagonal cell shapes in the RPUF hybrid composites are highlighted by red circles in Figure 2. It was observed that when a small amount of graphene filler was added, as depicted in Figure 2(b), the structure of the PU foam cells was improved. This enhancement is characterised by a reduction in the cell diameter, a smoother surface, and a decrease in voids, as shown in Figure 2(b). These improvements can be attributed to the effective dispersion and enhanced bonding between the graphene and RPUF within the hybrid composites. However, as the graphene content increased, as shown in Figures 2(b), 2(c) and 2(d), the uniformity of the cells deteriorated, resulting in rougher surfaces and larger voids. Graphene triggers changes in cell morphology, subsequently affecting the process of cell nucleation (Liu et al., 2021; Shivakumar et al., 2020). Overall, these findings indicate that adding a small amount of graphene filler to the hybrid composites improves the cell structure of the PU foam, leading to enhanced properties, such as reduced cell diameter, smoother surface, and diminished voids. However, an excessive graphene content can have a detrimental effect on cell uniformity, causing rough surfaces and larger voids. Understanding these morphological changes is crucial for optimising the fabrication process and achieving desired material properties in RPUF hybrid composites (Liu et al., 2021; Shivakumar et al., 2020).

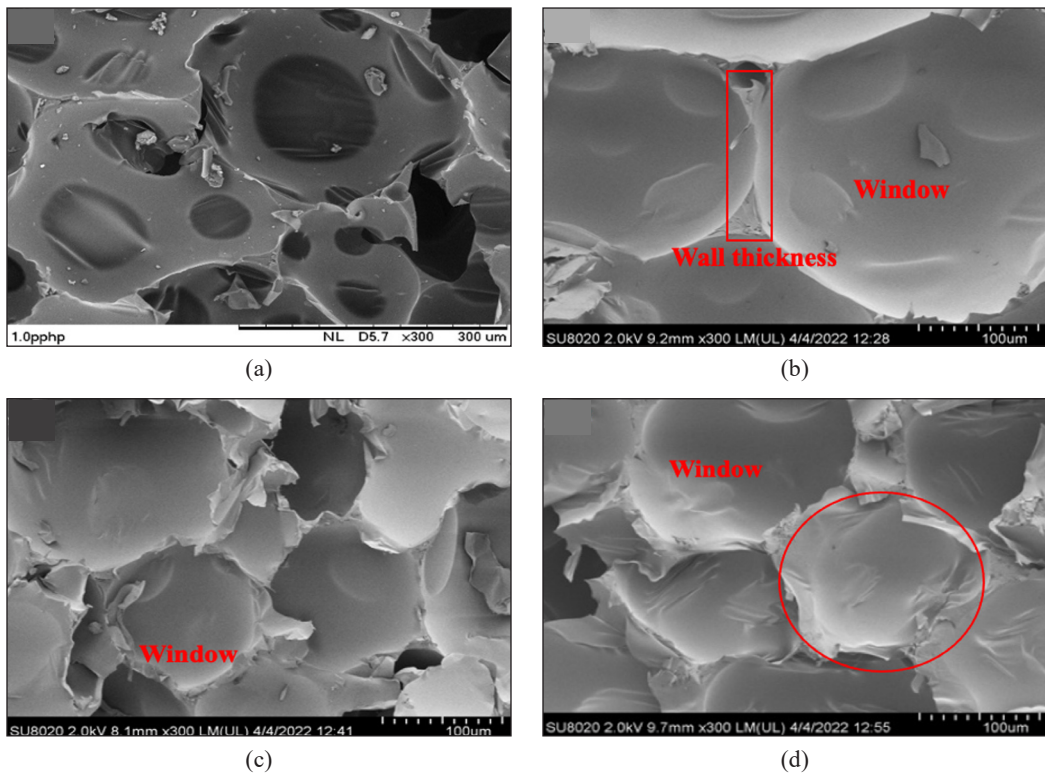


Figure 2. SEM micrographs of RPUF/ATH hybrid composites containing different graphene content: (a) 0 wt.%, (b) 0.5 wt.%, (c) 2.5 wt.%, (d) 3 wt.% (Magnification 300×)

Compressive Strength

In industrial applications, dimensional stability is crucial for foams, necessitating high compressive strength. Figure 3 illustrates the mechanical strength of RPUF hybrid composites with varying graphene contents. Among these composites, those containing 0.5 wt.% graphene exhibit the highest compression performance, with an optimal compressive strength of 12.58 KPa. This value surpasses pure RPUF (4.07 KPa) by 67.6% and RPUF/ATH (9.89 KPa) by 21.4%. The addition of graphene-enhanced compressive strength bolsters the durability and hardness of the pore walls, facilitating the formation of dense bubbles within the foam. Similar improvements in mechanical strength were reported by Pinto et al. (2020) and Liu et al. (2021), who introduced graphene and its derivatives as single and hybrid fillers in polyurethane foam and other matrices. Nevertheless, increasing the graphene component to 2.5 wt.% and subsequently to 3 wt.% reduces the compressive strength of the hybrid composite compared to the pure RPUF material. This reduction might be attributed to the stiffness of the hybrid fillers and the increase in the brittleness of the final composites. The SEM images in Figures 1(c) and 1(d) show evident foam cell rupture at higher graphene loadings.

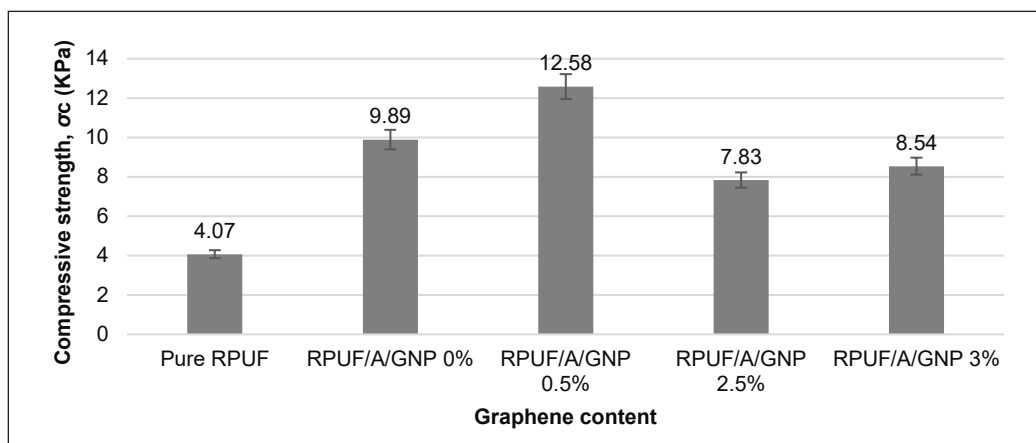


Figure 3. Compressive strength of pure RPUF and RPUF/ATH containing different graphene content

Fourier Transform Infrared (FTIR) Characterisation

FTIR spectroscopy is a versatile characterisation technique and a simple method for studying the formation of new bonds between polymers and nanoparticles or fillers in composites. This technique was employed to analyse virgin RPUF and RPUF/ATH-modified with and without graphene to observe any chemical reactions or the existence of new bonds in the materials. The FTIR spectra were acquired from 4000 to 500 cm^{-1} , as shown in Figure 4. The FTIR spectra revealed major IR vibration bands representing various oxygen-containing functional groups in the single and hybrid fillers. PU is a type of high polymer with a fundamental repeating unit of a urethane bond (-NHCOO-) manufactured by polymerising isocyanates and polyols (Mishra & Patel, 2020). Figure 4(a) shows the FTIR spectrum of the rigid PU foam in air at room temperature. The hydroxyl (OH) groups were observed at a wavenumber of 3,315 cm^{-1} , exhibiting wider peaks. The visible signals at 2,929 cm^{-1} and 2,358 cm^{-1} originate from symmetrical and asymmetrical stretch vibrations inside the CH_2 groups in the soft parts arising from polyols.

A prominent but relatively weak peak at 917 cm^{-1} , attributed to the symmetric stretching vibration of the N-CO-O bond and adsorption bands observed at approximately 765 cm^{-1} , indicates the presence of a C-H bond derived from an aromatic ring. The presence of carbonyl groups (C=O) at 1,709 cm^{-1} , N-H groups at 1,511 cm^{-1} (exhibiting a medium-strong peak), and hydrogen cyanide (C-N) at 1,221 cm^{-1} provided evidence for the establishment of urethane linkages (-RNHCOO-). Several researchers have reported these absorption bands (Alis et al., 2019; Wrzeźniewska-Tosik et al., 2020; Thiyagu et al., 2021). As shown in Figure 4(b), ATH was prepared using RPUF, and the composite was characterised by FTIR spectroscopy. The observed spectral bands of ATH were identified at 3,527 cm^{-1} , indicating the presence of hydroxyl (OH) group stretching. The hydroxyl groups on ATH react with the isocyanate group of the PU foam (Wang et al., 2017). In addition, the RPUF/

ATH peaks appear in the same position as the virgin RPUF. The Al-O and Al-O stretching and bending vibrations of ATH overlap those of RPUF with an increase in the strength of the peaks in the RPUF/ATH spectrum.

Hence, it can be asserted that the addition of ATH to RPUF did not produce significant changes in the strength of the bands observed in the foams. The pattern is similar to that in Figure 4(c), but the highest increase in the intensity of the C=O peaks ($3,734\text{ cm}^{-1}$) was recorded for the RPUF/0.5 wt.% graphene composite, matching the stretch vibrations of the amine (N-H) bond. Figure 4(c) also shows the slight effects of graphene on the spectra of the RPUF, demonstrating that it is difficult to detect the formation of urethane bonds between the RPUF and graphene because the PU backbones have the same chemical bonds. However, after the addition of graphene, there was a clear change in the intensity of the peaks of the composites. The strength of the peaks increases at $3,471\text{ cm}^{-1}$, $2,976\text{ cm}^{-1}$, $2,360\text{ cm}^{-1}$ (the second and third are ascribed to the alkene-CH stretch vibrations), $1,224\text{ cm}^{-1}$, and $1,067\text{ cm}^{-1}$ (attributed to C-O-C stretching vibrations). The increase in the intensity of the amide group (N-H) peak ($1,509\text{ cm}^{-1}$) indicates bending vibration (Hodlur & Rabinal,

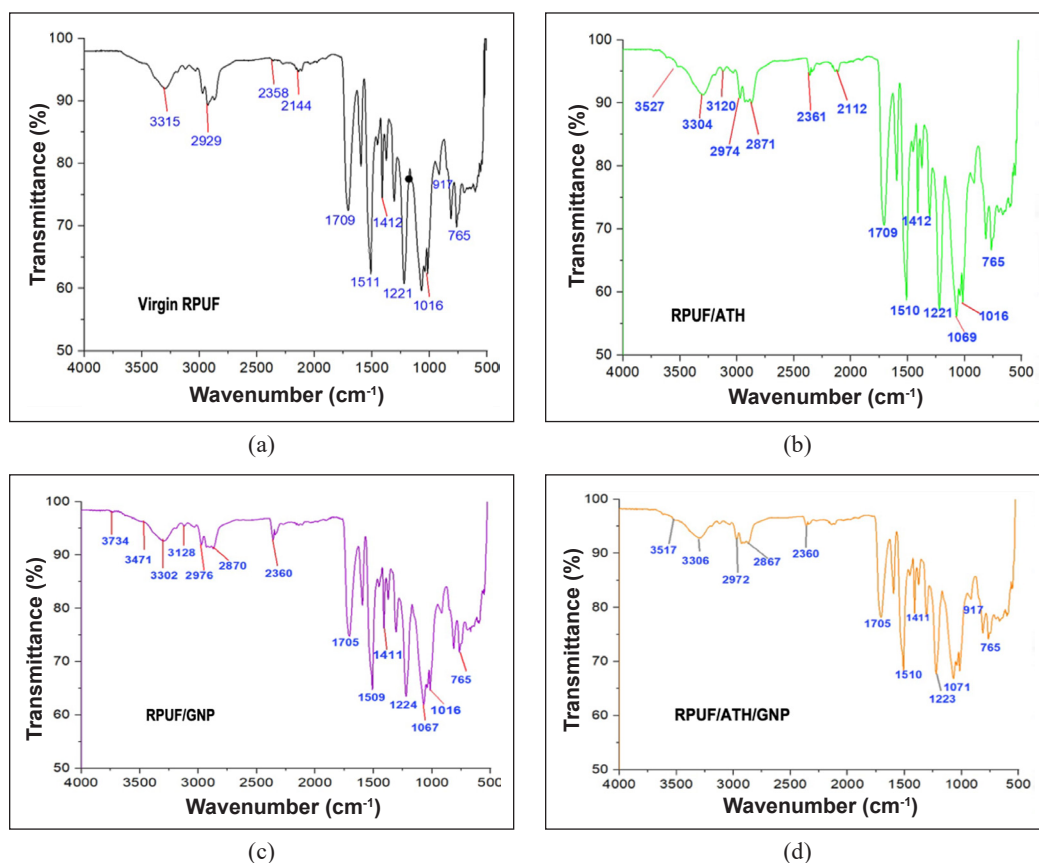


Figure 4. Infrared spectra: (a) Virgin RPUF; (b) RPUF/ATH; (c) RPUF/0.5 wt.% GNP; and (d) RPUF/ATH/0.5 wt.% GNP

2014). It suggests that the reaction between the -O-H and the NCO groups is catalysed by a combination of graphene and surfactant. The interface between the N and H bond of PU and the residual oxygenated groups of graphene was responsible for the disparity in the FT-IR spectra (Liu et al., 2017). Similar observations were reported in other studies on certain composites of RPUF and graphene (Gedam et al., 2019; Thiyagu et al., 2021). Figure 4(d) shows the FTIR spectra of the hybrid RPUF composites containing ATH and graphene fillers. Peaks related to virgin RPUF at $3,315\text{ cm}^{-1}$, $2,929\text{ cm}^{-1}$, $1,221\text{ cm}^{-1}$, and $1,016\text{ cm}^{-1}$ shifted to $3,517\text{ cm}^{-1}$, $2,972\text{ cm}^{-1}$, $1,223\text{ cm}^{-1}$, and $1,071\text{ cm}^{-1}$, respectively, owing to the interactions between ATH, graphene nanofiller, and polyurethane foam.

Many bands observed for virgin PU were also found in composites containing ATH, graphene, and surfactants. The band at $2,270\text{ cm}^{-1}$ was significant because it was missing in virgin PU and all its composites owing to the isocyanate (NCO) group. It proves that the entire supply of isocyanate was utilised to produce polyurethane (Pokharel et al., 2015). Due to the smaller quantity of graphene in the composite, obtaining solid evidence of physical or chemical interactions from the FTIR investigation was not easy. When the FTIR spectra of virgin RPUF were compared to those of its composites, no appreciable variation in the peak patterns was observed. Similar studies have reported comparable outcomes (Bera & Maji, 2017; Osman et al., 2021), demonstrating no filler matrix chemical interactions in the composites. All the chemical functional groups were unaltered because the filler was physically incorporated into the matrix.

Thermal Properties of RPUF and RPUF Hybrid Composites

Thorough comprehension of the flame retardancy mechanism requires analysis of the thermal characteristics during the combustion of RPUF-reinforced polyurethane foam (RPUF) and hybrid RPUF composites, which are commonly performed using thermogravimetric (TG) analysis. The thermal degradation of hybrid-reinforced polyurethane foam composites was examined using thermogravimetric analysis (TGA) and compared with the findings obtained for the virgin RPU foam. Table 3 lists the 5% mass loss temperature ($T_{5\%}$), the 50% mass loss temperature ($T_{50\%}$), the maximum degradation temperature (T_{max}), and the char residue at 800°C . The TGA and DTG thermograms of the virgin RPUF and hybrid RPUF foam composites are shown in Figures 5 and 6, respectively. The initial degradation temperature ($T_{5\%}$) of virgin RPUF was 23°C (Figure 5), and the release of volatile molecules, namely water molecules, was detected because of the high moisture uptake of the porous RPUF below 250°C .

In comparison, RPUF/ATH composites containing 0.5%, 2.5%, and 3.0 wt.% graphene, the $T_{5\%}$ values were 227°C , 253°C , and 256°C , respectively. It shows that increasing the amount of graphene in the RPUF improved the thermal firmness of the hybrid RPUF. It has been suggested that graphene slows the chain transfer reaction during the thermal

decomposition processes (Thiyagu et al., 2021). Generally, $T_{5\%}$, $T_{50\%}$, and T_{max} are higher for RPUF/graphene hybrid composites than for virgin RPUF, indicating the influence of graphene on enhancing the thermal stability of PU foam composites. For instance, while $T_{50\%}$ and T_{max} for RPUF/ATH were 334°C and 306°C, respectively, those of RPUF/ATH/graphene 0.5 wt.% were 539°C and 538°C, respectively. At the graphene loading of 3 wt.%, the hybrid composite reaches a maximum decomposition temperature of 592°C, representing a 50% and 48.3% increase in thermal stability compared to virgin RPUF (296°C) and RPUF/ATH (300°C). It is attributed to the high aspect ratio of graphene, which enables the formation of barricading layers and limits gaseous emissions during thermal degradation. The thermal stability of the RPUF hybrids was higher at a loading of 3.0 wt.% graphene, credited to the homogeneous and uniform dispersion of graphene.

Previous research has found that graphene sheets have a good barrier effect in preventing the transport of combustible decomposed products during the thermal degradation of composites and in slowing down the thermal decomposition process (Yuan et al., 2018). The initial breakdown of RPUF occurs within the temperature range of 231–424°C, attributed to the rupture of the urethane linkages. The second stage occurs at approximately 512–712°C and is ascribed to the cleavage of strong bonds such as aromatic groups, aliphatic carbon-carbon, and flame retardants (Kairytė et al., 2020). While the maximum degradation temperature (T_{max}) for virgin RPUF was observed to be 296°C, with a char residue of 15.18%, there was a significant increase in T_{max} for RPUF composites. For the case of RPUF/ATH composites, the T_{max} was 306°C, and the residual char reached 21.20%. The increases can be interpreted as an enhancement in thermal stability after the addition of ATH. These improvements can be attributed to the water molecules released from ATH. The presence of water molecules tends to cool the hot polymer, requiring a higher thermal energy to break down (Thirumal et al., 2010). In addition, water dilution reduces the concentration of combustible gases, and the development of a protective layer of aluminium oxide acts as a barrier, preventing the passage of oxygen and fuel into the polymers.

Figure 6 shows the DTG curves of the hybrid RPUF composites with different graphene concentrations. As observed, the RPUF/ATH/graphene hybrid composites displayed a shoulder peak, attributed to the removal of oxygen-containing complexes used in graphene

Table 3
Thermogravimetric data for pure RPUF and hybrid RPUF composites

Sample	T_5 (°C)	T_{50} (°C)	T_{max} (°C)	Char residue (%) at 800°C
Virgin RPUF	231	318	296	15.18
RPUF/A	278	334	306	21.20
RPUF/A/GNP 0.5%	227	539	538	15.50
RPUF/A/GNP 2.5%	253	579	547	16.66
RPUF/A/GNP 3.0%	256	591	592	17.46

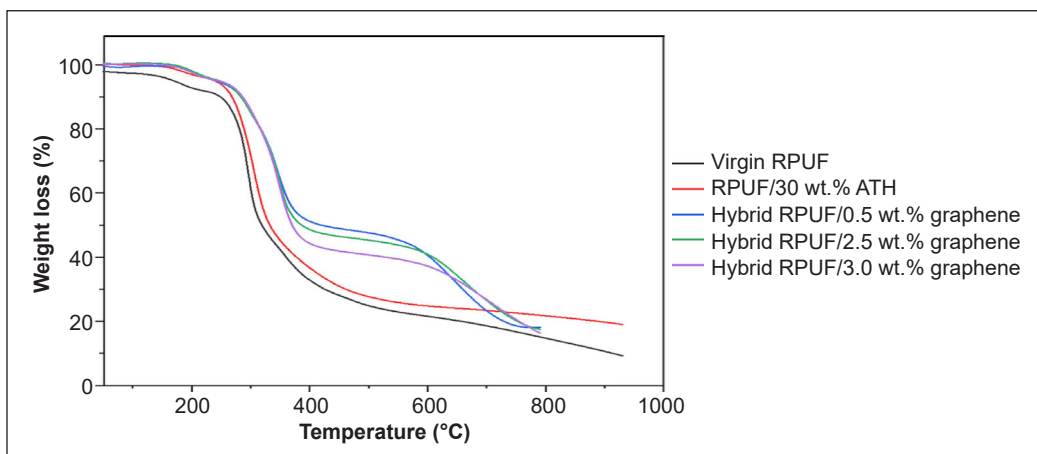


Figure 5. TGA curves of RPUF and hybrid RPUF with 0.5, 2.5, and 3.0 wt.% graphene

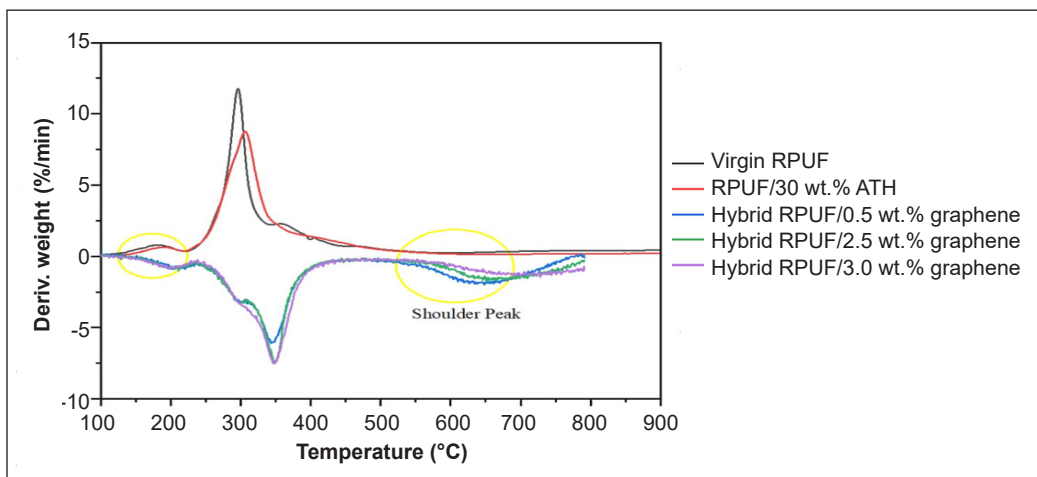


Figure 6. DTG curve for hybrid RPUF composites at different graphene concentrations

and ATH to enhance their dispersal in the polymer matrix. These changes were observed in the DTG thermograms, suggesting a notable reduction in the rate of mass loss during the second phase of thermal degradation in the system comprising all three graphene concentrations. At 2.5% and 3% graphene contents, the final stage of thermal degradation gradually diminished, indicating a significant quantity of solid residue ($> 20\%$). However, the decomposition temperatures for the last stage at 0.5%, 2.5%, and 3.0 wt.% graphene loading are 588°C , 613°C , and 672°C , respectively. The data in Table 3 reveal that the residual ash for the hybrid composites increases gradually with increasing graphene content. The emergence of chars impedes the transfer of heat, mass, and combustible gases at high temperatures, delaying the spontaneous scission of the polymer chain and increasing T_{max} (Huang et al., 2014).

The thermal stability of the RPUF/ATH composite increased to a higher decomposition temperature upon the addition of graphene, attributed to the better dispersion between graphene and ATH in the PU polymer system, as confirmed by the SEM results shown in Figure 1. During thermal degradation, adding graphene to the polymer system impedes the mass transfer of the generated volatile products (Zhu et al., 2021). This factor significantly improved the thermal stability of graphene-based materials. In other words, the thermal stability of the RPUF matrix increased after incorporating graphene loadings and ATH. This addition also improves the attraction and interface influence in the RPUF composites. These results align with previous studies that have shown the enhancement of thermal properties in polymer composites and their hybrids when graphene was used as a standalone filler or combined with other fillers (Sinh et al., 2019). Ultimately, these findings can be utilised to optimise the manufacturing process and produce high-quality hybrid rigid polyurethane composites with improved thermal stability. This cost-effective solution is promising for various industrial applications.

Fire Behaviour of ATH/Graphene Hybrid RPUF Composites

The LOI value was dependent on the surrounding temperature of the sample. The percentage of oxygen required for combustion decreased as the surrounding temperature increased. The LOI values of polymers and composites increase because of their ability to yield char in a fire, as char formation occurs at the expense of flammable volatiles (Chen et al., 2019). The fire-retardant behaviour of RPU foams was evaluated using the limiting oxygen index (LOI) and Underwriters Laboratories (UL-94) vertical burning test. The LOI assessment device was used to determine the percentage of oxygen volume required for polymer combustion, whereas the flammability of the specimens was assessed using a UL-94 vertical combustion analyser. The LOI value, burning time, ignition of the underlying cotton, and the UL-94 V classification during combustion are presented in Table 4. The Virgin RPUF exhibited an LOI value of 18% owing to its high flammability and low LOI value; the foam is highly flammable.

These substances readily evaporate at normal temperatures and release their components into the atmosphere. When heated, the chemicals ignite, causing the PU to burn. Virgin RPUF have poor fire response characteristics owing to their combustible hydrocarbon chains and high specific surface areas (Wang et al., 2019), which can be attributed to the significant amount of nitrogen in their structures. Typical PU foams emit highly poisonous smoke during combustion, particularly hydrogen cyanide (HCN) and carbon monoxide (CO) (Chattopadhyay & Webster, 2009). However, to impart non-flammable properties to virgin RPUF, the foam structure was modified by incorporating an organic flame retardant, such as aluminium hydroxide (ATH). As shown in Table 4, adding the 30 wt.% ATH to the virgin rigid PU foam increased the composite LOI value from 18% to 23% and achieved

a V-0 UL-94 test grade. This result indicates that the ATH-modified composite exhibits resistance to combustion with slow-burning characteristics. Composite materials with LOI values in the range of 21–27 tend to burn slowly, limiting their damage before the arrival of the fire rescue team (Fenimore, 1975)

The increase in the LOI value of RPUF/ATH can be attributed to ATH's fire-retardancy mechanism. ATH is an inorganic filler containing crystalline water in its chemical structure. During the endothermic reaction at (220–450°C), it releases approximately 34 wt.% steam. It reduces the composite temperature during combustion, and the released steam dilutes the combustible gases, resulting in an increased LOI. Additionally, ATH underwent a dehydration reaction, producing Al_2O_3 and carbonising the composites, as shown in Figure 7. It generates flammable volatiles and prevents the spread of flame (Wang et al., 2010; Zhu et al., 2014). As shown in Table 4, the incorporation of graphene into RPUF/ATH slightly decreased the LOI values for the hybrid RPUF composite compared with RPUF/ATH alone. The LOI values marginally decreased to 20% LOI for 0.5 wt.% graphene incorporation and 21% LOI for 2.5 wt.% graphene incorporation. Interestingly, at the graphene loading of 2.5 wt.%, the UL-94 test reveals a V-0 rating, and the burn time decreases to 10 s. It indicates a slight improvement in the flame resistance of the RPUF hybrid composite compared with that of the RPUF/ATH composite, which had a longer burn period of 16 s. However, for the 0.5% and 2.5 wt.% graphene-modified hybrid composites, the increase in their LOI values can be attributed to the dispersion state of the nanofiller, which has a noticeable effect on their reaction to small flames and fire behaviour under forced flaming conditions (Yuan et al., 2018). At a maximum graphene loading of 3.0 wt.%, the hybrid RPUF composite achieved an increased LOI value of 23%, indicating that a higher concentration of graphene, combined with other additives such as ATH, significantly enhances the fire resistance of the composites, confirming their synergistic flame-retardant effect.

Both graphene and ATH demonstrated better performance as hybrid flame retardants, as they can swell and block the spread of fire from the upper portion of the specimen to the bottom. All ATH and graphene-based flame-retardant blends exhibited higher LOI values than the virgin RPUF. This result demonstrates that the combination of ATH and graphene has a favourable impact, enhancing the fire characteristics of pristine RPUF. It was attributed to the synergistic effect of ATH/graphene at high filler contents. Graphene disperses heat within the samples (Dittrich et al., 2013), while ATH reduces the release of combustible gases by releasing water (Hull et al., 2011) and, in significant amounts, delays the combustion of the materials by reducing the availability of combustible fuel from the virgin RPUF. This finding is consistent with previous studies indicating that graphene, with its two-dimensional layered structure, can enhance polymer char formation during combustion by accumulating and re-irradiating heat (Han et al., 2013; Han et al., 2014). The combination of ATH with graphene and another flame retardant as a hybrid filler has

improved the fire behaviour of various hybrid polymer composites, making them suitable for use in high-performance engineering applications (Battig et al., 2021; Wang et al., 2017; Zielonka et al., 2022).

Table 4
Results of UL-94 and LOI test of hybrid RPUF composites incorporated with ATH and various quantities of graphene

Samples	Graphene Loading (wt.%)	Burn time (s)	Ignition of cotton	UL-94 Classification	LOI (%)
Virgin RPUF	0	25	YES	Failed	18
RPUF/A	0	16	NO	V-1	19
RPUF/A/GNP	0.5	16	NO	V-1	20
RPUF/A/GNP	2.5	10	NO	V-0	21
RPUF/A/GNP	3.0	8	NO	V-0	23

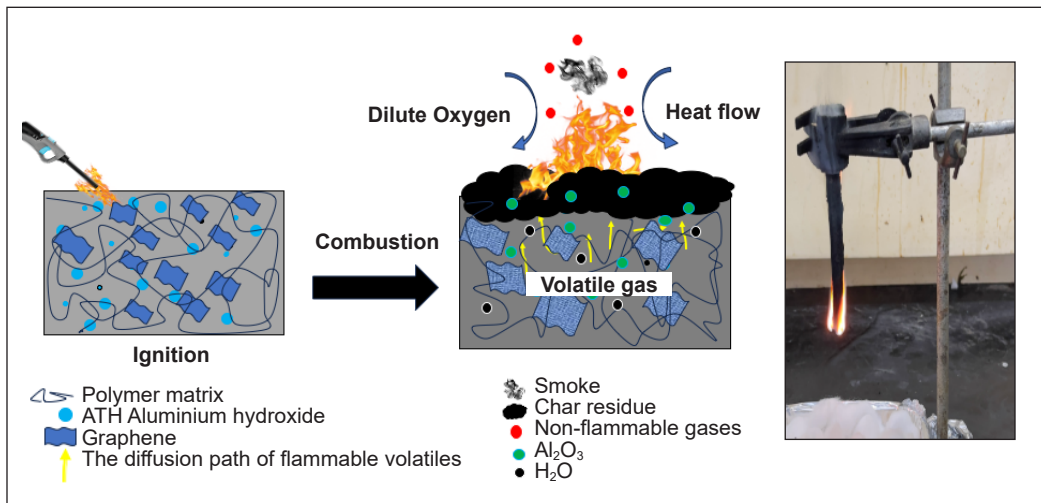


Figure 7. Schematic illustration of the flame retardant mechanism of ATH/graphene system in RPUF

CONCLUSION

This study successfully modified rigid polyurethane foams (RPUF) with aluminium hydroxide (ATH) and graphene to enhance their compressive strength, flame retardancy, and thermal properties. The addition of ATH and graphene to RPUF resulted in the development of synergistic effects, leading to improved performance of the hybrid composites. The results indicate that the incorporation of 0.5 wt.% graphene loading in the hybrid composite exhibited the best compression performance, with a compressive strength value of 12.58 KPa, surpassing both virgin RPUF (4.07 KPa) and RPUF/ATH (9.89 KPa). This enhancement in compressive strength can be attributed to the reinforcing

effects of ATH and graphene, which effectively distribute stress and improve the overall structural integrity of the hybrid composite. The characterisation of the hybrid composites using SEM micrographs revealed a more stable and uniform structure with the addition of 0.5 wt.% graphene. Infrared spectral analysis confirmed the presence of functional groups in the virgin RPUF and some modified composites, indicating the successful incorporation of ATH and graphene into the RPUF matrix. Thermal analysis demonstrated that the hybrid composites exhibited improved thermal stability compared to the virgin RPUF. The addition of 3.0 wt.% graphene resulted in a significant increase in the maximum decomposition temperature (539°C) and char residue (17.46%). These findings suggest that graphene is crucial in enhancing the hybrid composites' thermal stability and flame retardancy. Furthermore, LOI and UL-94 analyses revealed that the hybrid composites incorporated with 3.0 wt.% graphene exhibited increased LOI value and achieved V-0 classification, indicating enhanced fire resistance compared to the virgin samples. The hybrid composite is a promising material for high-performance applications, particularly building insulation. In summary, incorporating aluminium hydroxide and graphene into RPUF led to developing hybrid composites with improved compressive strength, thermal stability, and flame retardancy. The synergistic effects of ATH and graphene contributed to the enhanced properties of the hybrid composites. These findings contribute to the advancement of materials science and provide insight into developing novel flame-retardant RPUF composites for various industrial applications.

ACKNOWLEDGEMENTS

The authors acknowledge the financial support from the Ministry of Higher Education Malaysia under the Fundamental Research Grant Scheme (FRGS) (FRGS/1/2019/TK05/UTM/02/17) and Universiti Teknologi Malaysia for the funding under the UTM Fundamental Research Grant (UTMFR) Q.J130000.2551.21H44.

REFERENCES

- Alis, A., Majid, R. A., & Mohamad, Z. (2019). Morphologies and thermal properties of palm-oil based rigid polyurethane/halloysite nanocomposite foams. *Journal-Chemical Engineering Transactions*, 72, 415–420. <http://doi.org/10.3303/CET1972070>
- American Society for Testing and Materials. (2001). *Standard test method for compressive properties of rigid cellular plastics* (ASTM D1621-1). ASTM International.
- American Society for Testing and Materials. (1997). *Standard test Method for measuring the minimum oxygen concentration to support candle-like combustion of plastics (oxygen index)* (ASTM D2863-97). ASTM International.
- American Society for Testing and Materials. (2010). *Standard test method for measuring the comparative burning characteristics of solid plastics in a vertical position* (ASTM D3801-10). ASTM International.

- Baferani, A. H., Keshavarz, R., Asadi, M., & Ohadi, A. R. (2018). Effects of silicone surfactant on the properties of open-cell flexible polyurethane foams. *Advances in Polymer Technology*, 37(1), 71–83. <https://doi.org/10.1002/adv.21643>
- Baguian, A. F., Ouiminga, S. K., Longuet, C., Caro-Bretelle, A. S., Corn, S., Bere, A., & Sonnier, R. (2021). Influence of density on foam collapse under burning. *Polymers*, 23(1), Article 13. <https://dx.doi.org/10.3390/polym13010013>
- Battig, A., Fadul, N. A. R., Frasca, D., Schulze, D., & Schartel, B. (2021). Multifunctional graphene nanofiller in flame retarded polybutadiene/chloroprene/carbon black composites. *e-Polymers*, 21(1), 244–262. <https://doi.org/10.1515/epoly-2021-0026>
- Bera, M., & Maji, P. K. (2017). Effect of structural disparity of graphene-based materials on thermo-mechanical and surface properties of thermoplastic polyurethane nanocomposites. *Polymer*, 119, 118–133. <https://doi.org/10.1016/j.polymer.2017.05.019>
- Chattopadhyay, D. K., & Webster, D. C. (2009). Thermal stability and flame retardancy of polyurethanes. *Progress in Polymer Science*, 34(10), 1068–1133. <https://doi.org/10.1016/j.progpolymsci.2009.06.002>
- Chen, M. J., Xu, Y. J., Rao, W. H., Huang, J. Q., Wang, X. L., Chen, L., & Wang, Y. Z. (2014). Influence of valence and structure of phosphorus-containing melamine salts on the decomposition and fire behaviours of flexible polyurethane foams. *Industrial and Engineering Chemistry Research*, 53(21), 8773–8783. <https://doi.org/10.1021/ie500691p>
- Chen, X. Y., Huang, Z. H., Xi, X. Q., Li, J., Fan, X. Y. & Wang, Z. (2018). Synergistic effect of carbon and phosphorus flame retardants in rigid polyurethane foams. *Fire and Materials*, 42(4), 447–453. <https://doi.org/10.1002/fam.2511>
- Chen, X. Y., Romero, A., Paton-Carrero, A., Lavin-Lopez, M. P., Sanchez-Silva, L., Valverde, J. L., Kaliaguine, S., & Rodrigue, D. (2019). Functionalized graphene–reinforced foams based on polymer matrices. In M. Jawaid, R. Bouhfid & A. K. Qaiss (Eds.), *Functionalized Graphene Nanocomposites and their Derivatives* (pp. 121-155). Elsevier. <https://doi.org/10.1016/B978-0-12-814548-7.00007-6>
- Chen, X., Li, J., & Gao, M. (2019). Thermal degradation and flame retardant mechanism of the rigid polyurethane foam including functionalized graphene oxide. *Polymers*, 11(1), Article 78. <https://www.mdpi.com/2073-4360/11/1/78>
- Cheng, J. J., Shi, B. B., Zhou, F. B., & Chen, X. Y. (2014). Effects of inorganic fillers on the flame-retardant and mechanical properties of rigid polyurethane foams. *Journal of Applied Polymer Science*, 131(10), Article 40253. <https://doi.org/10.1002/app.40253>
- Członka, S., Kairyte, A., Miedzińska, K., Strakowska, A., & Adamus-Włodarczyk, A. (2021). Mechanically strong polyurethane composites reinforced with montmorillonite-modified sage filler (*Salvia officinalis* L.). *International Journal of Molecular Sciences*, 22(7), Article 3744. <https://doi.org/10.3390/ijms22073744>
- Dhaliwal, G. S., Anandan, S., Bose, M., Chandrashekhara, K., & Nam, P. (2020). Effects of surfactants on mechanical and thermal properties of soy-based polyurethane foams. *Journal of Cellular Plastics*. 56(6), 611–629. <https://doi.org/10.1177/0021955X20912200>
- Dittrich, B., Wartig, K. A., Hofmann, D., Mülhaupt, R., & Schartel, B. (2013). Flame retardancy through carbon nanomaterials: Carbon black, multiwall nanotubes, expanded graphite, multi-layer graphene

- and graphene in polypropylene. *Polymer Degradation and Stability*, 98(8), 1495–1505. <https://doi.org/10.1016/j.polyimdegradstab.2013.04.009>
- Eaves, D. (2004). *Handbook of polymer foams*. Rapra Technology Ltd.
- Eling, B., Tomović, Ž., & Schädler, V. (2020). Current and future trends in polyurethanes: An industrial perspective. *Macromolecular Chemistry and Physics*, 221(14), Article 2000114. <https://doi.org/10.1002/macp.202000114>
- Feng, C., Liang, M., Zhang, Y., Jiang, J., Huang, J., & Liu, H. (2016). Journal of analytical and applied pyrolysis synergistic effect of lanthanum oxide on the flame retardant properties and mechanism of an intumescent flame retardant PLA composites. *Journal of Analytical and Applied Pyrolysis*, 122, 241–248. <https://doi.org/10.1016/j.jaap.2016.09.018>
- Fenimore, C. P. (1975). Candle-type test for flammability of polymers. In M. Lewin, S. M. Atlas & E. M. Pearce (Eds.), *Flame-Retardant Polymeric Materials* (pp. 259-267). Springer. https://doi.org/10.1007/978-1-4684-2148-4_9
- Gedam, S. S., Chaudhary, A. K., Vijayakumar, R. P., Goswami, A. K., Bajad, G. S., & Pal, D. (2019). Thermal, mechanical and morphological study of carbon nanotubes-graphene oxide and silver nanoparticles based polyurethane composites. *Materials Research Express*, 6(8), Article 085308. <https://doi.org/10.1088/2053-1591/ab1db4>
- Han, Y., Wu, Y., Shen, M., Huang, X., Zhu, J., & Zhang, X. (2013). Preparation and properties of polystyrene nanocomposites with graphite oxide and graphene as flame retardants. *Journal of Materials Science*, 48(12), 4214–4222. <https://doi.org/10.1007/s10853-013-7234-8>
- Han, Z., Wang, Y., Dong, W., & Wang, P. (2014). Enhanced fire retardancy of polyethylene/alumina trihydrate composites by graphene nanoplatelets. *Materials Letters*, 128, 275–278. <https://doi.org/10.1016/j.matlet.2014.04.148>
- Hodlur, R. M., & Rabinal, M. K. (2014). Self assembled graphene layers on polyurethane foam as a highly pressure sensitive conducting composite. *Composites Science and Technology*, 90, 160–165. <https://doi.org/10.1016/j.compscitech.2013.11.005>
- Huang, G., Chen, S., Song, P., Lu, P., Wu, C., & Liang, H. (2014). Combination effects of graphene and layered double hydroxides on intumescent flame-retardant poly (methyl methacrylate) nanocomposites. *Applied Clay Science*, 88–89, 78–85. <https://doi.org/10.1016/j.clay.2013.11.002>
- Huang, S., Deng, C., Zhao, Z., Chen, H., Gao, Y., & Wang, Y. (2020). Phosphorus-containing organic-inorganic hybrid nanoparticles for the smoke suppression and flame retardancy of thermoplastic polyurethane. *Polymer Degradation and Stability*, 178, Article 109179. <https://doi.org/10.1016/j.polyimdegradstab.2020.109179>
- Hull, T. R., Witkowski, A., & Hollingbery, L. (2011). Fire retardant action of mineral fillers. *Polymer Degradation and Stability*, 96(8), 1462–1469. <https://doi.org/10.1016/j.polyimdegradstab.2011.05.006>
- Jeśiak, T., Hasiak, M., Łaszcz, A., Chęćmanowski, J., Gerasymchuk, Y., Stachowiak, P., Strek, W., & Hreniak, D. (2023). Thermo-smart composite materials: Exploring the potential of graphene-doped porous silica foams. *Construction and Building Materials*, 394, Article 132249. <https://doi.org/10.1016/j.conbuildmat.2023.132249>

- Jonjaroen, V., Ummartyotin, S., & Chittapun, S. (2020). Algal cellulose as a reinforcement in rigid polyurethane foam. *Algal Research*, 51, Article 102057. <https://doi.org/10.1016/j.algal.2020.102057>
- Ju, Z., He, Q., Zhang, H., Zhan, T., Chen, L., Li, S., Hong, L., & Lu, X. (2020). Steam explosion of windmill palm fibre as the filler to improve the acoustic property of rigid polyurethane foams. *Polymer Composites*, 41(7), 2893–2906. <https://doi.org/10.1002/pc.25585>
- Kairytė, A., Kremensas, A., Balčiūnas, G., Członka, S., & Strażowska, A. (2020). Closed cell rigid polyurethane foams based on low functionality polyols: Research of dimensional stability and standardised performance properties. *Materials*, 13(6), Article 1438. <https://doi.org/10.3390/ma13061438>
- Kavšek, M., Figar, N., Mihelič, I., & Krajnc, M. (2022). Melamine-formaldehyde rigid foams – Manufacturing and their thermal insulation properties. *Journal of Cellular Plastics*, 58(1), 175–193. <https://doi.org/10.1177/0021955X21997348>
- Kerche, E. F., Delucis, R. D. A., Petzhold, C. L., & Amico, S. C. (2020). Rigid bio-based wood/polyurethane foam composites expanded under confinement. *Journal of Cellular Plastics*, 57(5), 757–768. <https://doi.org/10.1177/0021955X20964018>
- Kim, J. M., Kim, D. H., Kim, J., Lee, J. W., & Kim, W. N. (2017). Effect of graphene on the sound damping properties of flexible polyurethane foams. *Macromolecular Research*, 25(2), 190–196. <https://doi.org/10.1007/s13233-017-5017-9>
- Kumar, M., & Kaur, R. (2017). Glass fibre reinforced rigid polyurethane foam: Synthesis and characterisation. *E-Polymers*, 17(6), 517–521. <https://doi.org/10.1515/epoly-2017-0072>
- Lee, C., Wei, X., Kysar, J. W., & Hone, J. (2008). Measurement of the elastic properties and intrinsic strength of monolayer graphene. *Science*, 321(5887), 385–388. <https://doi.org/10.1126/science.1157996>
- Lee, S. H., Lee, S. G., Lee, J. S., & Ma, B. C. (2022). Understanding the flame retardant mechanism of intumescent flame retardant on improving the fire safety of rigid polyurethane foam. *Polymers*, 14(22), Article 4904. <https://doi.org/10.3390/polym14224904>
- Liu, D., & Hu, A. (2020). The influence of environmentally friendly flame retardants on the thermal stability of phase change polyurethane foams. *Materials*, 13(3), Article 520. <https://doi.org/10.3390/ma13030520>
- Liu, D., Zou, L., Chang, Q., & Xiao, T. (2021). Preparation and properties of rigid polyurethane foams added with graphene oxide-hollow glass microspheres hybrid. *Designed Monomers and Polymers*, 24(1), 210–217. <https://doi.org/10.1080/15685551.2021.1954340>
- Liu, H., Dong, M., Huang, W., Gao, J., Dai, K., Guo, J., Zheng, G., Liu, C., Shen, C., & Guo, Z. (2017). Lightweight conductive graphene/thermoplastic polyurethane foams with ultrahigh compressibility for piezoresistive sensing. *Journal of Materials Chemistry C*, 5(1), 73–83. <https://doi.org/10.1039/C6TC03713E>
- Liu, X., Hao, J., & Gaan, S. (2016). Recent studies on the decomposition and strategies of smoke and toxicity suppression for polyurethane-based materials. *RSC Advances*, 6(78), 74742–74756. [10.1039/C6RA14345H](https://doi.org/10.1039/C6RA14345H)
- Lorusso, C., Vergaro, V., Conciauro, F., Ciccarella, G., & Congedo, P. M. (2017). Thermal and mechanical performance of rigid polyurethane foam added with commercial nanoparticles. *Nanomaterials and Nanotechnology*, 7(1–19), Article 184798041668411. <https://doi.org/10.1177/1847980416684117>

- Mishra, V. K., & Patel, R. H. (2020). Synthesis and characterization of flame retardant polyurethane: Effect of castor oil polyurethane on its properties. *Polymer Degradation and Stability*, 175, Article 109132. <https://doi.org/10.1016/j.polymdegradstab.2020.109132>
- Modesti, M., Lorenzetti, A., Simioni, F., & Camino, G. (2002). Expandable graphite as an intumescent flame retardant in polyisocyanurate-polyurethane foams. *Polymer Degradation and Stability*, 77(2), 195–202. [https://doi.org/10.1016/S0141-3910\(02\)00034-4](https://doi.org/10.1016/S0141-3910(02)00034-4)
- Mohamad, Z., Raji, A. M., Hassan, A., & Khan, Z. I. (2021). Novel intumescent flame retardant of ammonium polyphosphate/sepiolite/melamine on rigid polyurethane foam: Morphologies, and flammability properties. *Chemical Engineering Transactions*, 89, 619–624. <https://doi.org/10.3303/CET2189104>
- Osman, A., Elhakeem, A., Kaytbay, S., & Ahmed, A. (2021). Thermal , electrical and mechanical properties of graphene / nano-alumina / epoxy composites. *Materials Chemistry and Physics*, 257, Article 123809. <https://doi.org/10.1016/j.matchemphys.2020.123809>
- Pang, H., Wu, Y., Wang, X., Hu, B., & Wang, X. (2019). Recent advances in composites of graphene and layered double hydroxides for water remediation: A review. *Chemistry – An Asian Journal*, 14(15), 2542–2552. <https://doi.org/10.1002/asia.201900493>
- Peng, H., Wang, X., Li, T., Lou, C., Wang, Y., & Lin, J. (2019). Mechanical properties, thermal stability, sound absorption, and flame retardancy of rigid PU foam composites containing a fire-retarding agent: Effect of magnesium hydroxide and aluminium hydroxide. *Polymers for Advanced Technologies*, 30(8), 2045–2055. <https://doi.org/10.1002/pat.4637>
- Pinto, S. C., Marques, P. A. A. P., Vicente, R., Godinho, L., & Duarte, I. (2020). Hybrid structures made of polyurethane/graphene nanocomposite foams embedded within aluminum open-cell foam. *Metals*, 10(6), Article 768. <https://doi.org/10.3390/met10060768>
- Pokharel, P., Choi, S., & Lee, D. S. (2015). The effect of hard segment length on the thermal and mechanical properties of polyurethane/graphene oxide nanocomposites. *Composites Part A*, 69, 168–177. <https://doi.org/10.1016/j.compositesa.2014.11.010>
- Rocha, J. D. S., Escócio, V. A., Visconte, L. L. Y., & Pacheco, É. B. A. V. (2021). Thermal and flammability properties of polyethylene composites with fibers to replace natural wood. *Journal of Reinforced Plastics and Composites*, 40(19–20), 726–740. <https://doi.org/10.1177/07316844211002895>
- Salasińska, K., Leszczyńska, M., Celiński, M., Kozikowski, P., Kowiorski, K., & Lipińska, L. (2021). Burning behaviour of rigid polyurethane foams with histidine and modified graphene oxide. *Materials*, 14(5), Article 1184. <https://doi.org/10.3390/ma14051184>
- Shivakumar, H., Renukappa, N. M., Shivakumar, K. N., & Suresha, B. (2020). The reinforcing effect of graphene on the mechanical properties of carbon-epoxy composites. *Open Journal of Composite Materials*, 10(02), 27–44. <https://doi.org/10.4236/ojcm.2020.102003>
- Shoaib, S., Shahzad Maqsood, K., Nafisa, G., Waqas, A., Muhammad, S., & Tahir, J. (2014). A comprehensive short review on polyurethane foam. *International Journal of Innovation and Applied Studies*, 12(1), 165–169.
- Silva, E. H. P., Aguiar, J. C. F., Waldow, G., Costa, R. R. C., Tita, V., & Ribeiro, M. L. (2022). Compression and morphological properties of a bio-based polyurethane foam with aluminum hydroxide. *Proceedings of*

the Institution of Mechanical Engineers, Part L: Journal of Materials: Design and Applications, 236(7), 1408-1418. <https://doi.org/10.1177/14644207211059077>

- Sinh, L. H., Luong, N. D., & Seppälä, J. (2019). Enhanced mechanical and thermal properties of polyurethane/functionalised graphene oxide composites by in situ polymerisation. *Plastics, Rubber and Composites*, 48(10), 466–476. <https://doi.org/10.1080/14658011.2019.1664820>.
- Srihanum, A., Noor, M. T. T., Devi, K. P. P., Hoong, S. S., Ain, N. H., Mohd, N. S., Din, N. S. M. N. M., & Kian, Y. S. (2022). Low-density rigid polyurethane foam incorporated with renewable polyol as sustainable thermal insulation material. *Journal of Cellular Plastics*, 58(3), 485-503. <https://doi.org/10.1177/0021955X211062630>
- Stoller, M. D., Park, S., Yanwu, Z., An, J., & Ruoff, R. S. (2008). Graphene-based ultracapacitors. *Nano Letters*, 8(10), 3498–3502. <https://doi.org/10.1021/nl802558y>
- Thirumal, M., Singha, N. K., Khastgir, D., Manjunath, B. S., & Naik, Y. P. (2010). Halogen-free flame-retardant rigid polyurethane foams: Effect of alumina trihydrate and triphenylphosphate on the properties of polyurethane foams. *Journal of Applied Polymer Science*, 116(4), 2260–2268. <https://doi.org/10.1002/app.31626>
- Thiyagu, C., Manjubala, I., & Narendrakumar, U. (2021). Thermal and morphological study of graphene-based polyurethane composites. *Materials Today: Proceedings*, 45, 3982–3985. <https://doi.org/10.1016/j.matpr.2020.08.641>
- Titow, W. V. (2001). *PVC Technology*, 146. Rapra Technology Ltd.
- Tiuc, A. E., Borlea, S. I., Nemeş, O., Vermeşan, H., Vasile, O., Popa, F., & Pinţoi, R. (2022). New composite materials made from rigid/flexible polyurethane foams with fir sawdust: Acoustic and thermal behavior. *Polymers*, 14(17), Article 3643. <https://doi.org/10.3390/polym14173643>
- Wang, S., Du, X., Jiang, Y., Xu, J., Zhou, M., Wang, H., Cheng, X., & Du, Z. (2019). Synergetic enhancement of mechanical and fire-resistance performance of waterborne polyurethane by introducing two kinds of phosphorus–nitrogen flame retardant. *Journal of colloid and interface science*, 537, 197-205. <https://doi.org/10.1016/j.jcis.2018.11.003>
- Wang, Y., Wang, F., Dong, Q., Xie, M., Liu, P., Ding, Y., Zhang, S., Yang, M., & Zheng, G. (2017). Core-shell expandable graphite @ aluminum hydroxide as a flame-retardant for rigid polyurethane foams. *Polymer Degradation and Stability*, 146, 267–276. <https://doi.org/10.1016/j.polyimdegradstab.2017.10.017>
- Wang, Y., Wang, F., Dong, Q., Yuan, W., Liu, P., Ding, Y., Zhang, S., Yang, M., & Zheng, G. (2018). Expandable graphite encapsulated by magnesium hydroxide nanosheets as an intumescent flame retardant for rigid polyurethane foams. *Journal of Applied Polymer Science*, 135(39), Article 46749. <https://doi.org/10.1002/app.46749>
- Wang, Z. Y., Liu, Y., & Wang, Q. (2010). Flame retardant polyoxymethylene with aluminium hydroxide/melamine/novolac resin synergistic system. *Polymer Degradation and Stability*, 95(6), 945–954. <https://doi.org/10.1016/j.polyimdegradstab.2010.03.028>
- Wrześniewska-Tosik, K., Ryszkowska, J., Mik, T., Wesołowska, E., Kowalewski, T., Pałczyńska, M., Sałasińska, K., Walisiak, D., & Czajka, A. (2020). Composites of semi-rigid polyurethane foams with keratin fibers

- derived from poultry feathers and flame retardant additives. *Polymers*, 12(12), Article 2943. <https://doi.org/10.3390/polym12122943>
- Yao, Y., Jin, S., Ma, X., Yu, R., Zou, H., Wang, H., Lv, X., & Shu, Q. (2020). Graphene-containing flexible polyurethane porous composites with improved electromagnetic shielding and flame retardancy. *Composites Science and Technology*, 200, Article 108457. <https://doi.org/10.1016/j.compscitech.2020.108457>
- Yuan, B., Sun, Y., Chen, X., Shi, Y., Dai, H., & He, S. (2018). Poorly-/well-dispersed graphene: Abnormal influence on flammability and fire behaviour of intumescent flame retardant. *Composites Part A: Applied Science and Manufacturing*, 109, 345–354. <https://doi.org/10.1016/j.compositesa.2018.03.022>
- Zhang, W., Zhao, Z., & Lei, Y. (2021). Flame retardant and smoke-suppressant rigid polyurethane foam based on sodium alginate and aluminium diethyl phosphite. *Designed Monomers and Polymers*, 24(1), 46–52. <https://doi.org/10.1080/15685551.2021.1879451>
- Zhang, X., Sun, S., Yuan, D., Wang, Z., Xie, H., & Liu, Y. (2023). Fabrication of hydrolyzed keratin-modified rigid polyurethane foams and their thermal stability and combustion performance. *International Journal of Polymer Analysis and Characterization*, 28(7), 662-683. <https://doi.org/10.1002/pi.6616>
- Zhou, X., Jiang, F., Hu, Z., Wu, F., Gao, M., Chai, Z., Wang, Y., Gu, X., & Wang, Y. (2023). Study on the flame retardancy of rigid polyurethane foam with phytic acid-functionalized graphene oxide. *Molecules*, 28(17), Article 6267. <https://doi.org/10.3390/molecules28176267>
- Zhu, H., Peng, Z., Chen, Y., Li, G., Wang, L., Tang, Y., Pang, R., Khan, Z. U. H., & Wan, P. (2014). Preparation and characterization of flame retardant polyurethane foams containing phosphorus-nitrogen-functionalized lignin. *RSC Advances*, 4(98), 55271–55279. <https://doi.org/10.1039/C4RA08429B>
- Zhu, Q., Wang, Z., Zeng, H., Yang, T., & Wang, X. (2021). Effects of graphene on various properties and applications of silicone rubber and silicone resin. *Composites Part A: Applied Science and Manufacturing*, 142, Article 106240. <https://doi.org/10.1016/j.compositesa.2020.106240>
- Zielonka, P., Duda, S., Lesiuk, G., Błażejowski, W., Wiśniewska, M., Warycha, J., Stabla, P., Smolnicki, M., & Babiarczuk, B. (2022). The effect of flame retardant—Aluminum trihydroxide on mixed mode I/II fracture toughness of epoxy resin. *Polymers*, 14(20), Article 4386. <https://doi.org/10.3390/polym14204386>

Inoculations of *R. erythropolis* and *B. subtilis* Stimulate Indigenous Bacteria and Improve the Properties of Low-fertilized Agricultural Soils

Abd Aziz Amin^{1,2,3}, Hideki Okuda⁴, Mizuho Kawamura⁴, Nurjannah⁵ and Andi Kurniawan^{1,2,3*}

¹Coastal and Marine Research Center, Brawijaya University, Malang 65145, Indonesia

²Microbial Resources and Biotechnology Research Group, Graduate School, Brawijaya University, Malang 65145, Indonesia

³Faculty of Fisheries and Marine Science, Brawijaya University, Malang 65145, Indonesia

⁴Graduate School of Life Sciences, Ritsumeikan University, Shiga 525-8577, Japan

⁵Faculty of Mathematics and Natural Sciences, Brawijaya University, Malang 65145, Indonesia

ABSTRACT

Biodiversity and the number of bacteria present in the soil are two of the main parameters of soil quality, especially for agricultural purposes. Analysis of the low-fertilized soils suggested that the number and diversity of the bacterial communities in this soil are low. Hence, various methods have been used to stimulate bacterial activity and improve agricultural soil conditions. One of the popular methods is the inoculation of bacteria such as *B. subtilis* and *R. erythropolis*. These bacteria are potential species as bio-inoculants in soil management. However, the effectiveness of these bacteria in stimulating the activity of bacterial communities and improving soil properties of the low-fertilized soil is still sparsely explored. Therefore, this study aimed to analyze the impact of the inoculation of *B. subtilis* and *R. erythropolis* on the bacterial community structure and

soil properties of low-fertilized soil. The soil used is agricultural soil for tobacco farming activities using agrochemicals. Bacterial community structures were analyzed using the environmental DNA (eDNA) method. The soil properties analyzed were total nitrogen, carbon, phosphorous, potassium, and pH. This study suggests that *B. subtilis* and *R. erythropolis* may affect the bacterial community structure and increase the number of bacteria to reach the ideal limit

ARTICLE INFO

Article history:

Received: 16 October 2023

Accepted: 07 March 2024

Published: 15 August 2024

DOI: <https://doi.org/10.47836/pjst.32.5.11>

E-mail addresses:

abd.azizamin@ub.ac.id (Abd Aziz Amin)

hideki.okuda4@gmail.com (Hideki Okuda)

mizuhokawamura4@gmail.com (Mizuho Kawamura)

nj_anna@ub.ac.id (Nurjannah)

andi_k@ub.ac.id; andikur.ub@gmail.com (Andi Kurniawan)

* Corresponding author

for fertile soil. Adding bacterial inoculants could stimulate the growth of bacteria and the nutrient cycle in the soil environment, resulting in improved soil fertility.

Keywords: *B. subtilis*, microbial ecology, *R. erythropolis*, soil fertility, soil inoculation

INTRODUCTION

World food demand shows an increasing tendency toward food supply. According to Alexandratos and Bruinsma (2012), the food demand for developing countries will increase by 60% in 2030 and double in 2050. Various efforts have been made to improve food production, including agriculture (Bargaz et al., 2018). One of the main factors in increasing agricultural yields is tillage, which makes it more productive (Amini & Asoodar, 2015). Hence, chemical fertilizers and pesticides are often used on various agricultural lands. Conventional agriculture increases along with the intensification of agricultural production. High harvest targets primarily triggered this increase. Currently, the use of agrochemicals in agricultural land has become inevitable and continues to increase yearly (Aktar et al., 2009). However, conventional agricultural practices have been implicated in diminishing soil fertility by reducing the overall bacterial abundance. Such farming systems can alter the composition of beneficial microorganisms within the soil community, thereby influencing critical nutrient-cycling processes, such as nitrogen fixation and phosphorus solubilization (Yadav et al., 2023). Prolonged and unregulated utilization of conventional agricultural systems has been demonstrated to detrimentally impact soil fertility and ecosystem integrity, leading to alterations in soil microflora composition (Dhanker et al., 2021).

These materials can be a way to provide nutrients for plant growth quickly. With the availability of nutrients, plant growth can be accelerated more easily. However, the use of agrochemicals raises various problems. The increasing price of agrochemicals and their decreasing availability make it difficult for farmers to carry out their agricultural business (Jacquet et al., 2022). The use of agrochemicals at high prices also causes the profits of agricultural businesses to decrease even though the number of harvests can be maintained (Popp et al., 2013). The use of agrochemicals that interrupt a series of processes in the natural cycle of nutrients in the soil causes changes in soil conditions over time. The long-term application of agrochemicals can change soil properties and microbial activity (Maximillian et al., 2019; Meena et al., 2020). Agrochemicals can reduce microbial activity (Prashar & Shah, 2016), which plays an essential role in the decomposition of organic matter and provides nutrients in the soil (Bollag, 2008).

The high biodiversity of microbes is one of the leading indicators that can be used to analyze soil conditions (Kim et al., 2022). Various studies to assess soil conditions and increase its fertility are based on microbial biodiversity in the soil. The decrease in activity and the number of microbes causes a decrease in nutrient cycles in the soil, so soil

fertility decreases (Campbell, 2008). Hence, the low number of bacteria and the diversity of bacteria became one of the main characteristics of low-fertilized soils (Adhikari et al., 2014; Babalola & Glick, 2012; Xin-ling et al., 2021). Low-fertilized soils can be improved by stimulating the microbes in this soil (Jacoby et al., 2017). One alternative technique is providing bacterial inoculants to reduce agrochemicals and stimulate bacteria in nutrient cycles (Kumar et al., 2022). Soil inoculation with microbes operates through several mechanisms. One such mechanism involves reinstating natural microbial communities, which conventional agricultural practices may disrupt (Hermans et al., 2023). Another mechanism entails the recruitment and accumulation of beneficial microorganisms triggered by plant-pathogen interactions, leading to disease suppression (Wen et al., 2023). Moreover, soil inoculation can instigate directional shifts in soil and plant communities, fostering ecosystem restoration in degraded environments (Han et al., 2022). Various techniques, including soil biofertilization, trap crop utilization, and seed coating, are employed for soil inoculation (Han et al., 2022). These techniques offer valuable insights into root-microbe interactions, aiding in the comprehension of soil inoculation mechanisms. Understanding the intricacies of soil inoculation with microbes is imperative for devising strategies to enhance agricultural practices and ecosystem rehabilitation efforts. Inoculation with beneficial microbes, such as *B. subtilis* and *R. erythropolis*, has been proposed as an effective practice for enhancing plant growth and soil health (Angelina et al., 2020). *B. subtilis* is widely used as a Growth Promoting Rhizobacteria (Kamou et al., 2015), while *R. erythropolis* is a hydrocarbonoclastic bacteria (Liu et al., 2015).

The provision of bacterial inoculants affects not only soil properties but also the indigenous bacteria in the soil. However, the effect of *R. erythropolis* and *B. subtilis* inoculants on the bacterial community structure and properties of the low-fertilized soils has yet to be widely explored. Changes in the bacterial community structure and its relationship with soil properties after adding bacterial inoculants are critically important aspects of microbial ecology for developing microbial resources, such as efforts to improve food safety and security. Therefore, this study aims to analyze the bacterial community structure and soil properties after inoculating *B. subtilis* and *R. erythropolis* on low-fertilized soil.

MATERIALS AND METHODS

Soil and Material Preparation

This study used soil samples from a tobacco field in Miyazaki Prefecture, Japan. Rice straw from the same prefecture is used as organic matter to be added to the soil. Chemical properties and total bacterial numbers of soil samples and rice straw were analyzed (Table 1). The soil samples were categorized according to the Soil Fertile Index Database criteria established by Adhikari et al. (2014). Standardized soil fertility parameters include a total bacterial count of ≥ 6.0 cells/g soil, total nitrogen content of ≥ 2500 mg⁻¹ kg, total carbon

content of $\geq 25000 \text{ mg}^{-1} \text{ kg}$, total phosphorus content of $\geq 3000 \text{ mg}^{-1} \text{ kg}$, and total potassium content of $\geq 3000 \text{ mg}^{-1} \text{ kg}$ (Adhikari et al., 2014). Based on these categorizations in the Soil Fertile Index Database, the soil samples did not meet the criteria for being classified as fertile.

Table 1

Chemical properties of soil and rice straw as organic material used in this study

Sample	TB (cells/g-soil)	TC (mg/ kg)	TN (mg/ kg)	TP (mg/kg)	TK (mg/kg)	C/N ratio	pH
Rice Straw	n.d	470,000	25,000	60,000	18,000	19	6,8
Soil Sample	n.d	9000	530	1000	1200	16	6,9

Note. TB: Total Bacteria; TC: Total Carbon; TN: Total Nitrogen; TP: Total Phosphorous; TK: Total Potassium; n.d: not detected ($<1 \times 10^6$ cells/g-soil)

Before analyzing fresh soil samples, the soil was sieved through a 2 mm mesh sieve. Subsequently, 500 g of soil was placed into a 1 L pot with a moisture content of 30% and mixed with 1% (w/w) rice straw powder that had been pulverized using a chopper machine to eliminate any water content. *R. erythropolis* and *B. subtilis* were cultured in Luria Bertani broth medium (containing 1% peptone, 0.5% yeast extract, and 0.5% NaCl) at 35°C for 48 hours to prepare the bacterial inoculum.

The experimental design consisted of three pots with two replications of each treatment. Then, each bacterial inoculant *R. erythropolis* and *B. subtilis* (ca., 1×10^6 cells/g-soil) was added to each soil treatment. In comparison, Soil without bacterial inoculants was used as a control in this study. All soils (i.e., inoculated with bacteria and control) were incubated for 28 days (22°C/14 hr and 18°C/10 hr) in a plant factory incubator at Ritsumeikan University, Japan. The sampling parameter consisted of the total number of bacteria every week, soil chemical properties in week 4, and bacterial community structure in week 4.

Analysis of Chemical Properties

The chemical properties of soils (total carbon, total nitrogen, total phosphorous, and total potassium) were analyzed in the last final incubation on the 28th day or week 4. The soil carbon was determined using a total organic carbon analyzer machine (TOC-VCPH; Shimadzu, Kyoto, Japan) and the solid sample combustion unit (SSM-5000A; Shimadzu, Kyoto, Japan). To analyze the total nitrogen, total phosphorous, and total potassium, the soil was digested in a Kjeldahl digestion unit (Gerhardt, Königswinter, Germany) and then filtered (ADVANTEC No. 6; Toyo Roshi Co. Ltd., Tokyo, Japan). Total nitrogen, total phosphorous, and total potassium in the filtrate were determined using the indophenol blue method for nitrogen, the molybdenum blue method for phosphorous, and the atomic absorption spectrophotometry for potassium (Hitachi, Tokyo, Japan). The pH of soils was measured using the LAQUA pH/ion meter F-72 (Horiba, Ltd., Kyoto, Japan).

Analysis of Total Bacterial Number

The total number of bacteria in the soil every week was estimated by analyzing the environmental DNA (eDNA) with the low stirring method (Aoshima et al., 2006). A 1.0 g of soil was mixed with 8.0 mL of eDNA buffer and 1 mL of 20% sodium dodecyl sulfate (SDS) solution. The suspension was stirred at 1,500 rpm for 20 min, followed by centrifugation at $6,000 \times g$ for 10 min. The supernatant was mixed with chloroform-isoamyl alcohol (24:1 (v/v)), and centrifuged at $18,000 \times g$ for 10 min. Then, 500 μ l supernatant was taken as the crude nucleic acid in a new tube. 300 μ l of isopropanol was added, stirred gently, and centrifuged at 14,000 rpm for 20 min. The liquid was discarded gently, 1 ml of pre-cooled 70% ethanol was added, and centrifuged at 14,000 rpm for 5 minutes. The liquid was gently discarded and dried for about 30 min under a vacuum. The remaining was dissolved in 50 μ l of $1 \times$ TE buffer (10 mM Tris-HCl and 1 mM EDTA, pH 8.0). The eDNA was quantified based on the band's intensity after 1% agarose gel electrophoresis using KODAK 1 D 3.6 Image Analysis Software (Eastman Kodak Company, CT, USA).

PCR Amplification

The environmental DNA (eDNA) was extracted by following the eDNA extraction method described by Aoshima et al. (2006). The 16S rRNA bacterial gene was amplified using DGGE primers forward (5'-CGCCC GCCGC GCCCC GCGCC CGTCC CGCCG CCCCC GCCCG CCTAC GGGAG GCAGC AG-3') and reverse (5'-CCGTC AATTC CTTTG AGTTT-3'). The amplification PCR was taken in a 25 μ L PCR mixture containing 0.1 ng/ μ L of DNA template, 0.1 U rTaq DNA polymerase, 2.5 μ L of $10 \times$ buffer, 2.5 μ L of 2 mM dNTPs, and 0.5 μ L of 10 mM of each primer. DNA polymerase, dNTPs, and PCR buffer were purchased from Toyobo (Toyobo Co. LTD, Osaka, Japan), while all primers were synthesized by Sigma-Aldrich (Sigma-Aldrich Co. LLC, Tokyo, Japan). The condition of PCR is initial denaturation at 95°C for 1 min, followed by 40 cycles of denaturation at 95°C for 1 min, primer annealing at 55°C for 30 seconds, and extension at 72°C for 1 min, and then final extension at 72°C for 5 min.

DGGE Analysis

The amplified 16S rRNA bacterial genes were used for the Denaturing Gradient Gel Electrophoresis (DGGE) analysis. DGGE was performed using a D Code System (BioRad Laboratories Inc., California, USA). The 20 μ L of PCR product was loaded into 40% (w/v) polyacrylamide gel with a denaturant gradient of 27.5% - 67.5%. The gel was run in $1 \times$ TAE buffer (40 mM Tris (pH 7.6), 20 mM acetic acid, and 1 mM EDTA) at a constant voltage of 70 V at 60°C for 15 h. Thus, the gel was stained using SYBR Gold for 30 min and then rinsed with distilled water. Cluster analysis of the DGGE band pattern was conducted using the FPquest Bioinformatics Software (BioRad Laboratories Inc., California, USA).

Statistical Analysis

Statistical analysis was conducted to compare the bacterial density between treatment (soil inoculated with bacteria) and control (soil without bacterial inoculation) using Analysis of Variance (ANOVA). ANOVA was chosen for its suitability in determining whether there are any statistically significant differences in bacterial density between the treatment and control groups. Additionally, Multivariate Analysis of Variance (MANOVA) was employed to assess the variations in soil properties. MANOVA was deemed appropriate as it allows for the simultaneous analysis of multiple dependent variables, enabling the investigation of potential differences in various nutrient components between treatment and control groups. These statistical analyses were performed using SPSS version 29 (IBM Corp., Armonk, NY, USA) with a significance level set at $\alpha = 0.05$ to determine the statistical significance of the observed differences. Before analysis, assumptions of normality and homogeneity of variances were assessed, and, if necessary, appropriate transformations were applied to meet these assumptions.

RESULTS AND DISCUSSION

Effect of Microbial Inoculant on Bacterial Activity

Environmental DNA (eDNA) of bacteria in the low-fertilized agricultural soil was collected and then observed on gel electrophoresis gel (Figure 1). Soils subjected to the analysis in this study were the low-fertilized soil inoculated with *B. subtilis*, the low-fertilized soil inoculated with *R. erythropolis*, and the low-fertilized soil that was not inoculated with bacteria (used as controls). Hence, the greater the number of bacteria in the soil, the more eDNA will be obtained. In addition, the more eDNA collected, the brighter the light intensity of the band on the electrophoresis gel. The results of the analysis of bacterial populations during soil incubation using the eDNA method are shown in Figure 2. The eDNA method calculates the number of bacteria to evaluate the number of soil microorganisms by calculating the amount of DNA in the soil sample (Aoshima et al., 2006). Observations for 28 days of incubation showed that the total bacterial number in soil treatment with *R. erythropolis* increased to 5.2×10^8 cells/g-soil, while treatment with *B. subtilis* increased to 3.4×10^8 cells/g-soil. On the other hand, the total bacterial number in control gradually decreased to an undetectable level ($\leq 1 \times 10^6$ cells/g-soil) on day 28.

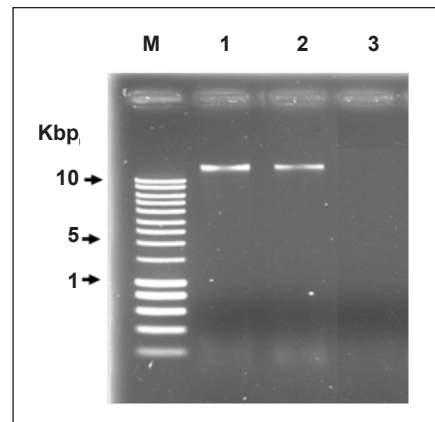


Figure 1. Analysis of the eDNA extracted after 28 days of incubation from soil inoculated with *R. erythropolis*. (Lane 1), *B. subtilis* (Lane 2), without bacterial inoculation (Lane 3). M is the lane of the marker.

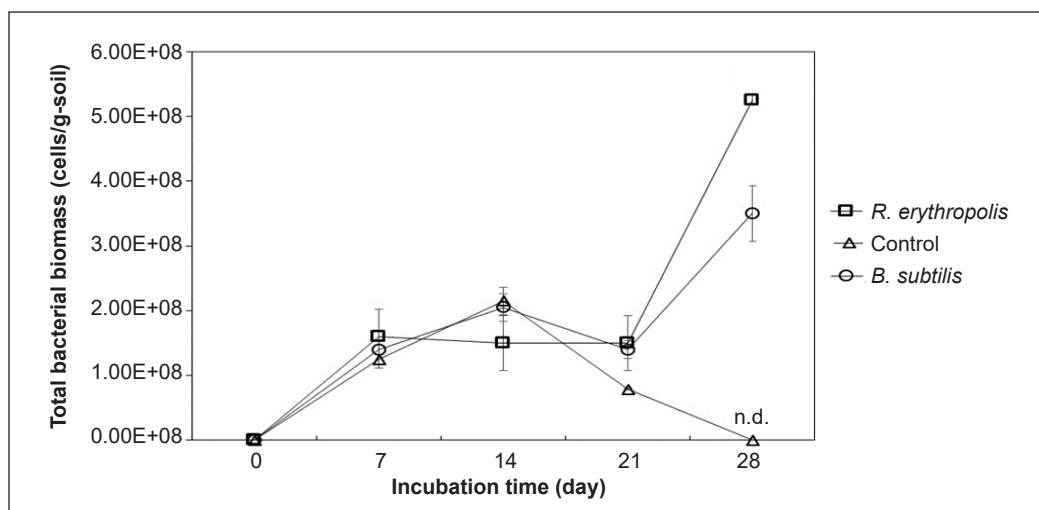


Figure 2. Effect of bacterial inoculant on the bacterial number in the soil during incubation

The bacterial densities of soils treated with bacterial inoculation (*R. erythropolis* and *B. subtilis*) were compared to that of the control (without bacterial inoculation) using Analysis of Variance (ANOVA) (Table 2). The results indicate significant differences in bacterial density between each treatment and the control ($\alpha < 0.05$). The most pronounced difference was observed on day 28. These findings suggest that bacterial inoculation significantly influences bacterial density in the soil. This bacterial density forms the foundation for supporting the nutrient cycling driven by microbial activities, thus facilitating the development of microbiota-based ecological agricultural systems.

This analysis underscores the efficacy of bacterial inoculation in influencing soil microbial communities, potentially enhancing soil fertility and ecosystem functioning. The observed increase in bacterial density corroborates previous studies indicating the role of bacterial inoculation in augmenting soil microbial populations. Additionally, the temporal dynamics of bacterial density, as evidenced by the significant difference on day 28, suggest

Table 2

The results of ANOVA analysis for the bacterial densities of soil dependent variable: Response

Source	Type III Sum of Squares	df	Mean Square	F	Sig.
Corrected Model	56766586666666750.000 ^a	14	40547561904761912.000	66.096	.000
Intercept	668416133333331970.000	1	668416133333331970.000	1089.572	.000
Treatment	68788266666666648.000	2	3439413333333324.000	56.065	.000
Day	269791200000000416.000	4	6744780000000104.000	109.945	.000
Treatment * Day	229086400000000256.000	8	2863580000000032.000	46.679	.000
Error	920200000000000.000	15	61346666666666.600		
Total	124528400000000000.000	30			
Corrected Total	57686786666666750.000	29			

a progressive establishment and proliferation of the inoculated bacterial strains within the soil environment. These findings contribute to our understanding of microbiota-mediated nutrient cycling mechanisms, highlighting the potential of microbial-based approaches in sustainable agriculture practices. Further investigations into the long-term effects of bacterial inoculation on soil microbial communities and ecosystem functioning are warranted to elucidate the full scope of its implications for agricultural sustainability and productivity.

Low bacterial numbers are among the main characteristics of low soil fertility (Adhikari et al., 2014). Various efforts have been made to increase the fertility of this type of soil for the benefit of agriculture. In the development of organic agriculture, efforts are often made to add organic materials such as rice straw and inoculate bacteria (Ramadass & Thiagarajan, 2017). Adding bacterial inoculants can help create conditions that can trigger the growth of indigenous bacteria (Hawrot et al., 2016; Santos et al., 2019) and increase the circulation of nutrients in the soil (Figure 6). Increasing agricultural soil fertility due to adding organic matter will accompany increased bacteria (Li et al., 2021). This study shows that adding inoculations of *R. erythropolis* and *B. subtilis* can increase the number of bacteria in low-fertilized soil until it meets the standard of the number of bacteria in fertile soil. The bacterial biomass values were divided into the following six groups: 1) shallow ($<1.0 \times 10^8$ cells/g); 2) very low (1.0×10^8 to 2.9×10^8 cells/g); 3) low (3.0×10^8 to 4.4×10^8 cells/g); 4) medium (4.5×10^8 to 5.9×10^8 cells/g); 5) high (6.0×10^8 to 9.9×10^8 cells/g); and 6) very high ($\geq 10.0 \times 10^8$ cells/g) (Adhikari et al., 2014).

In the case of control soil, the addition of bacteria continued until day 21 (increased to ca. 2.0×10^7 cells/g-soil), then continued to decrease. The increase in bacteria may occur because rice straw becomes a source of nutrients for the bacteria. However, the available nutrients can only support the bacteria until the 21st day. After that, the bacterial community in the soil cannot utilize the remaining nutrients, resulting in a decrease in the bacteria population. The bacterial community in the soil can be affected by changes in nutrient availability, which can result in a decrease in the bacterial population. Nutrient limitations, such as decreased phosphorus availability, can limit microbial growth and community structure (François et al., 2021). It is related to the fact that the total phosphorous decreased during control treatment compared to soil treatment with inoculant bacteria (Figure 6). Moreover, the remaining chemical substances in the soil can negatively affect microbes that cannot utilize these remaining nutrients (Nayak et al., 2018). The highest total number of bacteria in this study was shown by the soil treatment using *R. erythropolis*. Treatment using *B. subtilis* inoculation also showed higher total bacteria values than the control but lower than *R. erythropolis*.

The soil used in this study is the former soil of a tobacco field in Miyazaki prefecture, Japan. In this tobacco farming activity, chemicals and pesticides containing chloropicrin are used (Ota, 2013). These agrochemicals can interfere with the growth of indigenous

bacteria and make this soil low in fertility. Adding inoculated bacteria such as *R. erythropolis* and *B. subtilis* can positively impact the degradation of these agrochemicals (Choi et al., 2021; Prashar & Shah, 2016). Once the number of agrochemicals can be reduced, more indigenous bacteria can grow in the soil. *R. erythropolis* is a type of bacteria that can live in contaminated soil and is often used in bioremediation activities (Wolińska et al., 2016). This species is also very likely to degrade agrochemicals better than *B. subtilis*, resulting in a higher total number of bacteria than soil inoculated with *B. subtilis*.

The results of the total bacteria number analysis indicate that adding bacterial inoculants can stimulate the growth of bacteria, impacting soil fertility levels. Hence, applying bacterial inoculants enhances the activity of indigenous soil bacteria (Babalola & Glick, 2012). Moreover, the PCR-DGGE method was used in this study to compare the bacterial community structure in the soils.

Bacterial Community Structure

PCR-DGGE analysis was performed for eDNA samples collected from soils (i.e., inoculated with *R. erythropolis*, inoculated with *B. subtilis*, and control) of the beginning (day 0) and the end of incubation (day 28). The PCR amplification of the eDNA shows that the fragment bands were 600 bp (Figure 3). Then, the results of the DGGE observations indicated that the structures of the bacterial diversity were shown in Figure 4. The bands in the DGGE gel may indicate the main species of bacteria in the soils (Vendan et al., 2012). The structural communities of bacteria in the three soils sampled in this study were compared through the Cluster Analysis of the DGGE results (Figure 5). The dendrogram analysis results showed that the bacterial communities in the soil inoculated with bacteria at the beginning of the incubation period differed from that of the non-inoculated (control) (Figure 5A). In the case of inoculated soils, the difference in bacterial community is most likely due to

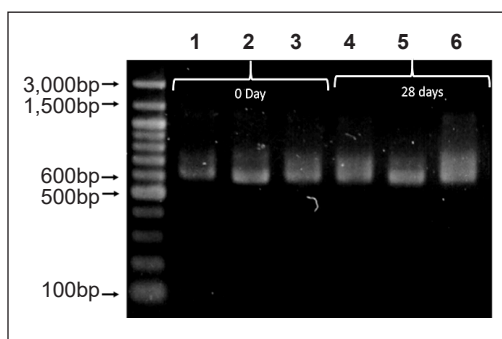


Figure 3. 16S rRNA amplified by PCR separated on 1.5% agarose gel (1, 4 = Control; 2, 5 = *R. erythropolis*; 3, 6 = *B. subtilis*)

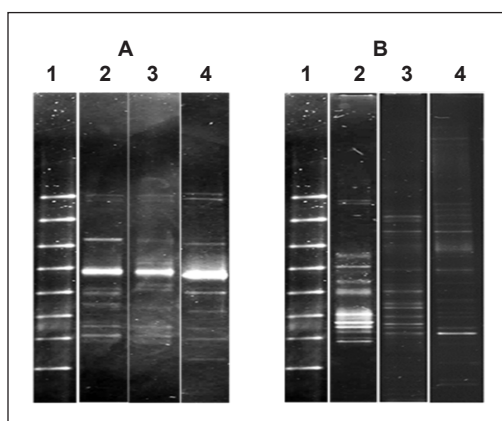


Figure 4. DGGE analysis of 16S rRNA fragments obtained from soils before (A) and after incubation (B) (Lane 1: DGGE marker, Lane 2: *R. erythropolis*, Lane 3: *B. subtilis*, Lane 4: Control)

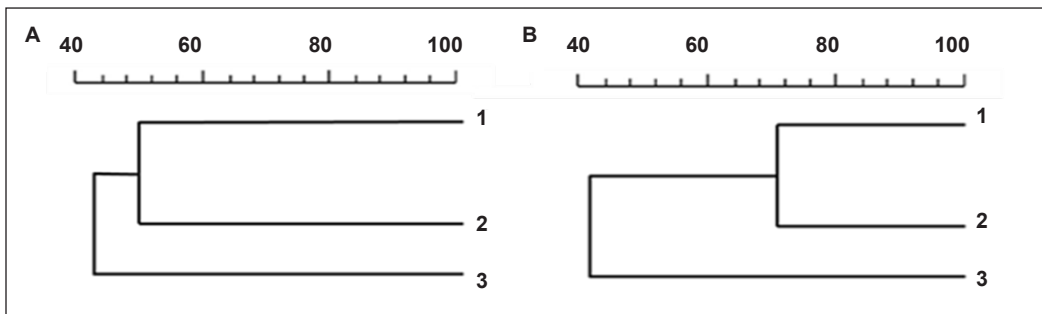


Figure 5. Cluster analysis of 16S rRNA obtained from soils before (A) and after incubation (B) (Lane 1: DGGE marker, Lane 2: *R. erythropolis*, Lane 3: *B. subtilis*, Lane 4: Control)

the different types of bacteria added (i.e., *R. erythropolis* dan *B. subtilis*). The dendrogram of the bacterial community structure analysis after 28 days of incubation is shown in Figure 5B. This analysis showed that the bacterial community in the bacterial-inoculated soil differed from the uninoculated soil.

However, the community structure became more similar to the control compared to the initial incubation. This result indicates that the provision of bacterial inoculation can stimulate the growth of indigenous bacteria. The addition of bacterial inoculation makes soil conditions more suitable for the life of indigenous bacteria, increasing the number of bacteria in the soil (Figure 2). This more favorable soil condition may occur because bacteria such as *R. erythropolis* and *B. subtilis* reduce the concentration of agrochemicals in the soil (Choi et al., 2021; Prashar & Shah, 2016). Bacterial inoculants change the structure of the bacterial diversity, which has an essential role in soil fertility. Applying microbial inoculants may improve the condition of the low-fertilized soils (Trabelsi & Mhamdi, 2013).

Effect of Microbial Inoculant on Soil Properties

This study analyzed soil properties after 28 days of incubation to explore the impact of adding bacterial inoculants to the soil (Figure 6). This analysis showed that adding bacterial inoculants made the total carbon, total phosphorus, and CN ratio values of the soils given bacterial inoculation higher than those of the control. In contrast, pH and Total Nitrogen were lower than the control. The difference in impact occurs in the Total Potassium parameter. When compared with the control, the value of this parameter was higher in the soil that was inoculated with *R. erythropolis* while lower in the addition of *B. subtilis* inoculation.

The soil properties in this study were compared using Multivariate Analysis of Variance (MANOVA). The results, depicted in Figure 6, illustrate variations in the soil samples, denoted by different letters (a, b, c). Similar letters indicate no significant differences between samples, while different letters denote significant differences. The analysis revealed significant differences in soil properties between soil samples with and without bacterial

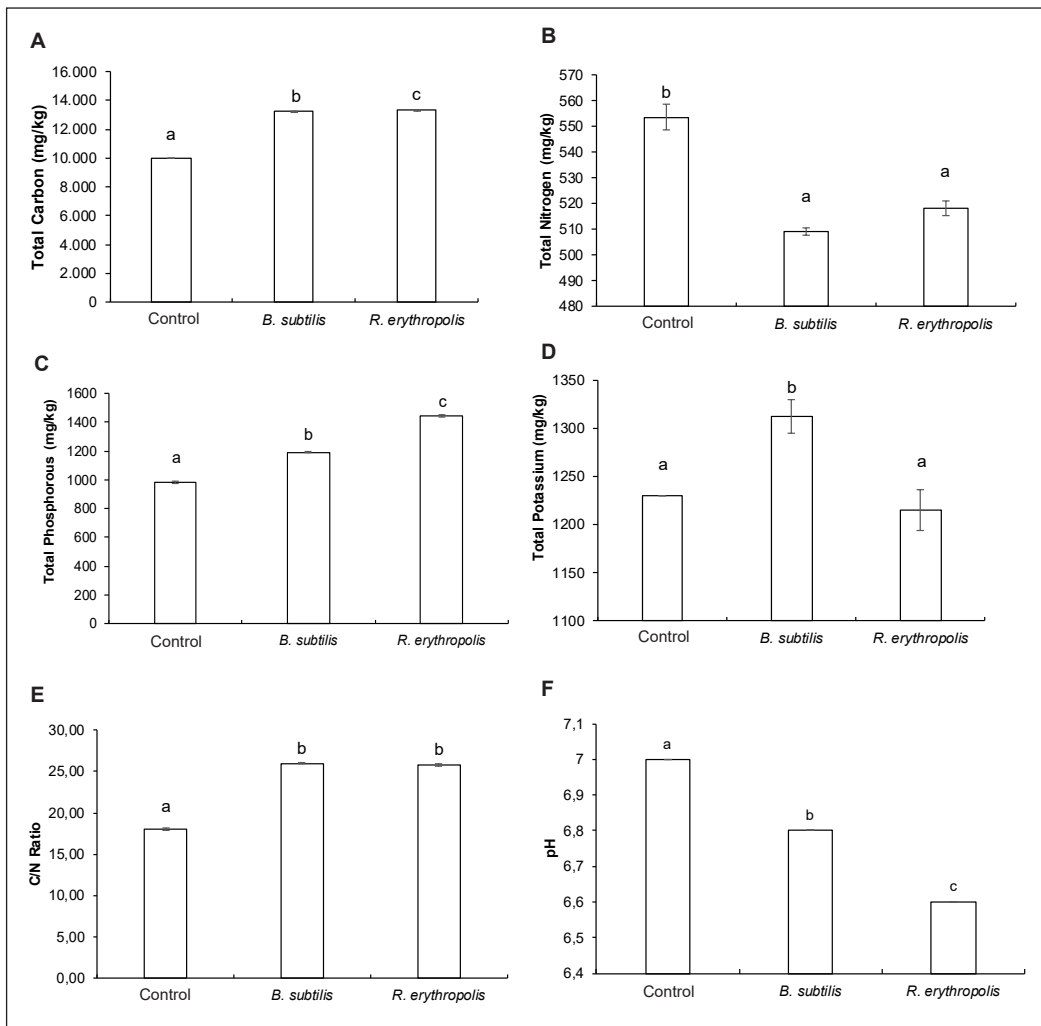


Figure 6. Total carbon (A), total nitrogen (B), total phosphorus (C), total potassium (D), CN ratio (E), and soil pH (F) of the soils on the 28th day

inoculation. It appears that bacterial inoculation stimulates the activity of soil bacteria, resulting in distinct soil conditions. Interestingly, the Total Nitrogen content between soil samples inoculated with *R. erythropolis* and those inoculated with *B. subtilis* did not differ significantly. This finding suggests that, regarding nitrogen conditions in the soil, the type of bacteria inoculated does not exert a significant influence, contrary to other soil properties.

This discrepancy in the response of Total Nitrogen content to bacterial inoculation warrants further investigation. Several factors may contribute to this observation, including the specific metabolic activities of the inoculated bacterial strains, their interactions with indigenous soil microbial communities, and the availability of nitrogen sources in the soil. Further research could focus on elucidating the mechanisms underlying the modulation of

nitrogen dynamics by different bacterial species in soil ecosystems. Additionally, examining the long-term effects of bacterial inoculation on nitrogen cycling processes and soil fertility could provide valuable insights into optimizing microbial-based approaches for sustainable soil management practices.

The decrease in pH in the soil given inoculants is possible because the bacterial community can stabilize soil pH in the ideal range for agriculture (ca. pH 5–7) (Carvalho, 2019). Moreover, the decrease in pH during decomposition is probably due to the production of organic acids, such as lactic acid, due to microbial activity (Qi et al., 2016). Stabilizing the pH indicates that the decomposition process reaches a state of equilibrium where the production and consumption of organic acids are balanced. The difference in the trend in the value of Total Potassium indicates that the activities of *R. erythropolis* and *B. subtilis* are different in recycling potassium from organic matter. Hence, *R. erythropolis* shows a more remarkable ability to recycle potassium from organic substrates (Carvalho, 2019). The results of this study suggested that adding bacteria seems to influence the nutrient cycle in the soil environment (Feirer et al., 2012; Zhang et al., 2016), resulting in a change in soil properties.

CONCLUSION

This investigation delved into the effects of *R. erythropolis* and *B. subtilis* inoculation on the properties of agriculturally fertilized soil. Our findings underscore the potential of bacterial inoculation in stimulating the proliferation of indigenous bacterial populations and enhancing nutrient cycling within the soil matrix. Notably, the inoculation with *R. erythropolis* and *B. subtilis* exerted discernible impacts on the structure of bacterial communities, leading to an augmentation in bacterial abundance towards the threshold indicative of fertile soil. Consequently, our study posits bacterial inoculation as a promising intervention for ameliorating the conditions of low-fertilized soil, particularly following its prior use in agriculture employing agrochemicals. These results hold significant implications for sustainable soil management practices, suggesting a viable strategy to revitalize soil fertility in agricultural contexts. By harnessing the potential of bacterial inoculants, agricultural systems can mitigate the deleterious effects of conventional practices and pave the way toward enhanced soil health and productivity. Further research is warranted to elucidate the mechanistic underpinnings of bacterial-mediated improvements in soil properties and to refine strategies for optimizing the efficacy of bacterial inoculation in diverse agricultural settings.

ACKNOWLEDGEMENTS

The authors thank Professor Motoki Kubo from the the Bioengineering Laboratory, Graduate School of Life Sciences, Ritsumeikan University Japan, and SOFIX Agriculture

Promotion Center, Japan, for supporting this research. This research is supported by the Grant of International Research Collaboration (HAPKI), the Institute of Research and Community Services (LPPM), and the University of Brawijaya, Indonesia (Contract number 960.2/IIN10.C 10IPN/2022).

REFERENCES

- Adhikari, D., Kai, T., Mukai, M., Kiwako, S. A., & Kubo, M. (2014). Proposal for a new soil fertility index (SOFIX) for organic agriculture and construction of a SOFIX database for agricultural fields. *Current Topics in Biotechnology*, 8, 81-91.
- Aktar, M. W., Sengupta, D., & Chowdhury, A. (2009). Impact of pesticides use in agriculture: Their benefits and hazards. *Interdisciplinary Toxicology*, 2(1), 1-12. <https://doi.org/10.2478/v10102-009-0001-7>
- Alexandratos, N., & Bruinsma, J. (2012). *World agriculture towards 2030/2050: The 2012 revision*. Food and Agriculture Organization of the United Nations. <https://doi.org/10.22004/ag.econ.288998>
- Amini, S., & Asoodar, M. (2015). The effect of conservation tillage on crop yield production (The Review). *New York Science Journal*, 8(3), 25–29. <https://doi.org/10.7537/marsnys080315.04>
- Angelina, E. M., Papatheodorou, T., Demirtzoglou, N., & Monokrousos. (2020). Effects of *Bacillus subtilis* and *Pseudomonas fluorescens* inoculation on attributes of the lettuce (*Lactuca sativa* L) soil rhizosphere microbial community: The role of the management system. *Agronomy*, 10(9), Article 1428. <https://doi.org/10.3390/agronomy10091428>
- Aoshima, H., Kimura, A., Shibutani, A., Okada, C., Matsumiya, Y., & Kubo, M. (2006). Evaluation of soil bacterial number using environmental DNA extracted by slow-stirring method. *Applied Microbiology and Biotechnology*, 71, 875-880. <https://doi.org/10.1007/s00253-005-0245-x>
- Babalola, O. O., & Glick, B. R. (2012). The use of microbial inoculants in African agriculture: Current practice and future prospects. *Journal of Food, Agriculture & Environment*, 10(3&4), 540-549.
- Bargaz, A., Lyamlouli, K., Chtouki, M., Zeroual, Y., & Dhiba, D. (2018). Soil microbial resources for improving fertilizers efficiency in an integrated plant nutrient management system. *Frontiers Microbiology*, 9, Article 1606. <https://doi.org/10.3389/fmicb.2018.01606>
- Bollag, J. M. (2008). Interactions of soil components and microorganisms and their effects on soil remediation. *Revista de la ciencia del suelo y nutrición vegetal*, 8(ESPECIAL), 28-32. <https://doi.org/10.4067/s0718-27912008000400006>
- Campbell, L. C. (2008). Managing soil fertility decline. *Journal of Crop Production*, 1(2), 29-52. https://doi.org/10.1300/J144v01n02_02
- Carvalho, C. C. C. R. D. (2019). Adaptation of rhodococcus to organic solvents. In H. M. Alvarez (Ed.), *Biology of Rhodococcus* (pp. 103-135). Springer. https://doi.org/10.1007/978-3-030-11461-9_5
- Choi, Y., Han, S. W., Kim, J. S., Jang, Y., & Shin, J. S. (2021). Biochemical characterization and synthetic application of aromatic L-amino acid decarboxylase from *Bacillus atrophaeus*. *Applied Microbiology Biotechnology*, 105, 2775–2785. <https://doi.org/10.1007/s00253-021-11122-3>

- Dhanker, R., Goyal, S., Kumar, K., & Hussain, T. (2021). Bacterial community response to pesticides polluted soil. In S. D. Mandal & A. K. Passari (Eds.), *Recent Advancement in Microbial Biotechnology* (pp. 339-355). Academic Press. <https://doi.org/10.1016/B978-0-12-822098-6.00010-0>.
- Feirer, N., Lauber, C. L., & Ramirez, K. S. (2012). Comparative metagenomic, phylogenetic and physiological analyses of soil microbial communities across nitrogen gradients. *The ISME Journal*, 6(5), 1007-1017. <https://doi.org/10.1038/ismej.2011.159>
- François, P. T., Hans, L., Esther, E. E., Etienne, L., Sven, M., & Ellen, K. (2021). Soil microbial communities are driven by the declining availability of cations and phosphorus during ecosystem retrogression. *Soil Biology and Biochemistry*, 163, Article 108430. <https://doi.org/10.1016/j.soilbio.2021.108430>.
- Han, X., Li, Y., Li, Y., Du, X., Li, B., Li, Q., & Bezemer, T. M. (2022). Soil inoculum identity and rate jointly steer microbiomes and plant communities in the field. *ISME Communications*, 2(1), Article 59. <https://doi.org/10.1038/s43705-022-00144-1>
- Hawrot, P. M., Mikiciuk, G., Mikiciuk, M., Izwilow, M., & Kiniorska, J. (2016). Number and activity of microorganisms in soil Inoculated with the Rhizocell C biopreparation in strawberry cultivation (*Fragaria × Ananasa Duch*). *Journal Ecological Engineering*, 17(2), 135-140. <https://doi.org/10.12911/22998993/62307>
- Hermans, S. M., Lear, G., Case, B. S., & Buckley, H. L. (2023). The soil microbiome: An essential, but neglected, component of regenerative agroecosystems. *iScience*, 26(2), Article 106028. <https://doi.org/10.1016/j.isci.2023.106028>.
- Jacoby, R., Peukert, M., & Succurro, A. (2017). The role of soil microorganisms in plant mineral nutrition—current knowledge and future directions. *Frontiers in Plant Science*, 8, Article 1617. <https://doi.org/10.3389/fpls.2017.01617>
- Jacquet, F., Jeuffroy, M. H., Jouan, J., Cadre, E., Litrico I., Malausa T., Reboud X., & Huyghe, C. (2022). Pesticide-free agriculture as a new paradigm for research. *Agronomy for Sustainable Development*, 42(1), Article 8. <https://doi.org/10.1007/s13593-021-00742-8>
- Kamou, N. N., Karasali, H., Menexes, G., Kasiotis, K. M., Bon, M. C., Papadakis, E. N., Tzelepis, G. D., Lotos, L., & Lagopodi, A. L. (2015). Isolation screening and characterisation of local beneficial rhizobacteria based upon their ability to suppress the growth of *Fusarium oxysporum* f. sp. *radicis-lycopersici* and tomato foot and root rot. *Biocontrol Science and Technology*, 25(8), 928–949. <https://doi.org/10.1080/09583157.2015.1020762>
- Kim, H., Park, Y. H., Yang, J. E., Kim, H. S., Kim, S. C., Oh, E. J., Moon, J., Cho, W., Shin, W., & Yu, C. (2022). Analysis of major bacteria and diversity of surface soil to discover biomarkers related to soil health. *Toxics*, 10(3), Article 117. <https://doi.org/10.3390/toxics10030117>
- Kumar, S., Diksha, Sindhu, S. S., & Kumar R. (2022). Biofertilizers: An ecofriendly technology for nutrient recycling and environmental sustainability. *Current Research in Microbial Sciences*, 3, Article 100094. <https://doi.org/10.1016/j.crmicr.2021.100094>
- Li, X., Su, Y., Ahmed, T., Ren, H., Javed Y., Yao, Q. A. J., & Yan, B. Li. (2021). Effects of different organic fertilizers on improving soil from newly reclaimed land to crop soil. *Agriculture*, 11(6), Article 560. <https://doi.org/10.3390/agriculture11060560>

- Liu, W., Wang, Q., Wang, B., Hou, J., Luo, Y., Tang, C., & Ashley, F. E. (2015). Plant growth-promoting rhizobacteria enhance the growth and Cd uptake of *Sedum plumbizincicola* in a Cd-contaminated soil. *Journal of Soils and Sediments*, *15*(5), 1191-1199. <https://doi.org/10.1007/s11368-015-1067-9>
- Maximillian, J., Brusseau, M. L., Glenn, E. P., & Matthias, A. D. (2019). Chapter 25 - Pollution and environmental perturbations in the global system. In M. L. Brusseau, I. L. Pepper & C. P. Gerba (Eds.), *Environmental and Pollution Science* (3rd ed.; pp. 457-476). Academic Press. <https://doi.org/10.1016/B978-0-12-814719-1.00025-2>
- Meena, R. S., Kumar, S., & Datta, R. (2020). Impact of agrochemicals on soil microbiota and management: A review. *Land*, *9*(2), Article 34. https://doi.org/10.1007/978-981-16-9310-6_3
- Nayak, S. K., Dash, B., Baliyarsingh, B. (2018). Microbial remediation of persistent agro-chemicals by soil bacteria: An overview. In J. K. Patra, G. Das & H. S. Shin (Eds.), *Microbial Biotechnology* (pp. 275-301). Springer. https://doi.org/10.1007/978-981-10-7140-9_13
- Ota, H. (2013). Historical development of pesticides in Japan. *Japanese Journal of Pesticide Science*, *38*(2), 161-166. <https://doi.org/10.1584/jpestics.w13-02>
- Popp, J., Pető, K., & Nagy J. (2013). Pesticide productivity and food security. A review. *Agronomy for Sustainable Development*, *33*, 243-255. <https://doi.org/10.1007/s13593-012-0105-x>
- Prashar, P., & Shah, S. (2016). Impact of fertilizers and pesticides on soil microflora in agriculture. In E. Lichtfouse (Ed.), *Sustainable Agriculture Reviews* (pp. 331-361). Springer. https://doi.org/10.1007/978-3-319-26777-7_8
- Qi, Y., Zhu, J., Fu, Q., Hu, H., Huang, Q., & Violante, A. (2016). Sorption of Cu by organic matter from the decomposition of rice straw. *Journal of Soils and Sediments*, *16*, 2203-2210. <https://doi.org/10.1007/s11368-016-1413-6>
- Ramadass, M., & Thiagarajan, P. (2017). Effective pesticide nano formulations and their bacterial degradation. *IOP Conference Series: Materials Science and Engineering*, *263*, Article 022050. <https://doi.org/10.1088/1757-899X/263/2/022050>
- Santos, M. S., Nogueira, M. A., & Hungria M. (2019). Microbial inoculants: Reviewing the past, discussing the present and previewing an outstanding future for the use of beneficial bacteria in agriculture. *AMB Expr*, *9*(1), Article 205. <https://doi.org/10.1186/s13568-019-0932-0>
- Trabelsi, D., & Mhamdi R. (2013). Microbial inoculants and their impact on soil microbial communities: A review. *BioMed Research International*, *2013*(1), Article 863240. <https://doi.org/10.1155/2013/863240>
- Vendan, R. T., Lee, S. H., Yu, Y. J., & Rhee, Y. H. (2012). Analysis of bacterial community in the ginseng soil using Denaturing Gradient Gel Electrophoresis (DGGE). *Indian Journal of Microbiology*, *52*(2), 286-288. <https://doi.org/10.1007/s12088-011-0193-3>
- Wen, T., Ding, Z., Thomashow, L. S., Hale, L., Yang, S., Xie, P., Liu, X., Wang, H., Shen, Q., & Yuan, J. (2023). Deciphering the mechanism of fungal pathogen-induced disease-suppressive soil. *New Phytologist*, *238*(6), 2634-2650. <https://doi.org/10.1111/nph.18886>
- Wolińska, A., Kuźniar, A., Szafranek-Nakonieczna, A., Jastrzębska, N., Roguska, E., & Stępniewska, Z. (2016). Biological activity of autochthonic bacterial community in oil-contaminated soil. *Journal Water Air Soil Pollution*, *227*, Article 130. <https://doi.org/10.1007/s11270-016-2825-z>

- Xin-ling, M., Jia, L., Xiao-fen, C., Wei-tao, L., Chun-yu, J., Meng, W., Ming, L., & Zhong-pe, L. (2021). Bacterial diversity and community composition changes in paddy soils that have different parent materials and fertility levels. *Journal of Integrative Agriculture*, 20(10), 2797-2806. [https://doi.org/10.1016/s2095-3119\(20\)63364-0](https://doi.org/10.1016/s2095-3119(20)63364-0)
- Yadav, S. L., Birla, D., Inwati, D. K., Yadav, M., Yadav, I. R., Makwana, S. N., & Lakshman, P. N. (2023). Impact of agrochemicals on soil biota and ways to mitigate it: A review. *International Journal of Environment and Climate Change*, 13(5), 366–375. <https://doi.org/10.9734/ijecc/2023/v13i51779>
- Zhang, C., Liu, G., Xue, S., & Wang G. (2016). Soil bacterial community dynamics reflect changes in plant community and soil properties during the secondary succession of abandoned farmland in the Loess Plateau. *Soil Biology and Biochemistry*, 97, 40-49. <https://doi.org/10.1016/j.soilbio.2016.02.013>

Application of UAV Technology for Vegetation Community Identification in Coastal BRIS Wetland

Syazuani Mohd Shariff^{1,2}, Edlic Sathiamurthy^{1*}, Rohani Shahrudin¹,
Idham Khalil¹ and Mohd Sofiyon Sulaiman³

¹Faculty Science and Marine Environment, Universiti Malaysia Terengganu, 21030, Kuala Nerus, Terengganu, Malaysia

²Faculty of Applied Science, School of Biology, UiTM Cawangan Negeri Sembilan, Kampus Kuala Pilah, 72000, Kuala Pilah, Negeri Sembilan, Malaysia

³Faculty of Ocean Engineering Technology and Informatics, Universiti Malaysia Terengganu, 21030, Kuala Nerus, Terengganu, Malaysia

ABSTRACT

Unmanned aerial vehicles (UAV) based methods for reconnaissance activities aim to update wetlands' health status and are safer and cost-effective considering that wetlands normally have saturated soils, dense vegetation and wildlife. Vegetation survey work in wetland areas needs many staff to ensure the safety of researchers and equipment. This paper describes the application of UAV technology to identify and demarcate vegetation communities in a dense BRIS (beach ridges interspersed with swales) coastal wetland. The methodology employed in this research has two steps. The first step involves the utilisation of UAV imagery and Geographic Information System (GIS) technology. The second step entails ground truthing, which involves validating tree species using 15 quadrants. The utilisation of UAVs in conjunction with ArcGIS 10.3 demonstrated that the unique characteristics of tree canopy morphology and tree heights could be assessed and analysed. The UAV-GIS results are compared to ground truthing results to validate

tree communities' demarcation. The findings indicate that integrating two datasets, particularly tree canopy morphology and tree height, produced an acceptably accurate vegetation community demarcation. The tree canopy form of *Hibiscus tiliaceus* (Bebaru) was differentiated from the canopies of *Acacia mangium* and *Nypa fruticans* by analysing the image. The tree height analysis involved using ArcGIS 10.3 software to

ARTICLE INFO

Article history:

Received: 20 October 2023

Accepted: 25 March 2024

Published: 15 August 2024

DOI: <https://doi.org/10.47836/pjst.32.5.12>

E-mail addresses:

syazuani@uitm.edu.my; syazuani226@gmail.com (Syazuani

Mohd Shariff)

edlic@umt.edu.my (Edlic Sathiamurthy)

rohanishahrudin@umt.edu.my (Rohani Shahrudin)

idham@umt.edu.my (Idham Khalil)

sofiyan@umt.edu.my (Mohd Sofiyon Sulaiman)

* Corresponding author

generate the digital surface model (DSM) and digital terrain model (DTM). Validation results indicate an 87% accuracy in the demarcation work. Hence, identification and demarcation of the vegetation communities could be achieved by utilising both tree canopy morphology and tree height data obtained from UAV.

Keywords: BRIS coastal wetland, canopy morphology, *Hibiscus tiliaceus*, UAV method

INTRODUCTION

Coastal BRIS wetlands are very challenging environments to study. They are usually waterlogged and have soft soil and dense trees that restrict accessibility. Moreover, the presence of wild animals, such as poisonous snakes and wild boars, makes such environments potentially hazardous to work in (Hu et al., 2017). Additionally, a sizable workforce is needed, which is inefficient from a cost standpoint and raises the possibility of disrupting delicate plant and animal species (Pinton et al., 2020). Right now, remote sensing presents a viable answer to the problems brought on by this predicament.

Satellites and aircraft have previously been used in remote sensing operations (Thomson et al., 2003). However, their application is sometimes limited due to cloud cover, rigid data acquisition frequency, and cost. In contrast, UAVs or drones could capture high-resolution multi-spectral images even during cloudy weather as they flew at lower altitudes (i.e. below cloud cover), with a high degree of manoeuvrability, easy deployment and flexible data acquisition schedule (Tagle, 2017; Durgan et al., 2020).

The UAV image approach could differentiate various vegetation communities from an aerial perspective based on canopy characteristics (Mahmud et al., 2023). It could facilitate the process of locating wetlands and enhance plant species identification. UAV with RGB (i.e. red-green-blue light spectrum) sensor is typically used for the field sampling. UAVs with near-infrared (NIR) band and Cubert UHD 185 hyperspectral sensors have been used for more detailed vegetation observation and analysis and could distinguish between different species of mangrove trees (Abeyasinghe et al., 2019; Darwin et al., 2014; Durgan et al., 2020).

This paper describes the application of UAV technology to identify and demarcate coastal BRIS wetland vegetation communities. It demonstrated a viable means of aiding wetland vegetation survey work. Vegetation community identification helps evaluate the wetland's health state and monitor vegetation alterations in a target area (Lawley et al., 2016; Zungu et al., 2018; Fang et al., 2021; Alsfield et al., 2010).

METHODOLOGY

Study Area

The study was conducted at the BRIS wetland on the campus of Universiti Malaysia Terengganu, 20 km north of Kuala Terengganu (Figure 1). The wetland is approximately 5.26

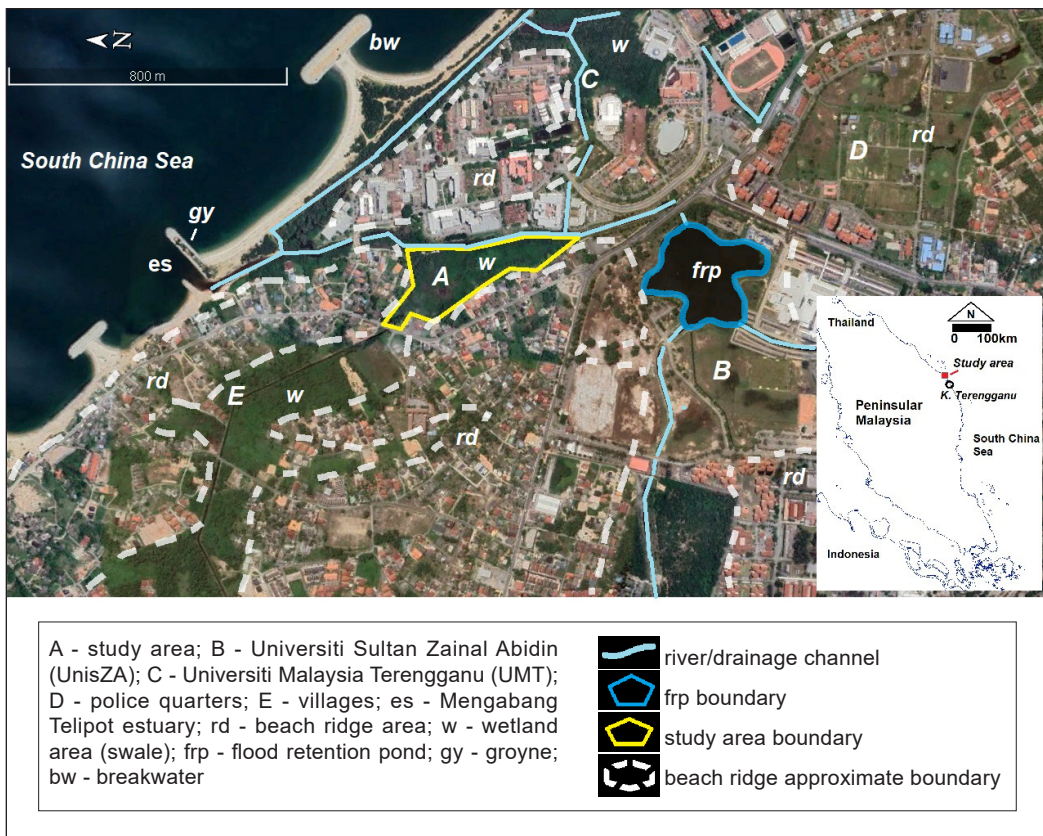


Figure 1. Study area (Source: Google Earth)

ha and is beside a tidal river (Figure 1). It would be flooded when the adjacent rivers overflow, resulting from high upstream flows during the northeast monsoon season and high tide.

Remote Sensing and GIS Technique

The study area was surveyed using an unmanned aerial vehicle (UAV) on July 19, 2022. This UAV method produces high-resolution images compared to aerial photography methods. A DJI Matrice 100 drone was used. Flight missions were conducted 60 meters above ground level (AGL) at 38 km/hr cruising speed. The spatial resolution was 8 cm × 8 cm. The flight paths for the drones were designed in a way similar to mowing a lawn to account for projected overlap, with 75% front-lap and 75% side-lap, respectively (Otto et al., 2018). The Zenmuse X3 camera (<https://www.dji.com/>) mounted on the drone captured true-colour photographs at a resolution of 12.0 megapixels (4000 × 3000 pixels).

Litchi (version 4.0.1; available at <https://flylitchi.com>) was used to construct flight routes and monitor progress while data was collected (Figure 2). Three hundred and seventy-eight individual pictures were digitally merged using the pix4d program (<https://www.pix4d>).

com). It allowed for a realistic 3D mapping and modelling ArcGIS 10 to analyse and interpret the generated image to identify the vegetation communities based on canopy morphology and height. Tree height is the elevation difference between the canopy's top and ground surfaces. For this purpose, a digital terrain model (DTM) and digital surface model (DSM) of the study area are used. The DTM represents the ground surface elevation, and the DSM represent the top canopy surface elevation. DTM and DSM use the National Geodetic Vertical Datum or NGVD as a standard elevation reference system. The Survey and Mapping Department of Malaysia developed this system. Practically, elevations were calculated using a reference level from a surveying benchmark using the NGVD system. While DSM data was acquired from the UAV survey, DTM was generated from secondary data sources from earlier (2007 and 2020) on-the-ground topographic surveys conducted by land surveyors for Universiti Malaysia Terengganu campus development projects.



Figure 2. Flight paths for drone mapping using Litchi software

Vegetation Community Demarcation and Validation

Tree height data aided vegetation identification work as different species have different height ranges. The identified vegetation communities were demarcated using ArcGIS 10.3 software. After that, the demarcation was validated with data collected from the ground truthing work. The vegetation species and community surveyed within the quadrates discussed earlier served as ground-truthing data. It should be noted that the UAV combined with the GIS method identify and demarcates communities based on physical characteristics alone. Hence, it is not meant to demarcate species even though it may be useful under some clear circumstances, e.g., differentiating a coconut tree from a Nypa tree.

Vegetation Sampling

The vegetation sampling was carried out from October 6 to 16, 2022, in two stages: the quadrat establishment and the plant sampling (Figure 3). First, the study area was divided into a grid of 10 m × 10 m cells or quadrates and numbered. Using the random number

generator in Microsoft Excel, 15 quadrants were selected. A ground check was done to ascertain the accessibility of the selected area. The finalised quadrat locations are shown in Figure 4. Plant samples (such as leaves, fruits, and flowers) found in the quadrates were collected and preserved in 70% alcohol in a plastic container. The species were identified by referring to the voucher specimens in the UMT herbarium and expertise.

Figure 3 represents the flowchart of the methodology, comprising study site monitoring, remote sensing, GIS techniques, and vegetation sampling. Quadrates measuring 10 m x 10 m were established using measuring tape and rope. The grid was drawn and numbered on the UAV image using ArcGIS software. Fifteen quadrat locations were selected based on random numbers generated in Microsoft Excel and consideration of field conditions such as accessibility and safety.

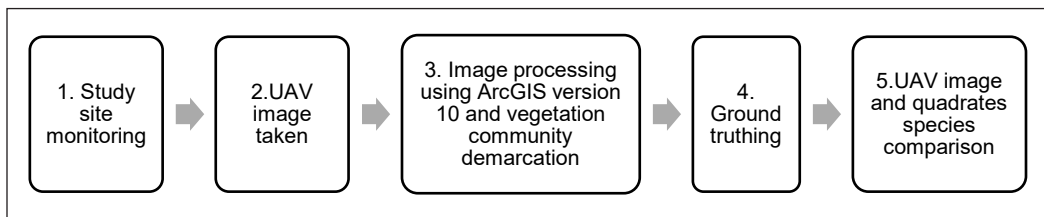


Figure 3. Flowchart of the methodology

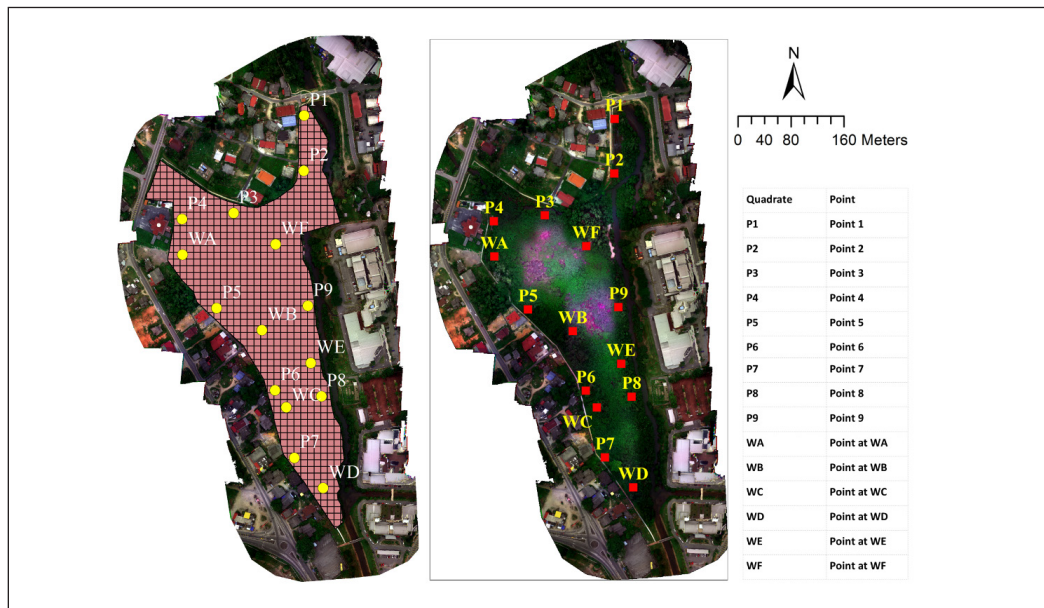


Figure 4. Fifteen quadrants are scattered in the coastal BRIS wetland, Kuala Nerus, Terengganu (Source: UAV Image)

Note. ‘P1–P9’ are just transects, whereas ‘WA–WF’ are transects locations with groundwater monitoring wells. The middle section is inaccessible; hence, no quadrates were assigned. It does not affect the sampling work’s validity as this section has the same type of vegetation as the surrounding quadrates based on visual observation from the top floor of a faculty building located just beside the wetland on the eastern side

RESULTS AND DISCUSSION

Vegetation Canopy Morphology Identification

The study area is dominated by *Hibiscus tiliaceus* (Bebaru) (Table 1; Figure 5). It is commonly found in tropical regions. This pantropical mangrove species usually occurs in coastal ecosystems with high salinity (Santiago et al., 2000). This tree offers a wider canopy with a short trunk sprawling and intertwined branches that form an impenetrable thicker. It posed accessibility challenges during the field survey. The leaf is heart-shaped, 8–20 cm long, wavy, and bright green colour on the upper surface and greyish green and hairy below (Figures 5 and 7). It has a yellowish, short-lived, and fragile flower (Elevitch & Thomson, 2006).

The vegetation canopy morphology was identified using the UAV image (Figure 6). The Bebaru (*H. tiliaceus*) tree canopy morphology differs from the *Acacia mangium* and *Nypa fruticans* canopy (Figure 7). The *A. mangium* leaves were usually large, 11–27 cm long (Figure 7) and 3–10 cm broad and have acute-angled, glabrous and stout branchlets (Maslin &



Figure 5. The *Hibiscus tiliaceus* plant is dominant in the study area

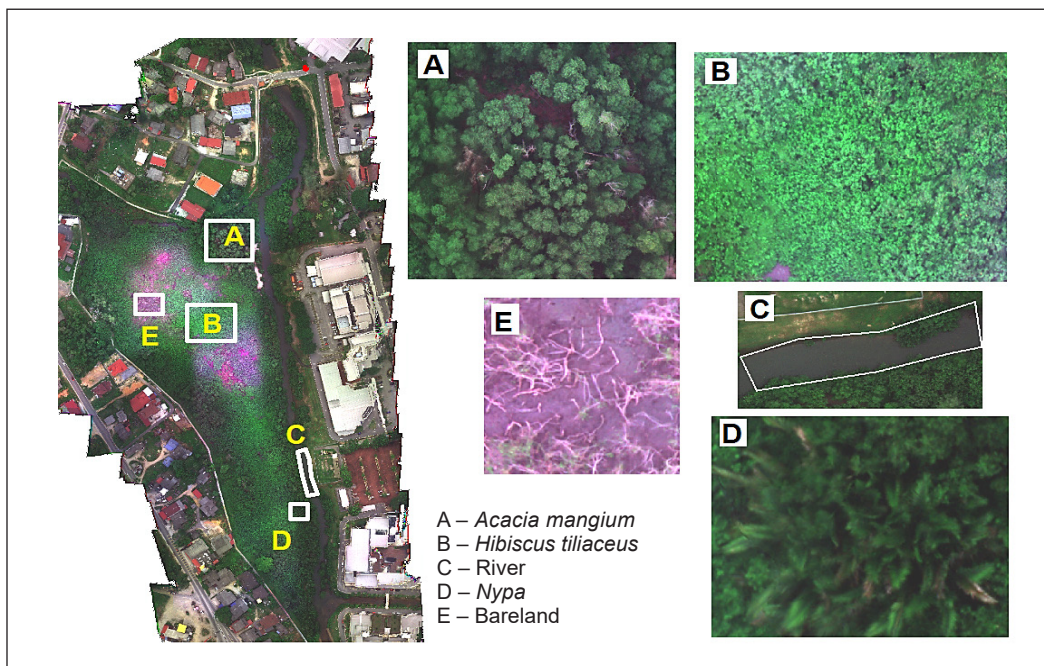


Figure 6. UAV images of canopy morphology of vegetation with location examples in the study area
 Note. Bare land and waterbody (river) compare vegetated and non-vegetated

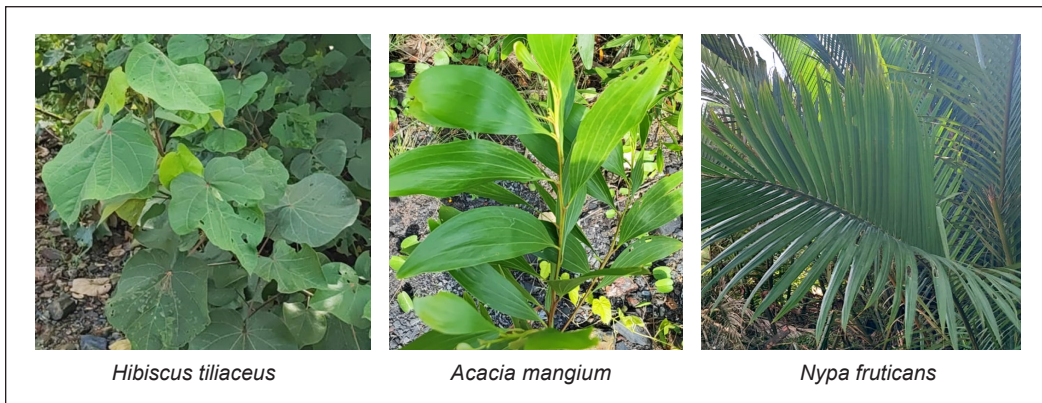


Figure 7. Leaves characteristic

McDonald, 1996). *Nypa fruticans* leaves appear from the ground, lacking a visible upright trunk with a single leaf that can grow up to 8 m (Figure 7) (Zakaria & Aslzaeim, 2010).

Vegetation Height Estimation

The digital surface model (DSM) represents the top of the canopy surface, while the digital terrain model (DTM) shows the ground level in the study area (Figure 8). The DTM was generated from topographic survey data from Universiti Malaysia Terengganu (UMT), whereas the DSM was generated from UAV data. The DTM represents the ground surface

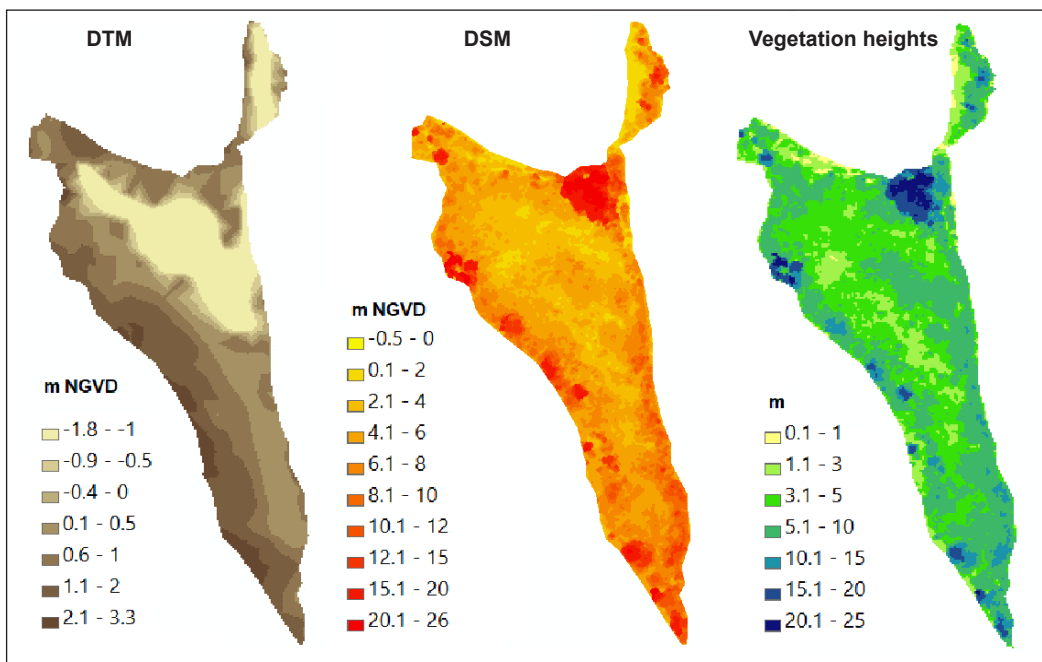


Figure 8. DTM, DSM and vegetation heights

elevations, while the DSM represents the canopy top surface elevations. DTM and DSM elevations used the same vertical datum with reference to the NGVD system; hence, they are comparable. The difference in elevations between DSM and DTM represents the vegetation height, represented by the 'Vegetation Heights' map. This vegetation heights map illustrates the diverse range of plant heights resulting from vegetation species variations. This data aided vegetation community demarcation because different species of vegetation could have different average heights. The Bebaru tree typically grows to 3–10 m in height, whereas *A. mangium* can grow to 25–35 m in height, and the *N. fruticans* tree can reach up to 9 m (Hegde et al., 2013; Zakaria & Alzaeim, 2010). Hence, when an area with certain canopy morphology (Figure 6), e.g. Berbaru, the vegetation heights range, in the case of the study area, 3 to 7 m, would help to further affirm that the area is most likely Berbaru. This approach is not meant to be used in vegetation identification, as other vegetation types could also have the same height range. It is meant to aid in identification work, especially in inaccessible areas.

Vegetation Species Identification from Quadrates Sampling

A vegetation community is the primary or prevailing vegetation type within a specific abiotic setting in a region (Diekmann, 2003). In this study, the community's determination was based on identifying the dominant species, which collectively contributes to the highest coverage within a defined quadrat. Hence, the community in each quadrat was determined based on the species dominance.

The vegetation communities have been identified using aerial photos and data from ground truthing/field surveys. UAV images provided two sorts of information: crown morphology and vegetation height. These data produced variances in canopy morphology, which may be translated into various vegetation communities. The finding was then confirmed using a field survey. A total of 29 species were identified across all quadrants. Based on this data, the dominant species for each quadrat was indicated. The dominant species, represented by the one with the highest coverage in each quadrat, reflected the composition of the community. In this study, if there is more than one dominant species, the dominancy was determined based on the highest crown cover.

The communities' assessment was made based on UAV images. Based on the variations identified by the UAV image, the field surveys identified 13 floristically and physiognomically unique plant groups. Meanwhile, the 29 species mentioned were listed from ground truthing (vegetation sampling), and some did not fit into the recognised plant groups from the aerial images.

The vegetation samples have been incorporated into the analysis conducted in ArcGIS to generate the wetland map, which includes the spatial distribution of the communities (Table 1).

Table 1
Species of vegetation collected in the quadrates

No.	Species	P1	P2	P3	P4	P5	P6	P7	P8	P9	WA	WB	WC	WD	WE	WF
1	<i>Hibiscus tiliceus</i>	\	*	*	*	*	-	*	*	*	*	*	-	*	*	\
2	<i>Acacia mangium</i>	-	-	-	-	-	\	-	\	-	-	\	\	-	-	-
3	<i>Cyperus esculentus</i>	*	\	-	-	-	\	\	-	-	-	-	*	-	-	-
4	<i>Sonneratia alba</i>	\	-	-	-	-	-	-	-	-	-	-	-	-	-	-
5	<i>Melastoma malabathricum</i>	-	-	-	-	-	\	\	-	-	-	-	-	-	-	-
6	<i>Nephrolepis acutifolia</i>	-	-	-	-	-	*	\	-	-	-	-	-	\	-	-
7	<i>Fagraea fragrans</i>	-	-	-	-	-	\	-	-	-	-	-	-	-	-	-
8	<i>Acrostichum aureum</i>	\	-	-	-	-	-	-	-	-	-	-	-	-	-	-
9	<i>Passiflora foetida</i>	\	-	-	-	-	-	-	-	-	-	-	-	-	-	-
10	<i>Casuarina equisetifolia</i>	\	-	-	-	-	-	-	-	-	-	-	-	-	-	-
11	<i>Sphagneticola tribolata</i>	\	-	-	\	-	-	-	-	-	-	-	-	-	-	-
12	<i>Mimosa pudica</i>	\	-	-	-	-	-	-	-	-	-	-	-	-	-	-
13	<i>Flagellaria</i> sp.	-	\	\	\	\	-	\	\	\	\	\	\	\	\	\
14	<i>Annona glabra</i>	-	-	-	-	-	-	-	-	-	-	\	-	-	-	-
15	<i>Catunaregam spinosa</i>	-	-	-	-	\	-	-	-	-	-	-	-	-	-	-
16	<i>Passiflora edulis</i>	-	-	-	\	-	-	-	-	-	-	-	-	-	-	-
17	<i>Zingiber zerumbet</i>	-	-	-	-	-	\	-	-	-	-	-	-	-	-	-
18	<i>Dolichandrone spathacea</i>	\	-	-	-	-	-	-	-	-	-	-	-	-	-	-
19	<i>Derris trifoliata</i>	\	\	\	-	-	-	\	\	-	-	-	-	-	\	-
20	<i>Causonis trifolia</i>	\	\	-	\	-	-	-	-	-	-	\	-	-	\	-
21	<i>Spermacoce exilis</i>	\	-	-	-	-	-	-	-	-	-	-	-	-	-	-
22	<i>Tylophora flexuosa</i>	-	-	-	-	-	-	-	-	-	-	-	-	-	-	\
23	<i>Salacia chinensis</i>	-	-	-	-	-	-	-	-	-	-	-	-	-	-	\
24	<i>Olax imbricata</i>	-	-	\	-	\	-	-	-	-	-	-	-	-	-	\
25	<i>Mikania micrantha</i>	-	-	-	-	\	\	\	-	-	-	\	\	\	-	-
26	<i>Cyperus mindorensis</i>	-	-	-	-	-	-	\	-	-	-	-	-	-	-	-
27	<i>Coccoloba diversifolia</i>	-	-	-	-	-	\	-	-	-	-	-	\	-	-	-
28	<i>Vitex trifolia</i>	-	-	-	-	-	-	-	-	-	-	-	\	-	-	-
29	<i>Melothria pendula</i>	-	-	-	\	-	-	-	-	-	-	-	-	-	-	-

Note. * represents the dominant species in the quadrate, \ represents the species presence in the quadrate

UAV Vegetation Community Validation

Based on their canopy morphology and general height, vegetation communities were demarcated into polygons in ArcGIS. These polygons visually implied the boundaries of various plant species. The quadrat data of vegetation species sampled on the ground were spatially compared with the demarcated community boundaries by overlapping them in

ArcGIS. It must be noted that the purpose of doing this is not to show that UAVs can detect vegetation at the species level. Rather, it is to verify the accuracy of the vegetation community's demarcation. Such demarcation work would contribute to the optimisation of time, cost, and safety when vegetation species surveys are done for large and low-accessible areas. The most dominant species would define the canopy morphology characteristics and general heights. Hence, in Table 1, the dominant species are indicated and used to ascertain the accuracy of the UAV-based demarcation work.

The community was identified by analysing canopy morphology and vegetation height estimation using UAV image analysis with ArcGIS. In this study, the community's determination relied on recognising the dominant species that collectively contributed to the highest coverage within a specified quadrat.

Hibiscus tiliaceus or Bebaru was the most prevalent species in the study area (Table 1). Fifteen quadrants were randomly placed around the wetland area to avoid potential biases in species data collection and enhance the accuracy of vegetation identification within the designated study region (Figure 3). The results of vegetation sampling in each quadrat and the vegetation communities demarcated are shown in Figure 9.

The *H. tiliaceus* species has been distinguished based on the analysis of canopy morphology, specifically the differences in leaf size and arrangement compared to other plant species. However, identifying small-sized plants, such as *Flagellaria* sp., was challenging in the unmanned aerial vehicle (UAV). It is a limitation caused by the spatial resolution of the UAV image. The presence of overlapping foliage can obstruct the visibility of leaves, hence reducing detectability. It is important to note that the image obtained from UAVs demonstrates a tendency towards capturing plants characterised by greater leaf size.

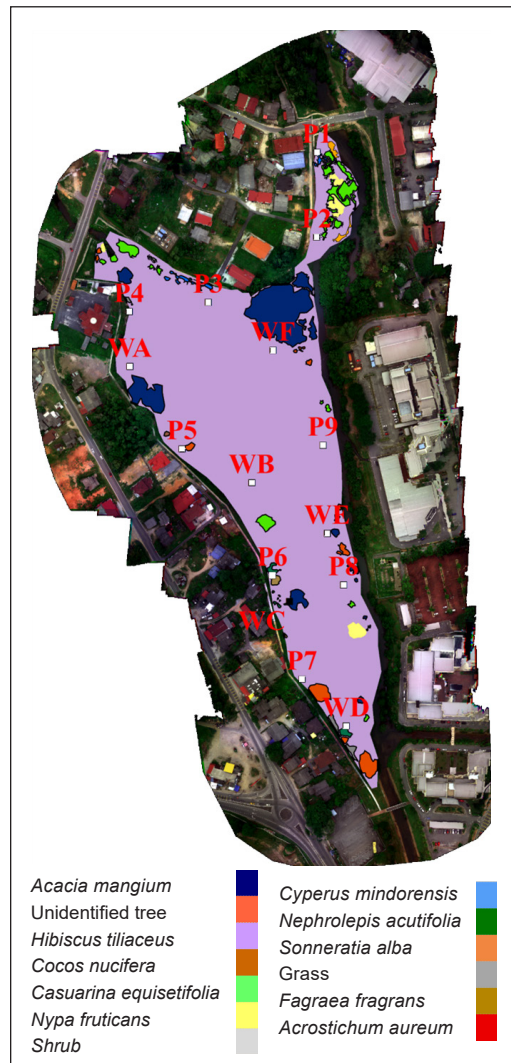


Figure 9. Vegetation communities identified via UAV technique and quadrat locations

Leaf size has a notable impact on the identification of canopy morphology, as evidenced by unimodal patterns of leaf size concerning tree size. It implies leaf size influences canopy morphology (Thomas, 2010; Ollinger, 2011). Consequently, identifying small leaves poses difficulties in UAV image processing for vegetation analysis, potentially influencing the efficiency of demarcating vegetation communities.

The demarcated vegetation communities were compared with the data from the quadrates. It means the result of fieldwork sampling, observation, and the vegetation community demarcation is independently done, making such comparison valid. All the communities were classified into 13 based on their canopy morphology and vegetation height estimation. These two parameters were determined by analysis of UAV images using ArcGIS software.

Of 15 quadrants, two did not match their community (Figure 9). Quadrat P6 has *Nephrolepis acutifolia* as its dominant species but was demarcated under Community 3, which has *H. tiliaceus* as the dominant species. Quadrat WC has *Cyperus esculentus* as its dominant species but was also demarcated under Community 3. These two quadrants were located very close to Community 3; hence, the error could be caused by the inability of the UAV's spatial resolution to discriminate them from *H. tiliaceus*, which dominates Community 3. Overall, 13 out of 15 quadrates indicated that the vegetation community did demarcate the dominant species correctly; hence, the accuracy is about 87%. If more quadrates are used, the reliability of this UAV technique could be further attested.

CONCLUSION

UAV technology could identify and demarcate coastal BRIS wetland vegetation communities. *Hibiscus tiliaceus* was the dominant species in this study region, with 13 quadrates out of 15 displaying its presence. Through the utilisation of ground truthing, it was determined that roughly 87% of the quadrates showed correct identification and demarcation. A higher spatial resolution would produce even better results as the detection depends on the leaf size. This technology is both cost-effective and safe. Ecologists could identify vegetation communities and demarcate their areas as an initial work before actual vegetation species survey work on the ground. The design of survey transects and locations can be more effective as the availability of a vegetation community map would enable targeted work. These benefits would be even more worthwhile when applied to larger areas, especially when they are challenging terrains.

ACKNOWLEDGEMENT

The authors sincerely thank Universiti Malaysia Terengganu for permitting this study. The first author expressed her appreciation to UiTM for supporting this research.

REFERENCES

- Abeyasinghe, T., Simic Milas, A., Arend, K., Hohman, B., Reil, P., Gregory, A., & Vázquez-Ortega, A. (2019). Mapping invasive *Phragmites australis* in the Old Woman Creek estuary using UAV remote sensing and machine learning classifiers. *Remote Sensing*, *11*(11), Article 1380. <https://doi.org/10.3390/rs11111380>
- Alsfeld, A. J., Bowman, J. L., & Deller-Jacobs, A. (2010). The influence of landscape composition on the biotic community of constructed depressional wetlands. *Restoration Ecology*, *18*, 370-378. <https://doi.org/10.1111/j.1526-100X.2009.00628.x>
- Darwin, N., Ahmad, A., & Zainon, O. (2014). The potential of unmanned aerial vehicle for large scale mapping of coastal area. In *IOP Conference Series: Earth and Environmental Science* (Vol. 18, No. 1, p. 012031). IOP Publishing. <https://doi.org/10.1088/1755-1315/18/1/012031>
- Diekmann, M. (2003). Species indicator values as an important tool in applied plant ecology - A review. *Basic and Applied Ecology*, *4*(6), 493-506. <https://doi.org/10.1078/1439-1791-00185>
- Durgan, S. D., Zhang, C., Duecaster, A., Fourney, F., & Su, H. (2020). Unmanned aircraft system photogrammetry for mapping diverse vegetation species in a heterogeneous coastal wetland. *Wetlands*, *40*, 2621-2633. <https://doi.org/10.1007/s13157-020-01373-7>
- Elevitch, C. R., & Thomson, L. A. (2006). *Hibiscus tiliaceus* (beach hibiscus). Species Profiles for Pacific Island Agroforestry.
- Fang, X. S., Liu, S., Chen, W. Z., & Wu, R. Z. (2021). An effective method for wetland park health assessment: A case study of the Guangdong Xinhui National Wetland Park in the Pearl River Delta, China. *Wetlands*, *41*, 1-16. <https://doi.org/10.1007/s13157-021-01418-5>
- Hegde, M., Palanisamy, K., & Yi, J. S. (2013). *Acacia mangium* willd - A fast growing tree for tropical plantation. *Journal of Forest and Environmental Science*, *29*(1), 1-14. <http://dx.doi.org/10.7747/JFS.2013.29.1.1>
- Hu, S., Niu, Z., Chen, Y., Li, L., & Zhang, H. (2017). Global wetlands: Potential distribution, wetland loss, and status. *Science of The Total Environment*, *586*, 319-327. <https://doi.org/10.1016/j.scitotenv.2017.02.001>
- Lawley, V., Lewis, M., Clarke, K., & Ostendorf, B. (2016). Site-based and remote sensing methods for monitoring indicators of vegetation condition: An Australian review. *Ecological Indicators*, *60*, 1273-1283. <https://doi.org/10.1016/j.ecolind.2015.03.021>
- Mahmud, M. S., He, L., Heinemann, P., Choi, D., & Zhu, H. (2023). Unmanned aerial vehicle based tree canopy characteristics measurement for precision spray applications. *Smart Agricultural Technology*, *4*, Article 100153. <https://doi.org/10.1016/j.atech.2022.100153>
- Maslin, B. R., & McDonald, M. W. (1996). *A key to useful Australian Acacias for the seasonally dry tropics*. CSIRO Publishing.
- Ollinger, S. V. (2011). Sources of variability in canopy reflectance and the convergent properties of plants. *New Phytologist*, *189*(2), 375-394. <https://doi.org/10.1111/j.1469-8137.2010.03536.x>
- Otto, A., Agatz, N., Campbell, J., Golden, B., & Pesch, E. (2018). Optimization approaches for civil applications of unmanned aerial vehicles (UAVs) or aerial drones: A survey. *Networks*, *72*(4), 411-458. <https://doi.org/10.1002/net.21818>

- Pinton, D., Canestrelli, A., Wilkinson, B., Ifju, P., & Ortega, A. (2020). A new algorithm for estimating ground elevation and vegetation characteristics in coastal salt marshes from high-resolution UAV-based LiDAR point clouds. *Earth Surface Processes and Landforms*, 45(14), 3687-3701. <https://doi.org/10.3390/rs13224506>
- Santiago, L. S., Lau, T. S., Melcher, P. J., Steele, O. C., & Goldstein, G. (2000). Morphological and physiological responses of Hawaiian *Hibiscus tiliacues* populations to light and salinity. *International Journal Plant Science*, 161(1), 99-106. <https://doi.org/10.1086/314236>
- Tagle, X. (2017). *Study of radiometric variations in unmanned aerial vehicle remote sensing imagery for vegetation mapping*. [MSc thesis]. Lund University, Sweden. <https://lup.lub.lu.se/luur/download?func=downloadFile&recordOid=8918735&fileOid=8918738>
- Thomas, S. C. (2010). Photosynthetic capacity peaks at intermediate size in temperate deciduous trees. *Tree Physiology*, 30(5), 555-573. <https://doi.org/10.1093/treephys/tpq005>
- Thomson, S. J., Smith, L. A., Ray, J. D., & Zimba, P. V. (2003, December). Remote sensing and implications for variable-rate application using agricultural aircraft. In *Ecosystems' Dynamics, Agricultural Remote Sensing and Modeling, and Site-Specific Agriculture* (Vol. 5153, pp. 13-20). SPIE. <https://doi.org/10.1117/12.506053>
- Zakaria, M. R., & Aslzaeim, N. (2010). A demographic study of a mangrove palm, *Nypa fruticans*. *Scientific Research and Essays*, 5(24), 3896-3902.
- Zungu, N. S., Mostert, T. H., & Mostert, R. E. (2018). Plant communities of the uMlalazi Nature Reserve and their contribution to conservation in KwaZulu-Natal. *Koedoe* 60(1), 1-14. <https://doi.org/10.4102/koedoe.v60i1.1449>

Comparative Analysis of Filtering Techniques for AGV Indoor Localization with Ultra-Wideband Technology

Nuradlin Borhan¹, Izzati Saleh¹ and Wan Rahiman^{1,2,3*}

¹*School of Electrical and Electronic Engineering, Universiti Sains Malaysia Engineering Campus, 14300 Nibong Tebal, Malaysia*

²*Cluster of Smart Port and Logistic Technology (COSPALT), Universiti Sains Malaysia Engineering Campus, 14300 Nibong Tebal, Malaysia*

³*Daffodil Robotics Lab Department of Computer Science and Engineering, Daffodil International University, Bangladesh*

ABSTRACT

This paper investigates the filtering techniques to enhance the accuracy of indoor localization for Autonomous Guided Vehicles (AGVs) using Ultra-Wideband (UWB) technology. A comprehensive comparative analysis of various filtering approaches, including the Kalman Filter (KF), Moving Average Filter (MA), Savitzky-Golay Filter (SG), Weighted Average Filter (WAF), and their combinations, are conducted. The primary focus of this paper is the integration of a Moving Average-Kalman Filter (MAKF) with an extended window size of 201. Experimental findings reveal significant performance differences among these filtering techniques. The most effective approach is the MAKF technique, achieving an accuracy of 85.13% and the lowest path deviation of 0.17 meters. Conversely, the MA exhibits the lowest accuracy at 68.83%. Notably, the WAF attains an accuracy of 72.46% but exhibits a significantly higher path deviation of 2.65 meters compared to 1.45 meters of the MA filtering technique. The proposed MAKF acknowledged for its ability to effectively reduce noise with real-time responsiveness, represents a significant advancement in AGV indoor localization techniques.

Keywords: AGV, indoor localization, Kalman filter, moving average, Savitzky-golay, UWB

ARTICLE INFO

Article history:

Received: 22 November 2023

Accepted: 07 March 2024

Published: 15 August 2024

DOI: <https://doi.org/10.47836/pjst.32.5.13>

E-mail addresses:

nuradlinnadhira@student.usm.my (Nuradlin Borhan)

izzatisaleh@student.usm.my (Izzati Saleh)

wanrahiman@usm.my (Wan Rahiman)

* Corresponding author

INTRODUCTION

Indoor localization poses intricate challenges for Autonomous Guided Vehicles (AGVs) operating within industrial environments. Precise AGV positioning is imperative for

optimizing operational efficiency and ensuring safe navigation (Liu et al., 2022). Unlike outdoor scenarios where the Global Positioning System (GPS) is readily available, indoor environments lack consistent satellite-based positioning and are often cluttered with obstacles and sources of interference.

Integrating Ultra-Wideband (UWB) technology with advanced filtering techniques has emerged as a promising solution to address these challenges. UWB technology, known for its ability to provide accurate distance measurements (Flueratoru et al., 2020) and resistance to signal reflections, is a key enabler for indoor localization. However, in an indoor environment, interference can introduce noise and inaccuracies into the raw UWB data (Borhan et al., 2023), necessitating filtering techniques to enhance accuracy.

This research aims to comprehensively evaluate and compare various filtering methods, including the established Kalman Filter (KF), the straightforward Moving Average Filter (MA), the polynomial-based Savitzky-Golay Filter (SG), and the Weighted Average Filter (WAF). This paper also explores the integration of these filters and their impact on AGV indoor localization.

The primary objective of this research is to provide insights into the effectiveness of filtering techniques in reducing noise and improving AGV positioning accuracy within an indoor environment. This study is supported by conducting experiments involving AGV platforms equipped with UWB hardware in an indoor scenario.

Furthermore, this research introduces the Moving Average-Kalman Filter (MAKF) with a large window size of 201 as an innovative approach for balancing noise reduction and real-time responsiveness, crucial for AGV operations in dynamic environments. The decision to employ a window size of 201 reflects a deliberate choice to capitalize on the advantages of an odd window size. This choice ensures that important dynamic patterns in the data are well-preserved and contribute to the overall robustness of the filtering processes. Moreover, a larger window size helps reduce the impact of fluctuations or noise in the input data.

Filtering Techniques for Indoor Localization

Numerous filtering methods have been explored to enhance the accuracy of AGV indoor localization. KF has been a prominent choice due to its ability to assimilate noisy measurements and provide state estimates with optimal accuracy. Yi et al. (2021) have demonstrated the efficacy of KF in AGV positioning. MA, known for its relatively high accuracy and low computational overhead, has also been investigated (Dangkham, 2018). MA filters offer real-time responsiveness, making them suitable for AGV applications in dynamic environments. However, MA alone may exhibit inaccuracies in speed measurement due to factors such as multipath effects and environmental interferences (Fakhoury & Ismail, 2023).

SG has been applied to smoothen UWB data (Laanen et al., 2023). SG filters use polynomial regression to eliminate high-frequency noise components while preserving underlying trends. This characteristic makes them appealing for certain AGV scenarios. WAF has been introduced for its ability to improve the accuracy of indoor localization with lower computation complexity (Cheng et al., 2011). WAF filters allow practitioners to adapt filter behavior to specific AGV localization requirements by assigning varying weights to data points.

Ultra-Wideband Technology for Indoor Localization

Li et al. (2019) have explored the integration of UWB hardware into AGV systems to retrieve the position of the AGV. UWB localization system generally involves anchors, which are stationary UWB transceiver modules placed in known positions throughout the environment and a tag, which is a transceiver module installed on the AGV (Bae et al., 2022). Moreover, the UWB technology possesses the capability to execute two-way-ranging (TWR) (Wei et al., 2018), a process that involves the precise measurement of time-of-flight (TOF) from the tag to the anchor, subsequently multiplied by the speed of light.

Table 1 shows the comparison of filtering techniques through the existing literature. Notably, a lack of attention is dedicated to utilizing the MA filter for AGV indoor localization, as highlighted in Table 1, specifically in real-time applications—a critical consideration for AGVs operating dynamically in indoor environments. This research gap raises fundamental questions about the untapped potential of the MA filter in improving AGV indoor positioning accuracy, noise reduction, and real-time responsiveness, as currently, there are minimal applications of the MA filter. The motivation for this study is to comprehensively address this conspicuous research gap by conducting a thorough assessment of the suitability of the MA filter and exploring its potential integration with the KF to fill this significant gap in academic research.

METHODS

The MAKF combines the KF and MA filter characteristics with a distinctive window size of 201 data points. It focuses on effectively reducing noise while preserving dynamic patterns. The algorithmic details of MAKF were also discussed, providing insights into its filtering methods.

Moving Average-Kalman Filter (MAKF)

This paper proposed the MAKF technique, which integrates the KF and MA filter characteristics, as shown in Figure 1. Sadowski and Spachos (2019) found that Kalman has better accuracy, while MA has better precision. Therefore, the MAKF in this research differs from the conventional method by integrating the recursive, optimal estimation

Table 1
Comparison of filtering techniques

References	KF	MA	SG	Other filtering techniques		AGV	UWB	Simulation	Real-time application	Reason for choosing the technique
Li et al., 2019	✓	-	-	Weighted Fusion Technique	✓	✓	-	-	To reduce the impact of positioning in line-of-sight (LOS) and non-line-of-sight (NLOS) states. To mitigate multipath fading in indoor wireless positioning.	
Wisammongkol et al., 2019	-	-	-	WAF	-	-	-	✓	Its ability to smooth data points without distorting the signal tendency.	
Bergmann et al., 2020	-	-	✓	-	-	-	✓	-	It effectively removes random noise from the collected spatial data obtained from the IPS. Its lightweight and accurate performance.	
Gyulai et al., 2020	-	-	✓	-	-	-	✓	-	It helps to smooth out the data and reduce noise or fluctuations in the signal.	
Singh et al., 2020	-	-	✓	-	-	-	-	-	It helps to improve the accuracy of the location results obtained from the UWB technology.	
Rykala et al., 2020	-	✓*	-	-	-	✓	-	✓	Its effectiveness in addressing the challenges of NLOS environments and improving positioning accuracy.	
Le Minh & Xuan, 2021	✓	-	-	-	✓	✓	-	-	Its ability to combine and optimize the UWB positioning and U-PDR techniques enhances the accuracy of indoor localization.	
Lee et al., 2021	✓	-	-	-	✓	✓	-	✓	To provide better location accuracy in indoor environments with systematic noise and inadequate measuring information.	
Yi et al., 2021	-	-	-	Adaptive Kalman filter	✓	✓	-	✓	To improve the positioning accuracy in NLOS environments.	
Zhou et al., 2021	-	-	-	Standard Kalman filter based on expectation maximization (SKF-EM)	✓	✓	-	✓		

Table 1 (continue)

References	KF	MA	SG	Other filtering techniques	AGV	UWB	Simulation	Real-time application	Reason for choosing the technique
Qiang et al., 2021	-	-	-	Fuzzy Kalman filter	✓	-	-	✓	To handle the large fluctuation caused by NLOS factors in complex indoor environments.
Li et al., 2022	✓	-	-	-	✓	-	-	✓	To correct ranging errors caused by UWB multipath interference.
Guo et al., 2022	-	-	-	KF + Dilution of Precision (DOP)	-	✓	-	✓	To enhance UWB positioning accuracy in narrow spaces.
Sofianidis et al., 2022	-	✓*	-	Low pass filter	-	✓	-	✓	To improve the accuracy of the UWB-based localization system.
Alonge et al., 2022	-	-	-	Kalman-Bucy filter (KBF)	-	✓	-	✓	To deal with the velocity estimation problem in UWB localization.
Mehrabian & Ravanmehr, 2023	-	-	-	Weight-Based Optimization (WBO)	-	-	-	✓	To optimize raw RSSI values and enhance the accuracy of the IPS.

Note. * Refers to reference wherein the MA filter has been applied

```

1: Input:  $input_{MAKF}$  – Noisy measurement data matrix
2: Output:  $output_{MAKF}$  – Smoothed estimate data matrix
3: Initialize variables:
4:  $N \leftarrow$  Window size for moving average
5: Apply Kalman Filter to  $input_{MAKF}$  to obtain  $kalman\_output$ 
6: for  $i \leftarrow 1$  to number of rows in  $kalman\_output$  do
7:   Calculate  $avg$  (moving average):
8:    $avg \leftarrow$  Moving average of  $kalman\_output(1 : i, :)$  over window size  $N$ 
9:    $signal \leftarrow kalman\_output(i, :)$ 
10:   $avg \leftarrow avg + signal$ 
11:  Append  $avg$  to  $output_{MAKF}$ 
12: end for
    
```

Figure 1. Moving Average-Kalman filter algorithm

capabilities of the KF with the simple, non-recursive smoothing features of the MA filter to mitigate the limitations of each method and provide a more effective solution for specific applications such as AGV indoor localization.

The MAKF algorithm begins with noisy measurement data, $input_{MAKF}$. The algorithm's output, labeled $output_{MAKF}$, represents a smoothed version of the measurement data, providing a more accurate representation of the AGV's position.

The first step in the MAKF algorithm is initializing the parameters, where the window size for the moving average, denoted as N , is defined. This window size determines the extent of smoothing applied to the noisy data. A larger N value results in more extensive smoothing, while a smaller value retains more of the dynamics of the original data.

Subsequently, KF is applied to the $input_{MAKF}$ data to obtain $kalman_output$. The KF component of the MAKF processes the raw measurements and utilizes a prediction correction algorithm to estimate the state of the AGV, compensating for noise and uncertainties.

For each data point in $kalman_output$, the algorithm calculates a moving average, or avg , using a rolling window of size N . This moving average operation acts as a smoothing mechanism, reducing the influence of noisy fluctuations and enhancing the overall precision of the data. In this step, the algorithm ensures that the filtered signal retains its real-time responsiveness while mitigating noise and inaccuracies.

Finally, the average value, representing the smoothed estimate, is combined with the KF-processed signal to create an optimized estimate of the AGV's position. This updated estimate is then appended to the $output_{MAKF}$ data matrix, ensuring that the final output reflects the improved accuracy achieved through the MAKF technique.

EXPERIMENTAL SETUP

The experiments were conducted in a controlled indoor environment to simulate complex industrial settings, such as manufacturing plants and warehouses. The environment consists of a 6.47 meter \times 8 meter area with various obstacles, representing a challenging scenario for AGV navigation. The experimental environment can be seen in Figure 2.

UWB technology was utilized to gather localization data. The UWB technology employed in this research is the DWM1001-Development Board (Figure 3), which consists of anchor nodes strategically placed throughout the environment and an AGV equipped with a UWB tag. The specifications of the DWM1001 are outlined in Table 2. In this experiment, the UWB updates every 0.1 sec.

The AGV utilized in this study is a compact indoor mobile robot designed for robotics research and education. It is equipped with sensors for navigation and safety, including encoders, and a laser scanner for obstacle detection and avoidance. The AGV is shown in Figure 4.

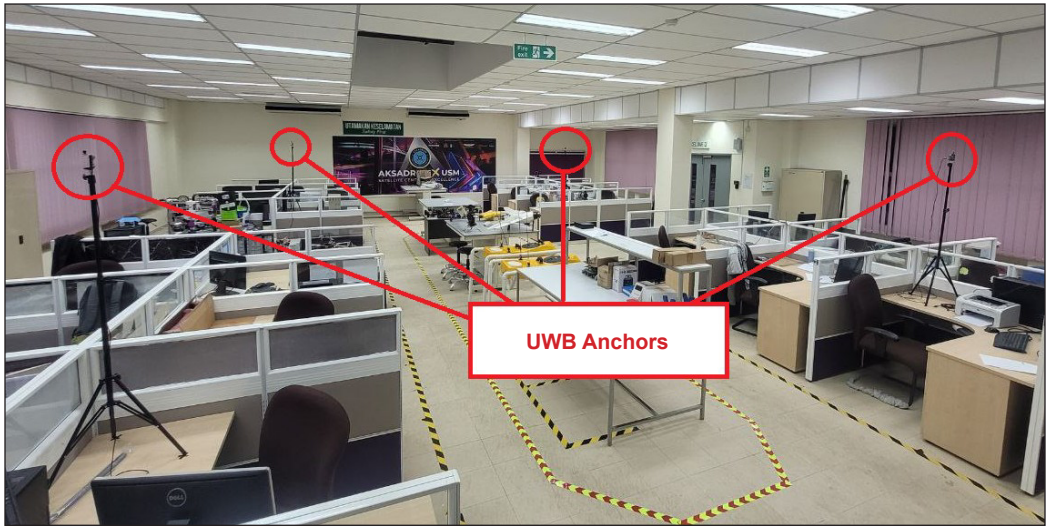


Figure 2. The experimental environment set up in a cluttered space

Table 2
DWM1001-Development board specifications

Specifications	
Accuracy range	Within 10 cm
Line-of-sight range	60 m
Data rate	6.8 Mbps
Supply voltage	3.6 V–5.5 V
Size	54 mm × 43 mm
UWB Channel 5	6.5 GHz



Figure 3. DWM1001-Development Board

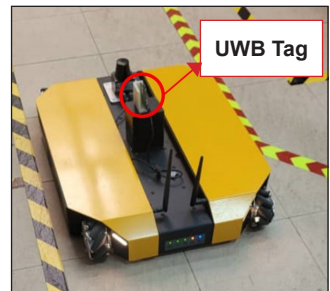


Figure 4. AGV equipped with UWB tag

The data collection procedure involved the AGV navigating the predefined route within the experimental environment. The predefined route, which is also the reference trajectory, is a straight path starting at (2,0) meter and ending at (2,8) meter, where the coordinate origin (0,0) meter is based on Anchor 2.

As the AGV moved, UWB signals were exchanged between the AGV equipped with the UWB tag and the anchor nodes. These signals were used to calculate the AGV’s position and trajectory. Raw UWB data obtained during the experiments were subjected to preprocessing, which included data filtering and noise reduction to enhance the accuracy and reliability of the collected data.

Following the collection and preprocessing of the raw UWB data, the AGV operates in accordance with the reference trajectory derived from the UWB data subjected to filtration by five distinct filtering techniques: KF, MA filter, SG filter, WAF, and MAKF. For more information on these filtering techniques’ working mechanisms and algorithms, please

refer to the Appendix. The movement of the AGV is executed in real time rather than in a simulated environment. This real-time execution enables a comprehensive comparative assessment of the performance of the filtering techniques. Figure 5 displays the overall experimental setup.

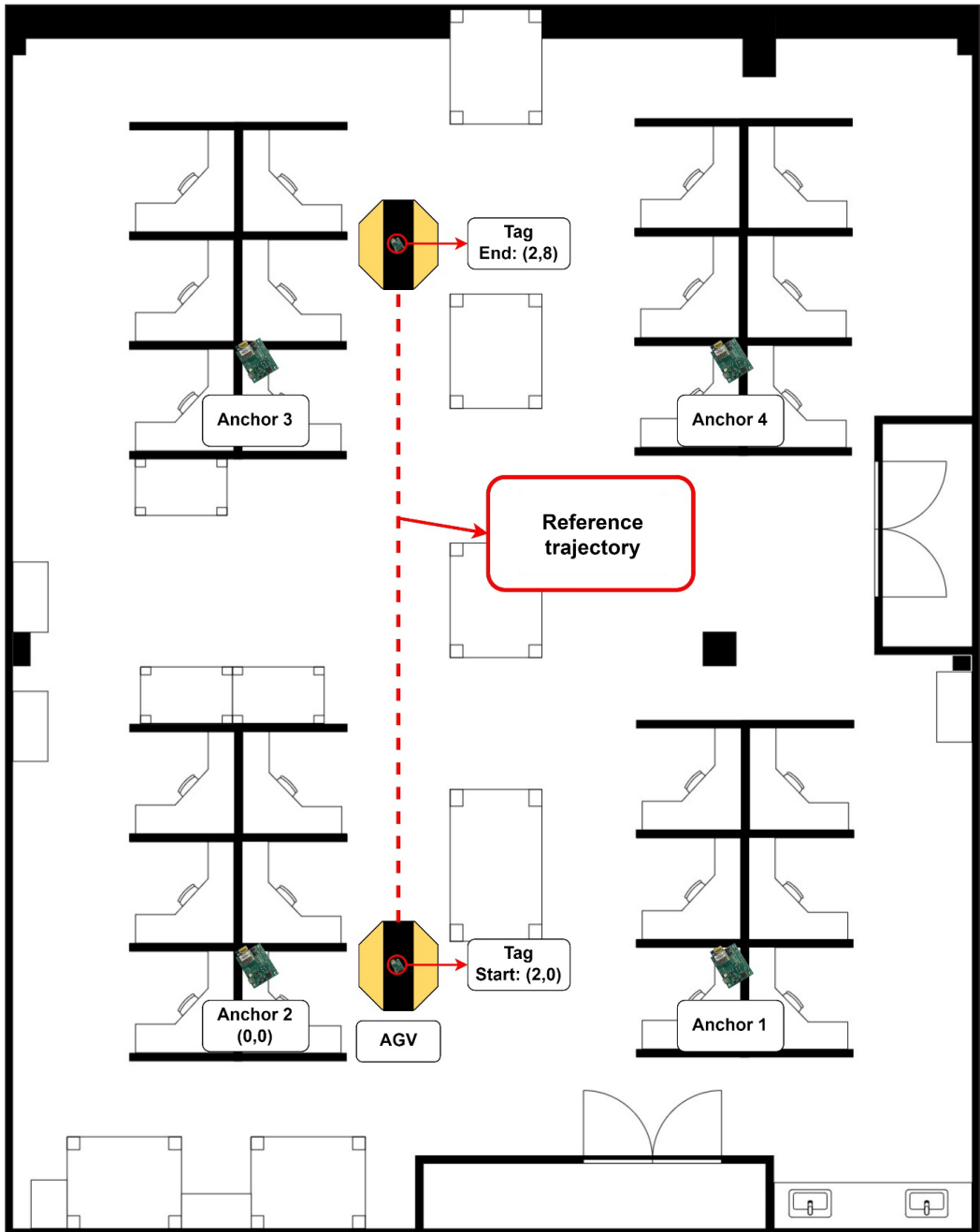


Figure 5. Overall experimental setup in an indoor environment

RESULTS AND DISCUSSION

The study provides a comprehensive analysis of the trajectories of the AGV employing various filtering techniques. These techniques offer varying trade-offs between trajectory smoothness and alignment with a reference path, as visually illustrated in Figure 6. The AGV employing the KF technique showcases generally accurate positioning, although it exhibits noticeable fluctuations, resulting in a lack of smoothness. In contrast, the AGV utilizing the MA filtering technique exhibits a smoother trajectory but deviates from the reference trajectory. It is important to note that, despite the visual deviation, smoothness is a desirable attribute for AGV operations in some contexts.

Among the analyzed techniques, the AGV trajectory employing the SG filtering technique stands out. Figure 6(c) shows that this method delivers a trajectory that aligns

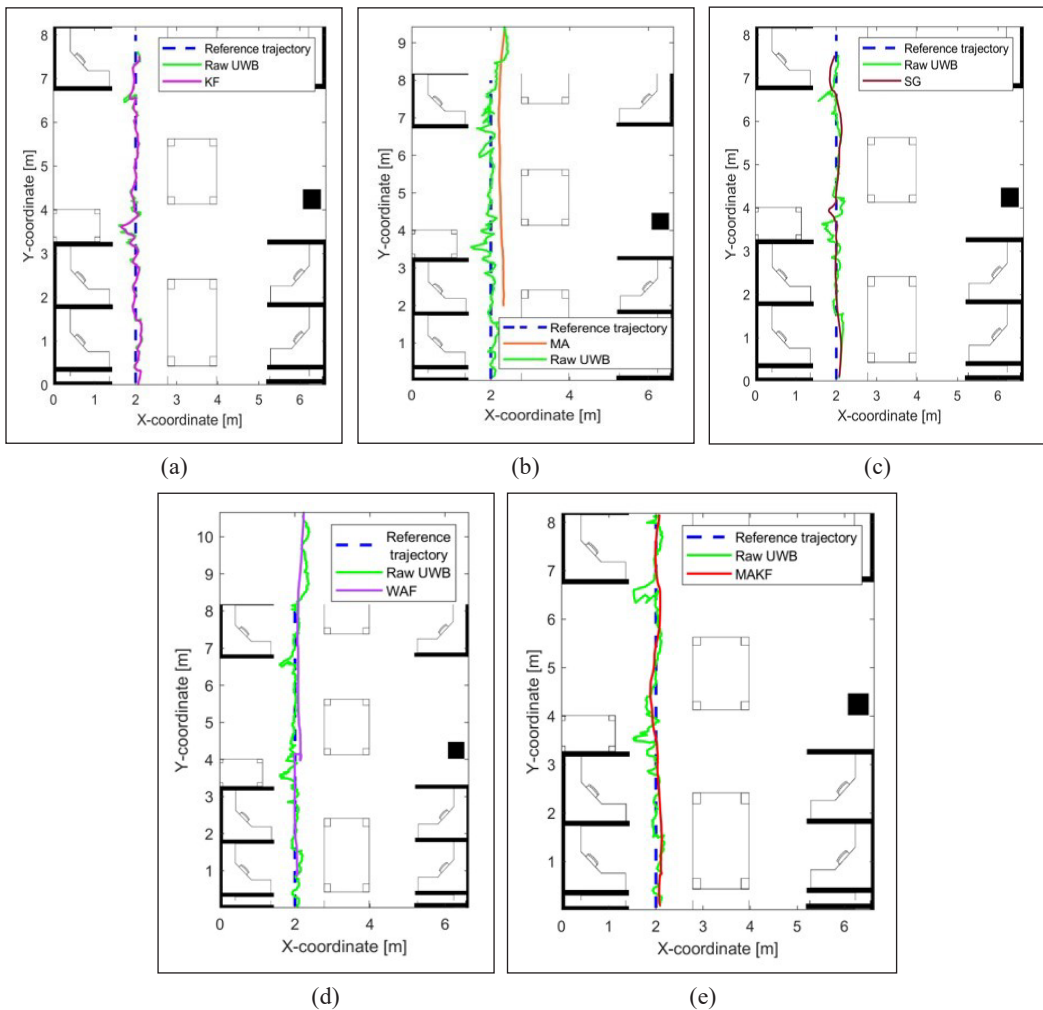


Figure 6. Real-time AGV trajectory using different filtering techniques: (a) KF, (b) MA, (c) SG, (d) WAF, and (e) MAKF

closely with the reference path, offering the best balance between trajectory accuracy and smooth movement. It is important to highlight that the visual results reflect the actual movement of the AGV and are crucial in selecting the most suitable filtering technique.

Moreover, Figure 6(d) displays the AGV’s trajectory using the WAF technique. While it provides exceptionally smooth movement, the deviation from the reference trajectory is more pronounced than with the SG filter. This trade-off between smoothness and trajectory accuracy emphasizes the importance of selecting the filtering technique that aligns with specific AGV requirements.

In this comparative analysis, the proposed MAKF technique, as displayed in Figure 6(e), emerges as the most promising solution. The movement of the AGV is notably smoother compared to the conventional KF method, while it still closely follows the reference trajectory, distinguishing it from the MA filtering technique alone.

The analysis extends to key metrics such as path deviation, MSE, RMSE, and accuracy. These metrics provide a quantitative basis for evaluating the performance of the filtering techniques. Figure 7 displays the path deviation results for different filtering techniques, while Table 3 shows the accuracy, MSE and RMSE of the filtering techniques. As displayed in Figure 7, the KF method presents a low path deviation at 0.49 meters, emphasizing its accuracy in positioning. In contrast, the MA filter exhibits a higher path deviation of 1.45 meters, implying less precision in its positioning estimates.

The SG filter and WAF technique demonstrate path deviations of 0.48 meters and 2.65 meters, respectively, signifying their capability to provide accurate positioning with varying degrees of smoothness. However, the most remarkable result in the proposed MAKF with a path deviation of 0.17 meters indicates significant improvements in AGV indoor localization

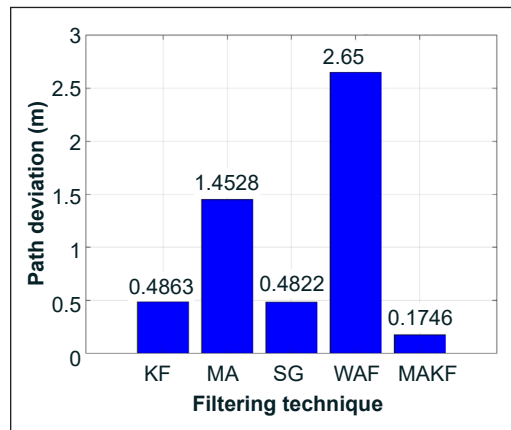


Figure 7. Path deviation results for different filtering techniques

Table 3
MSE, RMSE and accuracy results for different filtering techniques

Filtering Techniques	MSE (m)	RMSE (m)	Accuracy (%)
KF	2.0438	1.4296	82.0375
MA	6.1544	2.4808	68.8305
SG	2.244	1.4980	81.1786
WAF	4.8049	2.1920	72.4593
MAKF	1.4004	1.1834	85.1319

precision. The effectiveness of the MAKF technique in improving accuracy is supported by its RMSE of 1.18 meters and an MSE of 1.4, the lowest among the techniques evaluated.

The results obtained reveal a close relationship between accuracy, MSE and RMSE. KF demonstrates an accuracy of 82.04% with an MSE of 2.04 meters and RMSE of 1.43 meters, highlighting its effectiveness in AGV positioning. Conversely, the MA filter presents a lower accuracy of 68.83% with a higher RMSE of 2.48 meters and MSE of 6.15 meters, indicating less reliable positioning.

The SG filter strikes a balance with an accuracy of 81.18% and an RMSE of 1.5 meters, signifying the trade-off between accuracy and precision. Its MSE of 2.24 meters suggests a moderate level of accuracy in the AGV positioning compared with other filtering techniques. WAF delivers an accuracy of 72.46% but comes with a higher value of MSE and RMSE, which are 4.8 and 2.19 meters, respectively, again highlighting the intricate relationship between accuracy and precision.

The proposed MAKF excels in both accuracy and precision. With a high accuracy of 85.13% and the lowest RMSE value among the evaluated techniques at 1.18 meters, the MAKF establishes itself as a promising choice for applications demanding high accuracy and minimal positioning errors. Additionally, the MAKF recorded the lowest value of MSE, which was 1.4 meters. The low value of MSE indicates that the estimation of the filter is closer to the true positions, which further supports the efficacy of the MAKF. The comparison reveals the advantages of merging the KF and MA filters, effectively addressing their limitations.

The choice of filtering technique significantly influences AGV operations, particularly in complex indoor environments where safety and efficiency are paramount. These implications extend to various industrial sectors, where AGVs are critical in automation and logistics.

CONCLUSION

The findings presented in this study revealed significant variations in performance among the assessed filtering techniques. The highlight of this research was the introduction and assessment of MAKF, which outperformed all other techniques with an accuracy of 85.13%, an MSE and an RMSE of 1.4 and 1.18 meters, respectively. Additionally, the filter recorded the lowest value for path deviation, which was 0.17 meters. MAKF effectively improved the AGV indoor localization, combining the advantages of accuracy, minimal positioning errors, and real-time responsiveness. In contrast, the MA filter exhibited the lowest accuracy at 68.83%, and the WAF, reaching an accuracy of 72.46%, displayed a significantly higher path deviation of 2.65 meters.

These results carry significant implications for AGV indoor localization. The demonstrated effectiveness of MAKF, especially with extended window size, presents

a promising solution to tackle challenges related to noise and dynamic environments in AGV operations. This study provides practical guidance for researchers and practitioners in automation and logistics, aiding filter selection and parameter optimization. Such guidance ultimately enhances the efficiency and safety of AGV applications in diverse industrial and logistical scenarios.

ACKNOWLEDGEMENT

This work was sponsored by Collaborative Research in Engineering, Science and Technology Center (CREST) (grant no.: 304/PELECT/6050423/C121).

REFERENCES

- Alonge, F., Cusumano, P., D’Ippolito, F., Garraffa, G., Livreri, P., & Sferlazza, A. (2022). Localization in structured environments with UWB Devices without acceleration measurements, and velocity estimation using a Kalman–Bucy filter. *Sensors*, 22(16), Article 6308. <https://doi.org/10.3390/s22166308>
- Bae, K., Son, Y., Song, Y. E., & Jung, H. (2022). Component-wise error correction method for UWB-based localization in target-following mobile robot. *Sensors*, 22(3), Article 1180. <https://doi.org/10.3390/s22031180>
- Bergmann, J., Gyulai, D., Morassi, D., & Váncza, J. (2020). A stochastic approach to calculate assembly cycle times based on spatial shop-floor data stream. *Procedia CIRP*, 93, 1164–1169. <https://doi.org/10.1016/j.procir.2020.03.052>
- Borhan, N., Saleh, I., Yunus, A., Rahiman, W., Novaliendry, D., & Risfendra. (2023). Reducing UWB indoor localization error using the fusion of Kalman filter with moving average filter. In *2023 IEEE International Conference on Automatic Control and Intelligent Systems (I2CACIS)* (pp. 55-59). IEEE Publishing. <https://doi.org/10.1109/I2CACIS57635.2023.10193663>
- Cheng, L., Wu, C. D., & Zhang, Y. Z. (2011). Indoor robot localization based on wireless sensor networks. *IEEE Transactions on Consumer Electronics*, 57(3), 1099–1104. <https://doi.org/10.1109/TCE.2011.6018861>
- Dangkham, P. (2018, June 28-30). The smoothing filter for mobile augmented reality using the moving average. In *Proceedings of 2018 the 8th International Workshop on Computer Science and Engineering (WCSE)* (pp. 497–501). Bangkok, Thailand.
- Fakhoury, S., & Ismail, K. (2023). Improving pedestrian safety using ultra-wideband sensors: A study of time-to-collision estimation. *Sensors*, 23(8), Article 4171. <https://doi.org/10.3390/s23084171>
- Flueratoru, L., Wehrli, S., Magno, M., & Niculescu, D. (2020). On the energy consumption and ranging accuracy of ultra-wideband physical interfaces. In *GLOBECOM 2020-2020 IEEE Global Communications Conference* (pp. 1-7). IEEE Publishing. <https://doi.org/10.1109/GLOBECOM42002.2020.9347984>
- Guo, Y., Li, W., Yang, G., Jiao, Z., & Yan, J. (2022). Combining dilution of precision and Kalman filtering for UWB positioning in a narrow space. *Remote Sensing*, 14(21), 1–17. <https://doi.org/10.3390/rs14215409>
- Gyulai, D., Pfeiffer, A., & Bergmann, J. (2020). Analysis of asset location data to support decisions in production management and control. *Procedia CIRP*, 88, 197–202. <https://doi.org/10.1016/j.procir.2020.05.035>

- Laanen, R., Nasri, M., van Dijk, R., Baratchi, M., Koutamanis, A., & Rieffe, C. (2023). *Automated classification of pre-defined movement patterns: A comparison between GNSS and UWB technology*. ArXiv Preprint. <https://doi.org/https://doi.org/10.48550/arXiv.2303.07107>
- Le Minh, T., & Xuan, D. T. (2021). Applying Kalman filter to UWB positioning with DS-TWR method in LOS/NLOS scenarios. In *2021 International Symposium on Electrical and Electronics Engineering (ISEE)* (pp. 95-99). IEEE Publishing. <https://doi.org/10.1109/ISEE51682.2021.9418707>
- Lee, G. T., Seo, S. B., & Jeon, W. S. (2021). Indoor localization by kalman filter based combining of UWB-positioning and PDR. In *2021 IEEE 18th Annual Consumer Communications & Networking Conference (CCNC)* (pp. 1-6). IEEE Publishing. <https://doi.org/10.1109/CCNC49032.2021.9369588>
- Li, J., Xue, J., Fu, D., Gui, C., & Wang, X. (2022). Position estimation and error correction of mobile robots based on UWB and multisensors. *Journal of Sensors*, 2022(1), Article 7071466. <https://doi.org/10.1155/2022/7071466>
- Li, P., Xu, Y., Shen, T., & Bi, S. (2019). INS/UWB integrated AGV localization employing Kalman filter for indoor LOS/NLOS mixed environment. In *2019 International Conference on Advanced Mechatronic Systems (ICAMechS)* (pp. 294-298). IEEE Publishing. <https://doi.org/10.1109/ICAMechS.2019.8861620>
- Liu, X., Wang, G., & Chen, K. (2022). High-precision vision localization system for autonomous guided vehicles in dusty industrial environments. *NAVIGATION: Journal of the Institute of Navigation*, 69(1), 1-21.
- Mehrabian, H., & Ravanmehr, R. (2023). Sensor fusion for indoor positioning system through improved RSSI and PDR methods. *Future Generation Computer Systems*, 138, 254–269. <https://doi.org/10.1016/j.future.2022.09.003>
- Qiang, G., Yufeng, M., Liudan, X., Xufeng, Z., & Penghao, L. (2021). UWB/INS location via fuzzy Kalman filtering for electrical apparatuses in complex indoor environment. In *2021 6th International Conference on Control and Robotics Engineering (ICCRE)* (pp. 118-122). IEEE Publishing. <https://doi.org/10.1109/ICCRE51898.2021.9435659>
- Rykała, Ł., Typiak, A., & Typiak, R. (2020). Research on developing an outdoor location system based on the ultra-wideband technology. *Sensors*, 20(21), 1–24. <https://doi.org/10.3390/s20216171>
- Sadowski, S., & Spachos, P. (2019). Optimization of BLE beacon density for RSSI-based indoor localization. In *2019 IEEE International Conference on Communications Workshops (ICC Workshops)* (pp. 1-6). IEEE Publishing. <https://doi.org/10.1109/ICCW.2019.8756989>
- Singh, J., Dhuheir, M., Refaey, A., Erbad, A., Mohamed, A., & Guizani, M. (2020). Navigation and obstacle avoidance system in unknown environment. In *2020 IEEE Canadian Conference on Electrical and Computer Engineering (CCECE)* (pp. 1-4). IEEE Publishing. <https://doi.org/10.1109/CCECE47787.2020.9255754>
- Sofianidis, I., Serasidis, V., Konstantakos, V., & Siozios, K. (2022). Application of energy efficient filtering for UWB indoor positioning. In *2022 11th International Conference on Modern Circuits and Systems Technologies (MOCASST)* (pp. 1-4). IEEE Publishing. <https://doi.org/10.1109/MOCASST54814.2022.9837493>

- Wei, Z., Lang, Y., Yang, F., & Zhao, S. (2018, May 25-27). A tof localization algorithm based on improved double-sided two way ranging. In *2018 International Conference on Computer Science and Software Engineering (CSSE 2018)* (pp. 307-315). Nanjing, China.
- Wisnmongkol, J., Klinkusoom, L., Sanpechuda, T., Kovavisaruch, L. O., & Kaemarungsi, K. (2019). Multipath mitigation for RSSI-Based bluetooth low energy localization. In *2019 19th International Symposium on Communications and Information Technologies (ISCIT)* (pp. 47-51). IEEE Publishing. <https://doi.org/10.1109/ISCIT.2019.8905164>
- Yi, C., Da, A. Z., Hui, C., Shan, C., & Xuan, Z. (2021). A UWB location algorithm - Based on adaptive Kalman filter. In *Journal of Physics: Conference Series* (Vol. 1757, No. 1, p. 012176). IOP Publishing. <https://doi.org/10.1088/1742-6596/1757/1/012176>
- Zhou, T., Xiao, M., Liu, Y., Cheng, Y., & Liu, Y. (2021). Research on indoor UWB positioning based on expectation maximization in NLOS environment. *Concurrency and Computation: Practice and Experience*, 33(17), 1–12. <https://doi.org/10.1002/cpe.6278>

Review Article

Exploring Probability of Detection (POD) Analysis in Nondestructive Testing: A Comprehensive Review and Potential Applications in Phased Array Ultrasonic Corrosion Mapping

Jan Lean Tai¹, Mohamed Thariq Hameed Sultan^{1,2,3*}, Farah Syazwani Shahar¹, Noorfaizal Yidris¹, Adi Azriff Basri¹ and Ain Umaira Md Shah¹

¹Department of Aerospace Engineering, Faculty of Engineering, Universiti Putra Malaysia, 43400 UPM Serdang, Selangor, Malaysia

²Laboratory of Biocomposite Technology, Institute of Tropical Forest and Forest Product (INTROP), University Putra Malaysia, 43400 UPM Serdang, Selangor, Malaysia

³Aerospace Malaysia Innovation Centre [944751-A], Prime Minister's Department, MIGHT Partnership Hub, Jalan Impact, 63600 Cyberjaya, Selangor Darul Ehsan, Malaysia

ABSTRACT

In nondestructive testing (NDT), ensuring defect detection, measurement accuracy, and reliability guarantees various components' structural integrity and safety. The Probability of Detection (POD) concept has emerged as a fundamental measure of the effectiveness of an inspection technique in identifying defects. Since NDT plays a crucial role in aerospace, manufacturing, and infrastructure industries, enhancing POD has become critical. POD refers to the likelihood that a flaw or defect of a certain size will be detected using the NDT technique. The “ \hat{a} versus a ” and the “hit/miss” methods are particularly notable among the commonly employed POD estimation methods. The POD curve is determined

based on crack size measurements in the “ \hat{a} versus a ” approach, typically used in ultrasonic testing. On the other hand, the “hit/miss” method establishes the POD curve by analysing binary outcomes, where a “hit” signifies successful detection and a “miss” denotes detection failure. This review focuses on POD in the context of NDT, specifically in phased array ultrasonic corrosion mapping (PAUCM), to uncover current uncertainty parameters and explore

ARTICLE INFO

Article history:

Received: 10 January 2024

Accepted: 12 April 2024

Published: 15 August 2024

DOI: <https://doi.org/10.47836/pjst.32.5.14>

E-mail addresses:

taijanlean2008@hotmail.com (Jan Lean Tai)

thariq@upm.edu.my (Mohamed Thariq Hameed Sultan)

farahsyazwani@upm.edu.my (Farah Syazwani Shahar)

nyidris@upm.edu.my (Noorfaizal Yidris)

adiazriff@upm.edu.my (Adi Azriff Basri)

ainumaira@upm.edu.my (Ain Umaira Md Shah)

* Corresponding author

an innovative avenue for enhancing POD assessment by incorporating the material surface temperature as an additional parameter.

Keywords: â versus a, hit/miss, model-assisted probability of detection, nondestructive testing, phased array ultrasonic testing, probability of detection

INTRODUCTION

In nondestructive testing (NDT), ensuring defect detection and measurement accuracy and reliability is crucial for guaranteeing various components' and structures' structural integrity and safety. Probability of detection (POD) provides a quantitative measure of the effectiveness of an inspection technique for defect identification. POD has emerged as a fundamental concept in the aerospace, manufacturing, and infrastructure industries.

The POD measures the likelihood that an NDT technique can detect flaws of a specific size. It is a key performance indicator influencing maintenance, quality control, and risk management decisions. POD analysis empowers engineers, inspectors, and decision-makers to make informed choices based on confidence in defect detection outcomes. The significance of POD lies in bridging the gap between theoretical expectations and real-world applications, ensuring that inspection methodologies align with the safety and quality requirements. Exploring POD is crucial for maintaining inspection accuracy as technology advances in the NDT landscape.

This review aims to comprehensively explore the concept of POD in the context of NDT, specifically emphasising its application in phased-array ultrasonic corrosion mapping (PAUCM). The primary focus was to investigate the intricacies of POD, particularly concerning PAUCM, to uncover the current uncertainty parameters associated with this technique. Furthermore, this review aims to explore an innovative avenue for enhancing POD assessment by incorporating material surface temperature as an additional parameter.

However, owing to the apparent dearth of existing studies in this specific niche, the focus was redirected toward the broader realm of POD assessment within the context of phased-array ultrasonic testing (PAUT). Despite its distinct applications, PAUT is commonly utilised with an angle beam for weld inspection, and the PAUCM employs a straight beam for corrosion detection. The two techniques have the same technology and equipment; there is also a similar mode of operation and the presentation of defects. Therefore, this review broadly explores historical processes, theoretical foundations, methodological strategies, illuminating case studies, and emerging trajectories in the field of POD assessment with a particular focus on the context of PAUT.

This review analyses in-depth contributions from researchers, industry experts, and practitioners to help comprehensively understand the evolution, challenges, and potential opportunities for POD assessment within the PAUT field.

Essentially, this endeavour intends to highlight the critical role of POD as a vital tool in maintaining the reliability and credibility of NDT practices, especially within the PAUT framework. Furthermore, investigating the potential role of the material surface temperature as a POD enhancer will pave the way for innovations that refine the accuracy and effectiveness of PAUCM in corrosion detection.

PROBABILITY OF DETECTION

POD analysis is a fundamental task in assessing the ability of NDT techniques to detect defects. This comprehensive review aims to outline the intricacies of POD analysis and trace its developmental trajectory, methodology, and significance in protecting material and structural integrity.

Meeker (2000) traced the origins of POD to the 1970s. However, real advancement and widespread adoption began after 2000, as evidenced by a literature review of 90 articles. In the mid-1970s, an estimation of the probability of flaw detection based on specific flaw sizes using uniform POD assumptions was attempted. Initially, binomial distribution methods were used for the estimation. However, this approach proved inadequate, as researchers discovered the multifaceted behaviour of POD curves (Georgiou, 2007).

The NDT community shifted towards more intricate models in the 1980s, which can capture the relationship between POD and flaw size. Log-logistic and ‘log-normal’ distributions are now utilised as sophisticated approximations of POD behaviour, illustrating the growing comprehension of this intricate phenomenon (Annis et al., 2015a).

The three-parameter model expands upon the two-parameter model by introducing the Signal Amplitude Distribution (SAD), the POD, and the Signal-to-Noise Ratio (SNR). This inclusion offers a more comprehensive representation of the detection process, recognising that flaws may exhibit various signal amplitudes. This change began a new era in POD analysis, leading to more accurate and relevant estimates (Knopp & Zeng, 2013).

Integrating simulation methodologies and advanced statistical techniques offers a more comprehensive and accurate approach to estimating the POD, accounting for a wide range of complex variables and uncertainties. Simulation-based approaches, such as Model-Assisted Probability of Detection (MAPOD), gained prominence during this period. The MAPOD approaches leverage computer simulations to replicate real-world inspection scenarios, assess the probability of flaw detection in different materials with varying sizes and characteristics, and generate realistic data that reflects the complexities of actual NDT operations (Rentala et al., 2018).

MAPOD has gained significant traction since its inception by the MAPOD Working Group in 2004. Its widespread adoption can be attributed to its capability to simulate NDT data for POD assessment, which leads to substantial resource savings (Dominguez et al., 2012).

Simulations have explored multiple variables such as material properties, defect geometries, inspection configurations, and environmental conditions. This holistic approach has enabled researchers to identify optimal parameters and strategies for flaw detection and quantifying uncertainties associated with different scenarios.

In 2009, the US Department of Defence published a notable handbook, MIL-HDBK-1823A, titled “Nondestructive Evaluation System Reliability Assessment.” This handbook thoroughly explains POD applications and is frequently cited in various POD research articles, indicating its widespread circulation and influence in the field (DOD, 2009).

Advanced statistical techniques, including Bayesian methods, have been integrated into simulation-based approaches to enhance the accuracy and reliability of POD predictions. By combining the simulation results with statistical analyses, researchers can generate more robust POD curves that account for the variability and uncertainties introduced during inspection (Dominguez et al., 2012). POD estimation methods fall under two primary categories: the “*a* versus *a*” and the “hit/miss” methods.

POD computing and evaluation have witnessed the emergence of various techniques over time. In addition to Bayesian methods, the Monte Carlo simulation approach is another commonly employed technique. This approach entails generating random samples from probability distributions and simulating the inspection process to estimate the POD. Monte Carlo simulation accounts for uncertainties, such as defect variability and measurement error, and precisely estimates POD and associated uncertainties (Abdelli et al., 2019).

The 29/29 method calculates the POD using a set of 29 flawed samples. The inspection results are then meticulously analysed to determine the proportion of successfully detected flaws. If all 29 flawed samples were accurately identified, the POD is considered 100% (Bato et al., 2017).

Maximum Likelihood Estimation (MLE) is an established statistical method for determining the parameters of a probability distribution based on observed data. The objective of MLE is to identify the parameter values that provide the highest likelihood of observing the actual detection outcomes, given a hypothesised model. Nevertheless, MLE-based approaches have been known to have certain limitations, such as convergence issues with algorithms. Despite the findings suggesting an increase in POD with crack length, there may be instances in which operators fail to identify large crack sizes, as evidenced by preliminary research (Poudel et al., 2022).

Spies and Rieder (2018) employed the Rayleigh-Rice model to develop MAPOD. The Rayleigh component represents noise, whereas the Rice component represents the signal. This model is particularly relevant in ultrasonic testing because flaw signals are commonly concealed within background noise. By separately characterising the signal and noise components and subsequently combining them, the Rayleigh-Rice model assesses the detectability of flaws.

After thoroughly examining extensive literature, it is apparent that the “ \hat{a} versus a ” and binary “hit/miss” methods are the most widely used and central to this article’s focus.

In the “ \hat{a} versus a ” approach, such as in ultrasonic testing, the echo amplitude “ \hat{a} ” is proportional to the crack size measurement “ a ”. The objective was to establish a decision threshold “ \hat{a} ” that maximised crack detection while minimising false alarms attributed to noise. To address the variability in the “ \hat{a} versus a ” relationship, ASTM-E3023 and MIL-HDBK-1823A employ linear functions to assign “ \hat{a} ” to “ a ” and incorporate prediction intervals to factor in noise and statistical uncertainty (Virkkunen et al., 2019).

The accuracy of the output in POD is affected by the amount of the input data. Inadequate data may lead to bias. For instance, MIL-HDBK-1823A recommends analysing at least 40 representative defect data points for “ \hat{a} versus a ” and signal strength “ \hat{a} ” measurements, as well as crack sizes “ a ” (Carboni & Cantini, 2016). Conversely, the “hit/miss” method determines the POD curve based on binary outcomes, with “hit” indicating successful detection and “miss” indicating failure. This “hit/miss” technique requires a larger dataset, with a minimum of 60 data sets, to ensure an unbiased and reliable POD curve (Virkkunen et al., 2019).

The receiver operating characteristic (ROC) is a vital metric for binary decisions (“hit/miss” technique). It illustrates four potential prediction outcomes in the binary decision scenarios, particularly for defect presence/absence determinations (Topp & Strothmann, 2021).

- True Positive (TP): When the system correctly spots a problem in a sample with an issue.
- True Negative (TN): When the system correctly says everything is fine with a sample that is indeed problem-free.
- False Positive (FP): When the system mistakenly thinks a problem in a sample is okay. It is like a false alarm.
- False Negative (FN): When the system misses a real problem in a sample, failing to identify it. It is like overlooking an actual issue.

Reliability in NDT is often expressed in the defect size, which has a 90% probability of being detected, referred to as “ a_{90} .” This value is presented with a 95% confidence interval to address statistical uncertainty denoted as “ $a_{90/95}$ ” (Annis, 2014).

Design of Experiment POD (DOEPOD) is a methodology pioneered by the National Aeronautics and Space Administration (NASA). This approach builds on prior NASA work on POD, based on binomial distribution, by introducing the concept of $a_{90/95}$ (Poudel et al., 2022). Virkkunen et al. (2019) utilised the DOEPOD model, which extends the binomial perspective of hit/miss data. The primary motivation behind the DOEPOD model is to address the limitation of assuming POD as a function of flaw size following a specific model, as in MAPOD estimation.

DOEPOD aims to provide an efficient and accurate methodology for estimating the observed POD and confidence limits for both hit/miss and signal amplitude testing

scenarios. Unlike MAPOD, DOEPOD does not assume that the prescribed POD functions, such as logarithmic or similar, are adequate across a wide range of discontinuity sizes and testing system technologies. Therefore, multi-parameter curve fitting or model optimisation approaches are unnecessary to generate a POD curve (Generazio, 2009).

The various methods for calculating POD have their unique efficacy, and the application of POD may vary depending on the scope of application. Table 1 concisely compares the different POD computing methods, highlighting their advantages and limitations.

Table 1
POD computing and evaluation method comparison

POD method	Advantage	Limitation
Binary Hit/ Miss	<ul style="list-style-type: none"> • Easy to understand, and quick assessments are appropriate. • Provide clear-cut results for making decisions. 	<ul style="list-style-type: none"> • Neglecting subtleties and uncertainties, the detection procedure is oversimplified. • Does not offer a probabilistic framework for quantifying uncertainty.
â versus a	<ul style="list-style-type: none"> • Provides a methodology based on probability to estimate POD and related uncertainty. • Provides for the estimation of several parameters, increasing adaptability. 	<ul style="list-style-type: none"> • Demands rigorous consideration when choosing the model’s parameters and assumptions. • Complicated models or high-dimensional parameter spaces could need a lot of processing power.
Bayesian Approaches	<ul style="list-style-type: none"> • Flexibility in handling complex models and incorporating prior information. • Provides a structure for assessing uncertainty and drawing probabilistic conclusions. 	<ul style="list-style-type: none"> • Computationally demanding, particularly for models with extensive parameter spaces. • The inclusion of subjectivity in the specification of prior distributions may result in the introduction of bias.
Monte Carlo Simulation	<ul style="list-style-type: none"> • POD estimations that are realistic and include related uncertainties. • Ideal for intricate examination situations when there are multiple sources of uncertainty. 	<ul style="list-style-type: none"> • Depends on presumptions of the model’s parameters and underlying probability distributions. • Computationally costly, especially when doing large-scale models.
29/29 Method	<ul style="list-style-type: none"> • Straightforward approach. • Suitable for routine inspections, this system is simple to use and understand. 	<ul style="list-style-type: none"> • Its breadth is restricted because it is based on a predetermined set of faulty samples. • It might not fully represent the variety and ambiguities in actual inspection situations.
Maximum Likelihood Estimation (MLE)	<ul style="list-style-type: none"> • Statistically sound methodology for estimating parameters. • Effective model parameter estimation from observable data. 	<ul style="list-style-type: none"> • Vulnerable to problems with convergence, especially with limited data or sophisticated models. • Assumes that the process of generating the data is accurately represented by the model that is being fitted.
Rayleigh-Rice Method	<ul style="list-style-type: none"> • Particularly ultrasonic testing, which improves the evaluation of defect detectability. • Accuracy is increased by characterising the signal and noise components separately. 	<ul style="list-style-type: none"> • Makes assumptions regarding the distributions of the signal and noise. • Restricted application to different inspection settings or NDT techniques.

POD Application in NDT Methods

The concept of POD revolves around quantifying the likelihood of successfully detecting a flaw of size 'a' through a probabilistic function known as POD. This function serves a twofold purpose: it measures the efficacy of NDT methods in identifying such flaws and contributes to developing risk-based maintenance strategies (Yusa et al., 2016).

The integration of POD analysis is essential to ensure the credibility of the NDT inspection procedures. Its fundamental role in validating the dependability of inspection methods is widely recognised, and it is commonly mandated as an integral component of qualification projects, particularly in safety-critical sectors such as aeronautics (Bato et al., 2020). Not all discontinuities can be classified as harmful defects, and it is crucial to assess the size of the discontinuity to determine whether detection is required because small discontinuities within thick structures may not be detrimental.

Ultrasonic Testing (UT) and Phased Array Ultrasonic Testing (PAUT)

Ultrasonic Testing (UT) techniques are essential for NDT because they can detect internal structures and defects in materials. UT has been used for POD analysis and has gained significant attention for improving the reliability of defect detection. POD analysis originated in the 1970s; however, its development accelerated after 2000, with a notable presentation of diverse defects and POD in UT (Meeker, 2000). Exploration of depth as a parameter for model predictions has also begun. POD curves are constructed based on the defect length, depth, orientation, defect type, shape, operator differences, and inspection environment, which can influence inspection accuracy (Subair et al., 2014).

Current methods for determining the probability of detecting the defect length, size, or depth through POD curves involve model simulations, expert insights, experimental trials, or their combinations. Human elements play a crucial role, particularly in inspection methods such as UT and Radiography testing (RT), where human judgment is essential. Automated NDT methods and computer-aided calculations have been employed to address the problem of inconsistencies at actual construction sites (Wall et al., 2009).

Kojima et al. (2019) explored the effect of human factors on POD parameters during ultrasonic inspection. They found that certified and uncertified inspectors had a similar failure risk when detecting stress corrosion cracking in stainless steel pipes.

Flat-bottom holes (FBH) and side-drilled holes (SDH) are commonly used for calibration during ultrasonic testing. FBHs are easy to manufacture and mimic various defects; however, their circular shape may not match them (Stubbs, 2005). An experiment was conducted to detect fatigue cracks and POD using a 0.5 mm diameter and 5 mm high FBH. Actual FBH dimensions represented "a" and ultrasonic defect echo amplitude represented "â" Statistical analysis determined the best linear fit between "a" and "â" (Rentala et al., 2016).

This approach optimises the probability of detecting common in-service fatigue cracks (Carboni & Cantini, 2016). Apart from the manufacturing phase NDT, periodic inspections are crucial for identifying deteriorated structures in service. In-service inspections are more challenging owing to the complexity of defects. Fatigue cracks are a frequent problem when structures or equipment are in regular use, and POD can aid in fatigue life inspection. The Probability of Failure (POF) can be estimated using ultrasonic-detected defect data and actual defect data (Guan et al., 2014).

PAUT utilises POD curves based on binary ‘hit/miss’ data but does not account for defect location and dimension accuracy on welds. Consequently, a follow-up “*â* versus *a*” analysis was conducted, enhancing accuracy. The ongoing research has been extended to stainless steel and dissimilar materials welds by incorporating real defects and artificial Electrical Discharge Machining (EDM) notches (Kurz et al., 2012; Kurz et al., 2013). One practical application of POD studies lies in PAUT, mainly using reference blocks made from composite materials with FBHs. These studies aim to gauge the reliability and capabilities of PAUT in detecting flaws such as FBHs in composite materials, offering insights into inspection technique performance and sensitivity (Dominguez et al., 2016).

In recent years, researchers have emphasised the integration of the Total Focusing Method (TFM) and Full Matrix Capture (FMC) to enhance the imaging capabilities of PAUT significantly. The TFM technique synthesises multiple ultrasonic waves captured by an array of transducers. Subsequently, the received signals are processed, and the ultrasonic energy is focused on specific points within the material, generating high-resolution images with improved defect detection and characterisation (Caulder, 2018). FMC was developed to address the limitations of conventional PAUT data acquisition methods, which typically capture only a subset of the available ultrasonic data. This approach records the complete set of ultrasonic signals captured by the transducer array, providing a comprehensive dataset that can be utilised for various post-processing techniques, including TFM.

The increasing popularity of TFM and FMC has led to research efforts to refine their underlying algorithms (Zhao et al., 2023). The TFM/FMC algorithm consists of four main steps: (1) data acquisition, which involves obtaining raw ultrasonic data from transducers; (2) signal processing, where noise is removed from the raw data, and system imperfections are corrected; (3) beamforming, in which the processed signals are combined to focus ultrasonic energy on a specific point within the material, and (4) image reconstruction, where the focused signals are utilised to generate a high-resolution image.

Advancements in signal processing, beamforming, and image reconstruction have enhanced performance and reduced computational time for these algorithms. Moreover, machine learning and artificial intelligence techniques are being investigated to further enhance the capabilities of TFM and FMC in PAUT (He et al., 2024). These advanced algorithms enable high-resolution imaging and accurate defect quantification, ultimately improving the overall effectiveness of the inspection process.

POD is a crucial performance metric for TFM and FMC techniques. It is influenced by signal-to-noise ratio, spatial resolution, defect orientation, and defect size (Bajgholi et al., 2023). The ongoing development and enhancement of TFM and FMC algorithms improve POD in PAUT, ultimately leading to more accurate and reliable defect detection and characterisation in various industrial applications.

Eddy Current Testing (ECT)

Eddy Current Testing (ECT) is modelled using complex electromagnetic equations, such as Maxwell's, which are challenging to solve analytically. A numerical approach is preferred for accurate modelling (Abdelli et al., 2019). During the ECT of metallic structures, the probe induces eddy currents in the material, and changes in the coil impedance are detected as the probe traverses a surface or near-surface crack. These changes are measurable parameters and typically increase with the defect size.

A POD demonstration test was conducted to evaluate the performance of the ECT system using standardised specimens with known crack sizes and distributions. The procedure involved scanning the specimens to gather the ECT response data for specific crack sizes, and the POD curve was developed using a two-step analysis:

1. Establishing “ \hat{a} versus a ” Relationship: This step employs advanced regression techniques to establish a mathematical link between the measured EC signal response “ \hat{a} ” and actual crack size “ a ,” accounting for factors such as depth and inspection process variability (Zhu et al., 2018).
2. Constructing the POD Curve: Building on normal probability theory, this phase involves creating the POD curve, depicting the probability of detecting a flaw of size “ a ” based on measured EC signal response “ \hat{a} ”. This curve gauges the reliability of the EC inspection system for detecting various flaw sizes.

While the “ \hat{a} versus a ” relationship provides average ECT signal responses for specific crack sizes, variations can occur in measured responses even for identically sized cracks due to physical attributes of flaws like depth and fluctuations in the ECT process. Statistical techniques can be used to evaluate the capability and reliability of ECT for detecting cracks and defects (Brown, 2009).

Repeated stresses can lead to fatigue-induced cracks, even below a material's breaking point, such as the circular crack growth around a hole. A method called “bolt-hole eddy current” (BHEC) uses a sensor inserted into a hole to detect changes indicative of cracks or issues (Underhill et al., 2018).

Similarly, Underhill and Krause (2011) inspected fatigue cracks in aluminium bolt-holes, generating POD using the crack depth and length as uncertain parameters. A follow-up study by Underhill and Krause (2016) examined corner cracks with 45 EDM notches and 72 fatigue cracks using BHEC.

Finland secures nuclear waste using copper canisters and ensures that their leak-free integrity is crucial. Kanzler et al. (2019) constructed a POD curve for a canister using the ECT method.

However, Xu et al. (2023) emphasised that POD would decrease due to the decrease in eddy current density, leading to the deterioration of SNR.

Radiography Testing (RT)

Weld defects exhibit diverse shapes, which makes it challenging to establish reliable and efficient POD assessments (Kanzler & Müller, 2016a). RT features a dynamic threshold adjusted based on defect size. This method tailors the detection thresholds according to the defect dimensions. However, acquiring sufficient data for POD assessment can be resource-intensive. Weld defects exhibit diverse shapes, which makes it challenging to establish reliable and efficient POD assessments (Kanzler & Müller, 2016a).

Innovative methodologies are required to address the complexity of utilising the actual defects for POD calculations. One such strategy is an indication size-dependent evaluation that addresses two key defect parameters. However, this approach requires a large amount of data. A smoothing algorithm is introduced to enhance the evaluation accuracy, which considers physical characteristics and defect detection capabilities (Kanzler & Müller, 2016b).

The Bayesian approach is useful for calculating POD curves, especially in situations with few defects. This method is essential when detailed results are required, such as nuclear fuel disposal canisters. The Bayesian approach was used to derive POD curves in this context because it meets the strict safety requirements for nuclear applications, and few actual defects are owing to high-quality production techniques. This method combines available data, expert knowledge, and statistical reasoning to provide reliable insights into the performance and capabilities of RT (Kanzler et al., 2012).

The influence of RT techniques on POD evaluation for planar flaws, such as cracks, is affected by various factors, including the flaw orientation relative to the beam direction, human factors, application conditions, accessibility, equipment sensitivity and resolution, manufacturing processes, and material properties. Equations were used to construct POD curves for cracks using varying parameters, such as grain diameter, thickness sensitivity percentage, crack width, and number of orientations. The results showed that increasing the number of orientations and crack width increased POD, whereas higher sensitivity values and larger object diameters decreased POD (Ghose, 2013).

Computed Radiography (CR) uses reusable storage phosphor plates instead of films for industrial Radiography. Research has shown that medium-resolution CR systems perform better for flaw detection at certain dose thresholds, which affect the computed POD. It suggests that medium-resolution CR systems are more effective for detecting flaws detection at these dose levels (Mohr & Willems, 2008).

It is crucial to compare the POD of various defect detection algorithms using artificial X-ray Computed Tomography (XCT) data from industrial specimens. Artificial XCT data were generated through numerical XCT simulations, which enabled the controlled incorporation of specific defects or pores at predefined locations (Yosifov et al., 2023). XCT, a vital volumetric imaging technique, is widely used in X-ray-based digital radiography (XDR) and POD computation. This approach often involves creating specimens with distinct artificial defects to capture the shape and size variations.

XCT simulations have applications in the biomedical and material science sectors for virtual radiographic testing optimisation and forecasting NDT systems' reliability using ray-tracing algorithms similar to SimCT to generate radiographic images (Yosifov et al., 2022).

A study by Kim et al. (2021) carried out an XCT experiment where NDT signals' \hat{a} were compared with direct measurements of the actual property value. Statistical modelling accounted for the inherent noise in the NDT signal. Notably, the same types of flaws may not consistently produce the same signal, and even flaws of identical size might result in different signals. The estimation of a POD curve is grounded in NDT measurements taken from flaws of different sizes. Initially, this method was employed to evaluate flaws during the operational lifespan of a component.

Structural Health Monitoring (SHM) and Guided Wave (GW)

Structural Health Monitoring (SHM) involves embedding sensors in a system to continuously evaluate structural health throughout its operational life. Guided waves, or Lamb waves, are sequentially emitted and received by the sensors to generate a comprehensive structure scan. Comparing these scans with a baseline scan captured when the structure was pristine provides a visual representation of the structural condition (Calmon et al., 2019).

These waves effectively identify surface and internal structural anomalies such as delamination, holes, cracks, corrosion, and wear in lap joints. Assessment of NDT capabilities often uses the Berens model, which employs POD curves to illustrate the likelihood of flaw detection based on size (Gianneo et al., 2016a). However, POD curves may exhibit nonlinear patterns with respect to the crack size, reflecting fluctuations supported by numerical simulations and empirical data (Gianneo et al., 2016b).

Forsyth (2016) proposed a novel approach using a single specimen with a growing crack to address the variability in crack responses and the impact of repeated inspections on the POD estimation. Forsyth (2016) emphasised that in many POD studies, the primary source of variability is not the measurement process but rather the diverse responses among cracks of similar sizes. It implies that reducing the sampling may lead to inaccurate POD estimates. Although treating repeated inspections as independent events to enhance POD is appealing, it contradicts the literature.

NDT and SHM share similarities, but their sensor setups affect POD curve interpretation. Portable sensor arrays are fundamental to NDT methods, such as ultrasonic wave testing, whereas guided wave monitoring in SHM employs permanently fixed transducers. POD curves help to evaluate the damage-detection capabilities within a predefined setup and damage location for SHM systems (Bayoumi et al., 2021).

Tschoke et al. (2021) project focussed on creating an SHM system for safety-critical components made from carbon fibre-reinforced polymer (CFRP) in the automotive sector. POD varies based on the defect size, as shown in the POD curves. However, the regulatory framework for SHM is still evolving, and a significant challenge is the lack of reliable methods for assessing POD in SHM systems.

POD Application in Diverse NDT Methods

The UT and ECT are prominent NDT techniques. However, NDT encompasses diverse methods, each significant in defect detection and characterisation.

Fluorescent Penetrant Testing (PT) is a versatile technique used throughout the various stages of manufacturing to identify surface cracks. The objective was to detect linear indications using POD curves that encapsulate the inspector's ability to detect specific crack sizes. The analysis categorises outcomes as hits, misses, or false calls and quantifies an inspector's proficiency (Herberich, 2009).

A comprehensive case study on PT was delved into a POD investigation across 27 titanium samples involving multiple inspectors. The resulting POD curve provides insights into crack detection effectiveness, accounting for factors such as inspector performance and testing conditions (Caturano et al., 2009).

Acoustic Emission (AE) monitoring is a valuable technique for detecting wire failures because it captures audible sounds from material defects. AE technology provides a comprehensive solution for identifying cable breaks, fatigue cracks, and corrosion (Lembersky et al., 2012). However, challenges arise due to the unique nature of diagnostic signals and source dynamics, making distinguishing genuine AE signals from noise difficult. A holistic approach, including stress stimuli, source behaviour, wave propagation, sensor sensitivity, and detection threshold, provides insights into the POD (Hossain et al., 2013).

Incorporating Infrared thermography (IR) into CFRP materials involves creating POD curves through experimental methods. Testing CFRP samples with known defects provided a statistical analysis, offering insights into the technique's defect identification performance (Peeters et al., 2018).

Pulsed Thermography is effective for materials exhibiting rapid heat diffusion. POD analysis aids in quantifying defects and assessing accuracy by stimulating materials with energy bursts and capturing thermal data (Accardi et al., 2023).

Model-Assisted Probability of Detection

Recent advancements in POD analysis have involved incorporating computational models and simulations to improve defect detection. This study examines the evolution of MAPOD by tracing its development from traditional POD analysis to advanced simulation techniques. MAPOD originated in the early 2000s when scholars first recognised the potential of computer-aided models in ultrasonic corrosion mapping for POD estimations (Burch et al., 2005).

The MAPOD working group was established in the US in 2004, and later, similar initiatives emerged in Europe, such as SISTAE in France and PICASSO (Dominguez et al., 2016). These efforts aimed to bridge the gap between mathematical models and experimental data, thereby allowing the prediction of a broader range of defect types and inspection scenarios.

As POD models evolve, diverse mathematical frameworks have emerged to support the MAPOD analyses. MAPOD simulates data using statistical or finite element methodologies, reducing reliance on resource-intensive experimental data (Wright, 2016). Conventional POD analyses are limited by their reliance on a single parameter; however, Yusa et al. (2018) advocated for a multi-parameter POD model facilitated by numerical simulations. Baskaran et al. (2021) extended the MAPOD paradigm to ECT, harnessing multiple flaw response signals, including the defect length and coil impedance at different frequencies.

Although MAPOD offers efficiency, validating the resulting probabilistic POD curves is also essential. A study by Le Gratiet et al. (2017) compared POD curves generated using four methods: Behrens, binomial-Barens, polynomial chaos, and kriging. The study found subtle differences in the lower 95% bounds of the a90/95 estimates, highlighting the complexity of the detectable defect size estimation.

Rodat et al. (2017) applied the MAPOD methodology to the ultrasonic inspection of composite materials, incorporating input vectors such as material thickness, FBH diameter, and surface defect depth (FBH depth). The resultant output vector captured defect characteristics.

Mh1823 POD Software

The MIL-HBDBK-1823A manual provides a comprehensive guide for constructing POD studies (DOD, 2009). It also includes a helpful Mh1823 POD software download guide built on the R statistical and graphics engine, which can be accessed on the Statistical Engineering website (<https://www.r-project.org/>).

Tschoke et al. (2021) demonstrated the automotive industry's application of POD analyses in creating SHM systems for CFRP components. They emphasised the international recognition of the MIL-HBDBK manual and Mh1823 software as well-established standards for conducting these evaluations.

Forsyth and Aldrin (2009) provided a practical demonstration for conducting a POD curve study on BHEC using the Mh1823 software. Choi et al. (2022) replaced RT with UT and PAUT and detected volumetric defects through round-robin tests on various materials. POD analysis was performed using the Mh1823 POD analysis software, while a simulation using finite element techniques explored the potential of eddy current testing for detecting stress corrosion cracking signals (Yusa, 2017). The resulting POD curves were generated using the R software.

Kurz et al. (2012) documented using Mh1823 in the PAUT domain. TFM, a synthetic focusing technique, was integrated with Mh1823. It uses full-matrix capture to capture fundamental ultrasonic signals, enhances defect boundary delineation, generates coherent signals, and mitigates noncorrelation artefacts (Bajgholi et al., 2023).

Ground-penetrating radar (GPR) is used in civil engineering to detect rebar and tendon ducts within concrete structures. Its effectiveness is highlighted by its ability to uncover the subsurface features. Mh1823 software was employed for uncertainty analysis to evaluate GPR's reliability of the GPR. This software is a reliable tool for determining the precision of GPR in identifying subsurface features within concrete structures (Feistkorn & Taffe, 2014). Remarkably, Mh1823 has additional applications beyond NDT, including predicting driving behaviour (Ameyaw et al., 2019).

Computational Intelligence for Visual Applications (CIVA) Software

CIVA began in the early 1990s and evolved into a comprehensive toolkit with modules for various NDT methods, including UT, GW, ECT, RT, and CT. It is now an all-encompassing solution for simulating and analysing diverse NDT techniques across industries (Foucher et al., 2018). CIVA enables the generation of POD curves more efficiently and cost-effectively based on the precision, consistency, and repeatability of theoretical POD simulations. In pulsed-echo ultrasonic inspection, parameters such as defect length or size are crucial for generating POD curves. CIVA facilitates MAPOD through Monte Carlo simulations and establishes relationships between the input parameters and POD outcomes (Schneider et al., 2012).

CIVA is useful for calculating various uncertainty parameters. Dominguez et al. (2012) show how CIVA can be used to calculate the uncertainty parameters for PAUT. Automation reduces human errors during the inspection process. Parameters such as the water parts, defect angular position, and radial position were used for the uncertainty analysis for the PAUT. The study confirmed that a well-designed PAUT procedure can achieve 90% probability and 95% confidence in detecting a 0.5 mm diameter void.

Ribay et al. (2017) examined the use of CIVA for generating 'hit/miss' studies in the PAUT of centrifugally cast stainless steel pipes. This study focuses on high-attenuation surfaces with coarse grain structures and material thicknesses as crucial parameters for the

analysis. Haapalainen and Leskelä (2012) used CIVA to generate defect-size-dependent ‘a’ vs. signal response ‘â’ curves to detect service-induced cracks.

Marcotte and Liyanage (2017) combined multiple NDT techniques for inspection. They used ECT and PAUT and obtained promising results for detecting target defects. The study validated the CIVA software and suggested using multi-technique inspection systems.

Dominguez et al. (2010) and Jenson et al. (2011) conducted High-Frequency Eddy Current Testing (HFET) to detect fatigue cracks in titanium alloys. Their study demonstrated a close alignment between simulated POD and experimental POD, bolstering confidence in the CIVA’s predictive capabilities.

Similarly, CIVA is instrumental in simulating ECT scenarios. Goursolle et al. (2016) simulated ECT on fatigue cracks in Inconel 718 material, emphasising the influence of parameters such as inspectors, air gap, and frequency settings. Bato et al. (2017) and Bato et al. (2020) highlight how CIVA offers advantages in evaluating the impact of human factors on POD through simulation rather than experimentation. This approach contributes to the enhanced credibility of the model.

After that, CIVA extends its reach to RT. Tisseur et al. (2019) elaborated on CIVA’s version 11, which introduced a POD simulation tool within the RT module. This tool caters to scenarios where the radiation source is aligned with the defect or circumferentially misaligned, demonstrating the platform’s versatility.

Other Software Recommended by Researchers

Lei et al. (2022) highlighted the significance of various factors in POD analysis, such as test methods, materials, defects, equipment, and human factors. These multifaceted influences are owed to the complexity of POD estimation. They introduced SimSUNDT software, designed by the Chalmers University of Technology in Sweden, to enhance PAUT’s capability to replicate intricate inspection scenarios.

Subair et al. (2014) used simulation-driven POD estimation with ABAQUS software to explore pulsed electron ultrasound propagation for stainless steel surface notch detection. They evaluated the impact of various factors, including probe position, incident wave angle, and ultrasound frequency. The authors compared logarithmic scatter plots of simulated and experimental defect response signals using a simulation-experimental correlation approach and validated their findings using linear regression analysis in MATLAB.

Volker et al. (2004) introduced the “POD-generator” software, designed to enhance the structural integrity of pipes and pipelines through corrosion inspections using an ultrasonic technique. The software integrates data from the inspection and degradation models to determine the integrity of the three components. It produces a curve based on POD in specific scenarios, thereby improving the reliability in assessing structural conditions.

Fusing simulated and experimental data enhances the NDT performance evaluation and reduces costs. Gollwitzer et al. (2011) introduced the concept of merging these datasets to enhance the NDT performance estimation. The aRTist tool is the foundation for this approach. SimuPOD provides a user-friendly interface for defining the calculation series and automating the analysis, focusing on POD studies. This innovation streamlines the reliability and effectiveness of the NDT methods and increases their practical applicability.

Literature Review Summary

NDT techniques must be accurate, reliable, and critical across aerospace, manufacturing, petrochemical, and civil engineering industries. POD analysis is a powerful tool that quantifies inspection reliability by considering the defect size, materials, inspection configuration, and human factors. Linking NDT methods and risk assessment enhances decision-making and improves safety and efficiency.

An exploration encompassing around 70 articles titled “POD” or “probability of detection” from 2000 to 2023 reveals that the concept of POD has garnered extensive application across various NDT methods. The trajectory of its usage has revealed an intriguing pattern shaped by both temporal evolution and technological advancements.

POD originated in the aerospace industry owing to its strict demands. ECT is a crucial tool because of its widespread use in the aerospace industry. UT was among the first to adopt POD. In this review of 70 articles, ECT methods were mentioned in 18 papers, whereas UT was mentioned in 17 papers, totalling half of the corpus.

PAUT closely followed ten papers, indicating its established position in the NDT landscape. However, as the software landscape matured, there was a shift towards more sophisticated analytical capabilities. This is evident from the substantial growth in RT and GW SHM, which will account for 20% of the literature combined. This evolution shows the profound impact of software advancements in facilitating intricate analyses, expanding the POD’s purview to include crucial domains such as SHM.

Despite having a smaller proportion, other NDT methods play a significant role in defect detection. PT and AE accounted for 4%, indicating their values in the field. The IR and other combined methods comprised the remaining portions. This distribution highlights the diverse avenues through which POD affects NDT, as shown in Figure 1.

The articles’ analyses showed the evolution of POD in NDT methods and its correlation with software development. ECT and UT initially had a stronghold, but broader adoption of POD occurred in RT and SHM. POD enhances defect detection and is critical in various industries. The trend of employing POD software is set to expand with the increase in the MAPOD methodology, leading to greater efficiency and cost-effectiveness.

MAPOD is undeniable owing to technological evolution, offering time and cost savings and rapid generation of accurate POD curves using simulation data. It expedites defect detection and assessment while maintaining reliability.

Throughout the reviewed literature, other researchers’ utilisation of POD software has been documented in Table 2.

The specific testing method used can influence the parameter variations. Although general factors remain relevant, additional considerations arise in RT, such as the direction

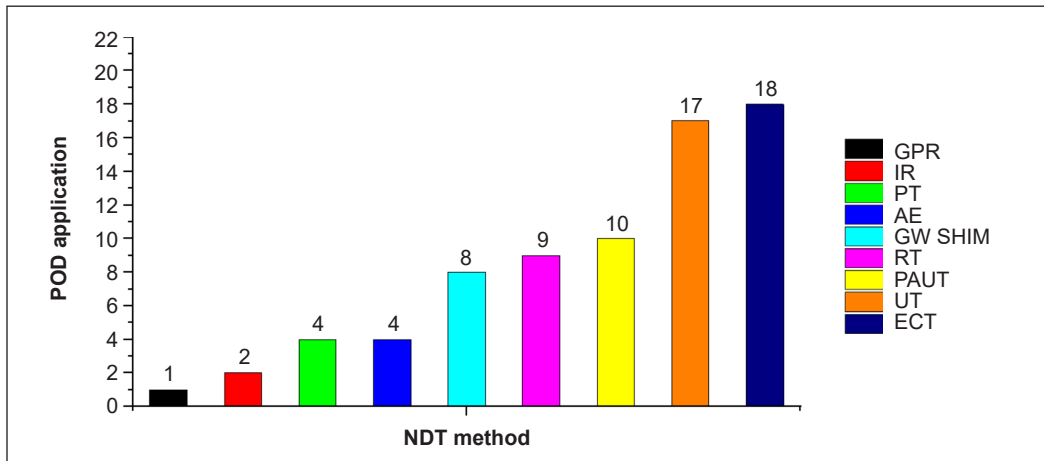


Figure 1. Distribution of POD application in different NDT methods

Table 2
Selected software for POD studies by other researchers

Software	Description	Reference
Mh1823 POD	Is a free software that can be accessed from the Statistical Engineering website (https://statistical-engineering.com/)	Forsyth & Aldrin, 2009; Kurz et al., 2012; Yusa, 2017; Tschoke et al., 2021; Choi et al., 2022; Bajgholi et al., 2023
CIVA	The CIVA software is a versatile commercial tool that extends its utility beyond POD analysis. It encompasses a range of simulation software for various NDT methods.	Dominguez et al., 2010; Jenson et al., 2011; Schneider et al., 2012; Haapalainen & Leskelä, 2012; Dominguez et al., 2012; Dominguez et al., 2016; Goursolle et al., 2016); Ribay et al., 2017; Marcotte & Liyanage, 2017; Bato et al., 2017; Foucher et al., 2018; Calmon et al., 2019; Tisseur et al., 2019; Bato et al., 2020
MATLAB	MATLAB provides various built-in functions and toolboxes for various applications, including mathematics, engineering, physics, finance, image processing, machine learning, and more.	Subair et al., 2014
simSUNDT	It is a simulation software for UT	Lei et al., 2022
aRTist SimuPOD	The aRTist is a computer simulation of both film and digital radiography. SimuPOD is one of the modules.	Gollwitzer et al., 2011

of the testing beam and the testing process itself. In the PAUT, the defects' water paths, as well as the angular and radial positions, need to be considered. These method-specific variations highlight the complexity of parameter selection in the POD analysis.

DISCUSSION

The primary objective of this literature review is to identify existing examples of utilising POD in the context of PAUCM. While PAUCM boasts numerous advantages in corrosion detection, recent studies have highlighted its adaptability for in-line inspections, particularly in elevated surface temperature conditions (Tai et al., 2023). Despite the robust presentation of detection data, integrating POD as a crucial tool for upholding the reliability and credibility of the PAUCM process would provide additional substantiation for the dependability of this application.

Although specific instances of applying POD in the context of PAUCM have not been uncovered, the review has elucidated the widespread utilisation of POD in other NDT methods. Concurrently, it has underscored the significance of uncertain critical parameters as pivotal inputs. By commencing with considerations of defect length and depth, the investigation expanded to encompass various factors, including defect type, size, dimensions, orientation, shape, and location, while also addressing the influence of human factors.

The application of PAUCM could explore an innovative avenue for enhancing POD assessment by incorporating the material surface temperature as an additional parameter, potentially yielding more robust results.

Additionally, this review indicates the existence of two primary POD models: the “hit/miss” model for image-type defects and the “ \hat{a} versus a ” model for defects represented in signal amplitude forms, as illustrated in Figures 2 and 3.

PAUCM, a manifestation of PAUT, presents information through A-, B-, C-, and S-scan images, thus providing a comprehensive three-dimensional perspective of the defects.

The A-scan mode resembles the traditional UT mode and displays the ultrasound echo amplitudes. The B, C, and S scans offer essential imaging tools for accurate defect localisation, as shown in Figure 4. The PAUCM ultrasound beam is aligned perpendicular to the test object, like the 0-degree normal probe in the UT.

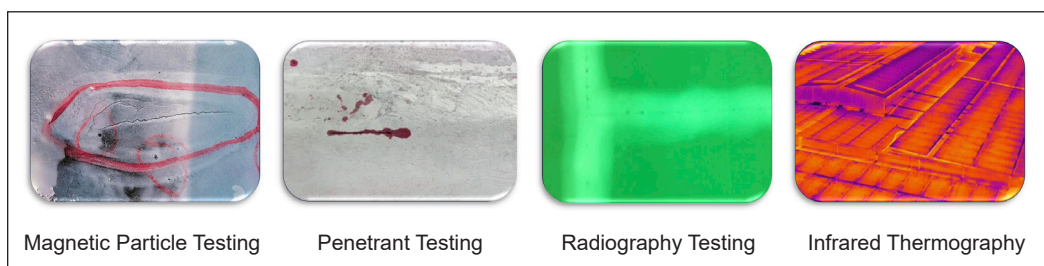


Figure 2. Image type NDT methods suitable for “Hit/Miss” POD

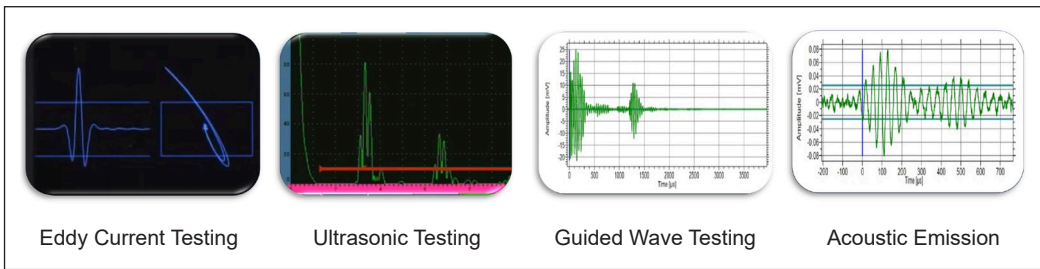


Figure 3. Amplitude type NDT methods suitable for “a versus a” POD

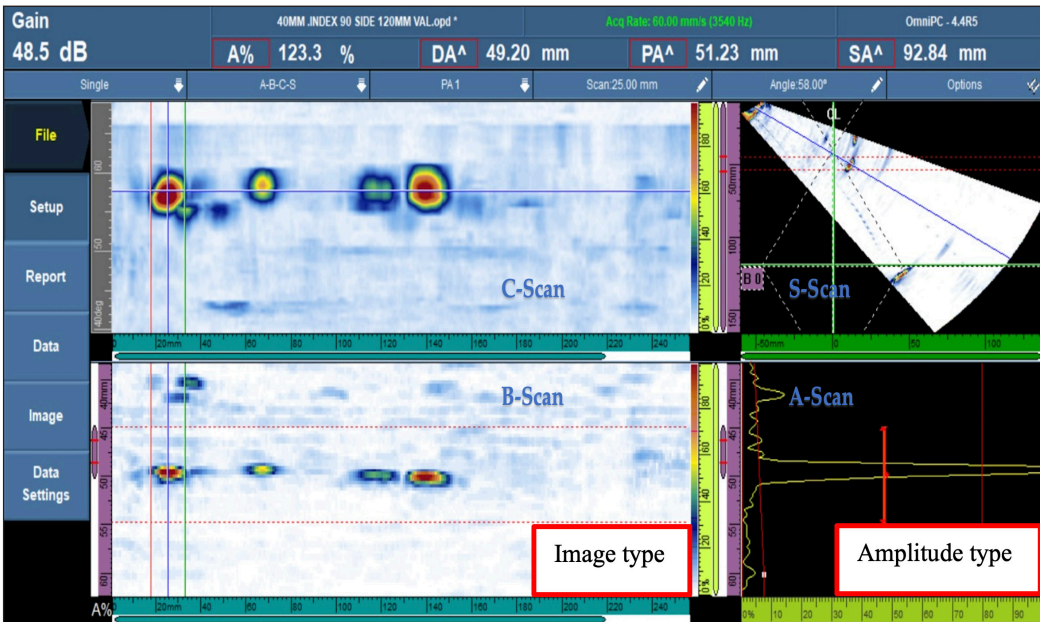


Figure 4. PAUT A-, B-, C- and S-scan presentation

PAUCM simultaneously presents information in image type and signal amplitude forms, making it suitable for both primary POD models. This dual representation not only enhances the feasibility of POD but also allows for relative comparisons.

The primary challenge currently lies in the practical application of POD despite a clear understanding of its foundational concepts. While other researchers have employed various POD computing methods, there remains a gap in translating this knowledge into practical implementation. Moving forward, the focus will be on mastering the utilisation of the MH1823 POD software, using the comprehensive guidance outlined in its accompanying handbook. In addition, dedicated experimental studies will be conducted for PAUCM, allowing for the precise collection of data. Subsequent analyses will rigorously examine various uncertainty parameters to construct and compare POD curves carefully, thereby improving the reliability of the assessments.

CONCLUSION

This comprehensive review highlights the dynamic evolution of POD and its multifaceted applications to various NDT methods. The exploration encompasses the nuanced utilisation of both “hit/miss” and “a versus a” approaches, the emergence and significance of MAPOD, the expedient role of cutting-edge POD software in curve generation, and the exciting prospect of PAUCM within the POD framework.

The journey through this scholarly terrain underscores the remarkable versatility of POD, traversing a broad spectrum of NDT methods and catering to diverse application domains. POD is a unifying metric for assessing the efficacy of defect detection techniques, whether employing UT, ECT, RT, or GW SHM, which mirrors the intricacies of real-world inspection scenarios, where the choice of the NDT method depends on the specific inspection goal and context.

A pivotal insight gleaned from the literature is the significance of parameter selection in the POD analysis. The dichotomy of “red and green apples,” as eloquently shared by one of the POD luminaries, encapsulates the essence of this challenge (Annis et al., 2015b). Selecting appropriate uncertainty parameters is critical to ensure that the chosen parameters accurately represent the characteristics of actual defects and align with the intended applications.

Concluding the literature review, it is evident that further exploration of PAUCM is worthwhile. The practical implementation of POD in real-world inspection scenarios remains a vital milestone. This journey necessitates a harmonious interplay between theoretical and practical insights, allowing for the effective integration of POD concepts into the operational landscape of PAUCM.

ACKNOWLEDGEMENTS

The authors thank Universiti Putra Malaysia for the financial support through Geran Inisiatif Putra Siswazah (GP-IPS) with grant number 9739200. The authors would also like to express their gratitude to the Department of Aerospace Engineering, Faculty of Engineering, Universiti Putra Malaysia, and the Laboratory of Biocomposite Technology, Institute of Tropical Forestry and Forest Product (INTROP), Universiti Putra Malaysia (HICOE) for their close collaboration in this study.

REFERENCES

- Abdelli, D. E., Nguyen, T. T., Clenet, S., & Cheriet, A. (2019). Stochastic metamodel for probability of detection estimation of eddy-current testing problem in random geometric. *IEEE Transactions on Magnetics*, 55(6), 1–4. <https://doi.org/10.1109/TMAG.2019.2893421>
- Accardi, E. D., Palumbo, D., Errico, V., Fusco, A., Angelastro, A., & Galietti, U. (2023). Analysing the probability of detection of shallow spherical defects by means of pulsed thermography. *Journal of Nondestructive Evaluation*, 42(1), 1–16. <https://doi.org/10.1007/s10921-023-00936-y>

- Ameyaw, D. A., Deng, Q., & Söffker, D. (2019). Probability of detection (POD)-based metric for evaluation of classifiers used in driving behavior prediction. *Proceedings of the Annual Conference of the Prognostics and Health Management Society, PHM, 11(1)*, 1–7. <https://doi.org/10.36001/phmconf.2019.v11i1.774>
- Annis, C. (2014). Influence of sample characteristics on probability of detection curves. *40th Annual Review of Progress in Quantitative Nondestructive Evaluation AIP Conference Proceedings, 1581*, 2039–2046. <https://doi.org/10.1063/1.4865074>
- Annis, C., Aldrin, J. C., & Sabbagh, H. A. (2015a). Profile likelihood: What to do when maximum probability of detection never gets to one. *Materials Evaluation, 73(1)*, 96–100.
- Annis, C., Aldrin, J. C., & Sabbagh, H. A. (2015b). What is missing in nondestructive testing capability evaluation? *Materials and Design, 73(1)*, 44–54.
- Bajgholi, M. E., Rousseau, G., Ginzler, E., Thibault, D., & Viens, M. (2023). Total focusing method applied to probability of detection. *International Journal of Advanced Manufacturing Technology, 126(7–8)*, 3637–3647. <https://doi.org/10.1007/s00170-023-11328-x>
- Baskaran, P., Pasadas, D. J., Ramos, H. G., & Ribeiro, A. L. (2021). Integration of multiple response signals into the probability of detection modelling in eddy current NDE of flaws. *NDT and E International, 118*, Article 102401. <https://doi.org/10.1016/j.ndteint.2020.102401>
- Bato, M. R., Hor, A., Rautureau, A., & Bes, C. (2017). Implementation of a robust methodology to obtain the probability of detection (POD) curves in NDT: Integration of human and ergonomic factors. *LES JOURNÉES COFREND 2017*, 1–16.
- Bato, M. R., Hor, A., Rautureau, A., & Bes, C. (2020). Experimental and numerical methodology to obtain the probability of detection in eddy current NDT method. *NDT and E International, 114*, 1–35. <https://doi.org/10.1016/j.ndteint.2020.102300>
- Bayoumi, A., Minten, T., & Mueller, I. (2021). Determination of detection probability and localization accuracy for a guided wave-based structural health monitoring system on a composite structure. *Applied Mechanics, 2(4)*, 996–1008. <https://doi.org/10.3390/applmech2040058>
- Brown, J. H. (2009). *Probability of detection analysis for eddy current inspection systems*. The American Society for Nondestructive Testing.
- Burch, S. F., Stow, B. A., & Wall, M. (2005). Computer modelling for the prediction of the probability of detection of ultrasonic corrosion mapping. *Insight: Non-Destructive Testing and Condition Monitoring, 47(12)*, 761–764. <https://doi.org/10.1784/insi.2005.47.12.761>
- Calmon, P., Mesnil, O., Miorelli, R., Artusi, X., Chapuis, B., & D’Almeida, O. (2019). Model assisted probability of detection for guided wave imaging structural health monitoring. *Proceedings of the 12th International Workshop on Structural Health Monitoring, 1*, 811–816. <https://doi.org/10.12783/shm2019/32190>
- Carboni, M., & Cantini, S. (2016). Advanced ultrasonic “Probability of detection” curves for designing in-service inspection intervals. *International Journal of Fatigue, 86*, 77–87. <https://doi.org/10.1016/j.ijfatigue.2015.07.018>

- Caturano, G., Cavaccini, G., Ciliberto, A., Pianese, V., & Fazio, R. (2009). Probability of detection for penetrant testing in industrial environment. In *Applied and industrial mathematics in Italy III* (pp. 186-195). World Scientific. https://doi.org/10.1142/9789814280303_0017
- Caulder, A. (2018). Full matrix capture and total focusing method: The next evolution in ultrasonic testing. *Materials Evaluation*, 76(5), 591–597.
- Choi, Y. M., Kang, D., Kim, Y. L., Cho, S., Park, T., & Park, I. K. (2022). Reliability assessment of PAUT technique in Lieu of RT for tube welds in thermal power plant facilities. *Applied Sciences*, 12(12), Article 5867. <https://doi.org/10.3390/app12125867>
- DOD. (2009). *MIL-HDBK-1823A, Nondestructive evaluation system reliability assessment*. Department of Defense Handbook.
- Dominguez, N., Feuillard, V., Jenson, F., & Willaume, P. (2012). Simulation assisted pod of a phased array ultrasonic inspection in manufacturing. *AIP Conference Proceedings*, 1430(31), 1765–1772. <https://doi.org/10.1063/1.4716425>
- Dominguez, N., Jenson, F., & Defense, E. A. (2010, June 7-11). Simulation assisted POD of a high frequency Eddy current inspection procedure. In *Proceedings of the 10th European Conference on Non-Destructive Testing. European Conference on Non-Destructive Testing* (pp. 1-10). Moscow, Russia.
- Dominguez, N., Rodat, D., Guibert, F., Rautureau, A., & Calmon, P. (2016). POD evaluation using simulation: Progress, practice and perspectives regarding human factor. *AIP Conference Proceedings*, 1706, 3–9. <https://doi.org/10.1063/1.4940651>
- Feistkorn, S., & Taffe, A. (2014). Methods to assess the quality of non-destructive testing in civil engineering using POD and GUM for static calculations of existing structures. *Materialpruefung/Materials Testing*, 56(7–8), 611–616. <https://doi.org/10.3139/120.110602>
- Forsyth, D. S. (2016). Structural health monitoring and probability of detection estimation. In *AIP Conference Proceedings* (Vol. 1706, No. 1). AIP Publishing. <https://doi.org/10.1063/1.4940648>
- Forsyth, D. S., & Aldrin, J. C. (2009, June 24-26). Build your own POD. In *Proceedings of the 4th European-American Workshop on Reliability of NDE* (pp. 1–8). Berlin, Germany.
- Foucher, F., Fernandez, R., Leberre, S., & Calmon, P. (2018). New tools in CIVA for model assisted probability of detection (MAPOD) to support NDE reliability studies. *NDE of Aerospace Materials & Structures 2018*, 32–43.
- Generazio, E. R. (2009). Design of experiments for validating probability of detection capability of NDT systems and for qualification of inspectors. *Materials Evaluation*, 67(6), 730–738.
- Georgiou, G. A. (2007). PoD curves, their derivation, applications and limitations. *Insight: Non-Destructive Testing and Condition Monitoring*, 49(7), 409–414. <https://doi.org/10.1784/insi.2007.49.7.409>
- Ghose, B. (2013). Evaluation of probability of detection (POD) and minimum number of exposures required for detection of planar flaw in cylindrical object by radiographic NDE method. *Asia Pacific Conference on Non-Destructive Testing*, 19, 1-6.
- Gianneo, A., Carboni, M., & Giglio, M. (2016a). Feasibility study of a multi-parameter probability of detection formulation for a lamb waves-based structural health monitoring approach to light alloy aeronautical plates. *Structural Health Monitoring*, 16(2), 225–249. <https://doi.org/10.1177/1475921716670841>

- Gianneo, A., Carboni, M., & Giglio, M. (2016b). Reliability aspects and multi-parameter POD formulation for guided wave based SHM techniques. *19th World Conference on Non-Destructive Testing 2016*, 1–11.
- Gollwitzer, C., Bellon, C., Deresch, A., & Ewert, U. (2011). On POD estimations with radiographic simulator aRTist. In *International Symposium on Digital Industrial Radiology and Computed Tomography (No. DGZfP-BB 128 [Tu. 2.3])* (pp. 1-8). Deutsche Gesellschaft für zerstörungsfreie Prüfung eV (DGZfP).
- Goursolle, T., Fauret, T., & Juliac, E. (2016, June 13-17). Effect of data amount on probability of detection estimation: Application to Eddy current testing. In *19th World Conference on Non-Destructive Testing 2016* (pp. 1-8). Munich, Germany.
- Guan, X., Zhang, J., Zhou, S., Rasselkorde, E. M., & Abbasi, W. (2014). Probabilistic modeling and sizing of embedded flaws in ultrasonic non-destructive inspections for fatigue damage prognostics and structural integrity assessment. *NDT and E International*, *61*, 1–9. <https://doi.org/10.1016/j.ndteint.2013.09.003>
- Haapalainen, J., & Leskelä, E. (2012, April 16-20). Probability of detection simulations for ultrasonic pulse-echo testing. In *18th World Conference on Nondestructive Testing* (pp. 1-5). Durban, South Africa.
- He, X., Jiang, X., Guo, J., Xu, L., & Mo, R. (2024). Ultrasonic evaluation of wire-to-terminal joints: integrating XGBoost machine learning with finite element feature analysis. *Nondestructive Testing and Evaluation*, 1–18. <https://doi.org/10.1080/10589759.2024.2304265>
- Herberich, J. (2009). Applying MIL-HDBK-1823 for POD demonstration on a fluorescent penetrant system. *Materials Evaluation*, *67*(3), 293–301.
- Hossain, M., Ziehl, P., Yu, J., Caicedo, J., & Matta, F. (2013). *Assessing probability of detection based on acoustic emission associated with fatigue crack extension in steel bridge elements*. The American Society for Nondestructive Testing.
- Jenson, F., Iakovleva, E., & Dominguez, N. (2011). Simulation supported POD: Methodology and HFET validation case. *AIP Conference Proceedings*, *1335*, 1573–1580. <https://doi.org/10.1063/1.3592117>
- Kanzler, D., & Müller, C. (2016a, June 13-17). Evaluating RT systems with a new POD approach. In *Proceedings of the 19th World Conference on Non-Destructive Testing* (pp. id-19535). Munich, Germany.
- Kanzler, D., & Müller, C. (2016b). How much information do we need? A reflection of the correct use of real defects in POD-evaluations. In *AIP Conference Proceedings* (Vol. 1706, No. 1). AIP Publishing. <https://doi.org/10.1063/1.4940652>
- Kanzler, D., Müller, C., Pitkänen, J., & Ewert, U. (2012, April 16-20). Bayesian approach for the evaluation of the reliability of non-destructive testing methods: Combination of data from artificial and real defects. In *18th world conference on nondestructive testing* (pp. 1-6). Durban, South Africa.
- Kanzler, D., Milsch, S., Pavlovic, M., Müller, C., & Pitkänen, J. (2019). Concept of total reliability of NDT methods for inspection of the EB weld of the copper canister used for a long-term storage of spent nuclear fuel. *Structural Integrity and NDE Reliability III Concept*, 1-6.
- Kim, F. H., Pintar, A., Obaton, A. F., Fox, J., Tarr, J., & Donmez, A. (2021). Merging experiments and computer simulations in X-ray computed tomography probability of detection analysis of additive manufacturing flaws. *NDT and E International*, *119*, Article 102416. <https://doi.org/10.1016/j.ndteint.2021.102416>

- Knopp, J. S., & Zeng, L. (2013). Statistical analysis of Hit/Miss data. *Materials Evaluation*, 71(3), 322–329.
- Kojima, M., Takahashi, H., & Kikura, H. (2019). Evaluation of capabilities on ultrasonic testing examiners using probability of defect detection and cumulative failure probability. *Journal of Advanced Maintenance*, 11(2), 65–78.
- Kurz, J. H., Jüngert, A., Dugan, S., & Dobmann, G. (2012, April 16-20). Probability of detection (POD) determination using ultrasound phased array for considering NDT in probabilistic damage assessments. In *South-African Institute for Non-destructive Testing: World Conference on Nondestructive Testing* (pp. 1-10). Durban, South Africa.
- Kurz, J. H., Jüngert, A., Dugan, S., Dobmann, G., & Boller, C. (2013). Reliability considerations of NDT by probability of detection (POD) determination using ultrasound phased array. *Engineering Failure Analysis*, 35, 609-617. <https://doi.org/10.1016/j.engfailanal.2013.06.008>
- Le Gratiot, L., Iooss, B., Blatman, G., Browne, T., Cordeiro, S., & Goursaud, B. (2017). Model assisted probability of detection curves: New statistical tools and progressive methodology. *Journal of Nondestructive Evaluation*, 36(8), 1–12. <https://doi.org/10.1007/s10921-016-0387-z>
- Lei, X., Wirdelius, H., & Rosell, A. (2022). Simulation-based investigation of a probability of detection (POD) model using phased array ultrasonic testing (PAUT) technique. *Journal of Nondestructive Evaluation*, 41(2), 1–13. <https://doi.org/10.1007/s10921-022-00873-2>
- Lembersky, L., Adams, R., Tamutus, T., & Watson, J. (2012). Suspension cable wire break monitoring using acoustic emission for economic and probability of detection advantages. In *Structural Materials Technology 2012* (pp. 169-176). PubGenius Inc.
- Marcotte, O., & Liyanage, T. (2017). *Nondestructive examination (NDE) used fuel containers probability of detection for increased probability of detection*. The American Society for Nondestructive Testing.
- Meeker, W. Q. (2000). A methodology for predicting probability of detection for ultrasonic testing. In *AIP Conference Proceedings* (Vol. 557, No. 1, pp. 1972-1978). AIP Publishing. <https://doi.org/10.1063/1.1373994>
- Mohr, G. A., & Willems, P. (2008, October 25-28). Factors affecting Probability of Detection with Computed Radiography. In *17th World Conference on Nondestructive Testing* (pp. 1-8). Shanghai, China.
- Peeters, J., Ibarra-Castanedo, C., Khodayar, F., Mokhtari, Y., Sfarra, S., Zhang, H., Maldague, X., Dirckx, J. J., & Steenackers, G. (2018). Optimised dynamic line scan thermographic detection of CFRP inserts using FE updating and POD analysis. *NDT and E International*, 93, 141–149. <https://doi.org/10.1016/j.ndteint.2017.10.006>
- Poudel, A., Galvan-Nunez, S., Lindeman, B., & Gonzalez, F. (2022). *A quantitative assessment of historical nondestructive evaluation (NDE) probability of detection (POD) data for railroad tank cars*. The American Society for Nondestructive Testing.
- Rentala, V. K., Mylavarapu, P., & Gautam, J. P. (2018). Issues in estimating probability of detection of NDT techniques – A model assisted approach. *Ultrasonics*, 87, 59–70. <https://doi.org/10.1016/j.ultras.2018.02.012>

- Rentala, V. K., Mylavarapu, P., K.Gopinath, Gautam, J. P., & Kumar, V. (2016, November 3-5). Model assisted probability of detection for lognormally distributed defects. In *8th International Symposium on NDT in Aerospace* (pp. 1-8). Bangalore, India.
- Ribay, G., Mahaut, S., Cattiaux, G., & Sollier, T. (2017, September 4-7). Assessment of the reliability of phased array NDT of coarse grain component based on simulation. In *Proceedings of the 7th European-American Workshop on Reliability of NDE* (pp. 1–8). Potsdam, Germany. <http://www.nde-reliability.de/portals/nde17/BB/21.pdf>
- Rodat, D., Guibert, F., Dominguez, N., & Calmon, P. (2017). Operational NDT simulator, towards human factors integration in simulated probability of detection. In *AIP Conference Proceedings* (Vol. 1806, No. 1). AIP Publishing. <https://doi.org/10.1063/1.4974719>
- Schneider, C. R. A., Sanderson, R. M., Carpentier, C., Zhao, L., & Nageswaran, C. (2012, September 11-13). Estimation of probability of detection curves based on theoretical simulation of the inspection process. In *51st Annual Conference of the British Institute of Non-Destructive Testing* (pp. 393–404). Northamptonshire, UK.
- Spies, M., & Rieder, H. (2018, June 11-15). An approach to the question ‘How to account for human error in MAPOD?’ In *12th European Conference on Non-Destructive Testing (ECNDT 2018)* (pp. 1–5). Gothenburg, Sweden. <https://www.ndt.net/article/ecndt2018/papers/ecndt-0571-2018.pdf>
- Stubbs, D. A. (2005). Probability of detection for embedded defects: Needs for ultrasonic inspection of aerospace turbine engine components. *AIP Conference Proceedings*, 760, 1909–1916. <https://doi.org/10.1063/1.1916903>
- Subair, S. M., Balasubramaniam, K., Rajagopal, P., Kumar, A., Rao, B. P., & Jayakumar, T. (2014). Finite element simulations to predict probability of detection (PoD) curves for ultrasonic inspection of nuclear components. *Procedia Engineering*, 86, 461–468. <https://doi.org/10.1016/j.proeng.2014.11.059>
- Tai, J. L., Grzejda, R., Sultan, M. T. H., Łukaszewicz, A., Shahar, F. S., Tarasiuk, W., & Rychlik, A. (2023). Experimental investigation on the corrosion detectability of A36 low carbon steel by the method of phased array corrosion mapping. *Materials*, 16(15), Article 5297. <https://doi.org/10.3390/ma16155297>
- Tisseur, D., Costin, M., Fournier, S., Reece, C., & Schumm, A. (2019, October 1-3). POD calculation on a radiographic weld inspection with CIVA 11 RT module. In *10th International Conference on NDE in Relation to Structural Integrity for Nuclear and Pressurized Components (JRC-NDE 2013)* (pp. 123–129). Cannes, France.
- Topp, M., & Strothmann, L. (2021). How can NDT 4.0 improve the Probability of Detection (POD)? *E-Journal of Nondestructive Testing (NDT)*, 26(4), 1–10. <http://www.ndt.net/?id=26013>
- Tschoke, K., Mueller, I., Memmolo, V., Moix-Bonet, M., Moll, J., Lugovtsova, Y., Golub, M., Venkat, R. S., & Schubert, L. (2021). Feasibility of model-assisted probability of detection principles for structural health monitoring systems based on guided waves for fiber-reinforced composites. *IEEE Transactions on Ultrasonics, Ferroelectrics, and Frequency Control*, 68(10), 3156–3173. <https://doi.org/10.1109/TUFFC.2021.3084898>

- Underhill, P. R., & Krause, T. W. (2011). Quantitative fractography for improved probability of detection (POD) analysis of bolt hole eddy current. *Research in Nondestructive Evaluation*, 22(2), 92–104. <https://doi.org/10.1080/09349847.2011.553349>
- Underhill, P. R., & Krause, T. W. (2016). Eddy current probability of detection for mid-bore and corner cracks in bolt holes of service material. *Research in Nondestructive Evaluation*, 27(1), 34–47. <https://doi.org/10.1080/09349847.2015.1045642>
- Underhill, P. R., Uemura, C., & Krause, T. W. (2018). Probability of detection for bolt hole eddy current in extracted from service aircraft wing structures. In *AIP Conference Proceedings* (Vol. 1949, No. 1). AIP Publishing. <https://doi.org/10.1063/1.5031619>
- Virkkunen, I., Koskinen, T., Papula, S., Sarikka, T., & Hänninen, H. (2019). Comparison of \hat{a} versus a and Hit/Miss POD-estimation methods: A European viewpoint. *Journal of Nondestructive Evaluation*, 38, 1-13. <https://doi.org/10.1007/s10921-019-0628-z>
- Volker, A. W. F., Dijkstra, F. H., Terpstra, S., Heerings, H. A. M., & Lont, M. A. (2004, August 30 – September 3). Modeling of NDE reliability: Development of a “POD-Generator”. In *Proceedings of the 16th World Conference on Nondestructive Testing* (pp. 1-8). Montreal, Canada.
- Wall, M., Burch, S., & Lilley, J. (2009). Human factors in POD modelling and use of trial data. *Insight: Non-Destructive Testing and Condition Monitoring*, 51(10), 553–561. <https://doi.org/10.1784/insi.2009.51.10.553>
- Wright, M. (2016, November 15-17). How to implement a PoD into a highly effective inspection strategy. In *NDT in Canada 2016 & 6th International CANDU In-Service Inspection Workshop* (pp. 1-8). Burlington, Canada. <https://www.ndt.net/search/docs.php3?id=20418>
- Xu, Z., Zhou, Z., Chen, H., Qu, Z., & Liu, J. (2023). Effects of the wire mesh on pulsed eddy current detection of corrosion under insulation. *Nondestructive Testing and Evaluation*, 38(2), 233–253. <https://doi.org/10.1080/10589759.2022.2102167>
- Yosifov, M., Reiter, M., Heupl, S., Gusenbauer, C., Fröhler, B., Fernández- Gutiérrez, R., De Beenhouwer, J., Sijbers, J., Kastner, J., & Heinzl, C. (2022). Probability of detection applied to X-ray inspection using numerical simulations. *Nondestructive Testing and Evaluation*, 37(5), 536–551. <https://doi.org/10.1080/10589759.2022.2071892>
- Yosifov, M., Weinberger, P., Reiter, M., Fröhler, B., Beenhouwer, J. De, Sijbers, J., Kastner, J., & Heinzl, C. (2023). Defect detectability analysis via Probability of defect detection between traditional and deep learning methods in numerical simulations. *E-Journal of Nondestructive Testing*, 28(3), 2–11. <https://doi.org/10.58286/27716>
- Yusa, N. (2017). Probability of detection model for the non-destructive inspection of steam generator tubes of PWRs. *Journal of Physics: Conference Series*, 860(1), 6–13. <https://doi.org/10.1088/1742-6596/860/1/012032>
- Yusa, N., Chen, W., & Hashizume, H. (2016). Demonstration of probability of detection taking consideration of both the length and the depth of a flaw explicitly. *NDT and E International*, 81, 1–8. <https://doi.org/10.1016/j.ndteint.2016.03.001>

- Yusa, N., Tomizawa, T., Song, H., & Hashizume, H. (2018). Probability of detection analyses of eddy current data for the detection of corrosion. *Nondestructive Testing and Diagnostics*, 4, 3–7. <https://doi.org/10.26357/BNiD.2018.031>
- Zhao, J., Yang, K., Du, X., Yao, S., & Zhao, Y. (2023). Automated quantification of small defects in ultrasonic phased array imaging using AWGA-gcForest algorithm. *Nondestructive Testing and Evaluation*, 1–22. <https://doi.org/10.1080/10589759.2023.2274001>
- Zhu, J., Min, Q., Wu, J., & Tian, G. Y. (2018). Probability of detection for eddy current pulsed thermography of angular defect quantification. *IEEE Transactions on Industrial Informatics*, 14(12), 5658–5666. <https://doi.org/10.1109/TII.2018.2866443>

Review Article

Formulation of Lubricating Grease from Waste Oil: A Review

Nur Amira Fatihah Bashari, Mohd Aizudin Abd Aziz*, Muhammad Auni Hairunnaja and Mohd Azmir Arifin

Faculty of Chemical Engineering Technology, Universiti Malaysia Pahang Al-Sultan Abdullah, 26300 UMPA, Gambang, Pahang, Malaysia

ABSTRACT

This paper demonstrates the potential of waste turbine oil (WTBO) as a base oil to substitute for mineral oil, which is usually used in grease formulations. This study will analyze the characteristics of used turbine oil, including its chemical composition and physical characteristics, including kinematic viscosity, viscosity index, moisture content, contamination, and density. The presence of antioxidants (butylated hydroxytoluene (BHT) and amine or phenyl-a-naphthylamine (PANA), anti-wear, and corrosion-inhibiting additives that can improve the formulated lubricating grease performance and lengthen service life are just a few of the useful remaining WTBO characteristics that can be used wisely as the base oil. It is crucial to create more environmentally friendly, economically sensible, and thrifty grease formulations to adhere to Malaysia's Green Technology Master Plan, which has outlined the strategic plans for developing green technologies. The new inventions must establish a resource- and carbon- efficient economy. The abundance of WTBO in the aviation industry and the unique characteristics of WTBO itself promise a reliable supply of base oil for lubricating grease in the future.

Keywords: Additives, base oil, grease formulation, grease lubricants, spent bleaching earth (SBE), thickener, waste turbine oil

ARTICLE INFO

Article history:

Received: 04 September 2023

Accepted: 01 February 2024

Published: 15 August 2024

DOI: <https://doi.org/10.47836/pjst.32.5.15>

E-mail addresses:

amirabashari97@gmail.com (Nur Amira Fatihah Bashari)

maizudin@ump.edu.my (Mohd Aizudin Abd Aziz)

mauliduni97@gmail.com (Muhammad Auni Hairunnaja)

mazmir@ump.edu.my (Mohd Azmir Arifin)

* Corresponding author

INTRODUCTION

Basic Components in Grease

Grease's basic function is to stay in contact with and lubricate the moving surfaces without sweeping out due to pressure, centrifugal force, or gravity. It is an oil-

based product that can form in solid to semifluid forms, and it is made up of base oil (70%–90%), thickener (5%–20%), and additives (1%–10%) (Rohim et al., 2021). The base oil, thickener and additive package significantly influence the behavior of grease. These three are the essential components on which grease formulas depend the most. The thickener is frequently described as a “sponge” that binds the base oil and additives (Alias et al., 2023). The thickener traps the oil that makes up most of the grease to stiffen or densify the finished product. Mineral oils and synthetic fluids are examples of base oils. The most used base is mineral oil. However, synthetic bases work best in extremely hot conditions (Suhaila et al., 2018).

Type of Grease

Grease is typically classified into two categories: soap-based and non-soap-based, depending on the thickener agent used in the lubricant. Soap-based grease uses a soap, such as lithium or sodium stearate, to maintain the even mixing of the oil and water components of the grease. In contrast, synthetic grease, also known as non-soap-based grease, employs a synthetic thickener, such as polyurea, to give the lubricant its structure (Aziz et al., 2017; Rawat & Harsha, 2019; Sofi et al., 2019).

Compared to soap-based grease, synthetic grease offers better lubrication, wear prevention, high-temperature stability, and higher resistance to water washout. Conversely, soap-based grease is commonly used in various industrial applications due to its good water resistance and ability to lubricate at low temperatures. Synthetic grease is often used in heavy-duty industrial and automotive applications with high temperatures and challenging operating conditions. In summary, the classification of grease as either soap-based or non-soap-based is based on the unique properties and capabilities of the two types of thickeners, as well as the specific applications in which they are used (Rahman & Aziz, 2022).

Based on a 2020 article from Tribology International, Figure 1 provides a mind map that displays some of the common types of oil greases (Chatra & Lugt, 2020; Johnson, 2008).

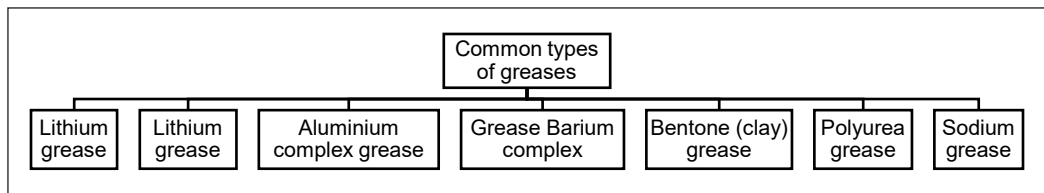


Figure 1. Common type of greases (Chatra & Lugt, 2020; Johnson, 2008)

General Grease Formulation from Waste Oil

The grease formulation is formed from a combination of base oils, additives and thickener. The mixture of the combination with the certain amounts will impact the characteristics of

the grease performance. Genuine grease combines an oil or other liquid lubricant with a thickening, usually soap, to create a solid. Grease typically contains (1) 70%–90% base oil, (2) 5%–20% soap-like gelling agents (thickener), and (3) 1%–10% additives such as rust inhibitors, antioxidants, metal deactivators, and anti-wear agents (Mang & Dresel, 2007). The Industrial Revolution significantly impacted technology for grease enhancement formulation. Nowadays, many researchers are concerned about innovating a greener grease formulation by substituting the base oil that is frequently from the mineral source with the waste oil. Many successful stories of grease formulation from waste oil have been recorded, such as waste oil from waste engine oil, transformer oil and waste cooking oil (Japar et al., 2018, 2019, 2020).

Base Oil

The base oil in grease is a carrier for the lubricant and lubricates the machine's moving parts. It controls a lot of lubricant characteristics, including viscosity, volatility, and thermal stability. Grease performance can be impacted by the base oil's characteristics under various loads, temperatures, and environmental conditions (Aziz et al., 2017; Zhang et al., 2021). The characteristics and performance of the lubricant can be impacted by the base oil's carbon chain length.

A chain of carbon atoms joined in a linear or branched pattern is referred to as an aliphatic hydrocarbon chain. Many organic molecules, including the hydrocarbons in crude oil, natural gas, and coal, are composed of carbon chains as their fundamental constituents. A few to several hundred carbon atoms can make up the length of the carbon chain, which is determined by the number of carbon atoms. The number of carbon atoms in the hydrocarbon molecules that make up the base oil is referred to as the carbon chain length. In comparison to long-chain hydrocarbons, short-chain hydrocarbons, such as those in mineral oil, have a lower viscosity and are less stable at high temperatures. They are also more flammable since they have a lower flash point (Kaperick, 2013).

In comparison to short-chain hydrocarbons, long-chain hydrocarbons, such as those found in synthetic oils, have a higher viscosity and are more stable at high temperatures. They are also less prone to catch fire since they have a greater flash point. The properties of hydrocarbons can be influenced by the length of the carbon chain, the kind of chemical connection between the carbon atoms, the existence of double bonds, and the presence of functional groups (Niu et al., 2019).

Figure 2 shows a common variety of base oils, including mineral oil, synthetic oil, vegetable oil, biodegradable oil, food-grade oil, and high-temperature oil that can be utilized as a base oil in grease. The choice of base oil depends on the application and the operating circumstances to which the lubricant will be exposed. Each type of base oil has its distinct qualities and benefits (Suhaila et al., 2018). The creation of the thickening structure

is substantially influenced by the type of base oil, which likely results in a distinct bleeding behavior and, consequently, a different lubricating mechanism (Fischer et al., 2018). Knowing that base oil provides lubrication, the viscosity factor will depend on it (the film thickness that depends on the base oil) (Kanazawa et al., 2017).

The most common base oil used in grease is mineral oil, derived from crude oil through refining. It is the cheapest and most widely used base oil in grease. However, they have disadvantages, such as less wear protection than synthetic-based greases, less thermal degradation and oxidation resistance, and not being biodegradable. If leaked or spilled, it can cause harm to the environment (Chandraseagar et al., 2019; Kuppusamy et al., 2020). Mineral oil can be further refined to create synthetic base oils (Rudnick, 2013).

Table 1 presents the API (American Petroleum Institute) classifications used to determine the level of refinement of base oils. Most industrial lubricants are derived from basic oils, and the API categorizes base oils into five groups based on their composition and how they are manufactured, as well as their response to different conditions, such as high temperatures. Groups I to III are produced by refining petroleum crude oil, while Group IV consists of fully synthetic (polyalphaolefin) base oils. Group V includes all other base oils that do not fall into Groups I to IV. Before any additives are mixed in, lubricating oils are initially categorized according to these five API groups (Aziz et al., 2017, 2018; Yano et al., 2013).

Turbine oil is a highly refined mineral produced from properly selected crude oil (ENEOS Corporation, 2018). It falls into Group 1 as it consists of mineral oil. Due to its strong oxidation stability and high viscosity index, it can be utilized as a lubricant for many

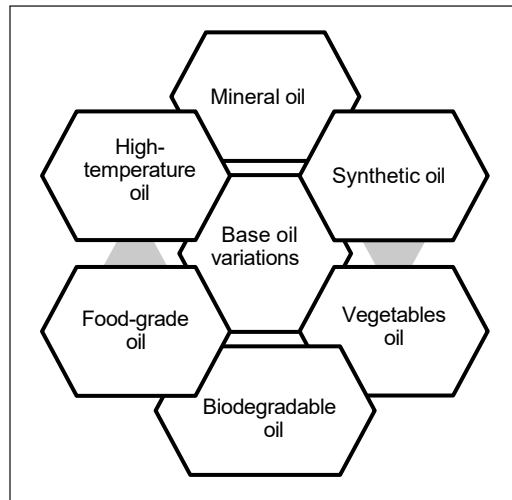


Figure 2. Base oil variations for grease formulation (Niu et al., 2019)

Table 1
API base stock categories

Groups	Base Oil	Viscosity Index	Vol % of Saturates	Mass of % Sulphur
I.	Mineral Oil	$80 \leq V1 < 120$	and < 90	> 0.03
II.		$80 \leq V1 < 120$	and ≥ 90	≤ 0.03
III.			≥ 90	≤ 0.03
IV.	Polyalphaolefin (PAO)		≤ 120	
V.	All other base stocks			

different types of machinery, particularly for compressors and general industrial equipment. The best viscosity grade can be selected because it ranges in viscosity from 32 to 220.

Thickener

The thickener is a substance that will create a solid or semifluid structure when it is combined with the chosen lubricant. The thickener provides grease by being a sponge that holds the lubricant in place by holding the combination of base oil and additives together. Thus, the stability and consistency of the grease will be directly impacted by the amount and type of thickener present (Razali et al., 2018). It has been discovered that the structure of the thickener and the viscosity of the base oil mostly affect how elastohydrodynamic lubrication films behave. The structure of the thickener, base oil viscosity, and rolling speed all have an impact on how the thickener adheres to or deposits on contacting surfaces, as well as how oil starvation affects film formation (Stahl & Jacobson 2003; Wu et al., 2023). Elastohydrodynamic Lubrication (EHL), a type of hydrodynamic lubrication (HL), is a lubrication regime where there is significant elastic deformation of the surfaces, which significantly changes the shape and thickness of the lubricant film in the contact (Mahadeshwara et al., 2023).

One of the most common types of thickener used in grease is metallic soap, which currently contains calcium, sodium, lithium, aluminum, clay, polyurea, and sodium. The traditional metallic soap is combined with a complex of ingredients to create complex greases. Lithium-based is the most popular type as it has widely been used. These are produced using a low-molecular-weight organic acid as the complexing agent in addition to normal lithium soap (Arki & Balköse, 2013). A soap is a metal salt of fatty acid by definition (Russo et al., 2023). If the grease contains soap, fatty acids are added; if not, basic oil is filled with the remaining elements. The long chain with complex of azelaic acid, acids tallow and sebacic acid (such as instances of typical acids) as well as the high-molecular-weight fatty acids, stearic acid and 12-hydroxystearic acid are the remaining elements. The metal base is added once the acid reaches the proper temperature, at which point the fatty acid melts. Making soap is referred to as saponification (Figure 3). In essence, it is a mix of acid and base equal/produces soap and water.

Then, all the water is removed because lubricants should have very little water. After finishing, the substance is cooled and allowed to gel; at this point, the mixture turns into grease. Next, base oil is added to the

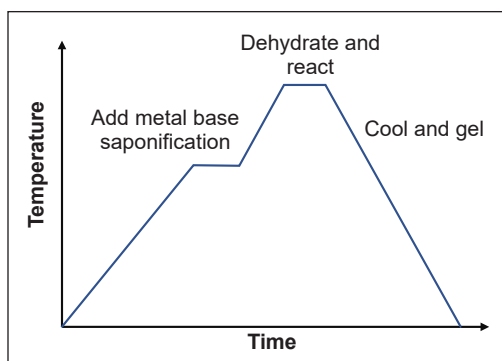


Figure 3. Grease essential process: acid + base = soap + water

mixture to modify consistency (additives might also be added). To achieve the consistency needed for the product, it might need to be heated, cooled, and tested multiple times. Most people mistakenly believe that grease is largely a thickener, whereas it is mostly oil. Usually, 10%– 20% of the oil in a container contains soap (Jeanna, 2017; Rawat & Harsha, 2019).

Non-soap thickeners are also becoming more and more common in specialized applications, like high- temperature settings. Two examples of thickeners that do not melt at high temperatures are bentonite and silica aerogel (Rawat & Harsha, 2019).

Figure 4 shows the crystalline structure of a few common thickeners that have always been used in the grease industry. Different crystalline structures are produced depending on the thickener’s component chemistry, which changes the qualities of the grease made with those thickeners. The crystals get denser and thicken less effectively, but they also get more thermal and shear stable. However, greases with a larger thickener content have worse pumpability and torque characteristics, as one might anticipate (Fan et al., 2018).

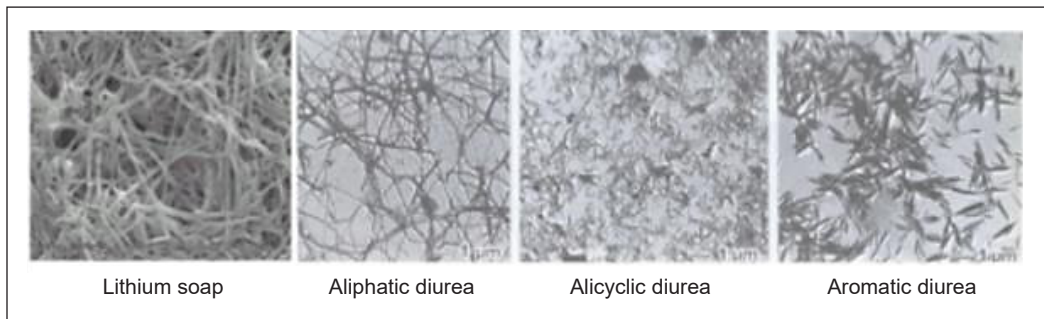


Figure 4. Crystalline structure in different thickener

Additives

Today, a wide range of additives are utilized to improve the service characteristics of lubricating grease. These additions alter the interfacial energy between the base oil and the thickening agent particles in a certain range and degree, and the volumetric fraction and nature of the additives have a major impact on their success. The characteristics of lubricating grease components and the microstructure attained during the production will determine how good the grease’s performance will be (Chatra & Lugt, 2020). There are a few ways to categorize additives that have been characterized, such as whether they work in the fluid’s center or on the surface, chemically active or inert, or via physical touch. Table 2 shows that the additives could be divided into two categories: performing in bulk or at a surface (Bhat & Charoo, 2019; Canter, 2012).

The grease formulation’s primary goal is to be able to choose additives that will not damage the grease. Hence, the choice of additives must take into consideration the structural stability of the thickener system that was used in the grease formulation. One of

Table 2

Additives category (Bhat & Charoo, 2019; Canter, 2012)

Additives performing in the bulk of the grease	
Antioxidants	Extend the life of the lubricant by inhibiting oxidation, thus minimizing base oil thickening, sludging and deposits
Scavengers	Chosen to react with undesirable contaminants such as acids or sulfur to render them less harmful.
Additives performing at a surface	
Anti-wear Agents	Inhibit wear typically under high-speed, low-load operating conditions.
Corrosion Inhibitors	Inhibit the corrosion of metals in contact with the lubricant, protecting equipment and extending the useful life of the lubricant.
Extreme Pressure (EP) Agents	Inhibit seizure under high loads and temperatures
Friction Modifiers	Reduce the friction between moving parts by surface adsorption
Metal Deactivators	Inhibit the metals from contacting the lubricant and catalyzing the oxidation of the lubricant.
Seal Swell Agents	Assist elastomer seals and gaskets in performing their function.

the thickener's characteristics that usually hinders the movement of additives is the polarity of the thickener. Inappropriate additives will create a physical barrier (Kaperick, 2013). Besides, it also can cause grease to soften, odor, corrosion with the intact surface, low-temperature performance, and decrease permeability (Bhat & Charoo, 2019; Canter, 2012).

PROBLEM STATEMENTS

Grease formulations based on mineral oil are frequently employed in a wide range of industrial and automotive applications because they effectively lubricate and safeguard moving parts. The base oil that is most generally used in the formation of grease is mineral oil, which is made from petroleum. The current trend in grease formulation nowadays is to create greases that are more sustainable and environmentally friendly while yet delivering the performance demands of various applications. Other than that, it needs to be cheap as well. One of the most cost-effective and sustainable methods of grease formulation that has been identified and is ongoing is using waste oil as a base oil in the grease formulation, where the typical base oil, usually from mineral oil, will be substituted with the waste oil (Okal et al., 2022). Research and development to employ waste oil as a base oil for grease formulation is actively happening. Numerous results and findings in the research that look into the performance and viability of using waste oil as a base oil have typically been encouraging. Studies demonstrated that in terms of wear resistance, load-carrying capacity, and high-temperature stability, waste oil used as a base oil in greases could perform on par with or even better than standard mineral oil-based greases. Besides, it is also mixed with selected thickeners and additives to enhance performance and increase service life, such as antioxidants, rust inhibitors, and anti-wear agents (Japar et al., 2020).

In the recently published study, many researchers claimed to have been able to develop grease using various waste oils such as waste cooking oil (WCO), waste engine oil (WEO), and waste transformer oil (WTO) as the base oil (Japar et al., 2019; Rahman & Aziz, 2022; Whitby, 2020). The performance of the produced grease may differ depending on the chemical qualities and composition of these three forms of waste oil. Usually, a vegetable oil, like WCO, that is used for frying food and is primarily made up of triglycerides, which are esters of glycerol and fatty, will create grease with low toxicity, good oxidation stability, high flash point, low pour point and high Viscosity Index (VI) (Herman et al., 2021). Meanwhile, WTO, an insulating and cooling fluid made primarily of paraffin, naphthene, and aromatics, is used in electrical transformers, and WEO is a lubricant that is used to lubricate internal combustion engines; it is primarily made up of hydrocarbons such as paraffins, naphthenes, and aromatics (Mahmud et al., 2019). Since both WTO and WEO are made up of almost similar hydrocarbon properties, they share almost similar properties of the grease produced, such as high viscosity, good lubrication, high-temperature resistance, good water resistance and good corrosion resistance (Japar et al., 2019; Rahman & Aziz, 2022).

Modern grease formulations employ waste oil as a base oil for its sustainability, cost-effectiveness, promising performance, and environmental-friendliness. Other than that, it is due to their availability, too. As numerous industrial processes constantly produce it, waste oil is readily available on the market and can serve as a reliable source of base oil. Although the idea of recycling waste oil to make new products has been put into practice in Malaysia (Razali et al., 2018, 2020), regrettably, WTBO has not discovered a means to recycle in any application despite the growing markets of turbine oil. WTBO is a useful by-product of turbine oil that is unavoidable while lubricating turbines for chemical synthesis (Glushkov et al., 2020). It is, nevertheless, can cause a serious environmental issue. Abundant WTBOs worldwide, present significant environmental, economic, and social problems (Liu et al., 2013).

A few research have found some valuable chemical and physical characteristics of waste turbine oil that can be utilized to formulate a high-quality grade at a low cost. WTBO also had been found to have a similar hydrocarbon chain as WEO and WTO, where WTBO also consisted of paraffins, naphthenes, and aromatics. Furthermore, as waste aviation turbine oil already contains a number of additives like antioxidants, rust inhibitors, and anti-wear agents that can enhance performance and lengthen service life, it can be thought of as a potential replacement for mineral oil as a base oil in grease composition (Vershina et al., 2019). Additionally, it is designed to offer lubrication and protection in extreme pressure, high load, and high-temperature circumstances typical of airplanes and other aircraft. Although no research claims that WTBO can be used as a base oil in grease formulations, its properties look promising in the grease formulation. Hence, this proposal will be the first research paper to initiate this study.

OBJECTIVE

The objective of this review paper is to study whether the recycling of WTBO as a base oil in the grease formulation (replacing the mineral oil as a common base oil) will be able to produce an industrial standard grease or not by evaluating the physical and chemical properties of WTBO.

Grease Formulation from Waste Oil

Greener alternatives began to become more and more popular in grease formulation. Due to urbanization and industrialization, waste oil production keeps increasing. The possibility to reuse waste oil as grease base oil has been demonstrated by research; nevertheless, the variable composition of waste oil upon collection, particularly for waste oil produced by the aviation industries, would result in uneven grease quality when employed in the formulation of grease (Rahman & Aziz, 2022). Research on current developments is actively carried out by utilizing and analyzing a variety of chemical compounds to follow the green trends. Environmental pollution is one such issue that has been and will continue to be. In connection with this, studies on creating new environmentally friendly grease formulations are carried out by utilizing waste, such as used oil and industrial waste and by investigating potential environmentally friendly grease components, such as the base fluid, thickener, or additive (Japar et al., 2020). Table 3 shows the successful research on grease formulation from waste oil.

Table 3
Successful grease formulation from waste oil

Aim	Grease Formulation	Parameter	Author/Ref
Formulation of grease using waste from a palm oil refinery.	Base oil: waste cooking oil thickener spent bleaching earth Additive: fumed silica	1. Consistency and dropping point 2. Corrosiveness on copper 3. Tribological properties	Waste-based, base oil and thickener (Japar et al., 2020)
Develop grease from waste oils as the base oil and red gypsum as one of the thickeners.	Base oil: waste oils Thickener: red gypsum/ fumed silica Additive: MoS ₂	1. Consistency and dropping point 2. Separation of oil	Waste-based base oil and thickener (Razali et al., 2018)
Formulation of lubricating grease from waste transformer oil	Waste Oil: WTO Thickener: fumed silica & sodium stearate Additives: molybdenum disulfate (MoS ₂)	1. Consistency and dropping point 2. Separation of oil	Nur Suhaila binti Anang Japar (Japar et al., 2019)
Characterization of lubricating grease formulated from waste engine oil	Waste Oil: WEO Thickener: fumed silica & sodium stearate Additives: molybdenum disulfate (MoS ₂)	1. Consistency and dropping point 2. Separation of oil	N. W. Abdu Rahman. (Rahman & Aziz 2022)

The similarities of all the waste oils listed in Table 3 that qualify them for grease formulation are due to their significant potential as a base fluid and/or a substitute for mineral oil. The variety of fatty acids present in each of the chemical compositions in each waste oil of each research will contribute to different values of grease formulated (Japar et al., 2019).

Turbine Oil

The main purpose of turbine oil is to lubricate the bearings and auxiliary machinery in steam and hydraulic turbines, turbo pumps, and air, gas, and refrigeration turbo compressors. Hence, it could be said that the primary purposes of turbine oil are for lubrication, speed control, and cooling (Fuskele et al., 2022). Basically, turbine oil is made from a combination of relatively simple ingredients: Base oil, oxidation, corrosion, defoaming inhibitors, and demulsifiers. The turbine oil formula typically makes up 97% or more of the base oil. A mineral or synthetic hydrocarbon base oil makes up the majority of turbine oil composition.

Additives are blended into the base oil at low amounts to preserve the oil and the turbine parts. According to OEM specifications, additives should give the turbine optimal performance. Original equipment manufacturer (OEM) lubrication requirements are designed to give the end user some assurance that the equipment will function properly and last as the specified amount of time stated if a certain lubricant is used. For example, antioxidants are one of the additives widely used in turbine oil. Antioxidants are a group of substances that have the capacity to inhibit oxidation. As a result, they can stop the turbine oil from breaking down and thickening (raising viscosity), improving the turbine's performance and extending its life too (Soleimani et al., 2018). The phenol and amine combinations are noteworthy for being utilized in turbine oil as antioxidants regularly (Shahnazar et al., 2016; Yano et al., 2013)

The turbine oil consumption is usually huge, approximately 3,700 gallons or 14,000 liters. That is an expensive oil supply of nearly 67 drums (Shekarchian et al., 2012). It typically lasts 3–5 years in a turbine, but this relies on the internal conditions of the system. Degradation would happen more quickly in a filthy system than in a clean one if the system encounters temperatures over the threshold, forms deposits, and otherwise is in good condition (Pirro et al., 2016; Vandervort et al., 2021). Turbine oils are recommended for use in situations where hydraulic oils, air compressor and vacuum pump oils, general shop lubricants, bearing lubricants, and heat transfer oils (Verified Market Research, 2022).



Figure 5. Turbine oil market size and forecast 2020–2028 (Verified Market Research, 2022)

According to Esomar Verified Market research, turbine oil was estimated to be worth USD 1.3 billion in 2020 and is expected to grow to USD 1.7 billion by 2028 (Figure 5). It will also grow at a compound annual growth rate (CAGR) of 3.7% from 2021 to 2028. The average price for turbine oil per gallon is 81.7 USD, and it is estimated that almost 1.5 million gallons of turbine oil will be widely produced in 2020 (Verified Market Research, 2022).

Properties of Used Turbine Oil

When evaluating grease performance, the qualities of the turbine oil used are crucial. Used turbine oil is an oil that no longer satisfies the quality requirement and has reduced qualities. An oil analysis needs to be done to guarantee the condition of the used turbine oil, as the characteristics of the used turbine oil were unknown at the time of collection. The properties of the turbine oil used, including kinematic viscosity, viscosity index, moisture content, and density, were examined in this study. Elemental analysis and FTIR characterization were also carried out to look for contamination, additives, or wear metal in used turbine oil (Tichy et al., 2021). In terms of chemical characteristics from Tables 5 and 6, it was found that the main constituents of the WTBO were C, O, and N, with metals making up only 4% of the sludge's mass. According to the analytical results, demulsifiers, defoamer, antirust, and antioxidants are also available. It is, therefore, practically a hydrocarbon (an organic substance made only of carbon and hydrogen (Gupta, 2017; Liu et al., 2016; Mortier et al., 2011)).

Tables 4 and 5 list the qualities and capabilities of both fresh and used turbine oil. In-service turbine oil keeps its excellent properties even after extensive use. Kinematic viscosity, the flow resistance brought on by gravity, increased from 45.20 to 46.68 mm² s⁻¹ at a particular temperature. After serving for a long period, alcohols, aldehydes, carboxylic acid, and other oxides were created (Hsu & Gates, 2000; Liu et al., 2016). The synthesis of carboxylic acids resulted in a small increase in acid number value (ASTM D974, 2014). Based on how quickly viscosity changes with temperature, The viscosity index (VI) is one of the most crucial elements in determining lubrication quality.

The term “viscosity index” refers to how the viscosity of an oil changes with temperature. For instance, high-VI oils experience less temperature-related viscosity change than low-VI oil. High-VI base oils are a prerequisite for the multigrade engine oils that vehicle manufacturers demand as a starting point in the formulation process. High-VI base oils have minimal volatility and are designed to work at low and high temperatures (Mang & Dresel, 2007). These oils are suitable for usage at temperatures between 32- and 150 degrees Fahrenheit. Group I base oils are refined using a solvent, a less complex refining procedure (Brown, 2015). Grease and gear lubricants frequently contain Group I base oils.

In other studies of the physical properties of the used turbine oil, the WTBO could be described as per Table 6, named Oil F. The viscosity of the used turbine oil is the lowest

compared to other used oils, such as engine oil, hydraulic oil, bearing oil and gear oil (Liu et al., 2013). Viscosity is the single most important performance property of a lubricant. The higher the viscosity, the greater the resistance to flow. The lower viscosity of these oils will result in less resistance and faster flow. In order to produce a great grease formulation that is high in viscosity, an extra thickener will be added (Tichy et al., 2021).

Table 4
Fresh turbine oil and in-service turbine oil: Properties and performance (Liu et al., 2016)

Description		Fresh Oil	In Service Oil	
Kinematic Viscosity (40°C)/mm ² s ⁻¹	41.4-50.6	45.2	46.68	ASTM D445
Viscosity Index	≥95	125	123	ASTM D2270
Acid Numbering KOH g ⁻¹	≤0.3	0.07	0.08	ASTM D974
Water Separability (54°C, 40-37-3 mL)/min	≤30	10	20	ASTM D1401
RPVOT/min	Report	788	470	ASTM D2272
Watering kg ⁻¹	≤100	90	158	ASTM D6304
Air Release (50°C)/min	≤10	1.7	4.9	ASTM D3427
Ruler/%	Amine	100%	52%	ASTM D6971
	Phenol	100%	31%	
Content/ppm				
Zn		0	1.7	ASTM D4951
Cu		-	0.15	
Fe		-	0.61	
Na		-	0.08	
P		22.38	26.62	
Si		<0.48	<0.48	
Ci		<0.0015	<0.0015	

Table 5
Sulphur content in the turbine oil residue (Liu et al., 2016)

	C	O	N	P	S	Ca	Fe	Zn	Si	Ai
Sludge/mass %	61.4	20.8	5.54	2.81	1.84	0.46	1.31	4.52	0.64	0.28
Residues of sludge after TG/ mass%	50.53	31.79	-	0.69	0.85	1.01	3.17	9.81	1.46	0.69

Table 6
Physical and chemical properties of fresh, used and reformed oils (Liu et al., 2013)

Samples	Viscosity 40°C (mm ² /s)	TAN (mgKOH/g)	H ₂ O Content (vol%)	H ₂ O Separability at 54°C (min)	Cu Corrosion	Mechanical Impurities (wt%)
Oil F Fresh Oil	32.56	0.02	-	40-37-3 (6.5)	1b	/
Used Oil	31.68	0.03	0.01	40-40-0 (20)	3b	/
Reformed Oil	32.08	0.02	0.01	40-40-0 (20)	1b	/

TAN is the Total Acid Number. It is a measure of acidity that is defined by the amount of potassium hydroxide in milligrammes that is required to neutralise the acids in one gram of oil (Decote et al., 2021). The standard acid value for lubricating is 0.1 (> 0.1 so corrosive and < 0.1 so non-corrosive). Oil F has recorded 0.03 mgKOH/g. Hence, a non-corrosive grease will be expected to be produced from this formulation.

The permissible water content in grease must be only 0.15% to 0.3% (Ismail et al., 2019; Sharma et al., 2022). The used turbine oil in Table 7 stated that only 0.01% of water content is found in it. Few costs will be saved as unnecessary processes like grease water washout need to be done to remove the water.

The 3b of copper corrosion recorded by Oil F is quite worrisome because it indicates an intermediate potential for Oil F to corrode the turbine (Tańczuk et al., 2017). Nevertheless, the additives like antioxidants and corrosion inhibitors used in the turbine oil were found to be hardly removed, although after going through the reclamation (the removal of water and particulate contamination from oil products and refortification process). Thus, the outcome of the grease formulation from the turbine oil used is predicted to not be corrosive.

FUTURE PROSPECT

Traditionally, mineral oils have been employed for lubrication purposes. Nevertheless, the long-term viability of fossil fuel-based energy sources is a significant concern. Moreover, the improper disposal of mineral oils can lead to environmental contamination in aquatic and terrestrial ecosystems (Borras et al., 2018). The combustion of mineral oils utilized as lubricants has the potential to release a tiny number of metallic elements, including phosphorus, zinc, calcium, magnesium, and iron nanoparticles (Cecilia et al., 2020). In this particular setting, using environmentally sustainable and non-hazardous bio-lubricants becomes essential. The utilization of bio-lubricants remains somewhat constrained compared to mineral oils, but this trajectory is growing and is contingent upon investments in research and development (R&D). The surge in demand for biodegradable lubricants can be attributed to the progression of environmental regulations, which have become increasingly stringent to mitigate the adverse environmental consequences of improper disposal practices (Negi et al., 2021).

The future prospects of bio-lubricants should prioritize enhanced lubricating qualities and reduced toxicity compared to conventional mineral oils. In addition to stringent environmental restrictions, there is an anticipation for developing more sustainable formulations utilizing WTBO as a fundamental base oil. The anticipated physical and chemical characteristics of WTBO following the treatment outlined in this study suggest a favorable potential to produce industrial grease.

Based on the findings of the Esomar Verified Market research, as depicted in Figure 5, it was projected that the market for turbine oil will have significant growth in the next

years. The production of waste turbine base oil (WTBO) is expected to expand significantly due to the global rise in turbine oil consumption over time (Efimov, 2020). The estimated proportion of waste oil in relation to the whole consumption of commercial products is approximately 50%, with waste oils specifically accounting for approximately 30% of this total (Hester & Harrison, 2010). The aviation industry has experienced a significant evolution in the aftermath of the Covid-19 pandemic. This transformation has led to an increased need for sustainable aviation oils. However, this surge in demand has also resulted in the generation and accumulation of WTBO. Consequently, it becomes imperative to ensure the proper disposal of these waste oils (Gong et al., 2020).

Table 7
2007 production of worldwide used oil source and classifications (Yu, Ma & Wang, 2012)

The Classification and Source of Worldwide Used oil Source	Production of Used oil (Million Ton)	Explanations
Used lubricating oil, chainsaw oil, Hydraulic fluid and lubricating grease	2925	According to a 45% efficiency factor, the Total National Production of Used Lubricants, hydraulic fluid, and lubricating grease is estimated to be around 2925 million tons.
Total of Worldwide Used oil Source	3753.7	Including other used oil likes (petroleum mining oil, dye, and ship industry)

Waste oil is harmful in two ways: it can be toxic to people and damage the natural environment. In 2007, the production of used oil in China was 37.537 million tons, with turbine oil falling under the lubricating oil category, contributing to 29.25 million tons of used oil production (Table 7). Different types of oil have various levels of additives, such as heavy metals, chlorine, and sulfur, which can be harmful to humans. When turbine oil is used, it can produce harmful substances due to high temperatures and oxidation, such as 3,4-Benzopyrene (PAH) and polychlorobiphenyl (PCB), which can seriously harm human health. Used oil pollution can also harm the ecosystem, soil, water, and plants (Aganbi et al., 2019; Ismail et al., 2021). A small amount of used turbine oil can contaminate a large amount of water, and waste oils can endanger aquatic life in rivers, lakes, and streams.

CONCLUSION

In conclusion, the idea of utilizing treated waste turbine oil for the grease formulation is promising to be viable based on the theoretical properties that have been analyzed. But a few things might need added for more valuable grease production. However, in this paper, the study covers only the grease formulation part. Hence, the WTBO collected from the supplier needs to be treated first before being substituted as a base oil to remove any impurities, such as metal, dust, debris, or moisture content. The formulated grease is expected to be long lasting due to the “natural” existence of antioxidants in the used oil

and useful to the moving machinery that metal made. Besides, the increased production of worldwide turbine oil means the increased amount of the used turbine oil will be in now and future is expected. Thus, this grease formulation is necessary for reducing the environmental impact and cost of the disposal process of used oil, which involves money and energy.

ACKNOWLEDGEMENTS

The authors wished to acknowledge the financial support from the Ministry of Higher Education, Malaysia, for funding this research under the Fundamental Research Grant Scheme (FRGS/1/2021/TKO/UMP/02/76; RDU 210147) and the Universiti Malaysia Pahang Al-Sultan Abdullah research fund (RDU 190398 & PGRS 200356).

REFERENCES

- Aganbi, E., Iwegbue, C. M. A., & Martincigh, B. S. (2019). Concentrations and risks of polychlorinated biphenyls (PCBs) in transformer oils and the environment of a power plant in the Niger Delta, Nigeria. *Toxicology Reports*, 6, 933-939. <https://doi.org/10.1016/j.toxrep.2019.08.008>
- Alias, N. H., Aziz, M. H. A., Adam, M. R., Aizudin, M., & Ang, E. H. (2023). Polymeric/ceramic membranes for water reuse. In M. Sillanpää, A. Khadir, & K. Gurung (Eds.), *Resource Recovery in Drinking Water Treatment* (pp. 65-92). Elsevier.
- Aziz, M. A. A., Isa, K. M., & Rashid, R. A. (2017). Pneumatic jigging: Influence of operating parameters on separation efficiency of solid waste materials. *Waste Management & Research*, 35(6), 647-655. <https://doi.org/10.1177/0734242X17697815>
- Aziz, M. A. A., Isa, K. M., Miles, N. J., & Rashid, R. A. (2018). Pneumatic jig: Effect of airflow, time and pulse rates on solid particle separation. *International Journal of Environmental Science and Technology*, 16, 11-22. <https://doi.org/10.1007/s13762-018-1648-4>
- Arki, E., & Balköse, D. (2013). Metal soap greases. In G. E. Zaikov, A. N. Goloshchapov & A. V. Lobanov (Eds.) *Progress in Organic and Physical Chemistry: Structures and Mechanisms* (pp. 55-75). CRC Press. <https://doi.org/10.1201/b13964-7>
- Bhat, S. A., & Charoo, M. S. (2019). Effect of additives on the tribological properties of various greases-A review. *Materials Today: Proceedings*, 18(7), 4416-4420. <https://doi.org/10.1016/j.matpr.2019.07.410>
- Borras, X., Rooij, M. B. D., & Schipper, D. J. (2018). Rheological and wetting properties of Environmentally Acceptable Lubricants (EALs) for application in stern tube seals. *Lubricants*, 6(4), Article 100. <https://doi.org/10.3390/lubricants6040100>
- Canter, N. (2012). Grease additives: Important contributors not to be overlooked. *Tribology and Lubrication Technology*, 68(12), Article 28.
- Cecilia, J. A., Plata, D. B., Saboya, R. M. A., de Luna, F. M. T., Cavalcante Jr, C. L., & Rodríguez-Castellón, E. (2020). An overview of the biolubricant production process: Challenges and future perspectives. *Processes*, 8(3), Article 257. <https://doi.org/10.3390/pr8030257>

- Chandraseagar, S., Abdulrazik, A. H., Abdulrahman, S. N., & Abdaziz, M. A. (2019). Aspen plus simulation and optimization of industrial spent caustic wastewater treatment by wet oxidation method. *IOP Conference Series: Materials Science and Engineering*, 702(1), Article 012011. doi:10.1088/1757-899X/702/1/012011
- Chatra, K. R. S., & Lugt, P. M. (2020). Channeling behavior of lubricating greases in rolling bearings: Identification and characterization. *Tribology International*, 143, Article 106061. <https://doi.org/10.1016/j.triboint.2019.106061>
- Decote, P. A., Negris, L., Vidoto, A. P., Mendes, L. A., Flores, E. M., Vicente, M. A., & Santos, M. F. (2021). Determination of the total acid number of Brazilian crude oil samples: Theoretical and experimental evaluation of three standard methods. *Fuel*, 313, Article 122642. <https://doi.org/10.1016/j.fuel.2021.122642>
- Efimov, P. (2020). *Finnish industrial area market research. Case company: Nordic access* [Unpublish degree thesis]. University of Applied Sciences.
- ENEOS Corporation (2018). *Product bulletin : TURBINE OIL turbine oil without additive*. ENEOS Corporation. <chrome-extension://efaidnbmninnibpcapjcgclclefindmkaj/https://www.eneos.co.jp/english/products/lubricants/pdf/ind-3502-2104e.pdf>
- Fan, X., Li, W., Li, H., Zhu, M., Xia, Y., & Wang, J. (2018). Probing the effect of thickener on tribological properties of lubricating greases. *Tribology International*, 118, 128-139. <https://doi.org/10.1016/j.triboint.2017.09.025>
- Fischer, D., Jacobs, G., Stratmann, A., & Burghardt, G. (2018). Effect of base oil type in grease composition on the lubricating film formation in EHD contacts. *Lubricants*, 6(2), Article 32. <https://doi.org/10.3390/lubricants6020032>
- Fuskele, V., Baredar, P., Sarviya, R. M., Lal, S., & Awasthi, S. (2022). Wind turbine nacelle cooling systems: A review. *Wiley Interdisciplinary Reviews: Energy and Environment*, 11(6), Article e456. <https://doi.org/10.1002/wene.456>
- Glushkov, D. O., Paushkina, K. K., & Shabardin, D. P. (2020). Co-combustion of coal processing waste, oil refining waste and municipal solid waste: Mechanism, characteristics, emissions. *Chemosphere*, 240, Article 124892. <https://doi.org/10.1016/j.chemosphere.2019.124892>
- Gong, H., Yu, C., Zhang, L., Xie, G., Guo, D., & Luo, J. (2020). Intelligent lubricating materials: A review. *Composites Part B: Engineering*, 202, Article 108450. <https://doi.org/10.1016/j.compositesb.2020.108450>
- Gupta, M. K. (2017). Requirement for successful production and delivery of the refined vegetable oils. In *Practical Guide to Vegetable Oil Processing* (pp. 1-5). Academic Press.
- Herman, I. T., Isa, K. M., Ibrahim, N., Kasim, F. H., & Aziz, M. A. A. (2021). A single step transesterification process to produce biodiesel from the spent cooking oil. *IOP Conference Series: Earth and Environmental Science*, 765, Article 012077. <https://doi.org/10.1088/1755-1315/765/1/012077>
- Hester, R. E., & Harrison, R. M. (2010). *Ecosystem services*. RSC Publishing.
- Hsu, S., & Gates, R. (2000). *Boundary lubrication and boundary lubricating films*. CRC Handbook of Modern Tribology

- Ismail, N. A., Aziz, M. A. A., Hisyam, A., & Abidin, M. A. (2021). Separation of samarium from medium rare earth mixture using multi-stage counter-current extraction. *Chemical Engineering Communications*, 208(5), 764-774. <https://doi.org/10.1080/00986445.2020.1746654>
- Ismail, N. A., Yunus, M. M., Aziz, M. A., & Abidin, M. A. (2019). Comparison of optimal solvent extraction stages between P204 and [A336][P204] for the separation of europium and gadolinium. *IOP Conference Series: Materials Science and Engineering*, 702(1), Article 012044. <https://doi.org/10.1088/1757-899X/702/1/012044>
- Japar, N. S. A., Aziz, M. A. A., & Rahman, N. W. A. (2020). Conversion of waste transformer oil into grease. In A. Z. Yaser (Ed.), *Advances in Waste Processing Technology* (pp. 23-35). Springer.
- Japar, N. S. A., Aziz, M. A. A., Razali, M. N., & Rahman, N. W. A. (2018). Grease and its application on electrical equipment: A review. *International Journal of Engineering and Technology(UAE)*, 7(3.26), 23-39. <https://doi.org/10.14419/ijet.v7i3.26.17455>
- Japar, N. S. A., Aziz, M. A., Razali, M. N., Zakaria, N. A., & Rahman, N. W. A. (2019). Preparation of grease using organic thickener. *Materials Today: Proceedings*, 19, 1303-1308. <https://doi.org/10.1016/j.matpr.2019.11.141>
- Jeanna, V. R. (2017). Thickener structure. *Tribology & Lubrication Technology*, 73(12), 26-30.
- Johnson, M. (2008). Understanding grease construction and function. *Tribology and Lubrication Technology*, 64(6), 32-38.
- Kanazawa, Y., Sayles, R., & Kadiric, A. (2017). Film formation and friction in grease lubricated rolling-sliding non-conformal contacts. *Tribology International*, 109, 505-518. <https://doi.org/10.1016/j.triboint.2017.01.026>
- Kaperick, J. P. (2013). Grease thickeners. In Q. J. Wang & Y. W. Chung (Eds.) *Encyclopedia of Tribology* (pp. 1562-1567). Springer.
- Kuppusamy, S., Maddela, N. R., Megharaj, M., & Venkateswarlu, K. (2020). An overview of total petroleum hydrocarbons. In *Total Petroleum Hydrocarbons* (pp. 1-27). Springer. https://doi.org/10.1007/978-3-030-24035-6_1
- Liu, J., Gu, K., Duan, H., Zhao, Y., & Li, J. (2013). Tribological and economic evaluation of recycled mineral lubricating oils. *Science China Technological Sciences*, 56, 2964-2972. <https://doi.org/10.1007/s11431-013-5408-x>
- Liu, Z., Wang, H., Zhang, L., Sun, D., Cheng, L., & Pang, C. (2016). Composition and degradation of turbine oil sludge. *Journal of Thermal Analysis and Calorimetry*, 125(1), 155-162. <https://doi.org/10.1007/s10973-015-5200-1>
- Mahadeshwara, M. R., Rosa, F., Vuchkov, T., Vilhena, L., Ramalho, A., Sharma, P., & Cavaleiro, A. (2023). Investigating the synergistic effect of electrochemical texturing and MoSeC coatings on the frictional behaviour of lubricated contacts. *Coatings*, 13(4), Article 692. <https://doi.org/10.3390/coatings13040692>
- Mahmud, M. S., Ishak, S., Razali, M. N., Aziz, M. A. A., & Musa, M. (2019). Grease quality issues on middle voltage switchgear: Corrosivity, resistivity, safety and ageing. *IJUM Engineering Journal*, 20(1), 216-228. <https://doi.org/10.31436/iiumej.v20i1.995>

- Mang, T., & Dresel, W. (2007). *Lubricants and lubrication*: John Wiley & Sons.
- Mortier, R. M., Fox, M. F., & Orszulik, S. (2011). *Chemistry and technology of lubricants*. Springer.
- Negi, P., Singh, Y., & Tiwari, K. (2021). A review on the production and characterization methods of bio-based lubricants. *Materials Today: Proceedings*, 46, 10503-10506. <https://doi.org/10.1016/j.matpr.2020.12.1211>
- Niu, M., Qu, J., & Gu, L. (2019). Synthesis of titanium complex grease and effects of graphene on its tribological properties. *Tribology International*, 140, Article 105815. <https://doi.org/10.1016/j.triboint.2019.06.008>
- Pirro, D. M., Webster, M., & Daschner, E. (2016). *Lubrication fundamentals, revised and expanded*. CRC Press.
- Rahman, N. W., & Aziz, M. A. A. (2022). The effects of additives on anti-wear properties of lubricating grease formulated from waste engine oil. *Egyptian Journal of Petroleum*, 31(3), 71-76. <https://doi.org/10.1016/j.ejpe.2022.07.002>
- Rawat, S. S., & Harsha, A. P. (2019). Current and future trends in grease lubrication. In J. K. Katiyar, S. Bhattachary, V. K. Patel & V. Kumar (Eds.), *Automotive Tribology* (pp. 147-182). Springer.
- Razali, M. N., Aziz, M. A. A., Jamin, N. F. M., & Salehan, N. A. M. (2018). Modification of bitumen using polyacrylic wig waste. *AIP Conference Proceedings*, 1930(1), Article 020051. <https://doi.org/10.1063/1.5022945>
- Razali, M. N., Isa, S., Md Salehan, N., Musa, M., Abd Aziz, M. A., Nour, A., & Yunus, R. (2020). Formulation of emulsified modification bitumen from industrial wastes. *Indonesian Journal of Chemistry*, 20(1), 96-104. <https://doi.org/10.22146/ijc.40888>
- Rohim, R., Isa, K. M., Abdullah, T. A. T., Rashid, R. A., & Aziz, M. A. (2021). Methanolysis of duckweed and azolla: A comparative analysis. *IOP Conference Series: Earth and Environmental Science*, 765(1), Article 012099. <https://doi.org/10.1088/1755-1315/765/1/012099>
- Rudnick, L. R. (2013). *Synthetics, mineral oils, and bio-based lubricants: Chemistry and technology* (2nd ed.). CRC Press.
- Russo, S., Brambilla, L., Thomas, J. B., & Joseph, E. (2023). But aren't all soaps metal soaps? A review of applications, physico-chemical properties of metal soaps and their occurrence in cultural heritage studies. *Heritage Science*, 11(1), Article 172. <https://doi.org/10.1186/s40494-023-00988-3>
- Shahnazar, S., Bagheri, S., & Hamid, S. B. A. (2016). Enhancing lubricant properties by nanoparticle additives. *International Journal of Hydrogen Energy*, 41(4), 3153-3170. <https://doi.org/10.1016/j.ijhydene.2015.12.040>
- Sharma, S., Gupta, V., & Mudgal, D. (2022). Current trends, applications, and challenges of coatings on additive manufacturing based biopolymers: A state of art review. *Polymer Composites*, 43(10), 6749-6781. <https://doi.org/10.1002/pc.26809>
- Shekarchian, M., Moghavvemi, M., Motasemi, F., Zarifi, F., & Mahlia, T. M. I. (2012). Energy and fuel consumption forecast by retrofitting absorption cooling in Malaysia from 2012 to 2025. *Renewable and Sustainable Energy Reviews*, 16(8), 6128–6141. <https://doi.org/10.1016/j.rser.2012.07.013>

- Sofi, S. N. A. M., Aziz, M. A. A., Japar, N. S. A., Rahman, N. W. A., Abdulhalim, A. R., & Yunus, M. Y. M. (2019). Preparation and characterization of grease formulated from waste transformer oil. *IOP Conference Series: Materials Science and Engineering*, 702(1), Article 012034. <https://doi.org/10.1088/1757-899X/702/1/012034>
- Soleimani, M., Dehabadi, L., Wilson, L., & Tabil, L. (2018). Antioxidants classification and applications in lubricants. In D. W. Johnson (Ed.), *Lubrication: Tribology, Lubricants and Additives*. IntechOpen.
- Staahl, J., & Jacobson, B. O. (2003). A lubricant model considering wall-slip in EHL line contacts. *Journal of Tribology*, 125(3), 523-532. <https://doi.org/10.1115/1.1537750>
- Suhaila, N., Japar, A., Aizudin, M., Aziz, A., & Razali, M. N. (2018). Formulation of lubricating grease using Beeswax thickener. *IOP Conference Series: Materials Science and Engineering*, 342(1), Article 012007. <https://doi.org/10.1088/1757-899X/342/1/012007>
- Tañczuk, M., Skorek, J., & Bargiel, P. (2017). Energy and economic optimization of the repowering of coal-fired municipal district heating source by a gas turbine. *Energy Conversion and Management*, 149, 885-895. <https://doi.org/10.1016/j.enconman.2017.03.053>
- Tichy, J., Menut, M., Oumahi, C., Muller, S., & Bou-Saïd, B. (2021). Grease flow based on a two-component mixture model. *Tribology International*, 153, Article 106638. <https://doi.org/10.1016/j.triboint.2020.106638>
- Vandervort, J., Lukasik, G., Ayyildiz, B., Solom, M., Delgado, A., Kirkland, K. V., & Patil, A. (2021). Performance evaluation of a Terry GS-2 steam impulse turbine with air-water mixtures. *Applied Thermal Engineering*, 191, Article 116636. <https://doi.org/10.1016/j.applthermaleng.2021.116636>
- Verified Market Research. (2022). *Global Turbine Oil Market Size by Type, by Application, by Viscosity Grade, by Geographic Scope and Forecast*. <https://www.verifiedmarketresearch.com/product/turbine-oil-market/#>
- Vershinina, K., Shabardin, D., & Strizhak, P. (2019). Burnout rates of fuel slurries containing petrochemicals, coals and coal processing waste. *Powder Technology*, 343, 204-214. <https://doi.org/10.1016/j.powtec.2018.11.052>
- Whitby, C. P. (2020). Structuring edible oils with fumed silica particles. *Frontiers in Sustainable Food Systems*, 4, Article 585160. <https://doi.org/10.3389/fsufs.2020.585160>
- Wu, C., Hong, Y., Ni, J., Teal, P. D., Yao, L., & Li, X. (2023). Investigation of mixed hBN/Al₂O₃ nanoparticles as additives on grease performance in rolling bearing under limited lubricant supply. *Colloids and Surfaces A: Physicochemical and Engineering Aspects*, 659, Article 130811. <https://doi.org/10.1016/j.colsurfa.2022.130811>
- Yano, A., Akiyama, Y., Matsuoka, M., & Takayanagi, K. (2013). Study on the evaluation method of sludge formation during the oxidation process of gear oils. *Tribology Online*, 8(2), 162-170. <https://doi.org/10.2474/trol.8.162>
- Zhang, E., Li, W., Zhao, G., Wang, Z., & Wang, X. (2021). A study on microstructure, friction and rheology of four lithium greases formulated with four different base oils. *Tribology Letters*, 69(3), Article 98. <https://doi.org/10.1007/s11249-021-01469-z>

Microwave Electro-technological Installation for Processing Vegetable-origin Organic Materials and Agricultural Crops

Midhat Tukhvatullin^{1*} and Eduard Khasanov²

¹*Department of Electric Power Supply and Technological Process Automation, Federal State Budgetary Educational Institution of Higher Education, Bashkir State Agrarian University, Ufa, Russia*

²*Department of Mechatronics Systems and Agricultural Machinery, Federal State Budgetary Educational Institution of Higher Education, Bashkir State Agrarian University, Ufa, Russia*

ABSTRACT

The research aims to conduct experimental studies of the drying schedule for processing vegetable-origin organic materials using a microwave electro-technological installation. The design and development of a microwave electro-technological installation for processing vegetable-origin organic materials and agricultural crops are based on the solution of an agreed boundary value problem of electrodynamics and heat and mass transfer. The experiments on the microwave processing of vegetable-origin organic materials using a microwave electro-technological installation allowed us to identify the preferred process conditions, which involve the work of 7 magnetrons and a rotation mechanism of vegetable-origin organic materials along their axis. The processing time is less than 15 hours; the final humidity does not exceed 7%. The temperature change is uniform. The temperature at a depth of 1/4 of the thickness of the samples differs from the temperature on the surface of the samples by 0.5–1.0°C. The differences in the calculated and experimental data on the humidity of organic materials of plant origin do not exceed 3.8%, and on temperature, it is 4.3%. The creation of a microwave installation for the simultaneous microwave processing of vegetable organic materials and agricultural crops will significantly increase the energy and economic efficiency of the installation by reducing the processing time and increasing the quality of dried material quality. Moreover, unlike the existing ones, the proposed

electro-technological installation contributes to the sale of more than two products with improved qualities, thus increasing the profits at the same energy costs.

ARTICLE INFO

Article history:

Received: 12 September 2023

Accepted: 01 February 2024

Published: 15 August 2024

DOI: <https://doi.org/10.47836/pjst.32.5.16>

E-mail addresses:

midhat_tukhvatullin@rambler.ru (Midhat Tukhvatullin)

edkhasanov43@rambler.ru (Eduard Khasanov)

* Corresponding author

Keywords: Agricultural crop, electro-technological installation, organic material

INTRODUCTION

Microwave energy is used for drying, heating, defrosting, and disinfection of different products, including agricultural crops such as barley, wheat, and soy. This technology has become popular with agricultural and processing enterprises since it has many positive features. The most attractive feature of microwave technology is the short processing time and the preservation of nutrients in the product after processing. Khasanov (2015) in his work states that the pre-sowing treatment of seeds with microwave current ensures high processing uniformity, at least 98%, with a productivity of 10 t / hour in the etching mode and 4 t / hour in the inlay mode.

Excess humidity reduction is one of the urgent tasks for cereal breeding centers producing elite and super elite seeds in western and eastern Canada (Saskatchewan, Alberta, Manitoba, Ontario, Quebec), as well as in China (the Songliao Plain) and the Ural and Volga Federal Districts of Russia. Excessive humidity shortens the product's best-before date, decreases its use efficiency, leads to deterioration in the product's commercial qualities after drying, and the rapid development of disease-producing agents that make grain useless (the average loss of grain without drying is 25%–28%) (Khasanov, 2015; Nirmaan et al., 2020).

Therefore, issue number one for enterprises that process vegetable-origin organic materials is to ensure their high-quality and uniform drying. The existing methods of drying vegetable-origin organic materials are atmospheric, convective, chamber, contact drying, flue gas drying, drying with infrared rays, high-frequency currents drying, induction and vacuum drying. Among the disadvantages of the above methods are high energy consumption and equipment cost, complex drying process control, low quality of the dried material, and the use of equipment polluting the environment (Arkhangelsky et al., 2018; Khasanov, 2015; Sivyakov & Grigorieva, 2019).

Using microwave energy eliminates the disadvantages of drying machines and reduces the seeds' moisture content. In their work, Tukhvatullin and Aipov (2019) state that the processing time is reduced to 9–12 hours due to the rotation of lumber along its axis in the microwave electromagnetic field; high uniformity of processing is ensured (95%–98%). Moreover, two-stage processing allows for a large increase (10%–20%) in yield compared to control due to the microwave field's various effects on seeds (Khasanov, 2015).

The authors propose a new technology for processing agricultural crops and vegetable-derived organic materials, which will allow obtaining better-quality products at low energy costs. Using the new technology will contribute to the transition to high-yielding and environmentally friendly agriculture for the selection and processing of plant products.

All of the above proves the research's relevance and great scientific and practical significance for the agro-industrial complexes of Europe, America, and the Russian Federation.

LITERATURE REVIEW

World literature covers the use of electromagnetic microwave energy for the thermal processing of materials. Some papers present information on agricultural use of microwave drying, such as farm products drying (Siviyakov & Grigorieva, 2019), assessment of corn germination by microwave priming (Lazim, 2023), microwave processing of materials at agricultural facilities (Aipov et al., 2019), and corn microwave drying (Zhou et al., 2019). Some of them give an analysis of microwave drying methods of rice varieties (Nirmaan et al., 2020), the effect of microwave treatment on disinfection and stimulation of seed germination followed by inlay (Khasanov, 2015). Papers devoted to the use of microwave drying in the food industry describe microwave mixture processing (Shishkina et al., 2019), sterilization of packaged food products (Patel et al., 2019) and polymer packaging for food products (Zhou et al., 2019).

They give an analysis of microwave disinfection of food products (Stepanenko & Kazhevnikov, 2017), the effect of microwave heat treatment on nutritional indicators (Waseem et al., 2022), synergistic effects of ultrasound and microwave treatment on the physicochemical properties and phytochemicals of watermelon (Navida et al., 2022), investigation of the effect of ultrasonic pasteurization on the physico-chemical profile and stability during storage of pumpkin (Nadeem, Tehreem et al., 2022), the effect of ultrasound treatment on the functional properties of various citrus juices (Nadeem, Ranjha et al., 2022); microwave processing of lemon cordial (Malik et al., 2022), convection combined microwave drying of essential oils (Monton et al., 2019), microwave processing of lime flavored drink (Patel & Bhise, 2023).

Some literature sources study the use of microwave drying in the woodworking industry: microwave electro-technological installation for drying rotating sawn timber (Tukhvatullin & Aipov, 2019), microwave bamboo vacuum drying (Lv et al., 2018), the effect of microwave radiation on the humidity of different wood species (Aniszewska et al., 2021), microwave timber processing (Tuhvatullin et al., 2019), drying of wood chips (Rezaei et al., 2017). There are papers presenting information on the use of microwave drying in the construction industry. They review the effects of microwave radiation on the geopolymers' properties (Sun et al., 2021), describe microwave processing of carbon-covered polymer composites (Galos, 2021), give an interpretation of the structure and properties of biological polyhydroxyalkanoates with different monomeric compositions (Ishak et al., 2021), present information on the electrification of microwave processing of materials (Amini et al., 2021), including microwave processing of bitumen (Abdrabou et al., 2023).

For example, in the work by Nirmaan et al. (2020), the microwave processing of rice for 7 minutes in a microwave installation with a power of 500 watts gives better results compared to traditional processing methods. The moisture content of rice decreases by

12%–20%, which is similar to the research results presented by Sivyakov and Grigorieva (2019) and Khasanov (2015).

The work by Navida et al. (2022) studies the effect of ultrasound and microwave energy treatment on the physico-chemical parameters of watermelon juice stored for 120 days. Microwave treatment increases acidity (0.15%), turbidity (3.00), vitamin C content (202.67 mg/100 ml), TP (852.57 mg/100 ml), TF (1970.9 mcg CE /100 ml) and TAC (8650.3 mcg ascorbic acid equivalent/ml juice) and the antioxidant content, which is similar to the research results presented in Nadeem, Ranjha et al. (2022) and Malik et al. (2022).

Aniszewska et al. (2021) studied the effect of microwave radiation on various types of wood. They found that the decrease in humidity for various fractions is 8–16 mm (14.60% and 17.66%) and 16–31.5 mm (14.68% and 16.77%), which indicates the effectiveness of continuous processing and is similar to the research results presented in the papers (Tuhvatullin & Aipov, 2019).

The work by Sun et al. (2021) proves the increase in the strength of geopolymers and changes in their microstructure under the effect of microwave radiation, similar to the research results presented in the work (Galos, 2021).

At the same time, microwave processing of different materials has some disadvantages. The effect of microwave energy on different materials is heterogeneous. Therefore, intensive controlled processing methods are needed to achieve the desired effect.

For example, Montenegro et al. (2021) studied the effect of microwave processing on the physical, physico-chemical and rheological properties of wheat grain. It is difficult to control the processing of the materials under study at high power values (from 100 W to 3000 W).

Qu et al. (2021) investigate the effect of microwave stabilization on the properties of whole-grain flour and prove that it significantly increases the product's storage time. However, the stabilization process is long and complicated.

Waseem et al. (2022) studied the effect of microwave processing on potatoes' nutritional parameters and properties. Microwave processing positively affects the material under study, making this method appropriate for processing food products.

As mentioned above, there are many studies on the effects of microwaves on different materials (vegetable-origin organic materials, seeds, and crop materials). Materials exposed to microwave processing are different. Some scientists study the properties of materials exposed to microwave energy; some investigate the process of microwave treatment (Aipov et al., 2019; Montenegro et al., 2021; Navida et al., 2022; Tuhvatullin et al., 2019; Waseem et al., 2022). The choice of materials for this study is justified by the fact that microwave processing allows obtaining better quality products, which contributes to the transition to high-yielding and environmentally friendly agriculture for selecting and processing plant products. Since most studies are aimed at investigating the properties of vegetable-origin

organic materials and agricultural crops (cereals) exposed to microwave energy, the study of microwave processing of vegetable-origin organic materials and agricultural crops is of particular interest both from the scientific and practical points of view (Khasanov, 2015; Monton et al., 2019; Nirmaan et al., 2020; Qu et al., 2021; Zhou et al., 2019).

The main problem of the intensive processing of vegetable-origin organic materials and agricultural crops is a decrease in the quality of the processed material. The long-term effects of microwave energy on agricultural crops, such as wheat, lead to the destruction of cellular structures and the deterioration of nutrients. As for vegetable-origin organic materials, the long-term microwave effect changes the internal and external structure of the material (deformation, torsion, charring) (Khasanov, 2015; Tukhvatullin & Aipov, 2019).

Thus, new solutions are necessary to preserve the quality of vegetable-origin organic materials and agricultural crops during microwave processing and reduce the processing energy intensity.

It is possible to combine two technological blocks (a block of thermal microwave modification of vegetable-origin organic materials and a block of non-thermal microwave modification of agricultural crops) into one working chamber of a microwave electro-technological installation to reduce the energy intensity of microwave processing of vegetable-origin organic materials and crops.

Thus, the combination of microwave and ultraviolet treatment inside one installation reduces the number of microorganisms or completely inhibits the pathogenic microflora on the material surface and increases raw materials' microbiological safety and stability (Kolokolova et al., 2020).

The main line of research in the world and scientific competitors: The development of the presented energy-saving technology, which allows obtaining agricultural products with improved quality, has been proposed for the first time.

The technology implies simultaneous thermal and non-thermal energy-saving processing of vegetable-origin organic materials and agricultural crops.

For the first time, the technology developed for simultaneous thermal and non-thermal processing of vegetable-origin organic material and agricultural crops has been presented.

The research aims to conduct experimental studies of the drying schedule for processing vegetable-origin organic materials using a microwave electro-technological installation with the following objectives:

1. Development of an automated control system for a microwave electro-technological installation.
2. Development of a simulation model of a microwave electro-technological installation.
3. Conducting experimental studies to determine the preferred schedule for processing vegetable-origin organic materials.

METHODS AND MATERIALS

Installation Model

The microwave electro-technological installation proposed by the authors for microwave processing of vegetable-origin organic materials and agricultural crops consists of two technological blocks—a block of thermal microwave processing of vegetable-origin organic materials and a block of non-thermal microwave processing of agricultural crops. A working chamber and a transmission line are the technological units of thermal microwave processing. The type of transmission line is a rectangular waveguide. A working chamber and a transmission line are the technological blocks of non-thermal microwave processing. The transmission line is a rectangular waveguide. Convenient placement and operation of the installation determine the length of the transmission line and the possible presence of a waveguide rotation.

The working chamber for non-thermal microwave processing of agricultural crops provides them with preferred technological properties. A waveguide should have the same cross-section as the transmission line, supplying it with microwave energy from a microwave energy source to reduce the reflection of the microwave electromagnetic wave from the entrance to the working chamber (Arkhangelsky & Grishina, 2007; Dobrodum & Arkhangelsky, 2017).

Figure 1 shows a diagram of a microwave electrotechnological installation for the microwave processing of plant material. Chamber 1 has shaft 3 with fasteners for vegetable-origin organic materials. Gearmotor 5 provides a rotation of vegetable-origin organic materials. The geometrical and technical characteristics of the installation model are presented in Table 1.

The microwave electro-technological installation has technological blocks for the non-thermal microwave processing of agricultural crops.

The microwave installation uses seven sources of microwave energy, making seven working chambers of non-thermal microwave processing possible. Each chamber can be assembled on a segment of a rectangular homogeneous waveguide with flanges and a round hole in the middle of wide walls. Agricultural crops (seed and plant material) are processed in those holes in a pipe made of organic glass.

It is important to note that each technological block of non-thermal microwave processing can produce the same or different agricultural products. Therefore, a microwave electro-technological installation can produce up to seven different materials.

If the water vapors from vegetable-derived organic materials are undesirable for agricultural crops, the technological block for non-thermal treatment can be protected from water vapor by a moisture-proof thin dielectric radio-transparent partition separating the zones where crops are located from the zones where vegetable-derived organic material rotates (Arkhangelsky et al., 2018; Dobrodum & Arkhangelsky, 2017).

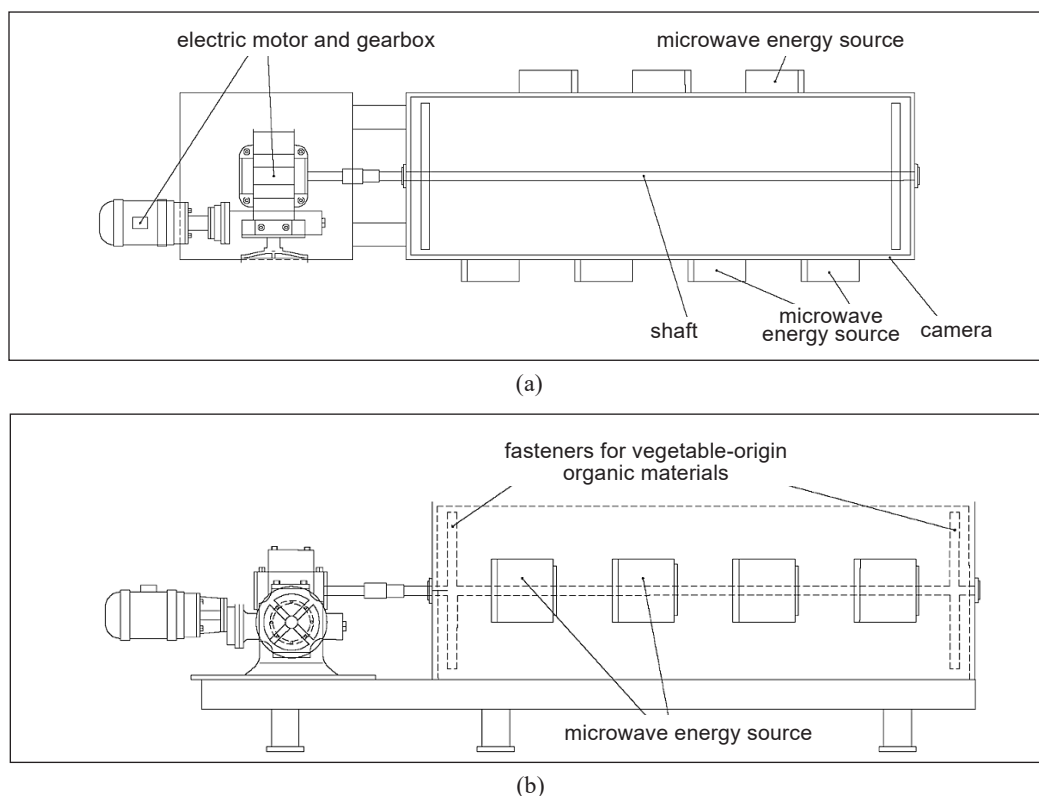


Figure 1. Diagram of a microwave electro-technological installation for microwave processing of plant material: (a) Top view; and (b) side view

The absence of horn radiators matching the working chamber with a microwave generator creates a problem for a microwave electro-technological installation assembled according to the diagram shown in Figure 2. The microwave energy reflected from the entrance to the working chamber creates a partially standing wave mode in the working chamber of non-thermal microwave processing. As a result, $\dot{A}(z)$ there is a dependence between a slit length and the crop processing quality. Thus, if a slit length is bigger than the wavelength in the waveguide, the processing quality decreases. A quarter-wave matching transformer should be used in the installation to avoid this. Therefore, using horn radiators and quarter-wave matching transformers increases the installation's economic efficiency and guarantees high production quality.

Table 1
Geometrical and technical parameters of the installation model

Parameter	Value
Installation dimensions, m	$2.42 \times 0.6 \times 0.6$
Number of magnetrons, pcs.	7
Power consumption of one magnetron, W	1,200
Output power of one magnetron, W	850
Radiation frequency, MHz	2,450
Dimensions of the waveguide energy output, mm	70×30

Installation Simulating Model

To simulate complicated processes, a simulation model of a microwave electro-technological installation for the microwave processing of vegetable-origin organic materials should be created in the MATLAB/Simulink software environment. The model is shown in Figure 2.

The simulation model consists of the following main blocks: a technological block for microwave processing of vegetable-origin organic materials (Subsystem), seven microwave energy sources (Rad1–Rad7), a device for determining the materials’ temperature (T, degrees C), a device for determining the materials’ moisture (W,%), an indicator (Scope) for displaying graphical dependences of changes in temperature and moisture of vegetable origin organic materials during microwave processing, a power source (Step), a block (Constant1) for setting the initial values of temperature and moisture of vegetable origin organic materials and the final processing moisture, a key ((Rotate Switch) for rotating vegetable origin organic materials around their axis in the technological block, a key (Magn Switch) for switching on the selected mode of vegetable origin organic materials’ processing.

The presented studies consider four modes of the simulation model operation: Mode 1: Switching on seven sources of microwave energy and vegetable-origin organic materials’ rotation; Mode 2: Switching on four sources of microwave energy and vegetable-origin organic materials’ rotation; Mode 3: Switching on seven sources of microwave energy and vegetable origin organic materials’ rotation, and Mode 4: Switching on four sources of microwave energy without the rotation of vegetable origin organic materials.

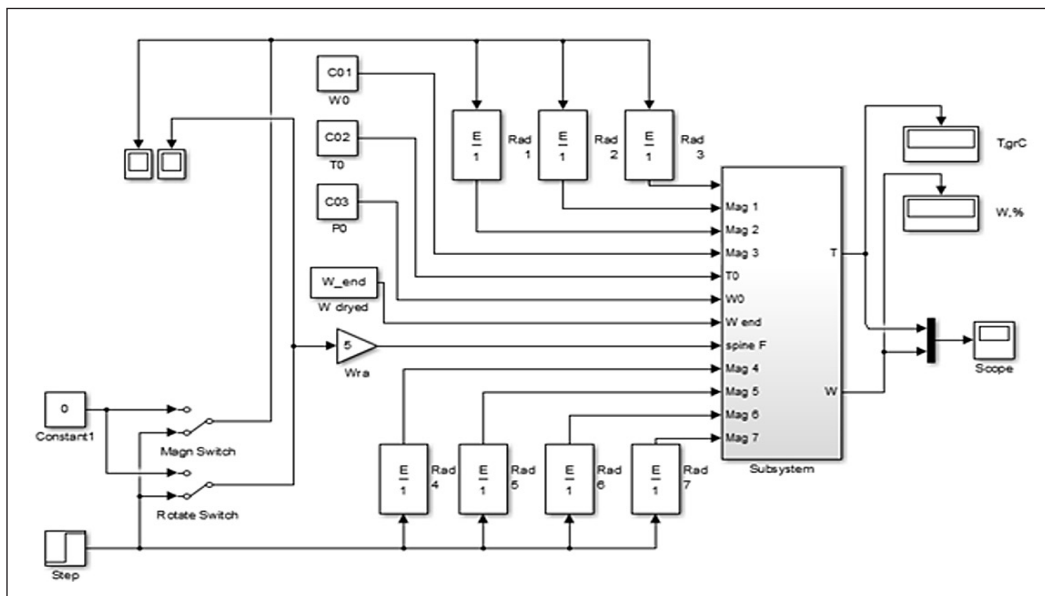
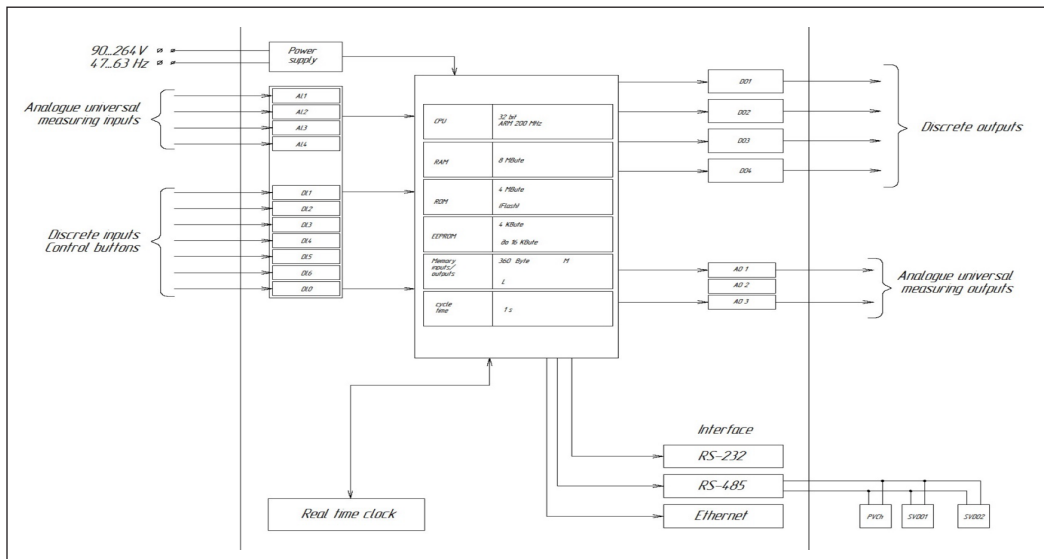


Figure 2. Simulation model of a microwave electro-technological installation for microwave processing of vegetable-origin organic materials

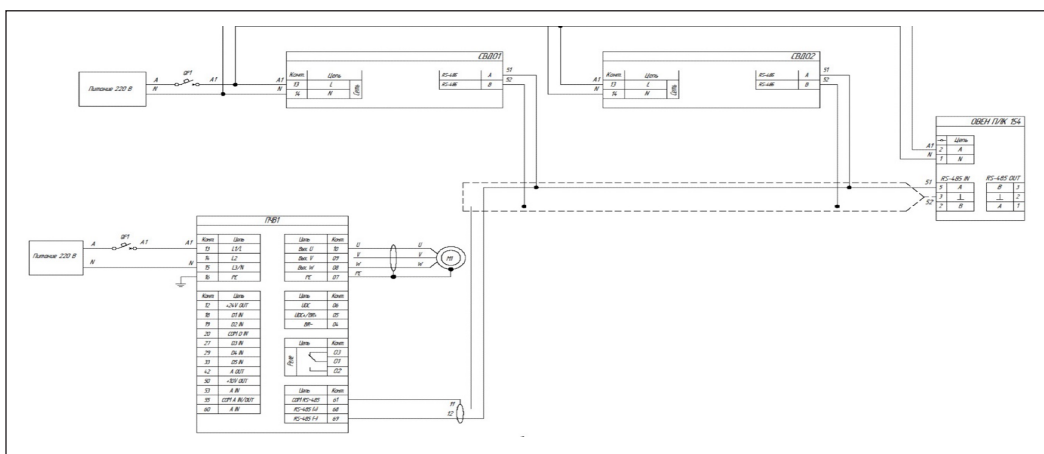
Methods Used to Measure the Processing Parameters

An automated control system has been developed to control the microwave processing organic materials of vegetable origin. Figure 3 shows the functional and circuit diagrams of the control system.

The automated control system for microwave processing organic materials of vegetable origin consists of four temperature sensors, four moisture sensors, a controller, two temperature and moisture measuring devices and a frequency transducer.



(a)



(b)

Figure 3. Diagram of an automated control system for microwave processing of vegetable-origin organic materials: (a) circuit diagram and (b) functional diagram

Note. OVEN PLC154—controller (PLC-programmable logic controller); SVD01, SVD02—temperature and moisture measuring device (SVD—wood moisture meter); PVCh1, PVCh—high-frequency transducer)

The humidity and temperature measuring device of the SVD series is designed for remote determination of humidity in drying chambers using four conductometric sensors. The device has one or two thermometers, depending on the model. The results of temperature measurements are transmitted via the RS-485 port according to the Modbus ASCII protocol. The length of the communication line is up to 1,000 meters; about 31 humidity meters can be connected to the line.

The technical characteristics of the OVEN PLK 154 controller are given in Table 2. The technical characteristics of the ARIES PCHV1 frequency converter are given in Table 3.

Table 2
Technical characteristics of the ARIES PLC 154 controller

Parameter	Value
Case protection level	IP20
Power supply voltage PLK154-220	90–264 V AC (rated voltage, 220 V), frequency of 47–63 Hz
Power consumption	6 Watts
Front panel display	1 Power indicator 6 digital input status indicators 4 output status indicators 1 indicator of connection with CODESYS 1 user program operation indicator
Interfaces	Ethernet 100 Base-T RS-232 RS-485
Exchange rate over RS interfaces	from 4800 to 115200 bps
Protocols	OVEN Modbus-RTU, Modbus-ASCII DCON Modbus-TCP GateWay (protocol CODESYS)

Table 3
Technical characteristics of the ARIES PCHV1 frequency converter

Parameter	Value
Power supply network	3 phases, 380–480 V (5.5–22 kW)
Output voltage (U, V, W), %	0–100
Output frequency, Hz	0–200 Hz(VC), 0–400 (U/F)
RS-485 protocol	Modbus RTU
Enclosure protection class	IP20

Testing Procedure

The purpose of the experimental studies is to determine the appropriate drying mode, which ensures fast processing and the preservation of nutrients in organic materials of vegetable origin.

Four modes of technological installation operation were studied. The first mode involves switching on seven magnetrons and materials' rotation. The second mode consists of actuating four magnetrons and materials' rotation. The third mode implies turning on seven magnetrons without the materials' rotation. The fourth mode involves actuating four magnetrons without materials' rotation.

Test characteristics are given in Table 4.

Table 4
Test characteristics

Parameter	Value
The first processing mode (7 magnetrons and the rotation mechanism of organic materials of plant origin along its axis are working)	
Initial humidity, %	85–92
Initial temperature, °C	21–23
Final humidity, %	6–10
Final temperature, °C	77–85
Processing time, hour	15
The second processing mode (4 magnetrons are working; the mechanism of rotation of organic materials of plant origin along its axis is disabled)	
Initial humidity, %	78–87
Initial temperature, °C	20–23
Final humidity, %	8–30
Final temperature, °C	78–93
Processing time, hour	39

Vegetable-derived organic materials are fastened horizontally to two frames of the working chamber of the microwave electro-technological installation. After the materials are laid, the lid is closed.

The moisture and temperature of vegetable-origin organic materials were measured every 60 minutes during microwave processing.

The experiments involved an infrared pyrometer, a surface thermometer, and a moisture-measuring device.

RESULTS

The paper presents the experimental results of the first and fourth processing modes. Figure 4 shows the modes of processing vegetable-origin organic materials in a microwave electro-thermal installation. Each mode gives the dependencies between moisture and time, temperature and time, and moisture and temperature.

- The drying time for the first mode was 15 hours; the final moisture was 7%.
- The drying time for the fourth mode was 39 hours; the final moisture was 12%.
- The first mode lasted 15 hours, and the fourth lasted 38 hours.

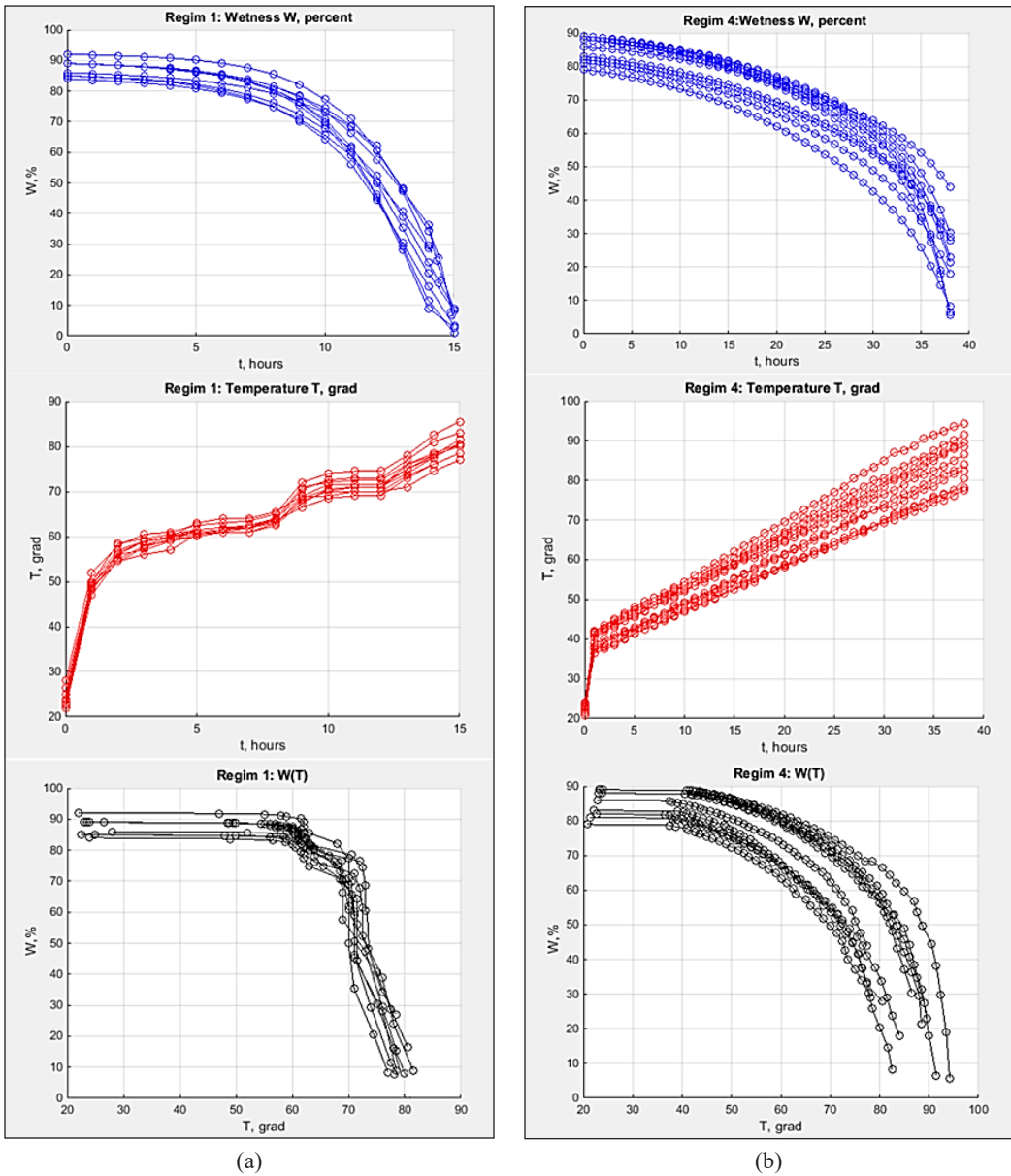


Figure 4. Modes of processing of vegetable-origin organic materials in a microwave electro-thermal installation: (a) the first mode; (b) the fourth mode

Figure 5 contrasts the simulation modeling results with the experimental studies of the microwave processing of vegetable-origin organic materials in the first and fourth modes.

The analysis of the results shows that the first mode is characterized by the absence of wrapping, charring, curving and twisting of the samples of vegetable-origin organic materials during their processing in the microwave electro-technological installation.

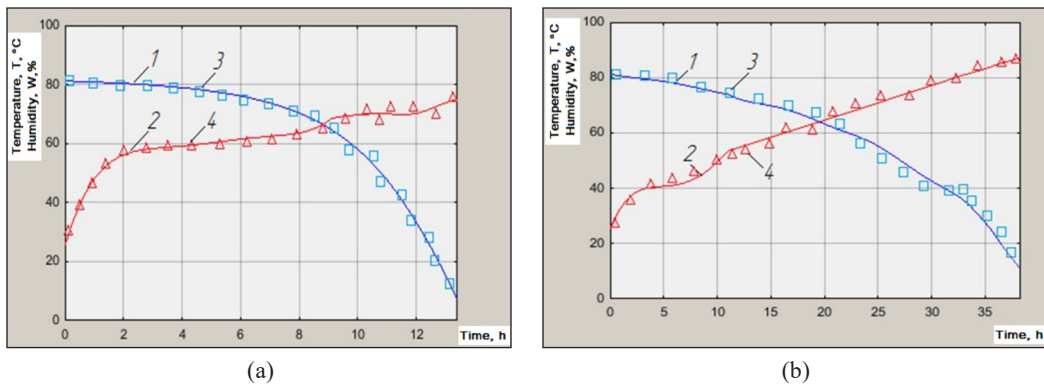


Figure 5. Comparison of the simulation modeling results and experimental studies of the microwave processing of vegetable-origin organic materials for the first and fourth modes: (a) the first mode, (b) the fourth mode

Note. 1, 2—simulation modeling results; 3, 4—experimental results

The fourth mode is characterized by wrapping and cracking the material, but there is no twisting, curving or charring.

Experimental studies and simulation modeling of the first and fourth modes of the microwave processing of vegetable-origin organic materials revealed the following:

- The drying time for the first mode was 15 hours; the final moisture was 7%.
- The drying time for the fourth mode was 39 hours; the final moisture was 12%.

The first mode provides a uniform temperature change of organic materials of vegetable origin. The surface temperature of the samples is almost the same as the temperature at half their thickness.

The fourth mode does not provide a uniform temperature change. The surface temperature of the samples differs by 8–13 °C from the temperature at half the depth of their thickness.

The simulation modeling of four modes of the technological installation operation provides a thorough and reliable analysis of changes in the temperature and moisture of vegetable-origin organic materials. The discrepancy between experimental data and simulation modeling does not exceed 4%.

Thus, the results of simulation modeling almost agree with the experimental results. The relative error does not exceed 3.5%.

DISCUSSION

Table 5 presents a comparative analysis of the results obtained and those of other authors.

The rotation of vegetable-origin organic material in the technological block of a thermal microwave installation has a positive effect, reducing the processing time and ensuring the required quality of the dried material, which is similar to the results of the studies

Table 5
Comparison of the results obtained with the results of other authors

Parameter	Results of experimental studies	Khasanov (2015)	Waseem et al. (2022)	Navida et al. (2022)	Malik et al. (2022)	Martins (2021)
Radiation frequency, MHz	2,450	2,450	2,450	2,450	2,450	2,450
Power, W	1,200	1,200	1,100	1,000	1,000	100–3,000
Uniformity processing, %	95–98	98	88.3	85	95	90
Productivity, t/hour	5–6	4	2.8–3.2	-	-	1.8–2.5
Positive effect	Reduction of processing time, improvement of properties	Increasing yields, improving seed quality	Improving the potato powder nutritional properties	Improving the watermelon juice's nutritional properties	Preservation of nutritional properties in a lemon drink	Improving the physical properties of grain

presented in the work (Aipov et al., 2019). The work states that the lumber pile rotation along its axis also reduces the processing time and provides a high-quality dried material.

Using two technological blocks (a block of thermal microwave processing of vegetable-origin organic materials and a block of non-thermal microwave processing of agricultural crops) in an electro-technological installation gives a positive economic effect since the processing of materials occurs simultaneously. The same findings are presented in Dobrodum and Arkhangel'sky (2017). They justify using a microwave electro-technological installation with a hybrid working chamber for processing dielectric and polymer materials and prove its commercial importance.

Non-thermal microwave processing of agricultural crops in an electro-technological installation does not worsen the nutritional value and organoleptic characteristics of the material. On the contrary, this method improves crops' properties (e.g., increases their nutritional value). The same findings are presented in Qu et al. (2021) and Waseem et al. (2022), which prove the increased nutritional value of a baked product made with the addition of less than 7.5% of potato powder. The product was processed in a microwave oven. Microwave processing did not damage potato starch.

Non-thermal microwave processing of agricultural crops, including grain, in an electro-technological installation increases storage time and provides a high-quality product. Qu et al. (2021) present similar findings, describing the process of lipase destruction in whole-grain flour by microwave heating, thus significantly increasing flour storage time and quality.

Combining two technological blocks in one electro-technological installation (a block of thermal microwave processing of vegetable-origin organic materials and a block of non-thermal microwave processing of agricultural crops) is a complex engineering problem under development. However, using this method will increase important economic and energy production indicators. The same findings are presented in Arkhangelsky and Grishina (2007) and Nadeem, Tehreem et al. (2022), which prove the economic and practical efficiency of combining two methods of processing different materials.

The creation of a microwave electro-technological installation for the microwave processing of vegetable-origin organic materials and agricultural crops implies combining two technological processes. Khasanov (2015) and Tukhvatullin and Aipov (2019) studied these processes, but their findings differ from those presented in this paper since they describe the microwave processing of various materials as one technological process. However, this method reduces the processing time and ensures the high quality of the processed materials.

Thus, the proposed prototype model for microwave processing of vegetable-origin organic materials and agricultural crops significantly increases the energy and economic efficiency of the installation by reducing the processing time and ensuring the required quality of the materials being dried, unlike existing electro-technological installations, which process only one material.

Moreover, unlike the existing ones, the proposed electro-technological installation increases the possibility of selling more than two products, thus significantly reducing costs and increasing the formation of positive financial results. In other words, the proposed installation contributes to profit growth at the same energy costs.

CONCLUSION

One of the options for designing a microwave electro-technological installation for microwave processing of vegetable-origin organic materials and agricultural crops is combining two technological blocks for non-thermal and thermal processing. Traveling wave chambers with a homogeneous rectangular waveguide are recommended to be used as blocks. A mechanism of rotation around their axis is used to ensure uniform processing of samples of vegetable-origin organic materials in a microwave electro-technological installation. As a result, the processing time decreases, and the quality of the processed material improves.

Experiments show that simulating the first and fourth modes of microwave processing of vegetable-origin organic materials decreases the drying time and the moisture rate. Thus, the drying time of the fourth mode is reduced from 39 to 15 hours, and the moisture rate is 12%. During the first mode, the moisture rate is 7%.

The first mode is characterized by a uniform temperature change (the temperature at the depth of half the thickness of the samples differs from the samples' surface temperature

by no more than 0.5–1.0°C). The fourth mode is characterized by an uneven temperature change (the temperature at a depth of half the thickness of the samples differs from the samples' surface temperature by 5–7°C).

Therefore, the first mode of microwave processing of organic materials of vegetable origin is preferable since it provides high-quality dried material in a short processing time.

Together with the heat treatment of vegetable-origin organic materials, the presented microwave electro-technological installation implements seven other technological processes of non-thermal microwave processing of agricultural products. In this case, after each of the seven sources of microwave energy (magnetron), a technological unit for non-thermal microwave modification of the corresponding material should be placed.

PRACTICAL APPLICATION OF THE FINDINGS

The creation of a microwave electro-technological installation for processing vegetable-origin organic materials and agricultural crops will solve the fundamentally new problem of coordinating technological blocks of thermal and non-thermal processing. This will contribute to the development of agriculture and allow the production of better-quality agricultural products.

Moreover, unlike the existing ones, the proposed electro-technological installation increases the possibility of selling more than two products with improved qualities, thus increasing profits at the same energy costs.

ACKNOWLEDGMENT

The work has been carried out within the framework of the grant of the Republic of Bashkortostan, Russia, as a science award for state support of young scientists–candidates of sciences (competition code: REC-GMU-2022).

REFERENCES

- Abdrabou, M. K., Han, X., Zeng, Y., & Zheng, Y. (2023). Harnessing the power of microwave irradiation: A novel approach to bitumen partial upgrading. *Molecules*, 28(23), Article 7769. <https://doi.org/10.3390/molecules28237769>
- Aipov, R. S., Gabitov, I. I., Tuhvatullin, M. I., Linenko, A. V., Tuktarov, M. F., & Akhmetshin, A. T. (2019). Process unit for drying sawn timber rotating in the ultra high frequency field with a discrete arrangement of magnetrons. *Bulgarian Journal of Agricultural Science*, 25(S2), 3-11.
- Amini, A., Latifi, M., & Chaouki, J. (2021). Electrification of materials processing via microwave irradiation: A review of mechanism and applications. *Applied Thermal Engineering*, 193, Article 117003. <https://doi.org/10.1016/j.applthermaleng.2021.117003>

- Aniszewska, M., Słowiński, K., Tulska, E., & Zychowicz, W. (2021). Effects of microwave irradiation on the moisture content of various wood chip fractions obtained from different tree species. *Journal of Wood Science*, 67(1), Article 28. <https://doi.org/10.1186/s10086-021-01958-8>
- Arkhangelsky, Y. S., & Grishina, E. M. (2007). Hybrid microwave electrotechnological installation. *Logistics and Economics of Resource Saving in Industry (Cross-Sectoral Research and Technology Centre of Renewable Energy Resources)*, 2, 277-280.
- Arkhangelsky, Y. S., Kalganova, S. G., & Yafarov, R. K. (2018). *Measurements in microwave electrotechnological installations*. Amirit Publication.
- Dobrodum, A. S., & Arkhangelsky, Yu. S. (2017). Microwave electrotechnological installations with hybrid cameras. *Electrical Engineering Issues*, 3(16), 16-22.
- Galos, J. (2021). Microwave processing of carbon fibre polymer composites: A review. *Polymers and Polymer Composites*, 29(3), 151-162. <https://doi.org/10.1177/09673911209038>
- Ishak, K. A., Velayutham, T. S., Annuar, M. S. M., & Sirajudeen, A. A. O. (2021). Structure-property interpretation of biological polyhydroxyalkanoates with different monomeric composition: Dielectric spectroscopy investigation. *International Journal of Biological Macromolecules*, 169, 311-320. <https://doi.org/10.1016/j.ijbiomac.2020.12.090>
- Khasanov, E. R. (2015). Influence of microwave current treatment modes on disinfection and stimulation of seed germination with subsequent inlay. *Bulletin of the Bashkir State Agrarian University*, 3(35), 77-81.
- Kolokolova, A. Y., Ilyuhina, N. V., Trishkaneva, M. V., & Korolev, A. A. (2020). The effect of combining microwave and ultraviolet methods of plant materials processing on Salmonella culture inhibition. *Proceedings of the Voronezh State University of Engineering Technologies*, 82(1), 76-81. <https://doi.org/10.20914/2310-1202-2020-1-76-81>
- Lazim, S. K. (2023). Evaluation of Maize (*Zea mays* L.) germination traits by hydro-and microwave priming. *Scholars Journal of Agriculture and Veterinary Sciences*, 10(11), 144-151. <https://doi.org/10.36347/sjavs.2023.v10i11.001>
- Lv, H., Chen, X., Liu, X., Fang, C., Liu, H., Zhang, B., & Fei, B. (2018). The vacuum-assisted microwave drying of round bamboos: Drying kinetics, color and mechanical property. *Materials Letters*, 223, 159-162. <https://doi.org/10.1016/j.matlet.2018.04.038>
- Malik, F., Nadeem, M., Ainee, A., Kanwal, R., Sultan, M., Iqbal, A., Mahmoud, S. F., Alshehry, G. A., Al-Jumayi, H. A., & Algarni, E. H. A. (2022). Quality evaluation of lemon cordial stored at different times with microwave heating (Pasteurization). *Sustainability*, 14(4), Article 1953. <https://doi.org/10.3390/su14041953>
- Martins, F. (2021). *Direitos Sociais em Tempos de Crise Econômica* [Social Rights in Times of Economic Crisis]. Saraiva Educação.
- Montenegro, F. M., Heffernan, R. B., Marsaioli Junior, A., Berteli, M. N., Campelo, P. H., & Clerici, M. T. P. S. (2021). Effect of microwave processing on the physical, physicochemical and rheological properties of wheat grain and its flour. *Research, Society and Development*, 10(8), Article e12610817033. <https://doi.org/10.33448/rsd-v10i8.17033>

- Monton, C., Luprasong, C., & Charoenchai, L. (2019). Convection combined microwave drying affect quality of volatile oil compositions and quantity of curcuminoids of turmeric raw material. *Revista Brasileira de Farmacognosia*, 29, 434-440. <https://doi.org/10.1016/j.bjp.2019.04.006>
- Nadeem, M., Ranjha, M. M. A. N., Ameer, K., Ainee, A., Yasmin, Z., Javaria, S., & Teferra, T. F. (2022). Effect of sonication on the functional properties of different citrus fruit juices. *International Journal of Fruit Science*, 22(1), 568-580. <https://doi.org/10.1080/15538362.2022.2079584>
- Nadeem, M., Tehreem, S., Ranjha, M. M. A. N., Ahmad, A., Din, A., Din, G. M. U., Javeria, S., Riaz, M. N., & Siddeeg, A. (2022). Probing of ultrasonic assisted pasteurization (UAP) effects on physicochemical profile and storage stability of jambul (*Syzygium cumini* L.) squash. *International Journal of Food Properties*, 25(1), 661-672. <https://doi.org/10.1080/10942912.2022.2058532>
- Navida, M., Nadeem, M., Qureshi, T. M., Pashameah, R. A., Malik, F., Iqbal, A., Sultan, M., Abo-Dief, H. M., & Alanazi, A. K. (2022). The synergistic effects of sonication and microwave processing on the physicochemical properties and phytochemicals of watermelon (*Citrullus lanatus*) juice. *Agriculture*, 12(9), Article 1434. <https://doi.org/10.3390/agriculture12091434>
- Nirmaan, A. M. C., Prasantha, B. D. R., & Peiris, B. L. (2020). Comparison of microwave drying and oven-drying techniques for moisture determination of three paddy (*Oryza sativa* L.) varieties. *Chemical and Biological Technologies in Agriculture*, 7, Article 1. <https://doi.org/10.1186/s40538-019-0164-1>
- Patel, D., & Bhise, S. (2023). Effect of thermal, and microwave treatment on bioactive compound, antioxidant activity, and sensory quality of lime-flavored dragon fruit RTS beverage. *Journal of Applied Science and Technology*, 42(30), 16-24. <https://doi.org/10.9734/cjast/2023/v42i304208>
- Patel, J., Al-Ghamdi, S., Zhang, H., Queiroz, R., Tang, J., Yang, T., & Sablani, S. S. (2019). Determining shelf life of ready-to-eat macaroni and cheese in high barrier and oxygen scavenger packaging sterilized via microwave-assisted thermal sterilization. *Food and Bioprocess Technology*, 12, 1516-1526. <https://doi.org/10.1007/s11947-019-02310-1>
- Qu, C., Yang, Q., Ding, L., Wang, X., Liu, S., & Wei, M. (2021). The effect of microwave stabilization on the properties of whole wheat flour and its further interpretation by molecular docking. *BMC Chemistry*, 15(1), Article 57. <https://doi.org/10.1186/s13065-021-00782-x>
- Rezaei, H., Lim, C. J., Lau, A., Bi, X., & Sokhansanj, S. (2017). Development of empirical drying correlations for ground wood chip and ground wood pellet particles. *Drying Technology*, 35(12), 1423-1432. <https://doi.org/10.1080/07373937.2016.1198912>
- Shishkina, N. S., Borchenkova, L. A., Karastoyanova, O. V., Shatalova, N. I., Korovkina, N. V., & Levshenko, M. T. (2019). Improvement of the process of welding blench with microwave application. *Food Processing Industry*, 1, 28-31.
- Sivakov, B. K., & Grigorieva, S. V. (2019). Installation of microwave drying of agricultural products in farms. *Electrical Engineering Issues*, 1(22), 9-13.
- Stepanenko, V. V., & Kazhevnikov, Y. V. (2017). Disinfection of food products by microwave electromagnetic field energy. *Questions of Electrotechnology*, 4(17), 19-22.

- Sun, Y., Zhang, P., Hu, J., Liu, B., Yang, J., Liang, S., Xiao, K., & Hou, H. (2021). A review on microwave irradiation to the properties of geopolymers: Mechanisms and challenges. *Construction and Building Materials*, 294, Article 123491. <https://doi.org/10.1016/j.conbuildmat.2021.123491>
- Tuhvatullin, M. I., Aipov, R. S., Linenko, A. V., Galiullin, R. R., & Kamalov, T. I. (2019). Microwave drying of wood, mathematical simulation of rotating lumber in the SHF field. *International Journal of Advanced Science and Technology*, 28(9), 208-218.
- Tukhvatullin, M. I., & Aipov, R. S. (2019). Efficiency of lumber materials' drying when rotating them in a microwave field. *Agroengineering Innovations in Agriculture*, 3(32), 272-277.
- Waseem, M., Akhtar, S., Ahmad, N., Ismail, T., Lazarte, C. E., Hussain, M., & Manzoor, M. F. (2022). Effect of microwave heat processing on nutritional indices, antinutrients, and sensory attributes of potato powder-supplemented flatbread. *Journal of Food Quality*, 2022, Article 2103884. <https://doi.org/10.1155/2022/2103884>.
- Zhou, J., Yang, X., Zhu, H., Yuan, J., & Huang, K. (2019). Microwave drying process of corns based on double-porous model. *Drying Technology*, 37(1), 92-104. <https://doi.org/10.1080/07373937.2018.1439952>.

Prevalence of *Vibrio parahaemolyticus*, *Vibrio cholerae*, and *Vibrio alginolyticus* in a White-leg Shrimp (*Litopenaeus vannamei*) Farm in Sarawak

Dalene Lesen¹, Elexson Nillian^{1*}, Dayang Najwa Awang Baki¹ and Tunung Robin^{2,3}

¹Faculty of Resource Science and Technology, University Malaysia Sarawak, 94300, Kota Samarahan, Sarawak, Malaysia

²Institut Ekosains Borneo, Universiti Putra Malaysia Kampus Bintulu, Jalan Nyabau, 97008 Bintulu, Sarawak, Malaysia

³Faculty of Humanities, Management and Science, Universiti Putra Malaysia Bintulu Sarawak Campus, Jalan Nyabau, 97008 Bintulu, Sarawak, Malaysia

ABSTRACT

Vibriosis in shrimp farms poses potential risks to the industry's sustainability and the consumers' health. Little is known about the dynamics and variation of *Vibrio* spp.—population in shrimp production in Sarawak, Malaysia. The apparent prevalence of three *Vibrio* species, *V. parahaemolyticus*, *V. cholerae*, and *V. alginolyticus*, were investigated in water (n=12), sediment (n=12), shrimp (n=12), and effluent (n=12) samples collected from two ponds in a coastal shrimp farm during one production cycle. Multiplex-PCR using specific primer sets showed the presence of the three *Vibrio* species. Based on the results, *V. parahaemolyticus* was the most prevalent in all four samples, with a contamination rate of 97.92% (95% CI: 89.10 to 99.89%), while *V. cholerae* and *V. alginolyticus* had a contamination rate of 47.92% (95% CI: 34.37 to 61.67%) and 25.0% (95% CI: 14.92 to 38.78%), respectively. High *Vibrio* load in the shrimp farm is due to favourable environmental factors, such as optimal temperatures, salinity, and pH ranges for the growth of these species. The study's findings offer important preliminary insights into the prevalence and distribution of these pathogenic *Vibrio* spp., within a shrimp farm in Kuching, Sarawak. This study serves as a potential model for monitoring *Vibrio* spp. prevalence in other shrimp farms across Sarawak, thereby addressing the scarcity of data on prevalence in the region.

ARTICLE INFO

Article history:

Received: 16 October 2023

Accepted: 07 March 2024

Published: 15 August 2024

DOI: <https://doi.org/10.47836/pjst.32.5.17>

E-mail addresses:

dalesen25@gmail.com (Dalene Lesen)

nelexson@unimas.my (Elexson Nillian)

dygnjw96@gmail.com (Dayang Najwa Awang Baki)

tunungrobin@upm.edu.my (Tunung Robin)

* Corresponding author

Keywords: Microbial load, most probable number, multiplex PCR, shrimp farm, *Vibrio* spp.

INTRODUCTION

The shrimp industry is a significant contributor to the aquaculture industry in Southeast Asia, with an estimated total area of marine shrimp farms in Malaysia alone at between 5,100 and 5,200 hectares as of 2012 and a total market value of RM1.13 billion in 2020 (Department of Fisheries Malaysia, 2012; Gilbert, 2023). However, the industry has faced challenges due to disease outbreaks, including vibriosis caused by *Vibrio* spp. These heterotrophic bacteria are prevalent in freshwater and marine environments and can inhabit a wide range of environments as free-living cells or symbionts. Approximately 110 species of the genus *Vibrio* have been identified to date, with many of these species being pathogenic to animals and humans (Farmer & Janda, 2015). *Vibrio* spp. Human infections often result from contact with polluted water or ingesting raw or undercooked seafood contaminated with the bacteria (Dutta et al., 2021). *Vibrio parahaemolyticus*, in particular, has been identified as a common cause of food poisoning cases in Malaysia (Sani et al., 2013). *Vibrio* spp. infection can pose serious health risks to immunocompromised individuals, including senior citizens and children, and can result in septicaemia and death (Song et al., 2020).

Some *Vibrio* spp, such as *V. cholerae*, are pathogenic and infectious, while others, such as *V. parahaemolyticus*, *V. alginolyticus* and *V. vulnificus*, are known as opportunistic pathogens (Haifa-Haryani et al., 2022; Valente & Wan, 2021). Shrimp infected with *Vibrio* spp. may exhibit clinical signs, including lethargy, a lack of moulting, abnormal swimming behaviour, reduced food intake, and potentially anorexia as indicated by empty guts and an off-white body colour (Valente & Wan, 2021). *V. parahaemolyticus* that causes acute hepatopancreatic necrosis disease (AHPND), for instance, causes the infected shrimp to exhibit an empty stomach and midgut, along with a hepatopancreas (HP) that appears pale to white (To et al., 2020). Meanwhile, *V. alginolyticus* is the causative agent of flaming bacterial disease that causes the infected shrimp to glow in the dark (Alifia et al., 2021). On the other hand, a few strains of *V. cholerae* are the causative agent of *Vibrio*-caused bacteremia, which is characterised by reduced hemocytes and lethargy in the infected crustaceans (Valente & Wan, 2021). Severe vibriosis in shrimp can even result in mortality. While *Vibrio* spp. is prevalent in the environment, its infection can be controlled when it occurs at low levels. However, environmental factors such as temperature and salinity can trigger the rapid growth of these bacteria, leading to outbreaks of vibriosis that can decimate an entire shrimp population in an infected pond, resulting in significant production losses (Mastan & Begum, 2016; Semenza et al., 2017). Contamination of seafood products with high concentrations of *Vibrio* spp. can also threaten consumer health. Therefore, early detection and enumeration of *Vibrio* spp. is essential for monitoring outbreaks in aquaculture farms, assessing the potential danger to public health, and preventing economic losses.

Currently, there is limited data available on the prevalence of *Vibrio* spp. in aquaculture farms in Sarawak, particularly in shrimp farms. Similar to other states in Malaysia,

shrimp farmers in Sarawak face significant challenges, with disease outbreaks being a major concern. However, the lack of official data poses a challenge, as most incidents are communicated verbally and not formally reported (Baker-Austin et al., 2018). Given Sarawak's goal to increase shrimp production to RM1 billion in export value by 2030, these disease challenges could significantly impede progress (Ling, 2022). Additionally, official data on disease incidents and *Vibrio* spp is scarce. prevalence in Sarawak, attributed to the absence of surveillance systems, under-reporting, or failure to report incidents, impedes a comprehensive understanding of the extent of these challenges and hinders the development of effective strategies for disease management and prevention in Sarawak's shrimp farming industry (Baker-Austin et al., 2018). This study aims to detect and isolate *Vibrio* spp. from water, sediment, shrimp, and effluent samples collected from a shrimp farm in Kuching, Sarawak.

This study has investigated the apparent prevalence of three *Vibrio* spp., *V. parahaemolyticus*, *V. cholerae*, and *V. alginolyticus*, in water, sediment, shrimp, and effluent samples collected from two ponds in a coastal shrimp farm. One production cycle of shrimp starts from the stocking of post-larvae shrimps to the harvesting of mature shrimps. To our knowledge, this report provides the first detection and quantification of these three *Vibrio* spp. in one cycle of shrimp production on a shrimp farm in Sarawak, Malaysia. This information offers novel perspectives on the challenges the shrimp aquaculture sector encounters in Sarawak. These challenges might diverge from those in other documented locations owing to the distinct geographical and climatic factors unique to the region. These factors contribute to variations in temperature, humidity, precipitation, soil properties, composition, and other environmental variables, consequently influencing the microbial composition in the region (Patel et al., 2023). The findings of this study will yield preliminary important information on the prevalence and distribution of this pathogenic *Vibrio* spp. in a shrimp farm in Kuching, Sarawak. Furthermore, it can serve as a model for prevalence studies in other shrimp farms around Sarawak. This approach will contribute to obtaining more comprehensive data on the prevalence and distribution of *Vibrio* spp. in Sarawak. Subsequently, these insights will aid in developing effective strategies for preventing and controlling vibriosis.

MATERIALS AND METHODS

Sample Collection

Samples were collected from Persatuan Nelayan Kawasan (PNK) Satang Biru, Lembaga Kemajuan Ikan Malaysia (LKIM), Telaga Air, Sarawak (0°N 110°11'51., 1°40'59, 1). Four sample types (water, sediment, shrimp, and effluent) were collected from two shrimp ponds (P1 and P2) every two weeks, from stocking to harvesting, which took approximately three months. Both earthen shrimp ponds have a surface area of one

hectare with a 1-meter depth. The sampling was done in August–October of 2020 for P1 and October–December of 2020 for P2. Every sampling was performed between nine and ten o'clock in the morning, and the entire period covered the warm season and the start of the rainy season.

The sampling method was adapted from the method by Kaysner et al. (1990) with modifications. Forty-eight (n=48) samples of twelve each of water (n=12), sediment (n=12), shrimp (n=12), and effluent (n=12) were obtained throughout the sampling process. During each sampling, each sample type was collected at three different spots (sampling points) to make up the triplicates. At least 1 L of surface water and effluent samples were collected in sterile polypropylene bottles at each sampling point. Shrimp were collected using a net and placed in sterile plastic bags. The shrimp were collected from the post-larvae stage, progressing through the juvenile and sub-adult stages until they reached the harvestable adult stage at the end of the sampling period. Meanwhile, sediment was collected using an ethanol-sterilised polyvinyl chloride (PVC) pipe and placed in sterile 50 mL microcentrifuge tubes. All samples were brought directly to the lab in an ice box and processed within 24 hours of sampling (Kaysner et al., 1990).

In addition to sample collection, the pond water's physical and chemical parameters (temperature, salinity, and pH) were also measured and recorded. These parameters were chosen because the water's temperature, salinity, and pH are commonly reported as one of the many factors influencing the distribution of *Vibrio* spp. (Valente & Wan, 2021). Water temperatures and pHs were measured on-site during every sampling using Fisherbrand™ accuMET™ AP125 Portable pH/Ion/mV/Temperature Meter Kit (Thermo Fischer Scientific, U.S.). Meanwhile, water salinity was measured using a salinity refractometer (Hisamatsu, Japan). The measurements were taken triplicate at three different pond spots and expressed as the mean values.

Enrichment and MPN Method

Before enrichment, the triplicate water and effluent samples were mixed in equal volumes in sterile microcentrifuge tubes. The triplicate sediment and shrimp samples were each mixed and homogenised using a sterilised conventional blender. One gram (solid samples) or 1 mL (liquid samples) of each sample was then thoroughly mixed with 9 mL of alkaline peptone water (APW) (Merck, Darmstadt, Germany) and pre-enriched by incubating overnight at 37°C. The suspension was then serially diluted 10-fold from 10⁻¹ to 10⁻⁵ in APW. Using the three-tube most probable number (MPN) method outlined in the Bacteriological Analytical Manual (BAM), 1 mL of each dilution was transferred into triplicate MPN tubes containing 10 mL APW broth. All tubes were incubated at 37°C under aerobic conditions for 24 hours. Prior to extracting the genomic DNA from the MPN tubes after incubation, the turbidity of the tubes was observed (Blodgett, 2000). Sterile APW broth was used as

the blank control throughout this experiment. Sterile APW was included in the experiment as the negative control.

Genomic DNA Extraction

Bacterial DNA from the turbid MPN tubes was extracted using the boiled-cell method with slight modifications (Queipo-Ortuno et al., 2008). One millilitre of each culture was transferred to a 1.5 mL microcentrifuge tube and centrifuged at 10,000 rpm for 5 min. The supernatant was removed, and the resulting pellet was resuspended in 100 µL sterile distilled water. The suspension was then boiled for 10 min and cooled at -21°C for 5 min. The DNA extract was centrifuged at 10,000 rpm for 10 min and then stored at -21°C for analysis.

Multiplex Polymerase Chain Reaction (mPCR)

Multiplex PCR was conducted using three sets of primers that specifically targeted *V. parahaemolyticus*, *V. cholerae*, and *V. alginolyticus*, respectively, as designed by Kim et al. (2015). The primers used are shown in Table 1. Each 15 µL of the PCR mixture consisted of the following components: 7.5 µL exTEN 2X PCR Master Mix (1st BASE), 0.6 µL of each primer with a concentration of 10 µM, 2.0 µL DNA template, and 1.9 µL sterile distilled water.

Table 1

Sequences, sources, and expected amplicon sizes of primer pairs used to target each *Vibrio* spp. in this study (Kim et al., 2015)

Target species	Primer name	Primer sequence (5'→ 3')	Amplicon size (bp)
<i>Vibrio parahaemolyticus</i>	VP 1155272 F	AGCTT ATTGG CCGTT TCTGT CGG	297
	VP 1155272 R	CKCAA GACCA AGAAA AGCCG TC	
<i>Vibrio cholerae</i>	VC C634002 F	CAAGC TCCGC ATGTC CAGAA GC	154
	VC C634002 R	GGGGC GTGAC GCGAA TGATT	
<i>Vibrio alginolyticus</i>	VA 1198239 F	ACGGC ATTGG AAATT GCGAC TG	199
	VA 1198239 R	TACCC GTCTC ACGAG CCCAA G	

PCR was run by using T100™ Thermal Cycler (Bio-Rad, USA) according to the following conditions: Initial denaturation at 94°C for 5 min; 30 cycles of denaturation at 94°C for 30 sec, annealing at 60°C for 30 sec, and extension at 72°C for 30 sec; final extension at 72°C for 10 min (Kim et al., 2015). The PCR products were electrophoresed on 1.5% (w/v) agarose gel at 80 V for two hours. GeneRuler 100-bp DNA ladder (Thermo Fisher Scientific, USA) was used as the molecular weight marker. A cocktail of *V. parahaemolyticus* ATCC 27969, *V. cholerae* KCDC 13589, and *V. alginolyticus* ATCC 17749 was used as the positive control. In contrast, sterile APW processed parallel with the samples was used as the negative control to replace the DNA template.

From the results of multiplex PCR, MPN values were analysed based on the MPN table for three tubes and expressed as MPN mL⁻¹ for water and effluent samples and MPN g⁻¹ for sediment and shrimp samples (Man, 1983).

Statistical Analysis

Data was analysed using GraphPad Prism (version 9.5.1, Dotmatics, San Diego, CA). The prevalence of *Vibrio* spp. was calculated with a 95% confidence interval (CI). Fisher's exact test was used to compare the overall prevalence of the three *Vibrio* spp. with the significant level set at $P < 0.05$. Spearman's r_s correlation statistic was performed using PAST 4.13 (University of Oslo, Norway) software to test the association between the environmental and chemical parameters (i.e., temperature, pH, and salinity) with each *Vibrio* spp. load.

RESULTS

Multiplex PCR

The expected sizes for the PCR products of *V. parahaemolyticus*, *V. cholerae*, and *V. alginolyticus* are 297 bp, 154 bp, and 199 bp, respectively. The agarose gel electrophoresis (AGE) of the PCR products showed the presence of bands according to the expected sizes (Figure 1). During the optimisation steps, the annealing temperature of 60°C was ideal for specific amplifications using the three primer sets. On the other hand, PCR products using annealing temperatures lower than 58°C did not produce any band during the AGE.

Based on positive PCR bands, the prevalence of *V. parahaemolyticus*, *V. cholerae*, and *V. alginolyticus* in four types of samples taken from the shrimp farm, from the stocking period to the harvesting period, were summarised in Table 2.

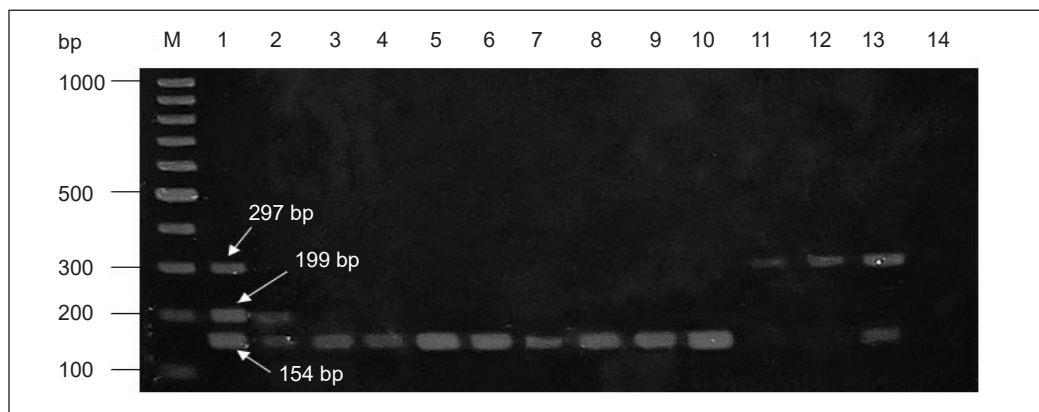


Figure 1. Gel electrophoresis of multiplex PCR of *Vibrio* spp. through amplification of random sequences for identification of *V. parahaemolyticus* (297 bp), *V. alginolyticus* (199 bp), and *V. cholerae* (154 bp). Lane M: 100 bp DNA ladder; Lane 1: positive control (cocktail of *V. parahaemolyticus* ATCC 27969, *Vibrio cholerae* KCDC 13589, and *V. alginolyticus* ATCC 17749); Lane 2–13: representative positive samples; Lane 14: negative control.

Table 2

Prevalence of *V. parahaemolyticus*, *V. cholerae*, and *V. alginolyticus* in water, sediment, shrimp, and effluent samples taken from stocking to harvesting period based on MPN-mPCR method

Sample	Prevalence (%)			
	n ^a	<i>V. parahaemolyticus</i>	<i>V. cholerae</i>	<i>V. alginolyticus</i>
Water	12	100.0 ^b (75.75–100) ^c	58.33 (31.95–80.67)	0.0 (0–24.25)
Sediment	12	100.0 (75.75–100)	33.33 (13.81–60.94)	0.0 (0–24.25)
Shrimp	12	91.67 (64.61–99.57)	16.67 (2.96–44.80)	66.67 (39.06–86.19)
Effluent	12	100.0 (75.75–100)	83.33 (55.20–97.04)	33.33 (13.81–60.94)
TOTAL	48	97.92 (89.10–99.89)	47.92 (34.47–61.67)	25.0 (14.92–38.78)

Note. ^a Number of samples; ^b Percentage of positive samples; ^c 95% confidence interval (%)

Throughout the sampling in the shrimp farm, 48 samples were collected from two ponds during six samplings. Of the entire samples examined, the prevalence of *V. parahaemolyticus*, *V. cholerae*, and *V. alginolyticus* was 97.92% (n=47, 95% CI: 89.10 to 99.89%), 47.92% (n=23, 95% CI: 34.47 to 61.67%), and 25.0% (n=12, 92% CI: 14.92 to 38.78%), respectively. Among the three *Vibrio* spp., *V. parahaemolyticus* had the highest prevalence, while *V. alginolyticus* had the lowest (P<0.05).

In comparison between samples, *V. parahaemolyticus* was the most prevalent in all four samples. In water samples, the prevalence of *V. parahaemolyticus* and *V. cholerae* were 100% (n=12, 95% CI: 75.75 to 100%) and 58.33% (n=7, 95% CI: 31.95 to 80.67%), respectively, while *V. alginolyticus* was not detected. *V. parahaemolyticus* was again the most prevalent in sediment samples, with 100% (n=12) positive detection, followed by *V. cholerae* with 33.33% (n=4, 95% CI: 13.81 to 60.94%). Meanwhile, *V. alginolyticus* was again not detected in the sediment samples. In shrimp samples, *V. alginolyticus* had the second highest detection after *V. parahaemolyticus*, with 66.67% (n=8, 95% CI: 39.06% to 86.19%) prevalence. In effluent samples, *V. parahaemolyticus*, *V. cholerae*, and *V. alginolyticus* were positively detected with a prevalence of 100% (n=12, 95% CI: 75.75 to 100%), 83.33% (n=10, 95% CI: 55.2 to 97.04%), and 33.33% (n=4, 95% CI: 6.6 to 60.0%), respectively.

Based on statistical analysis, it has been found that the overall prevalence among the three *Vibrio* spp. is significantly different (P<0.05). However, the prevalence of *V. parahaemolyticus* between sample types was not significantly different. The prevalence of *V. cholerae* significantly differs between sediment and effluent, as well as between shrimp and effluent samples. Meanwhile, the prevalence of *V. alginolyticus* significantly differed between shrimp and water samples and between sediment and shrimp samples.

The three physical and chemical parameters of the water samples were measured and recorded throughout the sampling period. Based on Figure 2, the water temperatures for P1 and P2 remained between 29°C and 34°C from stocking to harvesting. The salinity in P1 was 22–26 ppt, while the salinity in P2 was slightly lower, at 20–25 ppt. Meanwhile, the pH levels for water in both ponds ranged from acidic to neutral (pH 5.9 to pH 7.9).

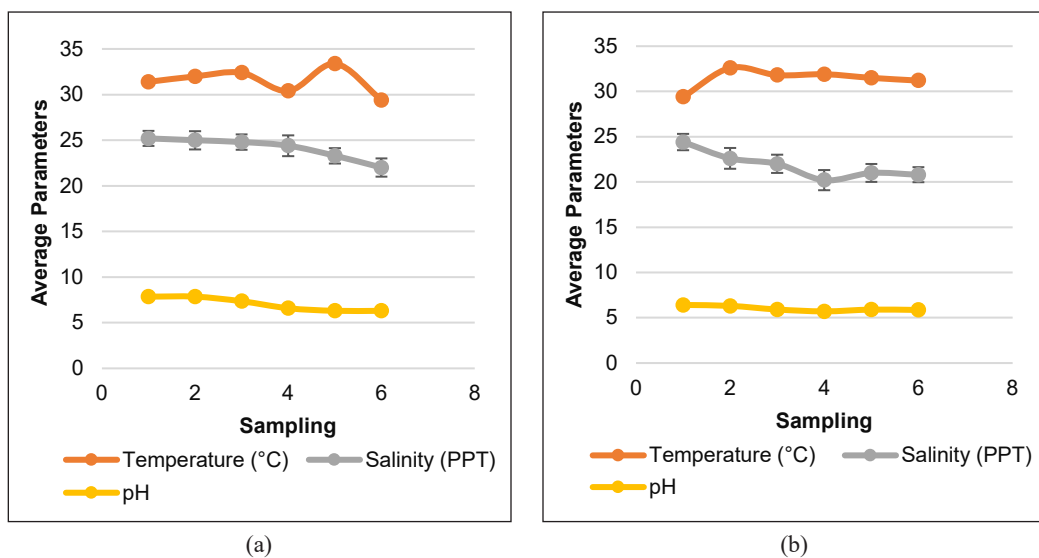


Figure 2. Average temperature, salinity, and pH of pond water in: (a) P1; and (b) P2 throughout the sampling periods

Concentration of *Vibrio* spp. in P1

Vibrio parahaemolyticus

Based on the MPN-mPCR method, it was found that the highest concentration of *V. parahaemolyticus* in water, sediment, and shrimp samples in P1 from stocking (Sampling 1) to harvesting (Sampling 6) was more than 1,100 MPN/mL (Table 3). Although a slight decrease in the detection of *V. parahaemolyticus* in the three samples was observed after the first sampling, the concentration eventually rose to more than 1,100 MPN mL⁻¹ at the last sampling. In the effluent samples, the highest concentration of *V. parahaemolyticus* was detected during sampling 5 with 110 MPN mL⁻¹. The concentration of *V. parahaemolyticus* in the effluent samples at P1 is the lowest compared to the other three sample types.

Based on Figure 3, it was observed that the concentration of *V. parahaemolyticus* in water, sediment, and shrimp samples increased to its highest concentration towards harvesting, and it has the highest concentration as compared to the other two *Vibrio* spp. Only in the effluent samples did the concentration of *V. parahaemolyticus* become the lowest compared to *V. cholerae* and *V. alginolyticus* at the end of the sampling period.

Based on the MPN-mPCR result in Table 3, the highest and lowest concentrations of *V. cholerae* in water samples were >1,100 MPN mL⁻¹ and <3 MPN mL⁻¹, respectively. The concentration of *V. cholerae* increased to more than >1,100 MPN mL⁻¹ on the second sampling but then decreased and remained low at >3 MPN mL⁻¹ until harvesting. In the sediment and shrimp samples, the highest detection was observed on sampling two at 38 MPN g⁻¹ and 180 MPN mL⁻¹, respectively. However, the concentrations of *V. cholerae* in

Table 3

Microbial load of *Vibrio* spp. (MPN g⁻¹ or MPN mL⁻¹) in samples collected from P1 throughout one production cycle

Sampling	Sample	<i>V. parahaemolyticus</i>			<i>V. cholerae</i>			<i>V. alginolyticus</i>		
		Min ^a	Med ^b	Max ^c	Min	Med	Max	Min	Med	Max
1	Water	420	>1,100	-	45	160	420	-	<3	9.5
	Sediment	210	1,100	4,100	3.6	11	38	-	<3	9.5
	Shrimp	-	<3	9.5	-	<3	9.5	180	1,100	4,100
	Effluent	8.7	36	9.4	4.5	16	42	-	<3	9.5
2	Water	18	93	420	420	>1,100	-	-	<3	9.5
	Sediment	40	210	430	3.6	11	38	-	<3	9.5
	Shrimp	1.3	7.4	20	9	43	180	3.7	15	42
	Effluent	1.3	7.2	42	420	>1,100	-	-	<3	9.5
3	Water	180	1,100	4,100	1.3	7.2	18	-	<3	9.5
	Sediment	4.5	16	42	-	<3	9.5	-	<3	9.5
	Shrimp	8.7	36	94	3.6	14	42	1.3	7.2	18
	Effluent	4.5	15	42	1.7	3.6	18	-	<3	9.5
4	Water	180	1,100	4,100	-	<3	9.5	-	<3	9.5
	Sediment	4.5	15	42	-	<3	9.5	-	<3	9.5
	Shrimp	3.6	11	38	-	<3	9.5	0.17	3.6	18
	Effluent	8.7	35	94	-	<3	9.5	-	<3	9.5
5	Water	420	>1,100	-	0.17	3.6	18	-	<3	9.5
	Sediment	420	>1,100	-	-	<3	9.5	-	<3	9.5
	Shrimp	420	>1,100	-	-	<3	9.5	-	<3	9.5
	Effluent	8.7	38	110	40	210	430	0.15	3	11
6	Water	420	>1,100	-	-	<3	9.5	-	<3	9.5
	Sediment	420	>1,100	-	-	<3	9.5	-	<3	9.5
	Shrimp	420	>1,100	-	-	<3	9.5	-	<3	9.5
	Effluent	4.5	15	42	90	290	1,000	8.7	35	94

^a Minimum MPN g⁻¹ or MPN mL⁻¹ value; ^b Median MPN g⁻¹ or MPN mL⁻¹ value; ^c Maximum MPN g⁻¹ or MPN mL⁻¹ value

(- = No minimum or maximum value)

both samples in the following weeks decreased and remained less than 3 MPN g⁻¹ until the harvesting. Unlike *V. parahaemolyticus*, the concentration of *V. cholerae* in the effluent samples was one of the highest among the four sample types. The highest detection was at more than 1,100 MPN mL⁻¹. Although the concentration decreased in sampling three and four, it increased again until harvesting to a maximum value of 1,000 MPN mL⁻¹ (Table 3).

From Figure 3, the concentration of *V. cholerae* in water, sediment, and shrimp samples steadily decreased and remained low towards the end of the sampling period, unlike *V. parahaemolyticus*. However, in the effluent samples, the concentration of *V. cholerae* increased until it became more prominent than *V. parahaemolyticus* and *V. alginolyticus*.

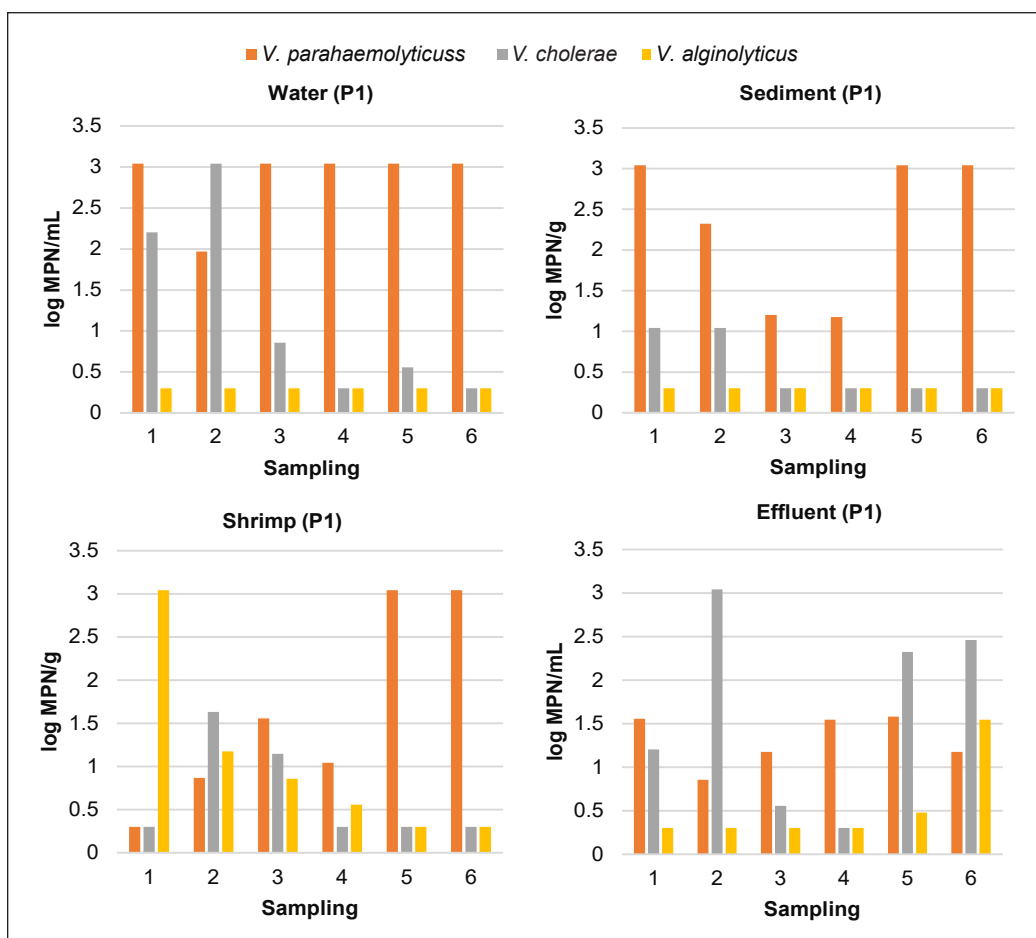


Figure 3. Estimated microbial load of *Vibrio* spp. in water, sediment, shrimp, and effluent samples collected from stocking (Sampling 1) to harvesting (Sampling 6) in P1. The concentrations are expressed in log median MPN mL⁻¹ for water and effluent samples and log median MPN g⁻¹ for sediment and shrimp samples. For values with no minimum or maximum limit, the log median is derived from the lowest or highest estimated number

In water and sediment samples, the concentration of *V. alginolyticus* detected was <3 MPN mL⁻¹ and <3 MPN g⁻¹, respectively, and remained low throughout the sampling period. *V. alginolyticus* was not detected during the MPN-mPCR of both samples from stocking to harvesting (Table 3). *V. alginolyticus* was detected in the shrimp sample on sampling one with the highest concentration of 4,100 MPN g⁻¹. However, the concentration decreased until it became as low as <3 MPN g⁻¹ in samples five and six. Meanwhile, in the effluent samples, *V. alginolyticus* concentration only increased in sampling five until it reached a maximum concentration of 94 MPN mL⁻¹ during harvesting (sampling six).

Based on the graphs in Figure 3, the concentration of *V. alginolyticus* in water and sediment samples remained the lowest among the three *Vibrio* spp. from stocking to harvesting. Meanwhile, in shrimp samples, *V. alginolyticus* started as the highest *Vibrio*

spp. detected, but the concentration steadily decreased towards harvesting until it became one of the lowest *Vibrio* spp. detected. In contrast, the concentration of *V. alginolyticus* in effluent samples increased towards harvesting to become the second-highest *Vibrio* spp. detected in the samples.

Concentration of *Vibrio* spp. in P2

Vibrio parahaemolyticus

Similar to P1, the highest concentration of *V. parahaemolyticus* in water samples collected from P2 was more than 1,100 MPN mL⁻¹ (Table 4). The concentration remained relatively constant throughout the sampling period, from stocking to harvesting. The highest concentration of *V. parahaemolyticus* in sediment samples was as high as >1,100 MPN g⁻¹. However, a decrease was observed in sampling three, with a maximum value of 94 MPN g⁻¹ of *V. parahaemolyticus* detected. The concentration increased again in the following weeks and remained constant at >1,100 MPN g⁻¹ until harvesting. Similar to shrimp samples from P1, the concentration of *V. parahaemolyticus* detected in shrimp samples from P2 started low at 42 MPN/g but eventually increased to >1,100 MPN g⁻¹ towards the harvesting. Meanwhile, the concentration of *V. parahaemolyticus* in the effluent samples increased from 420 MPN mL⁻¹ in sampling 1 to >1,100 MPN mL⁻¹ towards sampling 6.

Figure 4 shows that the concentration of *V. parahaemolyticus* in all four sample types increased to a maximum value of >1,100 MPN mL⁻¹ or > 1,100 MPN g⁻¹ towards harvesting. In addition, *V. parahaemolyticus* had the highest detection compared to the other two *Vibrio* spp. being studied.

The highest concentration of *V. cholerae* in water samples was >1,100 MPN mL⁻¹, which is on sampling two, as seen in Table 4. However, the concentration decreased until <3 MPN mL⁻¹ towards harvesting. Meanwhile, the highest concentrations of *V. cholerae* in sediment and shrimp samples were 38 MPN mL⁻¹ and 180 MPN mL⁻¹, respectively. Similar to water samples, the concentration of *V. cholerae* in both samples then decreased to <3 MPN mL⁻¹ or MPN g⁻¹ towards harvesting. On the other hand, the concentration of *V. cholerae* in the effluent samples increased to >1,100 MPN mL⁻¹ on sampling three and decreased to 18 MPN mL⁻¹ on harvesting.

Based on the graphs in Figure 4, the concentration of *V. cholerae* in water, sediment, and shrimp samples remained relatively low compared to *V. parahaemolyticus*. Although increments were observed in the middle, the concentration decreased towards the end of sampling. In effluent samples, the concentration of *V. cholerae* started high, even higher than the concentrations of *V. parahaemolyticus* and *V. alginolyticus*. However, the concentration decreased towards harvesting.

The concentrations of *V. alginolyticus* in both water and sediment samples remained constant at <3 MPN mL⁻¹ or MPN g⁻¹ from stocking to harvesting (Table 4). Meanwhile,

Table 4

Microbial load of *Vibrio* spp. (MPN g⁻¹ or MPN mL⁻¹) in samples collected from P2 throughout one production cycle

Sampling	Sample	<i>V. parahaemolyticus</i>			<i>V. cholerae</i>			<i>V. alginolyticus</i>		
		Min ^a	Med ^b	Max ^c	Min	Med	Max	Min	Med	Max
1	Water	420	>1,100	-	0.15	3	9.6	-	<3	9.5
	Sediment	8.7	29	94	-	<3	9.5	-	<3	9.5
	Shrimp	3.7	15	42	-	<3	9.5	3.6	14	42
	Effluent	37	150	420	180	1,100	4,100	90	290	1,000
2	Water	420	>1,100	-	-	<3	9.5	-	<3	9.5
	Sediment	420	>1,100	-	-	<3	9.5	-	<3	9.5
	Shrimp	8.7	35	94	-	<3	9.5	-	<3	9.5
	Effluent	420	>1,100	-	1.3	7.4	20	3.7	15	42
3	Water	180	1,100	4,100	0.15	<3	9.6	-	<3	9.5
	Sediment	8.7	35	94	1.2	6.1	18	-	<3	9.5
	Shrimp	4.5	15	42	-	<3	9.5	-	<3	9.5
	Effluent	180	1,100	4,100	420	>1,100	-	-	<3	9.5
4	Water	180	1,100	4,100	0.15	<3	11	-	<3	9.5
	Sediment	420	>1,100	-	1.3	7.2	18	-	<3	9.5
	Shrimp	37	150	420	-	<3	9.5	-	<3	9.5
	Effluent	420	>1,100	-	8.7	36	94	-	<3	9.5
5	Water	180	1,100	4,100	-	<3	9.5	-	<3	9.5
	Sediment	420	>1,100	-	-	<3	9.5	-	<3	9.5
	Shrimp	420	>1,100	-	-	<3	9.5	-	<3	9.5
	Effluent	180	1,100	4,100	3.6	14	42	-	<3	9.5
6	Water	180	1,100	4,100	-	<3	9.5	-	<3	9.5
	Sediment	420	>1,100	-	-	<3	9.5	-	<3	9.5
	Shrimp	420	>1,100	-	-	<3	9.5	-	<3	9.5
	Effluent	420	>1,100	-	1.3	7.2	18	-	<3	9.5

^a Minimum MPN g⁻¹ or MPN mL⁻¹ value; ^b Median MPN g⁻¹ or MPN mL⁻¹ value; ^c Maximum MPN g⁻¹ or MPN mL⁻¹ value (- = No minimum or maximum value)

in shrimp samples, *V. alginolyticus* was detected at a maximum concentration of 42 MPN g⁻¹ in sampling one but subsequently decreased and remained low at <3 MPN g⁻¹ until harvesting. Similarly, the concentration of *V. alginolyticus* in effluent samples in sampling one was relatively high at a maximum concentration of 1,000 MPN g⁻¹, even higher than both *V. parahaemolyticus* and *V. cholerae*. However, the concentration decreased and remained low at <3 MPN g⁻¹ until the last sampling.

From the graphs comparing the concentration of *Vibrio* spp. in different samples (Figure 4), *V. alginolyticus* has the lowest overall concentration in all four samples towards harvesting. Although the concentration started high in shrimp and effluent samples, unlike *V. parahaemolyticus*, *V. alginolyticus* decreased towards the end of the production cycle.

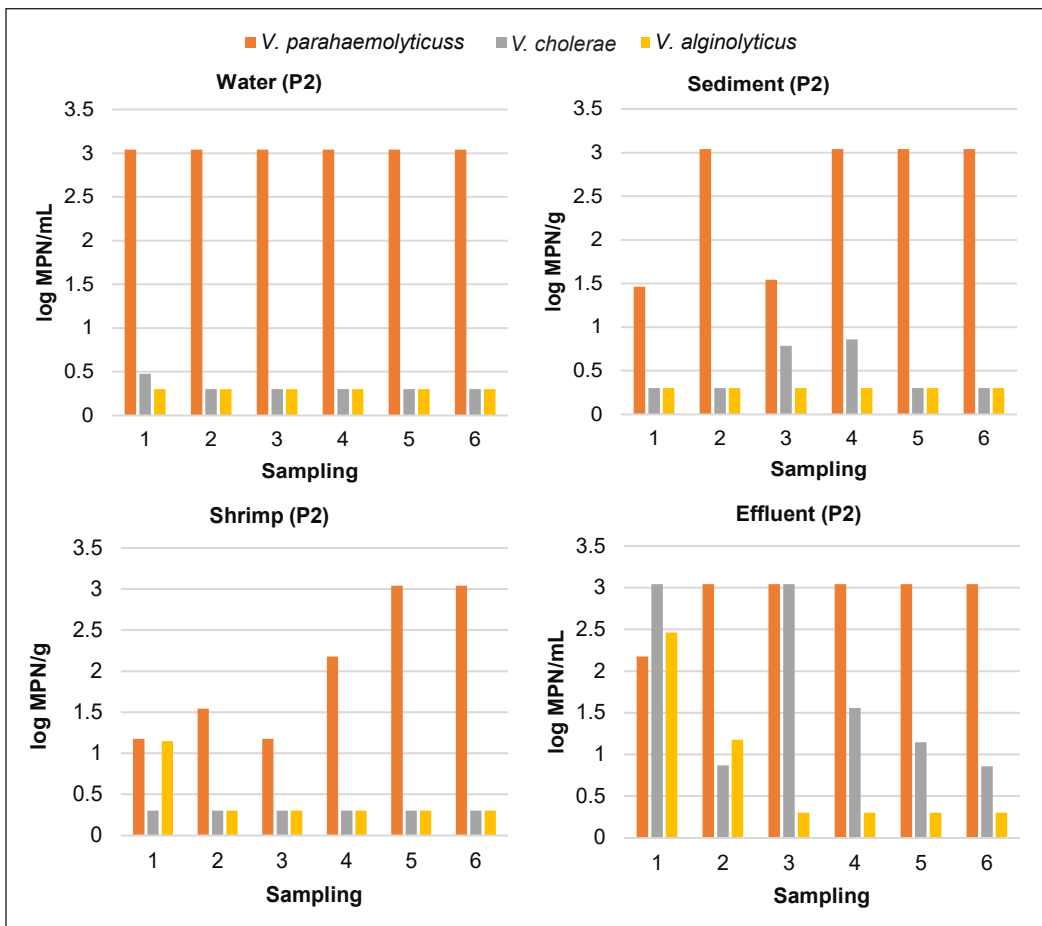


Figure 4. Estimated microbial load of *Vibrio* spp. in water, sediment, shrimp, and effluent samples collected from stocking (Sampling 1) to harvesting (Sampling 6) in P2. The concentrations are expressed in log median MPN mL⁻¹ for water and effluent samples and log median MPN g⁻¹ for sediment and shrimp samples. For values with no minimum or maximum limit, the log median is derived from the lowest or highest estimated number

Spearman's Correlation Analysis

Spearman's statistical analysis assessed the correlation between parameters and each *Vibrio* species. In P1, the temperature exhibited a weak negative correlation with the *V. parahaemolyticuss* population, a positive correlation with the *V. cholerae* population, and no correlation with the *V. alginolyticus* population. Additionally, water salinity displayed a weak negative correlation with the *V. parahaemolyticuss* population, a significant positive correlation with the *V. cholerae* population, and no correlation with the *V. alginolyticus* population in P1. Conversely, in P2, no correlation was observed between water salinity and all three *Vibrio* species. The pH of pond water in P1 was slightly negatively correlated with *V. parahaemolyticuss* population, positively correlated with *V. cholerae*, and not correlated with *V. alginolyticus* population (Figure 5A).

In P2, the temperature did not correlate with the three *Vibrio* species. Similarly, no correlation was observed between water salinity and all three *Vibrio* species in P2. Moreover, there was no correlation between pH values and all three *Vibrio* spp. in P2 (Figure 5B).

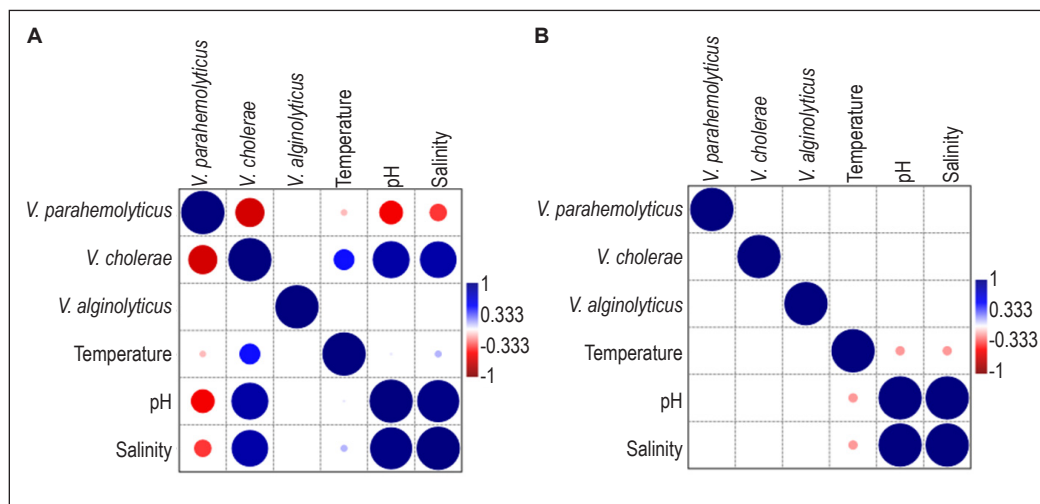


Figure 5. Spearman's rs analysis matrix shows the correlation between the three environmental and chemical parameters with each *Vibrio* spp. in (A) Pond 1 and (B) Pond 2. A rs of +1 (blue) represents a perfect association of ranks, a rs of zero (blank) shows no association between ranks, and a rs of -1 (red) indicates a perfect negative association of ranks. The closer rs is to zero, the weaker the association between the ranks

DISCUSSION

The vibriosis outbreaks in shrimp aquaculture can result in significant mortality rates and economic losses due to decreased production. The 2011 outbreak of Acute Hepatopancreatic Necrosis Diseases (AHPND) caused by *V. parahaemolyticus* in Peninsular Malaysia resulted in a mortality rate of 60%–90% in many shrimp farms and resulted in economic losses of approximately US\$ 0.1 billion (Kua et al., 2016; NACA, 2012). These incidents raise serious concerns for the aquaculture sector as well as the economy at large. Therefore, early detection of *Vibrio* spp. in shrimp aquaculture can help to prevent significant damage at the early stage.

Many methods can be used to detect and enumerate microbial loads in a sample, such as viable plate counts, direct microscopic counts, metabolism-based detection, luminescence-based detection, and immunological/serological-based detection (Logue & Nde, 2017). In our study, the MPN-multiplex PCR (MPN-mPCR) method is used instead of the MPN-plate method because it allows for the enhanced detection and enumeration of *V. parahaemolyticus*, *V. cholerae*, and *V. alginolyticus* simultaneously. Compared to direct plating using selective media, MPN-mPCR allows for the rapid processing of many samples at the same time, which helps to reduce the processing time (Russo et al., 2014).

This technique also helps to reduce the number of Petri dishes and the cost of selective media used for the enumeration process. The MPN-mPCR technique also provides a more sensitive and rapid detection and enumeration than the conventional MPN-plate method. Without isolating pure isolates, the possibility of getting false negatives through the MPN-mPCR method is lower than the MPN-plate method (Miwa et al., 2003). Therefore, the MPN-mPCR method holds significant potential for further development into a rapid test kit. A comprehensive *Vibrio* detection kit could include pre-packaged enrichment media for sample processing, a simplified genomic DNA extraction kit, and a ready-to-use Polymerase Chain Reaction (PCR) mix with primers specific for the targeted *Vibrio* species. This kit would aim to streamline the detection process, making it accessible for shrimp farmers to monitor *Vibrio* populations in their farms with ease.

Water samples were collected from a few points in each pond to ensure random sampling of the targeted *Vibrio* spp., and the samples were taken at the surface level to maintain standardisation throughout the sampling period. Additionally, given that *Vibrio* spp. is reported to favour warmer temperatures and surface water is typically warmer than deeper depths due to direct sunlight exposure, it is anticipated that *Vibrio* spp. will be more abundant at the water surface (Brumfield et al., 2023).

Based on the findings of this study, *V. parahaemolyticus* is the most prevalent among the three *Vibrio* spp., with the highest load in all four samples exceeding 10^3 MPN g⁻¹ or MPN mL⁻¹. Moreover, while *V. cholerae* and *V. alginolyticus* concentration decreased in most of the samples towards the harvesting period, *V. parahaemolyticus*, on the other hand, exhibited increments in all samples towards harvesting. The dominance of *V. parahaemolyticus* over *V. cholerae* and *V. alginolyticus* in all four samples may indicate that *V. parahaemolyticus* illustrates the “pathogen advantage theory”. According to this theory, one pathogen species may have a competitive advantage over others in their natural ecosystem, commonly brought by temperature rise. This situation will eventually lead to the overabundance of that domineering species (Colwell, 2004; Thornstenson & Ullrich, 2021). In this case, *V. parahaemolyticus* was able to exploit available resources better than *V. cholerae* and *V. alginolyticus*, resulting in the positive growth of *V. parahaemolyticus* and reduced growth of *V. cholerae* and *V. alginolyticus* (McLaren & Callahan, 2020).

In shrimp samples, the overall load of the three *Vibrio* spp. was low during the stocking period compared to the other samples. However, as the production cycle progressed, exposure to environmental factors and contamination with *Vibrio* spp., which are already present in nature, caused the counts to increase towards harvesting (Kim & Lee, 2017). *V. cholerae*, while not considered a serious pathogen to shrimps, with only a few studies reporting their ability to cause vibriosis in shrimps, can still cause infection in humans through consumption of contaminated products (Cao et al., 2015; Gopal et al., 2005; Haldar et al., 2007). It has been reported that about 42% of *V. cholerae* infections in humans are

caused by consuming seafood products (Chen et al., 2022). Meanwhile, *V. alginolyticus* is an opportunistic pathogen, indicating that once contamination in the host crosses a certain threshold, vibriosis can occur, and mortality is a possible outcome (Brown et al., 2012). The minimum bacterial load of *Vibrio* spp. that can cause vibriosis varies depending on several factors, including the specific *Vibrio* spp., the health and immune status of the host, and the route of exposure. Additionally, individual susceptibility to vibriosis can differ. In our study, the incidence of *V. alginolyticus* contamination in all samples, particularly in shrimp samples when harvested, is still low, making it less likely to cause vibriosis.

Despite the low counts of both *V. cholerae* and *V. alginolyticus*, the concentration of *V. parahaemolyticus* in shrimp samples during the harvesting is concerningly high. At the same time, it is impossible to get shrimps that are entirely free of *Vibrio* spp. contamination due to their ubiquitousness in the marine environment, there are standard acceptable contamination levels set by every country for export purposes. For example, Crustacean seafood products for export to the United States must have less than 10^4 MPN g^{-1} of *V. parahaemolyticus* contamination. In Australia and New Zealand, the contamination level of *V. parahaemolyticus* in their imported crustacean products must be less than 10^3 MPN g^{-1} (Lokkhumlue & Prakitchaiwattana, 2014). In raw or improperly cooked seafood products, pathogenic bacteria such as *Vibrio* spp. can become highly accumulated, rendering the seafood unsafe for consumption (Harrison et al., 2022).

One of the factors that may contribute to the increase in the microbial load of *Vibrio* spp. in the ponds is the high temperature, typically prevalent between August and December. Malaysia has a tropical climate with a fairly slight variation in the average monthly temperature. With a mean annual temperature of 26.4°C, Malaysia experiences high temperatures all year round (<https://climateknowledgeportal.worldbank.org/country/malaysia/climate-data-historical>). The relatively high temperature in the shrimp farm can explain the high occurrence of *Vibrio* spp. in P1 and P2, with average temperatures in the range of 29°C to 34°C throughout the sampling period. Our results show that temperatures in this range correlate with culturable *Vibrio* spp. at high concentration, particularly *V. parahaemolyticus*.

However, according to Spearman's statistical analysis, temperature exhibits varying correlations with different *Vibrio* spp. populations. The temperature in P1 has a weak negative correlation with the *V. parahaemolyticus* population, a positive correlation with the *V. cholerae* population, and no correlation with the *V. alginolyticus* population. Meanwhile, the temperature in P2 does not correlate with all three *Vibrio* spp. These statistical results are in contrast with the findings in our study, as well as in many reported studies. This observation may be due to only slight changes in the temperature throughout the sampling, and other factors can affect the growth of the *Vibrio* spp. Many studies reported the correlation between temperature and growth patterns of *V. parahaemolyticus*, *V. cholerae*,

and *V. alginolyticus* in coastal environments (Thornstenson & Ullrich, 2021; Vezzulli et al., 2016; Williams et al., 2022). It has been shown that temperatures of 20°C and above are optimum for the growth of *Vibrio* spp. in marine water. Many studies have shown that *V. parahaemolyticus*, *V. cholerae*, and *V. alginolyticus* have optimum growth at 37°C and can still grow at a wide temperature range between 20°C–42°C (Gu et al., 2016; Ravel et al., 1995; Sheikh et al., 2022). In the case of *V. parahaemolyticus*, it has been observed that the increase in temperature leads directly to an increase in growth (Kim et al., 2012).

This observation supports our finding, where the concentration of *V. parahaemolyticus* in all samples, especially in water, increased and remained high at $>10^3$ MPN mL⁻¹ when the temperature in P1 and P2 remained in the high range of $>30^\circ\text{C}$. Meanwhile, temperatures less than 15°C have been reported to induce a viable but non-culturable (VBNC) state in *Vibrio* spp. (Baker-Austin et al., 2018). Although this condition is not a concern for coastal farming since the temperature in Malaysia remains relatively high throughout the year, it may raise concern during post-harvesting and importing, when the seafood needs to be kept on ice or frozen to prevent spoilage. Although bacteria in the VBNC state become dormant and are not detectable using conventional culture methods, they remain viable. In addition, functions such as metabolic activity, antibiotic resistance, specific gene expression, virulence, and pathogenicity are sustained (Fernández-Delgado et al., 2015).

In addition to temperature, salinity is another factor that can affect the growth patterns of *Vibrio* spp. in marine ecosystems (Sampaio et al., 2022). The salinity of water samples taken from P1 and P2 fell in the 20–25 ppt range throughout the sampling period. This range of salinity is favourable for the growth of shrimps in the coastal shrimp farm (Chu & Brown, 2021). Unfortunately, this range is also optimum for the growth of *V. parahaemolyticus*. *V. parahaemolyticus* is reported to have rapid growth in coastal water with salinity in the range of 15 to 25 ppt (Givens et al., 2014). The results also indicate that as the pond water salinity in P1 and P2 decreased slightly towards harvesting, the overall load of the three *Vibrio* spp., notably *V. parahaemolyticus*, increased. It has been reported that a decrease in salinity, especially in brackish water, encourages the growth and spread of *Vibrio* spp. (Baker-Austin et al., 2018). However, statistical analysis showed a weak negative correlation between water salinity and the *V. parahaemolyticus* population, a significant positive correlation with the *V. cholerae* population, and no correlation with the *V. alginolyticus* population in P1. In P2, no correlation was observed between water salinity with all three *Vibrio* spp. The result of this statistical analysis may be due again to the only slight changes in the salinity and the microbial population. The consistency in water salinity in both ponds can also be attributed to the farm's adherence to recommended physio-chemical standards that create an environment conducive to the healthy growth of the shrimp.

Another factor that can significantly affect the growth and survival of *Vibrio* spp. is the pH of water. Most *Vibrio* spp. prefer slightly acidic to neutral pH levels (pH 6.5–7.5) (Ross

& Schreiber, 1998). This information supported our observation that the overall growth of the three *Vibrio* spp., especially *V. parahaemolyticus*, is rapid from stocking to harvesting. At the same time, the pH of water in both ponds remained in the range of pH 5.9–7.9. While this pH range is considered optimum for their growth, some *Vibrio* spp. such as *V. cholerae*, was reported to tolerate a wide range of pH, including alkaline pH as high as pH 9.0 (Nhu et al., 2021). However, according to statistical analysis, the pond water pH is slightly negatively correlated to *V. parahaemolyticus* population, positively correlated to *V. cholerae*, and no correlation with *V. alginolyticus* population in P1. No correlation was observed again between pH values with all three *Vibrio* spp. in P2.

In general, pH levels below pH 6.5 might inhibit the growth of *Vibrio* spp. since acidic conditions can denature proteins and disrupt cellular processes (Kayser & Kayser, 2007). On the other hand, pH levels above pH 7.5 were reported to affect the growth of *Vibrio* spp. by interfering with the bacterial enzymes and other proteins required for their cellular processes, thus preventing their proper functioning (Kieliszek & Błażejowski, 2005). For *V. parahaemolyticus* studies, they can grow at a wide range of pH values, with optimal growth occurring at a pH of 7.0–8.0 (Suzuki et al., 2014). However, *V. parahaemolyticus* can also survive and grow at lower pH values, as low as pH 4.0 (Suzuki et al., 2014).

In addition to affecting the growth and survival of *Vibrio* spp., the pH of water can also influence the expression of certain virulence factors, such as toxins and enzymes, which can contribute to the pathogenicity of these bacteria (Kim et al., 2008). For example, *V. cholerae* has been shown to produce higher levels of cholerae toxin (CTX) and toxin-coregulated pilus (TCP), two of the main virulence factors, at low pH levels (Faruque & Nair, 2010; Weber & Klose, 2011)). In a study conducted by Whitaker et al. (2010), it was observed that acidic conditions induced the expression of lysine decarboxylase, an enzyme responsible for regulating the bacterial acid stress response system in *V. parahaemolyticus* O3:K6. This mechanism enables the bacteria to survive in acidic conditions, enhancing their virulence potential (Whitaker et al., 2010). Overall, the pH of water can significantly impact the presence and activity of *Vibrio* spp. in aquatic environments, with optimal pH levels being critical for their growth and survival.

The overall growth of *V. cholerae* and *V. alginolyticus* decreased towards the end of sampling, while *V. parahaemolyticus* showed increment or constant high concentration throughout the sampling. *V. cholerae* and *V. alginolyticus* might have been outcompeted by the rapidly growing *V. parahaemolyticus*, which could utilise the resources better (Thornstenson & Ullrich, 2021). This statement agrees with Caburlotto et al. (2010), who stated that another reason for the different growth patterns is the difference in the sensitivity of the different *Vibrio* spp., towards environmental conditions, including temperature, salinity, and pH. In this case, *V. parahaemolyticus* may be more sensitive to environmental factors than *V. cholerae* and *V. alginolyticus*.

In addition to being sensitive to environmental and chemical parameters, overfeeding has been identified as a potential factor contributing to the abundance of *Vibrio* spp. in shrimp ponds. Overfeeding leads to the formation of nutrient-rich sludge, creating conditions favourable for the proliferation of harmful microorganisms, including *Vibrio* species (Horowitz & Horowitz, 2020). However, in the Telaga Air shrimp farm, no sludge formation was observed throughout the sampling period. Additionally, information from the manager revealed the implementation of a well-timed feeding schedule using automatic timers to prevent shrimp from being overfed. Further studies are necessary to thoroughly investigate the feeding conditions and their relationship with *Vibrio* spp. in the farm. In environmental samples, *V. parahaemolyticus* is often reported to be the dominant species isolated, especially in brackish waters. Such is the case that the number of other *Vibrio* spp. isolated in a sample is used to evaluate the presence and risk of *V. parahaemolyticus*.

A study by Ruiz-Cayuso et al. (2021) found that for each *Vibrio* spp. detected, the odds of isolating *V. parahaemolyticus* increased by 2.84-fold. This study proved and supported the findings by Blackwell and Oliver (2008), who also reported the correlation between *V. parahaemolyticus* with the total *Vibrio* spp. and other coliforms such as *Escherichia coli* isolated from an environmental sample (Ruiz-Cayuso et al., 2021). The dominance of *V. parahaemolyticus* against other *Vibrio* spp. is due to their ability to withstand a wide range of temperatures and salinities, as well as to adapt and thrive in various environments (Janda & Abbott, 2010). This characteristic allows *V. parahaemolyticus* to outcompete other *Vibrio* spp. in marine and freshwater environments.

According to the project manager of PNK Satang Biru shrimp farm, a complete harvest of adult *P. vannamei* from each pond can yield approximately seven to eight metric tons of shrimp in one production cycle. During the last sampling (the sixth sampling), conducted at the time of harvesting adult shrimps, the average size of the harvested shrimp was approximately 130 mm long. Overall, it took approximately 90 to 100 days for the post-larvae shrimp to grow to a harvestable size. While the direct effect of the high presence of *Vibrio* spp. was not observed on the overall growth and production of the shrimp in the shrimp farm, the risk for infection is still present. Without stressors, *Vibrio* spp., as an opportunistic pathogen, can reach significant concentration without triggering the onset of vibriosis (Newman, 2022). However, the ability of *Vibrio* spp. to cause disease should not be overlooked, considering the relationship between the shrimp and the stressors (Valente & Wan, 2021). In addition, the accumulation of *Vibrio* spp. in shrimp products can still pose health risks to consumers when not processed or cooked appropriately (Kaysner et al., 2004).

The findings in our study raise concern since the microbial load in the harvested shrimp product exceeds the standards acceptable in most importing countries. However,

early detection of *Vibrio* spp. in shrimp farms, especially during stocking, is crucial because it helps to prevent the spread of the bacteria to other shrimps and can lead to a more effective treatment plan. If *Vibrio* spp. is not detected until it has spread throughout the farm, it might lead to a significant loss of shrimp and finances for the farm. Additionally, *Vibrio* spp. can cause serious health problems for humans who consume contaminated shrimp, so early detection and treatment can protect public health. Early detection also allows for more targeted and potentially less disruptive treatment methods rather than implementing broad and potentially harmful measures if the infection has spread widely.

Shrimp farmers should pay attention to their management practices to ensure the quality of their products and to prevent the spread of diseases. Good practices include controlling water quality, preventing overcrowding, and maintaining good hygiene. Continuous real-time monitoring of the critical control points (HACCP) in shrimp aquaculture is also essential to ensure food safety and prevent disease outbreaks. Overall, good farm management is the key to preventing vibriosis and protecting the health and well-being of both the shrimps and the seafood consumers.

CONCLUSION

Vibrio parahaemolyticus, *V. cholerae*, and *V. alginolyticus* were successfully detected and enumerated in all four sample types in both ponds, from stocking until harvesting. This study has shown that *V. parahaemolyticus* is the most dominant species compared to *V. cholerae* and *V. alginolyticus* in the Telaga Air shrimp farm, suggesting that the ability of *V. parahaemolyticus* to exploit available resources more effectively than *V. cholerae* and *V. alginolyticus* contributes to the elevated *V. parahaemolyticus* load in the shrimp farm. It becomes a concern because *V. parahaemolyticus* is a well-recognised human pathogen associated with seafood-related infections, and its prevalence in shrimp farms can have implications for food safety. In the future, prevalence studies can be extended to encompass more shrimp farms across Sarawak, providing a more comprehensive dataset on the prevalence and distribution of *Vibrio* species.

The study's outcomes, serving as a valuable model, highlight the need for ongoing monitoring of *Vibrio* spp. prevalence in shrimp farms across Sarawak, addressing the current lack of comprehensive data on the subject in the region. This study also underscores the importance of employing the MPN-multiplex PCR technique to surveillance *Vibrio* spp. in shrimp farms. The method offers several advantages, including enhanced sensitivity and rapid simultaneous processing of multiple samples, which reduces processing time. The efficiency of this technique positions it as a promising tool for ongoing monitoring efforts, providing critical data for the prevention and control of vibriosis outbreaks in shrimp farms, thereby safeguarding public health and the sustainability of the shrimp industry.

ACKNOWLEDGEMENTS

The project was funded by Geran Putra IPM (9695800), Universiti Putra Malaysia (UPM), in collaboration with UNI/F07/GRADUATES/85816/2023, Postgraduate Student Research Grant, Universiti Malaysia Sarawak (UNIMAS). This work forms part of Dalene Lesen's research project in collaboration with Lembaga Kemajuan Ikan Malaysia (LKIM).

REFERENCES

- Alifa, F., Diba, D. F., Rusnita, & Basir, B. (2021). Conditions of clinical symptoms and life of Vaname shrimp in prevention of *Vibrio alginolyticus* infection using miana leaf extract. *Journal of Fish Health*, *1*(2), 40–48. <https://doi.org/10.29303/jfh.v1i2.230>
- Baker-Austin, C., Oliver, J. D., Alam, M., Ali, A., Waldor, M. K., Qadri, F., & Martinez-Urtaza, J. (2018). *Vibrio* spp. infections. *Nature Reviews Disease Primers*, *4*(1), 1–19. <https://doi.org/10.1038/s41572-018-0005-8>
- Blackwell, K. D., & Oliver, J. D. (2008). The ecology of *Vibrio vulnificus*, *Vibrio cholerae*, and *Vibrio parahaemolyticus* in North Carolina estuaries. *The Journal of Microbiology*, *46*(2), 146–153. <https://doi.org/10.1007/s12275-007-0216-2>
- Blodgett, R. (2000). *BAM appendix 2: Most probable number from serial dilutions*. U.S. Food & Drug Administration. <https://www.fda.gov/food/laboratory-methods-food/bam-appendix-2-most-probable-number-serial-dilutions>
- Brown, S. P., Cornforth, D. M., & Mideo, N. (2012). Evolution of virulence in opportunistic pathogens: Generalism, plasticity, and control. *Trends in Microbiology*, *20*(7), 336–342. <https://doi.org/10.1016/j.tim.2012.04.005>
- Brumfield, K. D., Chen, A. J., Gangwar, M., Usmani, M., Hasan, N. A., Jutla, A. S., Huq, A., & Colwell, R. R. (2023). Environmental factors influencing occurrence of *Vibrio parahaemolyticus* and *Vibrio vulnificus*. *Applied and Environmental Microbiology*, *89*(6), Article e00307-23. <https://doi.org/10.1128/aem.00307-23>
- Caburlotto, G., Haley, B. J., Lleò, M. M., Huq, A., & Colwell, R. R. (2010). Serodiversity and ecological distribution of *Vibrio parahaemolyticus* in the Venetian Lagoon, Northeast Italy. *Environmental Microbiology Reports*, *2*(1), 151–157. <https://doi.org/10.1111/j.1758-2229.2009.00123.x>
- Cao, H., An, J., Zheng, W., & He, S. (2015). *Vibrio cholerae* pathogen from the freshwater-cultured whiteleg shrimp *Penaeus vannamei* and control with *Bdellovibrio bacteriovorus*. *Journal of Invertebrate Pathology*, *130*, 13–20. <https://doi.org/10.1016/j.jip.2015.06.002>
- Chen, Y., Ai, X., & Yang, Y. (2022). *Vibrio cholerae*: A pathogen shared by human and aquatic animals. *The Lancet Microbe*, *3*(6), Article e402. [https://doi.org/10.1016/s2666-5247\(22\)00125-2](https://doi.org/10.1016/s2666-5247(22)00125-2)
- Chu, Y. T., & Brown, P. B. (2021). Evaluation of Pacific Whiteleg shrimp and three halophytic plants in marine aquaponic systems under three salinities. *Prime Archives in Sustainability*, *13*(1), Article 269. <https://doi.org/10.37247/pas.1.2021.38>
- Colwell, R. R. (2004). Infectious disease and environment: Cholerae as a paradigm for waterborne disease. *International Microbiology*, *7*(4), 285–289.

- Department of Fisheries Malaysia. (2012). *Annual Fisheries Statistics 2012*. Ministry of Agriculture and Agro-Based Industry Malaysia
- Dutta, D., Kaushik, A., Kumar, D., & Bag, S. (2021). Foodborne pathogenic Vibrios: Antimicrobial resistance. *Frontiers in Microbiology*, *12*, Article 638331. <https://doi.org/10.3389/fmicb.2021.638331>
- Farmer, J. J., & Janda, J. M. (2015). Vibrionaceae. In M. E. Trujillo, S. Dedysh, P. DeVos, B. Hedlund, P. Kämpfer, F. A. Rainey & W. B. Whitman (Eds.) *Bergey's Manual of Systematics of Archaea and Bacteria* (pp. 1–7). American Cancer Society.
- Faruque, S. M., & Nair, G. B. (2010). Cholerae toxins: A comprehensive review. *Toxins*, *2*(1), 51-71.
- Fernández-Delgado, M., García-Amado, M. A., Contreras, M., Incani, R. N., Chirinos, H., Rojas, H., & Suárez, P. (2015). Survival, induction and resuscitation of *Vibrio cholerae* from the viable but non-culturable state in the Southern Caribbean Sea. *Revista Do Instituto De Medicina Tropical De São Paulo*, *57*(1), 21–26. <https://doi.org/10.1590/s0036-46652015000100003>
- Gilbert, J. (2023, July 10). MAG plans to focus on downstream products. *New Straits Times*. <https://www.nst.com.my/business/2023/07/929327/mag-plans-focus-downstream-products>.
- Givens, C. E., Bowers, J. C., DePaola, A., Hollibaugh, J. T., & Jones, J. L. (2014). Occurrence and distribution of *Vibrio vulnificus* and *Vibrio parahaemolyticus* - potential roles for fish, oyster, sediment and water. *Letters in Applied Microbiology*, *58*(6), 503–510. <https://doi.org/10.1111/lam.12226>
- Gopal, S., Ota, S. K., Kumar, S., Karunasagar, I., Nishibuchi, M., & Karunasagar, I. (2005). The occurrence of *Vibrio* species in tropical shrimp culture environments; Implications for Food Safety. *International Journal of Food Microbiology*, *102*(2), 151–159. <https://doi.org/10.1016/j.ijfoodmicro.2004.12.011>
- Gu, D., Guo, M., Yang, M., Zhang, Y., Zhou, X., & Wang, Q. (2016). A σ -mediated temperature gauge controls a switch from LUXR-mediated virulence gene expression to thermal stress adaptation in *Vibrio alginolyticus*. *PLoS Pathogens*, *12*(6), Article e1005645. <https://doi.org/10.1371/journal.ppat.1005645>
- Haifa-Haryani, W. O., Amatul-Samahah, Md. A., Azzam-Sayuti, M., Chin, Y. K., Zamri-Saad, M., Natrah, I., Amal, M. N., Satyantini, W. H., & Ina-Salwany, M. Y. (2022). Prevalence, antibiotics resistance and plasmid profiling of *Vibrio* spp. isolated from cultured shrimp in Peninsular Malaysia. *Microorganisms*, *10*(9), Article 1851. <https://doi.org/10.3390/microorganisms10091851>
- Haldar, S., Chatterjee, S., Asakura, M., Vijayakumaran, M., & Yamasaki, S. (2007). Isolation of *Vibrio parahaemolyticus* and *Vibrio cholerae* (Non-O1 and O139) from moribund shrimp (*Penaeus Monodon*) and experimental challenge study against post-larvae and juveniles. *Annals of Microbiology*, *57*(1), 55–60. <https://doi.org/10.1007/bf03175050>
- Harrison, J., Nelson, K., Morcrette, H., Morcrette, C., Preston, J., Helmer, L., Titball, R. W., Butler, C. S., & Wagley, S. (2022). The increased prevalence of *Vibrio* species and the first reporting of *Vibrio jasicida* and *Vibrio rotiferianus* at K.U.K. shellfish sites. *Water Research*, *211*, Article 117942. <https://doi.org/10.1016/j.watres.2021.117942>
- Horowitz, A., & Horowitz, S. (2020, November 24). *Sludge: An obstacle to shrimp health - responsible seafood advocate*. Global Seafood Alliance. <https://www.aquaculturealliance.org/advocate/sludge-an-obstacle-to-shrimp-health/?headlessPrint=AAAAPIA9c8r7gs82oWZBA>

- Janda, J. M., & Abbott, S. L. (2010). The genus *Vibrio*. In *The Prokaryotes* (pp. 639-702). Springer.
- Kayser, O., & Kayser, Y. (2007). Acid stress in bacteria. *FEMS Microbiology Reviews*, *31*(5), 577-608.
- Kaysner, C. A., Abeyta, C., Stott, R. F., Krane, M. H., & Wekell, M. M. (1990). Enumeration of vibrio species, including *V. cholerae*, from samples of an oyster growing area, Grays Harbor, Washington. *Journal of Food Protection*, *53*(4), 300–302. <https://doi.org/10.4315/0362-028x-53.4.300>.
- Kaysner, C. A., DePaola, A., & Jones, J. (2004). *BAM Chapter 9: Vibrio*. U.S. Food and Drug Administration. <https://www.fda.gov/food/laboratory-methods-food/bam-chapter-9-vibrio>
- Kieliszek, M., & Błażejowski, J. (2005). The influence of pH and temperature on the growth of Enterobacteriaceae. *International Journal of Food Microbiology*, *102*(1), 1-10.
- Kim, H. J., Ryu, J. O., Lee, S. Y., Kim, E. S., & Kim, H. Y. (2015). Multiplex PCR for detection of the *Vibrio* genus and five pathogenic *Vibrio* species with primer sets designed using comparative genomics. *BMC Microbiology*, *15*(1), Article 239. <https://doi.org/10.1186/s12866-015-0577-3>
- Kim, J. Y., & Lee, J. L. (2017). Correlation of total bacterial and *Vibrio* spp. populations between fish and water in the aquaculture system. *Frontiers in Marine Science*, *4*, Article 147. <https://doi.org/10.3389/fmars.2017.00147>
- Kim, W. R., Park, J. H., Lee, S. Y., & Kim, J. M. (2008). Effect of pH on the expression of virulence factors in *Vibrio parahaemolyticus*. *Environmental Microbiology*, *10*(4), 873-880.
- Kim, Y., Lee, S., Hwang, I., & Yoon, K. (2012). Effect of temperature on growth of *Vibrio parahaemolyticus* and *Vibrio vulnificus* in flounder, salmon sashimi and oyster meat. *International Journal of Environmental Research and Public Health*, *9*(12), 4662–4675. <https://doi.org/10.3390/ijerph9124662>
- Kua, B. C., Iar, A., Zahrah, A. S., Irene, J., Norazila, J., Haiha, N. Y. N., Fadzilah, Y., Mohammed, M., Rokhaiya, B. S., Omar, M., & Teoh, T. P. (2016, February 22-24). *Current status of acute hepatopancreatic necrosis disease (AHPND) of farmed shrimp in Malaysia*. [Paper presentation]. Proceedings of the ASEAN Regional Technical Consultation on EMS/AHPND and Other Transboundary Diseases for Improved Aquatic Animal Health in Southeast Asia, Makati City, Philippines.
- Ling, S. (2022, September 7). Sarawak aims to export rm1bil worth of shrimp annually by 2030. *The Star*. <https://www.thestar.com.my/news/nation/2022/09/07/sarawak-aims-to-export-rm1bil-worth-of-shrimp-annually-by-2030#:~:text=KUCHING%3A%20Sarawak%20aims%20to%20increase,worth%20of%20shrimp%20a%20year>.
- Logue, C. M., & Nde, C. W. (2017). Rapid microbiological methods in food diagnostics. In F. Toldrá & L. M. L. Nollet (Eds.), *Advances in Food Diagnostics* (pp. 153–185). Wiley.
- Lokkhumlue, M., & Prakitchaiwattana, C. (2014). Influences of cultivation conditions on microbial profiles of Pacific white shrimp (*Litopenaeus Vannamei*) harvested from eastern and central Thailand. *Chiang Mai University Journal of Natural Sciences*, *13*(1), 67-75. <https://doi.org/10.12982/cmujns.2014.0022>
- Man, J. C. D. (1983). MPN tables, corrected. *European Journal of Applied Biotechnology*, *17*, 301-305. <https://doi.org/10.1007/BF00508025>
- Mastan, S. A., & Begum, S. K. A. (2016). Vibriosis in farm-reared white shrimp, *Litopenaeus vannamei* in Andhra Pradesh - Natural occurrence and artificial challenge. *International Journal of Applied Sciences and Biotechnology*, *4*(2), 217–222. <https://doi.org/10.3126/ijasbt.v4i2.15126>

- McLaren, M. R., & Callahan, B. J. (2020). Pathogen resistance may be the principal evolutionary advantage provided by the microbiome. *Philosophical Transactions of the Royal Society B: Biological Sciences*, 375(1808), Article 20190592. <https://doi.org/10.1098/rstb.2019.0592>
- Miwa, N., Nishio, T., Arita, Y., Kawamori, F., Masuda, T., & Akiyama, M. (2003). Evaluation of MPN method combined with PCR procedure for detection and enumeration of *Vibrio parahaemolyticus* in seafood. *Journal of the Food Hygienic Society of Japan (Shokuhin Eiseigaku Zasshi)*, 44(6), 289–293. <https://doi.org/10.3358/shokueishi.44.289>
- NACA. (2012). *Report of the Asia Pacific emergency regional consultation on the emerging shrimp disease: Early mortality syndrome (EMS)/ acute hepatopancreatic necrosis syndrome (AHPNS)*. Network of Aquaculture Centres in Asia-Pacific. <chrome-extension://efaidnbnmnihpcajpcgclefindmkaj/https://library.enaca.org/Health/Publication/ahpns-emergency-consultation-report.pdf>
- Newman, S. G. (2022). *An update on vibriosis, the major bacterial disease shrimp farmers face - Responsible seafood advocate*. Global Seafood Alliance. <https://www.globalseafood.org/advocate/an-update-on-vibriosis-the-major-bacterial-disease-shrimp-farmers-face/>
- Nhu, N. T., Lee, J. S., Wang, H. J., & Dufour, Y. S. (2021). Alkaline pH increases swimming speed and facilitates mucus penetration for *Vibrio cholerae*. *Journal of Bacteriology*, 203(7), Article e00607-20. <https://doi.org/10.1128/jb.00607-20>
- Patel, J., Grab, S., & De Maayer, P. (2023). Distinct microbial communities across a climatically versatile summit in the lesotho highlands. *Ecology and Evolution*, 13(3), Article e9891. <https://doi.org/10.1002/ece3.9891>
- Queipo-Ortuño, M. I., Colmenero, J. D. D., Macias, M., Bravo, M. J., & Morata, P. (2008). Preparation of bacterial DNA template by boiling and effect of immunoglobulin G as an inhibitor in real-time PCR for serum samples from patients with brucellosis. *Clinical and Vaccine Immunology*, 15(2), 293–296. <https://doi.org/10.1128/cvi.00270-07>
- Ravel, J., Knight, I. T., Monahan, C. E., Hill, R. T., & Colwell, R. R. (1995). Temperature-induced recovery of *Vibrio cholerae* from the viable but nonculturable state: Growth or resuscitation? *Microbiology*, 141(2), 377–383. <https://doi.org/10.1099/13500872-141-2-377>
- Ross, T., & Schreiber, M. (1998). *Vibrio* species in the natural environment. *Annual Review of Microbiology*, 52(1), 547-570.
- Ruiz-Cayuso, J., Trujillo-Soto, T., Rodriguez-Iglesias, M., & Almagro-Moreno, S. (2021). Effects of temperature and salinity interaction on *Vibrio* spp. and *Vibrio parahaemolyticus* in the intercontinental Euro-African Atlantic. *Research Square*, 2021, 1–17. <https://doi.org/10.21203/rs.3.rs-607386/v1>
- Russo, P., Botticella, G., Capozzi, V., Massa, S., Spano, G., & Beneduce, L. (2014). A fast, reliable, and sensitive method for detection and quantification of *Listeria monocytogenes* and *Escherichia coli* O157:H7 in ready-to-eat fresh-cut products by MPN-QPCR. *BioMed Research International*, 2014(1), Article 608296. <https://doi.org/10.1155/2014/608296>
- Sampaio, A., Silva, V., Poeta, P., & Aonofriesei, F. (2022). *Vibrio* spp.: Life strategies, ecology, and risks in a changing environment. *Diversity*, 14(2), Article 97. <https://doi.org/10.3390/d14020097>

- Sani, N. A., Ariyawansa, S., Babji, A. S., & Hashim, J. K. (2013). The risk assessment of *Vibrio parahaemolyticus* in cooked black tiger shrimps (*Penaeus Monodon*) in Malaysia. *Food Control*, *31*(2), 546–552. <https://doi.org/10.1016/j.foodcont.2012.10.018>
- Semenza, J. C., Trinanes, J., Lohr, W., Sudre, B., Löfdahl, M., Martinez-Urtaza, J., Nichols, G. L., & Rocklöv, J. (2017). Environmental suitability of *Vibrio* infections in a warming climate: An early warning system. *Environmental Health Perspectives*, *125*(10), Article 107004. <https://doi.org/10.1289/ehp2198>
- Sheikh, H. I., Najiah, M., Fadhilina, A., Laith, A. A., Nor, M. M., Jalal, K. C., & Kasan, N. A. (2022). Temperature upshift mostly but not always enhances the growth of *Vibrio* species: A systematic review. *Frontiers in Marine Science*, *9*, Article 959830. <https://doi.org/10.3389/fmars.2022.959830>
- Song, X., Zang, J., Yu, W., Shi, X., & Wu, Y. (2020). Occurrence and identification of pathogenic vibrio contaminants in common seafood available in a Chinese traditional market in Qingdao, Shandong Province. *Frontiers in Microbiology*, *11*, Article 1488. <https://doi.org/10.3389/fmicb.2020.01488>
- Suzuki, K., Ushijima, K., Ito, T., & Ono, T. (2014). Environmental pH affects growth and virulence factors of *Vibrio parahaemolyticus*. *Applied and Environmental Microbiology*, *80*(10), 3109–3116.
- Thornstenson, C. A., & Ullrich, M. S. (2021). Ecological fitness of *Vibrio cholerae*, *Vibrio parahaemolyticus*, and *Vibrio vulnificus* in a small-scale population dynamics study. *Frontiers in Marine Science*, *8*, Article 623988. <https://doi.org/10.3389/fmars.2021.623988>
- To, T. T. H., Yanagawa, H., Thuan, N. K., Hiep, D. M., Cuong, D. V., Khai, T. L., Taniguchi, T., Kubo, R., & Hayashidani, H. (2020). Prevalence of vibrio parahaemolyticus causing acute hepatopancreatic necrosis disease of shrimp in shrimp, molluscan shellfish and water samples in the Mekong Delta, Vietnam. *Biology*, *9*(10), Article 312. <https://doi.org/10.3390/biology9100312>
- Valente, C. D. S., & Wan, A. H. L. (2021). *Vibrio* and major commercially important vibriosis diseases in decapod crustaceans. *Journal of Invertebrate Pathology*, *181*, Article 107527. <https://doi.org/10.1016/j.jip.2020.107527>
- Vezzulli, L., Grande, C., Reid, P. C., Hélaouët, P., Edwards, M., Höfle, M. G., Brettar, I., Colwell, R. R., & Pruzzo, C. (2016). Climate influence on *Vibrio* and associated human diseases during the past half-century in the coastal North Atlantic. *Proceedings of the National Academy of Sciences*, *113*(34), E5062–E5071. <https://doi.org/10.1073/pnas.1609157113>
- Weber, G. G., & Klose, K. E. (2011). The complexity of ToxT-dependent transcription in *Vibrio cholerae*. *Indian Journal of Medical Research*, *133*(2), 201–206.
- Whitaker, W. B., Parent, M. A., Naughton, L. M., Richards, G. P., Blumerman, S. L., & Boyd, E. F. (2010). Modulation of responses of *Vibrio parahaemolyticus* O3:K6 to pH and temperature stresses by growth at different salt concentrations. *Applied and Environmental Microbiology*, *76*(14), 4720–4729. <https://doi.org/10.1128/aem.00474-10>
- Williams, N. L., Siboni, N., King, W. L., Balaraju, V., Bramucci, A., & Seymour, J. R. (2022). Latitudinal dynamics of *Vibrio* along the eastern coastline of Australia. *Water*, *14*(16), Article 2510. <https://doi.org/10.3390/w14162510>

Modeling Respiration Rate of Bell Pepper (*Capsicum annum* L.) Under Hypobaric Storage Through Dimensional Analysis

Dewi Maya Maharani^{1,2}, Nursigit Bintoro^{1*}, Joko Nugroho Wahyu Karyadi¹ and Arifin Dwi Saputro¹

¹Department of Agricultural Engineering and Biosystem, University of Gadjah Mada, Yogyakarta 55281, Indonesia

²Department of Biosystems Engineering, University of Brawijaya, Malang 65145, Indonesia

ABSTRACT

Knowing the respiration rate of fresh products during storage is very important. One can use direct measurement or available prediction equations to determine the respiration rate. However, the availability of the prediction equations still needs to be improved. This study aims to develop mathematical models of respiration rate for pretreated bell peppers during hypobaric storage. Model development was done by applying dimensional analysis. Mature green bell peppers were used as the experimental samples. Three pretreatments on the bell pepper before storage, namely control, ozone pretreatment, and UV-C pretreatment, combined with three hypobaric storage levels of 26, 64, and 101 kPa, were studied. An apparatus set was built to create hypobaric conditions. An ozone generator and UV-C lamp were used to apply pretreatments to the samples. It was found that respiration rate models could be developed by considering bell pepper surface area, weight, volume, storage time, storage volume, and pressure. At the storage pressures of 101 to 56 kPa, UV-C pretreatment was the best in suppressing the respiration rate of bell pepper. Meanwhile, at a storage pressure of 26 kPa, the application of ozone and UV-C pretreatment gave a higher respiration rate than the control. The three models were found to have different characteristics and showed high accuracy with the experimental results. The dimensionless product of π_3 was found to have the most significant effect on RCO_2 for the three models. This finding indicated that the ratio between bell pepper and jar volumes is critical to ensure the model works.

ARTICLE INFO

Article history:

Received: 17 October 2023

Accepted: 07 March 2024

Published: 26 August 2024

DOI: <https://doi.org/10.47836/pjst.32.5.18>

E-mail addresses:

mayamaharani@mail.ugm.ac.id (Dewi Maya Maharani)

nursigit@ugm.ac.id (Nursigit Bintoro)

jknugroho@ugm.ac.id (Joko Nugroho Wahyu Karyadi)

arifin_saputro@ugm.ac.id (Arifin Dwi Saputro)

* Corresponding author

Keywords: Bell pepper, hypobaric storage, ozone, respiration, UV-C

INTRODUCTION

Bell pepper (*Capsicum annuum* L.) plays an essential role in many different cuisines worldwide with its various flavors and colors (Frans et al., 2021). Green bell pepper is a vital source of antioxidants, vitamins, and dietary fiber (Howard et al., 2000; Bosland et al., 2012; Rubatzky & Yamaguchi, 2012; Chen et al., 2018). However, bell pepper is a perishable product with a relatively short shelf life. Therefore, some treatments should be applied to extend its shelf life.

Ozonation is one of the promising chemical treatments to inactivate microorganisms and degrade mycotoxins (Gomes et al., 2020; Trombete et al., 2017). Ozone is an unstable molecule that rapidly decays to diatomic oxygen without leaving food residues and has the GRAS (Generally Recognized As Safe) status (Gaou et al., 2005; Gutiérrez et al., 2018). This treatment is faster than other conventional disinfection methods and without harmful residues. Many studies of ozone application on fresh products have been carried out, such as the application of ozone on cantaloupe (Chen et al., 2020), apples (Lv et al., 2019), oranges (García-Martín et al., 2018), and carrots (de Souza et al., 2018). It was also reported that ozone pretreatment on cantaloupe reduces respiration rate, ethylene production, and the number of microorganisms and maintains a high hardness level (Chen et al., 2020). Ong et al. (2014) find that papayas treated with ozone at concentrations lower than 5 ppm have a lower respiration rate and delayed ripening compared to controls. Considering these findings, it is reasonable to apply ozone pretreatment on the bell pepper in this study.

Ultraviolet-C (UV-C) irradiation is another new potential and environmentally friendly technology to extend the shelf life of fruits and vegetables (Lwin et al., 2021). It has been applied in many research works to prolong the self-life and maintain the quality of fresh products. UV-C treatment reduces respiration rate and maintains the quality of fresh products (Zhang & Jiang, 2019; Rodoni et al., 2015). Lwin et al. (2021) reported that irradiation of UV-C with a dose of 4.4 kJ/m² maintains baby corn's texture and total sugar concentration. The effect of UV-C irradiation in reducing respiration rate has also been reported for many products in various research works. Vicente et al. (2005) found that UV-C irradiation at 7 kJ/m² reduced the respiration rate of red chili Rodoni et al. (2015) for fresh-cut peppers, and Ustun et al. (2021) for green beans. Therefore, UV-C radiation is feasible for reducing bell pepper's respiration rate in this study.

Storing fresh produce in an environment with low oxygen concentrations can also extend the product's shelf life. Low oxygen concentration can slow the respiration rate of fresh produce, remove ethylene and other metabolic volatiles, retard the progress of ripening and aging (Burg, 2014). Reducing oxygen concentration in the storage space can be done by lowering the chamber's air pressure, known as hypobaric. It is a cheap and easy way to reduce oxygen concentration in storage space. Wang and Dilley (2000) stated that better and easier preservation of fresh produce under hypobaric conditions is thought to be due

to modification of the low-oxygen atmosphere and removal of volatile metabolic products such as ethylene and α -pharmacies from the atmosphere of storage facilities. The effect of hypobaric treatment in suppressing respiration rate was also reported for strawberry fruit (An et al., 2009), tomato fruit (Kou et al., 2016) and asparagus (Li et al., 2006). Hashmi et al. (2014) point out that combining hypobaric and other treatments, such as UV-C, heat ultrasound or volatile chemicals, may improve the storability of strawberries.

Respiration can be defined as a metabolic process that provides energy for the biochemical processes of fresh products. The respiration rate must be known because it is essential to control ripening to ensure quality after harvest and monitor product quality during storage. The respiration rate is inversely related to the product's shelf life, and efforts for shelf-life enhancement focus mainly on decreasing respiration (Waghmare et al., 2013). Respiration rate, usually expressed as the rate of O_2 consumption or CO_2 evolution, helps predict the shelf life of the products. Measurement of the respiration rate is sometimes very difficult to do. In hypobaric storage, measuring the respiration rate is problematic since O_2 dan CO_2 measuring devices are commonly designed for atmospheric pressure. Therefore, it is necessary to build models that can be used to predict respiration rates in the hypobaric storage condition. There are still many other situations where theoretically developed models are essential for postharvest agricultural product handling. Because it is often that in many postharvest activities, the relationship among parameters is not known clearly, causing analytical solutions not to be applied. In such a situation, dimensional analysis can solve the problem.

Dimensional analysis is one of the methods that can be used to develop a mathematical model of any phenomenon, mainly for cases where the relationship among the variables that influence the phenomenon cannot be related analytically. Pexton (2014) stated that dimensional analysis helps explain a phenomenon found in a process and is described as a mathematical model. In addition, the dimensional analysis makes it possible to state which phenomena have a significant influence and which play a minor role (Kowalczyk & Delgado, 2007). Several researchers have utilized dimensional analysis in the postharvest handling of agricultural products to develop predictive equations for certain phenomena. Moradi et al. (2016) applied dimensional analysis to develop equations to predict the moisture content of aloe vera gel. Jimoh et al. (2016) formulated prediction models for cassava peeling performance.

Nwakuba et al. (2017) developed an equation to predict the drying rate of the cocoa beans. Saracoglu (2018) used dimensional analysis to construct a plum drag force model, Asonye et al. (2018) developed equations for the cutting energy of okra, and Moradi et al. (2019) developed models for the physical and mechanical properties of three cultivars of cucumber fruit. Because the relationship between respiration rate variables during hypobaric storage is unclear, dimensional analysis can be used to form a prediction equation

for the respiration rate. Considering the above descriptions, this study aimed to develop mathematical models of the respiration rate of bell peppers pretreated using ozone and UV-C during hypobaric storage by applying dimensional analysis.

MATERIALS AND METHODS

Respiration Rate Model Development Using Dimensional Analysis

The respiration rate in the form of CO₂ production (RCO_2) during storage of bell peppers in the hypobaric condition is affected by several parameters. There were unlimited parameters that might affect a particular phenomenon. However, considering too many parameters will make the resulting mathematical equation too long, impractical and complex (Sonin, 2001). In this study, the formulation of the respiration rate was intended for bell peppers stored under hypobaric conditions at room air temperature. They were pretreated using ozone and UV-C; no treatment was performed before storage. For that reason, the parameters, along with their dimensions and units considered to affect the respiration rate, were summarized in Table 1.

Table 1

Considered parameters in the development of the respiration rate model of bell pepper stored under hypobaric condition

No	Parameter	Symbol	Unit	Dimension
Dependent parameter				
1.	Respiration rate	RCO_2	$m^3 kg^{-1} day^{-1}$	$L^3 M^{-1} T^{-1}$
Independent parameter				
2.	Bell pepper surface area	A	m^2	L^2
3.	Bell pepper mass	w	kg	M
4.	Bell pepper volume	Vb	m^3	L^3
5.	Storage time	t	day	T
6.	Jar volume	Vr	m^3	L^3
7.	Jar absolute pressure	P	N/m^2	$ML^{-1} T^{-2}$

According to the Buckingham π theorem, these parameters could be related to Equation (1).

$$\pi = A^{k1}, w^{k2}, Vb^{k3}, t^{k4}, Vr^{k5}, P^k \tag{1}$$

The number of dimensionless products (π) formed was equal to the number of parameters involved minus the number of dimensions (Sonin, 2001; Thurairajasingam et al., 2002; Gibbings, 2011; Olmos et al., 2015; Loubière et al., 2019). Therefore, there were 7 parameters and 3 dimensions for the case studied here, so 4 dimensionless products will be obtained. Through some standard calculations of the Buckingham π theorem, the four dimensionless products are shown in Equations 2 to 5.

$$\pi 1 = \frac{R_{CO2} \cdot w^{1.5}}{Vb \cdot Vr^{0.17} \cdot P^{0.5}} \quad [2]$$

$$\pi 2 = \frac{A^{1.5}}{Vr} \quad [3]$$

$$\pi 3 = \frac{Vb}{Vr} \quad [4]$$

$$\pi 4 = \frac{t \cdot Vr^{0.17} \cdot P^{0.5}}{w^{0.5}} \quad [5]$$

These four dimensionless products could be related as a functional Equation 6.

$$\pi 1 = C (\pi 2)^a (\pi 3)^b (\pi 4)^c \quad [6]$$

Substituting Equations 2 to 5 into Equation 6 resulted in Equation 7. The constant values of C , a , b , and c of Equation 7 could be determined by applying multiple linear regression analysis to the experimental data. Then, a mathematical model for predicting the respiration rate could be expressed as Equation 8.

$$\frac{R_{CO2} \cdot w^{1.5}}{Vb \cdot Vr^{0.17} \cdot P^{0.5}} = C \left[\frac{A^{1.5}}{Vr} \right]^a \left[\frac{Vb}{Vr} \right]^b \left[\frac{t \cdot Vr^{0.17} \cdot P^{0.5}}{w^{0.5}} \right]^c \quad [7]$$

$$R_{CO2} = C \left[\frac{Vb \cdot Vr^{0.17} \cdot P^{0.5}}{w^{1.5}} \right] \left[\frac{A^{1.5}}{Vr} \right]^a \left[\frac{Vb}{Vr} \right]^b \left[\frac{t \cdot Vr^{0.17} \cdot P^{0.5}}{w^{0.5}} \right]^c \quad [8]$$

Materials

Green bell peppers of spider variety in a green mature state were used as the samples in this research. These bell peppers were bought directly from the farmer in Batu, East Java, Indonesia. The bell peppers were transported to the laboratory inside a closed box at night. On arrival at the laboratory, the peppers were cleaned using a wet cloth to remove adhering dirt, sorted and selected, where only fresh, free of defect, and homogenous in color were used in the research. The selected bell pepper's weight, volume, and surface area must be measured individually before being stored in the respirometer jar.

Apparatus

The arrangement of the hypobaric apparatus used in this research is presented in Figure 1. This apparatus consisted of a vacuum pump (Value VE180N, 3/4 HP), a holding tank (30 × 15 cm), a vacuum controller unit, a glass jar (123 × 150 mm), and other supported components such as valve, hose, and clamps. The arrangement of these components would create a vacuum condition in the glass jar or respirometer container automatically as desired. The vacuum pump functioned to create a vacuum pressure in the respirometer

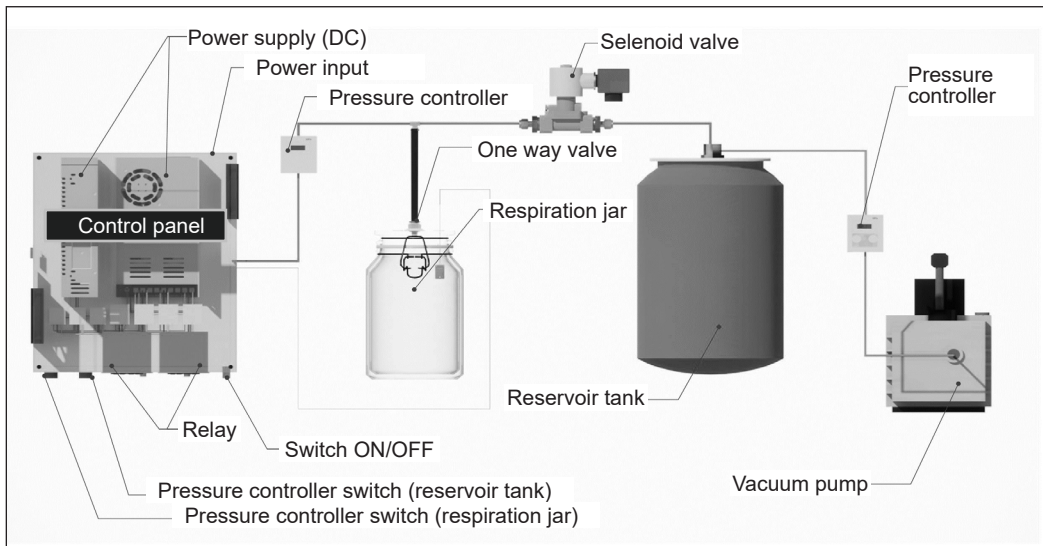


Figure 1. The arrangement of the hypobaric apparatus used in the experiment

jars. A holding or reservoir tank was used to stabilize the pressure in the system. The vacuum controller unit was used to regulate the desired pressure by opening and closing the solenoid valve and turning on and off the pump. Glass jar with a volume of 2118 ml was used as the respirometer container to store the bell pepper sample and was equipped with a pneumatic hose, one-way valve, and a vacuum pressure meter (SMC ZSE40-T1-22L and Panasonic DP-100). A total of 27 glass jars were used in this study to accommodate all treatment combinations.

In this research, the bell pepper sample was pretreated by exposing it to ozone gas or UV-C light before being stored in the respirometer glass jar. This pretreatment was carried out to better reduce the respiration rate and maintain the quality of the bell pepper sample. A UV-C fluorescent lamp (Sankyo Denki G40T10 and Philips TUV 36W/G36 T8) was used to apply the irradiation process to the bell pepper sample. The process was done in a specially designed exposure cabinet made from wood with $149.5 \times 45.3 \times 110$ cm dimensions. The magnitude of irradiation intensity was monitored using a UV-C light meter (Lutron, 254SD) with a white ball-shaped UVC-light probe constructed in a special housing with a measurement range of 2 mW/cm^2 . In this study, the intensity of UV-C radiation used was 0.834 mW/cm^2 for 6 minutes or 3 kJ/m^2 . This intensity was chosen based on the values commonly used in the various research works, where this value was in the range of the suggested intensities. Fonseca and Rushing (2008) suggested that the optimal UV-C dose for maximum hormesis effect ranged from 0.125 to 9 kJ/m^2 to control the growth of plant pathogens. Hassan et al. (2020) used UV-C intensities of 3.5, 7.0, and 10.4 kJ/m^2 for hot pepper, fennel and coriander; Ma et al. (2021) used 0.25 kJ/m^2 for paprika; and Yan et al. (2021) used 4 kJ/m^2 for tomato.

An ozone generator machine (PX-902) was used to apply another pretreatment to the bell pepper sample. The sample was put in a plastic container ($47 \times 32 \times 24$ cm) with inlet and outlet holes. Ozone gas from the generator then flowed through a plastic hose into the container until the concentration of ozone gas in the plastic container reached 4.99 ppm, which took about 4 minutes. This concentration was left until it reached 0 ppm, which took about 8 minutes. The concentration of ozone gas in the container was monitored using an ozone gas detector (Dienmern, Dm-509-O3). The concentration of ozone gas used in this study was selected based on various research reports on the application of ozone gas in various studies. Srilaong et al. (2013) used ozone concentrations of 2 and 10 ppm for mango fruit, Ali et al. (2014) used 0–5 ppm for papaya fruit, Han et al. (2017) applied ozone gas concentration of 2 ppm for mulberry fruit, García-Martín et al. (2018) used 1.6–60 ppm for orange fruit, Lv et al. (2019) used 2.5 ppm for apple, Lin et al. (2019) used 1.99 ppm for red suren, and Chen et al. (2020) applied 3, 5, and 7 ppm for melon fruit. The selected ozone gas concentration used in this study was in the range or about the average concentration value used by the above researchers.

Methods

Selected bell pepper was measured for dimension, weight, and volume and then pretreated by exposing it to the predetermined ozone gas or UV-C. Untreated bell pepper was also used as a control treatment. Therefore, this study carried three different pretreatments: gas ozone pretreatment, UV-C pretreatment, and no pretreatment (control). After being pretreated, a bell pepper was stored in the respirometer glass jar, and the cover was tightly closed. Each respirometer jar was filled with one of the bell pepper samples. The jar was vacuumed to the predetermined absolute pressure values by adjusting the vacuum controller unit. This research observed three different vacuum or hypobaric conditions of 26 kPa, 64 kPa and 101 kPa (atmospheric pressure). The hypobaric conditions of 26 kPa, 64 kPa and 101 kPa correspond with O_2 concentrations in the jar of 5%, 13% and 21%, respectively. A gas analyzer (Quantek 902D) was used to monitor the concentration of CO_2 in the jar. CO_2 gas measurements in vacuum conditions (under normal atmospheric pressure) are carried out by inserting the needle of the CO_2 measuring device (Quantek 902D) into the glass jar of the respirometer where the bell pepper is placed. Due to the pressure conditions in the vacuum respirometer jar, CO_2 gas from the respirometer jar will automatically flow into the CO_2 measuring device, and the CO_2 sensor in the measuring device will detect the CO_2 concentration value. In this measurement process, the suction pump from the CO_2 measuring device does not need to be turned on. In this way, CO_2 gas measurements can be carried out smoothly. The absolute pressure was monitored using a vacuum pressure meter (SMC ZSE40- T1-22L and Panasonic DP-100). The jar was then stored at tropical room temperature of about 25–28°C for 15 days. The change in CO_2 concentration in the

jar was measured daily for 15 days of storage. Three replications were carried out for each treatment combination.

Parameter Measurement

The weight of the bell pepper sample was measured using a digital balance (Model MH-200, range of 0–200 g/0.01 g). The volume was measured using the water displacement method. The surface area of the bell pepper was found by calculating the measured fruit and stalk dimensions of the sample using a digital caliper. The surface area was obtained by the sum of the fruit (A_f) and the stalk (A_s) surface area using Equations 9 and 10, respectively. In this calculation, the bell pepper was assumed to be a frustum for the fruit portion and a cylinder for the stalk. Figure 2 shows the measured dimensions of the fruit and stalk used in this research.

$$A_f = \pi \cdot (R + r) \left\{ h^2 + (R - r)^2 \right\}^{\frac{1}{2}} + \pi r^2 + \pi R^2 - \frac{1}{4} \cdot \pi \cdot \left(\frac{d_1 + d_2 + d_3}{3} \right)^2 \quad [9]$$

$$A_s = \pi \cdot \left(\frac{d_1 + d_2 + d_3}{3} \right) \cdot l + \frac{1}{4} \cdot \pi \cdot (d_1)^2 \quad [10]$$

The bell pepper sample's weight, volume, and surface area were assumed to be constant throughout the storage period. The same was true for the volume and absolute pressure in the respirometer jar. The concentration of CO_2 in the jar was monitored daily during storage. The bell pepper's respiration rate was calculated using Equation 11 (Kays, 1991; Fonseca et al., 2002).

$$R_{CO_2} = \frac{V_f (CO_{2t} - CO_{2i})}{W (t - t_i) 100} \quad [11]$$

Where R_{CO_2} was the respiration rate of the bell pepper (ml/kg.h); V_f was the free volume inside the jar (ml); CO_{2i} and CO_{2t} were CO_2 concentrations at the initial and at time t (%), respectively; W was the weight of the bell pepper sample (kg), and t and t_i were certain of storage time and initial storage time (hour).

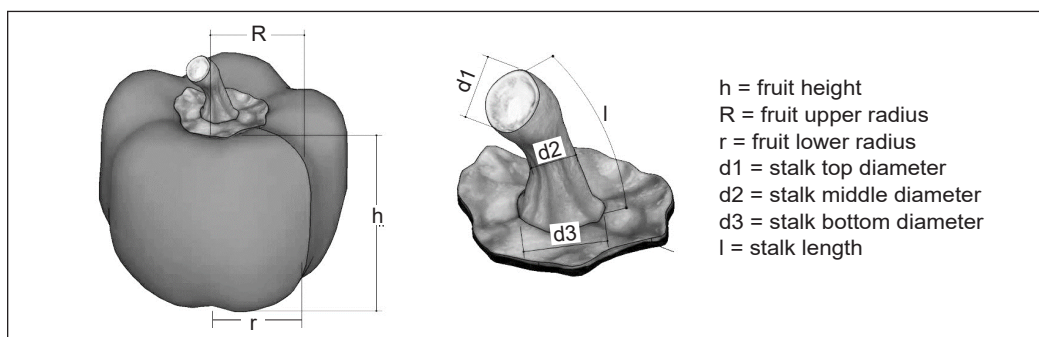


Figure 2. Schematic presentation of the dimensions of fruit and stalk of bell pepper

From the measurement of the involved parameters during the experiment, the values of $\pi 1$ to $\pi 4$ could be calculated, as shown in Table 2. The range of these values will also be the limits of the applicability of the developed equations.

Table 2
The range of π values calculated from measured parameters in the research

Pretreatment	$\pi 1$	$\pi 2$	$\pi 3$	$\pi 4$
Ozone	1.461×10^{-9} - 8.443×10^{-9}	1.296-2.406	0.094-0.161	0.114×10^8 - 3.746×10^8
UV-C	1.069×10^{-9} - 5.529×10^{-9}	0.748-2.060	0.094-0.151	0.099×10^8 - 4.117×10^8
Control	0.106×10^{-9} - 10.20×10^{-9}	1.471-2.372	0.104-0.179	0.107×10^8 - 3.361×10^8

RESULTS AND DISCUSSION

Model of Bell Pepper Respiration Rate

Based on the values of $\pi 1$ to $\pi 5$ obtained in this research, constant values of Equation 8 could be found using multiple regression analysis. Therefore, models or equations for the respiration rate of the three pretreatment conditions could be determined in Equations 12 to 14.

$$RCO_{2 \text{ Ozone}} = 4.692 \times 10^{-5} \left[\frac{Vb.Vr^{0.17}.P^{0.5}}{w^{1.5}} \right] \left[\frac{A^{1.5}}{Vr} \right]^{0.688} \left[\frac{Vb}{Vr} \right]^{1.555} \left[\frac{t.Vr^{0.17}.P^{0.5}}{w^{0.5}} \right]^{-0.360} \quad [12]$$

$$RCO_{2 \text{ UV-C}} = 1.52 \times 10^{-5} \left[\frac{Vb.Vr^{0.17}.P^{0.5}}{w^{1.5}} \right] \left[\frac{A^{1.5}}{Vr} \right]^{-0.622} \left[\frac{Vb}{Vr} \right]^{0.811} \left[\frac{t.Vr^{0.17}.P^{0.5}}{w^{0.5}} \right]^{-0.359} \quad [13]$$

$$RCO_{2 \text{ Control}} = 1.310 \times 10^{-2} \left[\frac{Vb.Vr^{0.17}.P^{0.5}}{w^{1.5}} \right] \left[\frac{A^{1.5}}{Vr} \right]^{-2.446} \left[\frac{Vb}{Vr} \right]^{4.403} \left[\frac{t.Vr^{0.17}.P^{0.5}}{w^{0.5}} \right]^{-0.274} \quad [14]$$

The constant values of the model for ozone, UV-C, and control were found to be different. The respiration rates of bell peppers in the three conditions differed. In other words, ozone or UV-C pretreatment would change the respiration rate of bell peppers. The enforceability of the respiration rate models resulting from this study had limits according to the range of $\pi 1$ to $\pi 4$ values, as shown in Table 2.

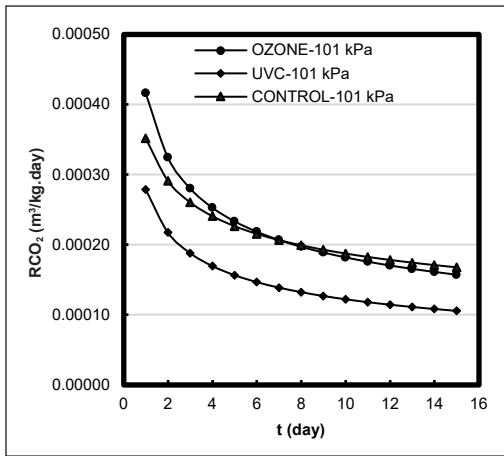
Figure 3 presents RCO_2 values according to the developed models for the storage pressures from 26 to 101 kPa in 15 kPa intervals. It could be observed that the respiration rate of the three treatments decreased with the storage time. At the beginning of the storage time until about five days, respiration rates decreased faster than the rest of the storage days, suggesting that the greatest decrease in the respiration rate occurred at the beginning

of the storage period, indicating that changes in the qualities of the bell pepper were likely to occur during this period. Collings et al. (2018) also found that the respiration rate of Fresh *P. nigrum* berries decreased faster at the beginning of the storage period. It was also reported that the rate of change of CO₂ and O₂ was faster in the early hours of mango packaging (Devanesan et al., 2012).

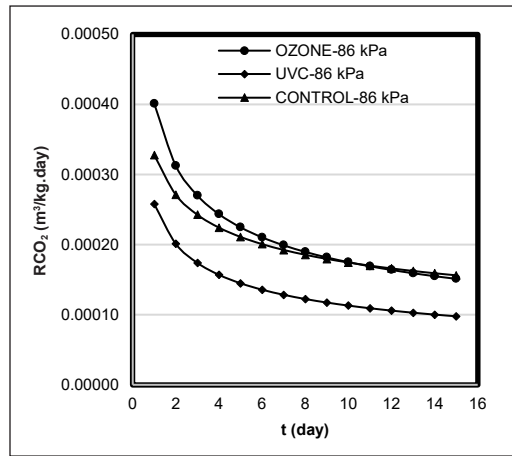
Ozone pretreatment showed the highest respiration rate at a storage pressure of 101 kPa to 71 kPa (Figures 3a to 3c) and was almost the same as the control but much higher than the UV-C pretreatment. It indicated that ozone pretreatment had no inhibitory effect on the respiration rate at those storage pressures. The effect of ozone in reducing respiration rate was getting better at 56 kPa storage pressure. However, further decreasing storage pressure to 41 kPa or lower (Figures 3e and 3f) decreases effectiveness, even giving a higher respiration rate than the control. The optimal ozone pretreatment storage pressure was about 56 kPa (Figure 3d). This result was very close to those reported by An et al. (2009) and Muhammad et al. (2023), who reported that a hypobaric pressure of 50 kPa was the best for strawberries and tomatoes, respectively. However, ozone pretreatment's effectiveness was less than UV-C for all studied storage pressures.

Templalexis et al. (2023) reported that the respiration rate of ozone-pretreated fresh-cut lettuce increased compared to the control. Arya et al. (2016) also found that the respiration rate of oyster mushrooms pretreated with 10 and 20 ppm ozone gas was larger than the control. Khawarizmi et al. (2018) stated that ozone was naturally decomposed into oxygen, which could contribute to a higher respiration rate of oxygen-sensitive commodities. On the contrary, Lin et al. (2023) found that the ozone-treated fresh-cut water fennel respiration rate was lower than that of the control. Cao et al. (2022) also found a lower ozone-pretreated kiwi fruit respiration rate than the control. The difference in research findings about the relationship between ozone treatment and respiration rate proves that more research is still needed to reveal ozone's true role in a product's respiration rate. As further stated by Khawarizmi et al. (2018), several parameters, such as ozone concentration, exposure time, and product sensitivity to ozone, were important factors that must be considered in research.

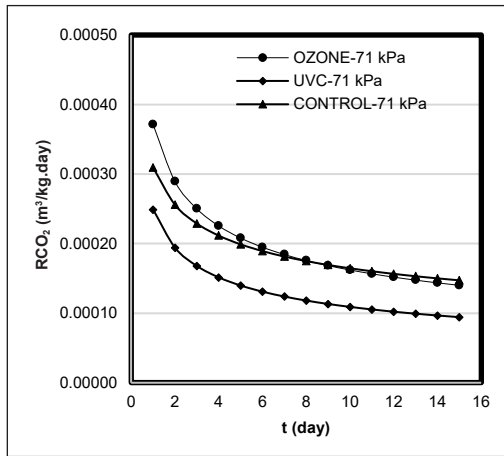
It was also observed that UV-C pretreated bell pepper showed the lowest respiration rate at storage pressure from 101 to 56 kPa (Figures 3a to 3d). However, further lowering the storage pressure to 41 kPa or lower, the respiration rate of UV-C pretreatment increased and was higher than that of the control (Figures 3e and 3f). It indicated that the effectiveness of UV-C pretreatment in suppressing respiration rate decreased as storage pressure decreased. It was the same phenomenon as ozone pretreatment, as mentioned above. According to this result, if UV-C pretreatment should be combined with the hypobaric storage, the lowest storage pressure could be applied at around 56 kPa. Therefore, it was suggested that reducing the respiration rate at a storage pressure of 101 to 56 kPa would be more effective if the bell pepper was treated with UV-C instead of using ozone.



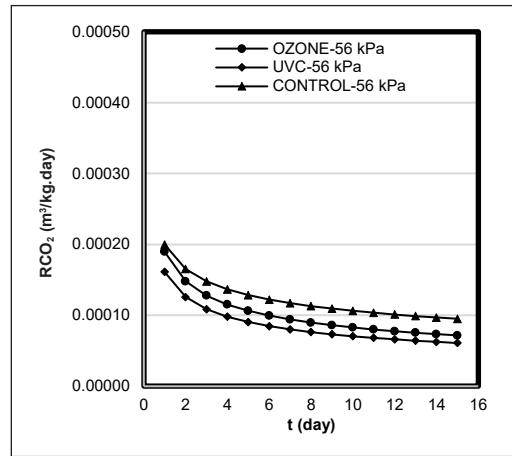
(a)



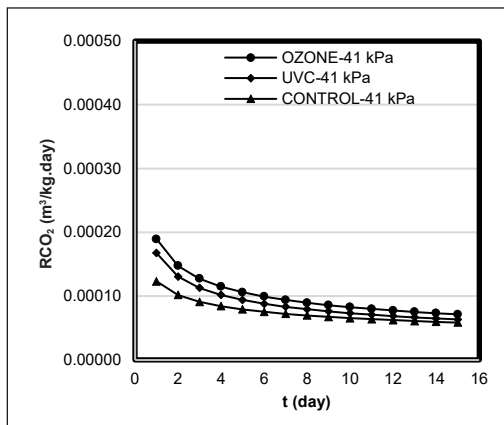
(b)



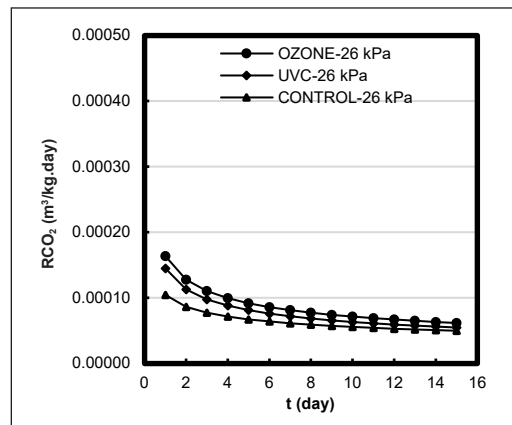
(c)



(d)



(e)



(f)

Figure 3. RCO_2 of the bell pepper during hypobaric storage, according to the developed models: (a) 101 kPa; (b) 86 kPa; (c) 71 kPa; (d) 56 kPa; (e) 41 kPa; and (f) 26 kPa storage pressures

Figure 3f showed that the effectiveness of UV-C pretreatments in reducing respiration rate was getting less at a storage pressure of 26 kPa compared to the control. The same was valid for ozone pretreatment, which meant that the effect of UV-C and ozone pretreatments on the respiration rate of bell pepper storage under hypobaric conditions depended on the storage pressure. At the storage pressure of 26 kPa, the control had the lowest respiration rate, meaning that ozone or UV-C pretreatment was not necessary at this storage pressure. In other words, for the storage pressure of 26 kPa and the temperature of 28°C, applying ozone or UV-C to the bell pepper would negatively affect the respiration rate. UV-C irradiation activates several biological processes and increases respiratory rate (Yemmireddy et al., 2022). Squash slices also experienced increased respiration rates with UV treatment ((Erkan et al., 2001) and shallots at a storage temperature of 28°C and RH 76.1% (Fauziah et al., 2020). The storage temperature used would also influence the effect of UV-C treatment on the respiration rate.

Kim et al. (2012) found that UV-LED irradiation decreased the respiration rate of cherry tomatoes at a storage temperature of 10°C while there was no obvious effect at 20°C. According to Allende et al. (2006), UV-C light has the potential to activate several biological processes in higher plants, including stimulation of respiration activity. Vunnam et al. (2014) reported that UV-C-treated cherry tomatoes had the highest respiration rate compared to the control treatment and fruit stored in modified atmospheres packaging (MAP). From these results, there are still many discrepancies regarding the effect of UV-C pretreatment on respiration rate. Its effectiveness depended on the irradiation dose, duration of the exposure time, storage temperature, and storage room pressure, and it was even found to not affect the respiration rate. Therefore, more comprehensive research was still needed to reveal the role of UV-C irradiation on the respiration rate of fresh produce. Similar statements were pointed out by other researchers in various research works, such as Gimeno et al. (2022) in a study about the application of UV-C in MAP.

Hashmi et al. (2014) in the study of hypobaric application for strawberry fruit. Furthermore, it is stated that the application of hypobaric in conjunction with other physical treatments such as UV-C, heat and ultrasound and volatile chemical treatments still needs to be evaluated. It was also observed that the respiration rate of the three pretreatment conditions consistently decreased with decreasing storage pressure. This finding indicated that storage pressure could effectively reduce the respiration rate of the bell pepper samples. Chen et al. (2013) reported similar results for bayberry fruit. Kou et al. (2016) also found that the respiration rates of tomatoes significantly decreased in the hypobaric condition. At the same time, Li et al. (2019) reported that hypobaric treatment only had little effect on the respiratory rate of blueberry fruit. The lower respiration rate in hypobaric conditions was due to the lower availability of oxygen in the space of the container, which caused the respiration rate to decrease.

As aforementioned, at 101 kPa, the concentration of oxygen in the container was the same as free air or about 21%, while at 64 kPa, the concentration of oxygen was reduced to 15%, and further reduction the storage pressure to 26 kPa, the concentration of oxygen was only 5%. This study showed that the combination of ozone or UV-C pretreatment and storage pressure was best at around 56 kPa, or about half of the atmospheric pressure. Some researchers also pointed out similar results for different treatment combinations. Muhammad et al. (2023) recommended that the best combination between the application of 400 ppm KMnO_4 with the storage pressure was found for the storage pressure of 50 kPa for tomato fruit. An et al. (2009) reported that a storage pressure of 50.7 kPa gave a slightly better ascorbic acid content and a lower growth of bacteria compared to the control for strawberry fruit.

Templalexis et al. (2023) found that the effectiveness of UV-C pretreatment in reducing the respiration rate of fresh-cut lettuce depended on the duration of the exposure time; as the exposure time increased, the effectiveness decreased. Mabusela et al. (2023) found that direct exposure to Vacuum Ultraviolet radiation on Fuji apple successfully reduced the respiration rate but damaged the skin, and UV-C pretreatment produced a lower respiration rate during the shelf life of Yellow Peaches (Zhou et al., 2020). Cote et al. (2013) reported that UV-C irradiation did not affect the respiration rate of tomatoes. Similar results were found by Collings et al. (2018) that UV-C treatment practically had no certain effect on the respiration rate of fresh piper nigrum berries compared to the control.

Model Validation

Comparisons between observed and predicted respiration rates using the developed model, as shown in Equations 13 to 15, are presented in Figure 4. The predicted respiration rate values were relatively close to the experimental results, meaning that the three developed models could be used to estimate the respiration rate in practice. As mentioned, it was still very rare and difficult to measure the respiration rate in the hypobaric condition; therefore, these equations would be very valuable in estimating the respiration rate of bell pepper in the hypobaric condition. An et al. (2009) pointed out that very few studies had directly reported respiration data as a function of the hypobaric partial pressure of the component gases. Thus, more measurement data were needed to quantitatively describe respiration as a function of hypobaric condition variables.

One of the advantages of using this model was that it was not necessary to measure O_2 and CO_2 concentrations directly on a respirometer, which was known to be quite difficult in hypobaric conditions because O_2 and CO_2 measuring instruments were generally designed for non-hypobaric conditions or atmospheric air pressure. The accuracy of the developed models to predict the respiration rate was evaluated using the determination coefficient (R^2) Equation 15, root mean square error (RMSE) Equation 16, percentage error (PE) Equation

17, mean absolute percentage error (MAPE) Equation 18, chi-square (χ^2) Equation 19 and the results are presented in Table 3.

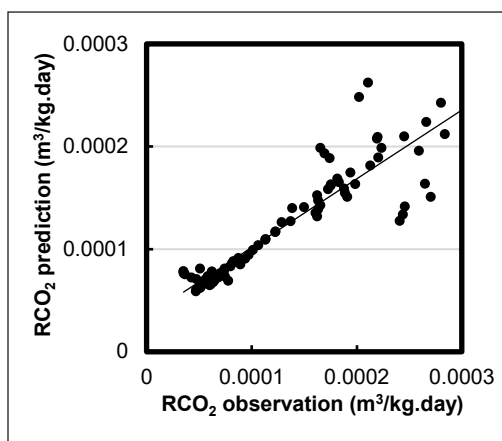
$$R^2 = \frac{\sum(MR_{exp} * MR_{pre})^2}{\sum(MR_{exp}^2 * MR_{pre}^2)} \quad [15]$$

$$RMSE = \left[\frac{1}{N} \sum_{i=1}^n (X_{i,exp} - X_{i,pre})^2 \right]^{1/2} \quad [16]$$

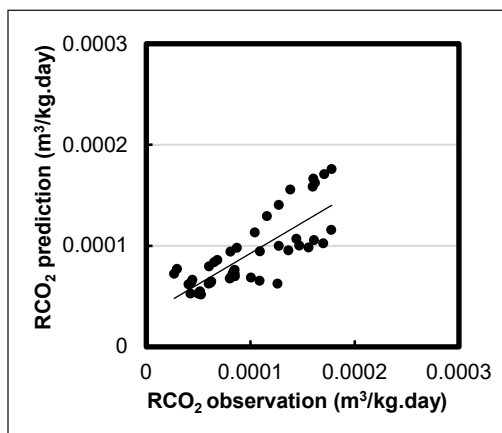
$$MAPE = \frac{\sum_{t=1}^n \left| \left(\frac{A_t - F_t}{A_t} \right) 100 \right|}{n} \quad [17]$$

$$\chi^2 = \frac{\sum_{i=1}^N (X_{i,exp} - X_{i,pre})^2}{N - Z} \quad [18]$$

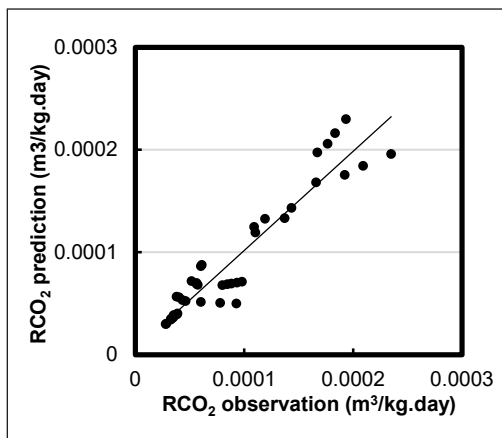
It could be seen that the R^2 values were relatively high, along with small values of RMSE, PE, MAPE, and χ^2 . The greater the R^2 value, the closer to 1, the higher the effect (Susmiati, 2022). MAPE has important, desirable features, including reliability, ease of interpretation, presentation clarity, and statistical evaluation support (Moreno et al., 2013). Meanwhile, a model has a very accurate forecast if the MAPE value is below 10% and a good forecast if the MAPE value is between 10% and 20% (Lewis, 1982). The smaller the RMSE and MAPE values, the smaller the deviation between the predicted and observed values so that the model used is more accurate. Models that provide smaller RMSE and MAPE values are more accurate and in accordance with actual conditions (Shintawati et al., 2020). The smaller the Chi-square value (χ^2), the more precise the prediction equation, but in general, there are no limitations. Table 3 indicated that the developed models of the respiration rate were accurate and might be used to predict the respiration rate of



(a)



(b)



(b)

Figure 4. Comparison between observed and predicted respiration rates: (a) ozone pretreatment, (b) UV-C pretreatment; and (c) control

Table 3

Parameters to evaluate the accuracy of the models

Pretreatment	<i>R</i> ²	<i>RMSE</i>	<i>PE</i> (%)	<i>MAPE</i>	χ^2
Ozon	0.956	3.476x10 ⁻⁵	0.199	19.468	0.0008
UV-C	0.933	3.639x10 ⁻⁵	0.447	25.009	0.0007
Control	0.879	6.579x10 ⁻⁵	0.374	20.959	0.0012

bell peppers in the hypobaric storage condition. It also suggested that the formulation of models for respiration rate could be carried out by applying dimensional analysis. Table 3 indicated that the developed models of the respiration rate were accurate and might be used to predict the respiration rate of bell peppers in the hypobaric storage condition. It also suggested that formulation of the model for respiration rate could be carried out by applying dimensional analysis.

Sensitivity Analysis

The effect of changing the values of the dimensionless products of π_2 to π_4 on RCO_2 can be seen from the sensitivity analysis in Table 4. It was found that within 10% increasing or decreasing the values of π_2 , π_3 , and π_4 , the dimensionless product of π_3 had the largest effect on RCO_2 for the three models. This finding indicated that the ratio between bell pepper volume to jar volume (π_3) was the most significant parameter affecting RCO_2 . It was also observed that for ozone-pretreated bell pepper, as the values of π_2 and π_3 increased, the values of RCO_2 would increase too; however, increasing the values of π_4 would decrease RCO_2 . Meanwhile, UV-C pretreatment and control were found to have the same tendency. Increasing the values of π_2 and π_4 would decrease RCO_2 while increasing π_3 would increase RCO_2 . These findings would be beneficial for estimating the respiration rate of bell peppers when designing a hypobaric storage system.

Table 4

Sensitivity analysis effect of π_2 , π_3 , and π_4 on RCO_2

Pretreatment	Dimensionless product	Change in RCO_2 value (%)		Average change in RCO_2 value (%)
		10% increase	10% decrease	
Ozone	π_2	24.325	21.389	22.857
	π_3	30.081	23.166	26.623
	π_4	21.595	23.060	22.327
UV-C	π_2	25.667	30.908	28.288
	π_3	31.641	25.413	28.527
	π_4	26.277	29.392	27.834
Control	π_2	22.601	48.765	35.683
	π_3	69.055	33.418	51.236
	π_4	25.572	29.135	27.353

CONCLUSION

The respiration rate models of bell peppers could be formulated during hypobaric storage by applying dimensional analysis. The parameters used to develop the models consisted of bell pepper surface area, bell pepper weight, bell pepper volume, storage time, storage volume, and storage pressure. Three respiration rate models were developed for control, ozone pretreated and UV-C pretreated bell peppers, and they were found to have different characteristics. At the storage pressures of 101 to 56 kPa, UV-C pretreatment was the best in suppressing the respiration rate of bell pepper. Meanwhile, at a storage pressure of 26 kPa, the application of ozone and UV-C pretreatment gave a higher respiration rate than the control. It was also observed that the developed respiration rate models had quite high accuracy, in which dimensionless products of π_3 , the ratio of bell pepper volume to jar volume parameter, had the largest effect on RCO_2 for the three models.

ACKNOWLEDGMENTS

The authors thank the University of Gadjah Mada, Indonesia, for providing financial support to this research through Program Rekognisi Tugas Akhir (RTA)-2023 No 5075/UN1.P.II/Dit-Lit/PT.01.01/2023 and BPPDN (Domestic Postgraduate Education Scholarship) the Ministry of Research, Technology and Higher Education Republic of Indonesia for providing the scholarship grant to the first author.

REFERENCES

- Ali, A., Ong, M. K., & Forney, C. F. (2014). Effect of ozone pre-conditioning on quality and antioxidant capacity of papaya fruit during ambient storage. *Food Chemistry*, *142*, 19-26. <https://doi.org/10.1016/j.foodchem.2013.07.039>
- Allende, A., Mcevoy, J. L., Luo, Y., Artes, F., & Wang, C. Y. (2006). Effectiveness of two-sided UV-C treatments in inhibiting natural microflora and extending the shelf-life of minimally processed 'Red Oak Leaf' lettuce. *Food Microbiology*, *23*(3), 241-249. <https://doi.org/10.1016/j.fm.2005.04.009>
- An, D. S., Park, E., & Lee, D. S. (2009). Effect of hypobaric packaging on respiration and quality of strawberry and curled lettuce. *Postharvest Biology and Technology*, *52*(1), 78-83. <https://doi.org/10.1016/j.postharvbio.2008.09.014>
- Arya, K. S., Yadav, B. K., & Santhakumaran, A. (2016). Effect of temperature and ozone treatment on the respiration of oyster mushroom. *International Journal of Agricultural Science and Research*, *6*(3), 377-388.
- Asonye, U. G., Nwakuba, N. R., & Asoegwu, S. N. (2018). Numerical and experimental studies on the cutting energy requirements of okra (*Abelmoschus Esculentus* L.). *Arid Zone Journal of Engineering, Technology & Environment*, *14*(SP.i4), 20-36.

- Bosland, P. W., Votava, E. J., & Votava, E. M. (2012). *Peppers: Vegetable and spice capsicums (2nd edition)*. Crop Production Science in Horticulture Series 22. CABI. <https://www.cabidigitallibrary.org/doi/book/10.1079/9781845938253.0000> CABI.
- Burg, S. P. (2014). Experimental errors in hypobaric storage research. In *Hypobaric Storage in Food Industry* (pp. 13-25). Academic Press. <https://doi.org/10.1016/b978-0-12-419962-0.00002-4>
- Cao, S., Meng, L., Ma, C., Ba, L., Lei, J., Ji, N., & Wang, R. (2022). Effect of ozone treatment on physicochemical parameters and ethylene biosynthesis inhibition in Guichang Kiwifruit. *Food Science and Technology*, 42, Article e64820. <https://doi.org/10.1590/fst.64820>
- Chen, C., Zhang, H., Zhang, X., Dong, C., Xue, W., & Xu, W. (2020). The effect of different doses of ozone treatments on the postharvest quality and biodiversity of cantaloupes. *Postharvest Biology and Technology*, 163, Article 111124. <https://doi.org/10.1016/j.postharvbio.2020.111124>
- Chen, H., Yang, H., Gao, H., Long, J., Tao, F., Fang, X., & Jiang, Y. (2013). Effect of hypobaric storage on quality, antioxidant enzyme and antioxidant capability of the Chinese bayberry fruits. *Chemistry Central Journal*, 7, Article 4. <https://doi.org/10.1186/1752-153X-7-4>
- Chen, H. Z., Zhang, M., Bhandari, B., & Guo, Z. (2018). Evaluation of the freshness of fresh-cut green bell pepper (*Capsicum annum* var. *grossum*) using electronic nose. *LWT-Food Science and Technology*, 87, 77-84. <https://doi.org/10.1016/j.lwt.2017.08.052>
- Collings, E. R., Gavidia, M. C. A., Cools, K., Redfern, S., & Terry, L. A. (2018). Effect of UV-C on the physiology and biochemical profile of fresh *Piper nigrum* berries. *Postharvest Biology and Technology*, 136, 161-165. <https://doi.org/10.1016/j.postharvbio.2017.11.007>
- Cote, S., Rodoni, L., Miceli, E., Concellón, A., Civello, P. M., & Vicente, A. R. (2013). Effect of radiation intensity on the outcome of postharvest UV-C treatments. *Postharvest Biology and Technology*, 83, 83-89. <https://doi.org/10.1016/j.postharvbio.2013.03.009>
- de Souza, L. P., Faroni, L. R. D. A., Heleno, F. F., Cecon, P. R., Gonçalves, T. D. C., Silva, G. J. da, & Prates, L. H. F. (2018). Effects of ozone treatment on postharvest carrot quality. *LWT 90*, 53-60. <https://doi.org/10.1016/j.lwt.2017.11.057>
- Devanesan, J. N., Karuppiyah, A., & Abirami, C. V. K. (2012). Effect of storage temperatures, O₂ concentrations and variety on respiration of mangoes. *Journal of Agrobiolgy*, 28(2), 119-128. <https://doi.org/10.2478/v10146-011-0013-8>
- Erkan, M., Yi, C., & Krizek, D. T. (2001). UV-C irradiation reduces microbial populations and deterioration in Cucurbita pepo fruit tissue. *Environmental and Experimental Botany*, 45(1), 1-9. [https://doi.org/10.1016/S0098-8472\(00\)00073-3](https://doi.org/10.1016/S0098-8472(00)00073-3)
- Fauziah, P. Y., Bintoro, N., & Karyadi, J. N. W. (2020). Effect of ultraviolet-C treatments and storage room condition on the respiration rate, weight loss, and color change of Shallots (*Allium ascalonicum* L.) during storage. In *IOP Conference Series: Earth and Environmental Science* (Vol. 449, No. 1, p. 012021). IOP Publishing. <https://doi.org/10.1088/1755-1315/449/1/012021>
- Fonseca, J. M., & Rushing, J. W. (2008). Application of ultraviolet light during postharvest handling of produce: Limitations and possibilities. *Fresh Produce*, 2(2), 41-46.

- Fonseca, S. C., Oliveira, F. A. R., & Brecht, J. K. (2002). Modelling respiration rate of fresh fruits and vegetables for modified atmosphere packages: A review. *Journal of Food Engineering*, 52(2), 99-119. [https://doi.org/10.1016/S0260-8774\(01\)00106-6](https://doi.org/10.1016/S0260-8774(01)00106-6)
- Frans, M., Aerts, R., Ceusters, N., Luca, S., & Ceusters, J. (2021). Possibilities of modified atmosphere packaging to prevent the occurrence of internal fruit rot in bell pepper fruit (*Capsicum annuum*) caused by *Fusarium* spp. *Postharvest Biology and Technology*, 178, Article 111545. <https://doi.org/10.1016/j.postharvbio.2021.111545>
- Gaou, I., Dubois, M., Pfohl-Leszkowicz, A., Coste, C., De Jouffrey, S., & Parent-Massin, D. (2005). Safety of Oxygreen®, an ozone treatment on wheat grains. Part 1. A four-week toxicity study in rats by dietary administration of treated wheat. *Food Additives and Contaminants*, 22(11), 1113-1119. <https://doi.org/10.1080/02652030500307156>
- García-Martín, J. F., Olmo, M., & García, J. M. (2018). Effect of ozone treatment on postharvest disease and quality of different citrus varieties at laboratory and at industrial facility. *Postharvest Biology and Technology*, 137, 77-85. <https://doi.org/10.1016/j.postharvbio.2017.11.015>
- Gibbins, J. C. (2011). *Dimensional analysis, 1st edition*. Springer.
- Gimeno, D., Gonzalez-Buesa, J., Oria, R., Venturini, M. E., & Arias, E. (2022). Effect of modified atmosphere packaging (MAP) and UV-C Irradiation on postharvest quality of red raspberries. *Agriculture*, 12(1), Article 29. <https://doi.org/10.3390/agriculture12010029>
- Gomes, T., Canever, S. B., Savi, G. D., Piacentini, K. C., Cargnin, M., Furtado, B. G., Feltrin, A. C., Quadri, M. B., & Angioletto, E. (2020). Modeling and experimental of mould disinfestation of soybean silos with ozone. *Ozone: Science and Engineering*, 42(2), 183-193. <https://doi.org/10.1080/01919512.2019.1630259>
- Gutiérrez, D. R., Chaves, A. R., & Rodríguez, S. del C. (2018). UV-C and ozone treatment influences on the antioxidant capacity and antioxidant system of minimally processed rocket (*Eruca sativa* Mill.). *Postharvest Biology and Technology*, 138, 107-113. <https://doi.org/10.1016/j.postharvbio.2017.12.014>
- Han, Q., Gao, H., Chen, H., Fang, X., & Wu, W. (2017). Precooling and ozone treatments affects postharvest quality of black mulberry (*Morus nigra*) fruits. *Food Chemistry*, 221, 1947-1953. <https://doi.org/10.1016/j.foodchem.2016.11.152>
- Hashmi, M. S., East, A. R., Palmer, J. S., & Heyes, J. A. (2014). Strawberries inoculated after hypobaric treatment exhibit reduced fungal decay suggesting induced resistance. *Acta Horticulturae*, 1053, 163-168. <https://doi.org/10.17660/ActaHortic.2014.1053.16>
- Hassan, A. B., Al, S. A., Sir, K. A., Elbadr, N. A., Alsulaim, S., Osman, M. A., & Mohamed, I. A. (2020). Effect of UV-C radiation treatment on microbial load and antioxidant capacity in hot pepper, fennel and coriander. *LWT*, 134, Article 109946. <https://doi.org/10.1016/j.lwt.2020.109946>
- Howard, L. R., Talcott, S. T., Brenes, C. H., & Villalon, B. (2000). Changes in phytochemical and antioxidant activity of selected pepper cultivars (*Capsicum* species) as influenced by maturity. *Journal of Agricultural and Food Chemistry*, 48(5), 1713-1720. <https://doi.org/10.1021/jf990916t>
- Jimoh, M. O., Olukunle, O. J., & Manuwa, S. I. (2016). Modeling of cassava peeling performance using dimensional analysis. *Agricultural Engineering International: CIGR Journal*, 18(2), 360-367.

- Kays, S. J. (1991). Metabolis processes in harvested products. In *Postharvest Physiology of Perishable Plant Products* (pp. 75-142). Van Nostrand Reinhold
- Khawarizmi, M. A., & Phebe, D. (2018). Ozone application in fresh fruits and vegetables. *Pertanika Journal of Scholarly Research Reviews*, 4(2), 29-35.
- Kim, N. Y., Lee, D. S., Lee, H. J., & An, D. S. (2012). Effect of UV-LED irradiation on respiration and ethylene production of cherry tomatoes. *Food Science and Preservation*, 19(1), 47-53. <https://doi.org/10.11002/kjfp.2012.19.1.047>
- Kou, X., Wu, J. Y., Wang, Y., Chen, Q., Xue, Z., Bai, Y., & Zhou, F. (2016). Effects of hypobaric treatments on the quality, bioactive compounds, and antioxidant activity of tomato. *Journal of Food Science*, 81(7), H1816-H1824. <https://doi.org/10.1111/1750-3841.13360>
- Kowalczyk, W., & Delgado, A. (2007). Dimensional analysis of thermo-fluid-dynamics of high hydrostatic pressure processes with phase transition. *International Journal of Heat and Mass Transfer*, 50(15-16), 3007-3018. <https://doi.org/10.1016/j.ijheatmasstransfer.2006.12.004>
- Lewis, C. D. (1982). *Industrial and business forecasting methods: A practical guide to exponential smoothing and curve fitting*. Butterworth Scientific.
- Li, H., James, A., He, X., Zhang, M., Cai, Q., & Wang, Y. (2019). Effect of hypobaric treatment on the quality and reactive oxygen species metabolism of blueberry fruit at storage. *CyTA - Journal of Food*, 17(1), 937-948. <https://doi.org/10.1080/19476337.2019.1674925>
- Li, W., Zhang, M., & Yu, H. Q. (2006). Study on hypobaric storage of green asparagus. *Journal of Food Engineering*, 73(3), 225-230. <https://doi.org/10.1016/j.jfoodeng.2005.01.024>
- Lin, F., Lv, K., Ma, S., Wang, F., Li, J., & Wang, L. (2023). Effects of ozone treatment on storage quality and antioxidant capacity of fresh-cut water fennel [*Oenanthe javanica*]. *Food Science and Technology*, 43, 1-11. <https://doi.org/10.1590/fst.108422>
- Lin, S., Chen, C., Luo, H., Xu, W., Zhang, H., Tian, J. J., Ju, R., & Wang, L. (2019). The combined effect of ozone treatment and polyethylene packaging on postharvest quality and biodiversity of *Toona sinensis* (A.Juss.) M.Roem. *Postharvest Biology and Technology*, 154(5), 1-10. <https://doi.org/10.1016/j.postharvbio.2019.04.010>
- Loubière, C., Delafosse, A., Guedon, E., Chevalot, I., Toye, D., & Olmos, E. (2019). Dimensional analysis and CFD simulations of microcarrier ‘just-suspended’ state in mesenchymal stromal cells bioreactors. *Chemical Engineering Science*, 203, 464-474. <https://doi.org/10.1016/j.ces.2019.04.001>
- Lv, Y., Tahir, I. I., & Olsson, M. E. (2019). Effect of ozone application on bioactive compounds of apple fruit during short-term cold storage. *Scientia Horticulturae*, 253, 49-60. <https://doi.org/10.1016/j.scienta.2019.04.021>
- Ma, L., Wang, Q., Li, L., Grierson, D., Yuan, S., Zheng, S., Wang, Y., Wang, B., Bai, C., Fu, A., Gao, L., Zhu, B., Luo, Y., Mu, J., & Zuo, J. (2021). UV-C irradiation delays the physiological changes of bell pepper fruit during storage. *Postharvest Biology and Technology*, 180, Article 111506. <https://doi.org/10.1016/j.postharvbio.2021.111506>

- Mabusela, B. P., Belay, Z. A., Godongwana, B., & Caleb, O. J. (2023). Impact of vacuum ultraviolet (VUV) photolysis on ethylene degradation kinetics and removal in mixed - fruit storage , and direct exposure to 'Fuji' apples during storage. *Journal of Food Science and Technology*, *60*, 2557-2567. <https://doi.org/10.1007/s13197-023-05775-3>
- Moradi, M., Balanian, H., & Taherian, A. (2019). Physical and mechanical properties of three varieties of cucumber: A mathematical modeling. *Journal of Food Process Engineering*, *43*(2), Article e13323. <https://doi.org/10.1111/jfpe.13323>
- Moradi, M., Niakosari, M., & Etemadi, A. (2016). Dimensionless modeling of thin layer drying process of aloe vera gel. *Iranian Food Science and Technology*, *12*(3), 362-370.
- Moreno, J. J. M., Pol, A. P., Abad, A. S., & Blasco, B. C. (2013). Using the R-MAPE index as a resistant measure of forecast accuracy. *Psicothema*, *25*(4), 500-506. <https://doi.org/10.7334/psicothema2013.23>
- Muhammad, A., Dayisoylu, K. S., Khan, H., Khan, M. R., Khan, I., Hussain, F., Basit, A., Ali, M., Khan, S., & Idrees, M. (2023). An integrated approach of hypobaric pressures and potassium permanganate to maintain quality and biochemical changes in tomato fruits. *Horticulturae*, *9*(1), Article 9. <https://doi.org/10.3390/horticulturae9010009>
- Lwin, N. T. N., Supapvanich, S., & Promyou, S. (2021). Ultraviolet-C irradiation maintaining texture and total sugars content of ready to cook baby corn during commercial storage. *Food Science and Biotechnology*, *30*, 47-54. <https://doi.org/10.1007/s10068-020-00854-z>
- Nwakuba, N. R., Ejebu, P. K., & Okafor, V. C. (2017). A mathematical model for predicting the drying rate of cocoa bean (*Theobroma cacao* L.) in a hot air dryer. *Agricultural Engineering International: CIGR Journal*, *19*(3), 195-202.
- Olmos, E., Loubiere, K., Martin, C., Delaplace, G., & Marc, A. (2015). Critical agitation for microcarrier suspension in orbital shaken bioreactors: Experimental study and dimensional analysis. *Chemical Engineering Science*, *122*, 545-554. <https://doi.org/10.1016/j.ces.2014.08.063>
- Ong, M. K., Ali, A., Alderson, P. G., & Forney, C. F. (2014). Effect of different concentrations of ozone on physiological changes associated to gas exchange, fruit ripening, fruit surface quality and defence-related enzymes levels in papaya fruit during ambient storage. *Scientia Horticulturae*, *179*, 163-169. <https://doi.org/10.1016/j.scienta.2014.09.004>
- Pexton, M. (2014). How dimensional analysis can explain. *Synthese*, *191*(10), 2333-2351.
- Rodoni, L. M., Zaro, M. J., Hasperu , J. H., Concell n, A., & Vicente, A. R. (2015). UV-C treatments extend the shelf life of fresh-cut peppers by delaying pectin solubilization and inducing local accumulation of phenolics. *LWT-Food Science and Technology*, *63*(1), 408-414. <https://doi.org/10.1016/j.lwt.2015.03.042>
- Rubatzky, V. E., & Yamaguchi, M. (2012). *World vegetables: Principles, production, and nutritive values*. Springer.
- Saracoglu, T. (2018). Development of prediction models of selected hydrodynamic properties of plum fruit (*Prunus domestica* L) in water. *International Journal of Engineering Science Invention*, *7*(5), 72-78.
- Shintawati, Analiasari, & Zukryandry. (2020). Kinetika Ekstraksi Minyak atsiri Lada Hitam (*Piper nigrum*) Secara Hidrodistilasi [Kinetics of Black Pepper (*Piper nigrum*) Essential Oil Extraction by

- Hydrodistillation]. *Chemical Engineering Research Articles*, 3(2), 63-70. <https://dx.doi.org/10.25273/cheesa.v3i2.7388.63-70>
- Sonin, A. A. (2001). *The physical basis of dimensional analysis (2nd ed.)*. Department of Mechanical Engineering, MIT.
- Srilaong, Jitareerat, & Wongs-Aree (2014). Fumigation with ozone to extend the storage life of mango fruit cv nam dok mai no.4. *Agricultural Science Journal*, 44(2), 663-672.
- Susmiati, Y. (2022). *Pengembangan distilator untuk pemurnian bioetanol dengan modifikasi internal reboiler* [Development of a bioethanol distillation process using a rectification distillation with an internally modified reboiler]. [Doctoral Dissertation]. Universitas Gadjah Mada, Indonesia.
- Templalexis, C., Lentzou, D., Samioti, A., & Xanthopoulos, G. (2023). The individual and combined effect of ozone and UV-C on mass loss respiration, texture and colour changes of fresh-cut lettuce. *Food Research*, 7(3), 29-41. [https://doi.org/DOI:10.26656/fr.2017.7\(3\).367](https://doi.org/DOI:10.26656/fr.2017.7(3).367)
- Thurairajasingam, E., Shayan, E., & Masood, S. (2002). Modelling of a continuous food pressing process by dimensional analysis. *Computers and Industrial Engineering*, 42(2-4), 343-351. [https://doi.org/10.1016/S0360-8352\(02\)00025-6](https://doi.org/10.1016/S0360-8352(02)00025-6)
- Trombete, F. M., Porto, Y. D., Freitas-Silva, O., Pereira, R. V., Direito, G. M., Saldanha, T., & Fraga, M. E. (2017). Efficacy of ozone treatment on mycotoxins and fungal reduction in artificially contaminated soft wheat grains. *Journal of Food Processing and Preservation*, 41(3), Article e12927. <https://doi.org/10.1111/jfpp.12927>
- Ustun, H., Ali, Q., Kurubas, M. S., Dogan, A., Balkhi, M., Peker, B., & Erkan, M. (2021). Influence of postharvest UV-C illumination on biochemical properties of green beans. *Scientia Horticulturae*, 289, Article 110499. <https://doi.org/10.1016/j.scienta.2021.110499>
- Vicente, A. R., Pineda, C., Lemoine, L., Civello, P. M., Martinez, G. A., & Chaves, A. R. (2005). UV-C treatments reduce decay, retain quality and alleviate chilling injury in pepper. *Postharvest Biology and Technology*, 35(1), 69-78. <https://doi.org/10.1016/j.postharvbio.2004.06.001>
- Vunnam, R., Hussain, A., Nair, G., Bandla, R., Garipey, Y., Donnelly, D. J., Kubow, S., & Raghavan, G. S. V. (2014). Physico-chemical changes in tomato with modified atmosphere storage and UV treatment. *Journal of Food Science and Technology*, 51, 2106-2112. <https://doi.org/10.1007/s13197-012-0690-3>
- Waghmare, R. B., Mahajan, P. V., & Annapure, U. S. (2013). Modelling the effect of time and temperature on respiration rate of selected fresh-cut produce. *Postharvest Biology and Technology*, 80, 25-30. <https://doi.org/10.1016/j.postharvbio.2013.01.012>
- Wang, Z., & Dilley, D. R. (2000). Hypobaric storage removes scald-related volatiles during the low temperature induction of superficial scald of apples. *Postharvest Biology and Technology*, 18(3), 191-199. [https://doi.org/10.1016/S0925-5214\(99\)00080-0](https://doi.org/10.1016/S0925-5214(99)00080-0)
- Yan, L., Zheng, H., Liu, W., Liu, C., Jin, T., Liu, S., & Zheng, L. (2021). UV-C treatment enhances organic acids and GABA accumulation in tomato fruits during storage. *Food Chemistry*, 338, Article 128126. <https://doi.org/10.1016/j.foodchem.2020.128126>

- Yemmireddy, V., Adhikari, A., & Moreira, J. (2022). Effect of ultraviolet light treatment on microbiological safety and quality of fresh produce: An overview. *Frontiers in Nutrition*, *9*, Article 871243. <https://doi.org/10.3389/fnut.2022.871243>
- Zhang, W., & Jiang, W. (2019). UV treatment improved the quality of postharvest fruits and vegetables by inducing resistance. *Trends in Food Science & Technology*, *92*, 71-80. <https://doi.org/10.1016/j.tifs.2019.08.012>
- Zhou, H., Zhang, X., Su, M., Du, J., Li, X., & Ye, Z. (2020). Effects of ultraviolet-C pretreatment on sugar metabolism in yellow peaches during shelf life. *HortScience*, *55*(4), 416-423. <https://doi.org/10.21273/HORTSCI114554-19>

A Reliable Multimetric Straggling Task Detection

Lukuman Saheed Ajibade^{1,2*}, Kamalrulnizam Abu Bakar¹, Muhammed Nura Yusuf^{1,3}
and Babangida Isyaku^{1,4}

¹Faculty of Computing, Universiti Teknologi Malaysia, 81310, Skudai, Johor, Malaysia

²Department of Computer Science, Federal Polytechnic Offa, Nigeria

³Department of Mathematical Sciences, Abubakar Tafawa Balewa University, Bauchi, Nigeria

⁴Department of Mathematics and Computer Science, Sule Lamido University, K/Hausa, Nigeria

ABSTRACT

One of the most difficult issues in using MapReduce for parallelising and distributing large-scale data processing is detecting straggling tasks. It is defined as recognising processes that are operating on weak nodes. When two steps in the Map phase (copy, combine) and three stages in the Reduce phase (shuffle, sort, and reduce) are included, the overall execution time is the sum of the execution times of these five stages. The main objective of this study is to calculate the remaining time to complete a task, the time taken, and the straggler(s) detected in parallel execution. The suggested method is based on the use of Progress Score (PS), Progress Rate (PR), and Remaining Time (RT) metrics to detect straggling tasks. The results obtained have been compared with popular algorithms in this domain, such as Longest Approximate Time to End (LATE) and Combinatory Late-Machine (CLM), and it has been demonstrated to be capable of detecting straggling tasks, accurately estimating execution time, and supporting task acceleration. RMSTD outperforms LATE by 23.30% and CLM by 19.51%.

Keywords: Big data, MapReduce, progress score, straggling tasks, stragglers

ARTICLE INFO

Article history:

Received: 23 October 2023

Accepted: 01 February 2024

Published: 26 August 2024

DOI: <https://doi.org/10.47836/pjst.32.5.19>

E-mail addresses:

saheed2066@graduate.utm.my (Lukuman Saheed Ajibade)

knizam@utm.my (Kamalrulnizam Abu Bakar)

ymnura@atbu.edu.ng (Muhammed Nura Yusuf)

babangida.isyaku@slu.edu.ng (Babangida Isyaku)

* Corresponding author

INTRODUCTION

This paper presents a Reliable Multimetric Straggling Task Detection algorithm (RMSTD) strategy for detecting straggling tasks among tasks executing in parallel. The main aim of the RMSTD is to present an approach that uses multiple metrics to make straggler detection much more reliable and

accurate. Straggler detection in the Hadoop MapReduce framework refers to identifying tasks that take longer than expected and are known as “stragglers” (Ouyang et al., 2016). In straggler detection, the overall execution time is the sum of the execution times of these five steps, consisting of two phases in the Map phase (copy, combine) and three stages in the Reduce phase (copy shuffle/sort, and reduce) (Katrawi et al., 2021).

Hadoop MapReduce and Apache Spark represent two widely adopted technologies for processing large datasets in the industry. Although both frameworks excel at managing substantial volumes of data, they diverge in terms of their architectural designs (Ketu et al., 2020). Hadoop MapReduce employs a cost-effective approach, utilising the Hadoop Distributed File System (HDFS) to execute batch processing. It is recognised for its stability and maturity, having been in use for an extended period and earned the trust of numerous organisations for handling extensive data volumes. The framework boasts a straightforward programming model, enhancing its usability. In contrast, Apache Spark offers a different approach and architecture for large-scale data processing.

Common methods of straggler detection include resource usage monitoring, where usage of system resources such as CPU, memory and disk utilisation is monitored as tasks execute, such that tasks that use fewer resources during their execution relative to other tasks may be declared as stragglers (Javadpour et al., 2020). Also, the Ensemble method integrates various straggler detection techniques to improve detection accuracy (Kumar et al., 2021). Profile-based analysis entails profiling tasks and finding outliers based on runtime, resource utilisation, or other factors. Another approach is the use of machine learning techniques where factors such as task running time, resource utilisation, input data records and cluster conditions are used to detect straggling tasks; this approach identifies trends in historical data in forecasting likely straggling tasks (Ouyang et al., 2018).

However, in resource usage monitoring, a task’s resource utilisation may be unreliable as an indicator of a straggler because it could legally use fewer resources if it has minimal data requirements or is executing on a node with limited resources. On the other hand, the ensemble approach, profile-based strategy, and machine learning techniques have the disadvantages of complexity, high profiling, and computational overheads. In most of the previous works on straggler detection, the use of a single metric to detect straggling tasks is quite common because the MapReduce framework is designed for a homogeneous environment where the computational power of the various machines is the same; hence, there is little consideration for the CPU capability since all the tasks are expected to run at the same rate. This assumption is not very true in all circumstances because, in a typical data centre, the resources are not dedicated exclusively to a particular job; hence, the resources are shared. Therefore, the load on each node varies, which may, in turn, affect the rate of execution of the tasks spread across the nodes. Therefore, this paper proposes a Reliable

Multimetric Straggler Detection Algorithm (RMSTD) to address the inadequacy of the previous studies and improve the effectiveness of straggler detection. The contribution of this paper includes:

- Improvement of the reliability of the straggling tasks detection by using Average Remaining Time (ART) to complete execution of the tasks to ensure that scenarios like the late start of execution of the task(s) due to the load on the node(s) and data skew problem rather than the usage of a single metric.
- The task's historical behaviour mitigates the impact of short-term oscillations or outliers in the Remaining Time, resulting in a more reliable estimate of job completion.
- RMSTD offers a more trustworthy approach by considering the past average, giving a more informed perspective on the anticipated completion timeframes of tasks.

RELATED WORKS

Phan et al. (2019) proposed a Framework for Assessing the Stragglers Detection (FASD) mechanism over MapReduce for straggler detection because other studies tend to focus more on the impact of stragglers. FASD presented a comprehensive straggler detection and reduction approach. However, the evaluation only applies to one application, and the study does not consider how it will be used in practice or include empirical data. The study also did not consider using optimal metrics in straggler detection, even though it offers a method for assessing straggler detection algorithms. Ghare and Leutenegger (2005) suggest task replication to enhance job response time. MapReduce. Dean and Ghemawat (2008) employ speculative execution to finish straggler jobs when parallel processing is nearing completion. Mantri reduces stragglers from MapReduce cluster processing nodes (Ananthanarayanan et al., 2019). Mantri's core strategies are straggler task restarting, network-aware task placement, and task output protection. Chen et al. (2014) introduce the speculative execution method of Maximum Cost Performance (MCP). Zaharia et al. (2019)'s Longest Approximate Time to End (LATE) improves Hadoop task scheduling.

In the LATE technique, the remaining running task time for each phase has been assumed to be the same; however, in the Reduce phase, the shuffle stage takes longer to complete than other stages as they are based on the prior task. According to Javadpour et al. (2020), Self-Adaptive MapReduce Scheduling Algorithm (SAMR), Enhanced Self-Adaptive MapReduce Scheduling Algorithm (ESAMR), and Speculative Execution Algorithm Based on Decision Tree (SECDDT) algorithms are unable to accurately anticipate the running duration. It is insufficient because the present task differs in several ways from the prior ones. While it is crucial to consider this because the node processing durations vary depending on their characteristics, ESAMR only uses executable information and ignores

node specifications (CPU and memory). A better job assignment scheme for Hadoop, the Earliest Completion Time (ECT) scheme, was presented by Dai and Bassiouni (2013). Two improved replica placement policies for Hadoop, the Partition Replica Placement Policy and the Slot Replica Placement Policy, were proposed by Qiang et al. (2014) and Dai et al. (2016). In contrast to the widely used Standard Deviation (SD) method, Tukey's method (Dai et al., 2017) adopts a statistical technique for identifying outliers that seems more suitable for identifying stragglers and starting speculative execution early. The sensitivity to extreme observations and the time it takes to find stragglers limit this strategy, too. As a result, most existing works declare non-stragglers as stragglers while ignoring true stragglers since they do not apply ideal parameters to recognise stragglers among parallel running tasks.

In summary, most existing studies on stragglers task detection are not based on optimum metrics and are usually focused on a specific situation; hence, their usage in other situations usually leads to failure. For example, if a system is designed to work in a homogeneous environment, it cannot be used in a heterogeneous environment because issues like skewness are not considered.

PROPOSED SOLUTION

This paper presents a Reliable Multimetric Stragglers Task Detection algorithm (RMSTD) strategy for detecting stragglers tasks among tasks; the RMSTD algorithm is designed to improve the stragglers detection strategy irrespective of the environments (homogeneous or heterogeneous). This approach uses optimal parameters to detect stragglers tasks applicable in all environments, including skew situations. The primary objective of this problem is to estimate the correct execution time in each stage of the MapReduce framework, which results in the correct total execution time. The constraints associated with this problem are the two stages in the Map phase (copy, combine) and three stages of Reduce (shuffle, sort, and reduce). The total execution time is the total sum of the execution time of these five stages.

The proposed method for solving this problem is calculating the Average Remaining Time (ART) to complete the execution of the tasks running in parallel. All tasks whose remaining time to complete execution is greater than the calculated ART is/are declared as stragglers. The computational complexity of the RMSTD algorithm is $O(n)$, where n is the number of tasks in the *Task_List*. The algorithm iterates through each task in the list once and performs constant work for each task. Therefore, the algorithm's time complexity is linear with respect to the input size. The design and operational process of RMSTD is structured into two phases: (1) the initial task allocation phase and (2) progress monitoring and the stragglers detection phase. Figure 1 presents the design flowchart, and Algorithm 1 shows the steps to achieve the desired result.

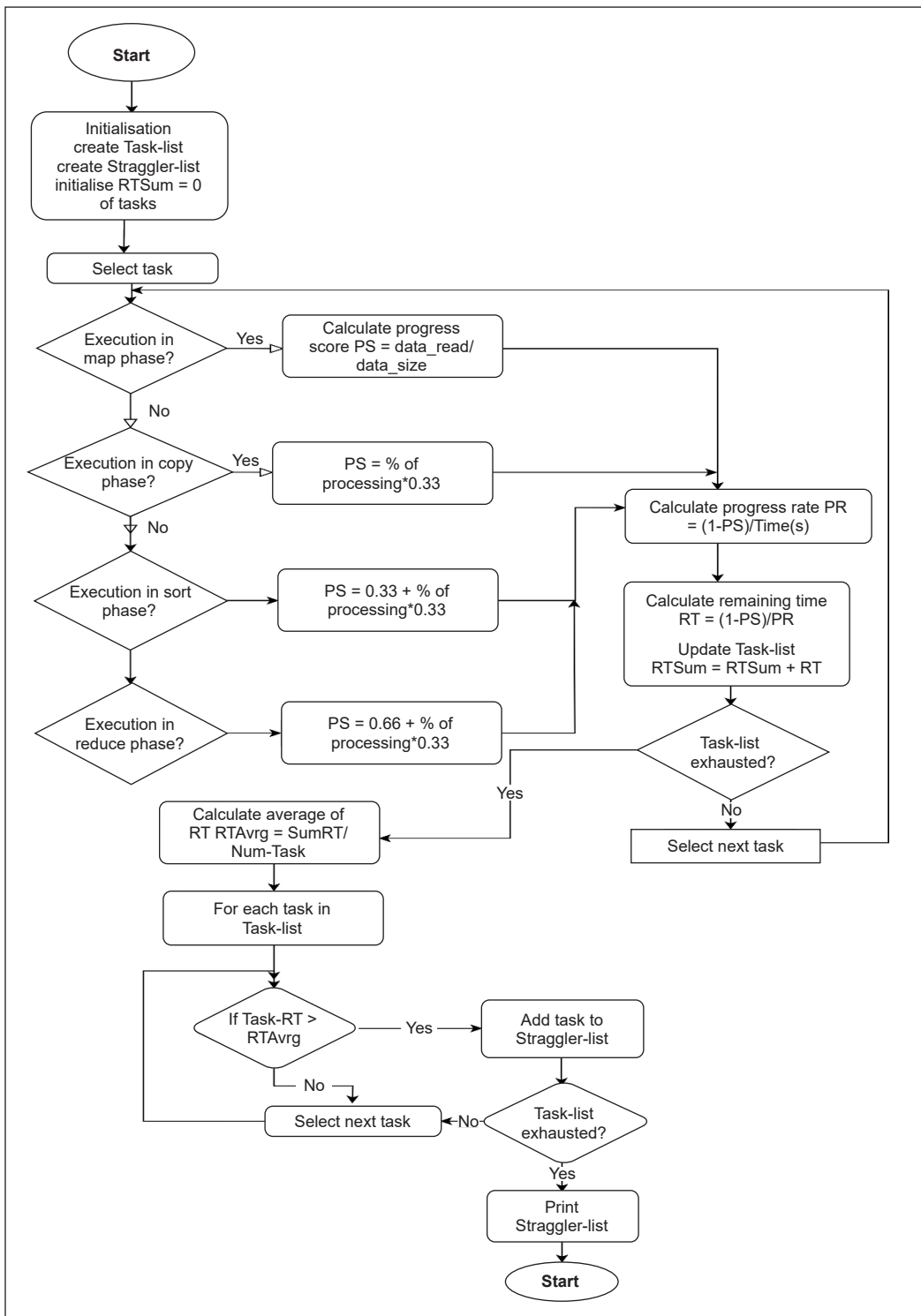


Figure 1. Flowchart of RMSTD design

Algorithm 1: RMSTD Algorithm

1. # Create a list of all tasks, "Task_list" with task_id, PS, PR, and RT attributes
 2. # Create a list of all Stragglers, "Straggler_list"
 3. Initialise RTSum = 0, Num-Task = total no of tasks
 4. For each task in Task_list
 5. If execution = map_phase
 6. PS = data read/data size
 7. Else
 8. If execution = copy_phase
 9. PS = %processing*0.33
 10. elseif execution = sort_phase
 11. PS = 0.33+ %processing*0.33
 12. elseif execution = reduce_phase
 13. PS = 0.66+ %processing*0.33
 14. endif
 15. Endif
 16. # Calculate the progress rate (PR)
 17. PR = PS/Time(s)
 18. calculate the remaining time to finish the task (RT)
 19. RT = (1-PS)/PR
 20. Update Task_list with PS, PR, and RT
 21. RTSum = RTSum+RT
 22. Endfor
 23. RTavg = SumRT/Num-Task
 24. For each task in task_list:
 25. If TaskRT > RTavg
 26. Add task to Straggler_list
 27. Endif
 28. Endfor
-

Data Generation for RMSTD

For testing the design using ART, a Java code (Algorithm 2) was used to generate test data for simplicity since all kinds of data can be handled by the design. Different data types to be processed will have a program to process the data exclusively.

Algorithm 2: Text data generator

```

1. function NewTextFile(filePath, fileSizeInBytes):
2.     open file at filePath for writing
3.     create a random number generator
4.     create a TextString object
5.     bytesWritten = 0

6.     while byteswritten < fileSizeInBytes
7.         clear the TextString
8.         lineLength = generate a random number between 1 and 10
9.         randomLine = LineOfText(lineLength)
10.        write randomLine to the file
11.        write a new line character to the file
12.        bytesWritten += length of randomLine + length of new line
            character
13.        if bytesWritten is a multiple of 10 MB
14.            flush the writer to free up memory
15.        endif
16.    endwhile
17.    close the file
18.    return NewTextFile

19. function LineOfText(lineLength):
20.    create a TextString object
21.    for i = 0 to lineLength - 1
22.        XterLetter = generate a random letter
23.        append XterLetter to the TextString
24.    endfor
25.    return the TextString as a string

26. main:
27. fileSizeInBytes = desired file size in bytes
28. filePath = path to the output file

29. NewTextFile(filePath, fileSizeInBytes)

```

Initial Task Allocation

The task allocation procedure in the Map phase is an important part of the MapReduce framework. It helps ensure that the MapReduce job is executed efficiently, and the results are timely. In this design phase, the input data is read and uploaded into HDFS together with

the job configuration. The allocation of input data to nodes is responsible for processing the input data and generating intermediate key-value pairs in this architecture phase. The Namenode begins the task allocation method by breaking the input data into chunks and assigning each chunk to the Map task. The Map jobs are run in parallel on the available nodes in the Hadoop cluster, and it also generates intermediate key-value pairs that are saved in HDFS, as depicted in Figure 2. The following are the steps involved in allocating tasks to selected nodes. The Namenode splits the input data into 64Mb/128MB/256Mb record-size chunks. Each split is assigned to a Map job. The Job Tracker considers the load on each node, the locality of the chunks' data, and the available resources on each one while allocating tasks to nodes. A task is often assigned to the nodes with the available resources and close to the data to improve the MapReduce job performance (Algorithm 3).

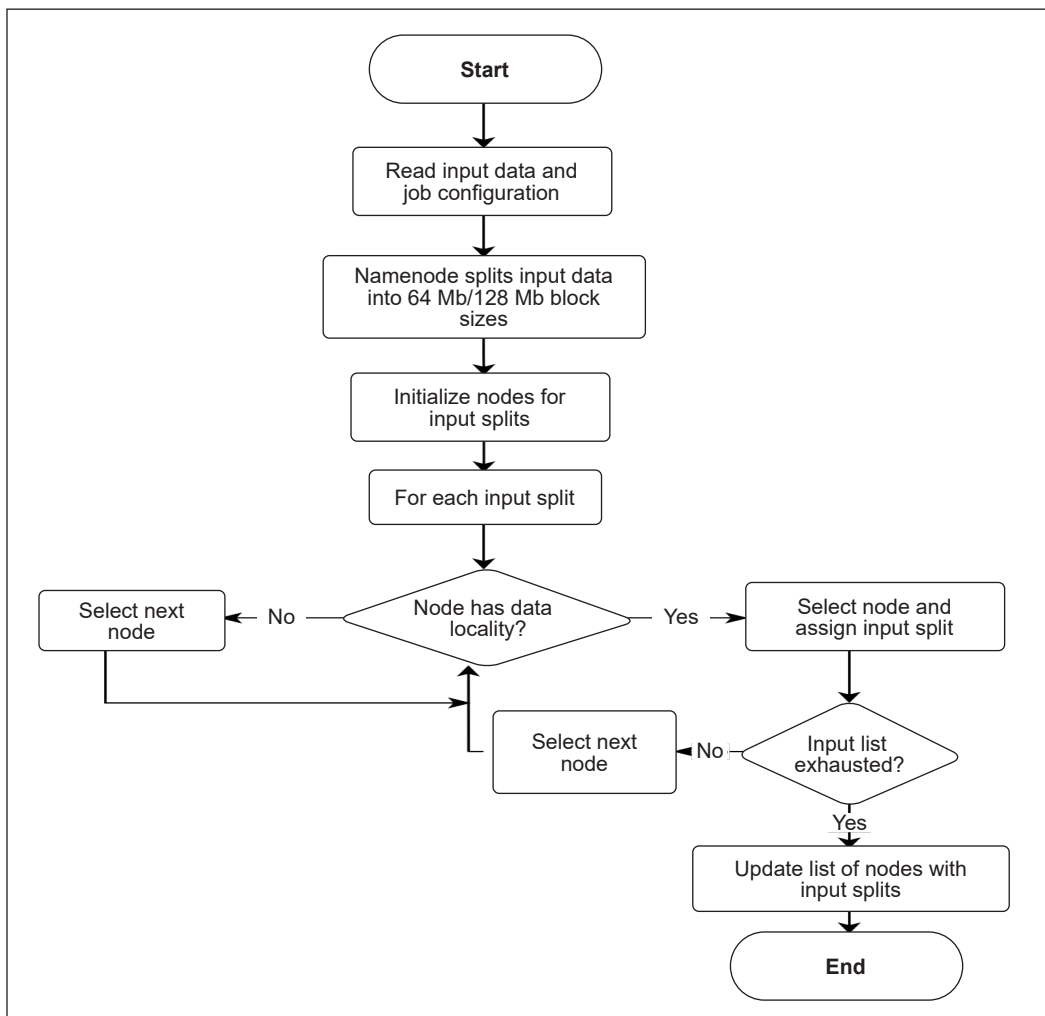


Figure 2. Flowchart of initial task allocation

Algorithm 3: Initial Task Allocation Algorithm

1. Input: MapReduce job configuration, input data
 2. Output: Map task assignments
 3. Split input data into input splits based on block size
 4. Initialise an empty map of nodes to assigned tasks
 5. For each input split:
 6. Select the nodes with data locality for the input split
 7. Assign the input split to a selected node with the least number of assigned tasks
 8. EndFor
 9. Update the map of the node to assigned tasks
 10. Return the map of the node to the assigned tasks
-

Progress Monitoring and Straggler Detection

The role of this phase in the operation of RMSTD is to use Progress Score, Progress Rate, and Remaining Time to complete and detect straggling tasks among tasks executing in parallel on the Hadoop cluster. In a Hadoop cluster, where tasks are executed in parallel, it is crucial to monitor the progress of individual tasks to ensure the timely completion of jobs. Straggling task(s) whose progress is/are slower than others can significantly impact the job's overall performance and completion time. To address this challenge, progress monitoring techniques employing metrics such as Progress Score, Progress Rate, and Remaining Time have emerged as valuable tools for detecting straggling tasks in Hadoop clusters.

Progress Score Calculation

The Progress Score metric provides an overview of the progress made by a task relative to the total amount of work it needs to complete. It is calculated by dividing the amount of work completed by the total amount of work. It is a score between 0 and 1 (from the literature), where 0 indicates that the task has not started, and 1 indicates that the task is complete. A high progress score indicates that a task is nearing completion, while a low score suggests that a task is lagging. Tracking each task's Progress Score makes it possible to identify tasks that have fallen behind in their progress. A lower Progress Score compared to others suggests a potential straggler.

In a homogeneous environment, that is, where all the nodes are the same in terms of processing capacity, the processing is expected to proceed at the same rate; hence, any task/node with a problem can be easily detected by using PS calculated as Equation 1:

$$PS[i] = \begin{cases} \frac{M}{N} & \text{for map tasks} \\ \frac{1}{3} \left(k + \frac{M}{N} \right) & \text{for reduce tasks} \end{cases} \quad [1]$$

where, $PS[i]$ is the i th task's P, N is the number of key/value pairs that must be processed in a task, M is the number of key/value pairs that have already been processed in a certain task, and K is the completed phase of a reduction task.

The PS for a Map is the fraction of input data read, but the execution of a Reduce is broken into three phases (copy, sort, and reduce), each accounting for one-third of the total PS. This weighting can be changed by modifying the scheduling parameters. For example, a task halfway through the copy phase will have a PS of $0.5 \times 0.33 = 0.165$. while a task halfway through the reduce phase will have a PS of $0.33 + 0.33 + (0.5 \times 0.33) = 0.66 + 0.165 = 0.83$

The value of the Progress score (PS) is taken for each task, and the task(s) whose PS < threshold (determined by individual work) is/are then declared as straggler(s). A threshold of 0.2 is commonly used for comparison as in (LATE) such that any task whose PS < 0.2 is identified as a straggler.

Progress Rate Calculation

The Progress Rate measures the speed at which a task is progressing. It is calculated by dividing the amount of work completed by the time taken to complete that work. A high progress rate indicates that a task is progressing quickly, while a low rate suggests that a task is progressing slowly. Monitoring the PR allows the identification of tasks that are progressing at a slower rate than expected, indicating a potential straggler calculated as Equation 2:

$$PR_i = \frac{PS[i]}{T} \quad [2]$$

where, PR_i is the Progress Rate of $Task_i$, and T is the time the task has been executed. A threshold is then determined for PR, at which point a task whose PR is less than the threshold is declared a straggler, which means that its progress is very slow.

There are certain disadvantages to using Progress Score or Progress Rate alone to identify straggling tasks in Hadoop.

- **Inaccuracy of Detection:** Progress Score and PR are not always accurate because PS is based on how much data has been processed by a task and the amount of time the task has been running, while PR is the rate of progress made by a task. Both can be misleading when a task is simply waiting for input data from a slow network connection or a slow input source. Such a task may have a low PS or PR that can make it be declared as a straggler when it is not.

- The PS or PR status of a job can change if additional parameters like the data collection size, the data locality, the number of concurrent tasks executing on the same node, and network congestion or latency are not considered.
- Lack of context: Progress Score and Progress Rate do not provide context for a task, such as the complexity of the data being processed or the degree of processing difficulty. Some jobs could seem to have a low PS or PR due to the volume of data they are handling, their inherent complexity, or their resource-intensive nature, leading to their being declared as stragglers when they are not.
- Unpredictable progress: Some tasks in Hadoop, particularly those that involve iterative algorithms or complex data dependencies, may exhibit non-linear progress, which causes an inaccurate assessment of their progress and may result in false positives or negatives when identifying straggling tasks using PS or PR alone.
- Data and Computational Skews: In Hadoop, data is frequently distributed unevenly between tasks because of the data's nature or the utilised partitioning method (Data Skew). The processing capacities will differ since the nodes' capacities in a heterogeneous environment are different (Computational skew). These metrics do not consider both skews, leading to some tasks taking longer than others to complete. Hence, the progress of the tasks might not be shown correctly.
- Wrong Assumption: It is usually assumed that tasks progress at a constant rate, which is not usually the case because the nodes are not dedicated to the job alone. The nodes are processing other tasks. Hence, not all the nodes' resources are always available to the tasks.

Remaining Time (RT) to Complete Calculation

The RT metric estimates the time required for a task to be completed based on its current PR. It is calculated by dividing the remaining work by the progress rate. A high remaining time to complete suggests that such a task will take a long time to finish, indicating a potential straggler. By comparing the estimated remaining time of each task, it is possible to identify tasks with significantly longer estimated completion times compared to others. Such tasks may be potential stragglers. RT of a task is calculated according to Equation 3.

$$RT_i = \frac{1 - PS[i]}{PR[i]} \quad [3]$$

where RT_i , $PS[i]$ Remaining Time (RT), Progress Score (PS) and Progress Rate (PR) of $Task_i$

Average Remaining Time (ART) to Complete Calculation

The performance and efficiency of a system rely largely on the timely completion of tasks in distributed computing systems such as Hadoop, where large-scale data processing tasks

are broken into smaller sub-tasks and completed across a cluster of nodes. However, certain tasks, known as stragglers, may take substantially longer time to run to completion than others. These straggling tasks can slow overall throughput and lengthen job completion times, reducing system efficiency and user experience. To address this challenge in this study, the use of Average Remaining Time (ART), a metric that estimates the time remaining for each task to complete based on their Progress Score (PS), Progress Rate (PR) and Remaining Time to Complete (RT), is employed. By continuously monitoring these metrics, the progress of tasks, and comparing their ART values, it becomes possible to identify potential stragglers among tasks being executed in parallel. The ART is calculated as Equation 4:

$$RT_{avg} = \frac{\sum \frac{1 - PS[i]}{PR[i]}}{n} \tag{4}$$

Where, RT_{avg} is the average of the remaining time of execution of all the tasks, PS is the progress score, PR is the progress rate, n is the number of tasks executed in parallel. Any $Task_i$ whose value is less than the calculated RT_{avg} is then declared/identified as a straggler.

PERFORMANCE EVALUATION

Experimental Setup of the proposed RMSTD

The experiment was set up and conducted on a Google Cloud platform. Eight nodes were used for this experiment. Tables 1 and 2 show the Cluster and Software configurations. Figure 3 shows the screenshot of the nodes running on the Google Cloud platform. 10 GB, 20 GB and 30 GB data (text) were generated using a Java program to test the design. The result of 10 GB data size, when executed using a single node (laptop) with other hardware specifications, is shown in Figure 4. For the 10 GB data on the Google Cloud platform, the readings were taken after 10 s of execution, and the average remaining time was calculated. In comparison, 20 GB and 30 GB data were taken after 30 s and 50 s, respectively, as shown in Figures 4, 5 and 6.

Table 1
Cluster configurations

Cluster Configurations				
Node	Main Memory	CPU Cores	Storage	
myclustertask-m (master)	16G	4	50G	
myclustertask-0 (slave-1)	12G	2	50G	
myclustertask-1 (slave-2)	12G	2	50G	
myclustertask-2 (slave-3)	12G	2	50G	
myclustertask-3 (slave-4)	12G	2	50G	
myclustertask-4 (slave-5)	12G	2	50G	
myclustertask-5 (slave-6)	12G	2	50G	
myclustertask-6 (slave-7)	12G	2	50G	
myclustertask-1 (slave-2)	12G	2	50G	
myclustertask-2 (slave-3)	12G	2	50G	

Table 2
Software configurations

Software Configurations	
Operating System	Ubuntu 20.04
Hadoop	2.8.5
JDK	1.8

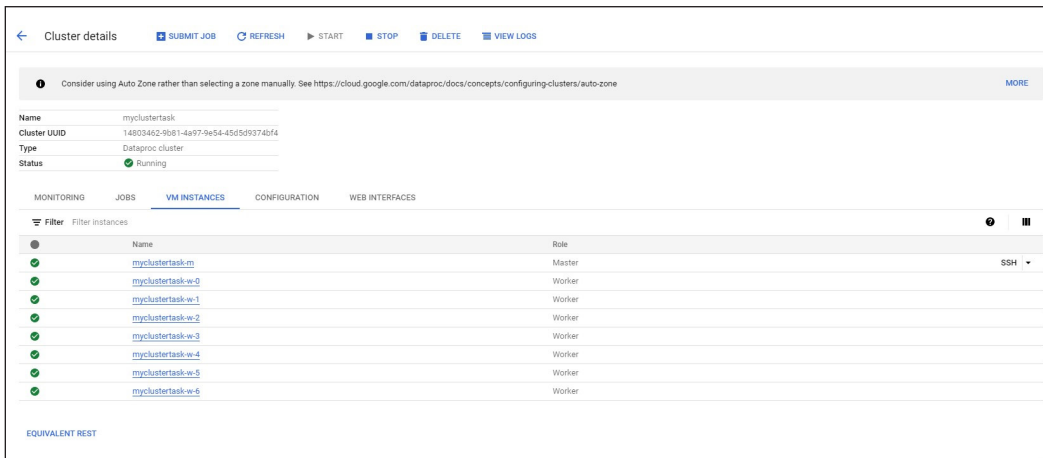


Figure 3. Screenshot of the nodes running on Google Cloud Platform

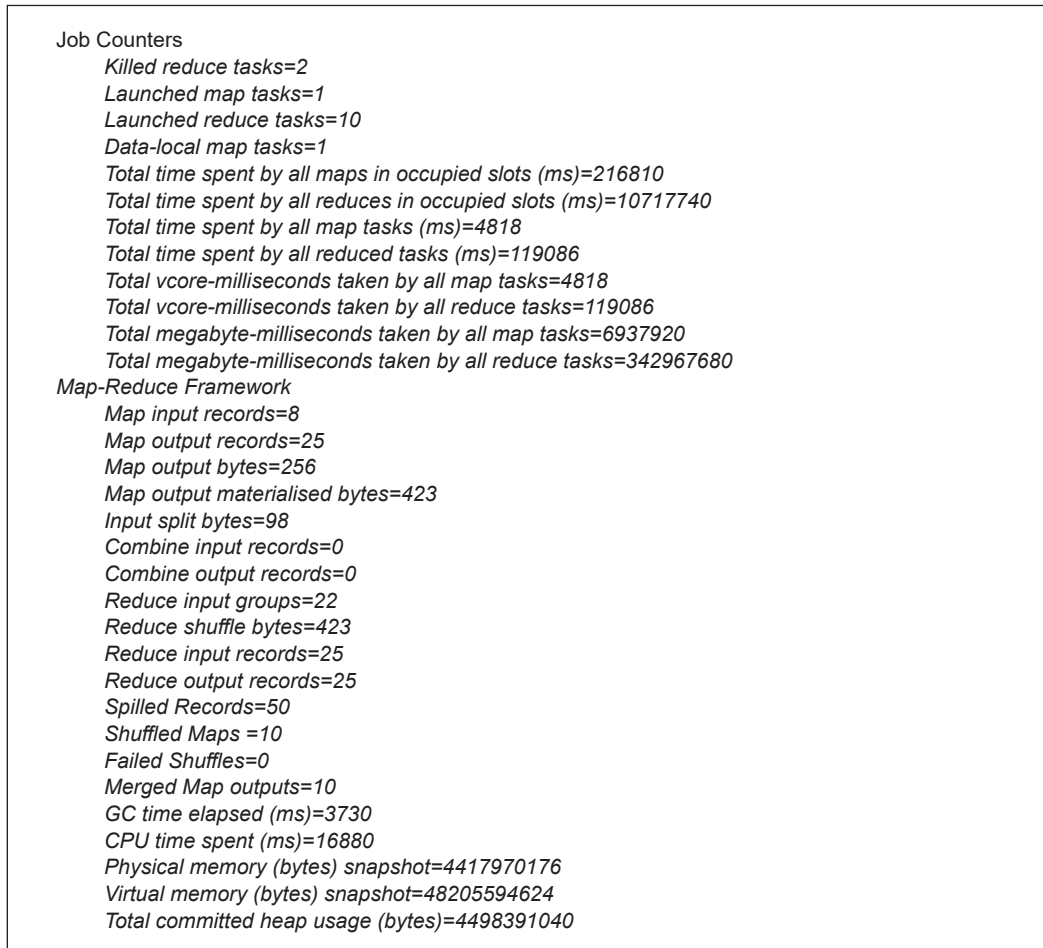


Figure 4. Result of the experiment (10 GB) on a single node (laptop)

RESULTS AND DISCUSSION

The experiment was set up and conducted on the Google Cloud platform and tested with 10 GB, 20 GB and 30 GB data; the ART was taken after 10 s, 30 s and 50 s, respectively, because of the data sizes. The result showed consistency for the number of tasks whose remaining time to complete was greater than the ART. At the 10 s threshold, two of the tasks (myclustertask-1 and myclustertask-3) RT were above the threshold of ART; at 30 s threshold, (myclustertask-1 and myclustertask-5) RT were above the threshold of ART and at 50 s threshold, (myclustertask-1 and myclustertask-4) RT were above the threshold of ART with consistency of number of straggling tasks detected. Table 3 shows the experiment results; a graphical representation of the result comparison for different data sizes is shown in Figures 5, 6, and 7. From the results when compared with Katrawi et al. (2020) (CLM) and Dean and Ghemawat (2008) (LATE) on straggling task detection, RMSTD shows an improvement of 19.51% and 23.30%, respectively.

PAPER CONTRIBUTIONS

The following are the contributions of this paper to the research work:

1. Increased accuracy: RMSTD using ART offers a more precise prediction of when the activity is anticipated to be finished by considering the task's typical behaviour over time. Temporary sluggishness, sporadic resource conflict, or network congestion that can lead to fluctuations in the RT have less of an impact

Table 3
Experimental data sizes and results

	RMSTD	CLM	LATE
Data size = 10 GB, Time threshold = 10 s			
No of Stragglers	2	3	4
Time Taken	12.86 s	17.20 s	20.30 s
ART	7.52 s	12.71 s	14.09 s
Data size = 20GB, Time threshold = 30 s			
No of Stragglers	2	4	3
Time Taken	31.20 s	37.30 s	37.10 s
ART	29.30 s	31.70 s	33.71 s
Data size = 30 GB, Time threshold = 50 s			
No of Stragglers	2	4	3
Time Taken	55.00 s	69.70 s	71.20 s
ART	49.55 s	62.90 s	64.81 s
Averages			
No of Stragglers	2	3.67	3.33
Time Taken	33.02	41.4	42.87
ART	28.79	35.77	37.54

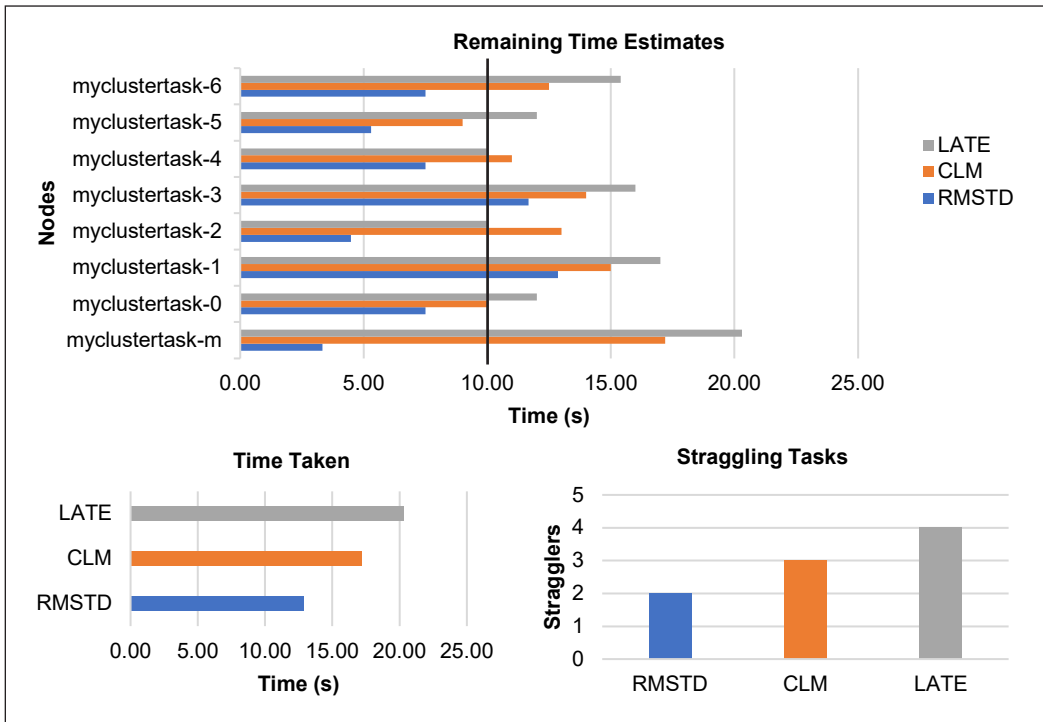


Figure 5. Experimental result with data size of 10 GB text file

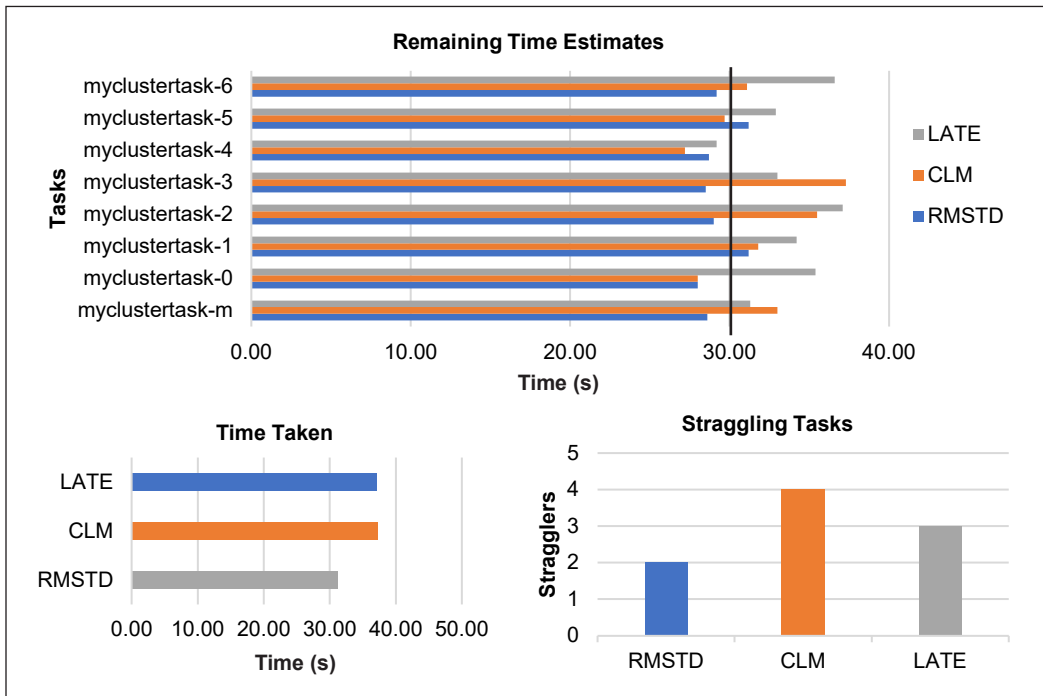


Figure 6. Experimental result with data size of 20 GB text file

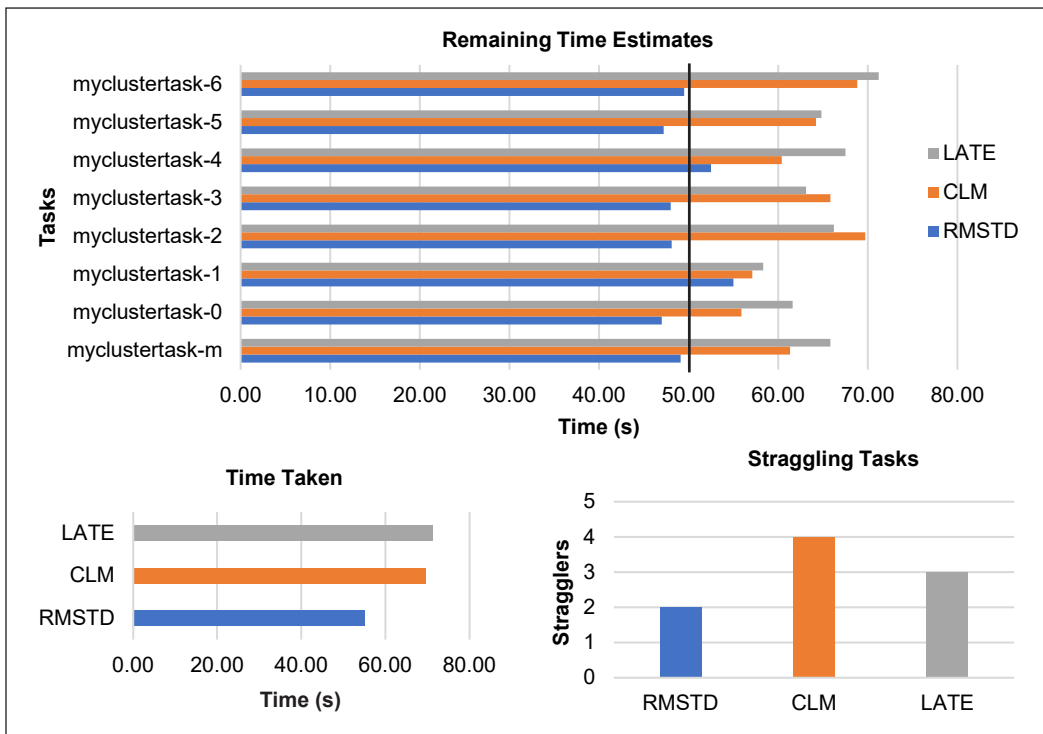


Figure 7. Experimental result with data size of 30 GB text file

- on this calculation. RMSTD through ART provides a more reliable and accurate indicator of work advancement.
2. Better straggler detection: Stragglers take significantly longer than the average or projected completion time. RMSTD makes detecting tasks that deviate from the norm and demonstrate straggling behaviour easier. This comparison aids in differentiating between jobs that may be suffering true performance concerns and those that are advancing at a normal rate.
 3. Smoothing out fluctuations: RMSTD provides a more reliable and smoothed estimate of the task's remaining time compared to other RT approaches. It considers the task's historical behaviour, considering the average time it has taken to accomplish identical pieces of work. It mitigates the impact of short-term oscillations or outliers in the Remaining Time, resulting in a more reliable estimate of job completion. Outliers and skews do not overly influence the average, and this can make it easier to identify tasks that are consistently taking longer than expected.
 4. Improved decision-making: When deciding on tasks, resources, or task scheduling, RMSTD offers a more trustworthy base in giving a more informed perspective on the anticipated completion timeframes of tasks by taking the past

average into account. Through this, it is easier to allocate resources more wisely and develop better task management plans, ultimately improving the efficiency of the work.

CONCLUSION

RMSTD provides a more stable, accurate, and reliable measure of task progress. It helps identify straggling tasks more effectively and facilitates better decision-making in Hadoop environments. It also offers a better advantage in detecting straggling tasks in Hadoop, and it has proven to be a useful approach for raising the effectiveness and performance of massively parallel data processing systems. Identifying stragglers and taking proactive steps to reduce their impact on job completion timeframes is feasible by continuously monitoring their progress and calculating the remaining execution time for tasks. In distributed computing systems, this strategy helps to optimise resource usage, shorten job execution times, and improve user experience.

ACKNOWLEDGEMENT

The authors acknowledged the contributions of all the authors to the successful completion of this article. The authors would also like to express their gratitude to Universiti Teknologi Malaysia for providing an enabling environment to carry out the study.

REFERENCES

- Ananthanarayanan, G., Kandula, S., Greenberg, A., Stoica, I., Lu, Y., Saha, B., & Harris, E. (2019). Reining in the outliers in MapReduce clusters using Mantri. In *9th USENIX Symposium on Operating Systems Design and Implementation (OSDI 10)* (pp. 265-278). USENIX Association.
- Chen, Q., Liu, C., & Xiao, Z. (2014). Improving MapReduce performance using smart speculative execution strategy. *IEEE Transactions on Computers*, 63(4), 954-967. <https://doi.org/10.1109/TC.2013.15>
- Dai, W., & Bassiouni, M. (2013). An improved task assignment scheme for Hadoop running in the clouds. *Journal of Cloud Computing*, 2, Article 23. <https://doi.org/10.1186/2192-113X-2-23>
- Dai, W., Ibrahim, I., & Bassiouni, M. (2016). Improving load balance for data-intensive computing on cloud platforms. In *2016 IEEE International Conference on Smart Cloud (SmartCloud)* (pp. 140-145). IEEE Publishing. <https://doi.org/10.1109/SmartCloud.2016.44>
- Dai, W., Ibrahim, I., & Bassiouni, M. (2017). An improved straggler identification scheme for data-intensive computing on cloud platforms. In *2017 IEEE 4th International Conference on Cyber Security and Cloud Computing (CSCloud)* (pp. 211-216). IEEE Publishing. <https://doi.org/10.1109/CSCloud.2017.64>
- Dean, J., & Ghemawat, S. (2008). MapReduce: Simplified data processing on large clusters. *Communications of the ACM*, 51(1), 107-113. <https://doi.org/10.1145/1327452.1327492>

- Ghare, G. D., & Leutenegger, S. T. (2005). Improving speedup and response times by replicating parallel programs on a SNOW. In D. G. Feitelson, L. Rudolph, U Schwiegelshohn (Eds.), *Job scheduling strategies for parallel processing. JSSPP 2004. Lecture Notes in Computer Science* (pp. 264-287). Springer. https://doi.org/10.1007/11407522_15
- Javadpour, A., Wang, G., Rezaei, S., & Li, K. C. (2020). RETRACTED ARTICLE: Detecting straggler MapReduce tasks in big data processing infrastructure by neural network. *Journal of Supercomputing*, 76, 6969-6993. <https://doi.org/10.1007/s11227-019-03136-6>
- Katravi, A. H., Abdullah, R., Anbar, M., & Abasi, A. K. (2020). Earlier stage for straggler detection and handling using combined CPU test and LATE methodology. *International Journal of Electrical and Computer Engineering*, 10(5), Article 4910. <https://doi.org/10.11591/ijece.v10i5.pp4910-4917>
- Katravi, A. H., Abdullah, R., Anbar, M., AlShourbaji, I., & Abasi, A. K. (2021). Straggler handling approaches in MapReduce framework: A comparative study. *International Journal of Electrical and Computer Engineering*, 11(1), 375-382. <https://doi.org/10.11591/ijece.v11i1.pp375-382>
- Ketu, S., Mishra, P. K., & Agarwal, S. (2020). Performance analysis of distributed computing frameworks for big data analytics: Hadoop vs Spark. *Computacion y Sistemas*, 24(2), 669-686. <https://doi.org/10.13053/CyS-24-2-3401>
- Kumar, G., Mohan, S., & Nagesh, A. (2021). An ensemble of feature subset selection with deep belief network based secure intrusion detection in big data environment. *Indian Journal of Computer Science and Engineering*, 12(2), 409-420. <https://doi.org/10.21817/indjese/2021/v12i2/211202101>
- Ouyang, X., Garraghan, P., McKee, D., Townend, P., & Xu, J. (2016). Straggler detection in parallel computing systems through dynamic threshold calculation. In *2016 IEEE 30th International Conference on Advanced Information Networking and Applications (AINA)* (pp. 414-421). IEEE Publishing. <https://doi.org/10.1109/AINA.2016.84>
- Ouyang, X., Wang, C., Yang, R., Yang, G., Townend, P., & Xu, J. (2018). ML-NA: A machine learning based node performance analyzer utilizing straggler statistics. In *2017 IEEE 23rd International Conference on Parallel and Distributed Systems (ICPADS)* (pp. 73-80). IEEE Publishing. <https://doi.org/10.1109/ICPADS.2017.00021>
- Phan, T. D., Pallez, G., Ibrahim, S., & Raghavan, P. (2019). A new framework for evaluating straggler detection mechanisms in MapReduce. *ACM Transactions on Modeling and Performance Evaluation of Computing Systems*, 4(3), Article 14. <https://doi.org/10.1145/3328740>
- Qiang, Y., Li, Y., Wei, W., Pei, B., Zhao, J., & Zhang, H. (2014). A job scheduling policy based on the job-classification and dynamic replica mechanism. *Information Technology Journal*, 13(3), Article 501. <https://doi.org/10.3923/itj.2014.501.507>
- Zaharia, M., Konwinski, A., Joseph, A. D., Katz, R., & Stoica, I. (2019). Improving MapReduce performance in heterogeneous environments. In *Proceedings of the 8th USENIX Symposium on Operating Systems Design and Implementation, OSDI 2008* (pp. 29-42). USENIX Association.

Comparative Analysis of Contaminant Levels in Leachate and Soil from Young and Old Landfills

Amir Detho, Aeslina Abdul Kadir* and Muhammad Aizat Azhar

Faculty of Civil Engineering and Built Environment, Universiti Tun Hussein Onn Malaysia, Batu Pahat, 86400, Johor, Malaysia

ABSTRACT

The leachate generated in municipal solid waste landfills tends to have extremely elevated levels of organic and inorganic pollutants influenced by the age and variety of landfills. This research aims to conduct a comparative analysis between two landfills, Krubong Landfill Sites (KLS) and Bukit Bakri Landfill Sites (BBLs). Based on the standard limit set by the Malaysia Environment Quality Act (MEQA), the average values of the leachate parameters at KLS and BBLs were recorded. These parameters include pH (8.84 for KLS and 9.08 for BBLs), temperature (30.22°C for KLS and 30.06°C for BBLs), Chemical Oxygen Demand (COD) (3695 mg L⁻¹ for KLS and 11289 mg L⁻¹ for BBLs), Biological Oxygen Demand (BOD) (1695 mg L⁻¹ for KLS and 3325 mg L⁻¹ for BBLs), and ammonia nitrogen (1107 mg L⁻¹ for KLS and 1390 mg L⁻¹ for BBLs). The findings of this research suggest that the age of the landfill indeed influences the characteristics of leachate and soil. KLS, being a mature landfill, demonstrated low biodegradability. On the other hand, BBLs, being a young landfill, exhibited high biodegradability. The highest heavy metal concentration in the soil sample of KLS was Barium (Ba), with 409 ppm, followed by Zirconium (Zr) at 297 ppm and Vanadium (V) at 114 ppm. For BBLs, Zirconium (Zr) and Thorium (Th) were 209 ppm, Rubidium (Rb) was detected at 86 ppm, and Chromium (Cr) was 57 ppm. In overall essence, the age of a landfill significantly influences its characteristics. Newly established landfills tend to contain a greater quantity of organic matter compared to older ones.

ARTICLE INFO

Article history:

Received: 02 November 2023

Accepted: 01 February 2024

Published: 26 August 2024

DOI: <https://doi.org/10.47836/pjst.32.5.20>

E-mail addresses:

amirdetho@gmail.com (Amir Detho)

aeslina@uthm.edu.my (Aeslina Abdul Kadir)

aizat@skveholdings.com (Muhammad Aizat Azhar)

* Corresponding author

Keywords: Heavy metal, mature landfill, organic material, soil characterisation, young landfill

INTRODUCTION

Leachate is a fluid percolated through diverse solid waste, acquiring dissolved or suspended matter. Landfilling is a widely preferred technique for solid waste disposal in numerous countries, with Malaysia as a prime example. Malaysia has over 230 landfills (Daud et al., 2022; Norsa'adah et al., 2020). Most are open dumpsites, which present grave environmental concerns to public health and societal well-being. Landfilling is considered the most cost-effective and environmentally sound method for solid waste disposal compared to other techniques like composting, incineration, and gasification. Nonetheless, leachate production from landfills is a significant issue related to this disposal method (Daud et al., 2020; Hussein et al., 2019).

In a landfill, a series of interconnected physical, chemical, and biological processes take place, leading to the degradation or transformation of the waste. As water permeates through the landfill, leachate is generated from the solid waste through these processes (Sackey & Miezah, 2022). The properties of the leachate and soil generated in landfills exhibit significant variability, influenced by factors such as the makeup of the solid waste, the rate of precipitation, the hydrology of the site, the degree of compaction, the design of the cover, the age of the waste, the sampling methods, the interaction of the leachate with its surroundings, as well as the design and functioning practices (Salami & Susu, 2019).

Other than that, leachate from landfills can contaminate surface water and groundwater, leading to diverse problems in forming leachate water and the amount of pollutants contained. This contamination occurs mainly when heavy rain accelerates the leachate percolating process through the soil layers at the base of the landfill, combining with groundwater to cause pollution (Detho et al., 2021a).

Leachate can be treated through various biological, chemical and physical treatments. The specific characteristics of the leachate govern the selection of a treatment method. In other words, the leachate treatment system is largely dictated by the individual properties of the leachate. The properties of leachate vary based on multiple factors, including climate, landfill age, amount of rainfall, operational practices at the landfill, and the volume and nature of the waste (Detho et al., 2021b; Zin, 2013).

Leachate from landfills contains high amounts of organic and inorganic material, heavy metals, and toxic chemicals in high concentrations. Landfill leachate constitutes a significant contributor to the contamination of both groundwater and surface water (Naveen et al., 2017). Leachate not only causes groundwater pollution but also soil contamination. Therefore, due to its characteristics, before leachate is discharged into the environment, it must be properly treated by physical, chemical and biological methods. The absorption of water leachate into the soil will cause pollution. Leachate from landfills causes pollution to ecosystems in the surrounding areas. In addition, soil contamination is also dangerous to surrounding landfills, the usage of landfills, and even to local communities that live nearby (Siddiqua et al., 2022).

Recently, researchers have been paying attention to leachate pollution and soil contamination around landfill areas due to the leachability of leachate from landfills. The soil serves as a natural filtration system for various substances present in water, including particles, toxic substances, acids, and some microorganisms. Its intricate layered composition helps reduce water runoff, capture larger particles, and neutralise acidic conditions in the soil (Dorioz et al., 2006).

In addition to leachate, soil plays a crucial role in landfill sites. It acts as a medium where contaminated materials are deposited and absorbs the leachate produced during the waste decomposition. Soil is a natural resource that requires careful monitoring due to its constant interactions with other media, such as air, groundwater, and surface water, through processes like evaporation, erosion, and infiltration (Ramaiah & Krishnaiah, 2014).

Soils have different textures like sandy, loamy, and clay soil, which were used as filters to reduce the quantity of organic and inorganic composition in leaching liquid. Texture and soil types will contribute to different absorption quantities and types of organic and inorganic compositions at a certain distance and depth of landfills. Therefore, soil is able to filter the content of inorganic substances present in the leachate water that goes through it. The type of inorganic substance that the soil can absorb depends on soil type and natural content in the soil itself. Therefore, soils become contaminated by leachate landfills because of their ability as a filter (Kanmani & Gandhimathi, 2013).

The age of a landfill strongly influences the properties of leachate. With an increase in landfill age, the biological decomposition of the deposited waste shifts from a relatively short decomposition phase to a longer phase, encompassing two sub-phases: acidic and methanogenic (Aziz, 2010). According to reports, the leachate from these two stages contains a variety of different substances. Volatile fatty acid concentrations in leachate from more recent landfills (young leachate) tend to be higher, which suggests that the leachate is more likely to be in the acidic phase. Younger landfills enter the acidic phase, and with time, they transition into the methanogenic phase. In the methanogenic phase, fatty acids from the acidic or acidogenic phase are converted into methane and carbon dioxide. This conversion between the two phases is time-consuming, as organic matter needs to decompose into gaseous and liquid fermentation products (Lindamulla et al., 2022). The properties of leachate and soil at the landfill were important to determine the lead of contamination and to identify the correct treatment for leachate and its pollutants.

Therefore, in this study, the characteristics of leachate and soil, two different ages of landfills, i.e., young landfill (<5 years) and old landfill (>10 years), were investigated. Moreover, this research aims to conduct a comparative analysis between two landfills, Krubong Landfill Sites (KLS) and Bukit Bakri Landfill Sites (BBLs). Thus, this study can better understand leachate and lead to more efficient managerial solutions and treatability options.

MATERIALS AND METHODS

Location of Landfills

The samples of leachate and soil were gathered from selected locations, namely the Bukit Bakri Landfill site (BBLs) in Muar and the Krubong Landfill site (KLS) in Melaka, Malaysia. During leachate and soil sample collection, safety equipment, storage for sample and procedure were followed. Leachate was kept in a closed container and labelled at cold storage at 4°C before being tested in the laboratory. For soil sample collection, grab samples with depths 0m and 1m were put in plastic bags and labelled separately. The landfill location shown in Figures 1 and 2 is selected based on the different ages of the landfill.

BBLs was selected because the landfill was constructed in 2010 and is less than five years old. BBLs is situated at Latitude 2.0417° and Longitude 102.6722° Muar to Melaka. It has a total land area of 14.6 hectares and a leachate-gathered pond. The site accepts approximately 200–270 tons of waste.



Figure 1. Location points and geomorphological map



Figure 2. Location of landfills

KLS is the oldest landfill, constructed in 1996 and classified as a mature landfill older than ten years. The landfill sites selected are classified as young and old landfills. KLS is situated at Latitude 2.286362° and Longitude 102.251043° Krubong to Melaka. It occupies a total area of 242 hectares and is equipped with a leachate-gathered pond and treatment plant. The site accepts approximately 900 tons of waste.

Leachate Samples Collection at the Site

Leachate was gathered from the collection pool using a submersible pump at a depth of 1500 mm, and the sample points were the routes of leachate that were active with stream flow. Sampling was done thrice a month, and the samples were taken throughout the study for February and March, which is within the dry season. The leachate samples were placed into a polytetrafluoroethylene (TFE) plastic bottle until it was full and tightly closed. Then, they were transported back to the laboratory to be tested for BOD, COD, and pH content. Then, the leachate sample brought back to the lab was filtered through a 0.7µm glass microfiber filter to ensure no suspended solids were in the leachate during the testing procedure. Each sample was duplicated and stored in a cool room.

Characteristics of Leachate

The samples were gathered and examined to evaluate their properties and stability. Physical characteristics such as temperature and pH measurements were assessed after the sampling process. The chemical characteristics, COD, BOD and ammonium nitrogen, were determined using a DR 6000, and the readings were recorded in units of mg L⁻¹ according to the standard method (Eaton & Franson, 2005). The concentration of metal Thorium (Th), Zirconium (Zr), Rubidium (Rb), Chromium (Cr), Vanadium (V), Gallium (Ga), and Cerium (Ce) was quantified using an inductively coupled plasma-optical mass spectrometer (ICPMS). Leaching tests are widely used to estimate the release of potentially hazardous elements from waste (Hashim et al., 2022). The test was conducted to ensure all the manufactured brick samples were satisfied and complied with standards. The USEPA SW 864 Method 1311 was used for the leachability testing in this research. All the experiment work was analysed at the Environment Laboratory, UTHM. The results were compared to those previously published by Eaton and Franson (2005).

Soil Collection at Site

Soil samples were collected using Soil Auger due to the hardness and compactness of the soil in this landfill, as illustrated in Figure 3. Soil samples were collected to test the heavy metal concentration. The method used to take the soil sample is the grab samples method. Ten sampling points have been identified and collected at 5 m to 10 m around the parameter area of the landfill with depths of 0 m and 1m around the parameter

area of the landfill to make a complete coverage around. The weight of each soil sample is about two kilograms. Collected samples were placed in plastic bags and labelled separately with each point. The same method is repeated at different points. Then, the soil samples were brought back to the laboratory for testing part.



Figure 3. Soil collection techniques

Soil Preparation

Soil samples were placed on plates and oven-dried at $100 \pm 5^\circ\text{C}$ for 24 hours to ensure they were dry. After drying, soil samples were ground and crushed to facilitate sieving. All this work was done in the Geotechnical Engineering Laboratory, UTHM.

Pellet Preparation

Soil samples were shaped into pellets. The pellet should be in fine powder condition because X-rays can only penetrate a few millimetres from the sample's surface. The soil samples that have been dried and crushed have to sieve through $63 \mu\text{m}$. Then, soil samples were mixed with wax at a ratio of 9:3, where 9 g were used for the soil sample, and 3 g were used for wax. Wax sticks the soil sample particles together in the pressed pellets process. Next, the samples were pressed into pellets using a compression machine and analysed. All the work has been done in the Environmental Analytical Laboratory, UTHM, as shown in Figure 4.

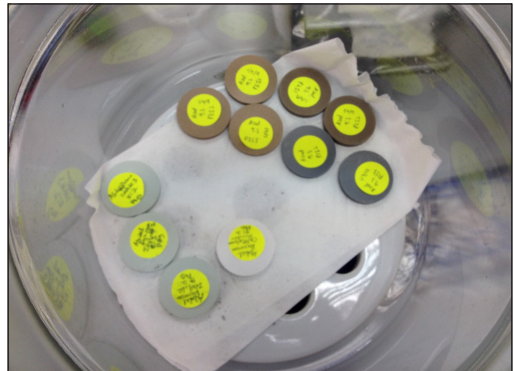


Figure 4. Pellet preparation

Laboratory Test for Soil Sample

Soil samples were analysed using X-Ray Fluorescence (XRF) to evaluate the heavy metal concentration in the soil sample. The soil samples were prepared in pellet shape before being used by the test XRF machine. The pellet processing should be in fine powder condition because X-rays can only penetrate a few millimetres from the surface of samples. Major element contents for the soil sample were measured using XRF equipment in the Environmental Analytical Laboratory at UTHM. XRF tool is a quantitative and qualitative analysis technique and very sensitive detection. The detection limit of this device depends on the elements to be analysed and the sample matrix, and detection limits are typically

between 10 and 100 ppm (part per million). XRF is frequently used for analysing major and trace elements in rock, minerals, and sediment due to its relatively easy and inexpensive sample preparation. This technique does not require sample digestion or fusion complex and is likely to increase the risk of errors.

RESULTS AND DATA ANALYSIS

Leachate Properties

Two landfills were selected in this study based on their age and activity characteristics of landfill. The leachate and soil collection samples were composed manually at two landfill sites, Bukit Bakri and KLS. The samples were preserved in a container filled with ice at 4°C upon collection. A bottle of each sample (90 mL) for each site was also preserved in the container in case of need for data reproduction, according to Eaton and Franson (2005). The results of samples obtained from both sites during laboratory testing are illustrated in Table 1. Two different ages of landfills, i.e., young landfills (<5 years) and old landfills (>10 years), were investigated in this study. The average leachate properties values at KLS and BBLs, i.e., temperature (30.22°C and 30.06°C), pH (8.84 and 9.08), COD (3695 mg L⁻¹ and 11289 mg L⁻¹), BOD (1695 mg L⁻¹ and 3325 mg L⁻¹), and ammonia nitrogen (1107 mg L⁻¹ and 1390 mg L⁻¹), were recorded based on MEQA standard limit.

Table 1
Properties of leachate at BBLs and KLS

Parameters	Bukit Bakri Landfill			Krubong Landfill		
	Range		Average	Range		Average
	High	Low		High	Low	
pH (0-14)	9.31	8.67	9.08	9.37	8.68	8.84
Temperature (°C)	29.72	28.12	30.06	32.58	28.12	30.22
COD (mg L ⁻¹)	18460	4425	11289	5210	3200	3695
BOD (mg L ⁻¹)	3690	3510	3325	2350	1073	1695
Ammonia, NH ₄ ⁺ (mg L ⁻¹)	1519.52	1231.05	1390	1407.21	950.74	1107

pH Measurement

Figure 5 shows the comparison of pH value between BBLs and KLS. Results from BBLs show that it increases from an 8.90 pH value to a 9.27 pH value. A stable landfill is frequently greater than a young landfill (Kulikowska et al., 2008). KLS shows that pH values rise from 8.80 to 8.97. The variation may arise from the stable leachate generated while fermenting methane, either during or after the process. The Environmental Quality Regulation 2009 and Malaysian Environmental Quality Act (Act-127) provide a permitted pH range of 6.0 to 9.0 (Aziz et al., 2010).

Temperature Measurement

Figure 6 shows the temperature values from both sites plotted against the time. The temperatures of the samples obtained from both sites are different. The temperatures highly depend on the local climate. From week 1 to week 2, the temperature is high because of sunny days in all locations, and from week 3 to week 4, the temperature drops from 30.06°C to 29.26°C due to rainy days. Figure 6 represents comparison temperatures between BBLs and KLS. The results show that from both landfill sites, the value of temperatures gradually decreased from 33.64°C to 28.30°C due to the sunny season to the rainy season. The decreasing trend for temperature in the site was affected by seasonal variations, ages of waste and location of waste, which have significant effects on temperatures (Keerio et al., 2020).

Chemical Oxygen Demand (COD) Analysis

From Figure 7, the trend of the COD measurements is increasing on rainy days. COD values from both sites increase from sunny days to rainy days because organic matter from solid waste increases with the rainy week, which increases COD values. The result we can see here is that the COD values of sample BBLs (young landfill) are higher than KLS (old landfill). The maximum values indicated for BBLs were 18293 mg L⁻¹, which seemed to exceed the acceptable levels stated by the Environmental Quality (Pollution Control from Solid Waste Transfer Stations and Landfills) Regulation 2009. COD values

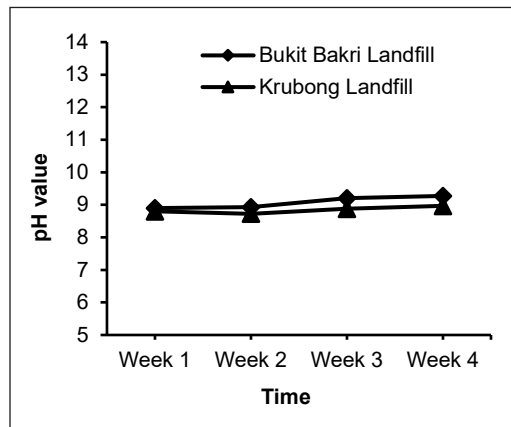


Figure 5. pH range comparison between BBLs and KLS

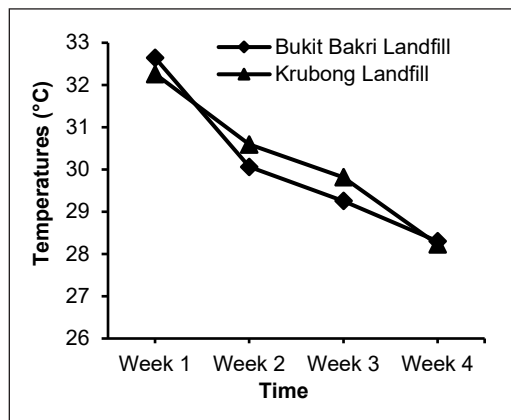


Figure 6. Temperature range comparison between BBLs and KLS

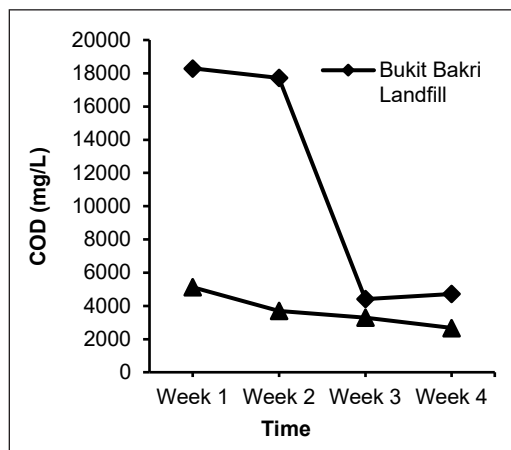


Figure 7. COD value of BBLs and KLS

were in the previous study, normally between (18000 and 2600 mg L⁻¹) (Aziz et al., 2010). Meanwhile, the COD value from KLS, the results show that (5123 to 2667 mg L⁻¹) were decreased due to dilution of seasonal variation, likely influenced by rainfall, which led to a reduction in the concentration of landfill leachate produced at the landfill site (Zainol et al., 2012). The results were a gradual decrease in both landfill COD values.

Biochemical Oxygen Demand (BOD) Analysis

Figure 8 demonstrates the BOD value of BBLs and KLS. BOD values from BBLs from week 1 to week 3 showed similar values, but in week 4, they decreased from 3583 mg L⁻¹ to 2552 mg L⁻¹. Meanwhile, the BOD value for KLS decreased from 2608 mg L⁻¹ to 1128 mg L⁻¹. In this study, BOD changes with landfill age. Generally, BOD levels for young landfills typically vary from 2000 to 30000 mg L⁻¹, while for older landfills, the range was 100 to 200 mg L⁻¹ (Tchobanoglous et al., 1993). The BBLs value in this research aligns with previous researchers' findings (Bashir et al., 2010). Nevertheless, the BOD for BBLs and KLS values seemed to exceed the acceptable levels (50 mg L⁻¹), and the landfill leachate required treatments to be environmentally accepted.

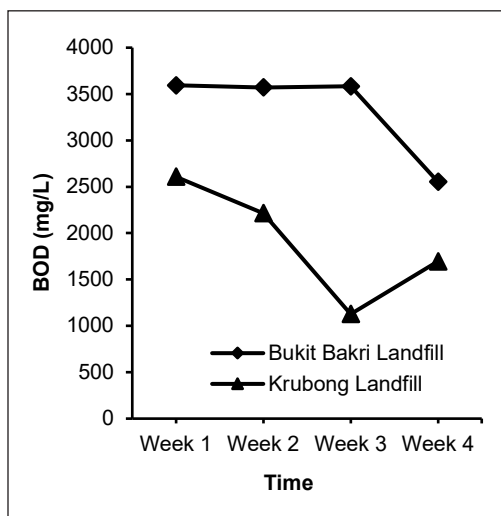


Figure 8. BOD value of BBLs and KLS

Ammonia Nitrogen Measurement

Figure 9 represents the ammonia-N value between BBLs and KLS, which slightly increases weekly. Ammoniacal nitrogen levels in leachate samples from the BBLs and KLS ranged between 1316-1337 mg L⁻¹ and 1112-1051 mg L⁻¹, respectively. However, higher values ranging from 1189 to 2117 mg L⁻¹ have been reported in previous studies by other researchers (Ghafari et al., 2010; Aziz et al., 2010). The high ammoniacal nitrogen content is the main cause of algal growth enhancement, eutrophication, biological treatment

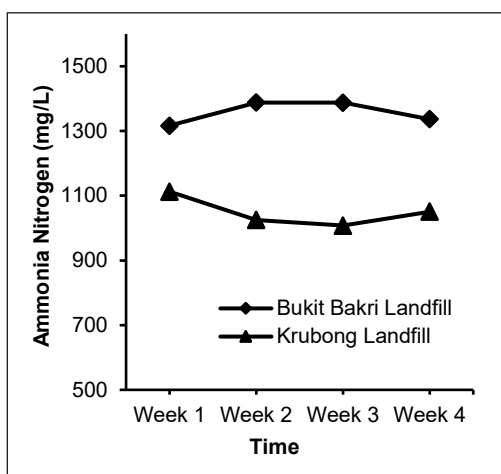


Figure 9. Ammonia Nitrogen value between BBLs and KLS

disruption and decreased dissolved oxygen (Keerio et al., 2022; Aziz et al., 2010). Consequently, its extreme toxicity, ammoniacal nitrogen poses a serious hazard to aquatic species (Bashir et al., 2010). Ammoniacal nitrogen concentrations typically vary from 10 to 800 mg L⁻¹ for young landfills (<5 years old) and from 20 to 40 mg L⁻¹ for mature landfills (> 10 years old), respectively.

Heavy Metal Concentration

Figure 10 shows the concentration of heavy metals and compares the concentrations of heavy metals in BBLS and KLS in leachate samples tested using ICPMS. Barium (Ba) represents the highest concentration value of heavy metals, with 362ppb for BBLS and 287ppb for KLS. Meanwhile, another heavy metal detected is Manganese (Mn) from both sites, with 277ppm in sample leachate from BBLS and 303 from KLS. The lowest heavy metals concentration in the leachate sample shows that Lead (Pb) with 14ppb and 16ppb were detected, respectively. In general, the concentration of heavy metals rises as the waste age increases, which raises the solubility of the metal. The stable leachate does have decreased heavy metal contents at this point (Kulikowska, 2008).

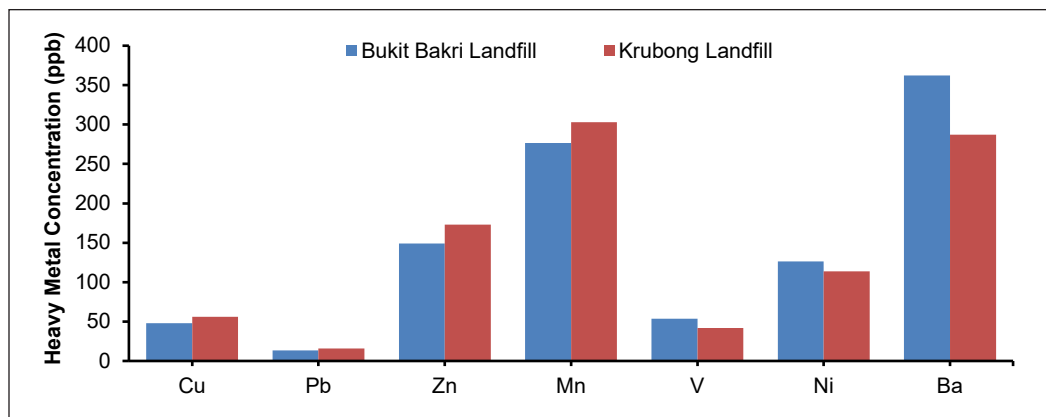


Figure 10. Heavy metal comparison between BBLS and KLS

Heavy Metal Concentration Composition of Soil

Figure 11 shows the soil heavy metals concentration composition from BBLS and KLS for this study findings. The result indicates that the soil from KLS exhibits the highest Barium (Ba) concentration at 409 ppm. Cesium (Cs) with 2 ppm was recorded as the lowest in soil sample BBLS. Meanwhile, soil samples from BBLS and KLS have a similar heavy metal concentration composition, Zirconium (Zr), with 209 ppm and 297 ppm. Most heavy metal concentrations in soil samples are BBLS and KLS, where certain chemical compounds have the lowest concentration value, for example, Cobalt (CO) with 4 ppm and 5 ppm.

Figure 11 shows a comparison of heavy metal concentration between BBLs and KLS with major elements that are contained in a soil sample. The result shows that the highest value of heavy metal concentration is Barium (Ba), with 409 ppm in the soil sample from KLS. Meanwhile, the sample soil from BBLs with a heavy metal concentration of Barium (Ba) is 32 ppm. The similar value of heavy metal concentration from both sample soil in KLS and BBLs is Chromium (Cr), with 56 ppm and 57 ppm. Other than that, the lowest value of heavy metals concentration is Cobalt (Co), with 5 ppm and 4 ppm from KLS and BBLs. The result from XRF also supported the result from ICPMS where certain chemical compounds, for example, Lead (Pb), Zinc (Zn), Manganese (Mn), Vanadium (V), Nickel (Ni) and Barium (Ba), where the heavy metals exist in leachate sample.

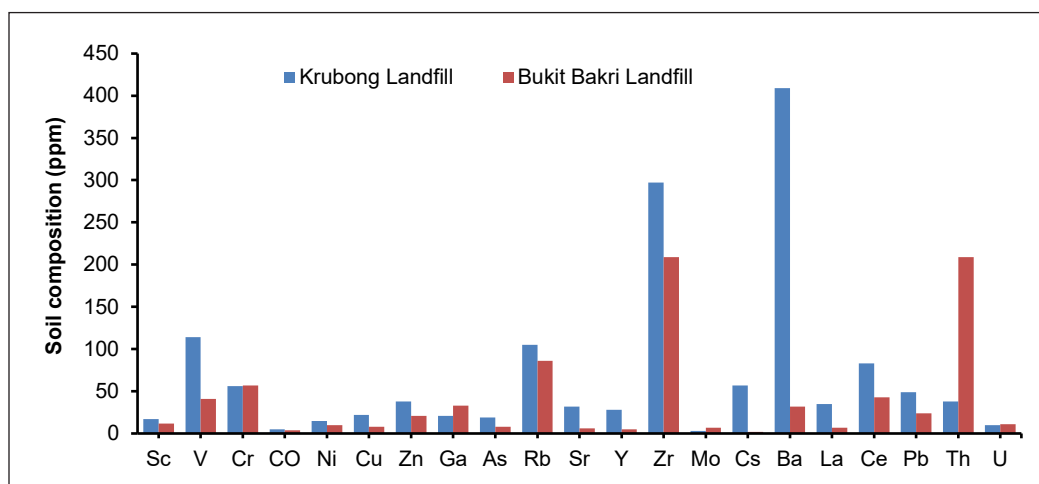


Figure 11. Comparison of heavy metals concentration between Bukit Bakri and KLS

CONCLUSION

The main objective of this study is to study the leachate and soil characteristics of BBLs (young landfill) and KLS (old landfill). Physical parameter characteristics were pH and temperature. The pH values in BBLs and KLS were almost the same, 9.08 and 8.84. Meanwhile, the temperature results from BBLs and KLS were almost the same, 30.06°C and 30.22°C.

The chemical parameters analysed includes COD, BOD, and ammonia nitrogen. The average COD values from BBLs were recorded at 11289 mg L⁻¹, and the COD value of KLS was recorded at 3695 mg L⁻¹. The BOD result was recorded at 3325 mg L⁻¹ from BBLs and 1695 mg L⁻¹ from KLS. Ammonia nitrogen results for BBLs and KLS were 1316–1337 mg L⁻¹ and 1112–1051 mg L⁻¹, respectively.

For soil characteristics, the concentration of heavy metals in the sample from site KLS and BBLs was detected using XRF. The highest heavy metal concentration in sample KLS

Site is Barium (Ba) at 409 ppm, followed by Zirconium (Zr) at 297 ppm and Vanadium (V) at 114 ppm. The highest heavy metal concentration in sample BBLs Site is Zirconium (Zr), and Thorium (Th) was 209 ppm. Rubidium (Rb) was detected at 86 ppm, and Chromium (Cr) was detected at 57 ppm. For leachate results, the highest value of heavy metal concentration from BBLs and KLS is Barium with 32 ppb, and for KLS, Manganese (Mn) with 303 ppm. The result shows that Lead (Pb) represents the lowest value of heavy metal concentration in the leachate sample from BBLs with 14 ppm; for KLS, the lowest heavy metal concentration is also Lead (Pb) with a value of 16 ppm, respectively.

The result shows that seasonal variations, ages of waste, and location of waste where available moisture have significant effects on temperatures. This study demonstrates that the age of the leachate and soil significantly influences their composition. The biodegradable portion of organic contaminants in the leachate decreases with increasing landfill age. The overall conclusions and the result of the comparison show clearly that a landfill's age affects its characteristics. In comparison to older landfills, more organic waste is often present in newer landfills. In general, new landfills have higher quantities of contaminants than older ones. In order to find a better understanding of this study, it is suggested that this study be extended to investigate leachate and soil characteristics in more specific detail with consideration of more aspects.

ACKNOWLEDGEMENT

This research was supported by UTHM Publisher's Office via Publication Fund E15216, Universiti Tun Hussein Onn Malaysia (UTHM), Batu Pahat, Johor, Malaysia, for providing the tools and facilities needed for this research.

REFERENCES

- Aziz, S. Q., Aziz, H. A., Yusoff, M. S., Bashir, M. J., & Umar, M. (2010). Leachate characterization in semi-aerobic and anaerobic sanitary landfills: A comparative study. *Journal of Environmental Management*, 91(12), 2608-2614.
- Bashir, M. J., Aziz, H. A., Yusoff, M. S., & Adlan, M. N. (2010). Application of response surface methodology (RSM) for optimization of ammoniacal nitrogen removal from semi-aerobic landfill leachate using ion exchange resin. *Desalination*, 254(1-3), 154-161. <https://doi.org/10.1016/j.desal.2009.12.002>
- Daud, Z., Detho, A., Rosli, M. A., Awang, H., Ridzuan, M. B. B., & Tajarudin, H. A. (2022). Optimization of mixing ratio, shaking speed, contact time, and pH on reduction of Chemical Oxygen Demand (COD) and Ammoniacal Nitrogen (NH₃-N) in leachate treatment. *Journal of the Air & Waste Management Association*, 72(1), 24-33. <https://doi.org/10.1080/10962247.2020.1862362>
- Daud, Z., Detho, A., Rosli, M. A., Abubakar, M. H., Samo, K. A., Rais, N. F. M., & Tajarudin, H. A. (2020). Ammoniacal nitrogen and COD removal from stabilized landfill leachate using granular activated carbon and green mussel (*Perna viridis*) shell powder as a composite adsorbent. *Desalination Water Treat*, 192, 111-117. <https://doi.org/10.5004/dwt.2020.25470>

- Detho, A., Daud, Z., Rosli, M. A., Ridzuan, M. B., Awang, H., Kamaruddin, M. A., & Halim, A. A. (2021a). COD and ammoniacal nitrogen reduction from stabilized landfill leachate using carbon mineral composite adsorbent. *Desalination and Water Treatment*, *210*, 143-151. <https://doi.org/10.5004/dwt.2021.26500>
- Detho, A., Daud, Z., Rosli, M. A., Ridzuan, M. B. B., & Awang, H. (2021b). Reduction of COD and ammoniacal nitrogen from landfill leachate using granular activated carbon and green mussel adsorbent. *Desalination and Water Treatment*, *223*, 218-226. <https://doi.org/10.5004/dwt.2021.27140>
- Dorioz, J. M., Wang, D., Poulencard, J., & Trevisan, D. (2006). The effect of grass buffer strips on phosphorus dynamics—A critical review and synthesis as a basis for application in agricultural landscapes in France. *Agriculture, Ecosystems & Environment*, *117*(1), 4-21. <https://doi.org/10.1016/j.agee.2006.03.029>
- Eaton, A. D., & Franson, M. A. H. (Eds.) (2005). *Standard methods for the examination of water and wastewater (21st edition)*. American Public Health Association.
- Ghafari, S., Aziz, H. A., & Bashir, M. J. K. (2010). The use of poly-aluminum chloride and alum for the treatment of partially stabilized leachate: A comparative study. *Desalination*, *257*(1-3), 110-116. <https://doi.org/10.1016/j.desal.2010.02.037>
- Hashim, A. A., Abdul Kadir, A., Sarani, N. A., Hassan, M. I. H., Kersnansamy, A., & Abdullah, M. M. A. B. (2022). Immobilization of metals in fired clay brick incorporated with aluminium-rich electroplating sludge: properties and leaching analysis. *Sustainability*, *14*(14), Article 8732. <https://doi.org/10.3390/su14148732>
- Hussein, M., Yoneda, K., Zaki, Z. M., & Amir, A. (2019). Leachate characterizations and pollution indices of active and closed unlined landfills in Malaysia. *Environmental Nanotechnology, Monitoring & Management*, *12*, Article 100232. <https://doi.org/10.1016/j.enmm.2019.100232>
- Kanmani, S., & Gandhimathi, R. (2013). Assessment of heavy metal contamination in soil due to leachate migration from an open dumping site. *Applied Water Science*, *3*, 193-205. <https://doi.org/10.1007/s13201-012-0072-z>
- Keerio, H. A., Bae, W., & Panhwar, S. (2022). Nitrite accumulation at low ammonia concentrations in wastewater treatment plants. *Sustainability*, *14*(24), Article 16449. <https://doi.org/10.3390/su142416449>
- Keerio, H. A., Bae, W., Park, J., & Kim, M. (2020). Substrate uptake, loss, and reserve in ammonia-oxidizing bacteria (AOB) under different substrate availabilities. *Process Biochemistry*, *91*, 303-310. <https://doi.org/10.1016/j.procbio.2019.12.023>
- Kulikowska, D., & Klimiuk, E. (2008). The effect of landfill age on municipal leachate composition. *Bioresource Technology*, *99*(13), 5981-5985. <https://doi.org/10.1016/j.biortech.2007.10.015>
- Lindamulla, L., Nanayakkara, N., Othman, M., Jinadasa, S., Herath, G., & Jegatheesan, V. (2022). Municipal solid waste landfill leachate characteristics and their treatment options in tropical countries. *Current Pollution Reports*, *8*, 273-287. <https://doi.org/10.1007/s40726-022-00222-x>
- Naveen, B. P., Mahapatra, D. M., Sitharam, T. G., Sivapullaiah, P. V., & Ramachandra, T. V. (2017). Physico-chemical and biological characterization of urban municipal landfill leachate. *Environmental Pollution*, *220*(Part A), 1-12. <https://doi.org/10.1016/j.envpol.2016.09.002>

- Norsa'adah, B., Salinah, O., Naing, N. N., & Sarimah, A. (2020). Community health survey of residents living near a solid waste open dumpsite in Sabak, Kelantan, Malaysia. *International Journal of Environmental Research and Public Health*, 17(1), Article 311. <https://doi.org/10.3390/ijerph17010311>
- Ramaiah, G. V., & Krishnaiah, S. (2014). Characterization of contaminated soil and surface water/ground water surrounding waste dump sites in Bangalore. *International Journal of Environmental Research and Development*, 4(2), 99-104.
- Sackey, L. N., & Miezah, K. (2022). Determining the quality of leachate at Sarbah landfill site at Weija, Ghana. *Emerging Challenges in Environment and Earth Science*, 4, 1-13.
- Salami, L., & Susu, A. A. (2019). A comprehensive study of leachate characteristics from three soluos dumpsites in Igando Area of Lagos State, Nigeria. *Greener Journal of Environmental Management and Public Safety*, 8(1), 1-14. <http://doi.org/10.15580/GJEMPS.2019.1.110118520>
- Siddiqua, A., Hahladakis, J. N., & Al-Attiya, W. A. K. A. (2022). An overview of the environmental pollution and health effects associated with waste landfilling and open dumping. *Environmental Science and Pollution Research*, 29, 58514-58536. <https://doi.org/10.1007/s11356-022-21578-z>
- Tchobanoglous, G., Theisen, H., & Vigil, S. A. (1993). *Integrated solid waste management: Engineering principles and management issues* (2nd ed.). McGraw-Hill.
- Zainol, N. A., Aziz, H. A., & Ibrahim, N. (2013). Treatment of Kulim and Kuala Sepetang landfills leachates in Malaysia using poly-aluminium chloride (PACl). *Research Journal of Chemical Sciences*, 3(3), 52-57.
- Zin, N. S. M., Aziz, H. A., Adlan, M. N., Ariffin, A., Yusoff, M. S., & Dahlan, I. (2013). A comparative study of Matang and Kuala Sembeling landfills leachate characteristics. *Applied Mechanics and Materials*, 361, 776-781. <https://doi.org/10.4028/www.scientific.net/AMM.361-363.776>

Physical and Mechanical Properties of Palm Frond-based Fiberboard Composite

Moraida Hasanah¹, Tengku Jukdin Saktisahdan¹, Susilawati^{2*}, Frannoto¹,
Adjie Padriansyah¹ and Irfan Hafizh¹

¹Department of Mechanical Engineering, Universitas Asahan, Asahan 21216, Indonesia

²Department of Physics, Faculty of Mathematics and Natural Sciences, Universitas Sumatera Utara, Medan 20155, Indonesia

ABSTRACT

Novel research has been conducted to characterize fiberboards made from palm frond fibers and polyester resin. In this study, polyester resin served as the matrix, and palm frond fibers with a size of 80 mesh were employed as the filler. The fiberboard composites were produced using a hot press at 70°C for 20 minutes, with varying mass compositions of polyester resin to palm frond fibers: S1 (60%:40%), S2 (65%:35%), S3 (70%:30%), S4 (75%:25%), and S5 (80%:20%). Parameters observed include physical properties (density and porosity), mechanical properties (impact, tensile, and flexural strength), and microstructure analysis using scanning electron microscope (SEM) and differential scanning calorimetry (DSC). The results indicate that S5 exhibits optimal properties, including a density value of 1.197 g/mL, low porosity at 0.232%, and mechanical characteristics with an impact strength of 271.251 J/m², tensile strength of 23.221 MPa, and flexural strength of 149.837 MPa. However, according to the DSC data, S1 stands out with a higher temperature water evaporating point at 82.48°C, indicating greater thermal stability. In addition, SEM results for the S5 sample reveal minimal voids, enhancing the fiberboard composites' physical and mechanical

properties and demonstrating high stability. This fiberboard can be classified as a High-Density Fiberboard (HDF) according to JIS A 5905:2003. It is a viable alternative for household furniture, offering a substitute for traditional wood.

ARTICLE INFO

Article history:

Received: 04 November 2023

Accepted: 01 February 2024

Published: 26 August 2024

DOI: <https://doi.org/10.47836/pjst.32.5.21>

E-mail addresses:

hasanahmoraida@gmail.com (Moraida Hasanah)

tjukdin@gmail.com (Tengku Jukdin Saktisahdan)

susilawati@usu.ac.id (Susilawati)

parnoto2001@gmail.com (Frannoto)

adjie211203@gmail.com (Adjie Padriansyah)

irfanhafizhnst@gmail.com (Irfan Hafizh)

* Corresponding author

Keywords: Composite, fiberboard, palm frond fiber, polyester resin

INTRODUCTION

The demand for construction materials is increasing rapidly due to global population growth and expanding infrastructure development (Krausmann et al., 2009). Unfortunately, this trend has led to higher deforestation, resulting in limited availability and higher wood prices (Deiningner & Minten, 1999). It is crucial to explore alternative materials that can be used as a substitute for wood to mitigate this problem. One promising option is fiberboard, which can be made from various types of natural fibers and composites (Chaharmahali et al., 2008). The use of fiberboard has gained increasing attention in the field of construction and is expected to play an important role in sustainable development (Vitrone et al., 2021).

Fiberboard is a composite material of lignocellulosic substances, including natural fibers or wood dust, that are compressed with specialized adhesives (Arévalo & Peijs, 2016). Its popularity as a construction material has increased due to its excellent mechanical strength and ease of processing. Numerous research studies have been conducted to improve the quality of fiberboard by using high lignocellulosic materials, such as corn cob waste strengthened with isocyanate resin and fibers from coconut husks and banana stems (Arévalo & Peijs, 2016; Kariuki et al., 2020; Sales et al., 2022; Wang & Hu, 2016). Exploring the use of natural fibers from various sources can expand the range of materials available for fiberboard production and potentially reduce waste in different industries.

Furthermore, using fiberboard can contribute to environmental conservation efforts as it is typically made from recycled materials and can be recycled again after use (González-García et al., 2009). It can help reduce waste and promote a more sustainable construction approach. Moreover, fiberboard has several advantages over traditional wood-based materials, including higher durability, better moisture resistance, and easier maintenance (Yuan et al., 2022). These properties make it a desirable option for various applications, such as furniture, flooring, wall panels, and decorative items.

Utilizing palm leaves as a raw material for fiberboard production provides an eco-friendly solution to waste management and has the potential to produce high-quality products due to its high lignocellulose content (Ali et al., 2022). Lignocellulose is a complex structure found in plant cell walls, composed of cellulose, hemicellulose, and lignin, which provides strength and rigidity to the plant and is highly resistant to degradation. The high lignocellulose content in palm leaves makes them ideal for fiberboard production, providing excellent mechanical properties and durability to the final product.

To further enhance the quality of fiberboard, a suitable adhesive is required to bond the fibers together. The choice of adhesive plays a crucial role in determining the mechanical properties of the composite product (Kazayawoko et al., 1999). Polyester resin, a commonly used adhesive, has several advantages, such as its low cost, ability to withstand extreme conditions like heat, acid, and base, and resistance to deformation (Gao et al., 2019). As

demonstrated in recent research, polyester has been recognized for its remarkable resistance to a wide range of chemicals, acids, and solvents (Zhang et al., 2023).

Incorporating palm frond fibers, which are emerging as a promising reinforcement agent for polymer composites, introduces the potential for our fiberboard to serve as an innovative thermal insulation material in construction applications (Mlhem et al., 2022). Therefore, this study aims to produce a novel fiberboard composite using palm frond fibers and polyester resin. The resulting fiberboard product is expected to possess desirable properties such as high strength, low density, and good dimensional stability, making it a viable wood alternative for construction needs and various equipment such as furniture (table or chair) and interior design. Eventually, this research will contribute to developing sustainable composite materials and provide an eco-friendly solution to address the environmental impact of wood used in the construction industry.

MATERIALS AND METHODS

The materials used were palm frond fibers (Figure 1), NaOH, polyester resin, methyl ethyl ketone peroxides (as a catalyst), and mirror glaze wax. The equipment includes an 80-mesh sieve, digital balance, hot press, two iron plates, a $100 \times 20 \times 10$ mm sample mold, a 500 mL glass beaker, aluminum foil, spatula, blender, stopwatch, vernier caliper, Universal Tensile Machine (UTM; GOTECH AI-7000M), Wolpert Impactor, Scanning Electron Microscope (SEM; JEOL-JSM-6510LV), and Differential Scanning Calorimetry (DSC; Linseis STA PT 1600). The production of fiberboard composites was carried out in the Basic Chemistry Laboratory of Universitas Sumatera Utara. In contrast, the characterization of the physical, mechanical, and microstructural properties of the fiberboard composites was conducted in the Integrated Research Laboratory of Universitas Sumatera Utara, Indonesia.



Figure 1. Palm frond fiber raw material

Preparation of Palm Frond

The preparation of palm frond fibers was carried out in several stages. First, palm frond fibers were cleaned with water and soaked in 2% NaOH for 24 hours. This stage was done to separate the fibers from organic materials and other debris that were still attached to the fibers. Next, the soaked fibers were immersed in 12% NaOH and heated to 130°C for 120 minutes on a hotplate. The purpose of this stage was to break the bonds between cellulose, lignin and hemicellulose, facilitating the easy separation and refinement of the

fibers (Cai et al., 2016). The processed fibers were then cleaned with water and sun-dried. After complete drying, the fibers were ground and sieved through an 80-mesh screen to ensure homogeneity in size.

Manufacturing of Fiberboard Composites from Palm Frond Fiber with Polyester Resin Matrix

The procedure for making fiberboard composites from palm frond fibers with polyester resin matrix began with weighing the fibers and polyester resin. The composition of the polyester resin matrix used for palm frond fibers is presented in Table 1. The polyester resin was then mixed with methyl ethyl ketone peroxides as a catalyst in a ratio of 100:1 to ensure a homogeneous mixture. Next, the mold was cleaned to prevent the mixture from sticking. An aluminum foil was placed on the iron plate as a base and cover for the mold. A mirror glaze was used to coat the mold, and an iron plate was used to prevent the sample from sticking when it was removed. The mold used complies with ASTM D256 standards and is sized at 100 × 20 × 10 mm.

The previously processed polyester resin mixture was then mixed with the palm frond fibers using a blender. The mixture was poured into the mold and leveled using a spatula. The mold was covered with an iron plate covered in aluminum foil and pressed for 20 minutes at a temperature of 70°C. Afterward, the sample was slowly removed from the mold. The appearance of the produced fiberboard composites can be seen in Figure 2. The sample was then subjected to physical and mechanical property testing. In this stage, tests such as density, porosity (Raza et al., 2023), impact strength (Ghori & Rao, 2021), tensile strength, and flexural strength (Patil et al., 2023) were performed to determine the quality of the fiberboard composites produced.

Density and Porosity Assessment

The density and porosity of the composites were determined by dividing the mass of

Table 1
Composition of polyester resin and palm frond fiber in composite

Sample Code	Composition	
	Polyester Resin (%)	Palm Frond Fiber (%)
S1	60	40
S2	65	35
S3	70	30
S4	75	25
S5	80	20

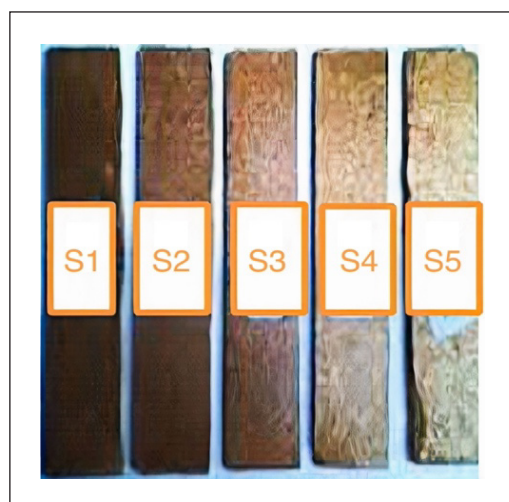


Figure 2. The produced fiberboard composites

the cylindrical samples by their volume. Three replicates were tested, and the averages of these measurements were reported. A digital balance and vernier caliper were used to measure the mass and dimensions by ASTM C134 (Raza et al., 2023).

Impact Strength Measurement

All samples were cut and prepared by ASTM D256, resulting in six replicas with $100 \times 20 \times 10$ mm dimensions. Subsequently, the specimens were conditioned at 22°C with a humidity level of 50% for 48 hours before conducting the tests. The impact test used the Wolpert Impactor instrument (Ghori & Rao, 2021).

Tensile Strength Measurement

The composites' tensile test was carried out using the UTM, following the standard test method ASTM D3039. The crosshead movement was set at 0.02 mm per minute to ensure consistent testing conditions (Patil et al., 2023).

Flexural Strength Measurement

ASTM D790, utilizing the UTM, assessed the flexural characteristics of the test specimens. The specimens were supported at both ends during the test, and a load was applied to the center until failure occurred, following a predetermined rate. The crosshead speed was 1 mm/min (Patil et al., 2023).

RESULTS AND DISCUSSION

Density and Porosity Testing

In this study, composite materials underwent density and porosity testing to determine the ratio of pore volume to the total composite volume. Typically, porosity is expressed as open porosity. The results of these tests are presented in Figure 3.

Figure 3 shows that the highest density was obtained by S5 (sample with the highest polyester resin percentage), which is 1.197 g/mL because polyester resin was used as the matrix in the highest proportion, resulting in the fiberboard composites having the highest density. Additionally, optimal use of resin during molding will result in physical and mechanical properties values with excellent stability of a composite when it is molded (Romanzini et al., 2013). Fiberboard composite made from palm frond fibers using polyester resin as the matrix can be used as a composite board according to JIS (Japanese Industrial Standard) A 5905:2003, which requires a fiber or particle board density value higher than 0.80 g/mL in the High-Density Fiberboard (HDF). Therefore, all fiberboard composites produced with variations in polyester resin and palm frond fibers have met the established requirements.

The highest porosity value was observed in S1, with a composition of 60% polyester resin and 40% palm frond fiber, reaching a porosity value of 0.403%. It can be attributed to the uneven distribution of raw materials, particularly due to the hydrophilic properties of palm frond fibers, which tend to absorb more resin (Essabir et al., 2016). Consequently, areas where the fibers were inadequately mixed with the resin resulted in an uneven surface, increasing the presence of open pores in the fiberboard composites. Conversely, the lowest porosity was achieved with S5, yielding a porosity value of 0.232%.

The raw materials were easily and evenly mixed in these compositions, resulting in a fiberboard composite with a sufficiently low percentage of pores.

Understanding the porosity of the board is crucial as this property plays a key role in hot-pressing simulation models (Rebolledo et al., 2018). The porosity of fiberboard significantly influences transfer mechanisms and the development of density profiles. Analyzing how fiber size and density impact the material's porosity can help determine optimal conditions for the vertical density profile, ultimately enhancing the overall quality of the fiberboard. The data in this study reveals a clear relationship between porosity and density (Rebolledo et al., 2018). Similarly, Shinoj et al. (2010) also observed a consistent trend: An inverse relationship between density and porosity. In other words, as porosity increases, density decreases, and vice versa. For instance, in the case of the S1 composite, an increase in porosity leads to more void spaces within the material, resulting in a lower overall density due to a reduced amount of solid material per unit volume. On the contrary, materials with lower porosity exhibit fewer void spaces, contributing to higher density.

Impact Strength

The impact strength test was conducted to determine the toughness of a sample under dynamic loading and whether the tested material was brittle or strong. It was performed using the Wolpert Impactor instrument. In this test, both ends of the sample were placed on supports, and then the impactor was quickly released towards the sample with dynamic load. The results of the impact strength test for the fiberboard composites are displayed in Figure 4.

Figure 4 shows that the highest impact strength of the composite was obtained by S5, with an impact strength value of 271.251 J/m². The results indicate that the impact

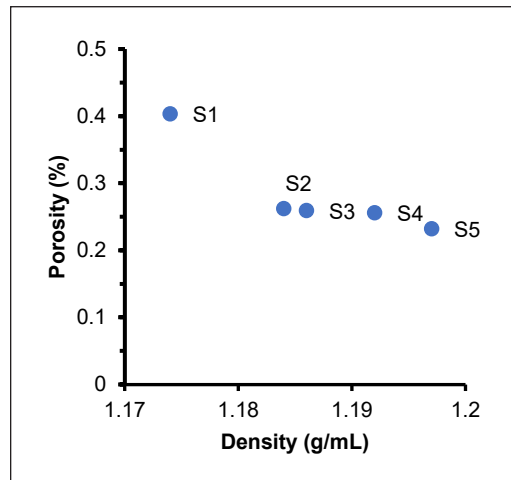


Figure 3. Density and porosity of palm frond-based fiberboard composite

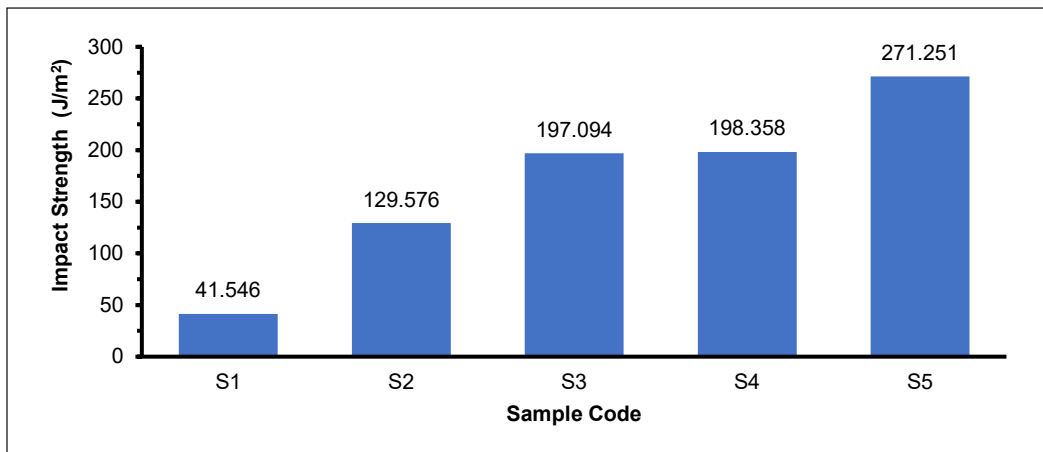


Figure 4. Impact strength of palm frond-based fiberboard composite

strength increases as the composition of polyester resin as the matrix increases because the mechanical properties of polyester resin improve resistance to deformation when it is evenly mixed with other base materials and, therefore, increasing the composition of polyester resin will affect the impact strength value of the fiberboard composite. In previous studies, Raju and Balakrishnan (2020) reported that palm fiber modified with epoxy and glass fiber yielded the highest impact strength, measured at 116 J. However, in this present study, it has been observed that palm frond fiber modified with polyester resin demonstrates a significantly higher impact strength. This substantial difference in impact strength can be attributed to using polyester resin. Known for its excellent resistance to stress-induced deformation, polyester resin substantially increases the impact strength upon its incorporation into the composite, as evidenced by the findings of Daramola et al. (2023). Additionally, polyester is recognized as a shatter-proof material, making it a viable alternative to glass in the production of containers (Seixas et al., 2023).

Tensile and Flexural Strengths

When subjected to a pulling force, the internal bond strength, or the tensile strength test, assesses a material's maximum load-bearing capacity. Meanwhile, the flexural strength test is designed to evaluate the composite's resistance to loading at three flexure points and to measure its elasticity. Tensile and flexural strength tests were performed using a UTM, with the test conducted by applying a load to both ends of the sample. The obtained values can be observed in Figure 5.

Based on Figure 5, S5 demonstrates the highest tensile and flexural strength among the composites, with values of 23.221 MPa and 149.837 MPa, respectively. This composite's tensile and flexural strengths are higher than the compressive strength. It can be attributed to the composite's composition of resin and palm fiber, where the fiber orientation

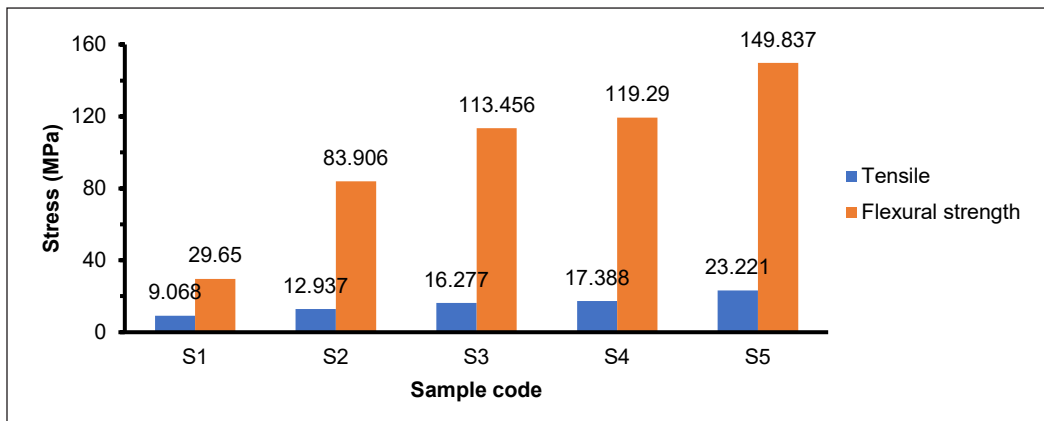


Figure 5. Tensile and flexural strength of palm frond-based fiberboard composite

contributes to enhanced stability in tensile and flexural strength (Hachaichi et al., (2021)). The results indicate an impact and flexural strength increase as the matrix's polyester resin composition increases. It aligns with Kalam et al. (2005), who found a decrease in tensile strength with higher palm fiber content in palm fiber epoxy composites. Additionally, as noted by Ramlee et al. (2021), several factors contribute to the lower tensile strength of palm composites, including poor adhesion capability, the hydrophilic nature of the fibers, and the random orientation of palm fibers within the matrix, resulting in inefficient stress transfer. Furthermore, decreased flexural strength with increasing palm fiber content leads to fiber failure and reduced composite strength (Karina et al., 2007).

The fiberboard produced in this study can be a viable alternative to wood, particularly for crafting furniture (Rosli et al., 2024). Moreover, because this fiberboard falls under the category of HDF, it can be used for furniture and other applications such as laminate flooring and siding (Rowell, 2014; Tang et al., 2017).

SEM Morphology

Surface analysis of the fiberboard composites was conducted using SEM on samples S1 and S5. Sample S1 was chosen because it had poor mechanical properties, while sample S5 had the highest mechanical properties compared to the other samples. Figure 6 shows the surface analysis results obtained using SEM.

The SEM test results on sample S1 suggest that many strands of palm frond fibers are not evenly distributed, resulting in clumps. It indicates that the composite is not homogeneously mixed, resulting in many unfilled spaces or voids not covered by the matrix, causing voids on the composite surface. Meanwhile, the SEM test results on sample S5 show that only a few palm frond fiber powders are unevenly mixed, and it is evident that the smooth surface reveals that the polyester resin binds the palm frond fibers evenly. It demonstrates that this composition's composite components with lower palm fiber are

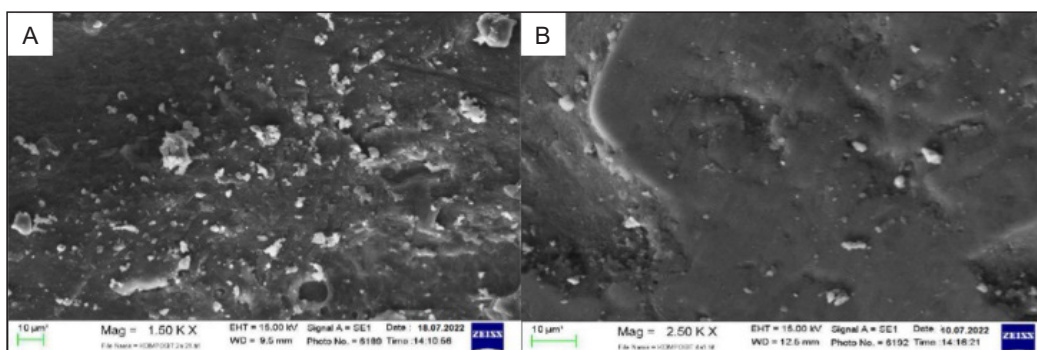


Figure 6. SEM morphology of palm frond-based fiberboard composite with a magnification of 1500× (A=S1 and B=S5)

more homogeneous (Chiromito et al., 2019). Similarly, as suggested by Raza et al. (2023), the homogeneity of the composite is influenced by the proportion of the polymer matrix. Composites with a higher proportion of polystyrene matrix compared to date surface palm fibers (DSF) exhibited no significant cleavage. This observation suggests DSF had a well-dispersed homogeneous distribution within the polystyrene matrix. Notably, voids within a composite can reduce mechanical strength, act as stress concentrators, and contribute to reduced stiffness. In addition, the image of sample S5 presented in this study indicates a relatively lower formation of voids, resulting in the fiberboard composite exhibiting the most optimal physical and mechanical properties.

DSC Analysis

We conducted a DSC analysis on the palm fronds-based fiberboard composite to compare the heat required to raise the sample's temperature. The analysis focused on the time- and temperature-dependent heat flow. Figure 7 displays the DSC thermogram.

The results of the DSC analysis were quantified in terms of degradation temperature values. The graph shows that the degradation of the materials began around 250°C. As depicted in Figure 7, during the heating phase lasting 5 to 10 minutes, an exothermic peak was observed in both the palm frond fiber raw material and composite thermograms. This peak indicates the evaporation of water, occurring at approximately 76.09°C. In the case of the palm frond fiber composite, a curing peak was also observed, which significantly decreased with a reduction in the percentage of palm fiber addition. As for samples S1 to S5, with decreasing percentages of palm frond fiber in the composites, there was a corresponding decrease in the water evaporation temperature, ranging from 82.48 to 67.82°C (Table 2). Notably, S1, containing the lowest polyester resin, exhibited the highest evaporation temperature.

These results suggest that an increase in palm fiber content has a diminishing effect on the thermal stability of the composites. As Ahmad et al. (2023) reported, the varying

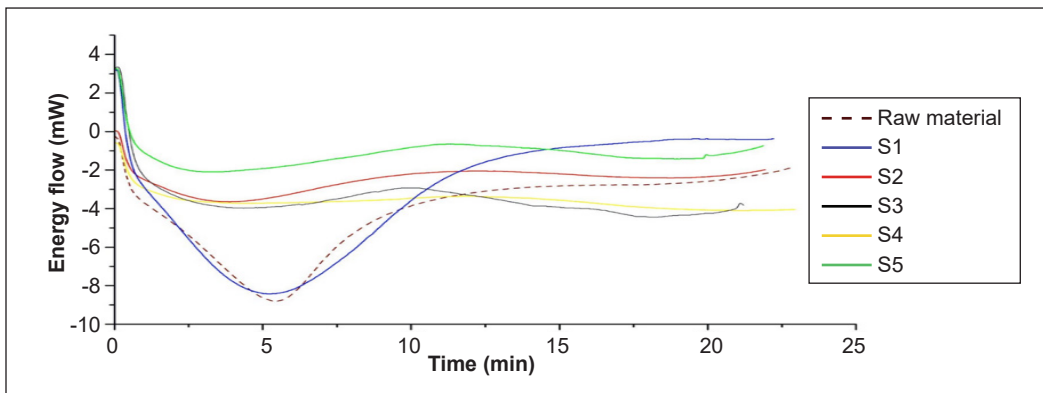


Figure 7. The DSC peaks for temperature degradation of palm fronds-based fiberboard with various composition

temperatures required for fibers to evaporate their water content can be attributed to the different non-substituted hydroxyl groups on their surfaces. Fibers with a higher affinity for water molecules require higher temperatures to evaporate their water content (Hachaichi et al., 2021). This study also found similar results, demonstrating that an increase in the percentage of polyhydroxybutyrate (decrease in degree of polymerization/DPF) in composite materials reduced their thermal stability. It was attributed to weakened hydrogen bonding and reduced mobility of cellulose chains in DPF, particularly after the composite’s dehydration process (Mlhem et al., 2022).

Table 2

Water evaporation temperature peaks (°C) from DSC analysis

Code	Peak of glass temperature (°C)
Raw material	76.09
S1	82.48
S2	72.36
S3	71.66
S4	67.45
S5	67.82

CONCLUSION

Mixing palm frond fibers with a polyester resin matrix resulted in the production of a fiberboard composite that can serve as a substitute for wood. The material fulfilled the JIS A 5095:2003 assessment requirements with a “hard board” classification and underwent physical and mechanical testing. S5 demonstrated the best physical and mechanical properties, indicating an optimal mass ratio composition of 80% polyester resin and 20% palm frond fibers, as shown by the microstructure of the fiberboard composite. Testing resulted in the highest density of 1.197 g/mL, the lowest porosity of 0.232%, the optimal impact strength of 271.251 J/m², tensile strength of 23.221 MPa, and flexural strength of 149.837 MPa. The SEM microstructure analysis showed the least number of voids formed, supporting the fiberboard composites’ maximum physical and mechanical properties. However, based on the DSC analysis, S1 emerges with a notably higher temperature for

water evaporation, recorded at 82.48°C. These results imply that while S5 may excel in specific mechanical and physical properties, S1 exhibits superior thermal characteristics.

This study has several limitations that merit consideration. While essential for controlled experimentation, the controlled laboratory conditions may not entirely replicate the variability encountered in real-world applications, thereby introducing a limitation regarding the study's external validity. Moreover, the study did not address the long-term durability of the fiberboard composite, leaving uncertainties about its performance in real-world environments over extended periods. Furthermore, the study predominantly focused on one manufacturing method—hot pressing—and did not explore alternative production techniques, limiting the understanding of potential material properties variations. Lastly, the evaluation of thermal stability was confined to the temperature of water evaporation, neglecting a broader exploration of other thermal properties and responses to diverse environmental conditions.

Future research should explore various avenues to enhance the understanding and applicability of the developed fiberboard composites. Investigating alternative fiber types or sizes beyond palm frond fibers would contribute to a more comprehensive understanding of the material's versatility. Similarly, exploring diverse resin types, including bio-based or environmentally friendly options, can open avenues for creating more sustainable composite materials. Long-term durability studies under real-world conditions are essential to assess the material's performance over extended periods and under varying environmental factors. A more thorough exploration of thermal properties, encompassing a broader range of temperatures and conditions, would provide valuable insights into the material's behavior. Environmental impact assessments, including recyclability and biodegradability, are essential to determine the ecological footprint of the composite. Furthermore, future research should address variability in manufacturing conditions, such as temperature, pressure, and curing time, to ensure robust and consistent material properties.

ACKNOWLEDGEMENT

The authors thank Universitas Asahan and Universitas Sumatera Utara, Indonesia, for providing facilities and instrumental testing in this research.

REFERENCES

- Ahmad, M. N., Ishak, M. R., Mohammad Taha, M., Mustapha, F., Leman, Z., & Irianto. (2023). Mechanical, thermal and physical characteristics of oil palm (*Elaeis Guineensis*) fiber reinforced thermoplastic composites for FDM-Type 3D printer. *Polymer Testing*, *120*, Article 107972. <https://doi.org/10.1016/j.polymeresting.2023.107972>
- Ali, M., Alabdulkarem, A., Nuhait, A., Al-Salem, K., Iannace, G., & Almuzaiqer, R. (2022). Characteristics of agro waste fibers as new thermal insulation and sound absorbing materials: Hybrid of date palm tree

- leaves and wheat straw fibers. *Journal of Natural Fibers*, 19(13), 6576-6594. <https://doi.org/10.1080/15440478.2021.1929647>
- American Society for Testing and Materials. (2017). *Standard test method for tensile properties of polymer matrix composite materials* (ASTM D3039). ASTM International. https://www.astm.org/d3039_d3039m-17.html
- American Society for Testing and Materials. (2017). *Standard test methods for flexural properties of unreinforced and reinforced plastics and electrical insulating materials* (ASTM D790). ASTM International. <https://www.astm.org/d0790-17.html>
- American Society for Testing and Materials. (2023). *Standard test methods for determining the Izod pendulum impact resistance of plastics* (ASTM D256). ASTM International. <https://www.astm.org/standards/d256>
- American Society for Testing and Materials. (2023). *Standard test methods for size, dimensional measurements, and bulk density of refractory brick and insulating firebrick* (ASTM C134). ASTM International. <https://www.astm.org/c0134-95r23.html>
- Arévalo, R., & Peijs, T. (2016). Binderless all-cellulose fibreboard from microfibrillated lignocellulosic natural fibres. *Composites Part A: Applied Science and Manufacturing*, 83, 38-46. <https://doi.org/10.1016/j.compositesa.2015.11.027>
- Cai, M., Takagi, H., Nakagaito, A. N., Li, Y., & Waterhouse, G. I. N. (2016). Effect of alkali treatment on interfacial bonding in abaca fiber-reinforced composites. *Composites Part A: Applied Science and Manufacturing*, 90, 589-597. <https://doi.org/10.1016/j.compositesa.2016.08.025>
- Chaharmahali, M., Tajvidi, M., & Najafi, S. K. (2008). Mechanical properties of wood plastic composite panels made from waste fiberboard and particleboard. *Polymer Composites*, 29(6), 606-610. <https://doi.org/10.1002/pc.20434>
- Chiromito, E. M. S., Trovatti, E., & Carvalho, A. J. F. (2019). Water-based processing of fiberboard of acrylic resin composites reinforced with cellulose wood pulp and cellulose nanofibrils. *Journal of Renewable Materials*, 7(5), 403-413. <https://doi.org/10.32604/jrm.2019.01846>
- Daramola, O. O., Akinwande, A. A., Adediran, A. A., Balogun, O. A., Olajide, J. L., Adedoyin, K. J., Adewuyi, B. O., & Jen, T. C. (2023). Optimization of the mechanical properties of polyester/coconut shell ash (CSA) composite for light-weight engineering applications. *Scientific Reports*, 13, Article 1066. <https://doi.org/10.1038/s41598-022-26632-x>
- Deiningner, K. W., & Minten, B. (1999). Poverty, policies, and deforestation: The case of Mexico. *Economic Development and Cultural Change*, 47(2), 313-344. <https://doi.org/10.1086/452403>
- Essabir, H., Boujmal, R., Bensalah, M. O., Rodrigue, D., Bouhfid, R., & Quaiss, A. E. K. (2016). Mechanical and thermal properties of hybrid composites: Oil-palm fiber/clay reinforced high density polyethylene. *Mechanics of Materials*, 98, 36-43. <https://doi.org/10.1016/j.mechmat.2016.04.008>
- Gao, Y., Romero, P., Zhang, H., Huang, M., & Lai, F. (2019). Unsaturated polyester resin concrete: A review. *Construction and Building Materials*, 228, Article 116709. <https://doi.org/10.1016/j.conbuildmat.2019.116709>

- Ghori, S. W., & Rao, G. S. (2021). Fiber loading of date palm and kenaf reinforced epoxy composites: Tensile, impact and morphological properties. *Journal of Renewable Materials*, 9(7), 1283-1292. <https://doi.org/10.32604/jrm.2021.014987>
- González-García, S., Feijoo, G., Widsten, P., Kandelbauer, A., Zikulnig-Rusch, E., & Moreira, M. T. (2009). Environmental performance assessment of hardboard manufacture. *The International Journal of Life Cycle Assessment*, 14, 456-466. <https://doi.org/10.1007/s11367-009-0099-z>
- Hachaichi, A., Kouini, B., Kian, L. K., Asim, M., & Jawaid, M. (2021). Extraction and characterization of microcrystalline cellulose from date palm fibers using successive chemical treatments. *Journal of Polymers and the Environment*, 29, 1990-1999. <https://doi.org/10.1007/s10924-020-02012-2>
- Kalam, A., Sahari, B. B., Khalid, Y. A., & Wong, S. V. (2005). Fatigue behaviour of oil palm fruit bunch fibre/epoxy and carbon fibre/epoxy composites. *Composite Structures*, 71(1), 34-44. <https://doi.org/10.1016/j.compstruct.2004.09.034>
- Karina, M., Onggo, H., Abdullah, A. H. D., & Syampurwadi, A. (2007). Effect of oil palm empty fruit bunch fiber on the physical and mechanical properties of fiber glass reinforced polyester resin. *Journal of Biological Sciences*, 8(1), 101-106. <https://doi.org/10.3923/jbs.2008.101.106>
- Kariuki, S. W., Wachira, J., Kawira, M., & Murithi, G. (2020). Crop residues used as lignocellulose materials for particleboards formulation. *Heliyon*, 6(9), Article e05025. <https://doi.org/10.1016/j.heliyon.2020.e05025>
- Kazayawoko, M., Balatinez, J. J., & Matuana, L. M. (1999). Surface modification and adhesion mechanisms in woodfiber-polypropylene composites. *Journal of Materials Science*, 34, 6189-6199. <https://doi.org/10.1023/A:1004790409158>
- Krausmann, F., Gingrich, S., Eisenmenger, N., Erb, K.-H., Haberl, H., & Fischer-Kowalski, M. (2009). Growth in global materials use, GDP and population during the 20th century. *Ecological Economics*, 68(10), 2696-2705. <https://doi.org/10.1016/j.ecolecon.2009.05.007>
- Mlhem, A., Abu-Jdayil, B., Tong-Earn, T., & Iqbal, M. (2022). Sustainable heat insulation composites from date palm fibre reinforced poly(β -hydroxybutyrate). *Journal of Building Engineering*, 54, Article 104617. <https://doi.org/10.1016/j.jobe.2022.104617>
- Patil, H., Sudagar, I. P., Pandiselvam, R., Sudha, P., & Boomiraj, K. (2023). Development and characterization of rigid packaging material using cellulose/sugarcane bagasse and natural resins. *International Journal of Biological Macromolecules*, 246, Article 125641. <https://doi.org/10.1016/j.ijbiomac.2023.125641>
- Raju, K., & Balakrishnan, M. (2020). Evaluation of mechanical properties of palm fiber/glass fiber and epoxy combined hybrid composite laminates. *Materials Today: Proceedings*, 21(Part 1), 52-55. <https://doi.org/10.1016/j.matpr.2019.05.359>
- Ramlee, N. A., Naveen, J., & Jawaid, M. (2021). Potential of oil palm empty fruit bunch (OPEFB) and sugarcane bagasse fibers for thermal insulation application - A review. *Construction and Building Materials*, 271, Article 121519. <https://doi.org/10.1016/j.conbuildmat.2020.121519>
- Raza, M., Al Abdallah, H., Kozal, M., Al Khaldi, A., Ammar, T., & Abu-Jdayil, B. (2023). Development and characterization of polystyrene-date palm surface fibers composites for sustainable heat insulation in construction. *Journal of Building Engineering*, 75, Article 106982. <https://doi.org/10.1016/j.jobe.2023.106982>

- Rebolledo, P., Cloutier, A., & Yemele, M. C. (2018). Effect of density and fiber size on porosity and thermal conductivity of fiberboard mats. *Fibers*, 6(4), Article 81. <https://doi.org/10.3390/fib6040081>
- Romanzini, D., Lavoratti, A., Ornaghi, H. L., Amico, S. C., & Zattera, A. J. (2013). Influence of fiber content on the mechanical and dynamic mechanical properties of glass/ramie polymer composites. *Materials & Design*, 47, 9-15. <https://doi.org/10.1016/j.matdes.2012.12.029>
- Rosli, M. A. A., Purwanto, N. B., Chen, L. W., Bhkari, N. M., Geng, B. J., Selamat, M. E. Bin, & Young, L. J. (2024). An overview of medium-density fiberboard and oriented strand board made from eucalyptus wood. In S. H. Lee, W. C. Lum, P. Antov, E. Krišťák, M. A. R. Lubis, & W. Fatriasari (Eds.), *Eucalyptus* (pp. 73-87). Springer. https://doi.org/10.1007/978-981-99-7919-6_5
- Rowell, R. M. (2014). The use of biomass to produce bio-based composites and building materials. In *Advances in Biorefineries* (pp. 803-818). Woodhead Publishing. <https://doi.org/10.1533/9780857097385.2.803>
- Sales, S. L. T., Aldamia, F. J., Gonzaga, P. S., Montesclaros, A. J. S., & Lawagon, C. P. (2022). Properties of fiber cement boards influenced by BSCH (banana stem and corn husk) fibers and citric acid addition. *Key Engineering Materials*, 913, 125-130. <https://doi.org/10.4028/p-qv513a>
- Seixas, A. A. A., Figueiredo, L. R. F., Santos, A. S. F., & Medeiros, E. S. (2023). Influence of the addition of glycerol-derived polymers on the properties of post-consumer recycled PET. *Journal of Polymer Research*, 30, Article 372. <https://doi.org/10.1007/s10965-023-03754-y>
- Shinoj, S., Visvanathan, R., & Panigrahi, S. (2010). Towards industrial utilization of oil palm fibre: Physical and dielectric characterization of linear low density polyethylene composites and comparison with other fibre sources. *Biosystems Engineering*, 106(4), 378-388. <https://doi.org/10.1016/j.biosystemseng.2010.04.008>
- Tang, Q., Fang, L., & Guo, W. (2017). Investigation into mechanical, thermal, flame-retardant properties of wood fiber reinforced ultra-high-density fiberboards. *BioResources*, 12(3), 6749-6762. <https://doi.org/10.15376/biores.12.3.6749-6762>
- Vitrone, F., Ramos, D., Ferrando, F., & Salvadó, J. (2021). Binderless fiberboards for sustainable construction. Materials, production methods and applications. *Journal of Building Engineering*, 44, Article 102625. <https://doi.org/10.1016/j.jobe.2021.102625>
- Wang, J., & Hu, Y. (2016). Novel particleboard composites made from coir fiber and waste banana stem fiber. *Waste and Biomass Valorization*, 7, 1447-1458. <https://doi.org/10.1007/s12649-016-9523-3>
- Yuan, T., Du, W., Bai, K., Huang, D., Nguyen, T. T., Li, J., & Ji, X. (2022). Preparation of an environment-friendly fiberboard with high mechanical strength using delignified wood fiber. *Vacuum*, 196, Article 110753. <https://doi.org/10.1016/j.vacuum.2021.110753>
- Zhang, J., Fang, Y., Zhang, A., Yu, Y., Liu, L., Huo, S., Zeng, X., Peng, H., & Song, P. (2023). A Schiff base-coated ammonia polyphosphate for improving thermal and fire-retardant properties of unsaturated polyester. *Progress in Organic Coatings*, 185, Article 107910. <https://doi.org/10.1016/j.porgcoat.2023.107910>

Smoothing RRT Path for Mobile Robot Navigation Using Bio-inspired Optimization Method

Izzati Saleh¹, Nuradlin Borhan¹ and Wan Rahiman^{1,2,3*}

¹*School of Electric & Electronic Engineering, Universiti Sains Malaysia Engineering Campus, 14300 Nibong Tebal, Pulau Pinang, Malaysia*

²*Cluster of Smart Port and Logistics Technology (COSPALT), Universiti Sains Malaysia Engineering Campus, 14300 Nibong Tebal, Pulau Pinang, Malaysia*

³*Daffodil Robotics Lab, Department of Computer Science and Engineering, Daffodil International University, Dhaka, Bangladesh*

ABSTRACT

This research addresses the challenges of using the Rapidly Exploring Random Tree (RRT) algorithm as a mobile robot path planner. While RRT is known for its flexibility and wide applicability, it has limitations, including careful tuning, susceptibility to local minima, and generating jagged paths. The main objective is to improve the smoothness of RRT-generated trajectories and reduce significant path curvature. A novel approach is proposed to achieve these, integrating the RRT path planner with a modified version of the Whale Optimization Algorithm (RRT-WOA). The modified WOA algorithm incorporates parameter variation (\vec{C}) specifically designed to optimize trajectory smoothness. Additionally, Piecewise Cubic Hermite Interpolating Polynomial (PCHIP) instead of conventional splines for point interpolation further smoothes the generated paths. The modified WOA algorithm is thoroughly evaluated through a comprehensive comparative analysis, outperforming other popular population-based optimization algorithms such as Particle Swarm Optimization (PSO), Artificial Bee Colony (ABC), and Firefly Algorithm (FA) in terms of optimization time, trajectory smoothness, and improvement from the initial guess. This research contributes a refined trajectory planning approach and highlights the competitive advantage of the modified WOA algorithm in achieving smoother and more efficient trajectories compared to existing methods.

ARTICLE INFO

Article history:

Received: 15 November 2023

Accepted: 28 February 2024

Published: 26 August 2024

DOI: <https://doi.org/10.47836/pjst.32.5.22>

E-mail addresses:

izzatisaleh@student.usm.my (Izzati Saleh)

nuradlinnadhrahb@student.usm.my (Nuradlin Borhan)

wanrahiman@usm.my (Wan Rahiman)

* Corresponding author

Keywords: Bio-inspired optimization, mobile robot navigation, obstacle avoidance, optimization, path planning, path smoothing, RRT

INTRODUCTION

There are four navigation difficulties in robotics: sensing, localization, motion control, and path planning. Path planning may be argued to be the most significant element for navigation procedures. It is the process of determining a collision-free path in a given environment, which is often cluttered in the real world (Alam & Rafique, 2015; Dao et al., 2016; Karur et al., 2021).

Since mobile robots are utilized in a variety of applications, researchers have devised ways to effectively adapt to their needs and overcome some of the key obstacles encountered while implementing fully or partially autonomous navigation in a cluttered environment (Dosoftei et al., 2021; Galli et al., 2017; Mac et al., 2016; Zhou et al., 2019). In order to simplify the path planning problem and ensure that the robot runs/moves smoothly in a cluttered environment while avoiding obstacles, the configuration space must be matched with the algorithm. Multiple path-planning and path-finding techniques exist, with their usefulness depending on the system's kinematics, the environment's dynamics, the computational capabilities of the robot, and the availability of input from sensors and other sources. The trade-offs between algorithm performance and complexity also rely on the use case.

Research in robotics, particularly in the subfield of autonomous navigation, significantly emphasizes the concept of robot path planning. Path planning algorithms build trajectories for robots to follow so that they can safely and effectively reach their destinations.

The Rapidly Exploring Random Tree (RRT) method is one of the most well-known approaches to path design. This sampling-based motion planning algorithm employs a "randomized" technique to explore the space for obstacles and generate a tree of possible paths. RRT was given its name because it uses a "randomized" approach. In the first step of the process, points in the space are sampled at random, and then a tree is constructed by linking the sampled points with edges. The tree's potential to reach new spots that have never been sampled increases as the tree continues to mature. As soon as it reaches its objective, it navigates the tree in reverse, looking for the most direct route from the beginning to the end.

Numerous enhancements to RRT, such as RRT-Connect, RRT*, and Bi-directional RRT (Bi-RRT), have been developed and implemented. RRT* is an extension of RRT that employs heuristics to select nodes more likely to lead to the objective. RRT was originally developed to determine which nodes are most likely to do so. It chooses which nodes are more promising based on a cost function and saves time by avoiding portions of the space that have already been searched. It is done to maximize the likelihood of finding useful information (Jeong et al., 2019; Li et al., 2014; Naderi et al., 2015; Yu & Xiang, 2021). Similarly, Bi-RRT is an RRT extension that generates two distinct trees, one starting at the start point and one starting at the goal point. It then looks for a path between the two

trees to identify the most efficient route from the beginning to the end of the maze. This method is more effective than the RRT technique since it only needs to search half of the space, which significantly increases speed (Xinyu et al., 2019).

Overall, RRT and its variants are powerful and flexible algorithms that can be used in a wide variety of applications. They are a great choice for path planning in unknown or dynamic environments. RRT's strength is that it uses minimal heuristics and arbitrary parameters and does not require state-to-state linkages. This facilitates the application of RRTs to non-holonomic and kinodynamic planning (Lavalle & Kuffner, 2001).

However, RRT may have several downsides. First, RRTs can be challenging to tune properly and may necessitate numerous tries to determine the ideal configuration. Second, RRTs are susceptible to local minima, which means that the algorithm may become stalled in a local optimum and unable to progress to a more optimal solution. Lastly, the path generated by RRT is typically jagged and not smooth (Abadi & Matousek, 2014).

Paper Scopes and Objectives

The primary objective of this paper is to enhance the smoothness of the trajectory generated by the RRT path planner. A secondary objective is to minimize significant curvature along the path, particularly in challenging areas characterized by tight turns or narrow passages. The final objective of this study is to ensure path validity and collision avoidance by devising an approach that guarantees the generated trajectory remains clear of obstacles within the given map environment.

RRT Path Smoothing Strategies

The RRT path smoothing strategies will be discussed in depth—the strategy employed is population-based optimization. Figure 1 shows the flowchart of the proposed method. Each step in the flowchart will be explained in great detail in the next subsections.

Generating Initial Path Using RRT

Figure 2 shows the sequence of RRT. The x_{tree} is initialized at the start point. While searching for the goal point, the algorithm will sample a random point x_{rand} inside a search space (in this case, an occupancy map). The algorithm will find the nearest node x_{near} inside x_{tree} to the sample point x_{rand} . Then, a new node, x_{new} , is generated along the line connecting x_{rand} and the nearest node, with a distance less than the calculated distance. The path between x_{new} and x_{near} is then checked for collision. If no collision is detected, the new point x_{new} is added to the tree x_{tree} . These steps are repeated until the goal point or the maximum iteration is reached. If a goal point is reached, the path $\overrightarrow{P_{RRT}}$ from the start point is traced until the goal point.

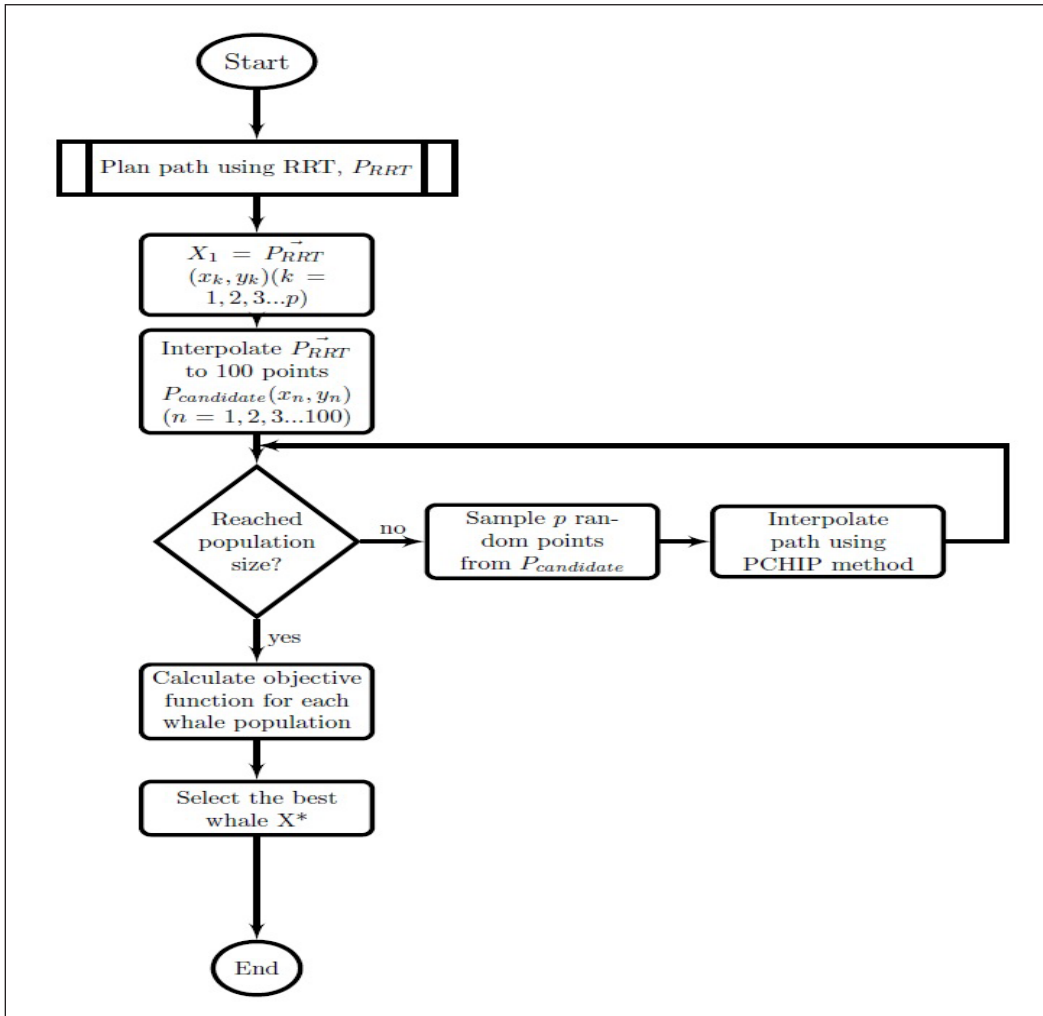


Figure 1. Flowchart of the proposed solution

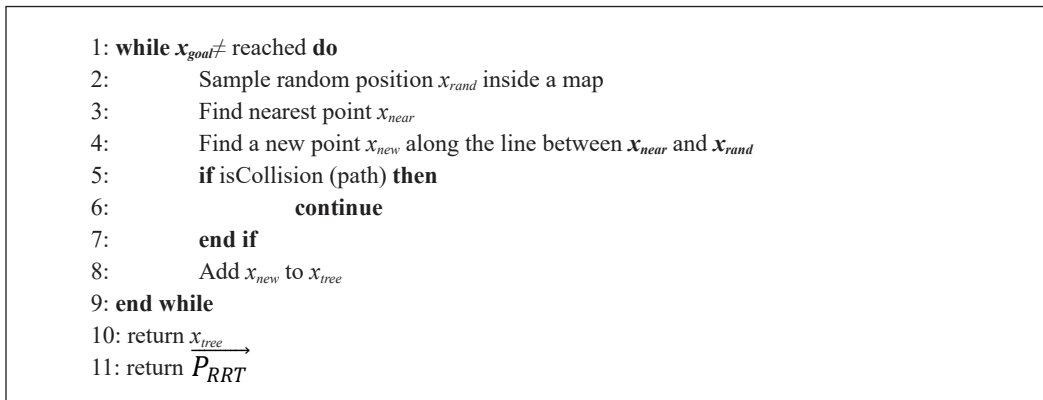


Figure 2. RRT algorithm

Population Initialization

Population-based optimization methods constitute a category of computational algorithms that derive inspiration from the collective behavior witnessed within natural populations, including animal groups and species evolution. The underlying principle intrinsic to these methods is the meticulous preservation of a population of candidate solutions, commonly referred to as individuals or agents, to methodically explore the vast search space and discern the globally optimal solution.

The population X with a solution size of n is generated. In our case, the first potential solution \vec{X}_1 will be the original RRT path \vec{P}_{RRT} . The original path \vec{P}_{RRT} consists of p number of points (x_k, y_k) , $(k = 1, 2, 3 \dots p)$ from start to goal point. In order to generate other possible solutions inside the population, the \vec{P}_{RRT} points were interpolated linearly to produce 100 (x, y) points $P_{candidate} = \{(x_1, y_1) \dots (x_{100}, y_{100})\}$ where the points were ranked from start point to goal point. This step samples the search space for the optimization algorithm. For the next consecutive solutions $\vec{X}_2 - \vec{X}_n$, p number of points will be randomly selected from the search area. Figure 3 shows the initialization of population X , where the first individual solution is assigned to \vec{P}_{RRT} .

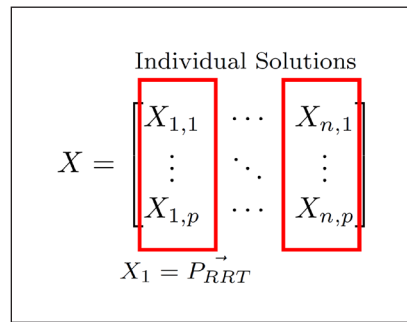


Figure 3. Initialization population solution

Piecewise Cubic Hermite Interpolating Polynomial (PCHIP)

Minimizing significant curvatures around corners, especially in confined spaces, is important as they can lead to inaccuracies to achieve a smooth trajectory path. Using the MATLAB function, Piecewise Cubic Hermite Interpolating Polynomial (PCHIP), instead of the conventional spline approach for point interpolation, as shown in Figure 4, helps

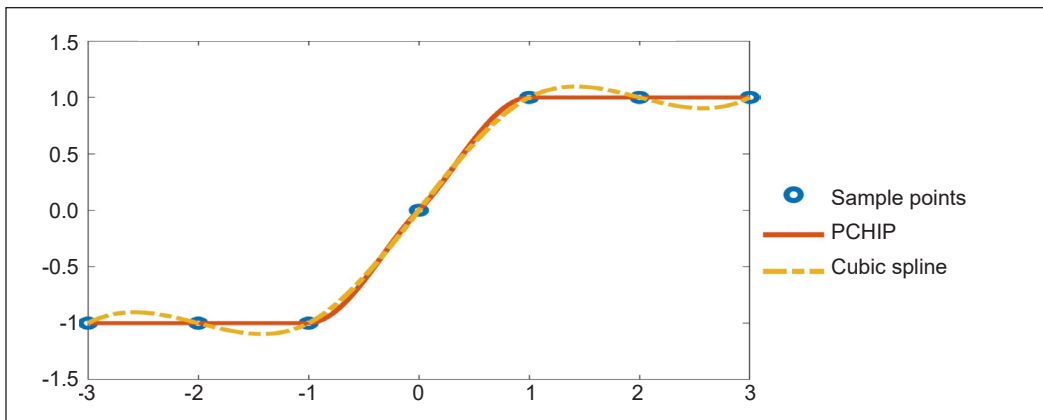


Figure 4. Comparison of different types of interpolation modes in MATLAB (adapted from MATLAB, 2020)

address this issue effectively. The cubic interpolant $P(x)$ maintains the shape of the data. The slopes at points x_j are chosen so that $P(x)$ preserves the data's shape and respects monotonicity. On intervals where the data are uniform, $P(x)$ is also uniform, and at intervals where the data have a local extremum, $P(x)$ also has a local extremum (MATLAB, 2020).

Objective Functions

Objective functions are devised to evaluate the fitness quality of solutions in the population. They comprise three essential components for improving global trajectory planning: smoothness cost ($f_1(\vec{X}_i)$), fuel cost ($f_2(\vec{X}_i)$), and safety cost ($f_3(\vec{X}_i)$), where \vec{X}_i represents the solution within the population.

It is important to note that the primary objective of this paper is to improve the smoothness of \vec{P}_{RRT} . However, to prevent the solution from getting trapped in the global minimum, it is crucial to consider the fuel cost and safety cost objectives. Without incorporating these two objectives, the resulting solution path may appear smooth but not accurately represent a valid trajectory from the start to the goal point.

It emphasizes the significance of a holistic approach, considering both smoothness and practical constraints. The proposed methodology ensures a smooth path and a viable and reliable trajectory by addressing the fuel cost and safety cost objectives alongside the smoothness objective.

Path Smoothness, $f_1(\vec{X}_i)$

Equation 5 can calculate the smoothness of each path. The path is viewed as a sequence of segments, and the angle of the triangle it forms is calculated. There is a total segment of $p - 1$, and $\cos \alpha$ for each segment i can be determined (Equations 1 to 3).

$$A = \sqrt{(x_{i+1} - x_i)^2 + (y_{i+1} - y_i)^2} \quad [1]$$

$$B = \sqrt{(x_{i+2} - x_i)^2 + (y_{i+2} - y_i)^2} \quad [2]$$

$$\cos \alpha_i = \frac{A^2 + B^2}{2AB} \quad [3]$$

The smoothness of the whole path can be calculated by taking the sum of the smoothness of all the segments (Equation 4).

$$\alpha(\vec{X}_i) = \sum_{k=1}^{p-1} \cos \alpha_i \quad [4]$$

The path smoothness function is then determined by taking the average value of all the $\alpha(X_i)$ (Equation 5).

$$f_1(\vec{X}_i) = \frac{\alpha(\vec{X}_i)}{p-1} \tag{5}$$

It is important to note that a lower value of the smoothness function indicates a smoother path. The smoothness function does not have a specific unit of measurement.

Fuel Cost, $f_2(\vec{X}_i)$

The fuel cost is determined by Equation 6.

$$f_2(\vec{X}_i) = \sum_{k=1}^{p-1} \sqrt{(x_{k+1} - x_k)^2 + (y_{k+1} - y_k)^2} \tag{6}$$

where $(x_k, y_k), (k = 1, 2, 3 \dots p)$ is the sequence of points inside path \vec{P}_{RRT} with a total number of sequences p . The fuel cost is measured in meters, m.

Valid Cost, $f_3(\vec{X}_i)$

The validity of the path sequence is examined according to Equation 7 to ensure the robot’s safety during navigation. A considerable penalty β is imposed on the cost function if the distance between the point (x_j, y_j) and the obstacle d_{obs} is smaller than the specified safety distance d_s . There is no unit for this objective function.

$$f_3(\vec{X}_i) = \begin{cases} \beta & d_{obs} \leq d_s \\ 0 & d_{obs} \geq d_s \end{cases} \tag{7}$$

The total cost function for each solution \vec{X}_i is determined by Equation 8.

$$f(\vec{X}_i) = f_1(\vec{X}_i) + f_2(\vec{X}_i) * (1 + f_3(\vec{X}_i)) \tag{8}$$

The resultant path example solution for X_1 to X_3 is shown in Figure 5.

Whale Optimization Algorithm (WOA)

The optimization algorithm can be employed after initializing the population and specifying the objective functions. This paper presents the application of the WOA as the chosen optimization method.

WOA was initially proposed by Mirjalili and Lewis (2016). It is an optimization

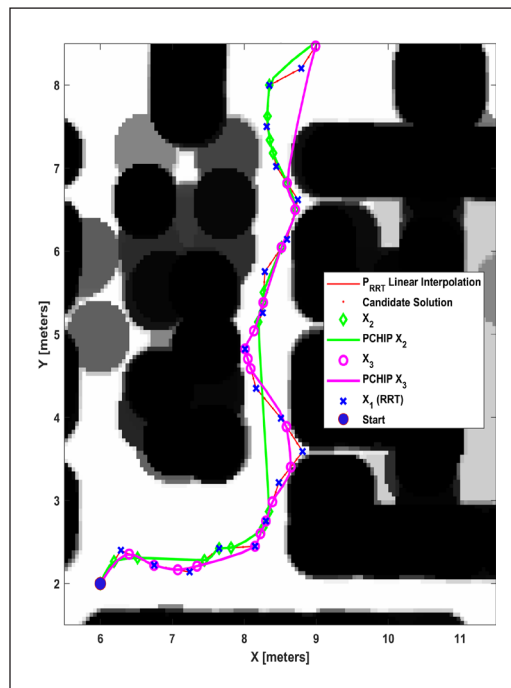


Figure 5. Example of initialization of population for X_1 to X_3 (zoomed)

algorithm that inspires humpback whales. Once they have discovered their target, humpback whales can encircle it. The WOA approach operates under the premise that the current best candidate solution is either the prey of interest or is very near to the optimal because the placement of the optimal design inside the search space is a priori unknown. Once the best search agent has been selected, the remaining search agents will attempt to draw closer to it. This behavior is demonstrated through Equations 9 and 10:

$$\vec{D} = |\vec{C} \cdot \vec{X}^*(t) - \vec{X}(t)| \quad [9]$$

$$\vec{X}(t + 1) = \vec{X}^*(t) - \vec{A} \cdot \vec{D} \quad [10]$$

where t indicates the current iteration, \vec{A} and \vec{C} are coefficient vectors, X^* is the position vector of the best solution obtained so far, and \vec{X} is the position vector. It is important to note that X^* should be adjusted after each iteration if a better solution exists.

The vectors \vec{A} and \vec{C} are calculated as Equations 11 and 12:

$$\vec{A} = 2\vec{a} \cdot rand() - \vec{a} \quad [11]$$

$$\vec{C} = 2 \cdot rand() \quad [12]$$

where \vec{a} is linearly decreased from 2 to 0 throughout iterations (in both exploration and exploitation phases), and the $rand()$ is a random vector in $[0,1]$.

Bubble-net Aattacking Method (Exploitation Phase)

In order to mathematically model the bubble-net behavior of humpback whales, two approaches are designed as follows:

Shrinking Encircling Mechanism

It is accomplished by reducing the value of \vec{a} in Equation 12. Note that the fluctuation range of \vec{A} is likewise decreased by \vec{a} . In other words, \vec{A} is a random number in the interval $[-a,a]$ where a is decreased from 2 to 0 throughout iterations.

Spiral Updating Position

A spiral equation is established between the whale's position and its prey to simulate the helix-shaped movement of humpback whales (Equation 13).

$$\vec{X}(t + 1) = \vec{D}^r \cdot exp^{bl} \cdot cos(2\pi l) + \vec{X}^*(t) \quad [13]$$

where \vec{D}^r is represented in Equation 14 and indicates the distance between the i -th whale to the prey (best solution obtained so far), b is a constant for defining the shape of the logarithmic spiral, l is a random number in $[-1,1]$ and \cdot is an element-by-element multiplication.

$$\vec{D} = |\vec{X}^*(t) - \vec{X}(t)| \tag{14}$$

Humpback whales swim simultaneously in a diminishing circle and spiral pattern around their prey. It is assumed that there is a 50% likelihood of picking either the shrinking encirclement mechanism or the spiral model to update the whales' position to characterize this concurrent behavior. In addition to the bubble-net method, humpback whales search for prey randomly. The mathematical model of the search is as follows.

Search for Prey (Exploration Phase)

Value $|\vec{A}| > 1$ emphasizes exploration and permits the WOA algorithm to perform a global search. The mathematical model looks like this (Equations 15 and 16):

$$\vec{D} = |\vec{C} \cdot \overrightarrow{X_{rand}}(t) - \vec{X}(t)| \tag{15}$$

$$\vec{X}(t + 1) = \overrightarrow{X_{rand}}(t) - \vec{A} \cdot \vec{D} \tag{16}$$

where X_{rand} is a random position vector (a random whale) chosen from the current population.

Proposed Modification

In order to further improve the smoothness of the path, an adaptive value of \vec{C} is proposed based on the occupancy of the X^* points instead of a constant number. The occupancy of a grid point inside an occupancy map is shown in Equation 17, where 0 is considered free space, 1 is considered occupied space and -1 is considered an unknown space. The constant value 2 is replaced with Equation 18, which means that \vec{D} and consequently $\vec{X}(t + 1)$ is only updated when the occupancy of the point is free space or an unknown space. The modified equation of C is shown in Equation 19.

$$\overrightarrow{occ_{X^*(t)}} \cup M = \begin{cases} 0 & \text{free space} \\ 1 & \text{occupied space} \\ -1 & \text{unknown space} \end{cases} \tag{17}$$

$$\vec{w} = 1 - \overrightarrow{occ_{X^*(t)}} \tag{18}$$

$$\vec{C} = \vec{w} \cdot rand() \tag{19}$$

The algorithm for the WOA is shown in Figure 6. The maximum iteration number t_{max} is set to 20 for all the experiments.

EXPERIMENTAL SETUP AND PERFORMANCE EVALUATION

An experimental setup was devised to assess the proposed method's robustness. Two factors were varied in the environment: the start-goal points and the randomness of RRT

```

1: Initialize the whales population  $X_i(i = 1, 2, \dots, n)$ 
2: Calculate the fitness of each search agent
3:  $X^*$  = the best search agent
4: while  $t < t_{max}$  do
5:   for each search agent do
6:     Update  $a, A, C, l$  and  $p$ 
7:     if  $p < 0.5$  then
8:       if  $|A| < 1$  then
9:         Update the position of the current search agent by eq. (10)
10:      else if  $|A| \geq 1$  then
11:        Select random search agent  $x_{rand}$ 
12:        Update the position of the current search agent by Eq. (17)
13:      end if
14:    else if  $p \geq 0.5$  then
15:      Update the position of the current search by using Eq. (14)
16:    end if
17:  end for
18: Check if any search agent goes beyond the search space and amend it
19:   Plot path using PCHIP
20: Calculate the fitness of each search agent
21: Update  $X^*$  if there is a better solution
22: end while
21: return  $X^*$ 

```

Figure 6. RRT-WOA Algorithm

path solutions. The algorithm's versatility and robustness in accommodating different configurations can be evaluated by altering the start-goal points.

The RRT algorithm generates paths based on random sampling, resulting in potential variations with each execution. The Random Number Generator (RNG) seeds were saved for data collection to ensure the planned path's reproducibility. Three sets of RNG seeds were selected to test the algorithm's robustness. The initial solution within the population, denoted as X , was recorded to facilitate a fair performance comparison among optimization algorithms. This guarantees that all optimization algorithms start with the same set of solutions and the same population size for each trial.

Environment Setup

Figures 7 and 8 illustrate the six different environmental setups used in the experiment. The occupancy map is based on the Engineering Design Lab in the USM Engineering Campus. It is inflated with a radius of 0.4m, corresponding to the physical size of the hardware robot. This inflation ensures that the initial planned path generated by the RRT algorithm is feasible for the robot to navigate. The simulation experiment was implemented using MATLAB ver. 2020b and executed on a laptop with an Intel Core i7-1065G7 CPU @1.30GHz.

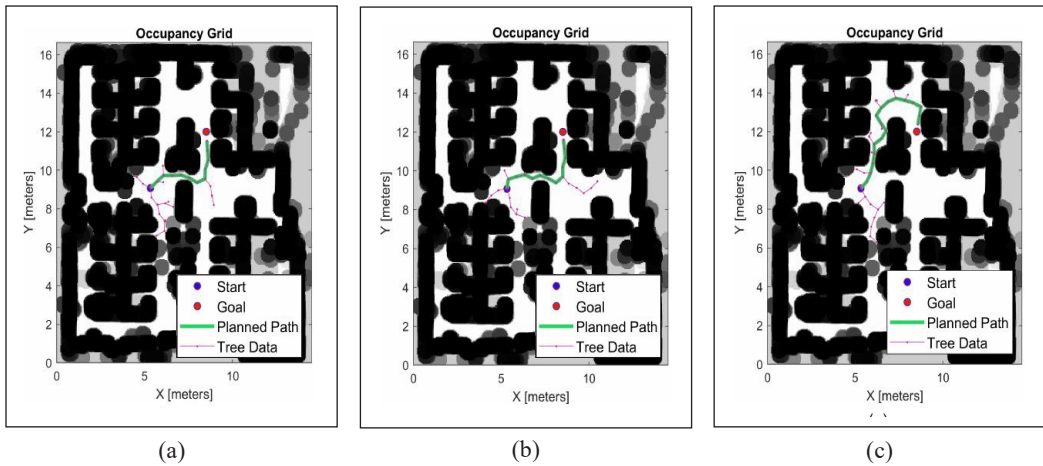


Figure 7. Generated RRT for Path 1 (Start point:(5.3,9.0) and Goal point: (8.5,12.0)) using (a) RNG 1, (b) RNG 2, and (c) RNG 3 *for ease of viewing, all plot legend used the same indicator

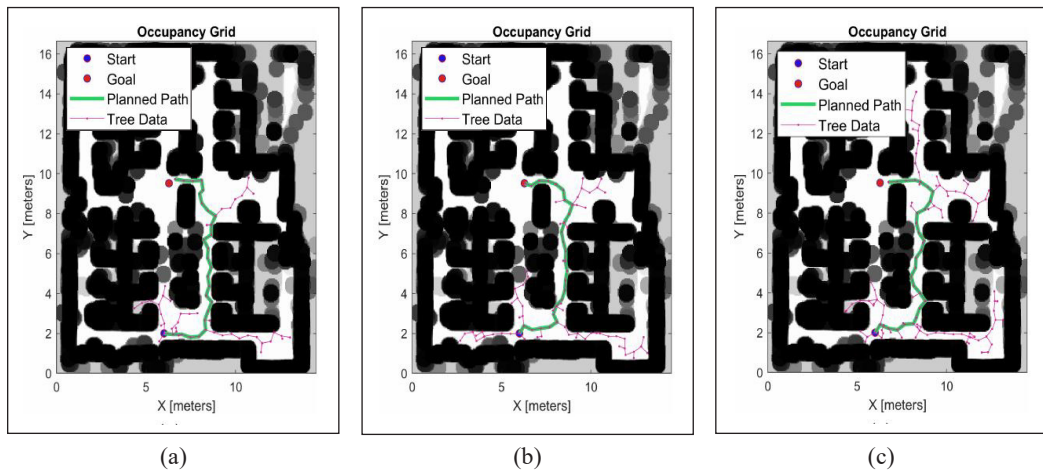


Figure 8. Generated RRT for Path 2 (Start Point: (6.0,2.0) and Goal point: (6.3,9.5)) using (a) RNG 1, (b) RNG 2, and (c) RNG 3 *for ease of viewing, all plot legend used the same indicator

Benchmark Test

A performance evaluation and comparison were conducted to determine whether the proposed method (denoted as WOA (modified) onwards) performs better in smoothing the RRT path than other population-based optimization algorithms, namely PSO, ABC, and FA. Table 1 presents the parameters used in the performance comparison of these algorithms.

The evaluation focused on key metrics to assess the effectiveness and efficiency of these algorithms. The metrics analyzed included the average optimization time, the mean smoothness of the resulting paths, and the percentage improvement achieved in path smoothing.

Table 1
Benchmark test parameters

Algorithm	Parameters	Values
Common	Population size, n	30
	Number of iterations, t_{max}	20
	Coefficient vector, \vec{C}	$2 \cdot rand()$
WOA (Mirjalili & Lewis, 2016)	Coefficient vector, \vec{A}	$2\vec{a} \cdot rand() - \vec{a}$
	Logarithmic spiral, l	$[-1,1]$
	Coefficient vector, \vec{C}	$\vec{w} \cdot rand()$
WOA (modified)	Coefficient vector, \vec{A}	$2\vec{a} \cdot rand() - \vec{a}$
	Logarithmic spiral, l	$[-1,1]$
PSO (Heris, 2017)	Cognitive component, c_1	1.5
	Social component, c_2	1.5
	Inertia weight, w_i	1
ABC (Heris, 2020)	Number of employed bees	n
	Number of onlooker bees	n
	Number of scout bees	n
	Trial limit, L	$0.6mn^*$
FA (Yang, 2009)	Mutation number, ϕ	$rand([-1,1])$
	Attraction coefficient, β_0	2
	Absorption coefficient, γ	1

RESULTS AND DISCUSSION

Benchmark Performance Analysis

The first benchmark test evaluated the optimization time of multiple algorithms. Figure 9 shows that WOA (modified) achieves the lowest median and second smallest spread for optimization time, indicating superior and consistent performance. WOA follows with the second-lowest median and a smaller spread. PSO demonstrates a slightly higher median and the smallest spread, indicating relatively better and consistent performance. ABC performs competitively with a higher median and small spread. FA exhibits the highest median and largest spread, indicating lower performance and greater variability.

The second benchmark test evaluated multiple optimization algorithms based on path smoothness. From the boxplot shown in Figure 10, WOA (modified) demonstrates the lowest median and the smallest spread,

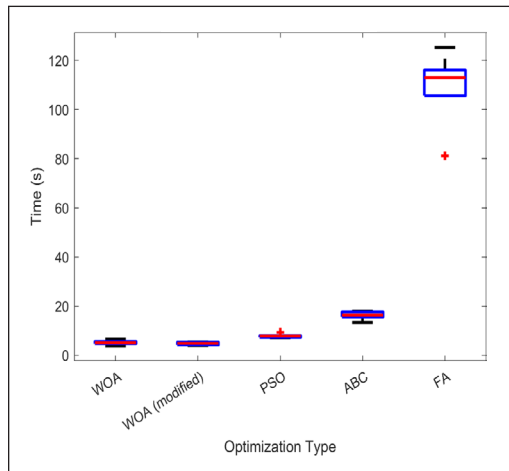


Figure 9. Boxplot analysis of optimization time for various optimization algorithms (lower values indicate better performance)

indicating better and more consistent performance. PSO shows a slightly higher median with a small spread, while ABC exhibits the highest median and the largest spread, indicating relatively poorer performance with more variability. FA falls in between, with a median higher than PSO but lower than ABC and a slightly larger spread than PSO.

The third benchmark test evaluated multiple optimization algorithms based on their ability to improve the smoothness of the initial RRT path. From boxplot data in Figure 11, WOA (modified) demonstrates the highest median and the smallest spread, indicating the best improvement percentage and most consistent performance. On the other hand, FA shows the lowest median with a smaller spread, suggesting relatively poorer but more consistent performance. PSO and ABC exhibit larger spreads, indicating more variability in their results, with PSO having a higher percentage of improvement compared to ABC.

The results of the benchmark performance test were visualized using a radar chart, as depicted in Figure 12. The chart concisely summarizes the algorithm rankings based on their overall performance. According to the plot, the algorithm that

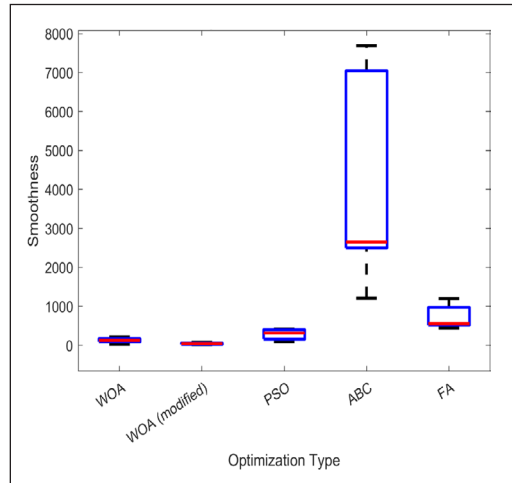


Figure 10. Boxplot analysis of optimization results in path smoothness for various optimization algorithms (lower values indicate better performance)

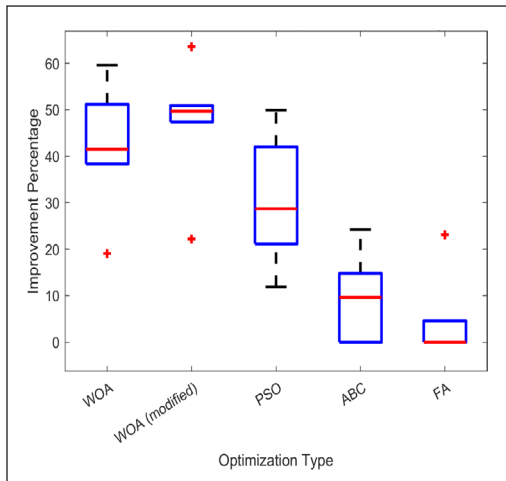


Figure 11. Boxplot analysis of optimization percentage improvement in path smoothness for various optimization algorithms (higher values indicate better performance)

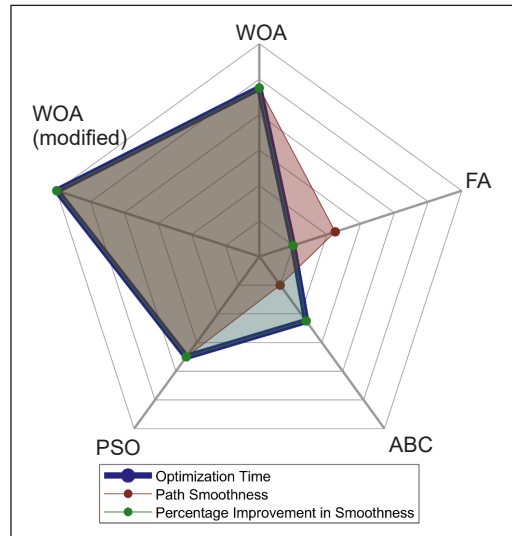


Figure 12. Radar chart for performance ranking (best to worst: WOA (modified), WOA, PSO, ABC & FA)

achieved the highest overall performance was WOA (modified), closely followed by WOA. PSO attained the third rank, while ABC and FA demonstrated the lowest performance among the tested algorithms. These rankings offer a clear representation of the relative performance of each algorithm in the benchmark test.

Results of Smoothed RRT Path

The result of the smoothed RRT path using WOA is shown in Figure 13 for Path 1 and Figure 14 for Path 2. From Figures 13 and 14, it could be observed that the optimized path (labeled with an orange line) is able to smooth out the original RRT path while still maintaining its path validity.

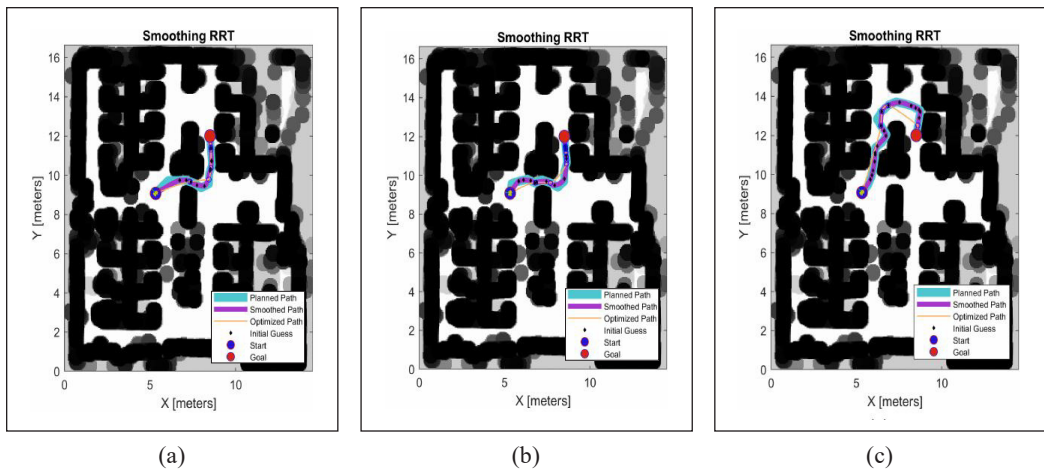


Figure 13. Smoothed RRT for Path 1 (Start point:(5.3,9.0) and Goal point: (8.5,12.0)) using (a) RNG 1, (b) RNG 2, and (c) RNG 3 *for ease of viewing, all plot legend used the same indicator

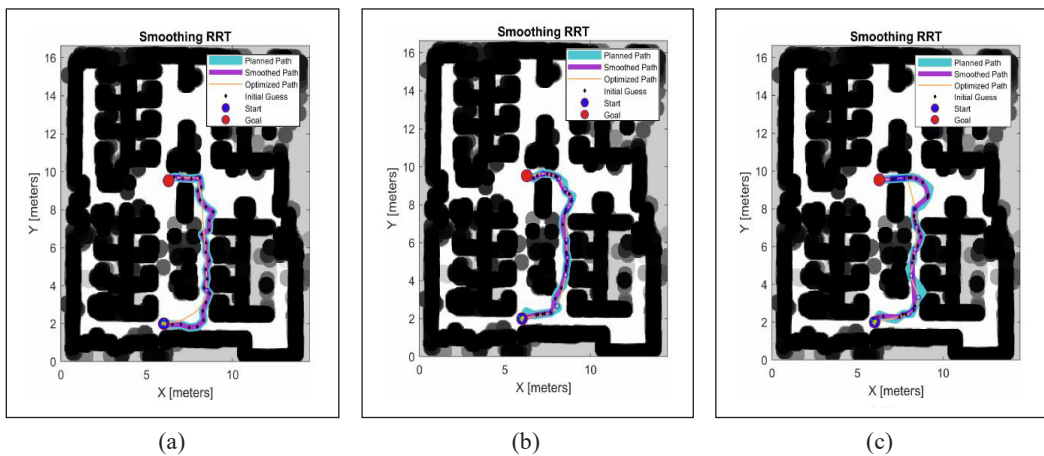


Figure 14. Smoothed RRT for Path 1 for Path 2 (Start Point: (6.0,2.0) and Goal point: (6.3,9.5)) using (a) RNG 1, (b) RNG 2, and (c) RNG 3 *for ease of viewing, all plot legend used the same indicator

CONCLUSION

In conclusion, this research has successfully addressed the challenges of using the RRT algorithm as a path planner. By integrating the RRT path planner with a modified version of the WOA (RRT-WOA), significant improvements have been made in trajectory smoothness and path curvature reduction. The novel approach of incorporating parameter variation (\vec{C}) in the modified WOA algorithm has effectively optimized trajectory smoothness. Additionally, using Piecewise Cubic Hermite Interpolating Polynomial (PCHIP) for point interpolation has further contributed to smoothing generated paths. The modified WOA algorithm has demonstrated its superiority over popular population-based optimization algorithms such as PSO, ABC, and FA through a comprehensive comparative analysis. The WOA (modified) algorithm outperformed these alternatives in terms of optimization time, trajectory smoothness, and improvement from the initial guess.

FUTURE WORKS

In future research, we hope to fine-tune the updated equations and parameters so that the proposed equation applies to all path types.

ACKNOWLEDGEMENT

This work was supported by Collaborative Research in Engineering, Science, and Technology (CREST), Malaysia, with grant no. 304/PELECT/6050423/C121.

REFERENCES

- Abbadi, A., & Matousek, R. (2014, November). *Path planning implementation using MATLAB*. [Paper presentation]. International Conference of Technical Computing Bratislava 2014, Bratislava, Slovakia. <https://doi.org/10.13140/2.1.3324.5767>
- Alam, M. S., & Rafique, M. U. (2015). Mobile robot path planning in environments cluttered with non-convex obstacles using particle swarm optimization. In *2015 International Conference on Control, Automation and Robotics* (pp. 32-36). IEEE Publishing. <https://doi.org/10.1109/ICCAR.2015.7165997>
- Dao, T. K., Pan, T. S., & Pan, J. S. (2016). A multi-objective optimal mobile robot path planning based on whale optimization algorithm. In *International Conference on Signal Processing Proceedings* (pp. 337-342). IEEE Publishing. <https://doi.org/10.1109/ICSP.2016.7877851>
- Dosoftei, C. C., Popovici, A. T., Sacaleanu, P. R., Gherghel, P. M., & Budaciu, C. (2021). Hardware in the loop topology for an omnidirectional mobile robot using matlab in a robot operating system environment. *Symmetry*, *13*(6), Article 969. <https://doi.org/10.3390/sym13060969>
- Galli, M., Barber, R., Garrido, S., & Moreno, L. (2017). Path planning using Matlab-ROS integration applied to mobile robots. In *2017 IEEE International Conference on Autonomous Robot Systems and Competitions (ICARSC)* (pp. 98-103). IEEE Publishing. <https://doi.org/10.1109/ICARSC.2017.7964059>

- Heris, M. K. (2020). *Artificial bee colony in Matlab*. Yarpiz. <https://yarpiz.com/297/ypea114-artificial-bee-colony>
- Heris, M. K. (2017). *Particle swarm optimization*. Yarpiz. <https://yarpiz.com/50/ypea102-particle-swarm-optimization>
- Jeong, I. B., Lee, S. J., & Kim, J. H. (2019). Quick-RRT*: Triangular inequality-based implementation of RRT* with improved initial solution and convergence rate. *Expert Systems with Applications*, 123, 82-90. <https://doi.org/10.1016/j.eswa.2019.01.032>
- Karur, K., Sharma, N., Dharmatti, C., & Siegel, J. E. (2021). A survey of path planning algorithms for mobile robots. *Vehicles*, 3(3), 448-468. <https://doi.org/10.3390/vehicles3030027>
- Lavalle, S. M., & Kuffner, J. J. (2001). Randomized kinodynamic planning. *The International Journal of Robotics Research*, 20(5), 378-400. <https://doi.org/10.1177/02783640122067453>
- Li, R., Liu, J., Zhang, L., & Hang, Y. (2014). LIDAR/MEMS IMU integrated navigation (SLAM) method for a small UAV in indoor environments. In *2014 DGON Inertial Sensors and Systems (ISS)* (pp. 1-15). IEEE Publishing. <https://doi.org/10.1109/InertialSensors.2014.7049479>
- Mac, T. T., Copot, C., Tran, D. T., & De Keyser, R. (2016). Heuristic approaches in robot path planning: A survey. *Robotics and Autonomous Systems*, 86, 13-28. <https://doi.org/10.1016/j.robot.2016.08.001>
- MATLAB. (2020). *Piecewise cubic hermite interpolating polynomial (PCHIP)*. MathWorks. <https://www.mathworks.com/help/matlab/ref/pchip.html>
- Mirjalili, S., & Lewis, A. (2016). The whale optimization algorithm. *Advances in Engineering Software*, 95, 51-67. <https://doi.org/10.1016/j.advengsoft.2016.01.008>
- Naderi, K., Rajamaki, J., & Hamalainen, P. (2015). RT-RRT*: A real-time path planning algorithm based on RRT*. In *Proceedings of the 8th ACM SIGGRAPH Conference on Motion in Games (MIG 2015)* (pp. 113-118). Association for Computing Machinery <https://doi.org/10.1145/2822013.2822036>
- Xinyu, W., Xiaojuan, L., Yong, G., Jiadong, S., & Rui, W. (2019). Bidirectional potential guided rrt* for motion planning. *IEEE Access*, 7, 95046-95057. <https://doi.org/10.1109/ACCESS.2019.2928846>
- Yang, X. S. (2009). Firefly algorithms for multimodal optimization. In O. Watanabe & T. Zeugmann (Eds.), *Stochastic Algorithms: Foundations and Applications* (pp. 169-178). Springer Berlin Heidelberg. https://doi.org/10.1007/978-3-642-04944-6_14
- Yu, Z., & Xiang, L. (2021). NPQ-RRT*: An improved RRT* Approach to hybrid path planning. *Complexity*, 2021(1), Article 6633878. <https://doi.org/10.1155/2021/6633878>
- Zhou, X., Gao, Y., & Guan, L. (2019). Towards goal-directed navigation through combining learning based global and local planners. *Sensors*, 19(1), Article 176. <https://doi.org/10.3390/s19010176>

Early Triage Prediction for Outpatient Care Based on Heterogeneous Medical Data Utilizing Machine Learning

Omar Sadeq Salman^{1*}, Nurul Mu'azzah Abdul Latiff¹, Sharifah Hafizah Syed Arifin¹ and Omar Hussein Salman²

¹School Faculty of Electrical Engineering, Universiti Teknologi Malaysia 81310 Johor Bahru, Malaysia

²Department of Network, Faculty of Engineering, AL Iraqia University, Baghdad, Iraq

ABSTRACT

Traditional triage tools hospitals use face limitations in handling the increasing number of patients and analyzing complex data. These ongoing challenges in patient triage necessitate the development of more effective prediction methods. This study aims to use machine learning (ML) to create an automated triage model for remote patients in telemedicine systems, providing more accurate health services and health assessments of urgent cases in real time. A comparative study was conducted to ascertain how well different supervised machine learning models, like SVM, RF, DT, LR, NB, and KNN, evaluated patient triage outcomes for outpatient care. Hence, data from diverse, rapidly generated sources is crucial for informed patient triage decisions. Collected through IoMT-enabled sensors, it includes sensory data (ECG, blood pressure, SpO₂, temperature) and non-sensory text frame measurements. The study examined six supervised machine learning algorithms. These models were trained using patient medical data and validated by assessing their performance. Supervised ML technology was implemented in Hadoop and Spark environments to identify individuals with chronic illnesses accurately. A dataset of 55,680 patient records was used to evaluate methods and determine the best match for disease prediction. The simulation results highlight the powerful integration of ML in telemedicine to analyze data from heterogeneous IoMT devices, indicating that the Decision Tree (DT) algorithm outperformed the other five machine learning algorithms by

93.50% in terms of performance and accuracy metrics. This result provides practical insights for developing automated triage models in telemedicine systems.

Keywords: Chronic disease, heterogeneous data, internet of medical things, machine learning, remote patient monitoring, triage

ARTICLE INFO

Article history:

Received: 19 November 2023

Accepted: 01 February 2024

Published: 26 August 2024

DOI: <https://doi.org/10.47836/pjst.32.5.23>

E-mail addresses:

o.sadeq@graduate.utm.my (Omar Sadeq Salman)

nurulmuazzah@utm.my (Nurul Mu'azzah Abdul Latiff)

shafizah@utm.my (Sharifah Hafizah Syed Arifin)

omarwsn@gmail.com (Omar Hussein Salman)

* Corresponding author

INTRODUCTION

The number of deaths from Cardiovascular diseases (CVDs), mainly heart disease and stroke, is projected to rise to 23.6 million by 2030, according to the World Health Organization (WHO) (Şahin & İlğün, 2022). Cardiovascular disease (CVD) and hypertension, also referred to as high blood pressure (BP), are chronic medical conditions with detrimental effects on the cardiovascular system, including the heart and blood vessels. These conditions are associated with a range of consequences, including myocardial infarctions (heart attacks), cerebrovascular accidents (strokes), and congestive heart failure. Individuals afflicted with chronic illnesses frequently require continuous medical surveillance, a factor that significantly influences their health status and can precipitate a rapid deterioration if not effectively controlled (Hussein et al., 2020). In addition, patients with low and high BP, especially the elderly ones, should be monitored and measured, as these values are vital to the patient's life and needed level of care and can determine the triage of severity level (Salman et al., 2014).

The Internet of Medical Things (IoMT) is an emerging technology that supports the application of Machine Learning (ML) techniques in healthcare services (Manickam et al., 2022). Integrating IoMT with ML algorithms has the potential to transform the field of medical sciences by enhancing the quality of healthcare, providing improved treatment options, and creating more efficient and affordable systems (Khan et al., 2021). Moreover, integrated IoMT provides many solutions ranging from point-of-care health monitoring and diagnosis to chronic disease management (Mujawar et al., 2020). Note that quality and healthy lifestyles include adequate support for monitoring and assessing human health performance (WHO, 2022).

Telemedicine is a form of medical care that enables providers to diagnose and treat various diseases remotely (Sims, 2018). It aims to support healthcare providers in delivering medical assistance remotely through Information and Communications Technology (Alshammari & Hassan, 2019). Telemedicine consists of three essential layers: body sensors in Layer 1 that collect data; a gateway-based system in Layer 2 that sends data to the preceding layer (the institution's server); and the hospital server in Layer 3 that provides the services remotely to the patient (Hussein et al., 2020; Salman et al., 2022). Figure 1 shows this traditional telemedicine framework.

ML algorithms have shown considerable promise in accurately forecasting various critical cases by evaluating extensive patient data to detect patterns and risk factors, especially when dealing with the analysis of extensive data sets (referred to as "big data") that contain numerous data records and input variables, as well as unorganized data fields like those found in image and text recognition algorithms (Barjouei et al., 2021). Machine learning models can take into account several characteristics, including age, gender, blood pressure, cholesterol levels, oxygen saturation, and other medical

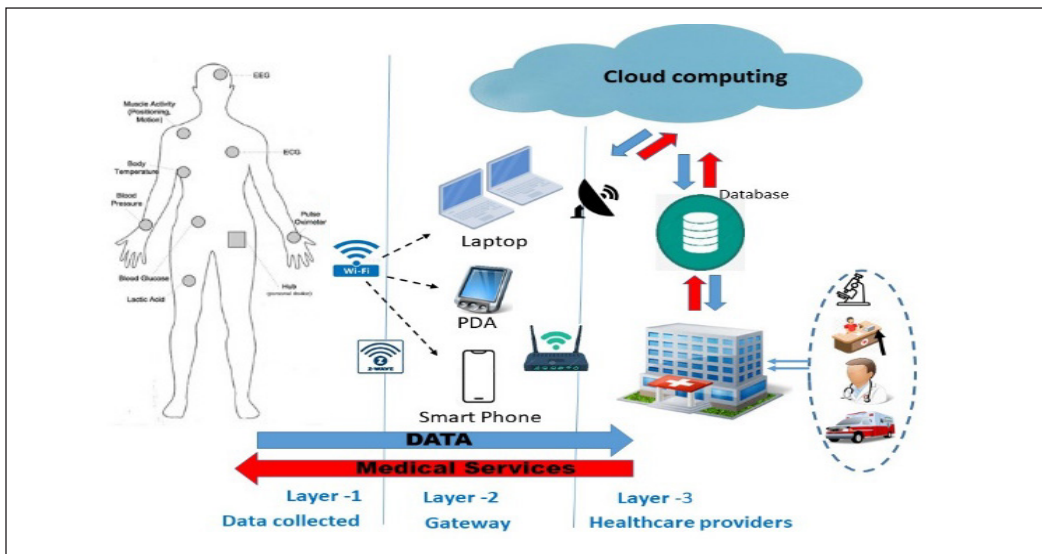


Figure 1. The telemedicine framework

issues, in order to predict the probability of developing CVD and BP diseases (Mohan et al., 2019). ML, a constituent of Artificial Intelligence (AI), has been embraced in healthcare domains due to its sophisticated capacity to analyze intricate and extensive data sets (Rashidi et al., 2021). The rapid growth of technologically driven systems, such as EHRs (electronic health records), yields substantial volumes of data that may be used to enhance decision-making processes. The utilization of AI facilitated a more comprehensive understanding of the data above, aiding in anticipating particular patient prognoses (Jampala et al., 2023). However, this requires substantial labeled data for effective learning and generalization (Onan, 2023).

Furthermore, Machine Learning (ML) refers to a collection of computer methods that acquire patterns from data without explicit programming (Kotwal et al., 2022). Therefore, machine learning (ML) is extensively utilized as a valuable computational tool in numerous industries. An important characteristic of machine learning is its ability to facilitate learning without a previous understanding of the intricate correlations between the underlying variables. ML models possess the capability to efficiently manage and process extensive datasets containing numerous variables, even when the relationships between these variables are non-linear and distributed in complicated manners (Kamali et al., 2022). Moreover, they employed ML to analyze their prediction performance models (Onan et al., 2017). Predictive clinical apps possess advantageous attributes that may be meticulously crafted to provide consistent prognostications and discern patterns within a provided data set. Consequently, these applications possess the capacity to predict patient outcomes and offer essential aid in the areas of diagnosis and therapy in various clinical conditions (Vasina et al., 2022).

This study implemented supervised ML algorithms, which include Decision Tree (DT), Naive Bayes (NB), Random Forest (RF), Support Vector Machine (SVM), K-nearest neighbor (KNN), and Logistic Regression (LR), based on Hadoop and Spark environments to predict two chronic disease types—heart disease and hypertension. The data set was upgraded from Salman, Aal-nouman, et al. (2021) to get 55,680 patient records. While Salman, Aal-nouman, et al. (2021) comprises 11 features and 580 records, our study has utilized 13 features with 55,680 records, using Hadoop and Spark environments.

This study investigates the potential benefits of supervised machine learning (ML) techniques in automating the triage process by analyzing heterogeneous, massive medical data. Additionally, it seeks to determine if implementing ML may enhance the decision-making process for remote patients. This study will employ a comparative methodology to evaluate several supervised ML approaches in forecasting triage outcomes for outpatients. The objective is to determine the most effective machine-learning strategy for addressing this challenge.

RELATED WORKS

The assessment of triage in emergency care systems has presented a significant issue owing to the exponential rise in the number of patients exhibiting varying acuity levels (Riedel et al., 2023). Although traditional triage methods have demonstrated satisfactory effectiveness in addressing hospital overcrowding (Abdalkareem et al., 2022), they are found to be inadequate in efficiently categorizing and managing patients, including during peak situations such as disasters and flooding (Mahon & Rifino, 2024). As a result of the overcrowding problem, nursing staff has been compelled to use the classified decision method to manage all patients, potentially resulting in fatal decision errors that could jeopardize patient safety (Abdalkareem et al., 2021; Elhaj et al., 2023).

ML technologies have prompted several academics to capitalize on their potential. Recent technological advancements have emerged as promising contenders for automating the triage decision-making process. These advancements also facilitate the development of models to predict patients' medical treatment needs and then prioritize them based on their level of urgency (AlSereidi et al., 2022). Advanced ML models can potentially improve the patient triage process, leading to better distinction among patients (Jiang et al., 2021). Automated triaging procedures can be established by applying machine learning classification algorithms. Automated E-triage yields exceptionally dependable classification outcomes, diminishing the need for extensive medical expertise (Liu et al., 2018). Machine learning systems, characterized by adaptable and intelligent computer algorithms, leverage data-driven methods to augment the autonomous learning and predictive capacities of diverse systems. These algorithms achieve cognition and learning by analyzing relationships among recorded data variables and identifying

patterns, ultimately enabling the creation of intelligent models for precise predictions and decision-making (Barjouei et al., 2021).

Several methods for using ML techniques to predict the severity of urgent cases have been implemented. Abe et al. (2022) proposed the adaptive model to develop a prehospital triage system for the identification of patients with head trauma according to trauma severity using XGBoost techniques, as well as to evaluate the predictive accuracy of these techniques. In addition, the work of Morrill et al. (2022) suggests developing a machine-learning strategy to offer immediate decision help to adults diagnosed with congestive heart failure. Compared to physician consensus opinion, the DT algorithm outperforms any physician in terms of exacerbation and triage classification.

The RF algorithm is an ensemble learning approach that uses trapping mechanisms. In RF, each model is trained separately and often simultaneously. Subsequently, the model utilizes the highest probability value to create a classification conclusion (Ghosh et al., 2021).

Moreover, it has been proposed in a previous study by Kadum et al. (2023) that the ML-Based Remote Triage (ML-ART) approach serves as a telemedicine framework. This framework involves collecting patient data, its transmission to telemedicine servers, and the subsequent classification of each patient into one of five distinct categories. The performance of the e-triage system was improved by utilizing the DT algorithm, which yielded the highest level of accuracy. Additionally, the study by Chatrati et al. (2022) proposed a smart home health monitoring system enabling patients to oversee their health, monitor the severity levels of their condition at home, and inform their healthcare practitioner of any problems using the SVM algorithm. In addition, the triage and priority model (TPM) presented by Salman et al. (2020) improves medical response time but requires an adaptive approach for heart monitoring. A study by Mohammed, Jaafar, et al. (2020) suggested that chronic diseases use vital signs and MCDM instruments. In addition, the work by Mohammed, Zaidan, et al. (2020) proposed the TROOIL method, which solves patient triage and ordering based on severity status but does not involve big data. A classification and prioritization framework for patients with chronic diseases in telemedicine was proposed by Hamid et al. (2022) based on a case study of 500 emergency patient records. The evaluation utilized the Dempster-Shafer theory and hybridized MLAHP and TOPSIS algorithms.

Several RF models may be utilized to assess the severity of emergencies in fail-safe and highly accurate operational scenarios (Etu et al., 2022). The work of Chen et al. (2023) utilizes multi-supervised ML, such as gradient boosting machines and RFs, to understand and aid in the progression of triage for CVD in young black women. Utilizing several ML algorithms accomplished the detection of Chronic Heart Disease (CHD). In studies conducted by Saranya and Pravin (2023) and Potdar et al. (2022), ML methods were employed to analyze historical medical data to predict the occurrence of CHD. The

researchers employed three supervised learning methodologies, namely NB, SVM, and DT, to detect potential connections within the CHD data set that might enhance the accuracy of predictions. In the work of Onan et al. (2017), the experimental investigation demonstrated that the combination of NB, SVM, RF, and LR produces encouraging outcomes by evaluating the efficacy of various data representations, including diverse textual features and different categorization techniques achieved through the fusion of several features. As the other study, Onan (2022) illustrates, conventional supervised machine learning models introduced an ensemble classification model based on bootstrap aggregation for text prediction. In addition, it assessed the predictive performance of six different texts and five supervised learning models (NB, Maximum Entropy Classifier (MEC), KNN, DT, and SVM) in conjunction with three considered ensemble learning models (Bagging, AdaBoost, and Random Subspace).

The development rates of countries around the globe are currently increasing tremendously and continuously, and the global population growth rate is on the rise (Ahmad et al., 2014). It has led to a growing population of individuals with chronic illnesses residing in remote regions, presenting challenges for healthcare professionals in accurately interpreting their vital signs and determining the urgency of their medical condition. Hence, it is imperative to prioritize the real-time triage of patients afflicted with chronic illnesses by including urgent case prediction. Inaccurate assessments have the potential to impede timely treatment and, in severe cases, result in fatalities. Hence, accurate prediction of patient classification before hospital admission or outpatient visits holds significant importance for medical facilities and telemedicine patients. Accurate triage holds significant importance in managing all illnesses, particularly in the older population (Salman, Taha, et al., 2021). Furthermore, managing the rising data heterogeneity on hospital servers poses an unresolved research challenge, requiring further inquiry and analysis (Kadum et al., 2023). In addition, the data's quality has a substantial impact on the models' quality. Training machine learning models using faulty data carries the risk of generating predictions that deviate from reality due to biases or errors (Onan, 2023).

Therefore, research must include every remote patient as a multi-tiered severity case-cohort component while considering various manifestations of symptoms and diseases. This strategy is particularly significant for patients residing in remote areas who also require precise diagnosis of the severity of their diseases.

A literature review revealed that no particular study considered managing big medical data with increasing patient populations for any chronic condition, and it is available, as demonstrated in Table 1.

Hence, we propose a method for identifying and predicting the presence of five categories for triage levels to overcome these limitations. Relevant studies by Chatrati

et al. (2022) and Kadum et al. (2023) have chosen these studies as benchmarks after thoroughly analyzing the existing literature. These studies align with our focus on triaging and determining urgent severity cases for patients through the utilization and evaluation of six models of supervised ML.

Table 1

Relevant state-of-the-art studies that addressed triaging patients in a scalable model of the healthcare monitoring system

References	Salman et al., 2020)	Mohammed, Jaafar, et al., 2020)	Mohammed, Zaidan, et al., 2020	Hamid et al., 2022	Chatrati et al., 2022	Kadum et al., 2023	Proposed work
Year	2020	2020	2020	2022	2022	2023	
MCDs	x	□	□	x	□	□	□
Remote monitoring out-patient	□	□	□	□	□	□	□
Remote monitoring in-patient	□	x	x	□	x	x	x
Scalability	□	□	□	x	x	□	□
The large scale of patients	□	□	□	□	□	□	□
Big Data Considered	x	□	x	x	x	x	□
Data pre-processing	x	x	x	x	x	x	□
Target Layer	Layer-2 and Layer-3	Layer-3 (server)	Layer-3 (server)	Layer-3 (server)	Layer-2	Layer-3 (server)	Layer-3 (server)
Time services Considered	□	x	x	x	x	x	x
Triage Considered	□	□	□	□	□	□	□
Priority Considered	□	□	□	□	□	□	x
IoMT	x	x	x	x	x	□	□
Temperature feature	x	x	x	x	x	□	□
Machine Learning	FCM	x	x	x	SVM KNN DT LR DA	NN SVM DT RF	SVM DT RF LR NB K-NN
Method	Evidence theory with FCM	Hybrid D.M. and voting method	TROOIL	Dumpster–Shafer and MLAHP and TROOIL	Support vector machine	Decision Tree	Decision Tree

METHODOLOGY

A comparative analysis was undertaken to assess the efficacy of several supervised machine learning models in assessing patients' real-time triage results. Using the dataset obtained from the data source (Salman, Aal-nouman, et al., 2021), the total data was upgraded to 55,680 patient records. While the original data set from Salman, Aal-nouman et al. (2021) comprises 11 features, our study utilized 14 features with 55,680 records using Hadoop and Spark environments. The Python 3.9 programming language and scientific libraries such as Pandas, NumPy, and Sklearn were utilized for data processing and analysis.

Data Preparation

Data preparation is a crucial stage in the machine learning pipeline and is among the most time-intensive activities in constructing machine learning models (Patel et al., 2022) (Rabash, Nazri, Shapii, & Hasan, 2023). Data pre-processing procedures were carried out after data collection, involving label encoding and imputation of missing data. The categorical feature labels were transformed into a numerical format to make them understandable by machines and to create easy-to-understand forms for ML algorithms. Missing values were computed by calculating the mean for each column that contains missing data in a provided data set and then filling in the missing value.

Data Set

The triage model incorporates a modified data set from a source, including sensors like BP, oxygen saturation, and ECG, and four non-sensory characteristics (Salman, Aal-nouman, et al., 2021). The model's performance is enhanced by adding temperature degree and non-sensory attributes like headache and left-hand discomfort, ensuring data organization by medical protocols. All the data has been formulated for patient triage information per medical guidelines, as shown in Table 2.

Table 2
Patient triage information

Summary	Mean	(-/+ Std.	Range
<i>Patients No.</i>			55680
<i>Patients Detail</i>			
Age	67	14.063	40-89
Sex Female%	27870	50.05%	Male / Female
<i>Vital Signs (Input)</i>			
<i>ECG Sensor</i>			
Peaks	90.505	25.405	40 - 139
QRS	0.278	0.098	0.2 - 0.4

Table 2 (continue)

Summary	Mean	(-/+ Std.	Range
P_P	0.321	0.467	Regular / Irregular
ST.El.	0.535	0.499	Yes / No
<i>Another sensor</i>			
Spo2	92.993	6.165	80 - 100
Temp	37.741	1.228	36 - 40
<i>Blood Pressures Measurements</i>			
H-Blood	15.764	3.689	11-23
L-Blood	8.902	1.779	6 -12
<i>Text Features</i>			
ChP.	0.514	0.500	Yes / No
SH.B.	0.549	0.498	Yes / No
Palip.	0.473	0.499	Yes / No
Rest	0.627	0.484	Yes / No
L.H.P.	0.589	0.492	Yes / No
Hed.	0.593	0.491	Yes / No
<i>Triage Outcome</i>			
Normal			10360
Risk			14914
Sick			11216
Urgent			11484
Cold Case			7706

Considering the symptoms and diagnoses of the patients, the probability of a change in the values was evaluated based on the medical guidelines (Salman et al., 2020). It is important to acknowledge that 55,680 simulated sequences were utilized to illustrate the presence of CHD and hypertension, classified as chronic ailments, among 55,680 individuals. The number of patient requests hypothesis is derived from data from the medical institution's data center, which is responsible for the city. Every patient has been evaluated by physicians specializing in chronic diseases, and each set of medical symptoms has been categorized into five categories (risk, urgent, sick, cold case, and normal) based on the severity of the ailment, as per medical guidelines.

Pre-processing Data

The study encountered a significant challenge of a high-class imbalance in the collected data set for designing ML triage models. The Synthetic Minority Over-sampling Data Generation Technique (SMODGT) was applied to handle this imbalance (Ratih et al., 2022; Rabash, Nazri, Shapii, & Al-Jumaily, 2023). This technique oversamples the minority class by creating synthetic examples along the line segments joining the minority class's

nearest neighbors. After applying SMODGT, the final training data set had a sample size of 55,680, with an equal distribution of samples across the target classes.

The start step was conducted to check and analyze the data to determine the correlation between attributes and comprehend the individual impact of each variable on the learning process. This technique facilitates the identification of the variable that keeps the most pertinent information, enabling prediction accuracy (Jebli et al., 2021). The next step is to check the missing values and fill out the missing data or modify it. Therefore, to improve the quality of the data set and reduce its size, the next step is to lower the dimensions between the features and the actual encoding. Additionally, since text features frequently appear in the data set, replacing them with values that the ML technique can understand and handle improves the quality of the results. All the values of the texts were replaced with integers. For instance, “male” or “female” were substituted with 1/0 in the gender feature and “yes” or “no” with 1/0 in the rest and short breath features, to name a few (Pan et al., 2018). Afterward, all integer values were converted to floats. Following this, it is necessary to normalize the ordinal variable and encode the category variable. In this study, the utilization of the Z score, also known as normalization Yang (2020), was implemented as a standardized approach for normalization. After subtracting the arithmetic mean from the variable, it is then normalized by dividing it by its standard deviation, as described in Equation 1:

$$X = (X - \mu) / \sigma \quad [1]$$

where “ X ” is the input data, “ μ ” is the mean value of data X , and “ σ ” is the standard deviation of data X .

In addition, the data were divided into 80% training and 20% assessment or testing.

Machine Learning Models

The growth of automation and advanced machine monitoring technologies has facilitated the generation of extensive digital datasets for analyzing system behavior, empowering machine learning (ML) systems to improve automated learning and prediction capabilities (Barjouei et al., 2021). The present work employed a conventional (supervised) machine learning technique to train several models using a carefully constructed dataset for triage. Several algorithms were initially chosen for the study, namely Logistic Regression (LR), Decision Trees (DT), k-nearest Neighbors (KNN), Support Vector Machines (SVM), Naive Bayes (NB), and Random Forest (RF). These algorithms were initially selected as they exhibit higher predictive ability in triage classification problems (Chatrati et al., 2022; Kadum et al., 2023; Salman, Taha, et al., 2021). The description of each classification technique is provided as follows:

Support Vector Machine (SVM)

SVM is a supervised learning technique (Ahmad et al., 2014; Barjouei et al., 2021; Onan, 2021; Ootom et al., 2020). Given a set of labeled training examples (i.e., every single instance in the training set is related to either the positive or negative class), SVM discovers the area of the hyperplane that best separates cases from each class and achieves the maximum distance between instances of data and the hyperplane. The learned hyperplane is then used to assign (or predict) a class label for each new test instance.

Naive Bayes (NB)

NB is a technique for supervised learning that computes model parameters using the Bayes theory. Calculating the probabilities, it assigns a class designation to any test instance. It is associated with each possible class label. The probability with the highest value determines the designation (Berrar, 2019).

Random Forest (RF)

RF is an ensemble-supervised ML model that uses DTs as the base learner and frequently constructs regression trees based on training data. Node selection in RF differs, with a random subset selection from the present attribute set and a selection of one optimized attribute in the sub-feature set. It has been widely employed in classification and regression problems (Barjouei et al., 2021; Hadi et al., 2020).

Logistic Regression (LR)

In the LR technique, classification is based on probabilities. It can be considered a particular regression case where the outcome is categorical. It uses a sigmoid non-linear activation function to produce the output. However, this also indicates that it suffers high sensitivity to attribute vector values. This classifier method is a widespread tool in disease prediction (Hadi et al., 2020).

Decision Tree (DT)

The procedure for constructing involves dividing the dataset into child subsets. The process of partitioning continues with repetitive partitioning of child subsets. The underlying concept of the tree method is to employ a series of partitions to identify the optimal class. Furthermore, DTs are characterized by feature selection capability, straightforward comprehension, interpretability, visualization, and independence from non-linear relationships between parameters (Barjouei et al., 2021; Shiwangi et al., 2023).

K-Nearest Neighbor (KNN) Algorithm

The K-Nearest Neighbors (KNN) algorithm is a supervised machine learning algorithm for prediction and classification tasks. One of its notable features is its simplicity and effectiveness. The algorithm identifies the 'k' training instances in its vicinity closest to a new, unseen data point based on a specified distance metric, commonly the Euclidean distance. The algorithm then classifies the new data point by a majority vote of its k-nearest neighbors (Lestari & Sumarlinda, 2022).

Peculiarity of the Method

Machine learning (ML) algorithms have shown promise in predicting urgent cases by analyzing vast amounts of patient data, particularly when processing large data sets. ML models can consider multiple factors (heterogeneity medical data) such as age, gender, BP, oxygen rate, and other medical conditions to predict the possibility of developing CVD and BP chronic diseases. Machine learning is extensively utilized in the healthcare industry due to its advanced ability to analyze complex and vast data sets. This study investigates the potential benefits of ML techniques in automating the triage process. The study revealed a promising future vision in the healthcare field by analyzing heterogeneous, massive medical data and assessing whether ML can enhance the decision-making process for remote patients.

Performance Evaluation Metrics

Multi-class classification problems play a crucial role in assessing the efficacy of learning methodologies and facilitating comparisons between various models. The selection of appropriate assessment measures is of utmost importance for reporting the success of prediction models, specifically within the sector of healthcare assessment models (Alsinglawi et al., 2022). Given that triage is an issue characterized by a high-class imbalance, relying just on a single assessment parameter, such as accuracy or precision, would be insufficient for assessing the performance of a model. Nevertheless, there is currently a lack of a globally approved set of performance metrics that apply to all multi-class issues. Since the current investigation pertains to a multi-class classification issue, it is important to note that the range of accessible performance metrics is restricted. Typically, these metrics include accuracy, recall, precision, and F1-score (Ozsahin et al., 2022). Moreover, Hameed et al. (2022) also suggested that the assessment of multi-class issues may be conducted using Receiver Operating Characteristics (ROC) and Areas Under The ROC Curve (AUC). However, it should be noted that the analytical difficulty escalates as the number of classes grows.

Hence, this research will only focus on the established assessment measures for assessing the performance of the chosen models. The next step involved the enervation of

the confusion matrix for each model. A confusion matrix is a fundamental concept in ML that offers insights into the expected and true categorization values produced by a prediction system (Huang & Wang, 2023). The data consists of two dimensions: the first dimension reflects the true class of the data, while the second dimension indicates the predicted class of the data set. The evaluation metrics designed for binary classification are not fully appropriate for multi-class classification problems, mainly because of the discrepancy in matrix dimensions between the two types of classification matrices (Hameed et al., 2022).

- True Positives (TP) refers to correctly identifying individuals who are correctly classified as patients with a certain chronic condition.
- True Negatives (TN) refer to instances where a forecast accurately identifies individuals who do not have a specific sickness or any other ailments.
- False positives (FP) refer to the erroneous identification of a healthy individual as being afflicted with a certain ailment.
- False negatives (FN) refer to the erroneous classification of the target as a non-healthy individual.

Performance metrics evaluate the performance of these ML algorithms. Various performance assessment metrics may be established using the confusion matrix, as presented in Table 3. The final review considered accuracy, precision, recall, and F1-score for each class, as represented in Performance Measure with formal in Table 4.

Table 3
Confusion matrix

	Predicted Negative	Predicted Positive
Actual Negative	TN	FP
Actual Positive	FN	TP

Table 4
Performance evaluation metrics

Performance Measure with formal	Description
$\text{Accuracy} = \frac{(\text{TP} + \text{TN})}{(\text{TP} + \text{TN} + \text{FP} + \text{FN})}$	It assesses the accuracy of a classification model in making predictions.
$\text{Precision} = \frac{\text{TP}}{(\text{TP} + \text{FP})}$	The assessment assesses the accuracy ratio of correctly predicted instances belonging to a certain class and the total number of instances anticipated as belonging to the same class.
$\text{Recall} = \frac{\text{TP}}{(\text{TP} + \text{FN})}$	The accuracy rate is assessed by calculating the proportion of accurate predictions for a certain class and the overall count of instances belonging to an actual class.
$\text{F1 - score} = \frac{2 * \text{Precision} * \text{Recall}}{\text{Precision} + \text{Recall}}$	This analysis aims to assess the harmonic mean of precision and recall.

RESULTS AND DISCUSSION

Several ML models were tested for the severity of urgent cases and for determining patient results on a dataset with a balanced number of classes (Table 2). In this study, the above-mentioned supervised ML classifiers made 11,088 predictions, and 11,088 patient records were used to test how to classify the triage levels for people with chronic heart and hypertension diseases. Of those 11,088 records, 2,083 are normal cases, 1,542 are cold cases, 2,936 are risk cases, 2,274 are urgent cases, and 2,253 are sick cases.

Table 5 summarizes the performance and accuracy results of the evaluated ML algorithms. The results indicate that three of the six models, namely DT, KNN, and RF, had higher accuracy than others. The DT and KNN models exhibited outstanding results compared to the other models, as evidenced by their better prediction metrics: accuracy (93.50%); precision (100.00%, 100.00%, 89.00%, 85.00%, 95.00%); recall (100.00%, 100.00%, 86.00%, 86.00%, 97.00%); and F1-score (100.00%, 100.00%, 88.00%, 86.00%, 96.00%) for triage levels (normal, cold state, risk, urgent, and sick, respectively). Meanwhile, the performance of the KNN algorithm regarding accuracy was (92.0%); precision (97.00%, 92.00%, 92.00%, 86.00%, 87.00%); recall (99.00%, 88.00%, 85.00%,

Table 5
Performance for all six algorithms (SVM, LR, DT, RF, KNN and NB) for triage categorization for normal, cold state, risk, urgent, and sick, respectively

Methods	Performance Metrics	NORMAL	COLD STATE	RISK	URGENT	SICK	Accuracy
SVM	Precision	83.00%	80.00%	57.00%	69.00%	64.00%	43.00%
	Recall	100.00%	93.00%	74.00%	1.00%	83.00%	
	F1-score	91.00%	86.00%	65.00%	3.00%	72.00%	
LR	Precision	98.00%	92.00%	59.00%	55.00%	70.00%	45.00%
	Recall	100.00%	95.00%	69.00%	32.00%	80.00%	
	F1-score	99.00%	93.00%	64.00%	41.00%	75.00%	
RF.	Precision	100.00%	98.00%	85.00%	80.00%	94.00%	91.00%
	Recall	100.00%	99.00%	82.00%	80.00%	97.00%	
	F1-score	100.00%	99.00%	83.00%	80.00%	96.00%	
KNN	Precision	97.00%	92.00%	92.00%	86.00%	87.00%	92.00%
	Recall	99.00%	88.00%	85.00%	90.00%	92.00%	
	F1-score	98.00%	90.00%	88.00%	88.00%	90.00%	
DT	Precision	100.00%	100.00%	89.00%	85.00%	95.00%	93.50%
	Recall	100.00%	100.00%	86.00%	86.00%	97.00%	
	F1-score	100.00%	100.00%	88.00%	86.00%	96.00%	
NB	Precision	80.00%	73.00%	55.00%	56.00%	52.00%	41.00%
	Recall	100.00%	93.00%	53.00%	6.00%	79.00%	
	F1-score	89.00%	81.00%	54.00%	11.00%	63.00%	
	Support	2083	1542	2936	2274	2253	11800

90.00%, 92.00%); and F1-score (98.00%, 90.00%, 88.00%, 88.00%, 90.00%) for triage levels (normal, cold state, risk, urgent, and sick, respectively), as shown in Figure 2.

Figure 2(d) illustrates that the DT algorithm outperforms other algorithms, particularly in the normal and cold cases (100% and 100%, respectively). However, on the other three levels (sick, urgent, and risk), the values are roughly close between the DT, KNN, and RF algorithms. However, the decision tree consistently holds the highest accuracy.

Figure 3 shows the model performance in the form of a confusion matrix displayed standalone for each algorithm.

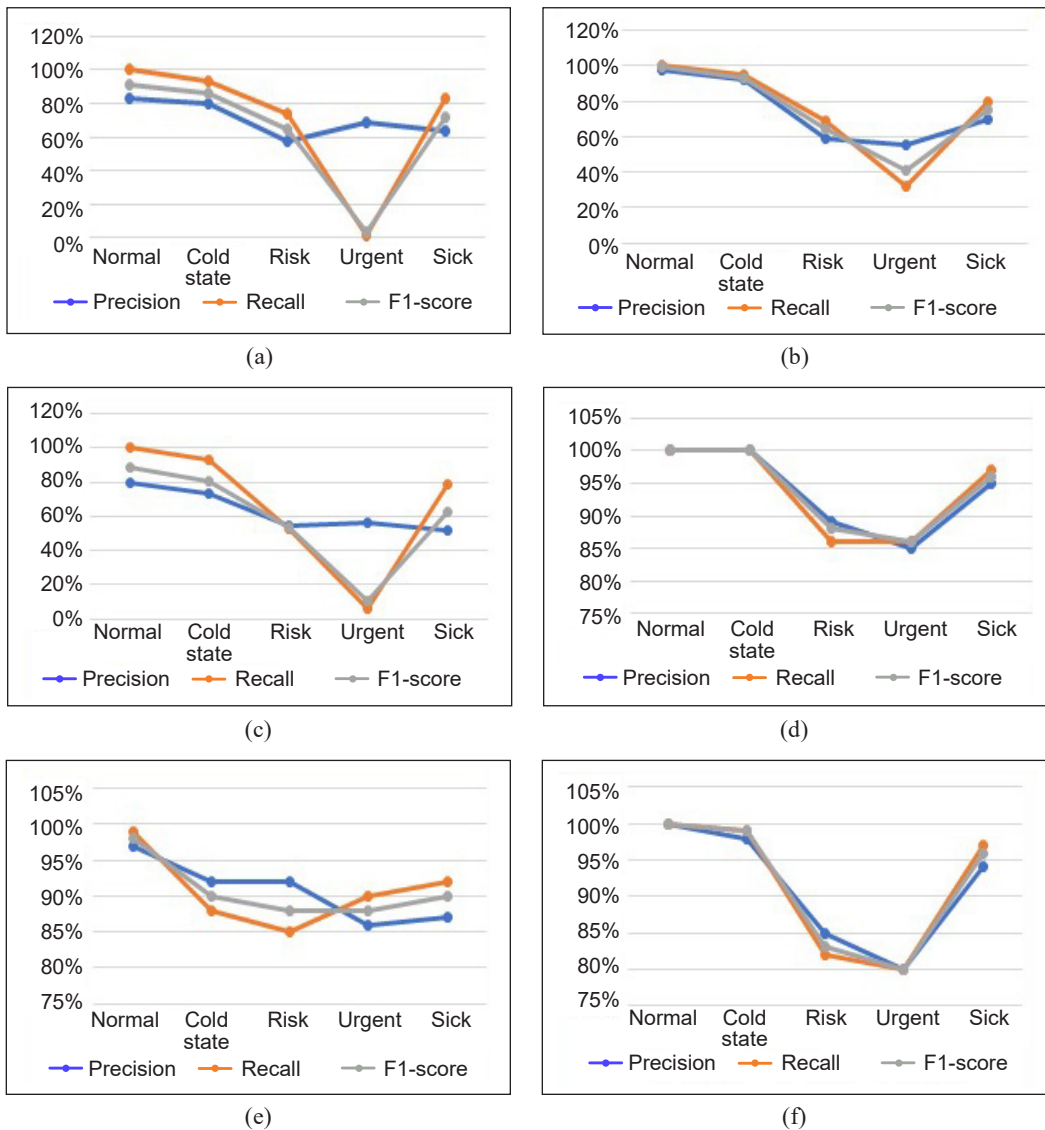


Figure 2. Performance metrics of six supervised machine learning methods: (a) SVM algorithm; (b) LR algorithm; (c) NB algorithm; (d) DT algorithm; (e) KNN algorithm; and (f) RF algorithm

		Prediction Value				
		NORMA L	COLD STATE	RISK	URGEN T	SICK
Actual Value	NORMAL	2067	159	25	52	147
	COLD STATE	652	266	0	79	493
	RISK	735	183	240	569	696
	URGENT	537	194	254	706	655
	SICK	411	129	64	275	1500

(a)

		Prediction Value				
		NORMA L	COLD STATE	RISK	URGEN T	SICK
Actual Value	NORMAL	2272	6	72	39	61
	COLD STATE	7	1472	0	1	10
	RISK	64	0	2186	35	138
	URGENT	35	1	39	2189	82
	SICK	68	13	122	58	2118

(b)

		Prediction Value				
		NORMA L	COLD STATE	RISK	URGEN T	SICK
Actual Value	NORMAL	1738	52	165	301	194
	COLD STATE	478	1	57	444	510
	RISK	351	48	688	843	493
	URGENT	263	53	433	1092	505
	SICK	160	59	428	302	1430

(c)

		Prediction Value				
		NORMA L	COLD STATE	RISK	URGEN T	SICK
Actual Value	NORMAL	1678	0	212	173	387
	COLD STATE	477	0	173	303	537
	RISK	549	0	562	60	704
	URGENT	507	0	392	733	714
	SICK	315	0	274	221	1569

(d)

		Prediction Value				
		NORMA L	COLD STATE	RISK	URGEN T	SICK
Actual Value	NORMAL	2111	4	150	75	110
	COLD STATE	30	1420	0	4	36
	RISK	50	48	2162	142	21
	URGENT	26	4	157	2087	72
	SICK	65	77	31	110	2096

(e)

		Prediction Value				
		NORMA L	COLD STATE	RISK	URGEN T	SICK
Actual Value	NORMAL	2323	10	49	20	48
	COLD STATE	21	1460	4	1	4
	RISK	108	17	2114	79	105
	URGENT	37	5	65	2161	78
	SICK	78	27	154	53	2067

(f)

Figure 3. Confusion matrix of six supervised machine learning methods: (a) SVM; (b) LR; (c) NB; (d) DT; (e) KNN; and (f) RF

A confusion matrix is a matrix used to evaluate the performance of a classifier on test data, where the actual values are believed to be known data values. In this work, the confusion matrix of each algorithm is r. The model performance in a confusion matrix is displayed as a standalone value for each algorithm, as shown in Figure 3. A confusion matrix is a matrix used to evaluate the performance of a classifier on test data, where the actual values are believed to be known data values. In this work, the confusion matrix of each algorithm is represented as a 5x5 matrix for the triage levels due to the result consisting of five category outputs: normal, cold case, risk, urgent, and sick. Each row in the matrix includes the number of actual classes, and each column includes the number of predicted classes. From the result of this matrix, we can determine the values for true positive (TP), false positive (FP), true negative (TN), and false negative (FN), as illustrated in Table 4. Moreover, the row values illustrate the prediction computed for each level within each triage class.

Consequently, using the actual and predicted values, the class precision and recall values are calculated (Figure 3). The class recall and class precision scores are useful for assessing the overall accuracy of the classifier. According to the values shown in the table, the decision tree classifier has the highest precision and recall values, whereas Naïve Bayes has the lowest values. The confusion matrix was applied to analyze model predictions in each class during testing.

In the DT algorithm, all the patients were accurately triaged, with false positives (FP) and false negatives (FN) being minimal, generally <100 or close to that, as explained in Figure 3(d).

A total of six models were trained and subsequently evaluated on the produced dataset, yielding a prediction accuracy range spanning 41.00% to 93.50%, as displayed in Figure 4, representing the correlation between algorithm accuracy and processing time.

On the other hand, the SVM, LR, and NB approaches seem to be the least effective models compared to the others, as they have the lowest prediction accuracy of 43.00%, 45.00%, and 41.00%, respectively.

However, the system has been verified and validated using another measure, the ROC-AUC score, which compares the relationship between TP and FP rates. In addition, it is ensured that the multi-class classification models perform well and make better decisions based on their predictions.

Figure 5 presents the ROC-AUC scores for various machine learning classification algorithms, facilitating a comparative assessment of their performance.

The ROC-AUC curve, a crucial metric for binary classification, visualizes the trade-off between recall and precision. The AUC, or area under the curve, quantifies a classifier's ability to differentiate between the two classes, with a desirable model exhibiting an AUC close to 1. The closer the ROC is to the top left of the graph, the better the model is. It

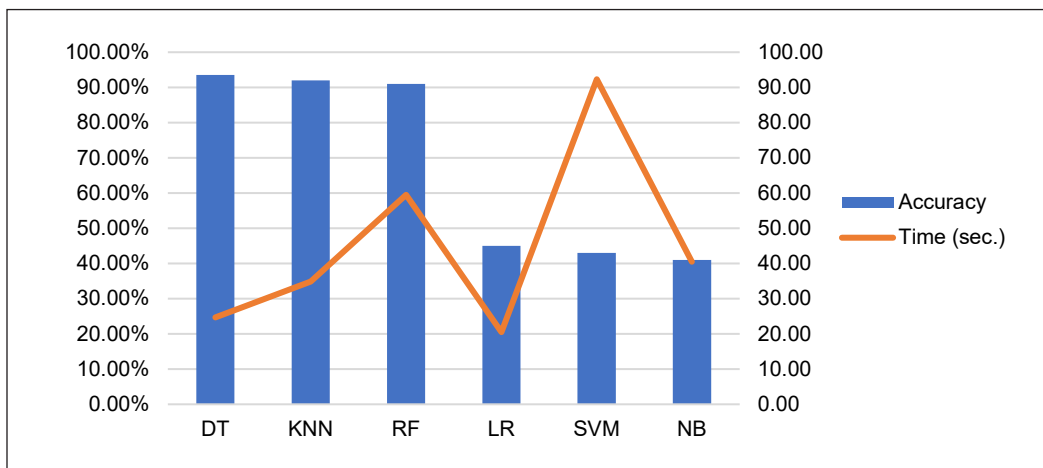


Figure 4. The Accuracy with the time process for six ML

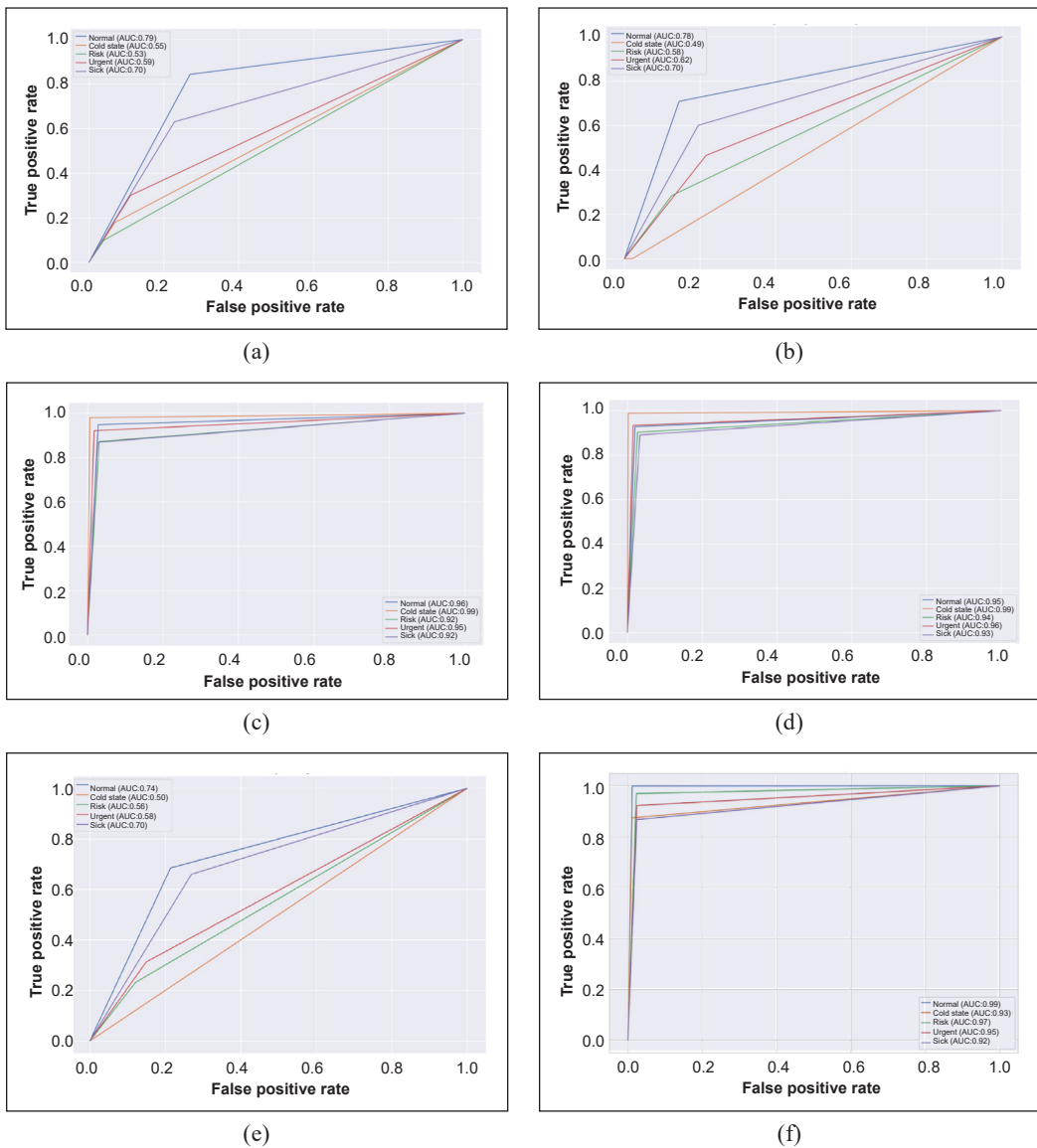


Figure 5. ROC Curves for six supervised machine learning methods: (a) SVM-AUC; (b) LR-AUC; (c) RF-AUC; (d) DT-AUC; (e) KNN-AUC; and (f) KNN-AUC

is an indication that the model has a good measure of separability. Therefore, the DT algorithm achieved the largest area under the ROC curve score of 0.9443, outperforming other algorithms, KNN, RF, LR, SVM, and NB, which had 0.9443, 0.9480, 0.6357, 0.6333, and 0.6135, respectively (Figure 5).

The DT algorithm outperforms other algorithms because it effectively combines decisions. In contrast, RF combines decisions from multiple trees, which may not always yield optimal results.

Additionally, KNN's reliance on proximity for decision-making can lead to inaccuracies in certain cases. Furthermore, the DT algorithm exhibits superior computational efficiency and reduced computational burden, making it particularly advantageous for handling categorical data. Also, the DT algorithm demonstrates enhanced capability in managing collinearity compared to SVMs. What is more, the DT algorithm demonstrates greater efficiency in managing outliers and missing values compared to the LR algorithm. Outliers do not influence DTs due to their ability to divide the data according to feature values. On the other hand, NB is not well-suited for intricate problems. In conclusion, the DT bears certain resemblances to the procedural steps followed by nursing staff in categorizing patients.

CONCLUSION

This paper suggests a way to find and predict the presence of five patient triage levels: normal, cold state, risk, urgent, and sick. These levels are for two chronic diseases: CVD and hypertension. The paper uses and evaluates six supervised machine learning models: SVM, NB, RF, DT, KNN, and LR. The goal is to make an automated triage model for remote patients in telemedicine systems and to provide more accurate health services. The DT algorithm obtained the highest accuracy and performance compared to the other five algorithms. This result was achieved by evaluating each algorithm as a standalone element and using three performance measurements: performance metrics (accuracy, precision, recall, and F1-score), confusion matrix, and ROC-AUC. All these measurements prove that the decision tree algorithm outperformed the other algorithms. Due to this, the results illustrate that the proposed system, with the DT algorithm, provides an accuracy of 93.50%, higher than that of the other algorithms. The suggested method supports the powerful combination of using machine learning in telemedicine and analyzing the huge amounts of medical data from different IoMT devices to make accurate decisions by predicting the triage levels of patients in real-time, particularly high-severity cases. Furthermore, it is advantageous to use structured and unstructured data from the data set with the proposed system Salman, Aal-nouman, et al. (2021), using 55,680 patient records. As a result of the proposed system, patients can be categorized based on the urgency and severity of the cases of patients suffering from CVD and hypertension. In future work, we need to consider adding new symptoms to help patients predict more chronic diseases, such as diabetes, through case studies.

ACKNOWLEDGEMENTS

We thank all the reviewers for their helpful comments and suggestions during the planning and execution of this research. We greatly appreciate their generosity with their time. Additionally, the authors would like to thank the doctors who validated the data generated.

REFERENCES

- Abdalkareem, Z. A., Al-Betar, M. A., Amir, A., Ehkan, P., Hammouri, A. I., & Salman, O. H. (2022). Discrete flower pollination algorithm for patient admission scheduling problem. *Computers in Biology and Medicine*, 141, Article 105007. <https://doi.org/10.1016/j.combiomed.2021.105007>
- Abdalkareem, Z. A., Amir, A., Al-Betar, M. A., Ekhan, P., & Hammouri, A. I. (2021). Healthcare scheduling in optimization context: A review. *Health and Technology*, 11(3), 445–469. <https://doi.org/10.1007/s12553-021-00547-5>
- Abe, D., Inaji, M., Hase, T., Takahashi, S., Sakai, R., Ayabe, F., Tanaka, Y., Otomo, Y., & Machara, T. (2022). A prehospital triage system to detect traumatic intracranial hemorrhage using machine learning algorithms. *JAMA Network Open*, 5(6), Article e2216393. <https://doi.org/10.1001/jamanetworkopen.2022.16393>
- Ahmad, A. S., Hassan, M. Y., Abdullah, M. P., Rahman, H. A., Hussin, F., Abdullah, H., & Saidur, R. (2014). A review on applications of ANN and SVM for building electrical energy consumption forecasting. *Renewable and Sustainable Energy Reviews*, 33, 102–109. <https://doi.org/10.1016/j.rser.2014.01.069>
- AlSereidi, A., Salih, S. Q. M., Mohammed, R. T., Zaidan, A. A., Albayati, H., Pamucar, D., Albahri, A. S., Zaidan, B. B., Shaalan, K., Al-Obaidi, J., Albahri, O. S., Alamoodi, A., Majid, N. A., Garfan, S., Al-Samarraay, M. S., Jasim, A. N., & Baqer, M. J. (2022). Novel federated decision making for distribution of anti-SARS-CoV-2 monoclonal antibody to eligible high-risk patients. *Journal of Information Technology & Decision Making*, 23(1), 197-268. <https://doi.org/10.1142/S021962202250050X>
- Alshammari, F., & Hassan, S. (2019). Perceptions, Preferences and experiences of telemedicine among users of information and communication technology in Saudi Arabia. *Journal of Health Informatics in Developing Countries*, 13(1), Article 20.
- Alsinglawi, B., Alshari, O., Alorjani, M., Mubin, O., Alnajjar, F., Novoa, M., & Darwish, O. (2022). An explainable machine learning framework for lung cancer hospital length of stay prediction. *Scientific Reports*, 12(1), Article 607. <https://doi.org/10.1038/s41598-021-04608-7>
- Barjouei, H. S., Ghorbani, H., Mohamadian, N., Wood, D. A., Davoodi, S., Moghadasi, J., & Saberi, H. (2021). Prediction performance advantages of deep machine learning algorithms for two-phase flow rates through wellhead chokes. *Journal of Petroleum Exploration and Production*, 11(3), 1233–1261. <https://doi.org/10.1007/s13202-021-01087-4>
- Berrar, D. (2019). Bayes' Theorem and naive bayes classifier. In S. Ranganathan, M. Gribskov, K. Nakai & C. Schonbach (Eds.), *Encyclopedia of Bioinformatics and Computational Biology* (pp. 403-412). Elsevier. <https://doi.org/10.1016/B978-0-12-809633-8.20473-1>
- Chatrati, S. P., Hossain, G., Goyal, A., Bhan, A., Bhattacharya, S., Gaurav, D., & Tiwari, S. M. (2022). Smart home health monitoring system for predicting type 2 diabetes and hypertension. *Journal of King Saud University - Computer and Information Sciences*, 34(3), 862–870. <https://doi.org/10.1016/j.jksuci.2020.01.010>
- Chen, M., Tan, X., & Padman, R. (2023). A machine learning approach to support urgent stroke triage using administrative data and social determinants of health at hospital presentation: Retrospective study. *Journal of Medical Internet Research*, 25, Article e36477. <https://doi.org/doi:10.2196/36477>

- Elhaj, H., Achour, N., Hoque, M., & Aciksari, K. (2023). A comparative study of supervised machine learning approaches to predict patient triage outcomes in hospital emergency departments. *Array*, *17*, Article 100281. <https://doi.org/10.1016/j.array.2023.100281>
- Etu, E. E., Monplaisir, L., Arslanturk, S., Masoud, S., Aguwa, C., Markevych, I., & Miller, J. (2022). Prediction of length of stay in the emergency department for COVID-19 patients: A machine learning approach. *IEEE Access*, *10*, 42229–42237. <https://doi.org/10.1109/ACCESS.2022.3168045>
- Ghosh, P., Azam, S., Jonkman, M., Karim, A., Shamrat, F. M. J. M., Ignatious, E., Shultana, S., Beeravolu, A. R., & Boer, F. D. (2021). Efficient prediction of cardiovascular disease using machine learning algorithms with relief and lasso feature selection techniques. *IEEE Access*, *9*, 19304–19326. <https://doi.org/10.1109/ACCESS.2021.3053759>
- Hadi, M. S., Lawey, A. Q., El-Gorashi, T. E. H., & Elmighani, J. M. H. (2020). Patient-centric hetnets powered by machine learning and big data analytics for 6G networks. *IEEE Access*, *8*, 85639–85655. <https://doi.org/10.1109/ACCESS.2020.2992555>
- Hameed, Z., Garcia-Zapirain, B., Aguirre, J. J., & Isaza-Ruget, M. A. (2022). Multiclass classification of breast cancer histopathology images using multilevel features of deep convolutional neural network. *Scientific Reports*, *12*(1), Article 15600. <https://doi.org/https://doi.org/10.1038/s41598-022-19278-2>
- Hamid, R. A., Albahri, A. S., Albahri, O. S., & Zaidan, A. A. (2022). Dempster–shafer theory for classification and hybridised models of multi-criteria decision analysis for prioritisation: a telemedicine framework for patients with heart diseases. *Journal of Ambient Intelligence and Humanized Computing*, *13*(9), 4333–4367. <https://doi.org/10.1007/s12652-021-03325-3>
- Huang, F., & Wang, Y. (2023). Introducing machine learning in auditing courses. *Journal of Emerging Technologies in Accounting*, *20*(1), 195–211. <https://doi.org/https://doi.org/10.2308/JETA-2022-017>
- Hussein, O., Aal-nouman, M. I., & Taha, Z. K. (2020). Reducing waiting time for remote patients in telemedicine with considering treated patients in emergency department based on body sensors technologies and hybrid computational algorithms: Toward scalable and efficient real time healthcare monitoring system. *Journal of Biomedical Informatics*, *112*, Article 103592. <https://doi.org/10.1016/j.jbi.2020.103592>
- Jampala, R., Gummadi, A. N., Santosh, K. D. S., Potharlanka, G., Goutham, C., & Chintala, R. R. (2023, August 3-5). *The evolution of digital health care: From stethoscopes to smart phones*. [Paper presentation]. 5th International Conference on Inventive Research in Computing Applications (ICIRCA), Coimbatore, India. <https://doi.org/10.1109/ICIRCA57980.2023.10220805>
- Jebli, I., Belouadha, F. Z., Kabbaj, M. I., & Tilioua, A. (2021). Prediction of solar energy guided by pearson correlation using machine learning. *Energy*, *224*, Article 120109. <https://doi.org/https://doi.org/10.1016/j.energy.2021.120109>
- Jiang, H., Mao, H., Lu, H., Lin, P., Garry, W., Lu, H., Yang, G., Rainer, T. H., & Chen, X. (2021). Machine learning-based models to support decision-making in emergency department triage for patients with suspected cardiovascular disease. *International Journal of Medical Informatics*, *145*, Article 104326. <https://doi.org/10.1016/j.ijmedinf.2020.104326>
- Kadum, S. Y., Salman, O. H., Taha, Z. K., Said, A. B., Ali, M. A. M., Qassim, Q. S., Aal-Nouman, M. I., Mohammed, D. Y., Al-baker, B. M., & Abdalkareem, Z. A. (2023). Machine learning-based telemedicine

- framework to prioritize remote patients with multi-chronic diseases for emergency healthcare services. *Network Modeling Analysis in Health Informatics and Bioinformatics*, 12(1), Article 11. <https://doi.org/https://doi.org/10.1007/s13721-022-00407-w>
- Kamali, M. Z., Davoodi, S., Ghorbani, H., Wood, D. A., Mohamadian, N., Lajmorak, S., Rukavishnikov, V. S., Taherizade, F., & Band, S. S. (2022). Permeability prediction of heterogeneous carbonate gas condensate reservoirs applying group method of data handling. *Marine and Petroleum Geology*, 139, Article 105597. <https://doi.org/10.1016/j.marpetgeo.2022.105597>
- Khan, M. F., Ghazal, T. M., Said, R. A., Fatima, A., Abbas, S., Khan, M. A., Issa, G. F., Ahmad, M., & Khan, M. A. (2021). An IoMT-enabled smart healthcare model to monitor elderly people using machine learning technique. *Computational Intelligence and Neuroscience*, 2021, Article 2487759. <https://doi.org/https://doi.org/10.1155/2021/2487759>
- Kotwal, S., Rani, P., Arif, T., Manhas, J., & Sharma, S. (2022). Automated bacterial classifications using machine learning based computational techniques: Architectures, challenges and open research issues. *Archives of Computational Methods in Engineering*, 29, 2469–2490. <https://doi.org/10.1007/s11831-021-09660-0>
- Lestari, W., & Sumarlinda, S. (2022). Implementation of K-Nearest Neighbor (KNN) and Support Vector Machine (SVM) for classification cardiovascular disease. *Multiscience*, 2(10), 30–36.
- Liu, J., Timsina, P., & El-Gayar, O. (2018). A comparative analysis of semi-supervised learning: the case of article selection for medical systematic reviews. *Information Systems Frontiers*, 20, 195–207. <https://doi.org/10.1007/s10796-016-9724-0>
- Mahon, S. E., & Rifino, J. J. (2024). Role of emergency medical services in disaster management and preparedness. In G. Ciottono (Ed.) *Ciottono's Disaster Medicine* (pp. 12–18). Elsevier. <https://doi.org/10.1016/B978-0-323-80932-0.00003-3>
- Manickam, P., Mariappan, S. A., Murugesan, S. M., Hansda, S., Kaushik, A., Shinde, R., & Thipperudraswamy, S. P. (2022). Artificial Intelligence (AI) and Internet of Medical Things (IoMT) assisted biomedical systems for intelligent healthcare. *Biosensors*, 12(8), Article 562. <https://doi.org/10.3390/bios12080562>
- Mohammed, K. I., Jaafar, J., Zaidan, A. A., Albahri, O. S., Zaidan, B. B., Albahri, A. S., Alsalem, M. A., & Alamoodi, A. H. (2020). A uniform intelligent prioritisation for solving diverse and big data generated from multiple chronic diseases patients based on hybrid decision-making and voting method. *IEEE Access*, 8, 91521–91530. <https://doi.org/10.1109/ACCESS.2020.2994746>
- Mohammed, K. I., Zaidan, A. A., Zaidan, B. B., Albahri, O. S., Albahri, A. S., Alsalem, M. A., & Mohsin, A. H. (2020). Novel technique for reorganisation of opinion order to interval levels for solving several instances representing prioritisation in patients with multiple chronic diseases. *Computer Methods and Programs in Biomedicine*, 185, Article 105151. <https://doi.org/10.1016/j.cmpb.2019.105151>
- Mohan, S., Thirumalai, C., & Srivastava, G. (2019). Effective heart disease prediction using hybrid machine learning techniques. *IEEE Access*, 7, 81542–81554. <https://doi.org/10.1109/ACCESS.2019.2923707>
- Morrill, J., Qirko, K., Kelly, J., Ambrosy, A., Toro, B., Smith, T., Wysham, N., Fudim, M., & Swaminathan, S. (2022). A machine learning methodology for identification and triage of heart failure exacerbations. *Journal of Cardiovascular Translational Research*, 15(1), 103–115. <https://doi.org/10.1007/s12265-021-10151-7>

- Mujawar, M. A., Gohel, H., Bhardwaj, S. K., Srinivasan, S., Hickman, N., & Kaushik, A. (2020). Nano-enabled biosensing systems for intelligent healthcare: Towards COVID-19 management. *Materials Today Chemistry*, 17, Article 100306. <https://doi.org/10.1016/j.mtchem.2020.100306>
- Onan, A. (2021). Sentiment analysis on massive open online course evaluations: A text mining and deep learning approach. *Computer Applications in Engineering Education*, 29(3), 572–589. <https://doi.org/10.1002/cae.22253>
- Onan, A. (2022). Bidirectional convolutional recurrent neural network architecture with group-wise enhancement mechanism for text sentiment classification. *Journal of King Saud University - Computer and Information Sciences*, 34(5), 2098–2117. <https://doi.org/10.1016/j.jksuci.2022.02.025>
- Onan, A. (2023). SRL-ACO: A text augmentation framework based on semantic role labeling and ant colony optimization. *Journal of King Saud University - Computer and Information Sciences*, 35(7), Article 101611. <https://doi.org/10.1016/j.jksuci.2023.101611>
- Onan, A., Korukoğlu, S., & Bulut, H. (2017). A hybrid ensemble pruning approach based on consensus clustering and multi-objective evolutionary algorithm for sentiment classification. *Information Processing and Management*, 53(4), 814–833. <https://doi.org/10.1016/j.ipm.2017.02.008>
- Otoom, M., Otoum, N., Alzubaidi, M. A., Etoom, Y., & Banihani, R. (2020). An IoT-based framework for early identification and monitoring of COVID-19 cases. *Biomedical Signal Processing and Control*, 62, Article 102149. <https://doi.org/10.1016/j.bspc.2020.102149>
- Ozsahin, D. U., Mustapha, M. T., Mubarak, A. S., Ameen, Z. S., & Uzun, B. (2022, August 2-4). *Impact of outliers and dimensionality reduction on the performance of predictive models for medical disease diagnosis*. [Paper presentation]. International Conference on Artificial Intelligence in Everything (AIE), Lefkosa, Cyprus. <https://doi.org/10.1109/AIE57029.2022.00023>
- Pan, Y., Zhang, J., Luo, G. Q., & Yuan, B. (2018, June 15-17). *Evaluating radar performance under complex electromagnetic environment using supervised machine learning methods: A case study*. [Paper presentation]. 8th International Conference on Electronics Information and Emergency Communication (ICEIEC), Beijing, China. <https://doi.org/10.1109/ICEIEC.2018.8473520>
- Patel, H., Guttula, S., Mittal, R. S., Manwani, N., Berti-Equille, L., & Manatkar, A. (2022, August 14-18). *Advances in Exploratory data analysis , visualisation and quality for data centric AI systems algorithms suitable for industry workloads*. [Paper presentation]. 28th ACM SIGKDD Conference on Knowledge Discovery and Data Mining, Washington, USA. <https://doi.org/10.1145/3534678.3542604>
- Potdar, V., Santhosh, L., & Jadhav, L. (2022). Coronary heart disease prediction using machine learning. *Journal of Emerging Technologies and Innovative Research*, 9(12), e390-e396.
- Rabash, A. J., Nazri, M. Z. A., Shapii, A., & Al-Jumaily, A. (2023). Stream learning under concept and feature drift: A literature survey. *Journal of Autonomous Intelligence*, 6(3), 1–16. <https://doi.org/10.32629/jai.v6i3.880>
- Rabash, A. J., Nazri, M. Z. A., Shapii, A., & Hasan, M. K. (2023). Non-dominated sorting genetic algorithm-based dynamic feature selection for intrusion detection system. *IEEE Access*, 11, 125080–125093. <https://doi.org/10.1109/ACCESS.2023.3328395>

- Rashidi, H. H., Tran, N., Albahra, S., & Dang, L. T. (2021). Machine learning in health care and laboratory medicine: General overview of supervised learning and Auto-ML. *International Journal of Laboratory Hematology*, 43, 15-22. <https://doi.org/10.1111/ijlh.13537>
- Ratih, I. D., Retnaningsih, S. M., Islahulhaq, I., & Dewi, V. M. (2022). Synthetic minority over-sampling technique nominal continuous logistic regression for imbalanced data. *AIP Conference Proceedings*, 2668(1), Article 070021. <https://doi.org/https://doi.org/10.1063/5.0111804>
- Riedel, H. B., Espejo, T., Bingisser, R., Kellett, J., & Nickel, C. H. (2023). A fast emergency department triage score based on mobility, mental status and oxygen saturation compared with the emergency severity index: A prospective cohort study. *QJM: An International Journal of Medicine*, 116(9), 774-780. <https://doi.org/10.1093/qjmed/hcad160>
- Şahin, B., & İlgin, G. (2022). Risk factors of deaths related to cardiovascular diseases in World Health Organization (WHO) member countries. *Health and Social Care in the Community*, 30(1), 73–80. <https://doi.org/10.1111/hsc.13156>
- Salman, O. H., Rasid, M. F. A., Saripan, M. I., & Subramaniam, S. K. (2014). Multi-sources data fusion framework for remote triage prioritization in telehealth. *Journal of Medical Systems*, 38(9), Article 103. <https://doi.org/10.1007/s10916-014-0103-4>
- Salman, O. H., Aal-Nouman, M. I., & Taha, Z. K. (2020). Reducing waiting time for remote patients in telemedicine with considering treated patients in emergency department based on body sensors technologies and hybrid computational algorithms: Toward scalable and efficient real time healthcare monitoring system. *Journal of Biomedical Informatics*, 112, Article 103592. <https://doi.org/10.1016/j.jbi.2020.103592>
- Salman, O. H., Aal-nouman, M. I., Taha, Z. K., Alsabah, M. Q., Hussein, Y. S., & Abdelkareem, Z. A. (2021). Formulating multi diseases dataset for identifying, triaging and prioritizing patients to multi medical emergency levels: Simulated dataset accompanied with codes. *Data in Brief*, 34, Article 106576. <https://doi.org/10.1016/j.dib.2020.106576>
- Salman, O. H., Taha, Z., Alsabah, M. Q., Hussein, Y. S., Mohammed, A. S., & Aal-Nouman, M. (2021). A review on utilizing machine learning technology in the fields of electronic emergency triage and patient priority systems in telemedicine: coherent taxonomy, motivations, open research challenges and recommendations for intelligent future work. *Computer Methods and Programs in Biomedicine*, 209, Article 106357. <https://doi.org/https://doi.org/10.1016/j.cmpb.2021.106357>
- Salman, O. S., Latiff, N. M. A. A., Arifin, S. H. S., Salman, O. H., & Al-Dhief, F. T. (2022, November 14-16). *Internet of medical things based telemedicine framework for remote patients triage and emergency medical services*. [Paper presentation]. IEEE 6th International Symposium on Telecommunication Technologies (ISTT), Johor Bahru, Malaysia. <https://doi.org/10.1109/ISTT56288.2022.9966532>
- Saranya, G., & Pravin, A. (2023). A novel feature selection approach with integrated feature sensitivity and feature correlation for improved prediction of heart disease. *Journal of Ambient Intelligence and Humanized Computing*, 14(9), 12005–12019. <https://doi.org/https://doi.org/10.1007/s12652-022-03750-y>
- Shiwangi, K. M., Sandhu, J. K., & Sahu, R. (2023, August 10-11). *Effective heart-disease prediction by using hybrid machine learning technique*. [Paper presentation]. International Conference on Circuit Power and Computing Technologies (ICCPCT), Kollam, India. <https://doi.org/10.1109/ICCPCT58313.2023.10245785>

- Sims, J. M. (2018). Communities of practice: Telemedicine and online medical communities. *Technological Forecasting & Social Change* 126, 53-56. <https://doi.org/10.1016/j.techfore.2016.08.030>
- Vasina, M., Velecky, J., Planas-Iglesias, J., Marques, S. M., Skarupova, J., Damborsky, J., Bednar, D., Mazurenko, S., & Prokop, Z. (2022). Tools for computational design and high-throughput screening of therapeutic enzymes. *Advanced Drug Delivery Reviews*, 183, Article 114143. <https://doi.org/10.1016/j.addr.2022.114143>
- WHO. (2022). *Health systems resilience toolkit: A WHO global public health good to support building and strengthening of sustainable health systems resilience in countries with various contexts*. World Health Organization. <https://www.who.int/publications/i/item/9789240048751>
- Yang, Y. (2020). Medical multimedia big data analysis modeling based on DBN algorithm. *IEEE Access*, 8, 16350–16361. <https://doi.org/10.1109/aACCESS.2020.2967075>

Finite Element Analysis of a Portable Bamboo Girder Used in Emergency Responses

Azrul Affandhi Musthaffa^{1*}, Norazman Mohamad Nor¹, Abdulrahman Alhayek², Mohammed Alias Yusof¹ and Mohd Yuhazri Yaakob³

¹Faculty of Engineering, Universiti Pertahanan Nasional Malaysia, Sungai Besi, Kuala Lumpur 57000, Malaysia

²Civil Engineering Department, College of Engineering, Universiti Tenaga Nasional, Jalan IKRAM - UNITEN, 43000 Kajang, Selangor, Malaysia

³Faculty of Engineering, Universiti Teknikal Malaysia Melaka (UTeM), Hang Tuah Jaya, 76100 Durian Tunggal, Melaka, Malaysia

ABSTRACT

This study uses numerical simulation to explore the performance of a portable bamboo girder designed for emergency scenarios and compares it to its steel counterpart. It underscores bamboo's appeal, offering a lightweight, quickly deployable, and eco-friendly alternative to steel. The research aims to assess bamboo's viability in emergency bridge construction, utilising SOLIDWORKS and ANSYS to create and simulate bamboo and steel girders. A bamboo girder aimed at humanitarian assistance and disaster relief (HADR) operations was analysed through ANSYS software under a Toyota Hilux truck's weight. Material properties, loads, and boundary conditions were defined for an accurate simulation. Three individual bamboo culms were tested in four-point flexural experiments, and the results revealed a modulus of elasticity of 14583 MPa and a local failure due to crushing and splitting with an ultimate strength of 263 MPa. Finite element analysis results indicated that the bamboo girder had a stress

of 85.56 MPa and a deflection of 84.68 mm. Although the steel girder showed lower deflection, it had significantly higher stresses and weighed 180% more than the bamboo version. The bamboo girder's deflection surpassed the recommended limit under a fully loaded truck, indicating room for improvement. However, stress analysis revealed that the bamboo's structural integrity remained below its design strength. Conversely, the steel girder

ARTICLE INFO

Article history:

Received: 08 December 2023

Accepted: 06 February 2024

Published: 26 August 2024

DOI: <https://doi.org/10.47836/pjst.32.5.24>

E-mail addresses:

azrulaffandhi.aa@gmail.com (Azrul Affandhi Musthaffa)

azman@upnm.edu.my (Norazman Mohamad Nor)

rahman.hayek@gmail.com (Abdulrahman Alhayek)

alias@upnm.edu.my (Mohammed Alias Yusof)

yuhazri@utem.edu.my (Mohd Yuhazri Yaakob)

* Corresponding author

exhibited higher stresses and considerably greater weight. Despite deflection concerns, the bamboo girder demonstrated structural soundness and lower weight compared to steel. This positions it as a viable solution for swift emergency deployment, warranting further refinement for enhanced performance.

Keywords: Bamboo girder, finite element method, simulation, sustainability

INTRODUCTION

Sustainable development and green technology have become the major engineering themes in the 21st century, specifically in civil and structural engineering. New environmentally friendly materials such as composite polymer and bio-composite materials are developed to partially replace conventional construction materials such as steel and concrete (Rahman et al., 2023; Najeeb et al., 2023). On the other hand, bamboo has been identified as one of the alternative construction materials for building and bridge structures. Bamboo is abundant and well-known for its ability to withstand high bending stress, tensile stress and compressive stress, according to Bahari and Krause (Bahari & Krause, 2016). Apart from exhibiting a high strength-to-weight ratio, bamboo culms are fast-growing, mature in three years, and reach the peak of their strength. In China, bamboo was used to construct simple suspension bridges by splitting the bamboo to make cables or twisting whole culms of pliable bamboo together (Akinlabi et al., 2017; Liu et al., 2018). The utilisation of bamboo as an alternative construction material for buildings and bridges has been widely known. Modern studies have proven the use of bamboo in the construction of houses (Salzer et al., 2016), multistorey buildings (Yang et al., 2020) and various types of bridges (Amede et al., 2021). Because of its unique rhizome-dependent system, bamboo is one of the fastest-growing plants in the world, growing three times faster than most other plant species (Liu et al., 2022).

Additionally, bamboo can be utilised as a stand-alone material. Bamboo may be a viable substitute for steel, concrete, and masonry (Egoh et al., 2020; Auwalu & Dickson, 2019). Numerous bridges and expansive roofs with long spans have been erected in regions where bamboo cultivation thrives. An instance from 1937 involves the United States army, which ingeniously employed bamboo for a bridge in the Philippines (Chung & Yu, 2002). This bamboo bridge extended to 15 meters and showcased a remarkable capacity to endure a load of 16 kN. In contemporary times, bridge construction has leveraged laminated bamboo techniques. In 2006, the inaugural prototype of a bamboo bridge was introduced to experiment with laminated bamboo's application. Yan et al. (2010) documented the creation of girder samples composed of bamboo, subsequently utilised in erecting a 10-meter pedestrian bridge in Daozi. The bridge's surface was covered with precast concrete formed from reinforced bamboo strips. In addition, two

bamboo bridge projects in China have also shown that using nature-based solutions like bamboo can result in significantly fewer CO₂ emissions compared to similar bridges made of concrete or steel (Rong et al., 2022).

During peacetime, rapid bridging construction is needed to temporarily replace a damaged bridge caused by natural disasters such as floods, landslides, earthquakes or tsunamis. In this situation, a portable bridge is usually utilised while the new bridge is constructed. Portable bridging has been identified as the fastest and the most effective solution to open up the line of communication for Humanitarian Assistance and Disaster Relief (HADR) operations (Musthaffa et al., 2018). In this study, a portable bridge girder intended for small vehicles and made primarily from bamboo was modelled and analysed. The girder has some steel parts to hold the bamboo culms together, ensure they work as one unit, and provide a way to connect multiple segments as needed. The finite element numerical simulation was conducted using ANSYS software to investigate the girder's performance and deformation under the gross weight of a Toyota Hilux truck. This design provides a quick deployment time and the ability to expand for longer spans while being environmentally sustainable using a natural and lightweight material.

MATERIAL EXPERIMENT

Based on availability in Malaysia, Buluh Semantan (*Gigantochloa scortechinii*) bamboo harvested from Hulu Selangor was obtained at 3 to 5 years old. These bamboo culms have a length of around 4.58 m, an outer diameter between 95 and 120 mm with an average of 100 mm, and a thickness between 6 and 13 mm with an average of 10 mm.

In order to establish the properties of the bamboo members used in the analysis, a set of four-point bending experimental tests was conducted to assess the structural behaviour of the material under applied loads according to ISO 22157:2004 (ISO 22157-2:2004, 2004). The tests were conducted on three full bamboo tubes with a length of 4 m in a four-point bending setup, as shown in Figure 1. The setup consisted of a rigid steel frame with two fixed supports and two loading points spaced at a specific distance along the specimens according to the distance of nodes. ISO 22157:2004 defines the minimum free span of the culm to avoid failure by a transverse force to be 30D, where D is the outer diameter. This minimum span is around 3054 mm for the bamboo culms used in the experiments.

The specimens were positioned, and load was incrementally applied at a uniformly constant speed of 0.5 mm/s to induce bending. The test results revealed that the material failed locally due to crushing and splitting, as displayed in Figure 2. The average modulus of elasticity was 14583 MPa, and the average ultimate strength was 263 MPa, which will be used in the numerical simulation. The flexural test results are summarised in Table 1.

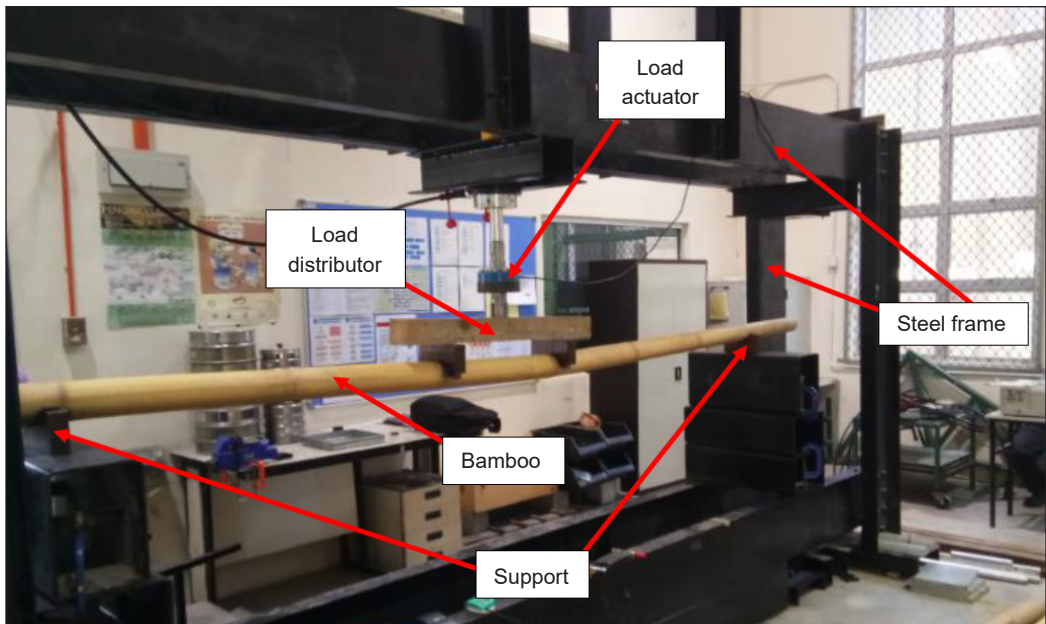


Figure 1. Test setup for bamboo in a four-point bending experiment



Figure 2. Local failure of bamboo due to crushing and splitting

Table 1
Summary of four-point bending experimental results

Sample ID	Inner diameter (mm)	Outer diameter (mm)	Thickness (mm)	Support span (mm)	Loading span (mm)	Modulus of elasticity (MPa)	Ultimate strength (MPa)
B1	80.5	98.3	8.9	3,260	580	13306.6	235.1
B2	78.3	104.5	13.1	3,760	855	15859.7	287.5
B3	78.8	102.4	11.8	3,450	765	14585.5	266.5
Average	79.2	101.8	11.3	-	-	14583.9	263.0

FINITE ELEMENT ANALYSIS METHODOLOGY

The 3D model of the girder is divided into two segments for ease of transportation and deployment. Each segment contains a 12-tube bamboo bundle, a steel connection at each end, and a steel plate on top. Figure 3 displays a flowchart for the methodology overview.

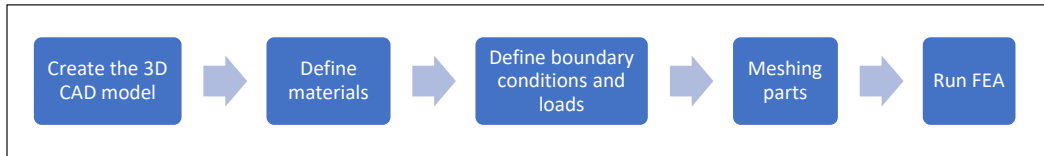


Figure 3. Methodology overview

Creating the 3D Model

The girder was created separately and assembled into the final girder in SOLIDWORKS. The bamboo bundle is 4 m long and is arranged in a 3×4 formation, as shown in Figure 4 (a). The average dimensions taken from Table 1 are used in creating the bamboo cross sections where each bamboo tube has an outer diameter of 100 mm and an inner diameter of 80 mm, giving the bundle a total width of 300 mm and a total depth of 400 mm. In addition, there are steel connections, which can be seen in Figure 4 (b), at each end with the same dimensions that provide a way to connect segments to create a longer-span girder. In order

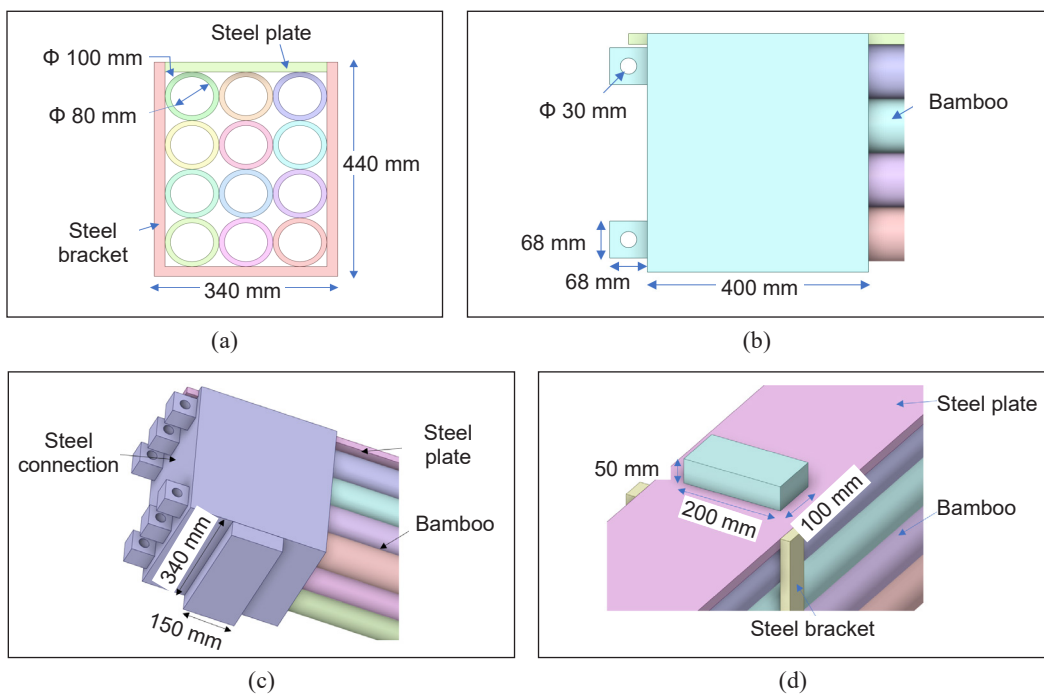


Figure 4. Parts dimensions: (a) cross-section of a bamboo bundle; (b) Steel connection; (c) Support pad; and (d) Loading pad

to keep the bundle in its 3×4 arrangement and work as one unit, four steel brackets were created at 800 mm spacing, as seen in Figure 5, each with a thickness of 20 mm. Moreover, load and support pads were created to apply the loading and boundary conditions on the girder, as displayed in Figures 4 (c) and (d). The loading pads' dimensions of 100×200 mm are the wheel patches that a car would form on the girder. At the same time, the loading span is 3085 mm based on the Toyota Hilux truck's dimensions and positioned on the girder to induce the maximum bending moment.

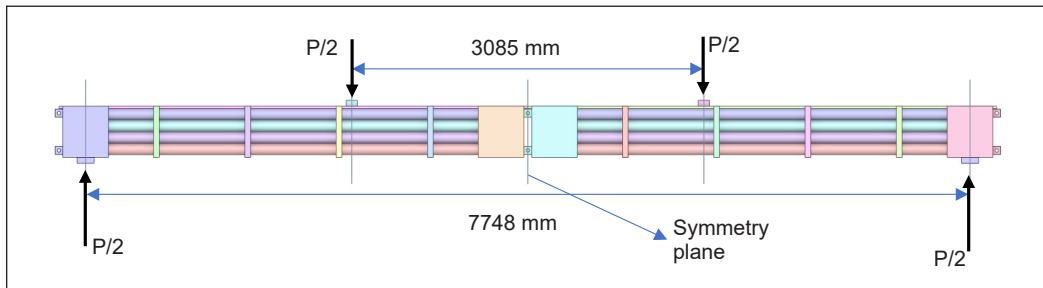


Figure 5. The full two segments girder

Generating the Numerical Model

After creating the fully assembled 3D model was transferred to ANSYS to generate the numerical model where materials are defined, loads and boundary conditions are assigned, and the simulation results are checked. Three materials were defined and used in the simulation, as shown in Table 2. A bamboo material is used for all the bamboo tubes, and structural steel is used for all the steel parts like the connections, brackets, and top plates. As for the loading and support pads, a soft, nearly incompressible material was created to transfer the loads while preventing stress concentrations at their locations and helping with convergence. The average modulus of elasticity obtained from the experimental flexural tests was used. On the other hand, design strength is used to assess the safety and feasibility of the bamboo girder design, which was obtained by utilising a factor of safety 1.5 for the ultimate strength, which would cover the uncertainty in bamboo strength, as shown in Equation 1.

$$Design\ strength = \frac{Ultimate\ strength}{1.5} \quad [1]$$

To take advantage of the symmetry in this girder and to reduce the computation time, only half of this girder was transferred to ANSYS, and a symmetry plane was created. As seen in Figure 5, the loading configuration follows the spacing and loads of a Toyota Hilux with a total gross weight of 28.5 kN. Furthermore, a dynamic amplification factor Φ that takes account of the dynamic magnification of stresses and vibration effects in the structure should be considered in a quasi-static analysis according to EN-1991-2 (Technical

Table 2
Material properties

Property	Bamboo	Structural Steel	Bearing Pads
Density (Kg/m ³)	740	7850	1
Modulus of Elasticity (MPa)	14583	200000	70
Poisson's Ratio	0.3	0.3	0.4999
Ultimate Strength (MPa)	263	460	-
Design/Yield Strength (MPa)	175	250	-

Committee CEN, 2003). Although the code disregards the dynamic factor for vehicles moving at low speed (not more than 5 km/h), it requires the inclusion of a dynamic factor for vehicles moving at normal speed (70 km/h). For the case of a vehicle moving at normal speed, this factor is taken as illustrated in Equation 2:

$$\phi = 1.40 - \frac{L}{500} \geq 1 \quad [2]$$

where L is the span length for a simply supported girder in meters, it is around 1.3 for this girder, which makes the total load 37.05 kN. Since this girder is part of a bridge system consisting of 2 girders, only half of the total load was applied on this girder, which comes to P = 18.53 kN, giving each loading pad a downward force of 9.26 kN. Moreover, the self-weight of the girder was added by defining the standard earth gravity acceleration of 9.81 m/s², and fixed support was applied to the bottom of the support pads, as illustrated in Figures 6 and 7.

For meshing, ANSYS offers a comprehensive library of elements that covers a wide range of engineering problems such as thermal, fluid, stress and many more. In this simulation, higher-order 3D solid elements exhibiting quadratic displacement behaviour were used for accuracy. Most solid elements were SOLID186, a higher-order 3D 20-node solid element that exhibits quadratic displacement behaviour. This element is defined by 20 nodes with three degrees of freedom per node: translations in the directions of the nodal x, y, and z. In addition, some elements of SOLID187 were used, such as a higher order 3D, 10-node element with a quadratic displacement behaviour well suited to modelling irregular meshes. Both elements above can be seen in Figure 8.

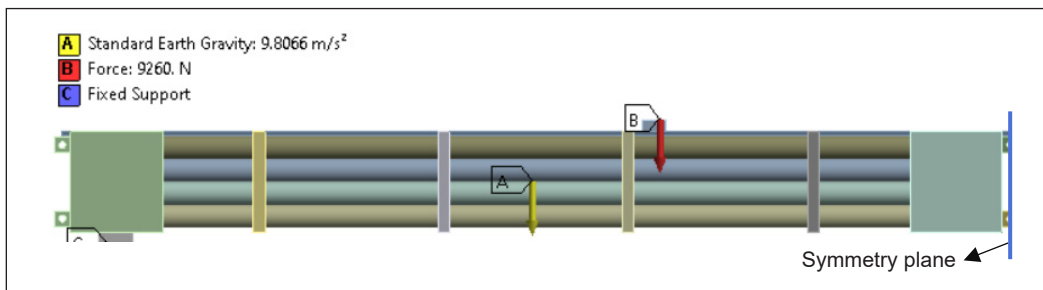


Figure 6. Defining self-weight, applied force, fixed support, and the symmetry plane

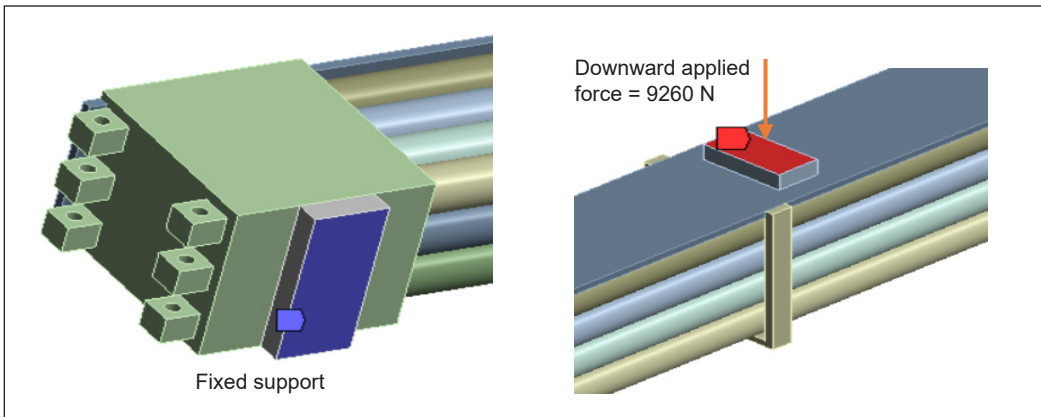


Figure 7. Defining boundary conditions and loads

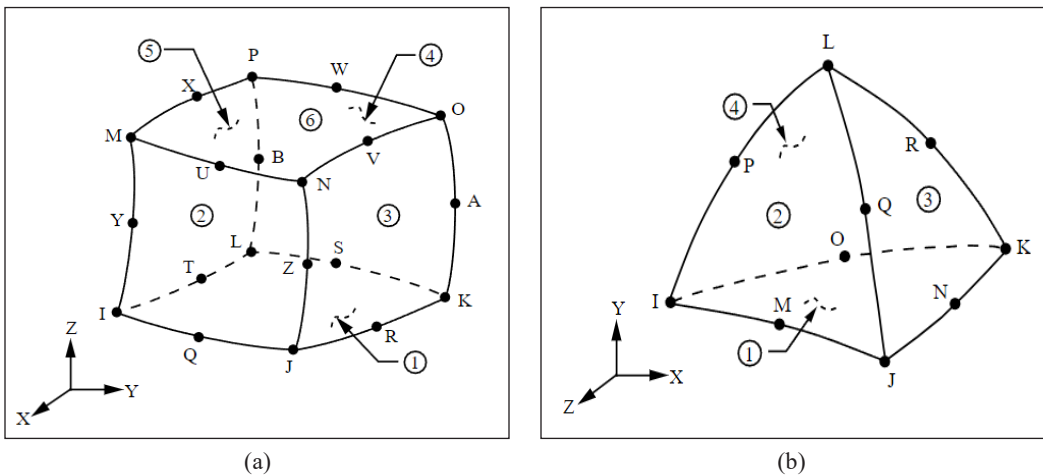


Figure 8. The geometry, node locations, and the element coordinate system for: (a) SOLID186; and (b) SOLID187 (Ansys Inc., 2017)

Furthermore, a mesh independence check was conducted, starting with a 20 mm mesh size while checking the maximum equivalent stress in bamboo (Table 3). Increasing the number of elements over six times to nearly 525000 resulted in a slight decrease in the stress.

Therefore, a global size of 20 mm was chosen to balance accuracy with computational time, as seen in Figure 9. It resulted in a total number of nodes 270572 and a total number of solid elements 79803. ANSYS offers many types of contacts to define the behaviour between different parts coming into contact with each other, such as bonded, frictional, and frictionless. The contacts between the support and loading pads and the steel parts they touch were defined as bonded, a linear contact that prevents sliding and separation. The contacts and interactions between bamboo tubes were defined as frictional contact with a friction coefficient of 0.1, a nonlinear contact type that allows separation and sliding with some

Table 3
Mesh independence study

Iteration	Equivalent Stress Bamboo (MPa)	Change (%)	Nodes	Elements
1	85.564	-	270572	79803
2	83.977	-1.85	926570	526237

friction. Moreover, the contact between bamboo tubes and surrounding steel parts was also defined as frictional contact with a friction coefficient of 0.1. Accordingly, the total number of contact elements is found to be 64090. The contact pair elements used are CONTA174 and TARGE170. The first element, CONTA174, represents contact and sliding between 3D target surfaces and a deformable surface defined by this element. It has the same geometric characteristics as the solid or shell element face with which it is connected, and the contact occurs when the element surface penetrates an associated target surface. On the other hand, TARGE170 is used to represent various 3D “target” surfaces for the associated contact elements, such as CONTA174, where the contact elements themselves overlay the solid, shell, or line elements describing the boundary of a deformable body and are potentially in contact with the target surface. As for the steel parts, they are considered to be welded together, and as a result, a mesh continuity was provided between them.

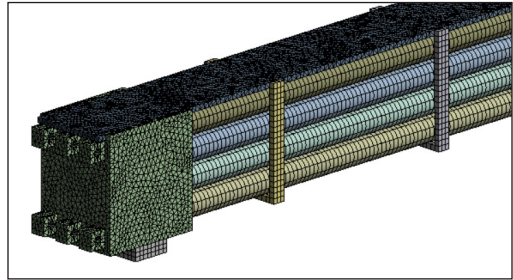


Figure 9. The meshing size is 20 mm

The Governing Equations

For many structures, it is difficult to determine the distribution of deformation and stress using conventional methods, and thus the finite element method (FEM) is necessarily used. This method is a powerful numerical technique for solving partial differential equations and analysing complex physical systems in engineering and science. FEM starts by creating what is known as a mesh which divides a complex physical domain into small elements connected at rigid points called nodes. Each element has a mathematical function, known as the shape function, which describes and approximates the behaviour of the physical quantities within the element based on the element’s geometry and connectivity. Additionally, these elements are bound and behave according to the governing equations, which are the equations that define the principles of physics and describe the behaviour of the system under consideration. In the case of static structural analysis, they are (1) material constitutive equations, (2) equilibrium equations, and (3) displacement-strain equations. These equations express the relationships between the physical quantities and external forces, ensuring that equilibrium and other physical laws are satisfied.

Three primary methods can be used to derive the finite element equations of a physical system. These are (1) the direct method or direct equilibrium method for structural analysis problems, which is typically used in analytical hand calculations; (2) the variational methods, such as the principle of minimum of potential energy and the principle of virtual work, and (3) the weighted residual methods. While the direct method gives exact solutions, solving complicated cases is much more difficult. Therefore, finite element analysis programs use weak forms, such as the variational method, to describe the problem in integral form and give an approximate numerical solution.

ANSYS uses the principle of virtual work to derive the governing equations, which state, “If a deformable body in equilibrium is subjected to arbitrary virtual (imaginary) displacements associated with a compatible deformation of the body, the virtual work of external forces on the body is equal to the virtual strain energy of the internal stresses.” The advantage of this principle over the minimum potential energy is that it applies more generally to both materials that behave in a linear elastic, as well as those that behave in a nonlinear fashion. Applying the principle to a finite element gives Equation 3:

$$\delta U^{(e)} = \delta W^{(e)} \tag{3}$$

Where $\delta U^{(e)}$ is the virtual strain energy due to internal stresses (the internal virtual work), and $\delta W^{(e)}$ is the virtual work of external forces on the element (the external virtual work). Another set of equations that relate stresses to strains are called the constitutive equations, which define the relationship between stress and strain within a material as in Equation 4:

$$\sigma_{ij} = C_{ijkl} \epsilon_{kl} \tag{4}$$

where σ_{ij} is the stress components, C_{ijkl} is the components of the elastic stiffness tensor, and ϵ_{kl} is the strain components. These equations form the basis for solving three-dimensional stress analysis problems, where the goal is to determine the stress and strain distribution within a solid body subject to applied loads and boundary conditions. The specific form of these equations can be modified for different material behaviours and boundary conditions. For isotropic linear elastic materials, the relationship is as in Equation 5:

$$\begin{bmatrix} \sigma_1 \\ \sigma_2 \\ \sigma_3 \\ \tau_{23} \\ \tau_{13} \\ \tau_{12} \end{bmatrix} = \frac{E}{(1+\nu)(1-2\nu)} \begin{bmatrix} 1-\nu & \nu & \nu & 0 & 0 & 0 \\ \nu & 1-\nu & \nu & 0 & 0 & 0 \\ \nu & \nu & 1-\nu & 0 & 0 & 0 \\ 0 & 0 & 0 & \frac{(1-2\nu)}{2} & 0 & 0 \\ 0 & 0 & 0 & 0 & \frac{(1-2\nu)}{2} & 0 \\ 0 & 0 & 0 & 0 & 0 & \frac{(1-2\nu)}{2} \end{bmatrix} \begin{bmatrix} \epsilon_1 \\ \epsilon_2 \\ \epsilon_3 \\ \gamma_{23} \\ \gamma_{13} \\ \gamma_{12} \end{bmatrix} \tag{5}$$

where E is the Young’s modulus, and ν is Poisson’s ratio. All aforementioned governing equations must satisfy the equilibrium equations, which, in the case of a 3D static stress state, are given by Equations 6, 7 and 8:

$$\frac{\partial \sigma_x}{\partial x} + \frac{\partial \tau_{xy}}{\partial y} + \frac{\partial \tau_{xz}}{\partial z} + \rho g_x = 0 \tag{6}$$

$$\frac{\partial \tau_{yx}}{\partial x} + \frac{\partial \sigma_y}{\partial y} + \frac{\partial \tau_{yz}}{\partial z} + \rho g_y = 0 \tag{7}$$

$$\frac{\partial \tau_{zx}}{\partial x} + \frac{\partial \tau_{zy}}{\partial y} + \frac{\partial \sigma_z}{\partial z} + \rho g_z = 0 \tag{8}$$

where σ is the normal stress, τ is the shear stress, $\tau_{xy} = \tau_{yx}$, $\tau_{xz} = \tau_{zx}$, and $\tau_{yz} = \tau_{zy}$, and ρg represents the body forces in three directions. Figure 10 shows the stress state of a 3D differential element in space.

The third governing equation for 3D static structural analysis is displacement-strain relations. It can be expressed in a matrix form by considering a vector of displacements (d) and a vector of strains (ϵ); the relationship is given by Equation 9:

$$\{\epsilon\} = [B]\{d\} \tag{9}$$

where B is the strain-displacement matrix and d is the nodal displacement in each degree of freedom. Consequently, the element stiffness matrix is calculated by Equation 10:

$$[k] = \iiint [B]^T [C] [B] dV \tag{10}$$

where B is the strain-displacement matrix, and C is the constitutive matrix. Assembling the element’s stiffness matrix $[k]$ into a global stiffness matrix $[K]$ and the global nodal forces $\{F\}$, the nodal displacements $\{d\}$ can be found from the global simple Equation 11:

$$\{F\} = [K]\{d\} \tag{11}$$

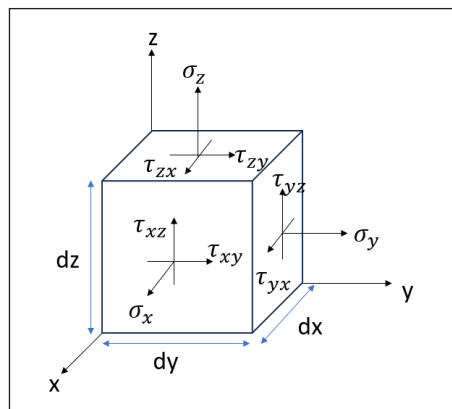


Figure 10. 3D stress state in a differential element

RESULTS AND DISCUSSION

A static structural analysis was carried out in ANSYS to evaluate the design of a bamboo girder used as a part of an emergency bridge system. Figure 11 shows the deformation of the girder along the Y-axis, which has a maximum downward deflection of 84.68 mm. In the American Association of State Highway and Transportation Officials (AASHTO) design guidelines 2020, deflection limitations are stated to be generally optional, except

for some cases, and some limits are given for steel, aluminium, and concrete vehicular bridges in the range of span/1000 to span/300, depending on the case. Since this girder is intended to be used as a temporary emergency system under small vehicles, the deflection limit is taken as span/100, which makes the limit for this girder $7748/100 = 77.48$ mm. It indicates that a fully loaded pickup truck, similar to a Toyota Hilux, might be too heavy for the serviceability requirements of this girder.

The von-Mises stress for the bamboo tubes shows a maximum of 85 MPa, as shown in Figure 12 (a), much lower than the design strength of 175 MPa. Moreover, this maximum stress is concentrated at the nodes of the bottom three tubes, and more specifically, where the bamboos coincide with the edge of the steel connection at the support side, as seen in Figure 13 (a). Table 4 shows the utilisation ratio and demand over the capacity ratio of the bamboo tubes based on design strength.

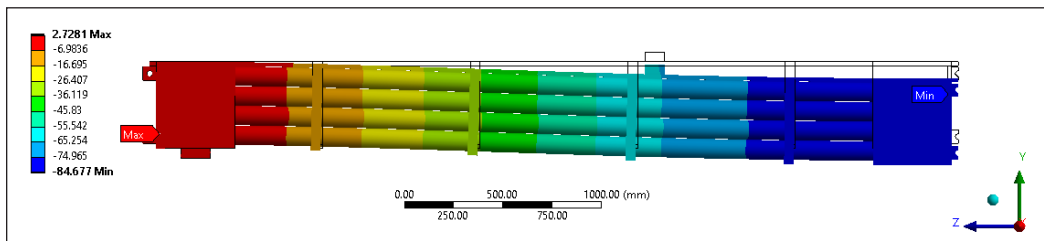


Figure 11. Directional deformation in the Y axis (true scale)

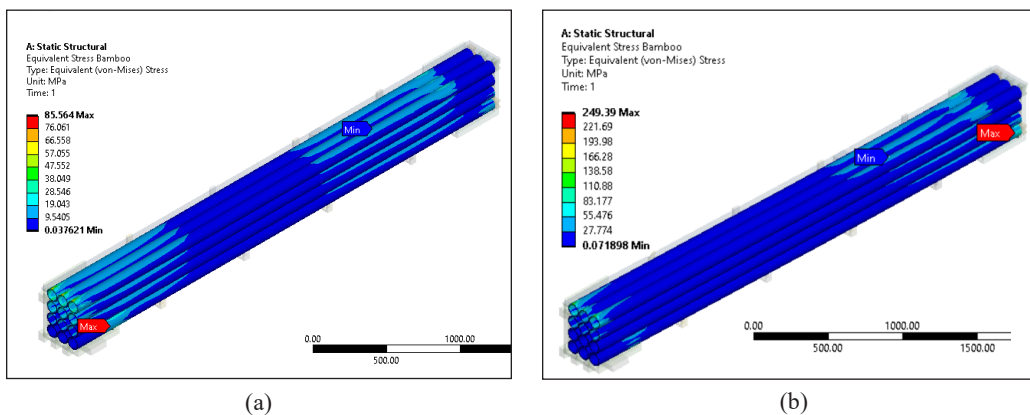


Figure 12. Equivalent von-Mises stress: (a) bamboo tubes; and (b) steel tubes

Table 4
The utilisation ratio for the bamboo tubes based on design strength

	Bamboo tubes	Utilisation (Design strength)
Max Equivalent stress Bamboo (MPa)	85.564	0.49
Min Normal Stress-Z Bamboo (MPa)	102.53	0.59
Max Normal Stress-Z Bamboo (MPa)	42.342	0.24

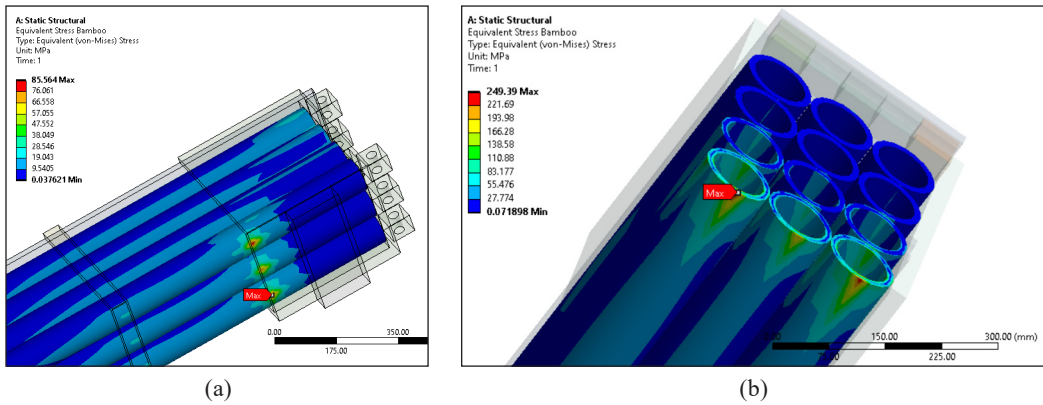


Figure 13. The Equivalent von-Mises stress at the location of stress concentration: (a) bamboo tubes; and (b) steel tubes

Figure 14 shows the normal stress in the Z direction with a maximum compressive stress of 102.5 MPa and a maximum tensile stress of 42.3 MPa, much lower than the design stress of 175 MPa. The maximum compressive stress happens at the same location as the maximum von-Mises stress.

The von-Mises stress for the steel parts shows a maximum of 410 MPa, as shown in Figure 15, which is much higher than the yield strength of 250 MPa but lower than the ultimate strength of 460 MPa. This high stress could be explained, considering it was achieved at a single node, indicating a numerical singularity. In addition, this maximum stress is concentrated at the node connecting the top steel plate with a steel connection, as seen in Figure 16.

An identical girder was simulated using steel tubes to compare the performance of the bamboo girder. The results are summarised in Table 5, where the deformation was 70% lower using steel tubes, as expected due to their remarkably higher stiffness. However, the maximum equivalent stress in

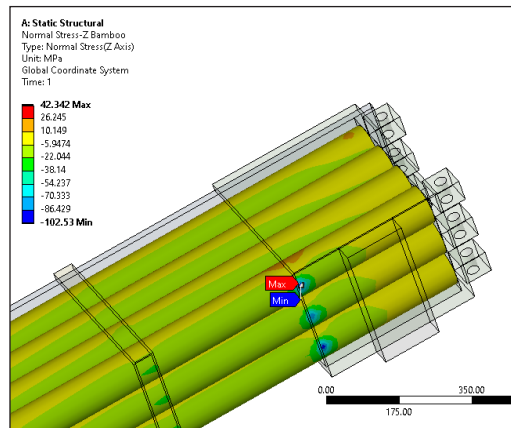


Figure 14. The location of the stress concentration on the bamboo tubes (normal stress Z axis)

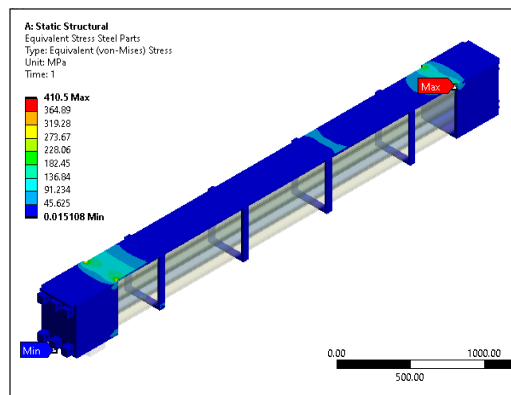


Figure 15. Equivalent von-Mises stress for the steel parts

the steel tubes was significantly higher, reaching the yield strength of 250 MPa, while the bamboo tubes stayed well below their design strength of 175 MPa, as shown in Figure 12. Nevertheless, the stress concentration was higher in the steel tubes, reaching 249.39 MPa at the middle span, Figure 13 (b), unlike the bamboo tubes, where the stress was much lower and concentrated at the support side, as seen in Figure 13 (a). Moreover, the total mass of the steel girder is almost 2.8 times the mass of the bamboo bridge, which makes it notably more difficult to carry and transport. Given that the main objective of this design is to be deployed quickly during emergencies, the relatively low weight of the bamboo girder gives it an advantage over its steel counterpart.

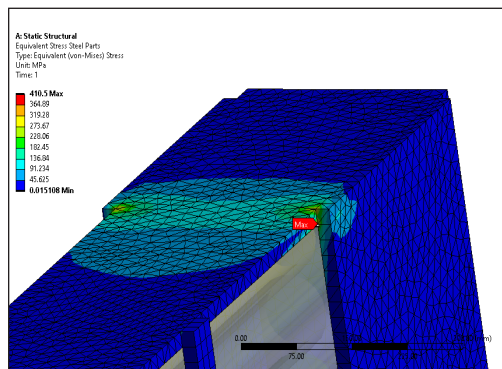


Figure 16. The location of the stress concentration on the steel parts (Equivalent von-Mises stress)

Table 5
Results comparison between bamboo tubes and steel tubes

2 Segments 4-point bending	Bamboo Tubes	Steel Tubes	Difference %
Load (N)	-9260	-9260	0%
Max deformation (mm)	84.678	25.53	70%
Max Equivalent stress tubes (MPa)	85.564	249.4	-191%
Min Normal Stress-Z tubes (MPa)	-102.53	-95.75	7%
Max Normal Stress-Z tubes (MPa)	42.342	65.41	-54%
Max Equivalent Stress Steel Parts (MPa)	410.5	388.58	5%
Volume (m ³)	0.19481	0.19481	0%
Mass (kg)	536.48	1501.4	-180%

CONCLUSION

This paper conducted a detailed finite element analysis of a bamboo girder for an emergency bridge system. The girder was made primarily from bamboo with some steel parts to hold the bamboo tubes together ens, where they work as one unit and provide a way to connect multiple segments as needed. The following points were concluded from this study:

- The four-point flexural experimental tests on individual culms showed that the material failed locally due to crushing and splitting. The average modulus of elasticity was 14583 MPa, and the average ultimate strength was 263 MPa.
- The maximum deflection was 84.68 mm, exceeding the limit of L/100, which is 77.48 mm. It indicates that a fully loaded pickup truck might be too heavy for the serviceability requirements of this girder.

- For the bamboo tubes, the maximum equivalent von-Mises stress reached 85 MPa, much lower than the design strength of 175 MPa. Moreover, the maximum normal compressive stress was 102.5 MPa, and the maximum normal tensile stress was 42.3 MPa along the longitudinal axis Z, lower than the design strength of 175 MPa.
- The steel parts had a stress of 410 MPa at a single node, exceeding the yield strength of 250 MPa but lower than the ultimate strength of 460 MPa. This high stress could be explained by numerical inaccuracy.
- The comparison with an identical girder using steel tubes showed that the steel girder resulted in lower deflection but significantly higher equivalent stresses. However, its weight was 180% higher than that of the bamboo girder, making it more difficult to transport and deploy quickly during emergencies.

ACKNOWLEDGEMENT

The authors thank everyone who has contributed to this project directly or indirectly.

REFERENCES

- Akinlabi, E. T., Anane-Fenin, K., & Akwada, D. R. (2017). *Bamboo the multipurpose plant*. Springer International Publishing. <https://doi.org/10.1007/978-3-319-56808-9>
- Amede, E. A., Hailemariam, E. K., Hailemariam, L. M., & Nuramo, D. A. (2021). A review of codes and standards for bamboo structural design. *Advances in Materials Science and Engineering, 2021*, Article 4788381. <https://doi.org/10.1155/2021/4788381>
- Ansys Inc. (2017). *ANSYS theory reference* (Release 18.2). <https://www.ansys.com/>
- Auwalu, F. K., & Dickson, P. D. (2019). Bamboo as a sustainable material for building construction in Nigeria. *Civil and Environmental Research, 11*(8), 30–36. <https://doi.org/10.7176/CER/11-8-03>
- Bahari, S. A., & Krause, A. (2016). Utilizing Malaysian bamboo for use in thermoplastic composites. *Journal of Cleaner Production, 110*, 16–24. <https://doi.org/10.1016/j.jclepro.2015.03.052>
- Chung, K. F., & Yu, W. K. (2002). Mechanical properties of structural bamboo for bamboo scaffoldings. *Engineering Structures, 24*(4), 429–442. [https://doi.org/10.1016/S0141-0296\(01\)00110-9](https://doi.org/10.1016/S0141-0296(01)00110-9)
- Egoh, A., Reed, K. S., & Kalu, P. N. (2020). A review of the current status of bamboo usage with special emphasis on orthopedic rehabilitation. *Materials Sciences and Applications, 11*(07), 415–430. <https://doi.org/10.4236/msa.2020.117028>
- ISO 22157-2:2004. (2004). *Bamboo-Determination of physical and mechanical properties-Part 2: Laboratory manual*. <https://www.iso.org/standard/38360.html>
- Liu, K. W., Xu, Q. F., Wang, G., Chen, F. M., Leng, Y. B., Yang, J., & Harries, K. A. (2022). Types and characteristics of bamboo materials for construction uses. In K. W. Liu, Q. F. Xu, G. Wang, F. M. Chen, Y. B. Leng, J. Yang & K. A. Harries (Eds.), *Contemporary Bamboo Architecture in China* (pp. 7–30). Springer. https://doi.org/10.1007/978-981-16-8309-1_2

- Liu, W., Hui, C., Wang, F., Wang, M., & Liu, G. (2018). Review of the resources and utilization of bamboo in China. In Khalil H. P. S. A. (Ed.), *Bamboo - Current and Future Prospects* (pp. 133-142). IntechOpen. <https://doi.org/10.5772/intechopen.76485>
- Musthaffa, A. A., Nor, N. M., Yusof, M. A., & Yuhazri, M. Y. (2018). New conceptual design of portable bamboo bridge for emergency purposes. *AIP Conference Proceedings*, 1930(1), Article 20043. <https://doi.org/10.1063/1.5022937>
- Najeeb, M. I., Syamsir, A., Amir, S. M. M., Khan, T., & Sebaey, T. A. (2023). Failure analysis of plant fibre-reinforced composite in civil building materials using non-destructive testing methods: Current and future trend. *Journal of Natural Fibers*, 20(2), Article 2246654. <https://doi.org/10.1080/15440478.2023.2246654>
- Rahman, M. A., Haque, S., Athikesavan, M. M., & Kamaludeen, M. B. (2023). A review of environmental friendly green composites: Production methods, current progresses, and challenges. *Environmental Science and Pollution Research*, 30(7), 16905–16929. <https://doi.org/10.1007/s11356-022-24879-5>
- Rong, K., Ekeland, A., Shao, C., Zhang, Y., & Shangguan, S. (2022). Bamboo bridges: A nature-based Solution. *Green Building & Construction Economics*, 3(1), 12–26. <https://doi.org/10.37256/gbce.3120221307>
- Salzer, C., Wallbaum, H., Lopez, L. F., & Kouyoumji, J. L. (2016). Sustainability of Social housing in asia: A holistic multi-perspective development process for bamboo-based construction in the Philippines. *Sustainability*, 8(2), Article 151. <https://doi.org/10.3390/su8020151>
- Technical Committee CEN. (2003). *Eurocode 1: Actions on structures - Part 2: Traffic loads on bridges*. <https://knowledge.bsigroup.com/products/eurocode-1-actions-on-structures-traffic-loads-on-bridges>
- Yan, X., Quan, Z., & Bo, S. (2010). Design and construction of modern bamboo bridges. *Journal of Bridge Engineering*, 15(5), 533–541. [https://doi.org/10.1061/\(ASCE\)BE.1943-5592.0000089](https://doi.org/10.1061/(ASCE)BE.1943-5592.0000089)
- Yang, D., Li, H., Xiong, Z., Mimendi, L., Lorenzo, R., Corbi, I., Corbi, O., & Hong, C. (2020). Mechanical properties of laminated bamboo under off-axis compression. *Composites Part A: Applied Science and Manufacturing*, 138, Article 106042. <https://doi.org/10.1016/j.compositesa.2020.106042>

Some Aspects of the Biology of Invasive Fish Species from a Langat River Tributary, Selangor, Malaysia

Abdulwakil Olawale Saba^{1,2}, Muhammad Shakir Zufayri Mohd Arshad¹, Muhammad Afifuddin Abdul Razak¹, Amirah Mustafa Kamal¹, Muhammad Rasul Abdullah Halim³, Intan Faraha A Ghani⁴, Mohd Lokman Ilham-Norhakim⁵ and Mohammad Noor Azmai Amal^{1*}

¹Department of Biology, Faculty of Science, Universiti Putra Malaysia, 43400 UPM, Serdang, Selangor, Malaysia

²Department of Fisheries, Faculty of Science, Lagos State University, 102101 Ojo, Lagos, Nigeria

³Institute of Biological Sciences, Faculty of Science, Universiti Malaya, 50603 Kuala Lumpur, Malaysia

⁴Department of Science and Biotechnology, Faculty of Engineering and Life Sciences, Universiti Selangor, Bestari Jaya Campus, 45600 Bestari Jaya, Selangor, Malaysia

⁵Environmental Management and Conservation Research Unit, Faculty of Applied Sciences and Technology, Universiti Tun Hussein Onn, Pagoh Campus, 84600 Pagoh, Johor, Malaysia

ABSTRACT

Invasive fish species pose several threats to aquatic biodiversity and health, necessitating a good understanding of their biology and ecology. This study aims to understand the biology of invasive fish species collected from a Langat River tributary, Selangor, focusing on their growth, reproduction, and feeding habits. Fish and water samples were collected between March and August 2022. A total of 171 specimens were recorded, including 71, 55, and 45 individuals of *Pterygoplichthys disjunctivus*, *P. pardalis*, and *Oreochromis* sp. The *b* values for length-weight relationships of *P. disjunctivus*, *P. pardalis*, and *Oreochromis* sp. were 2.79, 2.92, and 2.89, respectively.

The mean condition factor for *Oreochromis* sp. was significantly ($p < 0.05$) higher than that of the other two species. There were no significant differences between the observed and expected number of males and females for all three species. The females had higher mean gonadosomatic index values compared to males. The mean fecundity for *P. disjunctivus*, *P. pardalis*, and *Oreochromis* sp. were 973 ± 596 , 10562 ± 830 , and 1052 ± 1068 , respectively. The most important

ARTICLE INFO

Article history:

Received: 18 December 2023

Accepted: 25 March 2024

Published: 26 August 2024

DOI: <https://doi.org/10.47836/pjst.32.5.25>

E-mail addresses:

saba@upm.edu.my (Abdulwakil Olawale Saba)

shakirarshad0@gmail.com (Muhammad Shakir Zufayri Mohd Arshad)

muhd.afifuddin@gmail.com (Muhammad Afifuddin Abdul Razak)

amirahmustafa20@gmail.com (Amirah Mustafa Kamal)

mrasul87@gmail.com (Muhammad Rasul Abdullah Halim)

intanfaraha@unisel.edu.my (Intan Faraha A Ghani)

abgikanjmb6945@gmail.com (Mohd Lokman Ilham-Norhakim)

mnamal@upm.edu.my (Mohammad Noor Azmai Amal)

* Corresponding author

stomach contents of the three species were detritus, mineral particles, and diatoms, with a higher proportion of mineral particles found in the diets of *P. disjunctivus* and *P. pardalis*. The information on growth patterns, reproductive strategies, and dietary preferences provides valuable insights for controlling their invasion of local rivers.

Keywords: Feeding, fish ecology, food, gonadosomatic index, length-weight relationship, non-native species, water quality

INTRODUCTION

Invasive fish species pose a significant threat to native aquatic biodiversity, ecosystems, and fisheries worldwide because they can displace native species, alter habitats, and spread diseases (Xiong et al., 2023). These fish species might act as predators or rivals against indigenous species (Camacho-Cervantes et al., 2023), transmit parasites or pathogens (Šimková et al., 2019), or result in unexpected hybridization (Arndt et al., 2018). Thus, it may ultimately result in the loss of local biodiversity by eradicating indigenous species (Bezerra et al., 2019).

The Langat River is a crucial watercourse in Selangor, Malaysia, which ordinarily should be rich in diverse native fish species that have also been recorded in other adjoining water bodies. Native fishes are important because they can contribute to the river's ecological functioning (Wang et al., 2021). However, the presence of invasive fish species threatens the delicate balance and functioning of freshwater ecosystems (Nagelkerke et al., 2018).

Initially, alien fish species were imported to Malaysia for a variety of purposes, including the necessity to increase the nation's fish productivity and uses, such as ornamental fish keeping, sport fishing, and the biological control of undesirable species (Saba et al., 2020a). Unfortunately, when these fish are introduced into local waters, and their detrimental effects reach a tipping point, resulting in environmental dominance, alien fish become invasive (Havel et al., 2015; Piria et al., 2018). Besides that, they may spread to other water bodies, which may further increase their impact on the native ecosystem's biodiversity.

Alien fish species like tilapia (*Oreochromis* sp.) and sailfin catfishes (*Pterygoplichthys pardalis* and *P. disjunctivus*) have been imported intentionally and unintentionally for various purposes to Malaysia, including aquaculture, aquarium, recreational, and biological control purposes, resulting in their introduction and establishment of breeding populations in inland waters in Malaysia (Rahim et al., 2013; Saba et al., 2021). These invasive species can spread diseases, compete with native species for food and space, and predate on them, leading to population decline and the elimination of many native species (Ahmad et al., 2020). More so, some species have been categorized as invasive to Malaysia based on the

risk assessment using the fish invasiveness screening kit (FISK) and the aquatic species screening kit (AS-ISK) (Saba et al., 2020b; Vilizzi et al., 2021).

Research on different aspects of the biology of fish species, including the length-weight relationship, condition factor, reproductive biology, and the food and feeding habits of fish, are crucial for understanding how different species are likely to interact with each other and their possible roles in their resident aquatic ecosystems (Tran et al., 2021). Despite numerous introduced fish species present in Malaysia's inland waterbodies and the growing research on their negative impacts on native species and the aquatic ecosystem, there still exists a dearth of information on the biology of non-native fish species recorded in many other waterbodies in Malaysia. Apart from Samat et al. (2016) and Saba et al. (2021), most of the previous studies have focused mainly on distribution and occurrence (Aqmal-Naser et al., 2023; Hamid et al., 2022; Khaleel et al., 2020), and invasion risk screening (Kiat & Rahim, 2023; Saba et al., 2020b; Vythalingam et al., 2022) of these species. To better understand the potential impacts of these invasive species in the inland waters of Malaysia, this study aims to explore some aspects of the biology of invasive fish species from a Langat River tributary, Selangor. The objectives are, therefore, to assess the length-weight relationships and condition factors of the three important invasive fish species, evaluate the sex ratio, gonadosomatic index, and fecundity of the species, and determine the food and feeding habits.

MATERIALS AND METHODS

Study Area

The study area refers to a stream that flows through a dense residential area of Sungai Merab and into the Langat River, Selangor. The stream's bottom is shallow and sandy, with a depth ranging from 0.2 to 1.2 m and a width of 2.5 to 10.0 m. The riverbank is densely vegetated with tall grasses and several crops, such as banana trees, sugar cane, and coconut trees.

The sampling was undertaken over six months at three different times, which coincided with 18th March 2022, 26th May 2022, and 25th August 2022. The rainfall patterns are significantly influenced by two distinct monsoon seasons: the northeast monsoon, which takes place between October and March, and the southwest monsoon, which typically starts in May and concludes in September (Amirudin et al., 2022). Fish sampling was conducted within 200 m along the stream at points A (2°55'03.6"N 101°45'13.6"E), B (2°55'01.1"N 101°45'12.5"E), and C (2°54'57.5"N 101°45'13.7"E) (Figure 1).

Water Quality Measurement

Water quality was measured at three different points along a 200 m stretch of the sampling site. During each of the three times of sampling, a total of three readings were taken. Water

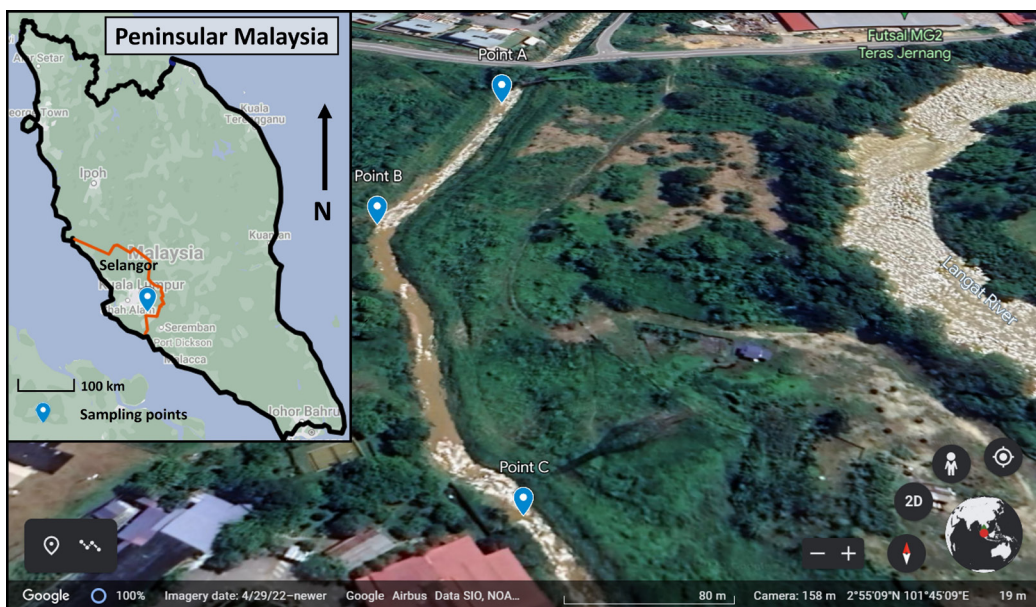


Figure 1. Map showing the location of the sampling points along the Langat River tributary, Selangor, Malaysia (Source: Google Earth)

quality parameters were measured, including dissolved oxygen, pH, water temperature, and total dissolved solids (TDS). On-site measurements were taken using a YSI 556 MPS probe (YSI, Yellow Springs, OH, USA). Additionally, chemical parameters, including ammonia, nitrite, nitrate, phosphate, and sulfate concentrations, were analyzed using a spectrophotometer (HACH, Loveland, CO, USA). The *ex-situ* measurements were conducted less than 24 hours after collecting the water samples using sterilized 500 mL polyethylene bottles.

Fish Sampling and Processing

Fish were sampled using a cast net with a length of 150 cm, a diameter of 305 cm, and a mesh size of 2 cm. The sampling activity was accomplished in 2 hours by four individuals for each sampling day, with the cast nets deployed approximately 24 times on each sampling day. All specimens collected were stored in a cool box containing ice cubes before being transported back to the laboratory for further assessment. Fishes were identified based on Zakaria-Ismail et al. (2019) and Saba et al. (2020c). All samples were dissected after the fish length and weight measurements were completed. The total length (TL), standard length (SL), and body weights (BW) of all collected specimens were measured to the nearest 0.1 cm and 0.1 g, respectively, by using a fish measuring board and a digital weighing scale. The ventral side of the fish was dissected to expose the viscera. The esophagus, intestine, stomach, and gonad (testis and ovary) were collected and separated from other visceral

organs. The collected gut and gonad were then measured for length and weight to the nearest 0.1 cm and 0.1 g, respectively. The gut was preserved in 5% of formalin, while the gonad was preserved in 10% of buffered formalin. The gut and gonad were labeled and stored in a separate bottle.

Length-weight Relationship and Condition Factor

The relationship between fish weight and length may be shown using Equation 1 (Fakoya et al., 2019):

$$W = aL^b \quad [1]$$

where: W = weight of the fish (g); L = total length of fish (cm); *a* = regression constant; and *b* = allometric coefficient.

Log-transformed data was utilized, and the least-square approach was used to estimate the values of constants *a* and *b* (Equation 2) (Zar, 1984).

$$\text{Log}W = a + b\text{Log}L \quad [2]$$

Condition Factor

The Equation 3 for condition factor (K) is as follows:

$$K = 100W/L^3 \quad (\text{Mozsár et al., 2015}) \quad [3]$$

where: K= condition factor; W= weight (g); and L= total length of fish (cm).

Kruskal-Wallis's test was used to compare the well-being of the three invasive fish species at a $p < 0.05$.

Sex Ratio, Gonadosomatic Index and Fecundity

To statistically assess the sex ratio, Pearson's chi-square goodness of fit test in IBM SPSS, ver. 26.0 (IBM Corp., Chicago, IL, USA) was used based on Equation 4 for the chi-square statistic, which is:

$$X^2 = \sum [(O - E)^2 / E] \quad [4]$$

where O is the observed frequency, and E is the expected frequency.

The gonadosomatic index (GSI) was determined after collecting ovaries from fish, blotting them, weighing them individually, and separating the eggs. Measurements of the weight of the fish gonad and the weight of the body without the gonad were then used to determine the GSI as in Equation 5:

$$GSI = 100 \times W_g / W \quad [5]$$

where: W_g = weight of wet gonad (g); and W = total wet body weight without gonad (g).

Small sub-samples from the posterior, middle, and anterior portions of the ovary were removed to calculate the fecundity. Then, each sub-sample was weighed to the nearest 0.1 g. The eggs within each sub-sample were counted using a dissecting microscope. The fecundity was, therefore, calculated according to Rahman and Samat (2021) as in Equation 6:

$$\text{Fecundity} = \frac{\text{Average number of eggs in sub-samples} \times \text{Weight of ovary (g)}}{\text{Weight of sub-sample (g)}} \quad [6]$$

Gut Content Extraction and Identification

Gut content analysis was performed by collecting the contents from the gut and transferring them to a petri dish containing 5 mL of distilled water to facilitate dilution. The occurrence frequency, volumetric approach, and index of preponderance were applied to obtain a more comprehensive perspective on dietary importance. The stomach contents were examined under a stereomicroscope using a 0.2 mm deep, 16×16 Fuchs Rosenthal counting chamber. The contents were then classified as multicellular green algae, unicellular green algae, red algae, plant parts, euglenoids, Xanthophyceae, Cyanobacteria, diatom, detritus, and mineral particles (Wickramaratne, 2021; Saba et al., 2021).

Frequency of Occurrence

The total number of stomachs containing prey items was expressed as a percentage of all non-empty stomachs to determine the frequency of occurrence (Hyslop, 1980). The frequency of occurrence method Equation 7 is as follows:

$$\%Oi = \frac{Ni}{N} \times 100 \quad [7]$$

where: $\%Oi$ = the frequency of occurrence of given food i ; Ni = number of stomachs containing prey I ; and N = total number of stomachs with food.

Percentage Volume

The percentage volume was calculated using the volumetric method, where the volume of each food item was expressed as a proportion of the total volume of food in the stomach (Silveira et al., 2020). The following Equation 8 was used:

$$\%Vi = \frac{Vi}{Vt} \times 100 \quad [8]$$

where: % V_i = percentage of food items I ; V_i = volume of item I ; and V_t = total volume of food (gut content).

Index of Preponderance

The index of preponderance was used to determine the relative significance of each food category based on the percent volume and frequency of occurrence values (Santi et al., 2017). This index's Equation 9 is as follows:

$$I = \frac{V_i O_i}{\sum V_t O_t} \times 100 \quad [9]$$

where: I = index of preponderance; V_i = percentage volume of food component; O_i = Percentage of occurrence of food item; V_t = total percentage volume of food component; and O_t = total percentage of occurrence of food item.

Data Analysis

Microsoft Excel spreadsheet software (Office 365, Version 2016, Microsoft Corp., Berkshire, UK) was used for record-keeping purposes and analyzed to obtain descriptive statistics. Data collected from the condition factor and length-weight relationship was analyzed using simple linear regression from the log equation. All inferential statistics were done in IBM SPSS, ver. 26.0 (IBM Corp., Chicago, IL, USA).

RESULTS

Water Quality Assessment

From March to August 2022, temperature, dissolved oxygen, and ammonia levels showed declining patterns, whereas pH, conductivity, and TDS demonstrated increasing tendencies. Phosphate and sulfate declined over time, with March showing the greatest average values for both parameters, while August had the lowest average values. The nitrate concentration gradually rose from March to May and declined from May to August. The nitrite concentration declined from March to August (Table 1).

Table 1
Summary of water quality parameter measurements from the three sampling months

Parameters	Readings (Mean \pm SD)		
	March	May	August
Temperature ($^{\circ}$ C)	28.8 \pm 0.2	27.8 \pm 0.2	27.7 \pm 0.3
Dissolve oxygen (mg/L)	4.5 \pm 0.3	4.9 \pm 1.1	5.6 \pm 0.8
Conductivity (μ S/cm)	0.1 \pm 0.0	0.2 \pm 0.0	0.2 \pm 0.0
Total dissolved solids (mg/L)	80.4 \pm 0.4	90.1 \pm 2.7	93.0 \pm 0.7

Table 1 (continue)

Parameters	Readings (Mean ± SD)		
	March	May	August
pH	7.63 ± 0.10	7.70 ± 0.00	8.00 ± 0.10
Phosphate (mg/L)	12.7 ± 0.8	11.6 ± 0.9	1.1 ± 0.4
Sulphate (mg/L)	20.2 ± 3.3	9.4 ± 1.9	7.3 ± 1.3
Nitrate (mg/L)	5.2 ± 0.7	7.2 ± 1.6	5.2 ± 0.6
Nitrite (mg/L)	0.1 ± 0.0	0.1 ± 0.0	0.1 ± 0.0
Ammonia (mg/L)	0.3 ± 0.0	0.2 ± 0.0	0.1 ± 0.0

Fish Length and Weight

A total of 171 specimens were collected, including 71, 55, and 45 individuals of *P. disjunctivus*, *P. pardalis*, and *Oreochromis* sp., respectively. The overall mean lengths and weights for the three species spanning the study duration are presented in Table 2, while Figure 2 shows the invasive species sampled.

Table 2
Overall length and weight information of the invasive fish species

Species		Mean ± SD	Min	Max
<i>P. disjunctivus</i>	Length (cm)	22.9 ± 6.8	12.3	46.1
	Weight (g)	125.7 ± 20.0	15.0	665.0
<i>P. pardalis</i>	Length (cm)	24.5 ± 6.2	11.6	42.6
	Weight (g)	149.9 ± 113.6	15.0	550.0
<i>Oreochromis</i> sp.	Length (cm)	16.3 ± 3.4	8.9	24.0
	Weight (g)	96.0 ± 59.3	15.0	275.0

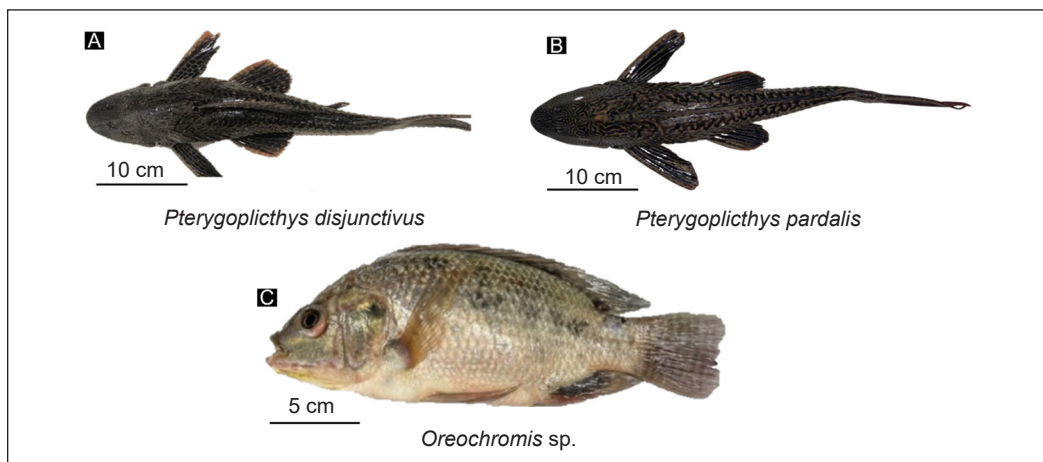


Figure 2. Invasive fish specimens: (A) *Pterygoplichthys disjunctivus*, (B) *P. pardalis*, and (C) *Oreochromis* sp.

A summary of length and weight information for the three different sampling months is presented in Table 3. In March, the average body weight of *P. disjunctivus* was 287.4 ± 215.5 g, with the highest recorded weight being 1125.0 g. In May, the weight reduced to 165.5 ± 135.9 g, while in August, it decreased even further to 72.4 ± 42.9 g. In March, the average body weight of *P. pardalis* was 146.0 ± 120.8 g, with the highest recorded weight being 550.0 g. In May, the weight rose to 176.2 ± 137.3 g and in August, it dropped to 126.8 ± 58.5 g. The average body weight of *Oreochromis* sp. was 72.7 ± 41.6 g in March, ranging from 15.0 g to 180.0 g. The average body weight in May rose to 133.5 ± 70.8 g, ranging from a minimum of 40.0 g to a maximum of 275.0 g. The average body weight in August declined to 94.8 ± 57.6 g, ranging from a minimum of 25.0 g to a maximum of 220.0 g.

Table 3
Monthly length and weight information of the invasive fish species

Month	Species	N	Mean BW (g) \pm SD	Min BW (g)	Max BW (g)	Mean TL (cm) \pm SD	Min TL (cm)	Max TL (cm)
March	<i>P. disjunctivus</i>	30	287.4 ± 215.5	15.0	1125.0	43.2 ± 6.9	12.3	41.1
May	<i>P. disjunctivus</i>	23	165.5 ± 135.9	45.0	665.0	26.4 ± 6.9	16.7	46.1
August	<i>P. disjunctivus</i>	18	72.4 ± 42.9	20.0	170.0	19.6 ± 4.6	12.4	28.4
March	<i>P. pardalis</i>	25	146.0 ± 120.8	15.0	550.0	24.2 ± 7.0	11.6	42.5
May	<i>P. pardalis</i>	16	176.2 ± 137.3	35.0	475.0	25.5 ± 6.8	16.0	40.2
August	<i>P. pardalis</i>	14	126.8 ± 58.5	45.0	235.0	23.9 ± 3.6	17.6	31.7
March	<i>Oreochromis</i> sp.	15	72.7 ± 41.6	15.0	180.0	15.1 ± 2.9	8.9	21.0
May	<i>Oreochromis</i> sp.	10	133.5 ± 70.8	40.0	275.0	18.8 ± 3.1	12.8	24.0
August	<i>Oreochromis</i> sp.	20	94.8 ± 57.6	25.0	220.0	16.0 ± 4.0	10.0	23.0

Length-frequency Distribution

The highest number of individuals in any size class for the entire sampling period was 34, as recorded for *P. disjunctivus* in the 15.0–19.9 cm size class. *Pterygoplichthys pardalis* recorded the largest number of individuals in the 20.0–24.9 cm and 25–29.9 cm size classes, while *Oreochromis* sp. recorded the largest number of individuals in the 15.0–19.9 cm size class (Figure 3).

Length-weight Relationship and Condition Factor

The results of the length-weight relationships (LWR) and condition factors (CF) are presented in Table 4. The *b* values for *P. disjunctivus*, *P. pardalis*, and *Oreochromis* sp. were 2.79, 2.92, and 2.89, respectively. *Oreochromis* sp. had the highest mean condition factor (1.97 ± 0.23) while the sailfin catfishes (*P. disjunctivus* and *P. pardalis*) recorded CF values less than 1.

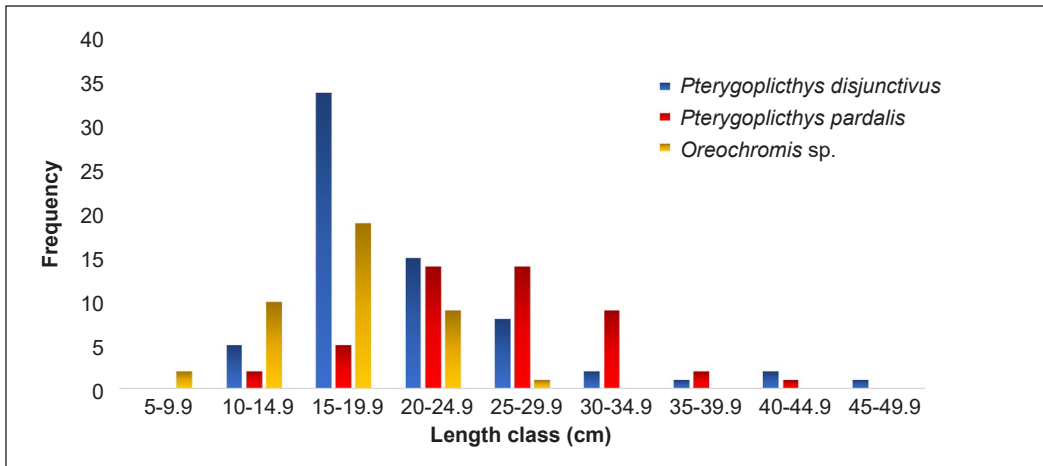


Figure 3. Length frequency distribution of invasive fish species

Table 4

The three invasive species' length-weight relationship and condition factor values over the entire sampling period

Species	N	Equation	R ²	Mean CF ± SD	Min CF	Max CF
<i>P. disjunctivus</i>	71	$y = 2.7939x - 1.7909$	0.9705	0.86 ± 0.14^a	0.50	1.16
<i>P. pardalis</i>	55	$y = 2.9232x - 1.9586$	0.9785	0.86 ± 0.11^a	0.80	1.12
<i>Oreochromis sp.</i>	45	$y = 2.8942x - 1.5834$	0.9761	1.97 ± 0.23^b	1.42	2.53

Note. Means with different superscripts indicate significant differences at $p < 0.05$

Throughout the study period, the b values recorded for *P. disjunctivus* in March (2.93), May (2.89), and August (2.61) were found to be less than 3. *Pterygoplichthys pardalis* recorded b values of 2.91, 2.87, and 2.93 in March, May, and August, respectively, while *Oreochromis sp.* was 2.95 in March, 3.09 in May, and 2.85 in August. All the b values were less than 3, indicating negative allometric growth, except for May, where *Oreochromis sp.* recorded a b value of 3.09, exhibiting positive allometric growth.

Sex Ratio, GSI and Fecundity

There were no significant differences between the observed and expected number of males and females for *P. disjunctivus* $X^2(1, N = 45) = 0.56, p = 0.456$, *P. pardalis* $X^2(1, N = 49) = 0.67, p = 0.184$ and *Oreochromis sp.* $X^2(1, N = 53) = 0.17, p = 0.680$. Therefore, the proportion of males and females was not significant ($p > 0.05$). The females had higher mean GSI values for all three species than males. However, female *Oreochromis sp.* had a lower mean GSI compared to the females of the two sailfin catfishes (Table 5).

The temporal variation in GSI for the three invasive species is presented in Figure 4. The highest GSI values for female *P. disjunctivus* were recorded in August (2.09), and the lowest GSI values were in March (0.61) during the study period. For the males, the highest

Table 5

Gonadosomatic index (GSI) values of the three invasive fish species

Species	Sex	N	Mean \pm SD	Min GSI	Max GSI
<i>P. disjunctivus</i>	Male	19	1.18 \pm 2.62	0.12	11.85
	Female	24	9.63 \pm 6.50 ^a	0.19	21.29
	Total	43	5.90 \pm 6.59	0.12	21.29
<i>P. pardalis</i>	Male	26	0.41 \pm 0.64	0.08	3.22
	Female	23	8.06 \pm 5.32 ^a	0.35	19.11
	Total	49	4.47 \pm 5.46	0.08	19.11
<i>Oreochromis</i> sp.	Male	19	0.38 \pm 0.52	0.03	2.22
	Female	18	1.72 \pm 1.32 ^b	0.23	4.93
	Total	37	1.03 \pm 1.19	0.03	4.93

Note. The same superscript for female *P. disjunctivus* and *P. pardalis* indicates no significant difference ($p > 0.05$) in their GSI values. GSI values were computed only for specimens with identifiable gonads

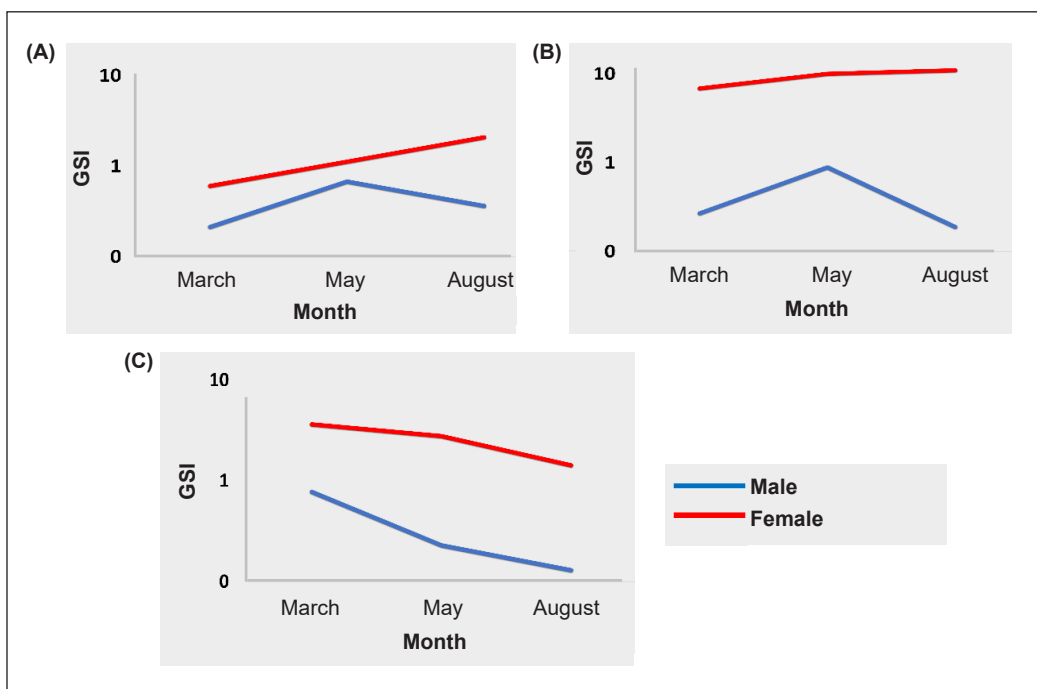


Figure 4. Temporal variation of the gonadosomatic index (GSI) for males and females of (A) *Pterygoplichthys disjunctivus*, (B) *Pterygoplichthys pardalis*, and (C) *Oreochromis* sp.

GSI values were recorded in May (0.68), and the lowest GSI values recorded were in March (0.21). For *P. pardalis*, the highest GSI value for males was in May (0.89), whereas the highest GSI value recorded for females was in August (11.01). The lowest GSI value for males was detected in August (0.19), whereas the lowest GSI value for females was recorded in March (6.88) for *P. pardalis*. The GSI for female *Oreochromis* sp. was found

to be the highest (2.87) in March and the lowest (1.30) in August. On the other hand, male GSI was highest (0.78) in March and the lowest (0.13) in August.

The mean fecundity for *P. disjunctivus*, *P. pardalis*, and *Oreochromis* sp. were 972.5 ± 595.7 , 10562.0 ± 829.6 , and 1052.3 ± 1068.1 , respectively. For *P. disjunctivus*, the highest fecundity was observed in May.

Food and Feeding Habits

Overall Stomach Contents

Details of food items found in the stomachs of the three invasive fish species throughout the study period are presented in Table 6. The food categories most important to *P. disjunctivus* and *P. pardalis* based on percentage frequency of occurrence, FO (%), and percentage index of preponderance, IP (%) were detritus, mineral particles, and diatoms. In contrast, detritus, mineral particles, and unicellular green algae were the most important factors for *Oreochromis* sp.

By percentage volume, VO (%), detritus, mineral particles, diatoms, and plant parts were the most important stomach contents to *P. disjunctivus* and *P. pardalis*, respectively, while by IP (%) detritus, mineral particles, diatoms were the most important for *P. disjunctivus* and *P. pardalis*. Detritus, mineral particles, and unicellular green algae were the most important stomach contents for *Oreochromis* sp. by IP (%).

Table 6
Summary of overall food items of three invasive species

Stomach content	FO (%)			VO (%)			IP (%)		
	PD	PP	OR	PD	PP	OR	PD	PP	OR
Mineral particles	95.56	100	86.67	22.66	29.82	6.84	4.68	34.59	0.89
Detritus	100	100	100	51.50	27.2	63.53	10.59	31.56	10.41
Diatom	61.80	81.57	56.67	5.11	9.59	2.49	0.71	9.09	0.23
Cyanobacteria	23.59	77.56	76.67	1.48	9.38	6.23	0.08	8.50	0.71
Unicellular green algae	55.27	30.32	77.78	5.81	1.96	6.74	0.65	0.69	0.82
Multicellular green algae	54.96	54.39	56.11	4.18	6.63	3.53	0.45	4.45	0.30
Red algae	0.00	63.01	43.33	1.91	3.99	1.32	0.00	2.90	0.10
Xanthophyceae	0.00	27.19	31.37	0.00	1.24	0.00	0.12	0.39	0.00
Euglenoids	18.21	41.92	0.00	1.23	2.18	0.06	0.00	1.11	0.00
Plant parts	58.17	70.43	90.00	6.13	8.01	5.98	0.70	6.72	0.82
Insect part	0.00	0.00	50.56	0.00	1.99	0.00	0.00	0.00	0.15
Zooplankton	0.00	41.11	0.00	0.00	1.36	0.00	0.00	0.00	0.09

Note. FO% = percentage frequency of occurrence, VO% = percentage volume, IP% = Percentage index of preponderance, PD = *P. disjunctivus*, PP = *P. pardalis*, OR = *Oreochromis* sp.

Monthly Stomach Contents

The feeding habits of the three invasive species over the sampling months indicated that detritus is the primary food source for all organisms (Table 7). *Pterygoplichthys disjunctivus* exhibits a debris predilection and a minimal inclination towards euglenoids. *Pterygoplichthys pardalis* mostly ingest mineral particles and shows minimal attraction towards Xanthophyceae. *Oreochromis* sp. exhibits a preference for debris; however, there is a transition to diatoms in March and August, and there is a minimal intake of unicellular algae in May.

Table 7

Most and least important stomach content in invasive fish species by sampling months

Species	Month	The most important food items	FO (%)	VO (%)	IP (%)
<i>P. disjunctivus</i>	March	Detritus	100	48.4	9.2
	May	Detritus	100	61.9	12.4
	August	Detritus	100	47.4	11.1
<i>P. pardalis</i>	March	Mineral particles	100	32.8	37.9
	May	Mineral particles	100	27.6	32.6
	August	Mineral particles	100	29.1	33.9
<i>Oreochromis</i> sp.	March	Detritus	100	52.6	7.5
	May	Detritus	100	57.8	6.7
	August	Detritus	100	80.2	17.1
Species	Month	Least important food items	FO (%)	VO (%)	IP (%)
<i>P. disjunctivus</i>	March	Euglenoids	31.1	1.1	0.1
	May	Euglenoids	13	0.4	0
	August	Euglenoids	6.6	0.3	0
<i>P. pardalis</i>	March	Xanthophyceae	28	1.1	0.4
	May	Xanthophyceae	25	1.5	0.5
	August	Xanthophyceae	28.6	1.1	0.4
<i>Oreochromis</i> sp.	March	Diatoms	40	1.7	0.1
	May	Unicellular Algae	0.9	0.5	0.2
	August	Diatoms	0.9	0.2	0.2

Note. FO% = percentage frequency of occurrence, VO% = percentage volume, IP% = Percentage index of preponderance

DISCUSSION

This study assessed some aspects of the biology of invasive fish species in the Langat River tributary, Selangor, Malaysia, based on growth, reproduction, and feeding habits over six months. Selangor, Malaysia, experiences considerable climatic variability throughout the year, which allowed the possibility of documenting aspects of fish biology during different seasons within the sampling duration.

Water Quality Assessment

Most physico-chemical parameters observed in this study were within the recommended ranges for the survival of tropical freshwater fish (Towers, 2015). However, it is worth noting that some parameters exhibited a high standard deviation, indicating the presence of readings that may not be optimal for fish. However, invasive fish species are known for their hardiness and may thrive in suboptimal water quality conditions.

Length-weight Relationship and Condition Factor

Although *P. pardalis* had the highest overall b value in this study, all three species exhibited negative allometry. *Oreochromis* sp., however, exhibited a positive allometry in May. More so, compared to *P. disjunctivus* and *P. pardalis*, *Oreochromis* sp., which had the highest mean CF, exhibited better well-being. It may translate to the fact that *Oreochromis* sp., despite a drop in some water quality parameters, could flourish, underscoring the significantly higher CF values for this species compared to its invasive counterparts. This competitive advantage could contribute to the outcompeting of the native species by *Oreochromis* sp. (Beatty et al., 2022; Saba et al., 2021). The invasive species' ability to flourish under suboptimal water quality conditions, coupled with their higher CF, may give them an upper hand in resource utilization and potentially lead to the displacement or decline in the diversity and abundance of native species.

Sex Ratio, GSI and Fecundity

The sex ratio in the three invasive species is not influenced by any factor that would lead to a non-random distribution of males and females. More so, for all three species, the female sex had higher mean GSI values compared to the males, indicating active reproduction. The significantly higher GSI values of *P. disjunctivus* and *P. pardalis* than *Oreochromis* sp. suggest better reproductive capacity. It is also indicated in the fecundity values. The highest GSI values for the female of each of the sailfin catfishes were recorded in August, while that of female *Oreochromis* sp. was in March. The highest fecundity for each of the three species was recorded in May, which coincides with the southwest monsoonal season (Amirudin et al., 2022).

The differences in LWR, CF, and reproductive biology among the invasive fish species in this Langat River tributary suggest that the sailfin catfishes have different life history strategies compared to tilapia, which may impact the native ecosystem in different ways. For example, species with a higher growth rate and CF may have a competitive advantage over native species for resources, while species with active reproduction may have a greater potential for population growth and expansion (Hudina et al., 2015; Paula et al., 2014).

Food and Feeding Habits

Detritus, mineral particles, and diatoms were the most important contents found in the stomachs of sailfin catfishes. Detritus is a significant carbon source in the global carbon cycle and serves as a food supply for detritivores, which are prominent elements of almost all ecosystems. The high percentage of mineral particles (mud and sand) in this species may be explained by a suction-type ventral mouth adapted to erode food from a rough surface, such as sand and mud at the base of rivers and lakes (Samat et al., 2016). This finding aligns with Iskandar (2021), who found a higher proportion of detritus and mineral particles in the stomach of *P. pardalis* collected from the Pusu River, Selangor.

Although detritus is difficult to digest for some fishes, *P. disjunctivus* and *P. pardalis* have well-developed gizzard-shaped pyloric stomachs, which helps them to digest the detritus (Samat et al., 2016). Besides, the preference for diatom (Bacillariophyta) as the essential natural diet of *P. pardalis* indicates that it is abundant in this area. In addition, it is an epilithic kind of microalgae, thus making it ideal for *P. pardalis*. Morphologically, *P. disjunctivus* and *P. pardalis* have ventrally oriented triangular mouth that supports their feeding habits (Elfidasari et al., 2020). Therefore, evidence suggests that *P. disjunctivus* and *P. pardalis* might be categorized as herbivores and detritivores. It agrees with the findings of Wickramaratne (2021) for the Victoria and Kalawewa reservoirs in Sri Lanka and Stolbunov et al. (2021) in Vietnam, detritus was the most important food found in the stomachs of loricariid fishes such as *P. disjunctivus* and *P. pardalis*.

Similarly, the most important food of *Oreochromis* sp. was detritus, coinciding with the finding of Shalloof and Khalifa (2009), who found a high proportion of detritus in the diet of *Oreochromis* sp. from Zabaal Lakes, Egypt. The findings of this study are also supported by Iskandar (2020), who found a high amount of detritus (48.99%) in the gut of *O. niloticus* from Pusu River, Selangor. Contrarily, Saba et al. (2021) found that diatoms were the most commonly occurring food item in the diet of *Oreochromis* sp. From the Gombak River, Selangor by occurrence, volume, and preponderance, and from the Klang River, diatoms and detritus were the most significant food items by volume. In the Langat River, detritus was the most important food item by volume and preponderance, followed by worms, suggesting that *Oreochromis* sp. from various Malaysian rivers have a diverse diet, with detritus and diatoms being the most essential components.

The high proportion of mineral particles indicates that *Oreochromis* sp. are bottom grazers, which agrees with Oso et al. (2006), while an abundance of detritus indicates their omnivorous nature (Shalloof et al., 2020). Also, the diet composition of fish species may be influenced by the abundance of specific food categories in the water body, making the fish explore what is available (Whitfield et al., 2022). According to Idowu et al. (2019), cichlids may adapt to numerous tropical functions, such as having a detritivorous, herbivorous, and planktivorous diet, and they could act as predators.

CONCLUSION

This study provides valuable information on the LWR, CF, reproductive biology, and food preferences of invasive fish species collected from a stream that flows into the Langat River in Selangor, Malaysia. During sampling for alien fish species, some samples of two native fish species, the blunt-snout barb *Mystacoleucus obtusirostris* and marble goby *Oxyeleotris marmorata*, were encountered. In this study, tilapia *Oreochromis* sp. recorded a better condition and well-being compared to the sailfin catfishes (*P. disjunctivus* and *P. pardalis*), which are likely to contribute more to the negative impact on native fish species through their prolific reproductive capacity. The results highlight the importance of understanding the life history traits of invasive fish species for their management and control and serve as a preliminary investigation of the potential of these species to impact the ecosystem of the Langat River. More so, the information gathered in this study serves as a baseline for further research and conservation efforts. It can guide informed decisions in managing invasive species by controlling their invasion of local rivers and preserving native fish populations.

ACKNOWLEDGEMENTS

The authors appreciate Malaysia's Ministry of Higher Education for providing financial support for this study under the Fundamental Research Grant Scheme (FRGS/1/2018/STG03/UPM/02/11) and the anonymous reviewers for their contributions to improving this article.

REFERENCES

- Ahmad, A. K., Nur-Hazwani, M. N. R., Omar, S. A. S., Aweng, E. R., & Taweel, A. (2020). Preliminary study on invasive fish species diffusion in selected Malaysian freshwater ecosystems. *Pakistan Journal of Biological Sciences*, 23(11), 1374-1379. <http://hdl.handle.net/123456789/1004>
- Amirudin, A. A., Salimun, E., Zuhairi, M., Tangang, F., Juneng, L., Mohd, M. S. F., & Chung, J. X. (2022). The importance of cumulus parameterization and resolution in simulating rainfall over peninsular Malaysia. *Atmosphere*, 13(10), Article 1557. <https://doi.org/10.3390/atmos13101557>
- Aqmal-Naser, M., Ali, N., Azmi, N., Fahmi-Ahmad, M., Rizal, S., & Ahmad, A. (2023). Freshwater fishes (Actinopterygii) of Kenyir Reservoir, Peninsular Malaysia: Updated checklist, taxonomic concerns and alien species. *Biodiversity Data Journal*, 11, Article e100337. <https://doi.org/10.3897/BDJ.11.e100337>
- Arndt, E., Marchetti, M. P., & Schembri, P. J. (2018). Ecological impact of alien marine fishes: Insights from freshwater systems based on a comparative review. *Hydrobiologia*, 817, 457-474. <https://doi.org/10.1007/s10750-018-3511-5>
- Beatty, S. J., Lear, K. O., Allen, M. G., Lymbery, A. J., Tweedley, J. R., & Morgan, D. L. (2022). What factors influence fin-nipping damage by the invasive *Gambusia holbrooki* (Poeciliidae) on native fishes in riverine systems? *Freshwater Biology*, 67(2), 325-337. <https://doi.org/10.1111/fwb.13843>

- Bezerra, L. A. V., Freitas, M. O., Daga, V. S., Occhi, T. V. T., Faria, L., Costa, A. P. L., Padial, A. A., Prodocimo, V., & Vitule, J. R. S. (2019). A network meta-analysis of threats to South American fish biodiversity. *Fish and Fisheries*, 20(4), 620-639. <https://doi.org/10.1111/faf.12365>
- Brewer, S. K., Rabeni, C. F., & Papoulias, D. M. (2008). Comparing histology and gonadosomatic index for determining spawning condition of small-bodied riverine fishes. *Ecology of Freshwater Fish*, 17(1), 54-58. <https://doi.org/10.1111/j.1600-0633.2007.00256.x>
- Camacho-Cervantes, M., Keller, R. P., & Vilà, M. (2023). Could non-native species boost their chances of invasion success by socializing with natives? *Philosophical Transactions of the Royal Society B*, 378(1878), Article 20220106. <https://doi.org/10.1098/rstb.2022.0106>
- Elfidasari, D., Wijayanti, F., & Sholihah, A. (2020). Trophic level and position of *Pterygoplichthys pardalis* in Ciliwung River (Jakarta, Indonesia) ecosystem based on the gut content analysis. *Biodiversitas*, 21(6), 2862-2870. <https://doi.org/10.13057/biodiv/d210665>
- Fakoya, K. A., Anetekhai, M. A., & Saba, A. O. (2019). Length-weight relationship and relative condition factor of Gorean snapper, *Lutjanus goreensis* (Valenciennes, 1830) in the coastal zone of Lagos, south-west Nigeria. *Zoologist (The)*, 17, 20-25. <https://doi.org/10.4314/tzool.v17i1.4>
- Hamid, M. A., Sahb, A. S. R. M., Nor, S. A. M., & Mansor, M. (2022). The distribution of invasive tilapia throughout a tropical man-made lake with special reference to Temengor Reservoir, Malaysia. *Indonesian Journal of Limnology*, 3(1), 47-57. <https://doi.org/10.51264/inajl.v3i1.26>
- Havel, J. E., Kovalenko, K. E., Thomaz, S. M., Amalfitano, S., & Kats, L. B. (2015). Aquatic invasive species: Challenges for the future. *Hydrobiologia*, 750, 147-170. <https://doi.org/10.1007/s10750-014-2166-0>
- Hudina, S., Žganec, K., & Hock, K. (2015). Differences in aggressive behaviour along the expanding range of an invasive crayfish: An important component of invasion dynamics. *Biological Invasions*, 17, 3101-3112. <https://doi.org/10.1007/s10530-015-0936-x>
- Hyslop, E. J. (1980). Stomach contents analysis - A review of methods and their application. *Journal of Fish Biology*, 17(4), 411-429. <https://doi.org/10.1111/j.1095-8649.1980.tb02775.x>
- Idowu, A. A., Ipadeola, A., Nwekoyo, V. E., & Popoola, O. C. (2019). Food and feeding habit of *Sarotherodon galilaeus* in Opeji River of Ogun State Nigeria. *Nigerian Journal of Agriculture, Food and Environment*, 15(2), 104-110.
- Iskandar, Z. R. (2020). *Community structures, well being, and gut contents of Alien Fishes in Pusu River, Gombak, Selangor* [Unpublished Bachelor Thesis]. Universiti Putra Malaysia.
- Khaleel, A. G., Nasir, S. A., Ismail, N., & Ahmad-Syazni, K. (2020). Origin of invasive fish species, peacock bass *Cichla* species in Lake Telabak Malaysia revealed by mitochondrial DNA barcoding. *Egyptian Journal of Aquatic Biology and Fisheries*, 24(3), 311-322. <https://dx.doi.org/10.21608/ejabf.2020.92251>
- Kiat, C. H., & Rahim, K. A. A. (2023). Risk screening of introduced African Catfish (*Clarias gariepinus*) (Burchell, 1822) in Sarawak using the fish invasiveness screening kit (FISK v2). *Borneo Journal of Resource Science and Technology*, 13(2), 151-160. <https://doi.org/10.33736/bjrst.5705.2023>

- Mozsár, A., Boros, G., Sály, P., Antal, L., & Nagy, S. A. (2015). Relationship between Fulton's condition factor and proximate body composition in three freshwater fish species. *Journal of Applied Ichthyology*, *31*(2), 315-320. <https://doi.org/10.1111/jai.12658>
- Nagelkerke, L. A., Onselen, E. V., Kessel, N. V., & Leuven, R. S. (2018). Functional feeding traits as predictors of invasive success of alien freshwater fish species using a food-fish model. *PLoS One*, *13*(6), Article e0197636. <https://doi.org/10.1371/journal.pone.0197636>
- Oso, J. A., Ayodele, I. A., & Fagbuaoro, O. (2006). Food and feeding habits of *Oreochromis niloticus* (L.) and *Sarotherodon galilaeus* (L.) in a tropical reservoir. *World Journal of Zoology*, *1*(2), 118-121. [http://idosi.org/wjz/wjz1\(2\)2006/8.pdf](http://idosi.org/wjz/wjz1(2)2006/8.pdf)
- Paula, A. F. D., Pires, D. D. O., & Creed, J. C. (2014). Reproductive strategies of two invasive sun corals (*Tubastraea* spp.) in the southwestern Atlantic. *Journal of the Marine Biological Association of the United Kingdom*, *94*(3), 481-492. <https://doi.org/10.1017/S0025315413001446>
- Piria, M., Simonović, P., Kalogianni, E., Vardakas, L., Koutsikos, N., Zanella, D., Ristovska, M., Apostolou, A., Adrović, A., Mrdak, D., Tarkan, A. S., Milošević, D., Zanella, L. N., Bakiu, R., Ekmeççi, F. G., Povž, M., Korro, K., Nikolić, V., Škrijelj, R., ... & Joy, M. K. (2018). Alien freshwater fish species in the Balkans - Vectors and pathways of introduction. *Fish and Fisheries*, *19*(1), 138-169. <https://doi.org/10.1111/FAF.12242>
- Rahim, K. A. A., Esa, Y., & Arshad, A. (2013). The influence of alien fish species on native fish community structure in Malaysian waters. *Kuroshio Science*, *7*(1), 81-93.
- Rahman, M. M., & Samat, A. F. (2021). Reproductive cycle, sexual maturity and fecundity of *Nemipterus furcosus* (Valenciennes, 1830). *Aquaculture and Fisheries*, *6*(4), 424-431. <https://doi.org/10.1016/j.aaf.2020.07.006>
- Saba, A. O., Ismail, A., Zulkifli, S. Z., Ghani, I. F. A., Halim, M. R. A., Ibrahim, M. A., Mukhtar, A., Aziz, A. A., Wahid, N. A. A., & Amal, M. N. A. (2021). Invasion risk and potential impact of alien freshwater fishes on native counterparts in Klang Valley, Malaysia. *Animals*, *11*(11), Article 3152. <https://doi.org/10.3390/ani11113152>
- Saba, A. O., Ismail, A., Zulkifli, S. Z., Shohaimi, S., Jamil, N. R., Nawi, N. M., Ghani, I. F. A., Halim, M. R. A., & Amal, M. N. A. (2020a). Checklists, production trends, and potential ecological and socioeconomic impacts of non-native freshwater fishes in Malaysia: A review. *Aquatic Invasions*, *15*(4), 646-670. <https://doi.org/10.3391/ai.2020.15.4.07>
- Saba, A. O., Ismail, A., Zulkifli, S. Z., Halim, M. R. A., Wahid, N. A. A., & Amal, M. N. A. (2020b). Species composition and invasion risks of alien ornamental freshwater fishes from pet stores in Klang Valley, Malaysia. *Scientific Reports*, *10*(1), Article 17205. <https://doi.org/10.1038/s41598-020-74168-9>
- Saba, A. O., Rasli, N. F., Ismail, A., Zulkifli, S. Z., Ghani, I. F. A., Muhammad-Rasul, A. H., & Amal, M. N. A. (2020c). A report on introduced Amazon sailfin catfish, *Pterygoplichthys pardalis* in Gombak Basin, Selangor, with notes on two body patterns of the species. *Pertanika Journal of Tropical Agricultural Science*, *43*(4), 693-703. <https://doi.org/10.47836/pjtas.43.4.19>
- Samat, A., Yusoff, F. M., Arshad, A., Ghaffar, M. A., Nor, S. M., Magalhaes, A. L. B., & Das, S. K. (2016). Reproductive biology of the introduced sailfin catfish *Pterygoplichthys pardalis* (Pisces: Loricariidae) in Peninsular Malaysia. *Indian Journal of Fisheries*, *63*(1), 35-41.

- Santi, E. P., Rahardjo, M. F., & Sulistiono, S. (2017). Diet of scalloped perchlet, *Ambassis nalua* (Hamilton, 1822) in Pabean Bay, West Java. *Jurnal Iktiologi Indonesia*, 17(1), 45-53. <https://doi.org/10.32491/jii.v17i1.303>
- Shalloof, K. A. S., & Khalifa, N. (2009). Stomach contents and feeding habits of *Oreochromis niloticus* (L.) from Abu-Zabal lakes, Egypt. *World Applied Sciences Journal*, 6(1), 1-5.
- Shalloof, K. A. S., Alaa, M., & Aly, W. (2020). Feeding habits and trophic levels of cichlid species in tropical reservoir, Lake Nasser, Egypt. *The Egyptian Journal of Aquatic Research*, 46(2), 159-165. <https://doi.org/10.1016/j.ejar.2020.04.001>
- Silveira, E. L. D., Semmar, N., Cartes, J. E., Tuset, V. M., Lombarte, A., Ballester, E. L. C., & Vaz-dos-Santos, A. M. (2020). Methods for trophic ecology assessment in fishes: A critical review of stomach analyses. *Reviews in Fisheries Science & Aquaculture*, 28(1), 71-106. <https://doi.org/10.1080/23308249.2019.1678013>
- Šimková, A., Řehulková, E., Rasoloariniaina, J. R., Jorissen, M. W., Scholz, T., Faltýnková, A., Mašová, Š., & Vanhove, M. P. (2019). Transmission of parasites from introduced tilapias: A new threat to endemic Malagasy ichthyofauna. *Biological Invasions*, 21, 803-819. <https://doi.org/10.1007/s10530-018-1859-0>
- Stolbunov, I. A., Gusakov, V. A., Dien, T. D., & Thanh, N. T. H. (2021). Food spectrum, trophic and length-weight characteristics of nonindigenous suckermouth armored catfishes *Pterygoplichthys spp.* (Loricariidae) in Vietnam. *Inland Water Biology*, 14, 597-605. <https://doi.org/10.1134/S1995082921050163>
- Towers, L. (2015, June 2). *Water quality: A priority for successful aquaculture*. The Fish Site. <https://thefishsite.com/articles/water-quality-a-priority-for-successful-aquaculture>
- Tran, H. D., Nguyen, H. H., & Ha, L. M. (2021). Length–weight relationship and condition factor of the mudskipper (*Periophthalmus modestus*) in the Red River Delta. *Regional Studies in Marine Science*, 46, Article 101903. <https://doi.org/10.1016/j.rsma.2021.101903>
- Vilizzi, L., Copp, G. H., Hill, J. E., Adamovich, B., Aislabie, L., Akin, D., Al-Faisal, A., J., Almeida, D., Amal, M. N. A., Bakiu, R., Bellati, A., Bernier, R., Bies, J. M., Bilge, G., Branco, P., Thuyet, B., Canning-clode, J., Cardoso Ramos, H. A., Costellanos-Gallindo, G. A., ... & Semenchenko, V. (2021). A global-scale screening of non-native aquatic organisms to identify potentially invasive species under current and future climate conditions. *Science of the Total Environment*, 788, Article 147868. <https://doi.org/10.1016/j.scitotenv.2021.147868>
- Vythalingam, L. M., Raghavan, R., Hossain, M., & Bhassu, S. (2022). Predicting aquatic invasions in a megadiverse region: Maximum-entropy-based modelling of six alien fish species in Malaysia. *Aquatic Conservation: Marine and Freshwater Ecosystems*, 32(1), 157-170. <https://doi.org/10.1002/aqc.3729>
- Wang, J., Chen, L., Tang, W., Heino, J., & Jiang, X. (2021). Effects of dam construction and fish invasion on the species, functional and phylogenetic diversity of fish assemblages in the Yellow River Basin. *Journal of Environmental Management*, 293, Article 112863. <https://doi.org/10.1016/j.jenvman.2021.112863>
- Whitfield, A. K., Able, K. W., Blaber, S. J., Elliott, M., Franco, A., Harrison, T. D., & Houde, E. D. (2022). Feeding ecology and trophic dynamics. In A. K. Whitfield, K. W. Able, S. J. M. Blaber, M. Elliott (Eds.), *Fish and fisheries in estuaries: A global perspective (pp.255-331)*. Wiley. <https://onlinelibrary.wiley.com/doi/abs/10.1002/9781119705345.ch5>

Abdulwakil Olawale Saba, Muhammad Shakir Zufayri Mohd Arshad, Muhammad Afifuddin Abdul Razak, Amirah Mustafa Kamal, Muhammad Rasul Abdullah Halim, Intan Faraha A Ghani, Mohd Lokman Ilham-Norhakim and Mohammad Noor Azmai Amal

Wickramaratne, I. U. (2021). Food habits of *Pterygoplichthys disjunctivus* (Vermiculated sailfin catfish) and coexisting fish species in Victoria and Kalawewa reservoirs, Sri Lanka. *Journal of Agriculture and Value Addition*, 4(2), 57-75. <https://doi.org/10.4038/java.v4i2.28>

Xiong, W., Guo, C., Gozlan, R. E., & Liu, J. (2023). Tilapia introduction in China: Economic boom in aquaculture versus ecological threats to ecosystems. *Reviews in Aquaculture*, 15(1), 179-197. <https://doi.org/10.1111/raq.12710>

Zakaria-Ismail, M., Fatimah, A., & Khaironizam, M. Z. (2019). *Fishes of the freshwater ecosystems of Peninsular Malaysia*. Lambert Academic Publishing.

Zar, J. H. (1984). Simple linear regression. In *Biostatistical Analysis* (pp. 324-359). Prentice Hall.

**REFEREES FOR THE PERTANIKA
JOURNAL OF SCIENCE & TECHNOLOGY**

Vol. 32 (5) Aug. 2024

The Editorial Board of the Pertanika Journal of Science and Technology wishes to thank the following:

Abdullah Hisam Omar
(UTM, Malaysia)

Guangyu Li
(ZUFE, China)

Abdulrahman S. M. Alqadami
(UQ, Australia)

Hai-Bo Zhao
(Sichuan University, China)

Adel A. Al-Azzawi
(Al-Nahrain University, Iraq)

Haidi Ibrahim
(USM, Malaysia)

Ahmad Sufian Abdullah
(UiTM, Malaysia)

Hamid Mortezapour
(University of Kerman, Iran)

Amirreza Talaiekhosani
(JIT, Iran)

Hamzeh Ghorbani
(Young Researchers and Elite Club, Iran)

Anne Juengert
(University of Stuttgart, Germany)

Hareef Ahmed Keerio
(Hanyang University, Korea)

Arien Heryansyah
(UTM, Malaysia)

Hassan Etesami
(University of Tehran, Iran)

Aweng Eh Rak
(UMK, Malaysia)

Hazleen Anuar
(IIUM, Malaysia)

Aytuğ Onan
(IKCU, Turkey)

Intan Sorfina Zainal Abidin
(USM, Malaysia)

Azura Che Soh
(UPM, Malaysia)

Jafar Ahmad Abed Alzubi
(BAU, Jordan)

Dayang Azra Awang Mat
(UNIMAS, Malaysia)

Kannan Thirumulu Ponnuraj
(USM, Malaysia)

Divya Chaturvedi
(SRMAP, India)

Khairun Nisa Kamarudin
(UiTM, Malaysia)

Edson Luis Maistro
(UNESP, Brazil)

Kurniawan Yuniarto
(Mataram University, Indonesia)

Elham Taghavi
(UMT, Malaysia)

Lam Man Kee
(UTP, Malaysia)

Erzam Marlisah
(UPM, Malaysia)

Mo Kim Hung
(UM, Malaysia)

Faieza Abdul Aziz
(UPM, Malaysia)

Mohammad Nishat Akhtar
(USM, Malaysia)

Goh Guo Liang
(NTU, Singapore)

Mohd Hanafi Idris
(UMT, Malaysia)

Mohd Salleh Rofiee
(UiTM, Malaysia)

Mohd Shawal Jadin
(UMPSA, Malaysia)

Mourad Abdelkrim
(UKMO, Algeria)

Muhammad Norhelmi Ahmad
(i-CATS University, Malaysia)

Mukhtiar Ali Soomro
(HKUST, Hong Kong)

Nadras Othman
(USM, Malaysia)

Nidal Al Said
(Ajman University, UAE)

Norharyati Harum
(UTeM, Malaysia)

Norizah Kamarudin
(UPM, Malaysia)

Nur Farhayu Ariffin
(UMPSA, Malaysia)

Nur Hidayah Zainan
(UTM, Malaysia)

Nurul Aini Mohd Ahyan
(UTM, Malaysia)

Rabia Musheer Aziz
(VIT Bhopal University, India)

Rajesh Devaraj
(NVIDIA Corp., India)

Rajkishor Kumar
(VIT, India)

Roslina Ahmad
(UM, Malaysia)

Shumpei Iehata
(UMT, Malaysia)

Sizo Ncube
(NUST, Zimbabwe)

Talha Burak Alakus
(Kirkkareli University, Turkey)

Tian Gui Yun
(UESTC, China)

Witdarko Yus
(Musamus University, Indonesia)

BAU – Al-Balqa' Applied University
HKUST – Hong Kong University of Science and Technology
IIUM – International Islamic University Malaysia
IKCU – Izmir Katip Celebi University
JIT – Jami Institute of Technology
NTU – Nanyang Technological University
NUST – National University of Sciences & Technology
SRMAP – SRM University Andhra Pradesh
UESTC – University of Electronic Science and Technology of China
UiTM – Universiti Teknologi MARA
UKMO – University of Kasdi Merbah Ouargla
UM – Universiti Malaya
UMK – Universiti Malaysia Kelantan

UMPSA – Universiti Malaysia Pahang Al-Sultan Abdullah
UMT – Universiti Malaysia Terengganu
UNESP – São Paulo State University
UNIMAS – Universiti Malaysia Sarawak
UPM – Universiti Putra Malaysia
UQ – The University of Queensland
USM – Universiti Sains Malaysia
UTeM – Universiti Teknikal Malaysia Melaka
UTM – Universiti Teknologi Malaysia
UTP – Universiti Teknologi Petronas
VIT – Vellore Institute of Technology
ZUFE – Zhejiang University of Finance & Economics

While every effort has been made to include a complete list of referees for the period stated above, however if any name(s) have been omitted unintentionally or spelt incorrectly, please notify the Chief Executive Editor, *Pertanika* Journals at executive_editor.pertanika@upm.edu.my

Any inclusion or exclusion of name(s) on this page does not commit the *Pertanika* Editorial Office, nor the UPM Press or the university to provide any liability for whatsoever reason.

Prevalence of <i>Vibrio parahaemolyticus</i> , <i>Vibrio cholerae</i> , and <i>Vibrio alginolyticus</i> in a White-leg Shrimp (<i>Litopenaeus vannamei</i>) Farm in Sarawak <i>Dalene Lesen, Elexson Nillian, Dayang Najwa Awang Baki and Tunung Robin</i>	2233
Modeling Respiration Rate of Bell Pepper (<i>Capsicum anuum</i> L.) Under Hypobaric Storage Through Dimensional Analysis <i>Dewi Maya Maharani, Nursigit Bintoro, Joko Nugroho Wahyu Karyadi and Arifin Dwi Saputro</i>	2259
A Reliable Multimetrix Straggling Task Detection <i>Lukiman Saheed Ajibade, Kamalrulnizam Abu Bakar, Muhammed Nura Yusuf and Babangida Isyaku</i>	2281
Comparative Analysis of Contaminant Levels in Leachate and Soil from Young and Old Landfills <i>Amir Detho, Aeslina Abdul Kadir and Muhammad Aizat Azhar</i>	2299
Physical and Mechanical Properties of Palm Frond-based Fiberboard Composite <i>Moraida Hasanah, Tengku Jukdin Saktisahdan, Susilawati, Frannoto, Adjie Padriansyah and Irfan Hafizh</i>	2313
Smoothing RRT Path for Mobile Robot Navigation Using Bio-inspired Optimization Method <i>Izzati Saleh, Nuradlin Borhan and Wan Rahiman</i>	2327
Early Triage Prediction for Outpatient Care Based on Heterogeneous Medical Data Utilizing Machine Learning <i>Omar Sadeq Salman, Nurul Mu'azzah Abdul Latiff, Sharifah Hafizah Syed Arifin and Omar Hussein Salman</i>	2343
Finite Element Analysis of a Portable Bamboo Girder Used in Emergency Responses <i>Azrul Affandhi Musthaffa, Norazman Mohamad Nor, Abdulrahman Alhayek, Mohammed Alias Yusof and Mohd Yuhazri Yaakob</i>	2369
Some Aspects of the Biology of Invasive Fish Species from a Langat River Tributary, Selangor, Malaysia <i>Abdulwakil Olawale Saba, Muhammad Shakir Zufayri Mohd Arshad, Muhammad Afifuddin Abdul Razak, Amirah Mustafa Kamal, Muhammad Rasul Abdullah Halim, Intan Faraha A Ghani, Mohd Lokman Ilham-Norhakim and Mohammad Noor Azmai Amal</i>	2385

The Riblet Short-Slot Coupler Using Substrate Integrated Waveguide (SIW) for High-frequency Applications <i>Nurehansafwanah Khalid, Siti Zuraidah Ibrahim, Mohd Nazri A Karim, Wee Fwen Hoon, Aliya Ashraf Dewani, Khuzairi Masrakin and Saidatul Norlyana Azemi</i>	2069
Cytotoxicity Assessment of α Helix Antarctic Yeast Oriented Antifreeze Peptide (Afp1m) on <i>M. dunni</i> (Clone III8C) Cells <i>Muhammad Shuaib Khan, Mohd Basyaruddin Abdul Rahman, Mohd Zuki Abu Bakar, Mohammed Mustapha Noordin, Shakeeb Ullah, Adamu Abdul Abubakar, Saifur Rehman, Aisha Saddiqua and Loqman Mohammad Yusof</i>	2083
Aluminium Hydroxide/Graphene-reinforced Rigid Polyurethane Foam Hybrid Composites <i>Aisha Elhadi Abosnina, Zurina Mohamad, Rohah Abdul Majid and Raji Muhammed Abdulwasii</i>	2095
Inoculations of <i>R. erythropolis</i> and <i>B. subtilis</i> Stimulate Indigenous Bacteria and Improve the Properties of Low-fertilized Agricultural Soils <i>Abd Aziz Amin, Hideki Okuda, Mizuho Kawamura, Nurjannah and Andi Kurniawan</i>	2121
Application of UAV Technology for Vegetation Community Identification in Coastal BRIS Wetland <i>Syazuani Mohd Shariff, Edlic Sathiamurthy, Rohani Shahrudin, Idham Khalil and Mohd Sofiyam Sulaiman</i>	2137
Comparative Analysis of Filtering Techniques for AGV Indoor Localization with Ultra-Wideband Technology <i>Nuradlin Borhan, Izzati Saleh and Wan Rahiman</i>	2151
<i>Review Article</i>	
Exploring Probability of Detection (POD) Analysis in Nondestructive Testing: A Comprehensive Review and Potential Applications in Phased Array Ultrasonic Corrosion Mapping <i>Jan Lean Tai, Mohamed Thariq Hameed Sultan, Farah Syazwani Shahar, Noorfaizal Yidris, Adi Azriff Basri and Ain Umaira Md Shah</i>	2165
<i>Review Article</i>	
Formulation of Lubricating Grease from Waste Oil: A Review <i>Nur Amira Fatimah Bashari, Mohd Aizudin Abd Aziz, Muhammad Auni Hairunnaja and Mohd Azmir Arifin</i>	2193
Microwave Electro-technological Installation for Processing Vegetable-origin Organic Materials and Agricultural Crops <i>Midhat Tukhvatullin and Eduard Khasanov</i>	2213

Pertanika Journal of Science & Technology

Vol. 32 (5) Aug. 2024

Content

Foreword	i
<i>Mohd Sapuan Salit</i>	
<i>Review Article</i>	
A Review on the Development of Microcarriers for Cell Culture Applications	1939
<i>Sia Yiik Swan, Muhammad Auni Hairunnaja, Nurhusna Samsuddin, Syed Mahmood, Mohd Aizudin Abd Aziz and Mohd Azmir Arifin</i>	
Facial Emotion Recognition with Deep Neural Network: A Study of Visual Geometry Group-16 (VGG16) Technique with Data Augmentation for Improved Precision	1963
<i>Sarthak Kapaliya, Debabrata Swain, Ritu Sharma, Kanishka Varyani and Jyoti Thakar</i>	
<i>Review Article</i>	
The Compatibility of Cement Bonded Fibreboard Through Dimensional Stability Analysis: A Review	1979
<i>Nurul Huda Azmi, Nik Mohd Zaini Nik Soh and Hasniza Abu Bakar</i>	
Mesh Optimisation for General 3D Printed Objects with Cusp-Height Triangulation Approach	1997
<i>Qais Ahmed Habash, Noor Ali Sadek, Ahmed Faeq Hussein and Abbas AlZubaidi</i>	
Comparing CNN-based Architectures for Dysgraphia Handwriting Classification Performance	2013
<i>Siti Azura Ramlan, Iza Sazanita Isa, Muhammad Khusairi Osman, Ahmad Puad Ismail and Zainal Hisham Che Soh</i>	
Learning Discriminative Features Using ANN-based Progressive Learning Model for Efficient Big Data Classification	2033
<i>Nandita Bangera and Kayarvizhy</i>	
Bending Effects on Polyvinyl Alcohol Thin Film for Flexible Wearable Antenna Substrate	2055
<i>Amirudin Ibrahim, Ahmad Rashidy Razali, Muzammil Jusoh, Najwa Mohd Faudzi and Aiza Mahyuni Mozi</i>	



Pertanika Editorial Office, Journal Division,
Putra Science Park,
1st Floor, IDEA Tower II,
UPM-MTDC Center,
Universiti Putra Malaysia,
43400 UPM Serdang,
Selangor Darul Ehsan
Malaysia

<http://www.pertanika.upm.edu.my>
Email: executive_editor.pertanika@upm.edu.my
Tel. No.: +603- 9769 1622

PENERBIT
UPM
UNIVERSITI PUTRA MALAYSIA
PRESS

<http://www.penerbit.upm.edu.my>
Email: penerbit@upm.edu.my
Tel. No.: +603- 9769 8851

